Quantitative weather radar and the effects of the vertical reflectivity profile

by

Miguel Angel Rico-Ramirez, B.Eng., M.Eng.

A dissertation submitted to the University of Bristol in accordance with the requirements of the degree of Doctor of Philosophy in the Faculty of Engineering, Department of Civil Engineering.

September 2004

Approximately 67,000 words

CONSULTATION RECORD

University of Bristol

THE LIBRARY

All readers must sign their names in the space below, in confirmation that they understand and agree to observe the above conditions.

NAME (Block capitals)	PERMANENT ADDRESS	SIGNATURE	DATE

Abstract

The variation of the vertical reflectivity profile (VRP) of rain is one of the major problems for quantitative precipitation estimation using weather radars. In particular, during stratiform rainfall a region of enhanced reflectivity associated with echoes from melting snowflakes causes overestimation of precipitation. This work is focused on the study of this region commonly known as the bright band. A new algorithm to detect the boundaries of the bright band from single-polarisation VRP has been developed. This algorithm has enabled the analysis of 1835 hours of vertically pointing X-band radar data and 1354 S-band RHI scans from the Chilbolton radar in order to study the characteristics of the bright band such as intensity, depth, height and variability at both frequencies. In addition, the differential reflectivity and the linear depolarisation ratio in the bright band are also included in the analysis. Using the results obtained, the Membership Functions (MF) of a Fuzzy Logic System (FLS) to classify hydrometeors have been proposed. The FLS receives as input parameters the conventional reflectivity factor, the differential reflectivity, the linear depolarisation ratio and the height of the hydrometeors and retrieves three types of hydrometeors: rain, snow and melting snow. The classification of rain and snow presents a high degree of uncertainty because of the large overlapping regions between the MF of both hydrometeors. The FLS is shown to perform a primary classification of melting snow because the depolarisation characteristics are distinct. By establishing the mean height of melting snow it is possible to modify the MF of the height of the hydrometeors in a more constrained way. A secondary classification is then performed with the new MF providing a much improved classification. The hydrometeor classification is followed by an algorithm to estimate the expected rain reflectivity from bright band contaminated reflectivity data. This correction is based on an idealised VRP typical of stratiform precipitation and obtained from the extensive analysis of the VRP at S-band frequencies.

Keywords: bright band, dual-polarisation radar, fuzzy logic system, hydrometeor classification, radar hydrology, rainfall estimation, vertical reflectivity profile, weather radar.

Esta tesis esta dedicada

a mis padres Fidel Rico González y Ma. Luz Soledad Ramírez Rubalcaba

a mis hermanos Adriana, Moisés y Olivia

a mi sobrina Maria Fernanda

y muy especialmente a Elena.

Acknowledgements

I would like to express my sincere gratitude to my supervisor, Professor Ian David Cluckie, for his invaluable help throughout the research project described in this thesis.

I would also like to thank Dr. Dawei Han, Dr. David Harvey and Dr. Richard Griffith who provide valuable comments. To all the present an past members of the Water and Environmental Management Research Centre (WEMRC), Gustavo Cerda, Efren González, Michael Hammond, Jongsook Park, Ali Reza, Yunqing Xuan, Rebecca Christian, Jun Quin, Gerald Rosenberg and Kathleen Kozyniak, who not only provided help whenever I needed it, but also made more fulfilling my time at Bristol. A big thank you to the secretary to the WEMRC, Marghi Peacock.

I acknowledge the Radio Communications Research Unit at the Rutherford Appleton Laboratory, in particular to John Goddard and Charles Kilburn, for providing the Chilbolton radar data.

I acknowledge all the people who participated and collected the vertically pointing X-band radar data during the experiments HYREX, SALPEX and EU HYDROMET.

I acknowledge the British Atmospheric Data Centre (BADC) for providing some of the radar data sets and EDINA for providing the UK digital elevation model.

This research work has been possible thanks to the National Research Council of Science and Technology (COnsejo NAcional de Ciencia Y Tecnología-CONACYT), who provided me with the funding under the scholarship 138598.

Author's declaration

I declare that the work in this dissertation was carried out in accordance with the Regulations of the University of Bristol. The work is original except where indicated by special reference in the text and no part of the dissertation has been submitted for any other degree. Any views expressed in the dissertation are those of the author and in no way represent those of the University of Bristol. The dissertation has not been presented to any other University for examination either in the United Kingdom or overseas.

SIGNED: 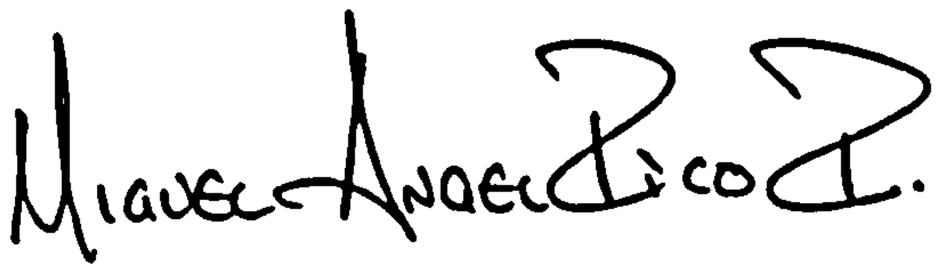 DATE: 15/Nov/2004

Miguel Angel Rico-Ramirez

Table of Contents

List of Figures

List of Tables

Chapter 1

Setting the scene

1.1 Introduction

One of the main advantages of weather radars is that they can scan large areas and take millions of measurements from a single location in real-time (Wilson and Brandes, 1979; Doviak and Zrnić, 1993). A network of rain gauges that can survey the same area with a similar spatial resolution would be practically impossible to maintain. However, weather radars have practical limitations and the estimation of precipitation using these devices is prone to several sources of errors. This is one of the reasons that radar meteorology has been a topic of active research.

This thesis is focused on the study of the bright band, which is a layer of enhanced echo power due to the scattering of microwaves from melting snowflakes. Because the power reflected back to the radar is related to the rainfall intensity, the interception of the radar beam with the melting layer is interpreted as an overestimation of rainfall. In order to improve the estimation of rainfall using weather radars, it is necessary to apply a correction to eliminate the effects of bright band. It is therefore necessary to study its intensity, depth, height and variability in space and time.

Chapter 2 describes firstly the general theory of weather radars and the development of the fundamental radar equations. It also describes the relationship between the backscattering cross section and the reflectivity factor, which is fundamental to the estimation of precipitation. The different measurements obtained with a dual-polarisation radar are also presented. The most important algorithms to estimate precipitation using single- and dual-polarisation measurements are described. The last part explains the main error sources in the estimation of precipitation using weather radars, in particular when the radar beam intercepts the melting layer.

Chapter 3 describes in detail the characteristics of an X-band Vertically Pointing

weather Radar (VPR). The data set obtained with this radar has been used for the development of this thesis. The fluctuations of the echo intensities have been analysed in order to obtain the standard error associated with the measurement of the reflectivity factor when averaging N independent samples. The proposal of using real-time digital filters is developed and explored to reduce the standard error in the reflectivity signal when fast data acquisition is required.

Chapter 4 describes a simple algorithm to detect the bright band boundaries from Vertical Reflectivity Profiles (VRP). This algorithm is based on an axis rotation algorithm to detect the height of the top and bottom of the bright band. However, one of the important steps in the detection process is the digital filtering of the VRP. Therefore, the frequency analysis of the reflectivity signal using the discrete Fourier transform is carried out in order to obtain the cut-off frequency of the digital filter to smooth the VRP. The cut-off frequency in filter design is important because a very narrow pass-band filter will produce excessive smoothing to the VRP, losing the important characteristics of the reflectivity signal such as the intensity, which is very important in this analysis. The cut-off frequency is dependent on the type of precipitation. The bright band detection algorithm has been tested on different events using height-time and range-height indicators types of data.

Chapter 5 presents the analysis of the bright band characteristics at X-band frequencies in different climatological regions: the North West of England, the South West of England, Bristol in England, Marseille in France and the Southern Alps in New Zealand. Around 1835 hr of X-band VPR observations have been analysed. The key parameters are the reflectivities above, within and below the bright band, their heights, the bright band thickness and the seasonal dependency of the height of the bright band.

Chapter 6 presents a similar analysis of the bright band characteristics at S-band frequencies in the South West of England. This analysis is important because it allows the comparison of the characteristics of the bright band at two different wavelengths. In addition, the analysis is extended to the polarimetric radar measurements in the bright band, which will establish the basis of the hydrometeor classification algorithm introduced in Chapter 8.

Chapter 7 presents the analysis of the effect of the spreading of the radar beam from a frequency-domain point of view. As the range increases from the radar, the volume of the radar beam increases and has an important effect on the echo measurements. This impact is simulated using vertical profiles of reflectivity, differential reflectivity and linear depolarisation ratio obtained from hundred of observations at S-band frequencies.

Chapter 8 describes a Fuzzy Logic System (FLS) to classify hydrometeors using data from a dual-polarisation radar. The FLS receives as input parameters the conventional reflectivity factor, the differential reflectivity, the linear depolarisation ratio and the height of the measurement and retrieves three types of hydrometeors: rain, snow and melting snow. The classification process is followed by an algorithm to correct for the increase in reflectivity in the melting layer. This correction is based on an idealised VRP obtained from the analysis of a considerable number of bright bands at S-band frequencies.

Chapter 9 presents the general conclusions from this research work and gives some suggestions and recommendations for future work.

A key aspect of the thesis is that it has been able to completely analyse data collected over a period of over thirteen years at a number of locations in the United Kingdom, Europe and the Southern Hemisphere (New Zealand). Additional data have been collected in a series of new experiments located in Bristol over the years 2000-2004. It is hoped that the results presented provide a seminal input to knowledge of the vertical reflectivity profile of precipitating storms and additionally provide a way forward in the development of correction algorithms and the potential introduction of polarisation diversity radars into the UK. This data is unique and only available to the Water and Environmental Management Research Centre (WEMRC) at the University of Bristol because the basic X-band VPR's were designed and commissioned by the group and the HYREX, SALPEX and HIRE key field programmes were designed and executed by the group since 1991. Future work in this area is likely to consolidate the results contained in this thesis, extend the dual-polarisation algorithms and improve the application potential of quantitative weather radar in Radar Hydrology.

Chapter 2

Radar observations of rainfall

2.1 Introduction

Since the beginning of weather radar research during the World War II, early researchers revealed many of the problems that weather radars face in quantitative precipitation estimation (Atlas and Ulbrich, 1990). Weather radars are subject to many sources of error and in order to obtain an accurate estimation of precipitation, it is necessary to understand each process involved in the estimation of precipitation.

The basic principles of radar meteorology are well described in Battan (1973); Doviak and Zrnić (1993); Collier (1996). This chapter only gives a general description of the theoretical basis of the estimation of precipitation by weather radars. It also covers several error sources affecting weather radar measurements, in particular when the radar beam intercepts melting snowflakes.

2.2 Development of weather radars

Before the World War II, the United States and the United Kingdom were carrying out intense research activity involving the development of radar (Atlas and Ulbrich, 1990). During the war, weather radar echoes were considered as annoyance rather than something of intrinsical interest (Probert-Jones, 1990). The major research work in the field of radar meteorology was carried out in the United Kingdom, where considerable work on radar propagation was carried out at the Telecommunication Research Establishment at Malvern (now QinetiQ) and at the General Electric Research Laboratories with the research work carried out by Ryde (Probert-Jones, 1990). Ryde (1946) who estimated the echo intensity and attenuation by atmospheric hydrometeors at centimetric wavelengths to determine the extent to which radars would be affected by weather. This established the basis of

radar meteorology by the end of the war (Atlas and Ulbrich, 1990; Probert-Jones, 1990). Marshall et al. (1947) were the first to show an excellent correlation between the received echo power from a 10-cm radar and the reflectivity, Z, computed from the drop size distribution of samples obtained from a filter paper on the ground. They stated that *"it may be possible therefore to determine with useful accuracy the intensity of rainfall at a point quite distant (say 100 km) by the radar echo from that point"*. Since then, this work has stimulated many researchers to estimate precipitation using radars.

2.3 Microphysics of precipitation

There are numerous physical processes that shape the evolution of precipitation. These physical processes are influenced and determined by the characteristics of the air mass, the liquid-water content of the cloud, the turbulence involving the vertical motion of the cloud and the time scales of the cloud (Cotton and Anthes, 1989). A cloud can be formed when moist air is brought to saturation through a physical process. Lifting is one of the most important processes, although there are others such as mixing of air parcels with different properties, radiative cooling and in situ pressure reductions (Jameson and Johnson, 1990). Lifting causes the air to expand and cool and when the air reaches saturation, condensation of water takes place.

An important factor for precipitation development is the initialization phase. There are warm, cold and mixed-phase processes. The warm processes involve the liquid and vapour phases. In this process, rain formation can be produced by collision and coalescence of water droplets (Cotton and Anthes, 1989). Mixed-phase processes involve the three water phases, but according to Jameson and Johnson (1990) the existence of supercooled cloud droplets is the distinguishing feature of this type of process. Cold processes may involve the three water phases, but the solid phase is dominant. In this process, there are several mechanisms of growth of ice crystals. The subsequent melting of ice can produce raindrops.

2.3.1 Microphysics of warm processes

The evolution of a cloud is controlled primarily by its liquid-water content, which reflects the cloud-base temperature and depth of the cloud (Jameson and Johnson, 1990). Another property to all clouds is the number of activated droplets or cloud droplet concentration. The cloud-base temperature influences the activation of cloud droplets (Cotton and Anthes, 1989). The cloud droplet concentration at cloud-base is an important factor that determine whether or not a cloud is going to precipitate (Cotton and Anthes, 1989) and

it can be the primary factor that determines the cloud's stability in the absence of large embryonic sources (Jameson and Johnson, 1990). This is because the limitation to precipitation production is the generation of large embryos by stochastic collisions between the activated droplets. For instance, clouds with high droplet concentrations are considered relatively stable (continental) whereas that clouds with low droplet concentrations are considered unstable (maritime) (Jameson and Johnson, 1990). Both, the liquid-water content and the cloud droplet concentration determine the mean droplet size. The United Kingdom being primarily maritime in influence is predominantly at the difficult end of the spectrum.

The precipitation development of warm processes is restricted to condensation and coalescence because it occurs below the 0°C isotherm. Effective coalescence growth not only depends on the availability of large embryos, but also on the liquid water content and mean size of the cloud droplets collected by the growing embryo (Jameson and Johnson, 1990). For instance, if the liquid water content is low, no embryo can grow effectively by coalescence (Jameson and Johnson, 1990). When sufficiently large embryonic precipitation droplets are formed, then turbulence, electric fields and drop charges influence the rates of drop collision and coalescence (Cotton and Anthes, 1989). When the droplets reach a radius of approximately 50 μm they are considered as raindrops. Raindrops grow up to a critical size of approximately 6 mm in diameter and then break up due to hydrodynamic instability (Cotton and Anthes, 1989), although a maximum drop size of 8 mm is physically more representative in the calculation of the reflectivity (See Eq. 2.21). Each fragment produced from the breakup process will act as a new precipitation embryo, which can again grow to breakup size creating more precipitation embryos (Cotton and Anthes, 1989). This process is limited by the height of the 0°C isotherm since this directly controls the maximum time available before raindrops reach the ground.

2.3.2 Microphysics of cold processes

Cold processes dominate winter storms. The parameterisation of the microphysical processes for the ice-phase is complicated because of the variety of shapes and physical processes involved in the formation of ice crystals. Cotton and Anthes (1989) described four growing processes of ice crystals:

Nucleation of ice crystals. There are several mechanisms for the nucleation of ice crystals:

Nucleation by vapour deposition, referring to the transfer of water vapour to a nucleus resulting in the formation of an ice crystal;

Nucleation by condensation, referring to the condensation of water vapour on a nucleus to form an embryonic droplet and then followed by freezing;

Nucleation by immersion freezing, referring to the nucleation of a droplet or raindrop on an ice nucleus immersed within the drop;

Nucleation by contact, referring to the nucleation by contact in a supercooled state of a droplet or raindrop on an ice nucleus.

Growth of ice particles by vapour deposition. The ice crystals can grow by vapour deposition providing that some kind of nucleation took place and if the environment is supersaturated with respect to the ice. The ice crystals then start growing by vapour deposition, reducing the vapour content and driving the environment below water saturation. But because an equilibrium must prevail, evaporation of droplets maintain the vapour pressure difference between ice and water.

Growth of ice particles by riming. When the ice crystals become very large, they become an ideal nucleator. Then supercooled cloud droplets collide and coalesce upon the ice surface, freezing and forming a thin layer called rime. The riming in convective clouds is very high because of the higher liquid water contents (more than 1 g m^{-3}) becoming graupel and hail.

Growth of ice particles by aggregation. Collision and coalescence among ice crystals form large aggregates. These aggregates form snowflakes. However, even when there are collisions between the ice crystals, they do not always come together, but experiments suggest that efficiency of coalescence is higher at warmer temperatures and is dependent on the type of ice crystal. Additionally, the aggregation rate is proportional to the concentration of ice crystals.

One of the most important growth processes is the aggregation of ice crystals, which can produce large snowflakes, which by subsequent melting can produce raindrops. The most interesting feature of snowfall to radar meteorologists is the so called bright band, which is associated with echoes from melting snow (See Section 2.8.1).

2.4 Propagation of electromagnetic waves

Electromagnetic Waves (EW) in free space propagate in straight lines at the speed of light. However, in the atmosphere, the variation of temperature, moisture and pressure produce small changes in the speed of propagation, which lead to potential refraction of the EW. The refractive index of the atmosphere (n) is related to the changes in the atmospheric

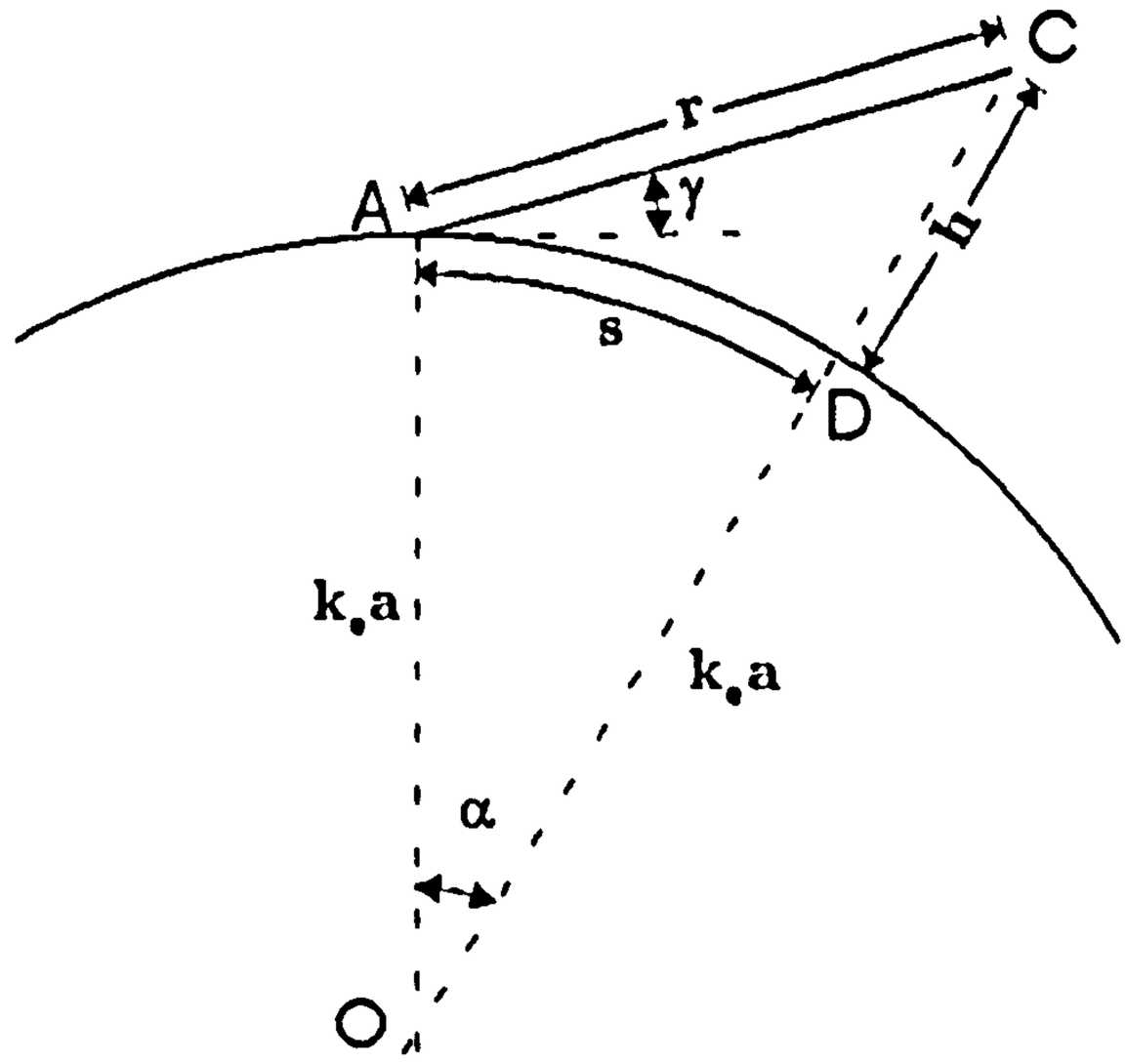

Fig. 2.1: Propagation of an EW in an equivalent Earth radius to account for atmospheric refraction.

conditions. A simple atmospheric model of the Earth considers the temperature and the humidity as horizontally homogeneous, which determines the refractive index as a function of height above the ground. Thus, the path of an electromagnetic wave depends on the variation of the refractive index with height (h). The curvature (C_0) of the path of an EW is approximately $-dn/dh$ under the assumption that the height of the EW is small compared to the earth radius (a), that is, $h \ll a$. So, if n is well approximated by a linear function in the height interval containing the EW, the path of an EW will have constant curvature. The common method of accounting for atmospheric refraction is by replacing the actual earth radius (a) by an equivalent earth radius ($k_e a$) and by replacing the actual atmosphere by an homogeneous atmosphere in which an EW propagates in straight line.

The value of k_e is given by (See Doviak and Zrnić, 1993):

$$k_e = \frac{1}{1 + a dn/dh} \tag{2.1}$$

Researchers have found that the gradient dn/dh is approximately constant with height and equal to $-1/(4a)$, thus the value of k_e is 4/3 resulting in an effective Earth radius of $4a/3$. From this, the path of an EW in the 4/3rds Earth approximation is shown in Fig. 2.1. Applying the law of Cosines to the triangle OAC, it is shown that:

$$(k_e a + h)^2 = (k_e a)^2 + r^2 - 2(k_e a) r cos(90 + \gamma) \tag{2.2}$$

where γ is the elevation angle and r is the range. Thus, its height h is given by:

$$h = [(k_e a)^2 + r^2 + 2 r k_e a sin(\gamma)]^{1/2} - k_e a \tag{2.3}$$

The distance s along the earth curvature of the point $[\gamma, r]$ is given by:

$$s = k_e a \alpha \tag{2.4}$$

Applying the law of Sines to the triangle OAC:

$$\frac{k_e a + h}{sin(90 + \gamma)} = \frac{r}{sin(\alpha)} \tag{2.5}$$

Solving Eq. 2.5 for α and substituting the result into Eq. 2.4, it is shown that:

$$s = k_e a sin^{-1}\left(\frac{r cos\gamma}{k_e a + h}\right) \tag{2.6}$$

Eqs. 2.3 and 2.6 relate the height h above the ground and distance s along the earth surface respectively of an EW with elevation angle γ and range r from the source.

A simplified form of Eq. 2.3 often employed in the literature is given by:

$$h = \frac{3r^2 cos\gamma}{8a} + r sin\gamma \tag{2.7}$$

Eqs. 2.3 and 2.7 are considered adequate in most circumstance for weather radar applications.

2.5 The radar theory

2.5.1 The radar equation

A radar sends a pulse of microwave energy in some specific direction. If a target (*e.g.* precipitation particles) lies along the path of the beam, then a small percentage of the energy is reflected back to the radar. Considering an isotropic radiating transmitter with power P_t located at a single point in space. At a range r, the power per unit area on the virtual sphere surface created by the radiated energy is $P_t/4\pi r^2$. If the transmitter concentrates that energy into a narrow beam through an antenna with gain G, thus a target at a range r with cross-sectional area A_t will intercept an amount of power P_σ given by (Battan, 1973):

$$P_\sigma = \frac{P_t G A_t}{4\pi r^2} \tag{2.8}$$

Assuming that the target does not absorb energy and re-radiates all the power isotropically, then the power intercepted by the radar antenna P_r with a cross section area A_e will be given by:

$$P_r = \frac{P_t G A_t A_e}{(4\pi r^2)^2} \tag{2.9}$$

A_e is related to the gain G and wavelength of the transmitter λ by:

$$A_e = G\lambda^2/4\pi \tag{2.10}$$

Therefore, Eq. 2.9 becomes:

$$P_r = \frac{P_t G^2 \lambda^2 A_t}{(4\pi)^3 r^4} \tag{2.11}$$

In reality, the target does not scatter isotropically and it is convenient to define the backscattering cross section, which is defined as *"the area intercepting that amount of power, which, if scattered isotropically, would return to the receiver an amount of power equal to that actually received"* (Battan, 1973). Thus, for a single scatterer, Eq. 2.11 becomes:

$$P_r = \frac{P_t G^2 \lambda^2 \sigma_i}{(4\pi)^3 r^4} \tag{2.12}$$

Eq. 2.12 applies for any type of target. In the case of raindrops, the radar beam illuminates a large number of scatterers within a volume defined by the beamwidth and pulse length of the radar (illuminated volume). The backscattered power from a volume of randomly distributed scatterers is the sum of the signals scattered by each of the scatterers. Because of the movement of the particles from pulse to pulse, it is necessary to average the power reflected over a large number of independent arrays. Thus, the average power is given by:

$$\bar{P}_r = \frac{P_t G^2 \lambda^2}{(4\pi)^3 r^4} \sum_{i=0}^{n} \sigma_i \tag{2.13}$$

The summation is carried out over the illuminated volume V_m, which is a function of the horizontal and vertical beamwidths (θ_h and θ_v respectively) and the pulse length in seconds (τ) of the radar. Thus, V_m can be approximated to:

$$V_m = \pi\left(r\frac{\theta_h}{2}\right)\left(r\frac{\theta_v}{2}\right)\left(\frac{c\tau}{2}\right) \tag{2.14}$$

where c is the speed of light. By substituting Eq. 2.14 into Eq. 2.13 the following is obtained:

$$\bar{P}_r = \frac{P_t G^2 \lambda^2 \theta_h \theta_v c\tau}{512\pi^2 r^2} \sum_{vol} \sigma_i \tag{2.15}$$

The term $\sum_{vol} \sigma_i$ is called the "radar reflectivity" (η) and represents the summation of σ over a unit volume. Eq. 2.15 needs to be corrected because the transmitted power per unit area is not constant between the half power points. Probert-Jones (1962) assumed that within the main lobe, the power per unit area can be represented by a Gaussian function and also took into account the two-way power density pattern. Thus, the power reflected is finally given by:

$$\bar{P}_r = \frac{P_t G^2 \lambda^2 \theta_h \theta_v c\tau}{512(2 \ln 2)\pi^2 r^2} \sum_{vol} \sigma_i \tag{2.16}$$

The signal intensity from precipitation echoes shows rapid fluctuations, which are caused by the movement, with respect to one another, of the randomly distributed particles within the illuminated volume (Battan, 1973). The backscattered power in a single radar pulse depends on the backscattering cross sections of the scatterers and their relative positions. The power averaging must be done over samples sufficiently separated in time or space to have zero correlation. A period of at least 10 ms is required to get uncorrelated samples (Battan, 1973).

2.5.2 Scattering theory

A plane-polarised wave passing over a spherical drop induces oscillating electric and magnetic dipoles within the drop. Energy is obtained from the incident field, a part of it is absorbed as heat by the drop, and part is re-radiated as a scattered electromagnetic field having the same wavelength as the incident wave (Battan, 1973). Mie (1908) described the scattering theory of a plane wave by a sphere. From Mie theory, it has been shown that the backscattering cross section of a spherical drop is (See Fig. 2.2):

$$\sigma = \frac{\pi a^2}{\alpha^2} \left| \sum_{n=1}^{\infty} (-1)^n (2n+1)(a_n - b_n) \right|^2 \tag{2.17}$$

where a is the drop radius, $\alpha = 2\pi a/\lambda$ and a_n and b_n are the coefficients for the scattering field; a_n are the coefficients from the induced magnetic dipoles, quadrupoles, etc., whereas that b_n are the coefficients from the induced electric dipoles, quadrupoles, etc.; n is the number of the terms in the expansion of the coefficients for the scattering field.

If the radii of the spheres are small compared with the wavelength, that is, $\alpha \ll 1$, the backscattering cross section of a single spherical drop is given by:

$$\sigma_i = \frac{\lambda^2}{\pi} \alpha^6 \left| \frac{m^2 - 1}{m^2 + 2} \right| = \frac{\pi^5}{\lambda^4} |K|^2 D_i^6 \tag{2.18}$$

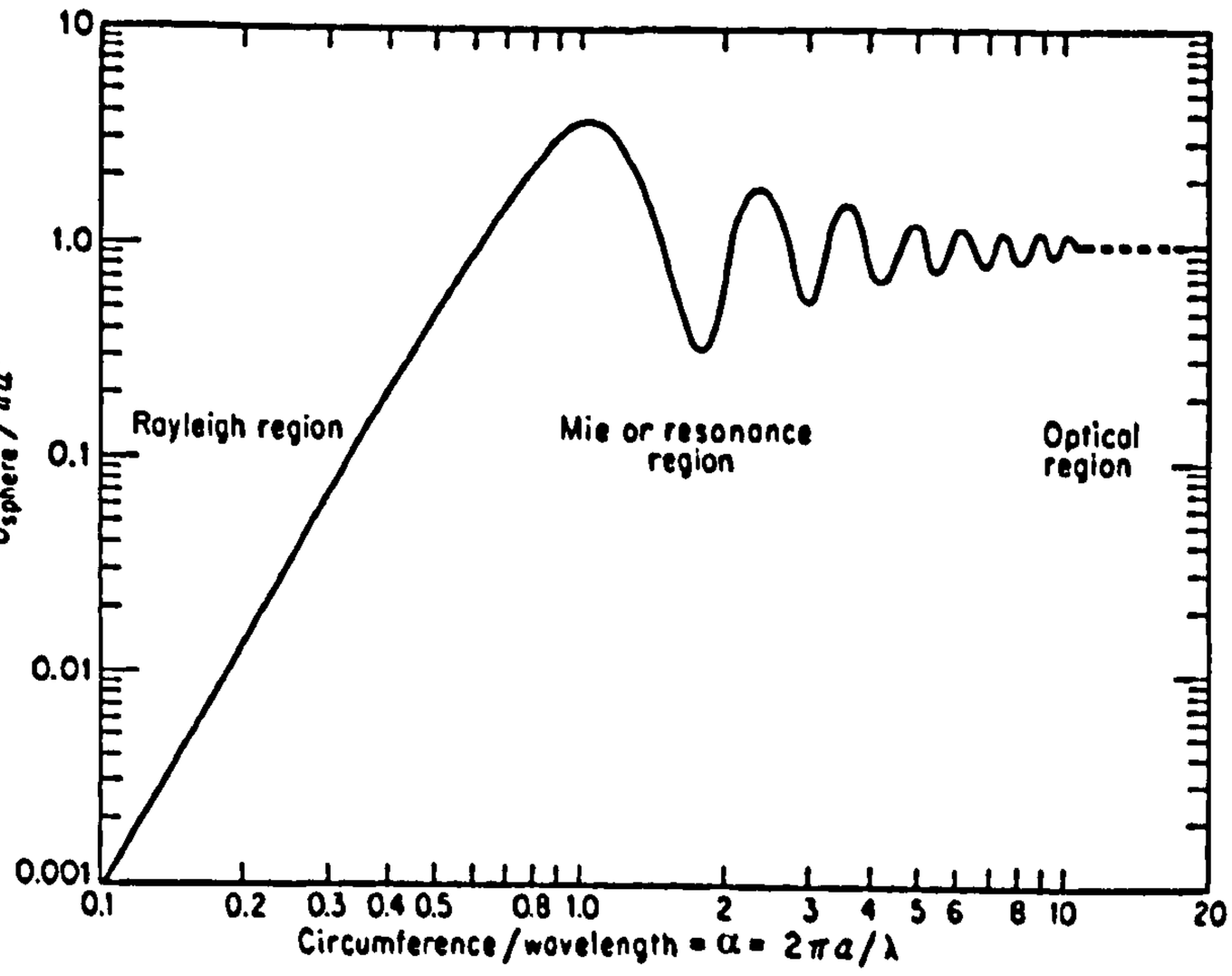

Fig. 2.2: Backscattering cross section of the sphere, where a is the radius and λ is the wavelength (after Skolnik, 1980).

where D_i is the particle diameter and $|K|^2$ is the complex refractive index of the particle. If the scatterers are known to be composed of water $|K|^2$ is 0.93 and 0.20 for ice. Eq. 2.18 is known as Rayleigh approximation of the backscattering cross section (See left side of Fig. 2.2). According to Battan (1973), Eq. 2.18 is valid for $D < 0.07\lambda$, otherwise the Rayleigh value of σ underestimates the true σ. For ice, Ryde (1946) indicated that the Rayleigh approximation holds for $D < 0.16\lambda$. Wexler and Atlas (1963) calculated the $\sum\sigma$ for rainfall rates between 0.01 and 100 mm hr^{-1} and for wavelengths between 3 and 10 cm using Mie and Rayleigh backscattering, concluding that the Rayleigh approximation is acceptable. However, if the wavelength is smaller than 3 cm, the discrepancies increase even at low rainfall rates.

2.5.3 The reflectivity factor

Assuming that the particle diameters are small compared to the wavelength, the backscattering cross section obtained in Eq. 2.18 can be substituted into Eq. 2.16 resulting in:

$$\bar{P}_r = \left(\frac{\pi^3 P_t G^2 \theta_h \theta_v c\tau}{1024\lambda^2 \ln 2}\right)\frac{|K|^2}{r^2}\sum_{vol} D_i^6 \tag{2.19}$$

$$\bar{P}_r = \frac{C|K|^2 Z}{r^2} \tag{2.20}$$

where C is a constant depending on the radar characteristics and Z is the "reflectivity factor". If the drop size distribution is given as a number of drops n_i, then $Z = \sum n_i D_i^6$.

Therefore, the echo intensities from precipitation particles are proportional to the sum of the sixth power of their diameters in the resolved volume illuminated by the radar beam providing that the Rayleigh scattering assumption is fulfilled. The reflectivity factor is then expressed as:

$$Z = \int_0^\infty D^6 N(D) dD; \qquad \mathrm{mm}^6\ \mathrm{m}^{-3} \tag{2.21}$$

where $N(D)$ is the drop size distribution and represents the number of drops with diameters between D and $D + dD$ in a unit volume. The units of $10\log(Z)$ are dBZ. If the Rayleigh approximation is not valid, the reflectivity factor is given as a function of the backscattering cross section $\sigma(D)$ given by:

$$Z = \frac{\lambda^4}{\pi^5 |K|^2} \int \sigma(D) N(D) dD \tag{2.22}$$

2.6 Dual-polarisation weather radar measurements

In order to fully exploit and interpret the backscattered electromagnetic radiation from hydrometeors, it is necessary to take into account the four fundamental properties of electromagnetic waves: amplitude, phase, frequency and polarisation (Jameson and Johnson, 1990). The use of reflectivity factor Z_h exploits the amplitude property and it has been the most important parameter in the estimation of precipitation using weather radars. However, there are several sources of uncertainty using only the reflectivity factor (See Wilson and Brandes, 1979; Collier, 1996). Some of these uncertainties can be minimized by the use of dual-polarisation techniques, which are sensitive to size, shape, orientation and phase of the hydrometeors (Herzegh and Jameson, 1992) and can improve the estimation of precipitation using weather radars (Zrnić and Ryzhkov, 1999).

An electromagnetic wave is produced by the interaction of time-varying electric and magnetic fields. The direction of propagation is normal to the plane formed by the electric and magnetic field vectors and according to Maxwell's equations both vectors are orthogonal. Polarisation refers to the orientation of the electric field vector when observed along the direction of propagation (See Staelin et al., 1994). The most general type of polarisation is elliptical and in this polarisation the electric field is rotating in such a way that draws an ellipse when viewed along the direction of propagation. If the direction of propagation is the $+\hat{z}$ axis in a xyz coordinate system, the electric field will have components in the $\hat{x}$ and $\hat{y}$ directions (E_x and E_y respectively). Depending on the amplitude and phase of the components E_x and E_y, the ellipse may become either circular or linear

(known as either circular or linear polarisation respectively). Therefore, circular and linear polarisations are special cases of the general elliptical polarisation. The electric field in linear horizontal polarisation is confined to the $\hat{x}$ direction and the component $E_y = 0$. On the other hand, the electric field in linear vertical polarisation is confined to the $\hat{y}$ direction and the component $E_x = 0$.

Weather radars with polarisation diversity provide either for the variation of the transmitted and/or received wave polarisations or provide for dual-channel reception of orthogonally polarised waves (Bringi and Hendry, 1990; Doviak and Zrnić, 1993). Dual-polarisation is the use of two orthogonal polarisation states such as linear horizontal (H) and vertical (V) or right-hand circular and left-hand circular. In simultaneous transmission/reception measurements, the transmitted H/V waves of equal amplitudes will generate, in general, a right- or left-handed elliptically polarised wave having a tilt of $\pm 45°$, but the received signals will always be the H/V components, which are not co-polar and cross-polar to the transmitted wave (Doviak et al., 2000).

2.6.1 Backscattering matrix

A dual-polarisation weather radar alternately transmits vertically and horizontally polarised electromagnetic waves and receives polarised backscattered signals. The backscattering characteristics of a single precipitation particle are described in terms of the backscattering matrix **S**. The reflected electric field at the antenna in the horizontal and vertical directions respectively (E_h^r, E_v^r) are related to the backscattering matrix **S** and to the incident electric field $\mathbf{E}^i$ by (See Doviak and Zrnić, 1993):

$$\mathbf{E}^r = \mathbf{S}\mathbf{E}^i\left(\frac{e^{-jk_0r}}{r}\right) \tag{2.23}$$

$$\begin{bmatrix} E_h^r \\ E_v^r \end{bmatrix} = \frac{e^{-jk_0r}}{r}\begin{bmatrix} S_{hh} & S_{hv} \\ S_{vh} & S_{vv} \end{bmatrix}\begin{bmatrix} E_h^i \\ E_v^i \end{bmatrix} \tag{2.24}$$

where k_0 is the free space propagation constant ($k_0 = 2\pi/\lambda$) and r is the distance from the scatterer. The first index of the scattering elements refers to the polarisation of the backscattered field and the second to the polarisation of the incident field. The backscattering cross sections at horizontal and vertical polarisations respectively of a single scatterer are given by:

$$\sigma_{h,v} = 4\pi|S_{hh,vv}|^2 \tag{2.25}$$

The polarimetric radar observables are related to the scattering elements of the backscattering matrix and they are (Adapted from Doviak and Zrnić, 1993):

1. The reflectivity factors at horizontal and vertical polarisations (From Eqs. 2.22 and 2.25):

$$Z_{h,v} = \frac{\lambda^4}{\pi^5 |K|^2} \int \sigma_{h,v}(D) N(D) dD \tag{2.26}$$

2. The differential reflectivity:

$$Z_{dr} = 10 \log \left(\frac{\langle |S_{hh}|^2 \rangle}{\langle |S_{vv}|^2 \rangle} \right) = 10 \log \left(\frac{Z_h}{Z_v} \right) \tag{2.27}$$

3. The linear depolarisation ratio:

$$\mathrm{LDR} = 10 \log \left(\frac{\langle |S_{vh}|^2 \rangle}{\langle |S_{hh}|^2 \rangle} \right) \tag{2.28}$$

4. The correlation coefficient:

$$\rho_{hv}(0) = \frac{\langle S_{hh}^* S_{vv} \rangle}{\langle |S_{hh}|^2 \rangle^{1/2} \langle |S_{vv}|^2 \rangle^{1/2}} \tag{2.29}$$

(The mathematical operation $\langle\ \rangle$ is the expected value of a set of samples and it is also named the ensemble average).

Differential reflectivity

Pruppacher and Beard (1970) found that large raindrops falling to the ground are distorted into oblate spheroids due to aerodynamic forces. Their maximal dimensions are horizontally oriented even when turbulence, drop collisions and aerodynamic instability may disturb their orientation. Taking advantage of this fact, Seliga and Bringi (1976) proposed the use of differential reflectivities at orthogonal polarisations to improve the estimation of precipitation. The backscattering cross-section for raindrops is larger for a horizontal polarised wave than for a vertical polarised wave.

Seliga and Bringi (1976) showed that the mean volumetric diameter of raindrops is related to the value of Z_{dr}. Therefore Z_{dr} is a measure of the mean particle shape. Large raindrops produce large values of Z_{dr}. On the other hand, the sensitivity of Z_{dr} to particle shape for ice is less than for water (Herzegh and Jameson, 1992). Ice particles tend to wobble and spin in their descent resulting in Z_{dr} values closer to zero.

Linear depolarisation ratio

The cross-polar return is obtained by transmitting an electromagnetic wave with horizontal polarisation and receiving the echo in the vertical polarisation receiver (Z_{vh}). In contrast, the co-polar return is the echo received in the horizontal polarisation receiver by a signal

sent out by the horizontal polarisation transmitter (Z_{hh}). The linear depolarisation ratio is defined as the ratio of the cross-polar to the co-polar returns and it is given by (Eq. 2.28):

$$\mathrm{LDR} = 10\log(Z_{vh}/Z_{hh}) \tag{2.30}$$

LDR provides a measure of depolarisation of the hydrometeors. When nonspherical hydrometeors fall with their major axis at an angle to the axis of polarisation, a small percentage of the transmitted energy is depolarised and yields a cross-polar return (Herzegh and Jameson, 1992; Illingworth, 2003). Depolarisation is a measure of the canting angle of the raindrops. A theoretical model when compared to radar observations shows that the mean canting angle of raindrops is narrowly distributed with a mean of zero and a standard deviation of the order of 4 degrees (Beard and Jameson, 1983). Similar to Z_{dr}, the response of LDR is also strongly tied to the dielectric constant of the hydrometeors (Herzegh and Jameson, 1992). Browne and Robinson (1952) were the pioneers in the study of polarisation radar measurements in the melting layer anticipated much of the modern work on polarisation diversity. They found that the cross-polarised component from melting snow particles is greater than the one from snow or rain.

Correlation coefficient

The correlation coefficient between horizontally and vertically polarised signals is affected by the variation in the ratio of the vertical-to-horizontal size of individual hydrometeors (Doviak and Zrnić, 1993). The correlation coefficient is the correlation between successive estimates of Z_h and Z_v and it gives a measure of the variety of shapes of the hydrometeors present in the volume illuminated by the radar beam (Illingworth, 2003).

The effects influencing the correlation coefficient are distributions of eccentricities, differential phase shifts on scattering, canting angles, irregular shapes of hydrometeors and mixtures of different hydrometeor types (Doviak and Zrnić, 1993). Measurements in rain reveal an average $|\rho_{hv}(0)|$ of 0.98, whereas that for wet spheroids is considerably less.

Specific differential phase

Electromagnetic waves experience phase shifts as they propagate through regions of precipitation. The horizontally polarised wave suffers larger phase shifts than the vertically polarised wave because raindrops are horizontally oriented as they fall. The differential phase Φ_{dp} is the difference between the received phases of horizontally and vertically polarised electromagnetic waves ($\Phi_{dp} = \Phi_{hh} - \Phi_{vv}$) and the specific differential phase (K_{dp}) is the rate of change of Φ_{dp} along the range, that is, $K_{dp} = \frac{1}{2} d\Phi_{dp}/dr$.

In terms of the drop size distribution $N(D)$, K_{dp} is given by (Doviak and Zrnić, 1993):

$$K_{dp} = \frac{180\lambda}{\pi}\mathrm{Re}\int[f_h(D_e) - f_v(D_e)]N(D_e)dD_e; \qquad ^\circ\,\mathrm{m}^{-1} \tag{2.31}$$

where λ is the wavelength, D_e is the equivalent volume diameter of a drop and $f_{h,v}$ are the forward scatter coefficients of the drop for horizontal and vertical polarisations. K_{dp} can also be expressed as (Bringi and Chandrasekar, 2001):

$$K_{dp} \approx \left(\frac{180}{\lambda}\right)10^{-3}CW(0.062D_m); \qquad ^\circ\,\mathrm{km}^{-1} \qquad \text{with} \qquad D_m = \frac{\int D^4N(D)dD}{\int D^3N(D)dD} \tag{2.32}$$

where λ is the wavelength in m, $C \approx 3.75$, W is the water content in g m^{-3}, D_m is the mass-weighted mean diameter in mm and $N(D)$ is the drop size distribution. Eq. 2.32 is important because K_{dp} is nearly linearly related to the liquid water content multiplied by the mean raindrop shape and therefore it provides the possibility of better estimates of the rainfall rate.

2.6.2 Typical dual-polarisation systems

There are two ways of implementing the dual-polarisation capability in weather radars: a) switching the transmitted polarisation between the horizontal and vertical polarised waves on a pulse-by-pulse basis using a single receiver (alternating transmission) and b) simultaneous transmissions of the horizontal and vertical polarised waves with simultaneous reception using dual receivers (See Doviak et al., 2000).

Alternating transmission means that the radar system switches between polarisation modes on a pulse by pulse basis. A primary issue using alternating transmission is the use of a high power switch. These switches are expensive and difficult to maintain. However, the main advantage of a high power switch is the excellent isolation properties between the horizontal and vertical channels (Doviak et al., 2000). The mechanical switch has been used in S-band radars, as in the case of the Chilbolton radar (See Bringi and Hendry, 1990) whereas a solid-state ferrite phase shifter switch has been used for C- and X-band radars. The latter is not used for S-band radars because with time there are changes in the crystalline structure of the ferrite material causing failures due to increased energy absorption, which is greater at longer wavelengths, because the size of the ferrite core is dependent upon the wavelength of the radar (Alford et al., 2002). The main benefits of alternating transmission are the use of single-channel rotating joints and a single receiver for the radar system. In addition, the cross-polar returns can be directly measured (as in the case of the linear depolarisation ratio).

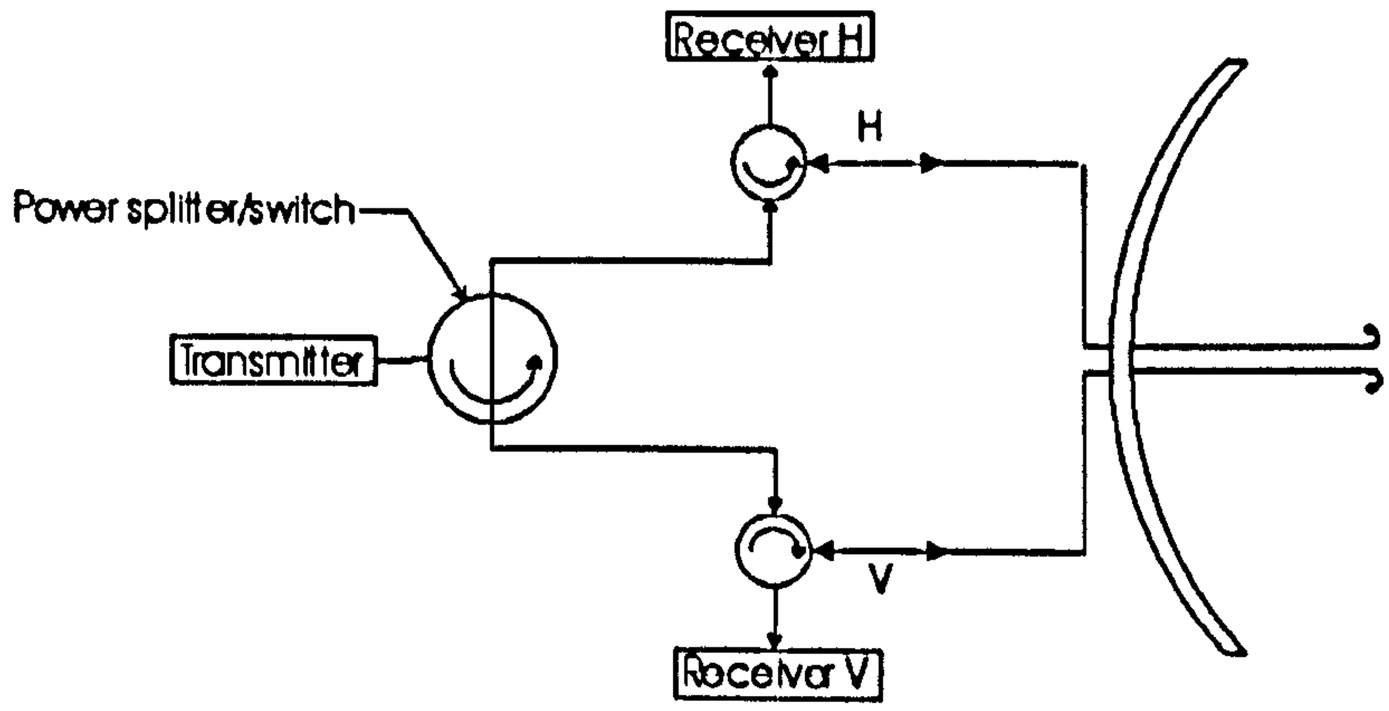

Fig. 2.3: Illustration to switch from simultaneous transmission and reception of H, V waves to transmission and reception of horizontally polarised waves (After Doviak et al., 2000).

Doviak et al. (2000) proposed the replacement of the dual-polarisation switch by a power divider in order to transmit the simultaneous horizontal and vertical polarised waves as an alternative polarimetric upgrade to the WSR-88D radars in USA (See Fig. 2.3). One of the main benefits of simultaneous transmission is the elimination of the expensive and hard to maintain dual-polarisation switch. However, the use of simultaneous transmissions precludes the measurements of cross-polar returns. To overcome this problem, Alford et al. (2002) proposed a mechanical transfer switch designed into the waveguide structure to bypass the power divider. In this way, the full transmit power can be achieved in a single polarisation mode. This solution helps to obtain the linear depolarisation ratio, which is useful in hydrometeor classification algorithms. Another drawback of using simultaneous transmission is that the Signal to Noise Ratio (SNR) decreases 3 dB as the result of the split of the transmitted power.

Both, alternating and simultaneous transmissions of horizontal and vertical polarised waves have proved to be the alternatives to implementing the dual-polarisation capability in weather radars. However, further research has to be done to estimate the errors in the resulting polarimetric variables when using any of these technologies.

2.7 Estimation of precipitation using weather radars

2.7.1 Raindrop size distribution

Raindrops grow to a critical size and will then suffer breakup due to hydrodynamic instability (Cotton and Anthes, 1989). The different sizes of raindrops define a Drop Size Distribution (DSD) given by $N(D)$. The DSD describes the probability density function of raindrops and it is one of the most important functions in rainfall rate algorithms. All the microphysical processes involved in the interaction between raindrops is reflected in

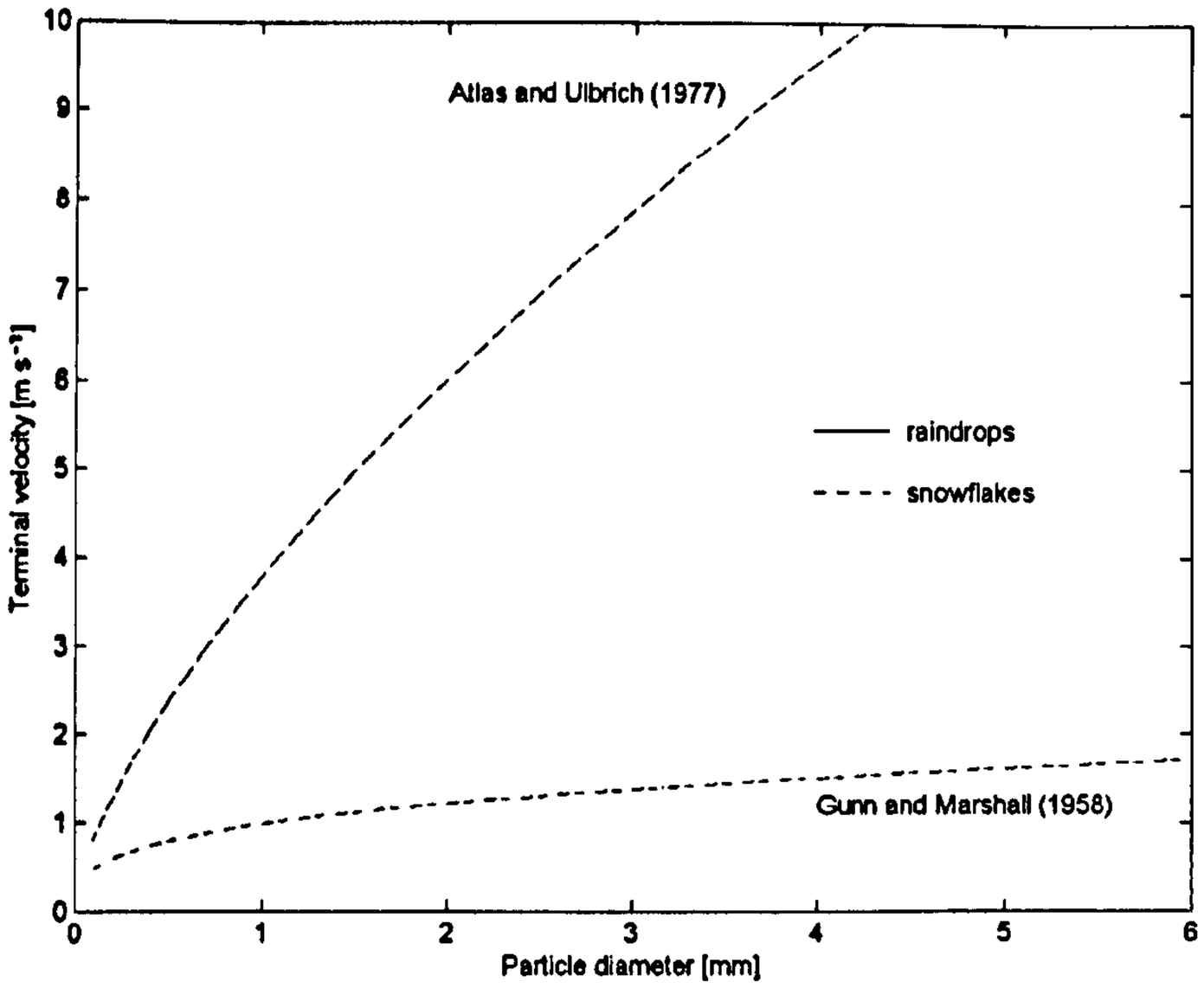

Fig. 2.4: Terminal velocities of raindrops (Atlas and Ulbrich, 1977) and snowflakes (Gunn and Marshall, 1958).

the DSD. For a given DSD, the rainfall rate is given by:

$$R = 0.0006\pi \int_0^\infty v(D) D^3 N(D) dD; \qquad \text{mm hr}^{-1} \tag{2.33}$$

where D is the raindrop diameter in units of mm, $N(D)$ is the number of drops m^{-3} in the interval D to $D + dD$ and $v(D)$ is the terminal velocity of the raindrops in m s^{-1} (See Fig. 2.4). Atlas and Ulbrich (1977) expressed the terminal velocity as a function of the particle diameter, given by $v(D) = 3.78D^{0.67}$ m s^{-1}. Eq. 2.33 assumes the absence of vertical air motions. Thus, R represents the 3.67^{th} moment of the DSD whereas Z represents the 6^{th} moment (See Eq. 2.21), with Z more sensitive to large drops than R. Similarly, the liquid water content (W) is given by:

$$W = \frac{\pi \rho_w}{6} \int_0^\infty D^3 N(D) dD \tag{2.34}$$

where ρ_w is the water density of the drop. It is clear that not only the reflectivity factor (Eq. 2.21) depends on the DSD, but also the rainfall rate and the liquid water content (Eqs. 2.33 and 2.34 respectively). Knowledge of the DSD is important because it establishes the interaction between the radar reflectivity and the rainfall rate. Marshall and Palmer (1948) (MP) observed an exponential DSD using dyed filter paper to measure the density of drop diameters at the surface. The exponential form of the DSD can always be applied when a large number of DSD are averaged in space or time (Bringi and Chandrasekar, 2001).

The MP DSD is given by:

$$N(D) = N_0 e^{(-\Lambda D)} \tag{2.35}$$

where N_0 is 8000 m^{-3} mm^{-1}, Λ is the slope factor of the distribution in mm^{-1} and D is the raindrop diameter in mm. The slope factor depends on the rainfall rate and it is given by:

$$\Lambda = 4.1 R^{-0.21} \tag{2.36}$$

where R is the rainfall rate in mm hr^{-1}. Substituting the MP DSD into Eq. 2.34, the following is obtained:

$$W = \frac{\pi \rho_w N_0}{\Lambda} \tag{2.37}$$

An important parameter is the median drop diameter D_0, which is defined as the drop diameter such that 50 per cent of the water content is comprised of drops with diameters less than D_0 (Doviak and Zrnić, 1993). This parameter can be obtained from:

$$\frac{1}{2} W = \frac{\pi \rho_w}{6} \int_0^{D_0} N(D) D^3 dD \tag{2.38}$$

Substituting Eqs. 2.35 and 2.37 into Eq. 2.38 and solving for D_0, it turns out that:

$$D_0 = 3.67/\Lambda \tag{2.39}$$

Thus, Eq. 2.35 becomes:

$$N(D) = N_0 e^{(-3.67 D/D_0)} \tag{2.40}$$

Eq. 2.40 is a more general form of the MP DSD because it depends on the median drop diameter. According to Marshall and Palmer (1948) the exponential DSD is slightly overestimated for raindrop diameters less than 1.5 mm. In reality there are larger variations in the shape of the DSD not represented by the MP DSD. Ulbrich (1983) proposed a more general three-parameter gamma DSD given by:

$$N(D) = N_0 D^{\mu} e^{(-(3.67+\mu) D/D_0)} \tag{2.41}$$

where the parameter μ can take values between -3 and 8. For $\mu = 0$, Eq. 2.41 takes the form of the MP DSD. The shape of the gamma DSD is determined by the exponent μ, that is, for positive values of μ the gamma DSD is concave downward whereas for negative

values it is concave upward. A gamma DSD can describe many of the natural variations in the shape of the DSD. When there is a substantial depth between the melting level and the ground surface, the parameterisation of a gamma DSD appears to be suitable for stratiform and convective rainfall events (Bringi and Chandrasekar, 2001). Testud et al. (2001) proposed the normalisation of the DSD to avoid any assumption about the shape of the DSD. Illingworth and Blackman (2002) proposed a normalised gamma DSD, which either total drop concentration, liquid water content or rainfall rate remain constant when the parameter μ is changed. In this way, N_0, D_0 and μ are independent parameters describing the concentration, mean size and breadth of drop spectra respectively.

The most commonly used polarimetric radar measurements for rainfall estimation are the reflectivity factor (Z_h), the differential reflectivity (Z_{dr}) and the specific differential phase (K_{dp}). Several relationships for rainfall estimation are given in the following section.

2.7.2 Algorithms to estimate rain from radar measurements

For many years, radar meteorologists have tried to find a useful equation relating the reflectivity factor to the rainfall rate. The rainfall rate given by Eq. 2.33 can be obtained assuming a drop size distribution and terminal velocity of raindrops. By comparing the rainfall rate with the actual reflectivity measured by the radar, it is possible to derive Z-R relationships of the form:

$$Z = aR^b \qquad \text{or} \qquad R = a^{-1/b} Z^{1/b} \tag{2.42}$$

where Z is the reflectivity factor in mm^6 m^{-3}, R is the rainfall rate in mm hr^{-1} and a and b are the parameters obtained from a regression analysis. Atlas and Ulbrich (1990) showed that the first Z-R relationship can be traced back to the research work carried out by Ryde (1946). They showed that this relationship is approximately $Z = 320R^{1.44}$. This relationship is very similar to that employed to estimate the rainfall rate from reflectivity measurements in the WSR-88D radar network, which is $Z = 300R^{1.4}$ (Serafin and Wilson, 2000). Marshall et al. (1947) reported one of the first Z-R relationships ($Z = 190R^{1.72}$), which was slightly modified to $Z = 220R^{1.6}$ (Marshall and Palmer, 1948). Years layer, Marshall et al. (1955) carried out a slight revision of the 1948 relationship, obtaining the well known Marshall-Palmer formula $Z = 200R^{1.6}$. This relationship is employed by the UK Meteorological office to estimate precipitation from reflectivity measurements (Harrison et al., 2000). Unfortunately, there is no single Z-R relationship that can be applied in every part of the world. Battan (1973) listed 69 different Z-R relationships derived from different climatological regions by several researchers. This variability is due

to the fact that the coefficient and exponent of the Z-R relationship depend on the shape of the DSD. Therefore, it is necessary to estimate in real-time the parameters of the DSD to allow flexibility in the variation of the parameters a and b of the Z-R relationship.

Calheiros and Zawadzki (1987) developed a statistical procedure called the Probability Matching Method (PMM) to derive Z-R relationships. This method relates the rainfall rate R to the observed radar reflectivity Z by matching the cumulative distribution function of R and Z. The cumulative distribution functions can be estimated independently from radar and raingauge measurements. Rosenfeld et al. (1994) proposed a modification of the PMM by matching raingauge intensities to reflectivity measurements taken from the same space-time window centered above the raingauges (known as Window Probability Matching Method-WPMM).

One of the main goals of dual-polarisation radars is the improvement in quantitative precipitation estimation. Seliga and Bringi (1976) proposed the use of differential reflectivities at orthogonal polarisations to estimate the parameters of an exponential DSD (Eq. 2.40). They suggested that the parameter D_0 is obtained with Z_{dr} whereas N_0 is obtained with Z_h and D_0. The main advantage of using the differential reflectivity Z_{dr}, is that the median raindrop diameter D_0 is related to the value of Z_{dr}. This advantage has been exploited by several researchers to obtain the shape of the DSD.

In order to derive relationships between the rainfall rate and the polarimetric radar measurements a common method is based on varying the parameters N_0, D_0 and μ of a theoretical gamma DSD and then calculating R, Z_h, Z_{dr} and K_{dp} assuming a scattering model (Holt, 1982, reviewed some methods to calculate the scattering of electromagnetic radiation by hydrometeors). In addition, the mean raindrop axis ratio $r(D)$ or raindrop deformation as a function of the diameter D must also be specified. The coefficients and exponents of the different rainfall rate algorithms are obtained by performing a non-linear regression between the rainfall rate and the polarimetric variables (Bringi and Chandrasekar, 2001). The deformation of raindrops is an important relationship that leads to different rainfall estimators. An important point made by Illingworth (2003) is that the choice of the drop shape model is crucial for the calculation of the rainfall rate estimator coefficients. Further research has to be done to reach a consensus on raindrop deformation.

Gorgucca et al. (1994) proposed an algorithm to estimate the rainfall rate based on Z_h and Z_{dr}, where the coefficients a, b and c of the rainfall estimator are wavelength dependent (See Table 2.1). The disadvantage of the algorithm $R(Z_h, Z_{dr})$ is that Z_h and Z_{dr} are prone to attenuation of the horizontal reflectivity and differential attenuation respectively at frequencies higher than 3 GHz, quite apart from the fact that Z_h is subject to radar

Rain estimator	f (GHz)	c	a	b	
$R = a^{-1/b} Z_h^{1/b}$	3	-	200	1.6 †	Marshall et al. (1955)
	3	-	300	1.4 ‡	
$R = c Z_h^a 10^{0.1bZ_{dr}}$	3	0.0067	0.93	-3.43	Bringi and Chandrasekar (2001)
	5	0.0058	0.91	-2.09	Bringi and Chandrasekar (2001)
	10	0.0039	1.07	-5.97	Bringi and Chandrasekar (2001)
$R = c K_{dp}^b$	3-10	$5.1\lambda^{0.866}$	-	0.866	Sachidananda and Zrnić (1987)
	3	50.7	-	0.85	Bringi and Chandrasekar (2001)
	3	40.5	-	0.85	Bringi and Chandrasekar (2001)
	3	50.1	-	0.70	Illingworth (2003)
	5	31.4	-	0.70	Illingworth (2003)
$R = c K_{dp}^a 10^{0.1bZ_{dr}}$	3	90.8	0.93	-1.69	Bringi and Chandrasekar (2001)
	5	37.9	0.89	-0.72	Bringi and Chandrasekar (2001)
	10	28.6	0.95	-1.37	Bringi and Chandrasekar (2001)

Table 2.1: Summary of relationships for rainfall estimation using polarimetric radar measurements at different frequencies f. R is in mm hr^{-1}, Z_h is in mm^6 m^{-3}, Z_{dr} is in dB, K_{dp} is in $°km^{-1}$ and λ in cm. † This relationship is used in the UK NIMROD system (Harrison et al., 2000); ‡ this relationship is used in the US NEXRAD system (Serafin and Wilson, 2000).

miscalibration. To some extent, the use of the differential phase K_{dp} may overcome these difficulties. The main advantages of rainfall estimation based on K_{dp} are its immunity to attenuation by precipitation, its immunity to radar miscalibration and K_{dp} is also less affected by partial blockage of the radar beam (Zrnić and Ryzhkov, 1996). Its immunity to attenuation and radar miscalibration is due to the fact that K_{dp} is a phase measurement. However, at shorter wavelengths or when there are large particles, Φ_{dp} (and consequently K_{dp}) is affected by the backscatter differential phase (δ). The backscatter differential phase decreases to zero for particles smaller than about a tenth of the radar wavelength, but exhibits an abrupt increase for larger particles (Zrnić and Ryzhkov, 1999). Therefore, the rainfall estimator $R(K_{dp})$ is more robust at 10-cm wavelengths than at shorter wavelengths (Zrnić and Ryzhkov, 1999). Rainfall estimators based on K_{dp} (Sachidananda and Zrnić, 1987) and K_{dp}-Z_{dr} (Bringi and Chandrasekar, 2001) have been proposed (Table 2.1).

Polarimetric measurements are affected by the hydrometeors located within the radar resolution volume (backscatter effect) and by the hydrometeors along the propagation path between the radar and the measurement (propagation effect) (Zrnić and Ryzhkov, 1999).

The propagation effects are attenuation of the H/V components (differential attenuation), depolarisation and differential phase shifts. Differential attenuation and differential phase shifts are caused by preferentially oriented hydrometeors whereas depolarisation is caused by nonspherical hydrometeors canted an angle with respect to the axis of polarisation.

It is clear that the different algorithms to estimate the rainfall rate have advantages and disadvantages. Relationships of the form $R(Z_h)$ have been used from just after World War II. However, this type of relationship presents uncertainty in the coefficients a and b because they are related to the shape of the DSD. Without extra information, apart from the reflectivity factor, a and b have to be obtained empirically by establishing a single climatological Z-R relationship. Even if the DSD is known, the $R(Z_h)$ relationship is critically dependent on the calibration of the radar system. To avoid any bias in the measurement of Z_h, it is necessary to calculate accurately the radar constant (See Eq. 2.20). In addition, Z_h is not immune to propagation effects and it is subject to attenuation due to rain at frequencies higher than 3 GHz.

Relationships involving Z_{dr} are also questionable because although Z_{dr} is independent of radar calibration, it is not immune to propagation effects being subject to differential attenuation in heavy precipitation and the depolarisation of the polarised waves. Illingworth (2003) discussed the accuracy of rainfall estimates using Z_h and Z_{dr}. He argued that the accuracy of $R(Z_h, Z_{dr})$ depends on several factors such as the accuracy of Z_{dr} to 0.2 dB for $R > 10$ mm hr^{-1} and less for lower rainfall rates. In practice, this is very difficult to achieve because there are other factors limiting the accuracy of Z_{dr}. For instance, Z_{dr} may be contaminated by the power of the sidelobes of the beam radiation pattern due to reflectivity gradients and it may also be affected by the mismatch between the horizontal and vertical beam radiation patterns causing the sampling of different volumes of precipitation (Illingworth, 2003).

On the other hand, relationships of the form $R(K_{dp})$ present several advantages as mentioned previously. However, Φ_{dp} is extremely noisy and consequently K_{dp} will be even noisier ($K_{dp} = \frac{1}{2} d\Phi_{dp}/dr$, See Section 2.6.1). To decrease the noise, K_{dp} is averaged for several kilometers along the beam. Ryzhkov and Zrnić (1996) suggested to average K_{dp} in a window of 2-4 km for high-reflectivity regions ($Z_h > 40$ dBZ) and 7-11 km for low-reflectivity regions ($Z_h < 40$ dBZ). This obviously leads to a considerable loss in resolution over the conventional $R(Z_h)$ rainfall estimator. Brandes et al. (2001) carried out an analysis between raingauge observations and rainfall rates estimated from K_{dp} and Z_h. They found similar bias factors and correlation coefficients between both estimators, concluding that no obvious benefit is obtained using K_{dp} to estimate rainfall rates over

using Z_h from a well-calibrated radar.

There is controversy whether or not polarimetry is going to improve radar rainfall estimates. Illingworth (2003) suggested that at the 2 km scale needed for an operational environment, the additional information provided by Z_{dr} and K_{dp} is not sufficiently accurate to improve rainfall estimates. However, some improvement in the quantitative precipitation estimation from polarimetric radar measurements may be realised by applying not only one particular rain estimator, but exploiting the attributes of the different polarimetric algorithms available depending on the circumstance. Ryzhkov and Giangrande (2004) proposed a "synthetic" algorithm, which makes use of different combinations of rain rate algorithm depending on the rain rate estimated using only the conventional $R(Z)$ relationship. They proposed the use of an algorithm of the form $R(R(Z_h), Z_{dr})$ for low rain rates ($R < 6$ mm hr^{-1}), and of the form $R(R(K_{dp}), Z_{dr})$ for medium rain rates ($6 < R < 50$ mm hr^{-1}) and the algorithm $R(K_{dp})$ for high rain rates ($R > 50$ mm hr^{-1}). Although the algorithms proposed by Ryzhkov and Giangrande (2004) are slightly different from the rainfall rate estimators presented in this section, it is clear that by exploiting the performance of different relationships $R(Z_h)$, $R(Z_h, Z_{dr})$, $R(K_{dp})$ and $R(K_{dp}, Z_{dr})$, it may be possible to improve the estimation of rainfall using dual-polarisation radars. However, the operational performance of such radars in practice is still to be identified.

2.8 Problems associated with the estimation of rain

The estimation of rain on the ground using weather radars is subject to many error sources, which become important for quantitative precipitation estimation. In the previous section the importance of the DSD has been described in relating the reflectivity factor Z_h (or any of the polarimetric variables Z_{dr}, K_{dp}) to the rainfall rate R. However, uncertainties in the knowledge of the DSD may not be the largest source of errors in radar rainfall measurements (Joss and Waldvogel, 1990) and there are additional errors that may require even more attention. Atlas et al. (1984) concluded that the average deviation in the rain rate estimation from reflectivity measurements due to DSD variability would be 33% whereas Doviak and Zrnić (1993) suggested errors of 30-35%. Joss and Waldvogel (1990) suggested that after averaging over space and time, the errors in rainfall estimates due to the variability of the DSD rarely exceeds a factor of 2.

On the other hand, problems associated with the variation of the vertical reflectivity profile of precipitation have received little attention (See Section 2.8.1). This variation is due to the growth or evaporation of precipitation, change of phase, in particular melting,

where a layer of enhanced reflectivity caused by melting snowflakes produces errors up to a factor of 5 (Joss and Waldvogel, 1990). Section 2.8.1 describes some correction algorithms.

Partial blockage of the beam is specially problematic in hilly terrains. The radar usually scans at low elevation angles in order to obtain measurements closer to the ground. Echoes from nearby mountains can be misinterpreted as heavy rainfall and therefore overestimations may occur. Correction for partial beam blockage is also difficult because not only the power from the mainlobe is reflected back to the radar, but also from the sidelobes. By knowing the shape of the antenna radiation pattern it may be possible to apply a correction for the partial blocking, but in conditions where the radar beam slightly departs from the standard propagation it is not straightforward. The use of the differential phase K_{dp} for rainfall estimation may overcome problems due to partial blocking to some extent, but as mentioned in the previous section K_{dp} is very noisy and it is only useful in very heavy precipitation. Therefore, it is important to establish accurate corrections to overcome the effects of partial blockage of the radar beam.

Attenuation by precipitation is another source of error that requires attention, specially at frequencies higher than 3 GHz (See Section 2.8.2). To some extent this is now recognised as posing a problem at C-band frequencies as well as X-band.

2.8.1 Variation of the vertical reflectivity profile

The variation of the vertical reflectivity profile may be one of the largest error sources in the estimation of precipitation from reflectivity measurements by weather radars. This variation is largely due to the growth or evaporation of precipitation, which is reflected in both, ice and liquid phases.

As the range increases from the radar, the radar beam is at some height above the ground (See Eq. 2.3). At far ranges, the hydrometeors intercepted by the radar beam may be composed of raindrops, melting snowflakes, snowflakes, hail, etc. This variability affects reflectivity measurements and the estimation of precipitation is not representative of the rainfall rate at the ground. There are three zones easily identified in stratiform precipitation: snow, melting snow and rain.

When the radar beam intercepts melting snowflakes, the result is an increase in the power reflected back to the radar. This enhanced reflectivity is known as the bright band and its increase is primarily due to the change of the dielectric constant of the hydrometeors from ice to raindrops (Battan, 1973). Interception of the radar beam with melting snow can cause overestimates of rain up to a factor of 5 (Joss and Waldvogel, 1990). Using polarimetric radar measurements to estimate the rainfall rate will not completely solve

this problem, because although K_{dp} is a useful estimator in heavy rain, it is also affected by melting snowflakes.

Additional error sources are due to horizontal winds (Doviak and Zrnić, 1993), which affect radar-raingauges inter-comparisons, because the radar beam is at some height above the ground. Raingauges obtain point measurements integrated in time whereas weather radars obtain volumetric measurements sampled with a given frequency (*e.g.* 5 min) and independent measurements from radars and raingauges are not necessarily comparable. In addition, vertical winds affect the DSD inducing errors in R by modifying the terminal velocity of the raindrops (See Eq. 2.33).

The bright band

The melting layer is the transition zone between ice particles and raindrops. Melting particles, as observed by a weather radar, present high values of reflectivity compared with the values observed above and below the melting layer (See Chapters 5 and 6). This important signature is called bright band and problems associated in the measurement of precipitation close to the ground arise when the beam from a scanning weather radar intercepts the melting layer causing an overestimation of the rainfall below. In addition, effects of absorption and scattering through the melting layer are important, as the frequency spectrum becomes crowded because of the use of shorter wavelengths for radar and satellite communications systems (Zhang, 1994).

Since the early observations of the bright band as seen by weather radars, there have been many attempts trying to quantify its causes (Ryde, 1946; Hooper and Kippax, 1950; Austin and Bemis, 1950; Wexler, 1955; Lhermitte and Atlas, 1963; Ekpenyong and Srivastava, 1970; Battan, 1973). The factors contributing to the increase in reflectivity in the upper part of the bright band are the increase of the dielectric constant of the hydrometeors because of the change from ice to liquid phase and the continuous growth of snowflakes by aggregation among ice crystals. On the other hand, the factors contributing to the decrease in reflectivity in the lower part of the bright band are an increase of fall velocity of raindrops followed by a decrease of particle concentration, a continuous breakup of raindrops and variations in particle shape from non-spherical to spherical particles. The change of the hydrometeor dielectric constant is the most important contributor to the bright band. The increase in reflectivity due to melting is calculated by (Hardaker, 1993):

$$\Delta Z = 10 \log \left| \frac{K_{water}}{K_{ice}} \right|^2 = 10 \log \left(\frac{0.93}{0.20} \right) = 6.67 \text{ dBZ} \tag{2.43}$$

There was controversy whether aggregation is dominant in the upper part of the bright band and breakup in the lower, mainly because of the lack of in-situ measurements of hydrometeor size distribution in the melting layer. Ohtake (1969) found no evidence to support the suggested pair of aggregation-breakup from observations of snow and rain at two different altitudes along a mountain slope. He observed similar patterns of particle size distributions sampled below and above the melting layer, concluding that each snowflake yields one raindrop without any breakup.

Uncertainties about the particle size distribution, composition and shape of the melting particles made it difficult to establish general consent as to whether or not the pair aggregation-breakup is important for the bright band signature (Battan, 1973). However, recent research (Stewart et al., 1984; Willis and Heymsfield, 1989; Barthazy et al., 1998) helped to support the existence of aggregation and breakup within the bright band.

Stewart et al. (1984) measured the particle size distributions in the melting layer using three different optical spectrometers fitted in an aircraft while ascending through the melting layer in widespread precipitation. The measurements were supported with a weather radar. Their observations showed that aggregation was occurring in the upper part of the bright band but the decrease in reflectivity in the lower part of the bright band was largely caused by the increase of the particle fall speed and the particle evolution from non-spherical to spherical particles. They pointed out that breakup of raindrops only contributes a small amount to the total decrease in reflectivity. They also concluded that the intensity of the bright band is dependent upon the sizes of the largest particles.

Similar experiments were carried out by Willis and Heymsfield (1989). They measured particle size distributions above, through and below the melting layer in stratiform precipitation using three different spectrometers and with the support of two weather radars. The measurements were taken following an advecting spiral descent in an aircraft. They showed that in the isothermal layer, larger particles continue growing, with an increase of large-particle concentration. They suggested that drop breakup below the melting layer may contribute for the decrease in reflectivity. However, they also concluded that evaporation in the drier air may contribute to most of the decrease, because of the low rainfall rates involved in their measurements.

Barthazy et al. (1998) measured the particle size distributions using an optical spectrometer placed on the top of a mountain and a disdrometer 450 m below. At the beginning of the measurements, both, the optical spectrometer and the disdrometer, were measuring raindrop sizes, and the melting layer was above both instruments; but due to the fact that the melting layer was slowly descending, it reached some point where it was located

between the optical spectrometer and the disdrometer, it then being possible to measure all the particle size distributions within the melting layer. Their work was supported with an X-band vertically pointing weather radar. Their results indicated that the flux density of particles measured with both instruments above and below the bright band respectively are the same, implying that on average, one snowflake melts into a single raindrop, which agrees with the results presented by Ohtake (1969). However, in relation to the measurements made by Ohtake (1969), Barthazy et al. (1998) had the opportunity to measure the particle size distributions within the bright band, concluding that aggregation dominates over breakup in the upper part and breakup dominates over aggregation in the lower part. They also observed the largest particle diameters at the maximum reflectivity in the melting layer.

Stewart et al. (1984); Willis and Heymsfield (1989); Barthazy et al. (1998) showed from different experiments that there is an increase of particle diameters due to aggregation of hydrometeors on the upper part of the bright band and the maximal radar reflectivity was associated with the biggest particle diameters that survive to warmer temperatures. If the aggregation efficiency of ice particles is higher at warmer temperatures (Cotton and Anthes, 1989; Stewart et al., 1984), then there is strong evidence to suggest that aggregation will take place in the onset of melting. Additionally, when large snowflakes start melting, the change in the dielectric constant becomes important because of the formation of liquid water on or within them, making them look like big raindrops to the radar (Fabry and Zawadzki, 1995). However, discrepancies exist whether or not breakup is the main cause that influences the decrease in reflectivity in the lower part of the bright band. While Barthazy et al. (1998) agree that breakup is dominant in the lower part of the bright band with significant increase of the fall speed of the raindrops, for Stewart et al. (1984), the latter is the most important. On the other hand, Willis and Heymsfield (1989) suggested that evaporation may contribute to most of the decrease.

Fabry and Zawadzki (1995) in a similar way to Wexler (1955) quantified the contribution of the enhancement of the bright band, concluding that the shape and orientation of melting snowflakes and the distribution of water within the snowflake account for the missing enhancement. The relative contribution of aggregation and breakup is small.

The influence of all the factors contributing to the increase-decrease effect of the bright band may differ from one vertical reflectivity profile to another because of the complex thermodynamic and microphysical processes around and within the bright band, which are influenced at the same time by the characteristics of the air mass, the vertical motion of the cloud, liquid water content, turbulence, crystal habit, temperature, relative humidity,

atmospheric pressure and even when there is a general trend in the shape of the bright band signature, differences in the factors contributing to the increase-decrease of reflectivity in the melting layer will be associated with the variation of any of these variables.

Correction for the vertical reflectivity profile

There are several techniques to correct for the variation of the vertical reflectivity profile. Some of these techniques are based on a idealised vertical reflectivity profile obtained from a considerable amount of observations (*e.g.* Smith, 1986; Kitchen et al., 1994).

The method proposed by Kitchen et al. (1994) has been adopted by the UK meteorological office to correct for the variation of the vertical reflectivity profile in radar reflectivity measurements. The profile shown in Fig. 2.5 is defined by the background reflectivity (the reflectivity in rain below the bright band), the height of the freezing level (0°C) derived from the temperature profile predicted by the UK mesoscale model and the cloud top height derived from IR satellite imagery. This algorithm requires the height of the bright band to be known within 200 m (Kitchen et al., 1994) and according to Marion and Illingworth (2003), operational forecast models can provide the height of the bright band with a Root Mean Squared Error (RMSE) of 150 m. The area of the bright band peak (A) against the background reflectivity factor (Z_b) is given by (Kitchen et al., 1994):

$$\log A = 1.42 \log(Z_b) + 2.1 \tag{2.44}$$

where A is in $\mathrm{mm}^6\ \mathrm{m}^{-2}$ and Z_b is in $\mathrm{mm}^6\ \mathrm{m}^{-3}$. The bright band is assumed to be triangular with a constant depth of 700 m. The correction is performed at each pixel of the radar scan by weighting the idealised vertical reflectivity profile with the beam power profile by an iterative method. This correction is not only intended to correct the increase in reflectivity in the melting layer, but also to correct measurements above the bright band and those due to orographic enhancement. According to Kitchen et al. (1994), this correction achieves a reduction of 63% in the RMSE in equivalent surface precipitation rates when compared to the raw radar data. However, systematic errors persist at ranges when the radar beam is above the bright band.

Recently Gray et al. (2002) developed a new approach to correct scanning weather radar measurements due to the changes in reflectivity between the ground and the height at which the radar is measuring. 89000 vertical reflectivity profiles were evaluated and a set of five typical reflectivity profile functions were found.

Szyrmer and Zawadzki (1999) pointed out that the complete understanding of the thermodynamic and microphysical processes around and within the bright band cannot be

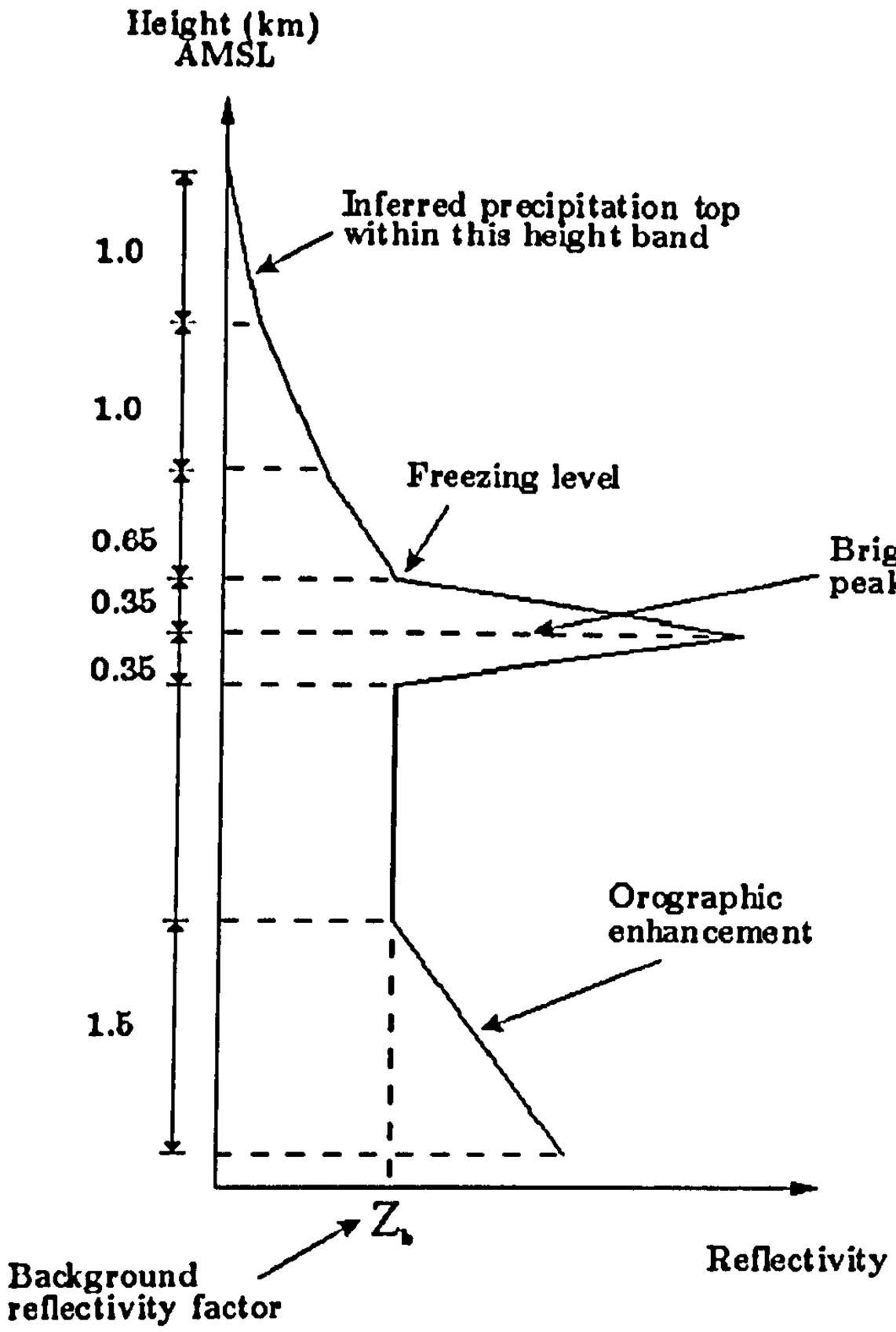

Fig. 2.5: Idealised vertical reflectivity profile utilised to correct scanning radar reflectivity measurements in the Nimrod system (from Kitchen et al., 1994).

obtained by observation. There are several bright band models in the literature (Hardaker, 1993; Hardaker et al., 1995; Gray et al., 2001), but the initialization of these models depends on factors such as the initial density of snowflakes, relative humidity and vertical temperature profile, which are not available in real-time. Therefore, although it is important to model the bright band, in reality it is difficult to apply a correction based on a microphysical model, because of the lack of the aforementioned factors.

2.8.2 Attenuation by rain

Attenuation of an electromagnetic wave is a measure of the amount of power lost by scattering and absorption through the medium. Radars with shorter wavelengths suffer more attenuation in rain in comparison to larger wavelengths ($\lambda = 10$ cm). It has been shown that the attenuation is directly proportional to the rain rate R and expressions of the form $A = \alpha R^b$ have been obtained. One-way attenuation relationships given by Doviak and Zrnić (1993) at 18°C are presented in Table 2.2. Note that the coefficient

Wavelength (cm)	Attenuation (dB km^{-1})
10	$0.000343R^{0.97}$
5	$0.0018R^{1.05}$
3.2	$0.01R^{1.21}$

Table 2.2: One-way attenuation at a temperature of 18°C (from Doviak and Zrnić, 1993).

α increases by two orders of magnitude for wavelengths from 10 to 3.2 cm, whereas the exponent b only suffers a light increase. This will produce an attenuation for wavelengths of 3.2 cm 100 times larger than at wavelengths of 10 cm. Therefore, attenuation effects at shorter wavelengths have to be considered when radars with this characteristic are used for hydrological purposes.

Larger wavelengths are required to avoid attenuation effects due to precipitation, but unfortunately at these wavelengths a large antenna diameter is required to obtain a small beamwidth, whereas for the same beamwidth shorter wavelengths require a smaller antenna diameter. Therefore, there is a trade-off between attenuation effects and resolution, which is related directly to costs.

The power loss suffered by the incident wave due to scattering and absorption can be determined by the extinction cross section of the precipitation particles σ_{ext}. Thus, σ_{ext} is proportional to the sum of the total scatterer cross section (σ_s) and the absorption cross section (σ_a). The specific attenuation (A) in units of dB km^{-1} is given by (See Doviak and Zrnić, 1993):

$$A = 4.343 \text{ x } 10^3 \int_0^\infty \sigma_{ext}(D)N(D)dD; \qquad \text{dB km}^{-1} \tag{2.45}$$

where $N(D)$ is the drop size distribution. σ_{ext} is proportional to $\sigma_{ext} \approx C_\lambda D^n$ (Bringi and Chandrasekar, 2001), where C_λ depends on the wavelength and n is approximately equal to 4. It follows that the attenuation is approximately proportional to the fourth moment of the drop size distribution, that is:

$$A \approx 4.343 \text{ x } 10^3 C_\lambda \int D^4 N(D)dD; \qquad \text{dB km}^{-1} \tag{2.46}$$

By substituting Eq. 2.34 into Eq. 2.32 and comparing the result with Eq. 2.46, it follows that the specific attenuation is proportional to K_{dp}, that is, $A = \alpha K_{dp}$. The specific attenuation at horizontal and vertical polarisations (A_h and A_v respectively), can be directly obtained from Eq. 2.46. Therefore, the differential attenuation $A_{dp} = A_h - A_v$ to correct Z_{dr} is $A_{dp} = \beta K_{dp}$. In reality, the exponent of K_{dp} for attenuation and differential

Frequency (GHz)	α	b_1	β	b_2
2.8	0.017	0.84	0.003	1.05
5.5	0.073	0.99	0.013	1.23
9.3	0.233	1.02	0.033	1.15

Table 2.3: Coefficients and exponents of temperature-averaged (0-30 °C) power-law fits given by Eqs. 2.47 at different frequencies (from Bringi and Chandrasekar, 2001).

attenuation departs from unity. Therefore, it is more convenient to express relationships of attenuation and differential attenuation respectively by:

$$A_h = \alpha K_{dp}^{b_1} \qquad \text{and} \qquad A_{dp} = \beta K_{dp}^{b_2} \tag{2.47}$$

Bringi and Chandrasekar (2001) give some values for the coefficients α and β and for the exponents b_1 and b_2 at different frequencies (See Table 2.3). Unfortunately, α and β are temperature dependent and different values have appeared in the literature. Bringi et al. (2001) have proposed a self-consistent constraint-based algorithm to avoid any assumption about the *a priori* values of α and β.

Attenuation correction algorithms are applied when the radar beam passes through rain-filled media. However, additional research has to be done to correct for attenuation when the radar beam passes through melting snow or mixed-phase precipitation.

2.9 Conclusions

Current research has sought to improve the estimation of precipitation using single- and dual-polarisation weather radar measurements. However, additional research has to be done to account for the variation of the vertical reflectivity profile, in particular, when the melting layer is at lower altitudes. This may not be a problem in regions where the melting level is at higher altitudes, but it is a real problem in regions such as the UK. Polarimetric radar measurements offer the possibility to classify hydrometeors (See Section 8.1), which provides the possibility of applying different rainfall estimators within the rain region. However, the difficulty still remains in estimating rainfall rates in snow and melting snow. It is concluded that polarimetric radar measurements potentially provide important advantages over the conventional reflectivity factor. Such advantages have to be exploited in the best way to improve the estimation of precipitation from weather radars and its quantitative use in operational hydrology.

Chapter 3

The high-resolution vertically pointing weather radar for atmospheric research

3.1 Introduction

This chapter describes the hardware and software characteristics of a low-power high-resolution X-band Vertically Pointing weather Radar (VPR) system for atmospheric research. The data set obtained from this VPR have been used for the development of this thesis. The VPR system has been used since 1991 and new real-time acquisition software has been written in order to obtain more accurately the reflectivity signal. The fluctuations of the echo intensities have been analysed to obtain an estimate of the accuracy of the standard error[1] associated when averaging N independent samples. The possibility has been explored of using real-time digital filters to reduce the high-frequency noise of the reflectivity signal when fast data acquisition is required.

3.2 Hardware characteristics

A VPR provides the capability to study the variability of the vertical reflectivity profile of precipitation. An X-band radar transceiver was originally designed by Racal Decca Ltd as a marine navigation device (Racal, 1988). This device was adapted for meteorological applications by the Radar Weather Observatory of McGill University, Montreal, Canada. In 1991, a new device was built and commissioned by the Water Resources Research Group

[1]The standard deviation is commonly called the standard error (See Rice, 1995).

Fig. 3.1: Bristol X-band vertically pointing weather radar.

at Salford University in association with McGill University for use in a vertically pointing mode (Tilford and Cluckie, 1991). The components were shipped from Canada and they were assembled at Salford University.

Initially, the VPR was mounted on the north-east corner of the roof of the Civil Engineering Department's Telford Building (Tilford and Cluckie, 1991). Later in 1994, two further devices were designed and built with identical hardware to the previous VPR, but mounted on a new trailer system (Tilford et al., 1995b; Cluckie et al., 2000). This fully mobile capability combined with a portable power generator allows the VPR to be deployed anywhere (See Fig. 3.1).

The VPR consists of the aerial system, the transceiver unit and the data acquisition system; the technical specifications of each subsystem are explained in detail in the following sections (See Table 3.1).

Aerial system	
Antenna diameter	1.2 m, parabolic reflector
Beamwidth at half power	1.8 degrees
Antenna relative gain	38 dB
Polarisation	Horizontal
Transmitter	
Radar frequency	9380-9440 MHz
Wavelength	3.2 cm (X-band)
Mean power supplied to antenna	12 dBW
Peak power	44 dBW (25 kW)
Pulse width	$0.05^{\dagger}$, $0.25^{\ddagger}$, $1^{\star}$ μs
Pulse repetition frequency	$1300^{\dagger\ddagger}$ and $650^{\star}$ Hz
Receiver	
Type	Logarithmic with balanced mixer
Tuning	Manual
Noise factor	Better than $10.5^{\ddagger\star}$ dB
IF	Centred on 60 MHz
IF bandwidth	$20^{\dagger}$ MHz and $4^{\ddagger\star}$ MHz
Acquisition system	
Sampling frequency	20 MHz
Spatial resolution	7.5 m
Temporal resolution	1 s
Averaged samples	256 pulses with 2048 data points

Table 3.1: Technical specifications of the Bristol X-band vertically pointing weather radar (After Tilford and Cluckie, 1991; Racal, 1988).

3.2.1 The aerial system

The aerial system comprises the antenna, which is a metallic paraboloid reflector. The paraboloid shape of the antenna produce a pencil beam, which is commonly used to measure the angular position of a target in both azimuth and elevation (Skolnik, 1980), being a suitable feature to detect precipitation echoes. The diameter of the antenna combined with the wavelength of the radar establishes the beamwidth, which is approximately 1.8° for this device.

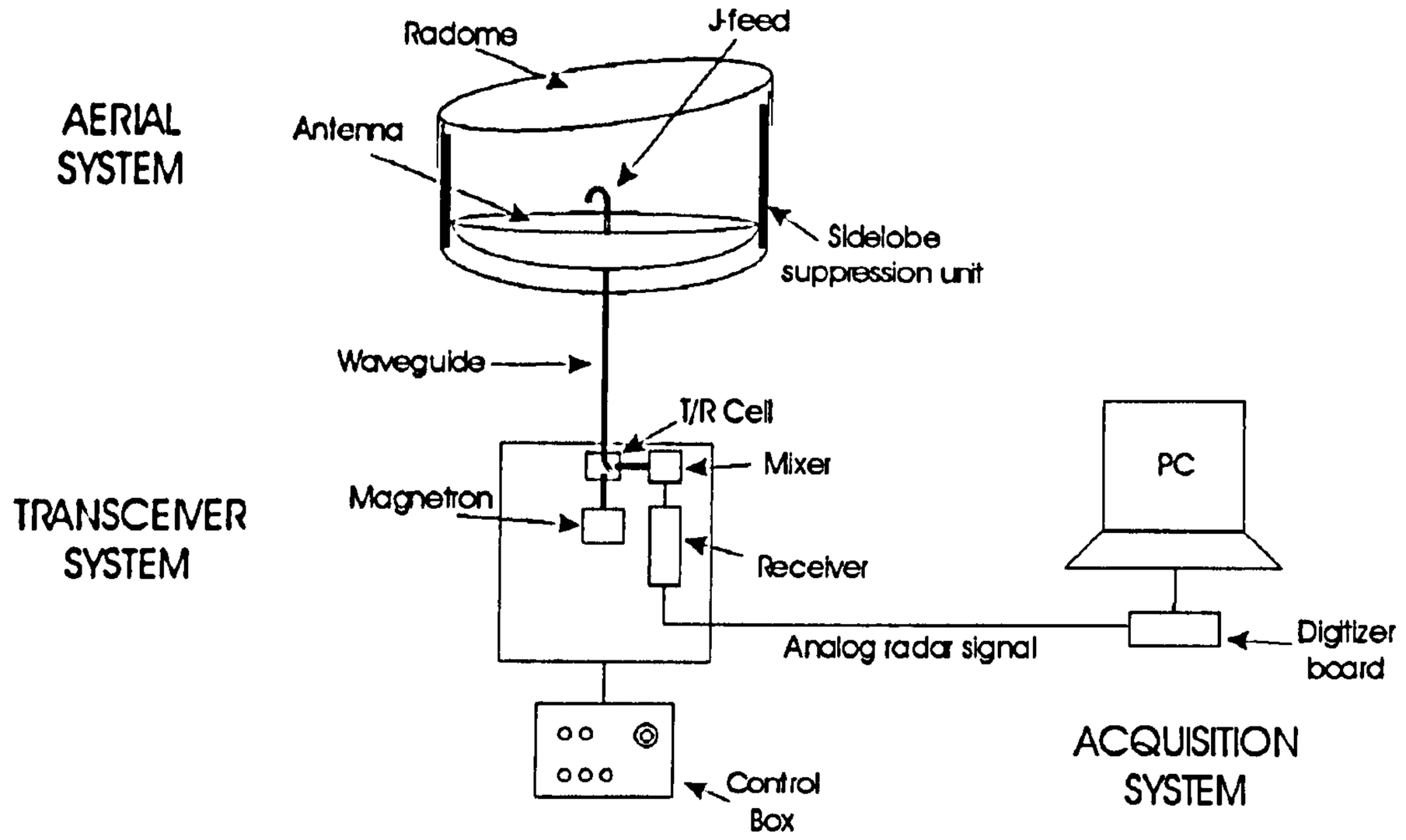

Fig. 3.2: Schematic representation of the VPR system.

The antenna is housed within a sidelobe suppression unit (See Fig. 3.2). This unit is coated on the inside with a foam substance designed to absorb the power from the sidelobes, which are typical of the antenna radiation pattern and could cause clutter echoes due to scattering from surrounding buildings. The antenna is inlayed approximately 75 cm into the sidelobe suppression unit. This unit is covered with a radome fabricated with a rubber-like material transparent to the microwaves to protect the antenna from the weather. During the first tests of the VPR at Salford, the radar signal presented strong echoes in the lowest 500 m. This effect was attributed to the accumulation of a layer of water on the radome due to its horizontallity (personal communication, Prof. Ian Cluckie). The problem was solved by tilting the radome a gradient of 10% and reducing at the same time the attenuation effects that precipitation echoes may suffer at long ranges due to the same layer of water (Tilford and Cluckie, 1991). The antenna itself has drainage holes to prevent the building-up of any water that may enter.

3.2.2 The transceiver

The transceiver comprises the circuits which generate the transmitted pulses and receive the echoes from precipitation (See Fig. 3.2). The high power microwave pulses are generated in the magnetron, an incoherent device, which means that the phase of the transmitted pulses is random and then no Doppler capability is obtained. The nominal frequency of the magnetron is 9410 MHz (X-band). The magnetron is connected directly through the circulator and waveguide to the J-feed which is fixed in the antenna dish. The length

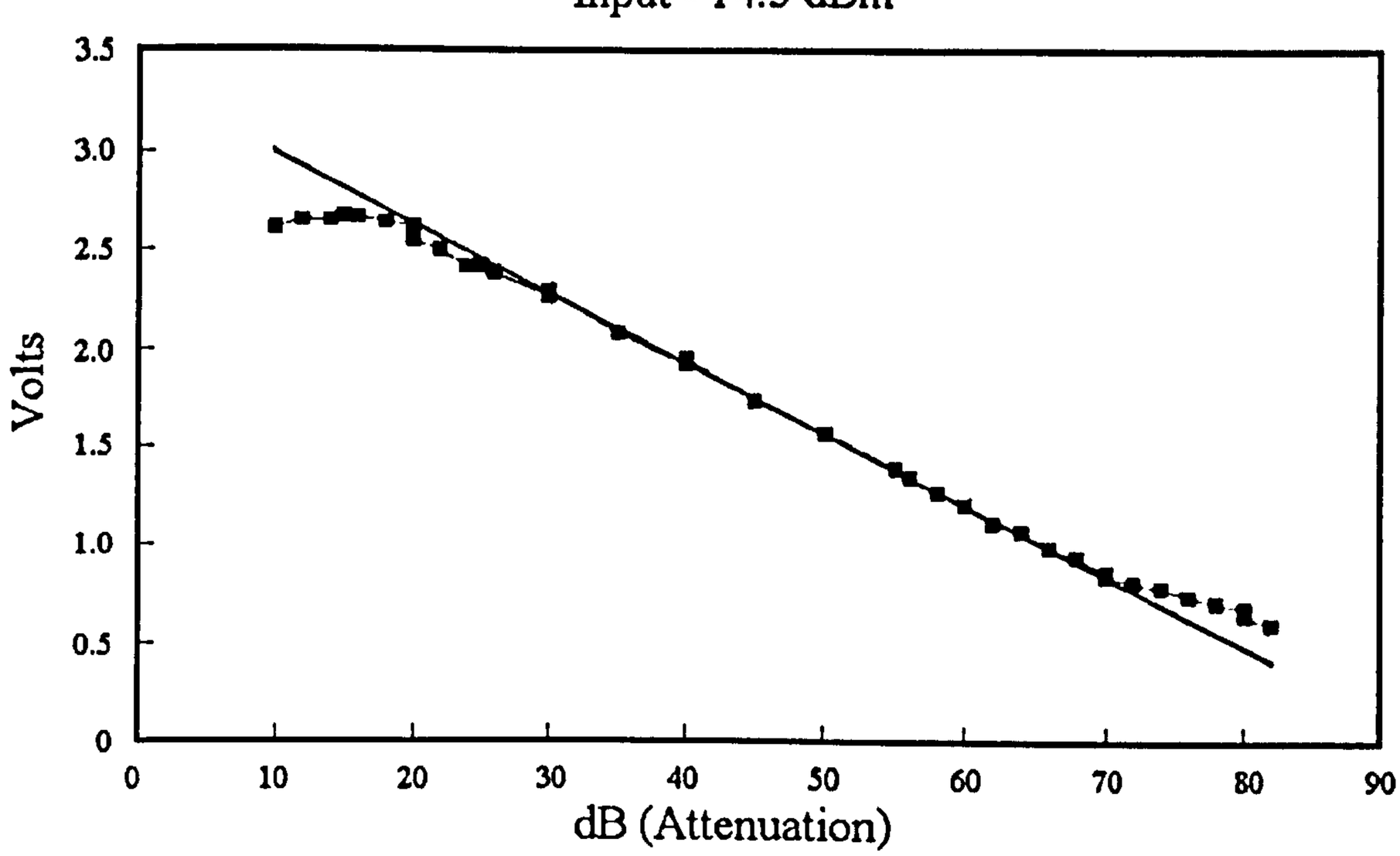

Fig. 3.3: Calibration curve for the VPR (From Duncan, 1993).

of the pulses generated by the magnetron are either 50 ηs (short pulse) or 250 ηs (medium pulse) or 1 μs (long pulse). The pulse length establishes the spatial resolution of the radar. For the short pulse the spatial resolution is 7.5 m, for the medium pulse the resolution is 37.5 m and for the long pulse the resolution is 150 m. The selection of the pulse length is through an external control box attached to the transceiver. The microwave pulses are modulated by the Pulse Repetition Frequency (PRF) which is either 1300 Hz for short pulse and medium pulse operation or 650 Hz for long pulse operation. Second or third trace echoes produced by superrefraction[2] are eliminated by a low frequency oscillator, which introduces a small sweep in the PRF giving them an irregular shape (Racal, 1988). The precipitation echoes received by the antenna go directly to the Transmit-Receive (TR) limiter, which prevents the high power of the outgoing magnetron pulses from reaching the receiver, which they would damage. The TR limiter is connected to the mixer, which combines the echo signals with the output of a local oscillator to produce an Intermediate Frequency (IF) of 60 MHz; the receiver amplifies and demodulates the IF signal to produce the radar signal (Racal, 1988). The linear response of the receiver is shown in Fig. 3.3. The local oscillator is tuned through a potentiometer attached to the external control box in order to match the frequency of the receiver therefore maximizing the strength of the echo signal (McGill, 1992). However, the tuning process is not an easy task. On a day of

[2]Superrefraction of the beam is an abnormal downward bending due to deviations in the atmospheric temperature and humidity from the standard radio atmospheric conditions. In some situations, the wave can be trapped in a duct, directing the energy long distances (Battan, 1973).

moderate rainfall rate, the potentiometer should be turned clockwise or anticlockwise in order to produce changes in the strength of the precipitation echoes. There are two ways of measuring the strength of the precipitation echoes, one of them is by maximizing the DC voltage of the terminals on the external control box and the other one is by maximizing the intensity of the averaged echo signal obtained directly through the acquisition system. Both methods are practically the same, although the second one is more reliable because the averaged signal can be taken only in the lowest 2000 m or 3000 m obtaining more accuracy. The problem of tuning is that the strength of the precipitation may change during the tuning process and there are 10 turns to cover the whole potentiometer. McGill (1992) recommends tuning the oscillator periodically, at least every month or two when the transmitter is operating in a room of constant temperature and weekly when it is operating in the field because the tuning is temperature dependant. One obvious improvement could be automatic tuning, which can be carried out by software, every time the VPR is receiving echoes at the beginning of a storm. However, this improvement would only be possible if the acquisition system was able to produce analog outputs to control the tuning.

3.2.3 The acquisition system

The continuous improvement in digital processing technology enables a huge amount of data to be processed in a relatively short period of time. The radar acquisition system comprises the A/D converter and the Personal Computer (PC) to process the precipitation echoes.

The A/D converter is a Metrabyte PCIP-Scope board which can digitize an analog signal in sets of 2048 data points with 8-bit resolution (256 levels) and with a maximal sampling frequency of 20 MHz (Keithley, 1996). This sampling frequency gives a maximal spatial resolution of 7.5 m. The digitizer board is attached to the PC as either ISA or PCI card. Providing the suitable software, the digitizer card is designed to allow the PC to be used as a digital oscilloscope. The digitizer board has two input analog channels and a third channel to connect an external trigger. There are two signals coming from the transceiver, the raw radar signal and the PRF signal to synchronize the data acquisition. While the capabilities of this digitizer board are suitable for radar signal digitization, new boards are available in the market, which offer more capabilities, such as, analog and digital outputs suitable for controlling the pulse length, switching and automatic tuning of the radar. In addition, the original Metrabyte PCIP-Scope board was to some extent sensitive to temperature changes which directly influenced the accuracy of the digitisation

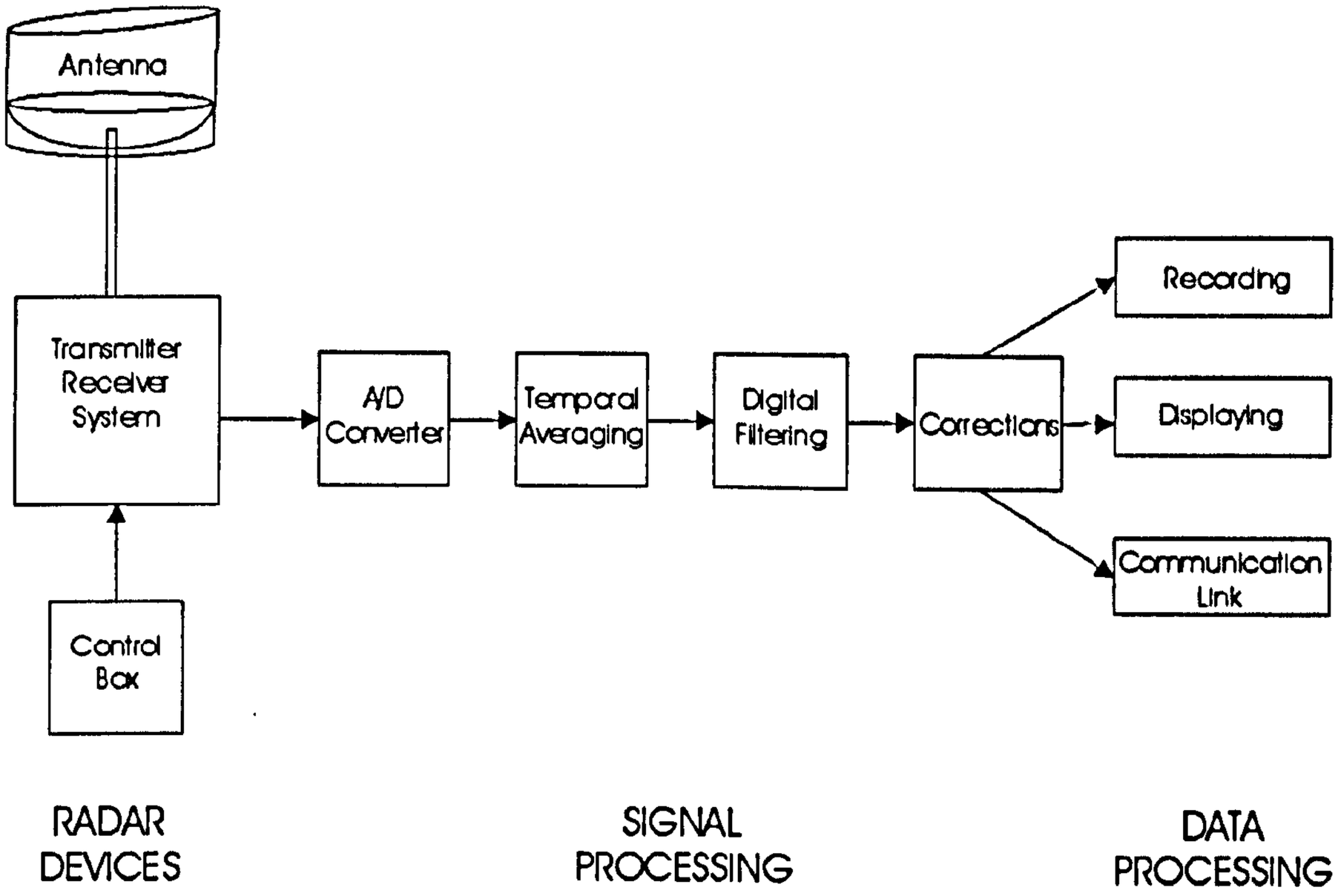

Fig. 3.4: VPR data acquisition system.

process (personal communication, Prof. Ian Cluckie).

3.3 Software characteristics

The raw signals coming from the receiver are digitized with the PCIP-Scope board and through software can be read directly from the memory locations of the digitizer board. A decade ago, the PC utilised to control the digitizer board was a 386 based-processor at 33 MHz, but with the advance and decrease of the prices in PC technology, it was replaced by a Pentium MMX based processor at 166 MHz. The speed of the processor has a big impact in the real-time digital processing of the precipitation echoes, allowing more tasks in the same period of time than a lower-speed processor. Additionally, faster-speed processors had an impact on the improvement of the data quality and provided a better understanding of the precipitation processes.

The original real-time data processing of the VPR data is described in Fabry (1994a, Chap. 2) and the acquisition software in Fabry (1994b). The software is called TRAILER and the acquisition and drawing routines were written in assembly language. Assembler is a very powerful low-level language, being the only way to tap the full power of the 80x86 processor family. A small part of the software was written in the Basic language, but the speed in this part of the code does not have any effect on the real-time data acquisition. This software runs quite fast but there were several drawbacks to the processing of the

radar signal. Additionally, there was a lack of modularity within the code, which made it difficult to add and test new real-time subroutines.

New real-time acquisition software called VIPER has been written in object oriented programming, conceptually based on the original TRAILER code. The acquisition-averaging subroutines have been written in assembler code to speed up the acquisition process. The signal processing of the precipitation echoes is divided in several blocks as shown in Fig. 3.4. The theory behind every block is explained in the following sections.

3.3.1 Averaging of N independent pulses

From radar theory, radar echoes produced by precipitation show fast fluctuations in the returned signal. These fluctuations are due to the movement of particles within the volume being examined by the radar beam (Battan, 1973). The average power reflected back to the radar must be computed over a sufficient number of uncorrelated samples, ensuring the microphysics of precipitation has not changed between consecutive samples. The averaging of independent samples is important in order to obtain accurate values of reflectivity increasing the Signal to Noise Ratio (SNR) (Keeler and Passarelli, 1990). Battan (1973) proposed a period of approximately 10^{-2} s to have independent samples. The most common averaging technique is the uniformly weighted average over a fixed number of independent samples. The averaging must be carried out in the power reflected, P_r. However, the receiver of the VPR uses logarithmic detection in order to increase the dynamic range of the radar, so the power reflected is proportional to $\log(P_r)$ instead of P_r. Therefore, it is required to convert each sampled logarithmic value to a linear power before averaging. An efficient way of doing this is using a look-up table, in which each log value has its corresponding antilog value in order to speed up the process. On the other hand, averaging in the logarithmic domain is easier and faster, but introduces a systematic bias in the estimation of the average power (Goddard et al., 1994). This bias can be around 2.5 dB for Rayleigh-distributed targets (Keeler and Passarelli, 1990). Using a look-up table for the estimation of the antilogarithm of $\log(P_r)$ is difficult because the estimation of $\log(P_r)$ must take into account the receiver calibration shown in Fig. 3.3. From this figure, a level of voltage delivered from the receiver corresponds to a certain value of $\log(P_r)$. Such a calibration curve is linear covering a range of nearly 60 dB, but there is a significant non-linearity at low/high received power (low/high voltages) which should not be neglected. If a constant calibration slope is assumed for the estimation of P_r in an anti-logarithmic look-up table, there will be an error associated with the extremes of received power. This error is embedded in P_r, which will be averaged with N more

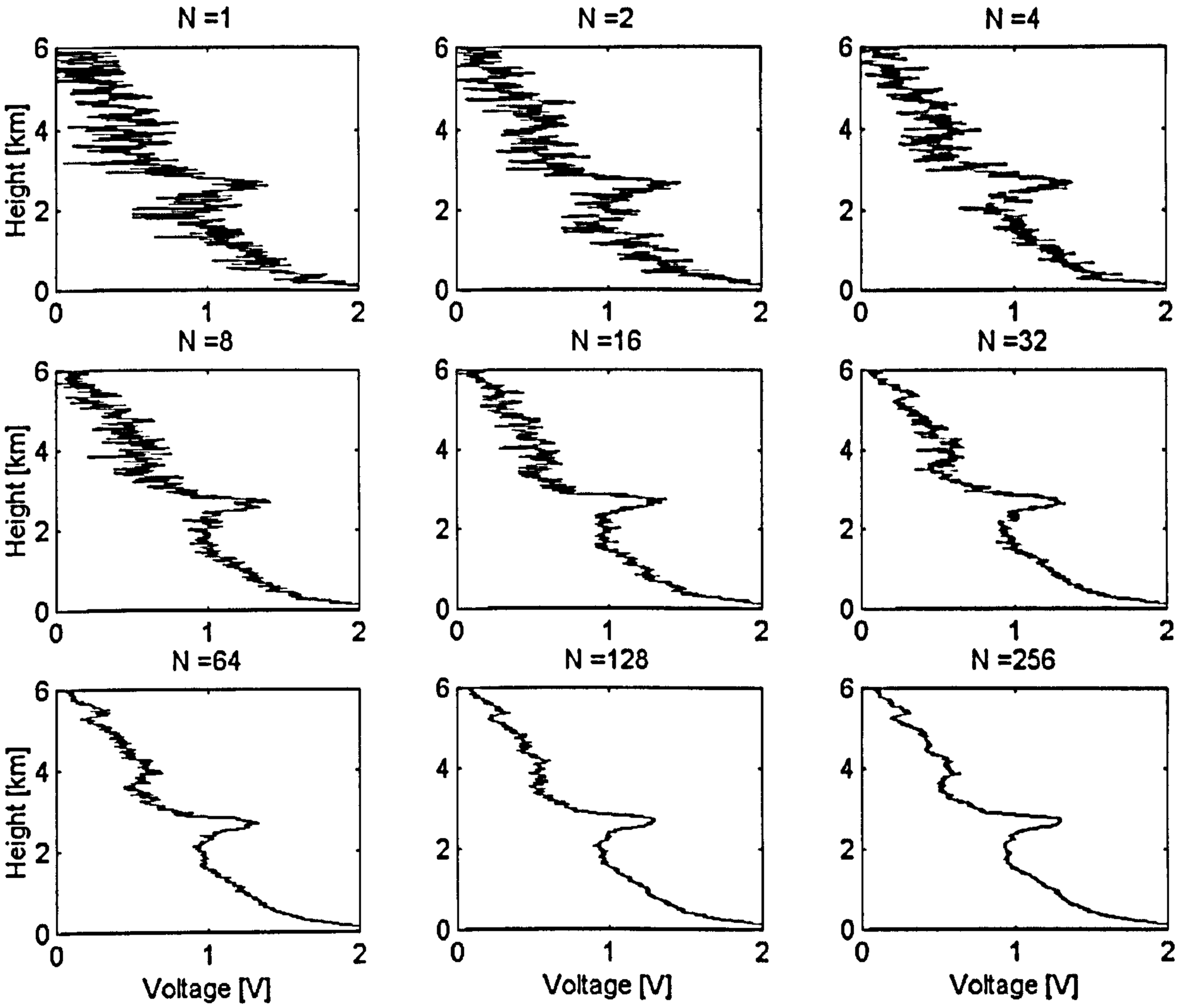

Fig. 3.5: Effects of averaging N independent samples from precipitation echoes measured with a VPR. The time interval between successive samples is 2.5 ms. The power reflected is related with the calibration curve shown in Fig. 3.3.

independent values. The result is an estimate of $\bar{P}_r$ which is heavily influenced by the calibration curve. On the other hand, if the averaging is carried out in $\log(P_r)$ - in the voltage domain - the value of $\bar{P}_r$ is calculated in the last stage, even when it is assumed to have a constant calibration slope, but there is always the possibility to recover the original signal. If the non-linearities are taken into account, they should be defined accurately by proper calibration and have an intensity-dependent correction. Therefore, the averaging is carried out in $\log(P_r)$ rather than in P_r, introducing a bias into the system, but avoiding the accumulative error from the non-linearity of the calibration curve. According to Collier (1996), a factor of +2.5 dB must be applied to the averaged radar signal to compensate for the averaging in the logarithmic domain.

The averaging routine has been implemented in assembly language for performance. The new data are read directly from the digitizer board memory. The number of independent pulses (N) to average is defined to be a power of 2, that is $N = 2^k$, where k is

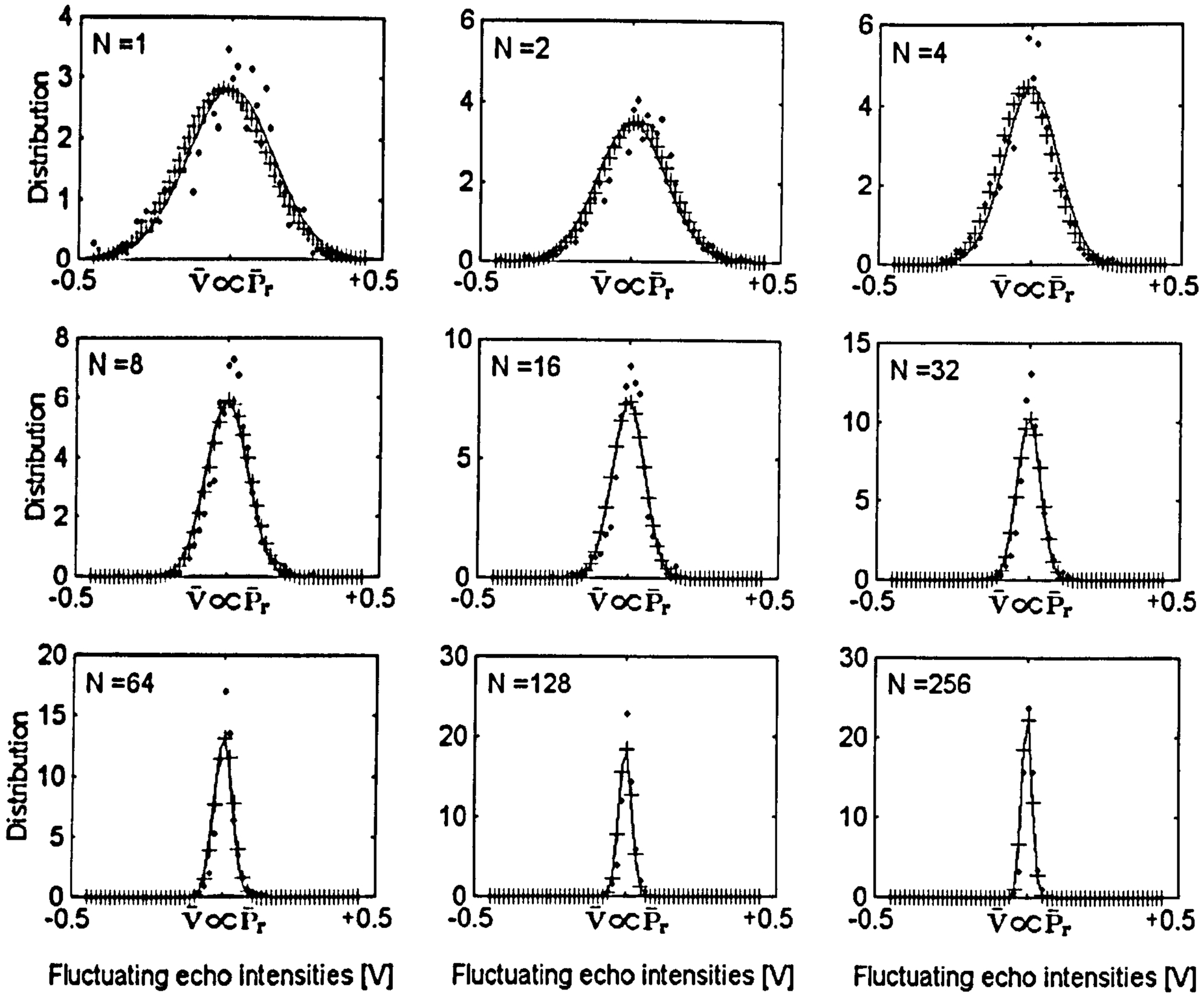

Fig. 3.6: Distributions of the fluctuating echo intensities for different number of averaging samples. The points represent the real distribution of the fluctuating echo intensities (the mean is μ_0 and the standard deviation is σ_0); the crosses represent the Gaussian distribution of the fluctuating echo intensities assuming $\mu = \mu_0$ and $\sigma = \sigma_0$; the solid line represent the Gaussian distribution assuming $\mu = 0$ and $\sigma = \sigma_0$. All the distributions integrate to 1.

an integer value between 0 and 10. In this way, the division to compute the averaging is avoided and the averaged value is obtained by performing a rotation of k bits to the right. The acquisition-averaging process of 256 independent arrays with 2048 samples takes around 650 ms in a Pentium-based processor at 166 MHz, being approximately 2.5 ms the time interval between successive samples. Fig. 3.5 shows the effect of averaging N pulses. Although the decorrelation time is 2.5 ms, compared with the rain decorrelation time of 10 ms, the effects of noise have been reduced considerably with a small number of samples. In order to estimate quantitatively the noise reduction, it is possible to assume that the true profile of precipitation is the one obtained averaging 512 pulses. By subtracting the true profile from every profile shown in Fig. 3.5 is obtained a distribution of the fluctuating precipitation-echo intensities for different number of averages. The distributions are shown in Fig. 3.6. From probability theory, a distribution is approximately

Gaussian when a random variable is the sum of a large number of independent random variables (See Rice, 1995). This type of distribution is observed in Fig. 3.6. It is interesting to note that the distribution of the fluctuating echo intensities can be represented as a Gaussian distribution with approximately zero mean and a standard deviation σ that depends on the number of independent samples being averaged. Marshall and Hitschfeld (1953) developed the theory of fluctuating echoes from randomly distributed particles. They found that when the number of independent samples exceeds 10, the distributions are Gaussian. However, Fig. 3.6 suggests that the distributions of the fluctuating echo intensities are Gaussian even for a small number of averages. From the definition of the Gaussian distribution (See Appendix C.1), it can be shown that the probability distribution of the fluctuating echo intensities can be approximated by:

$$f(A) = \frac{1}{\sigma\sqrt{2\pi}} e^{-A^2/2\sigma^2} \tag{3.1}$$

where A is the fluctuating echo intensity, and σ is the standard error related to the number of independent samples. Linear regression analysis between N against σ for 50 different events reveals that the standard error associated with the fluctuations of the echo intensities is estimated by:

$$\sigma = 0.1421 N^{-0.3883}; \qquad \text{V} \tag{3.2}$$

where N is the number of pulses with a time interval between successive pulses of 2.5 ms. Assuming a calibration slope of 27.63 dB/V (From Fig. 3.3), the standard error is estimated by:

$$\sigma = 3.9250 N^{-0.3883}; \qquad \text{dB} \tag{3.3}$$

Eq. 3.3 is plotted in Fig. 3.7. This equation is important because it allows a compromise to be found between the temporal resolution of the averaged data array and the reduction in error of the fluctuating echo intensities. The higher the number of independent arrays to be averaged, the lower the standard error associated because of the fluctuating echoes, but there is an increase of the processing time by a factor of $2.5N$ ms. For instance, 256 independent arrays gives a standard error of 0.45 dB or approximately 16.49 mV (Eq. 3.2). However, the resolution of the digitizer board is 15.62 mV (full scale is 4 V with 256 levels), and in order to reduce further the standard error, it is necessary not only to increase the number of independent samples to be averaged, but also the resolution of the board, *e.g.* to either 12 or 16 bits. It is concluded that 256 arrays, with a time interval between successive

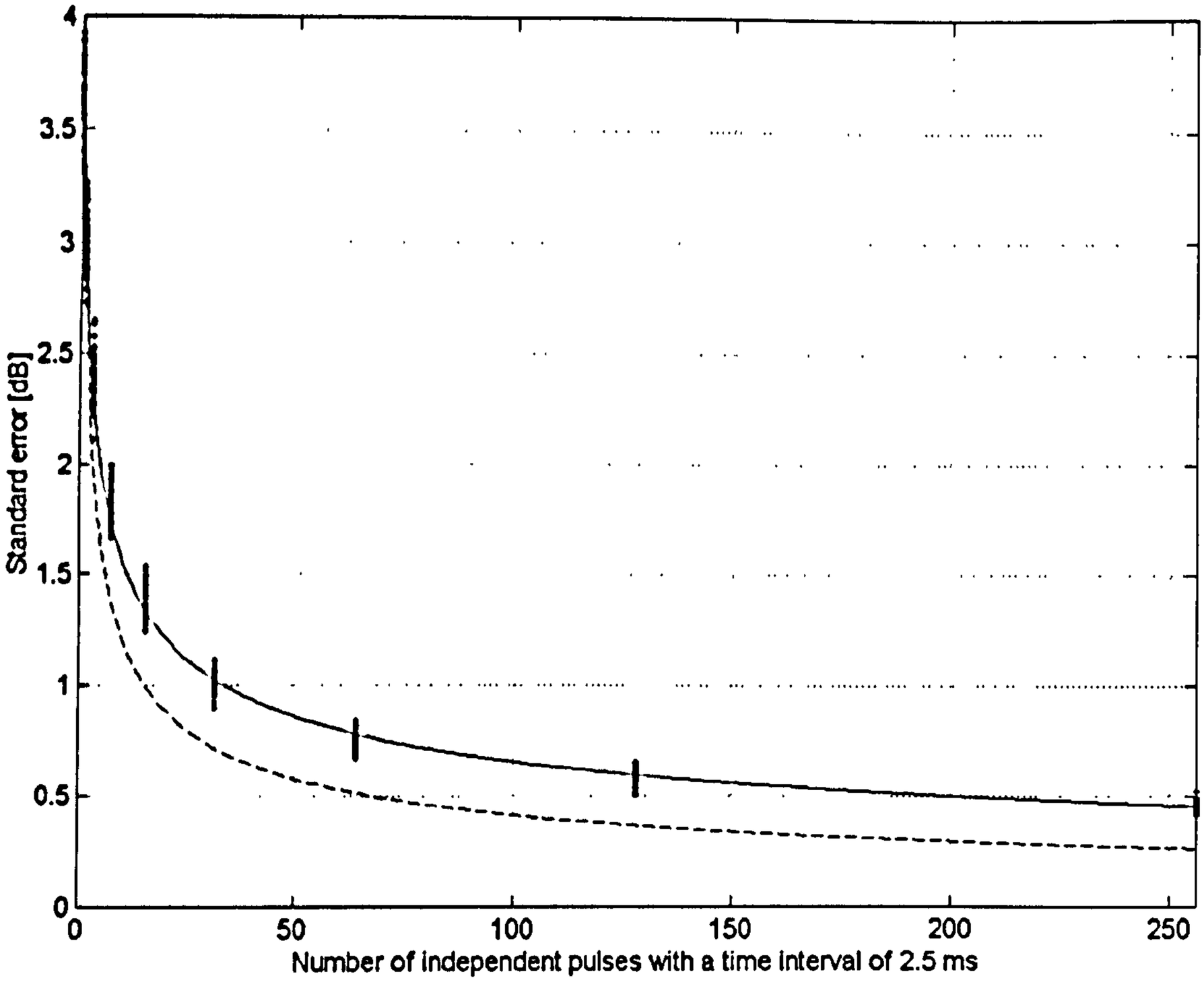

Fig. 3.7: Standard error of the fluctuating echo intensities for different number of averages. The solid line represents the empirical error with a time interval between successive pulses of 2.5 ms (Eq. 3.3, r=-0.9965) and the dashed line represents the theoretical error assuming uncorrelated samples, that is, $\sigma[\hat{\bar{P}}(\mathrm{dB})] \approx 10\log_{10}(1 + 1/\sqrt{N})$ (Bringi and Chandrasekar, 2001).

pulses of 2.5 ms, give the best quality of the precipitation signal, reducing the standard error of the fluctuating echo intensities up to 0.45 dB. However, a future modification which could have a significant impact would be to migrate to a 12 or 16 bit digitizer.

3.3.2 Correction for AC coupling

The averaged radar signal is AC coupled because of the characteristics of the radar receiver. AC coupling means that the average voltage of the radar signal for a single pulse is 0 Volts causing it to undergo a voltage shift (See Fig. 3.8). The original method in TRAILER to correct the voltage shift was inaccurate, revealing jumps between consecutive average radar signals. A new correction scheme has been implemented in order to locate the true base level more accurately. At 15 km above the ground, there are no echoes from precipitation and the voltage values obtained from the radar receiver at this height represent the true base level. However, small fluctuations of the echo intensities can introduce further errors when determining the base level. Averaging over a depth of 1 km at 15 km above the ground was found to be sufficient to obtain an accurate base level. Once this level is

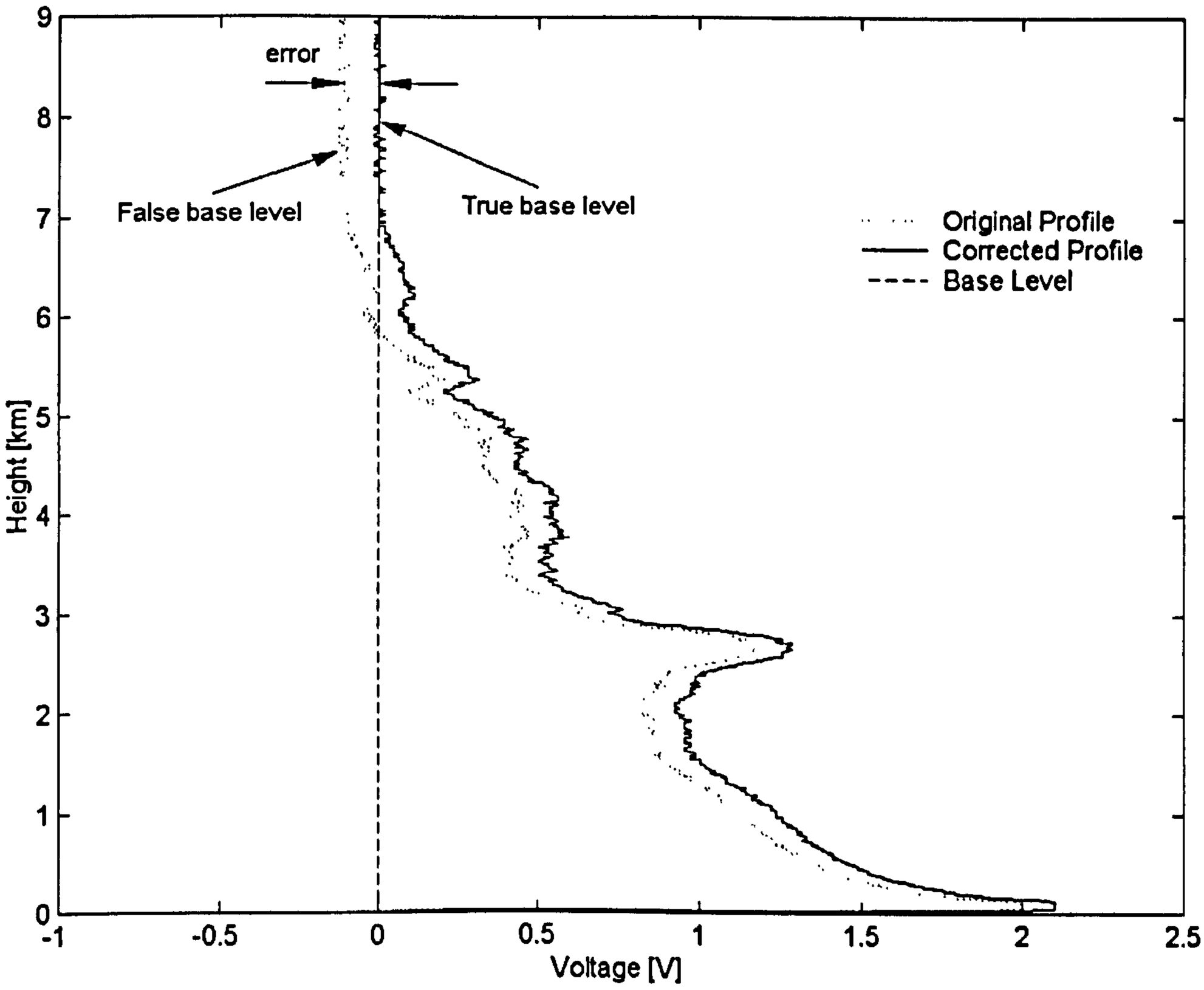

Fig. 3.8: True base level for AC coupling correction of VPR data.

obtained, the correction is applied by adding the estimated base level to the averaged radar signal. The correction for AC coupling must be done to every averaged radar signal. Fig. 3.8 shows the effect of applying this correction. In this example, the estimated error caused by the AC-signal characteristics is approximately -3.5 dB.

3.3.3 The minimum detectable signal

The averaging of N independent samples reduces considerably the noise caused by the fluctuating nature of precipitation echoes but, does not completely eliminate it. The noise energy limits the ability of a radar receiver to detect a weak echo signal, because both signal and noise occupy the same portion of the frequency spectrum (Skolnik, 1980). There is therefore a level called *minimum detectable signal*, which has been reduced considerably with the averaging, but some fluctuations still remain around the base level that result from noise rather than from precipitation. Selecting a low threshold increases the likelihood that noise would be mistaken for a real signal, but too high means that some echoes from precipitation would be missed. The fluctuating echo intensities of the noise follow the

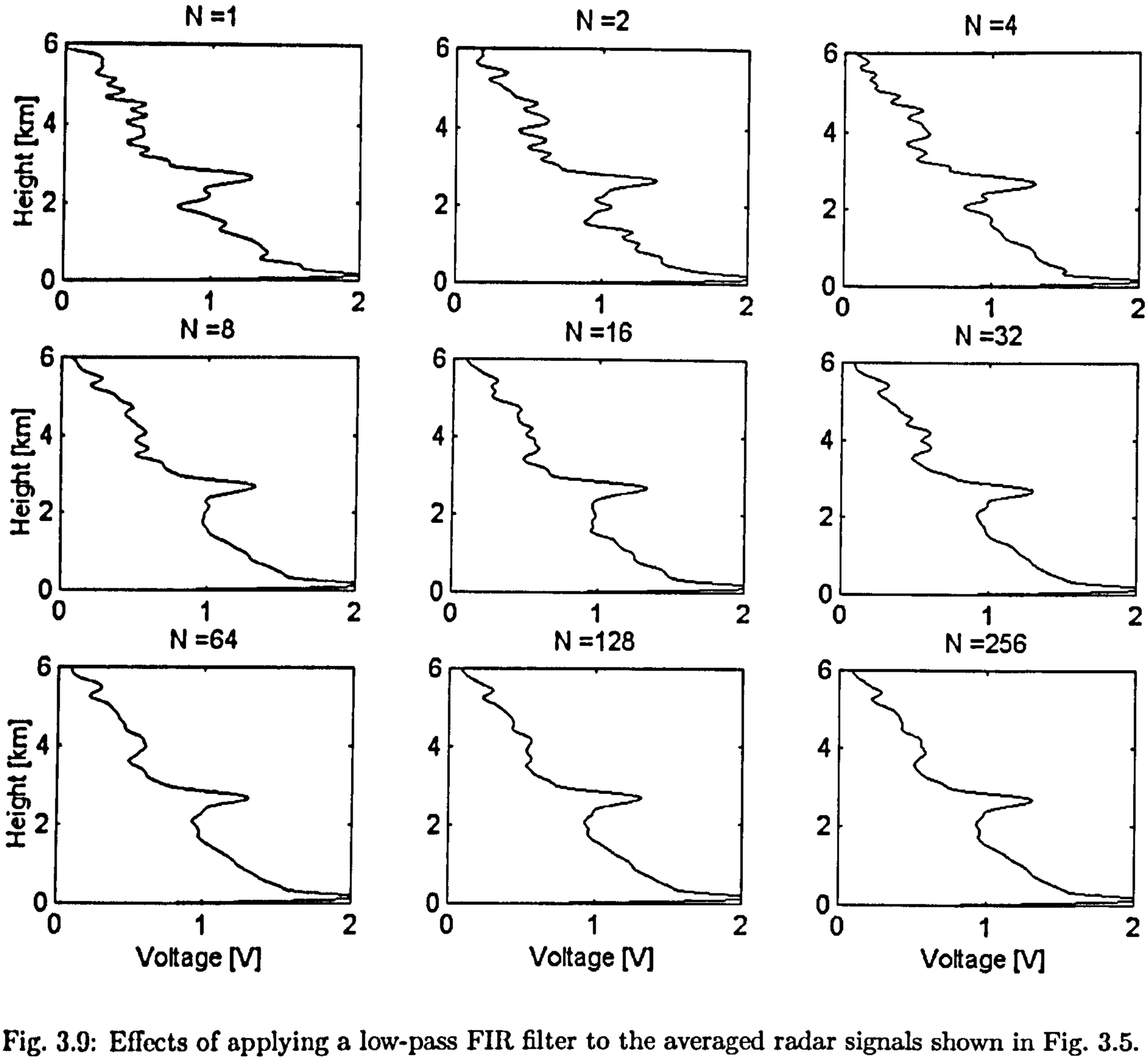

Fig. 3.9: Effects of applying a low-pass FIR filter to the averaged radar signals shown in Fig. 3.5. The quality of the signals has been improved considerably, reducing the effects of the echo fluctuations even when the number of independent samples is low.

same distribution given by Eq. 3.1. Depending on the number of independent arrays, the value of σ is given by Eq. 3.2. A threshold of one σ includes 68% of the fluctuating echo intensities of the noise, 2σ includes 95% and 3σ includes 99%; therefore, by choosing a threshold of 2σ guarantees that 95% of the noise at low levels of voltage is avoided. For instance, with 64 independent samples, the minimum detectable signal obtained is at 56.53 mV and all the values obtained below or equal to this level are neglected and equal to the base level (0 V). TRAILER utilises a threshold defined by the user, which is affected by the correction for AC coupling. VIPER utilises the improved algorithm.

3.3.4 Digital filtering

The averaging of N independent samples reduces considerably the effects of the fluctuating echo intensities and the inherent system noise. However, in applications where shorter temporal resolutions are required, digital filtering techniques can improve the quality of

the radar signal. For instance, a scanning weather radar system requires fast scanning at several elevation angles over a huge area. In such cases, the averaging intervals have to be reduced for real-time operation. Even when fast acquisition systems are used in the digitation process of the radar signal there will always be the constraint of averaging non-correlated samples. Therefore, real-time digital filtering techniques are proposed to reduce the standard error associated with the fluctuations of precipitation echoes when the number of independent samples being averaged is limited. Digital filters do not eliminate the averaging of independent samples, but they reduce the error associated with the fluctuations when the averaging is carried out over a limited number of samples.

Appendix B presents one of the techniques employed to design a digital filter. Providing the suitable cut-off frequency to smooth the radar signals, the filtering subroutine has been implemented in the VIPER software for real-time operation. Fig. 3.9 depicts the radar signals shown in Fig. 3.5, but smoothed with a low-pass FIR filter. There is a noteworthy improvement in the quality of the radar signal because the high-frequency variations of the fluctuating echo intensities have been significantly reduced with the filtering. It is important to take into account digital filters as a possible alternative way of reduction of the standard error of the fluctuating echo intensities when fast scanning is required.

Other applications of the digital filters described in Appendix B are in clutter suppression algorithms, as high-pass filters, in order to achieve attenuation of up to 40 dB in the low-frequency components (Keeler and Passarelli, 1990), but these uses are out of the scope of this research.

3.3.5 Measurement of the equivalent reflectivity factor

The calculation of reflectivity in the VPR is based on the Rayleigh approximation, where the radii of the hydrometeors should be much smaller than the radar wavelength (Battan, 1973). Using this assumption, the Mie backscattering cross section of a spherical rain drop is reduced to the sixth power of the particle diameters. However, at X-band frequencies, with a wavelength of 3 cm, questions arise with the validity of this approximation for large scatterers. In the bright band, for instance, large aggregates are found (Barthazy et al., 1998) and the Rayleigh approximation may be no longer valid.

The power reflected back to the radar is given by (From Section 2.5.3):

$$\bar{P}_r = \frac{C|K|^2 Z}{r^2} \tag{3.4}$$

where C is a constant dependent on the characteristics of the radar, $|K|^2$ is the dielec-

tric constant[3] of the hydrometeors, Z is the reflectivity factor and r the range from the radar to the scatterer.

Applying the logarithm to both sides of Eq. 3.4, it follows that:

$$10\log\bar{P}_r = 10\log(CK^2) + 10\log Z - 10\log r^2 \tag{3.5}$$

and the equivalent reflectivity factor in dBZ units is given by:

$$10\log Z = 10\log\bar{P}_r + 10\log r^2 - 10\log C - 10\log|K|^2 + 180 + 2.5 + X_{dB} \tag{3.6}$$

The first term in Eq. 3.6 is the average power reflected back to the radar and it is given by:

$$10\log\bar{P}_r = m_c\bar{V} + b_c \tag{3.7}$$

where $\bar{V}$ is the averaged raw voltage coming from the receiver and m_c and b_c are related to the calibration curve of the receiver (See Fig. 3.3). The calibration slope of the receiver (m_c) is approximately 27.63 dB V^{-1}. The second term in Eq. 3.6 is the range correction; the third term is constant and dependent on the radar characteristics; the fourth term is the dielectric constant of the hydrometeors and it is taken to be 0.93 for water (Battan, 1973); the fifth term is a factor that must be added to obtain $mm^6\ m^{-3}$ rather than $m^6\ m^{-3}$; the sixth term is the correction factor that must be added because the averaging is over the logarithm of the power reflected rather than over the power reflected; the seventh term is a correction factor to calibrate reflectivity measurements with other radar including system losses.

To speed up the real-time acquisition process, a look-up table with a value equal to the sum from the second to the seventh term of Eq. 3.6 is built. Every element of the look-up table, is the additive correction for an echo found at a range r from the radar.

3.3.6 Data compression and storage

There is a need for data compression before any data storage takes place. Assuming the VPR gets around 1400 samples (with a maximum resolution of 7.5 m) every second, and the size of every sample is 1 byte, the data supply is 1400 bytes per second; in one day of data, it is around 115 Megabytes of information. However, there is no need for

[3]The value of the dielectric constant depends on the complex index of refraction of the medium. For water is approximately 0.93, but for ice is 0.197 (Battan, 1973).

data storage in periods when it is not raining. Then, algorithms for data compression are quite important in order to optimize the storage capacity. According to Keeler and Passarelli (1990), there are two ways of compressing precipitation data; one of them is by keeping the data obtained at altitudes lower than the tropopause discarding any data above it. However, 1400 samples with a resolution of 7.5 m per sample cover 10.5 km in the vertical, which is just below the tropopause. The other way is by using a run length encoding algorithm, which compress strings of data having the same value. TRAILER had a compression algorithm to suppress the zeros (no echo condition) from the data set (McGill, 1992; Fabry, 1994b). This is based on the fact that regions with no precipitation usually contain long strings of zeros. When one region of no precipitation is found, the compression is carried out in two bytes, the first byte containing a 0 value which will indicate the beginning of compression and the second byte containing the number of zeros that were compressed. This compression algorithm is quite useful and valuable and reduces the file size by around 70% in a day of moderate precipitation. Better compression could be achieved by encoding strings of the same value, but it will be dependent on the type of precipitation being measured. If large variations are found in the vertical, as in the case of convection, the algorithm rather than compressing will be increasing the amount of information to be stored. Then, attention must be focused when higher ratios of compression are needed. Another point to take into account is that because the compression algorithm runs in real-time, it needs to be fast and easy to implement. It was therefore concluded that the zero-suppression algorithm is quite useful when compressing weather radar data and this was deployed in the VIPER code.

With the advance of magnetic recording technology, the data transfer rate in hard drives has also improved considerably, reaching around 100 MBps. However, in order to estimate the average time that a hard drive takes saving information, there are other factors that control the performance of the hard drive, such as the seek time and latency. The seek time is the time that a drive takes to position its Read-Write (R/W) heads over the tracks; typical values are around 8 ms. The latency is the settling time of the R/W head; for a typical 7200 RPM drive it is just less than 8 ms. The sum of the seek time and latency is the access time. With the current technology, if around 1.4 KB of data must be recorded every second, the average time spent by the hard drive saving that information is around 16 ms. Thus, with the current technology, hard drives are fast enough to record a number of VPR samples in real-time.

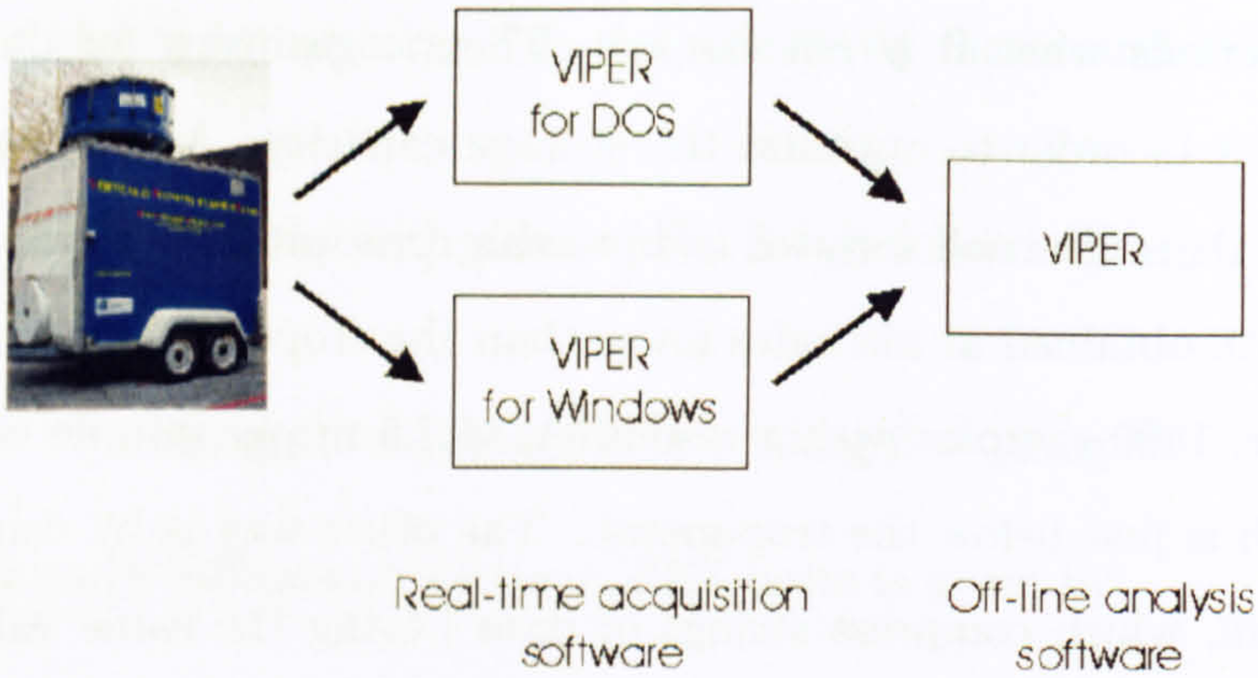

Fig. 3.10: Software developed for the acquisition and analysis of VPR data.

3.4 Software developed

3.4.1 Real-time acquisition software

Taking into account all the processing tasks discussed in Section 3.3, two different real-time applications have been developed to acquire VPR data. One of the applications runs under Microsoft Windows (MW) and the other under DOS (See Fig. 3.10).

Regarding the application running under MW, there are some support files on the web site of the board-manufacturer[4], which include an ActiveX (formerly OLE) custom control to interface the digitizer board with the applications being developed under MW. The ActiveX control packages all the functionality of the digitizer board in a very simple programming model. The ActiveX control is a low-level device driver that can be used with high-level languages as Visual C++ or Visual Basic. The applications using the ActiveX control run as two parallel tasks: the application runs as the foreground task while the ActiveX control runs as the background task in parallel with the digitizer board. In this way, the foreground task may be doing the digital signal processing while the background task is acquiring new data. The foreground and background tasks are synchronized using MW events. The MW events are messages, which indicate the finalization of some given activity, *e.g.* the acquisition of 2048 samples. When an event occurs, the application responds to the event by briefly suspending its current task and executing some specific code to process the new data. This is the principle of the event-driven multitasking environment under MW. There is a specific time interval over which the ActiveX control will check the hardware status, *e.g.* the end of data acquisition. The lowest interval that can be set is of 1 ms. However, doing some tests with a PIII based processor at 800 MHz the maximal interval obtained was of 10 ms. This polling interval is sufficient to acquire

[4]http://www.keithley.com.

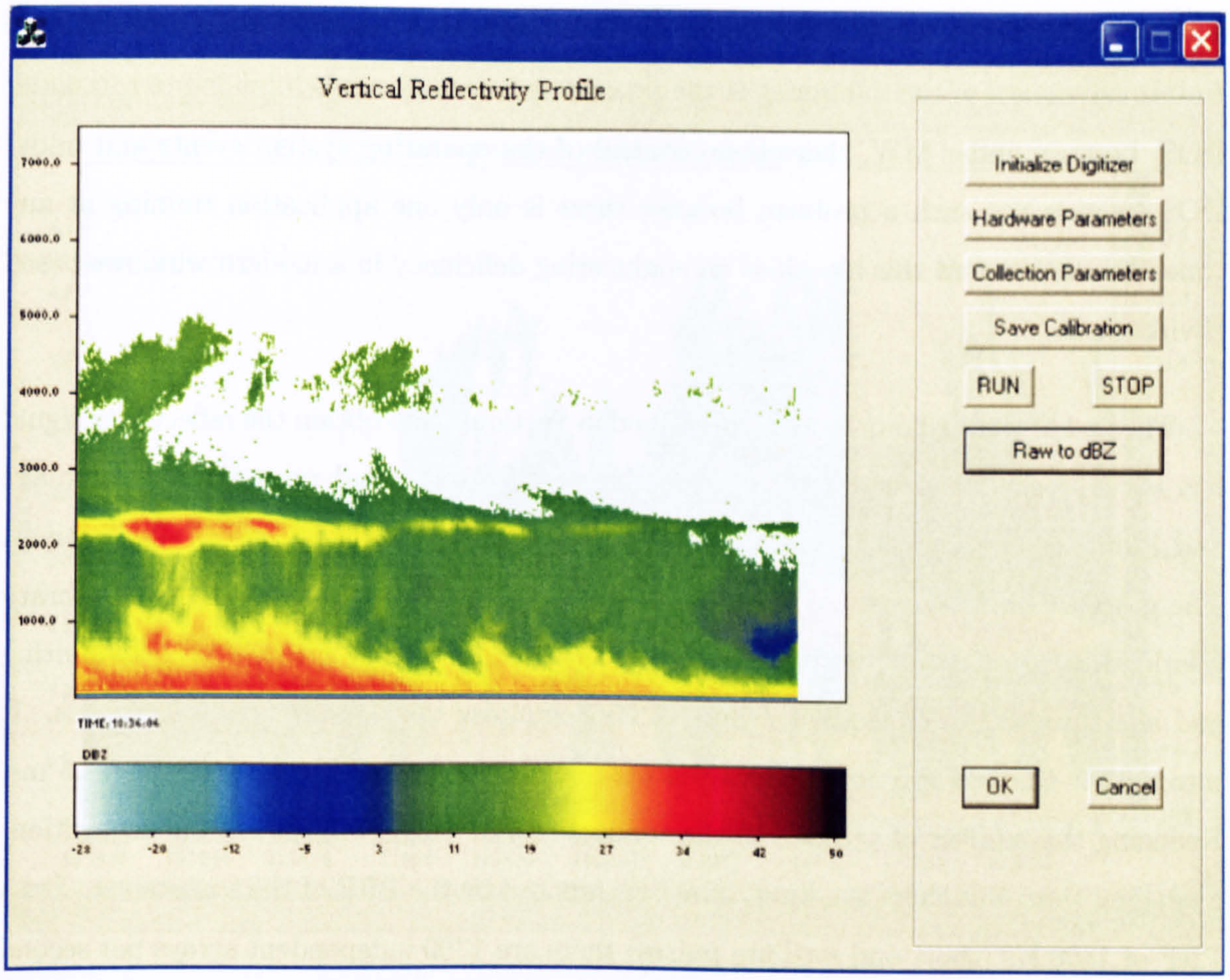

Fig. 3.11: Real-time VPR data acquisition software (VIPER for Windows).

precipitation echoes according to Battan (1973), but unfortunately it is dependent on the processor speed. In the Pentium MMX based processor at 166 MHz, the polling interval is around 50 ms. Additionally, there are many sources of events such as, mouse movement and clicking, keyboard, etc., which are running in parallel with the system. Every event has a priority, depending of how important it is in the system. But, more alarming than dependency on processor speed is the lack of predictability of MW events. Then, under MW it is difficult to control with accuracy the time taken to average N independent arrays. In Fig. 3.11 is shown the application running under MW, averaging 128 samples.

A second type of data acquisition software has been developed under the DOS environment. It follows what Fabry (1994b) stated: *"Every time I had to choose between elegance and speed (either programming or execution), speed was the winner"*. Then, the only way to tap the full power of the processor, is programming the acquisition code in a low-level language such as assembler. However, there is no need to program the whole software in assembly language. The most important subroutine in a weather radar acquisition system are the data acquisition and averaging of N independent arrays. For this reason, the acquisition-averaging subroutine has been written in assembly language (See

Appendix A), which can be easily linked to C++, Basic or some other high-level language to take advantage of the full power of the processor. The software is intended to run under DOS, because under MW, there is no control of the operating system events and under DOS there is not such a problem because there is only one application running at any time. To some extent this identifies an engineering deficiency in a modern windows-based environment.

The rest of the signal processing described in Section 3.3 to obtain the reflectivity signal has been programmed under C++, which is an object oriented programming language and it makes it easier than the Basic or C standard to develop complex applications. The graphics environment has been developed with the help of the Turbo C++ library (Borland, 1990). Several parameters can be modified in real-time, but in general, acquiring and averaging 256 independent arrays of 2048 samples takes approximately 650 ms. It means that the average time interval between successive pulses is approximately 2.5 ms. Reducing the number of samples in the vertical (*e.g.* < 2048) will reduce the acquisition-averaging time, but there is a limit, which is imposed by the PRF of the transceiver. For a PRF of 1300 Hz (short and medium pulses) there are 1300 independent arrays per second and for a PRF of 650 Hz (large pulse) there are 650 independent arrays per second. In theory, at 20 MHz acquisition frequency, it should be possible to obtain a sufficient amount of data (20 millions of bytes per second), but in practice, it is not possible. When the digitizer board finishes acquiring a set of samples, the application starts reading from the digitizer board memory and transferring the data to new memory locations. During the reading time, the digitizer board could have missed several pulses. Additionally, there are lost pulses due to internal errors in the digitizer board and it needs to be restarted.

On the other hand, the digital signal processing takes around 350 ms and includes the transformation to the equivalent reflectivity factor, and the compressing and storing of the data for further analysis. This is the reason why the temporal resolution of the VPR is set in approximately one second, averaging 256 independent pulses. Temporal resolutions of one second guarantee to track the evolution of any type of precipitation using the VPR. However, scanning weather radars require shorter temporal intervals, because they usually scan over a large area in a very short period of time; this mainly to guarantee the microphysics of precipitation has not changed considerably during the data acquisition phase. In such cases, fewer independent samples should be averaged and digital filtering techniques can be applied in real-time to reduce the high-frequency fluctuations of the reflectivity signal (See Section 3.3.4).

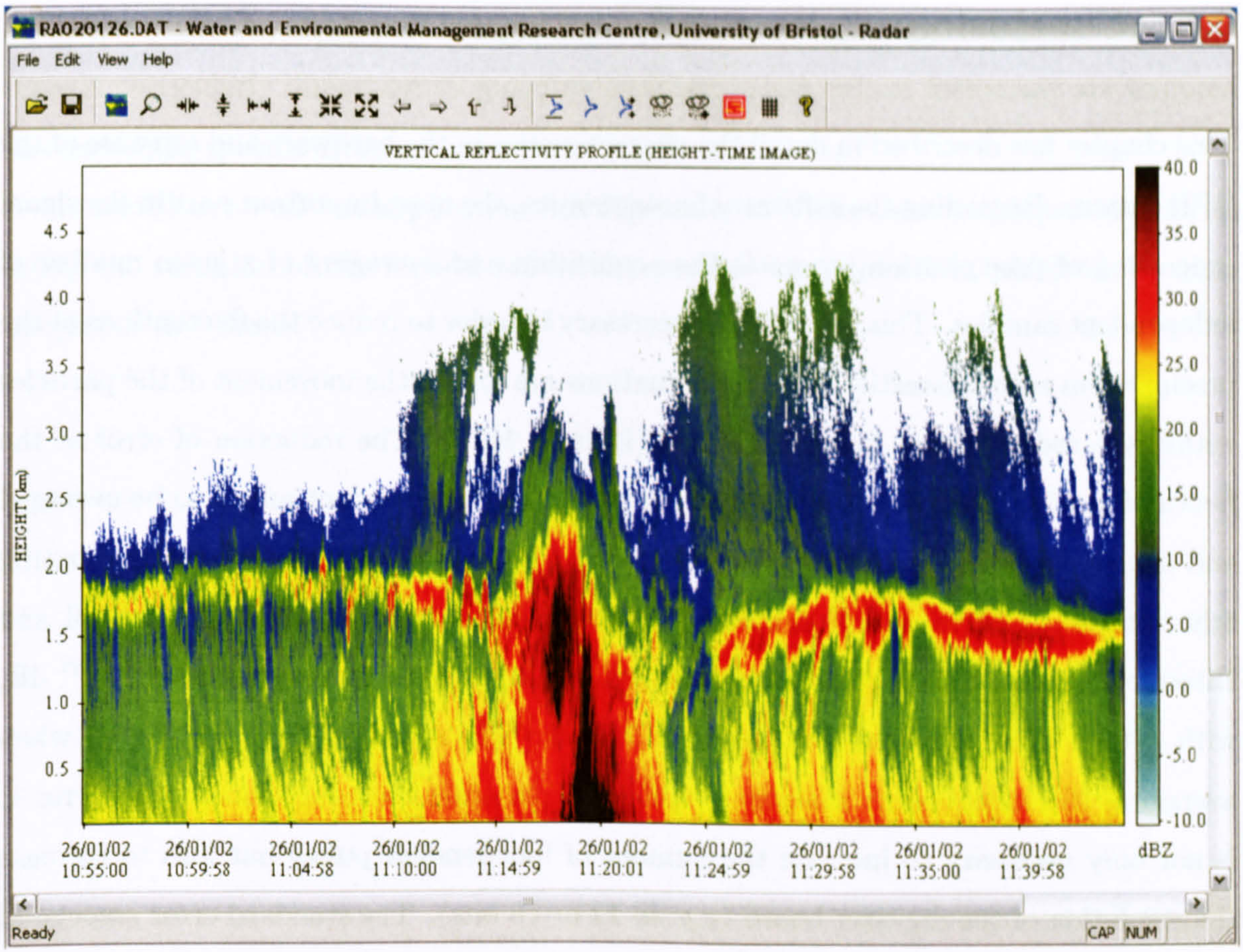

Fig. 3.12: Off-line VPR data analysis software (VIPER).

3.4.2 Off-line data analysis software

In order to carry out further analysis of the reflectivity data, an off-line application has been developed under MW (See Fig. 3.12). In this application time is not a constraint and several off-line processing tasks can be added to the software.

The standard display formed of VPR data is the Height Time Indicator (HTI), which has the time in the horizontal scale and height in the vertical. An example of HTI during stratiform rainfall is shown in the Fig. 3.12. Before 11:15 hr GMT, the bright band is located between 1.5 km and 2.0 km, with peak reflectivities between 25 dBZ to 30 dBZ. Below the bright band, the rainfall reflectivities are under 20 dBZ. At 11:15 hr GMT, the bright band disappeared and ice pellets with diameters less than 5 mm were observed during 10 minutes approximately. The vertical reflectivity profile presents large reflectivity variations reaching up to 45 dBZ. After 11:25 hr GMT, the bright band reappeared at the same height as the beginning, with peak reflectivities around 30 dBZ and rainfall reflectivities around 20 dBZ. Then, with the VPR is possible to study, in great detail, the natural variation of the vertical reflectivity profile.

3.5 Conclusions

This chapter has described in detail the characteristics in the hardware and software of the VPR system. Regarding the software characteristics, the most important part in the signal processing of precipitation echoes is the acquisition and averaging of a given number of independent samples. This averaging is necessary in order to reduce the fluctuations of the precipitation echo intensities. These fluctuations are due to the movement of the particles within the radar volume being examined (Battan, 1973). The reduction of error of the fluctuating echo intensities is related to the number of independent pulses to be averaged and the time interval between successive pulses. It has been found that the fluctuating echo intensities follow a well defined Gaussian distribution, as stated by Marshall and Hitschfeld (1953), with zero mean a standard deviation given by $\sigma = 3.9250N^{-0.3883}$ dB, with a time between successive pulses of 2.5 ms. The standard error associated when averaging 256 independent samples is 0.45 dBZ. In order to reduce further the error it is not only necessary to increase the number of independent pulses but also to increase the resolution of the digitizer board (*e.g.* to 12 or 16 bits). The standard error associated with the fluctuating echo intensities is also a helpful parameter to define the minimum detectable signal. A threshold of 2σ avoids 95% of the fluctuating echo intensities due to noise for values of voltage close to zero.

Taking into account the blocks involved in the signal processing of precipitation echoes (See Fig. 3.4), two different real-time applications have been developed to acquire VPR data. One of the applications runs under Microsoft Windows (MW) and the other under DOS. The former has been programmed in Visual C++, but it has been found to be dependent on the MW events and not reliable in real-time. The latter has been programmed in C++ under DOS. The acquisition and averaging subroutines have been written in assembly language, directing the whole processor power in carrying out the most important task in a weather radar data acquisition system. The DOS application has been found to be very reliable and it is possible to obtain a temporal resolution of 1 second averaging 256 samples with 2048 data points. The main advantage of this new software with respect to the TRAILER version is the modularity within the source code, facilitating to plug-in new real-time algorithms. Moreover, the processing of the reflectivity signal has been improved with the analysis of the echo fluctuations to produce a more accurate reflectivity signal.

In applications where shorter temporal resolutions are required, digital filtering techniques can improve the quality of the reflectivity signal by reducing considerably the effects of the echo fluctuations. FIR filters can be applied in real-time to the averaged radar sig-

nal, even when the number of independent samples is low (Compare Figs. 3.5 and 3.9). This is particularly important in scanning weather radars, where fast scans are required to cover some specific area.

In addition, an off-line application running under MW has been developed in order to study the variation of the vertical reflectivity profile of precipitation, which is the main subject of this thesis.

Chapter 4

Algorithm to detect the bright band from single-polarisation vertical reflectivity profiles

4.1 Introduction

Several algorithms have been proposed to detect the bright band boundaries from the Vertical Reflectivity Profile (VRP) of precipitation. Some of them involve single-polarisation reflectivity data (Klaassen, 1988; Fabry and Zawadzki, 1995; Tilford et al., 2001) and others dual-polarisation techniques (Hines, 1983; Hopper et al., 1991; Tan and Goddard, 1995; Bandera et al., 1998). Dual-polarisation over single-polarisation techniques are more advantageous in the determination of the size, shape, phase and orientation of the hydrometeors and it can be easier to identify the bright band. However, algorithms involving dual-polarisation techniques can not be applied when only single-polarisation reflectivity data are available.

Most of the bright band detection algorithms using single-polarisation VRP take into account the large reflectivity gradients associated with the bright band. Then, the variation of the vertical reflectivity profile $Z(h)$ is reflected in the first and second derivatives, that is, dZ/dh and d^2Z/dh^2. In image processing for instance, the object boundaries are related directly to the edge detection, being those places where the image intensity changes quickly. The use of the first and second derivative's is fundamental.

The bright band detection algorithm proposed by Tilford et al. (2001) makes use of the reflectivity gradient dZ/dh. The peak reflectivity of the bright band is located at a height h_0 where the reflectivity gradient is zero, that is $dZ(h_0)/dh = 0$. There are

two additional points below and above h_0, where the reflectivity gradient is maximal and minimal respectively. These points represent the state where the reflectivity inside the bright band reaches maximum and minimum slopes respectively. Beyond these points, the vertical reflectivity gradient will tend to decrease. The bright band top and bottom are estimated based on the fact that the maximum and minimum gradients mark the mid-points of the bright band boundaries. This is considering that these points define the mean reflectivity inside the bright band. However, the bright band signature changes constantly in space and time. The maximal gradients in the bright band are not always the mid-points of the bright band boundaries. For some cases, where the shape of the bright band is symmetric, the top and the bottom will be estimated correctly, but in most of the cases, it changes considerably and such an approximation often becomes invalid.

Bandera et al. (1998) proposed that for stratiform events the estimation of the bright band boundaries are better determined by the reflectivity gradient for the top and through the use of the linear depolarisation ratio (LDR) for the bottom. In convective situations where no bright band is apparent, LDR is used to detect the boundaries. As a first approximation, the estimation of the maximum and minimum gradients of reflectivity as in Tilford's algorithm is carried out. Then, taking advantage of the fact that the value of the reflectivity gradient in the bright band is higher than the value outside, an iteration process is performed comparing the average slopes inside and outside the bright band. This algorithm initially depends on the values of reflectivity taken outside the bright band. It assumes that there is a certain homogeneity outside the bright band, and even when there is a general trend outside the bright band, large local variations may influence the estimation of the real boundaries.

Klaassen (1988) defines the top of the bright band as either the point where the reflectivity is equal to the underlying rain or the height where the gradient $d^2Z/dh^2 > 0$; the bottom of the bright band is calculated when the Doppler velocity profile reaches its maximum value minus 0.5 m s^{-1}. One disadvantage of this proposal is that the weather radar must possess Doppler capability. Additionally, the value of the reflectivity at the top of the bright band is not necessarily the same value of reflectivity at the bottom of the bright band.

Fabry and Zawadzki (1995) define the top and bottom of the bright band as being where the curvature of the logarithm of the reflectivity is a maximum. No further details are given in the detection process, but assuming they make use of the curvature function $\rho = d\phi/ds$, for a function $Z(h)$, the curvature can be calculated by:

$$\rho(h) = \frac{d^2Z/dh^2}{[1 + (dZ/dh)^2]^{3/2}} \tag{4.1}$$

For instance, a large value of curvature is obtained on the peak of the bright band. However, around the bright band boundaries, there are several peak curvature values, which make it a bit confusing in the detection of the real boundary. Choosing the maximal from all these values does not mean the real boundary of the bright band has been identified. The use of the curvature function to detect the bright band boundaries requires a strong curvature in order to have clear detection. This fact was also recognized by Fabry and Zawadzki in the analysis of the bright bands in Montreal.

All the bright band detection algorithms discussed in this section have a good performance for certain types of profiles, but the variation of reflectivity in the bright band makes it difficult to detect the boundaries for any detection algorithm based on the gradient of reflectivity, dZ/dh. This chapter presents a new algorithm to detect the extent of the bright band from single polarisation vertical reflectivity profiles of precipitation. The proposed algorithm avoids the use of the reflectivity gradient dZ/dh by performing the detection process from a different perspective.

4.2 Data

An X-band Vertically Pointing weather Radar (VPR) has been deployed at several sites in order to study the variability of the vertical reflectivity profile. The overall characteristics of the VPR have been given in Chapter 3. The VPR measures echoes from precipitation along the vertical in the atmosphere at a specific time intervals (1 s averaging 256 independent samples). These averaged echoes are related directly to reflectivity and then through empirical equations to rainfall rate. The standard display formed with VPR data is called the Height Time Indicator (HTI) with height and time in the vertical and horizontal axis respectively. VPR data from Bristol, UK have been employed in this analysis.

On the other hand, it is not only possible to measure the variation of the vertical reflectivity profile with high-resolution VPR data, but also with a weather radar operating in a Range Height Indicator (RHI) mode. An RHI scan provides a cross-section of a storm and it gives information about the vertical structure of precipitation. It is composed, at some particular azimuthal angle, of several profiles at different elevation angles. The result, is a scan with range in the horizontal scale and height in the vertical. Every profile at different elevation angles should be fast enough to guarantee the microphysics of precipitation has not changed during the rest of the elevations. RHI scans from Chilbolton

Features of Chilbolton S-band radar	
Frequency	3075 MHz
Wavelength	10 cm (S-band)
Antenna diameter	25 m
Beamwidth	0.25 degrees
Peak power	600 kW
PRF	610 Hz
Pulse width	0.5 μs
Polarisation	linear: horz/vert
Spatial resolution	75 m
Temporal resolution	210 ms (64 pulses averaged)

Table 4.1: Features of the Chilbolton weather radar (From Goddard et al., 1994; Goddard, 1995)

weather radar have been used for this analysis.

The Chilbolton radar is operated by the Radio Communications Research Unit (RCRU). It is an S-band (10 cm wavelength) weather radar developed to study the effects of rain on communication systems (Goddard et al., 1994). It is the largest steerable meteorological radar in the world, with 25 m antenna diameter, allowing measurements with a very narrow beamwidth of 0.25 degrees. The short pulse width of 0.5 μs allows a range resolution of 75 m. The temporal averaging is done over 64 independent arrays in approximately 210 ms. The features of the Chilbolton radar are summarised in Table 4.1. The Chilbolton radar has dual-polarisation and Doppler capabilities, which allow the study of the size, shape, phase and orientation of the hydrometeors and wind field measurements respectively. Combining both capabilities, it may be possible to improve radar rainfall measurements. Similarly to the VPR, the reflectivity measurements from Chilbolton are obtained using the Rayleigh approximation. This assumption is valid even for large scatterers due to the long wavelength of the radar. Additionally, attenuation effects at 3 GHz frequency may be neglected.

An example of an RHI from 0 to 25 degrees is shown in the Fig. 4.1. The bright band is located at around 2 km height with peak reflectivities up to 50 dBZ. As the range increases, there is an increase in the sampled volume and a decrease of radar resolution. In RHI scans, the bright band loses its intensity due to the spreading of the radar beam at long ranges. The same effect occurs in conventional scanning weather radar measurements.

Both, HTI and RHI scans give information about the vertical structure of the storm,

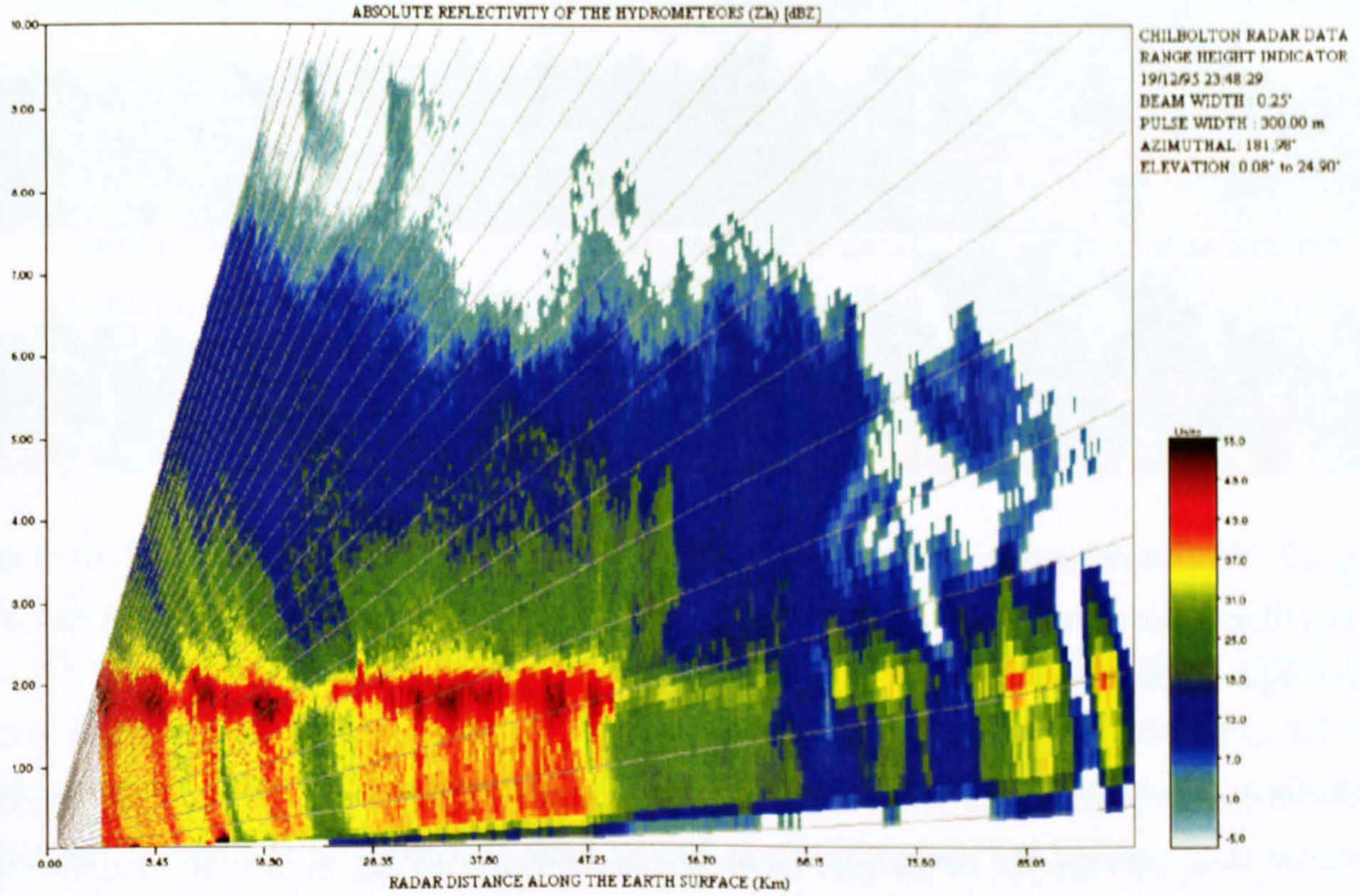

Fig. 4.1: RHI scan from Chilbolton on 19 December 1995.

however HTI scans are single point measurements, observing the precipitation passing overhead and RHI scans are cross section measurements observing precipitation over a long range. VRP from HTI scans are obtained directly because the radar beam is pointing vertically, but for an RHI scan, the VRP has to be constructed from beams at different elevations and taking into account the radar beam propagation through standard atmosphere.

4.3 Frequency analysis of reflectivity

The spatial and temporal variation of the VRP gives a clue to the nature of the storm. Fabry and Zawadzki (1995) define five different categories of VRP in rain: low level rain, rain with bright band, rain from compact ice, showers and deep convection. Towers (1996) includes all these profiles in three broad categories: true stratiform, mixed stratiform and convective, and showers. The typical bright band signature is common in stratiform precipitation, with small variations of reflectivity below and above the bright band. Sometimes wind shear effects are strong enough that they distort the typical bright band shape and the VRP presents large variations not only spatially (along the vertical) but also temporally (along the horizontal). This type of VRP can be classified as stratiform-convective and it is quite interesting because the bright band signature is not as well defined as in

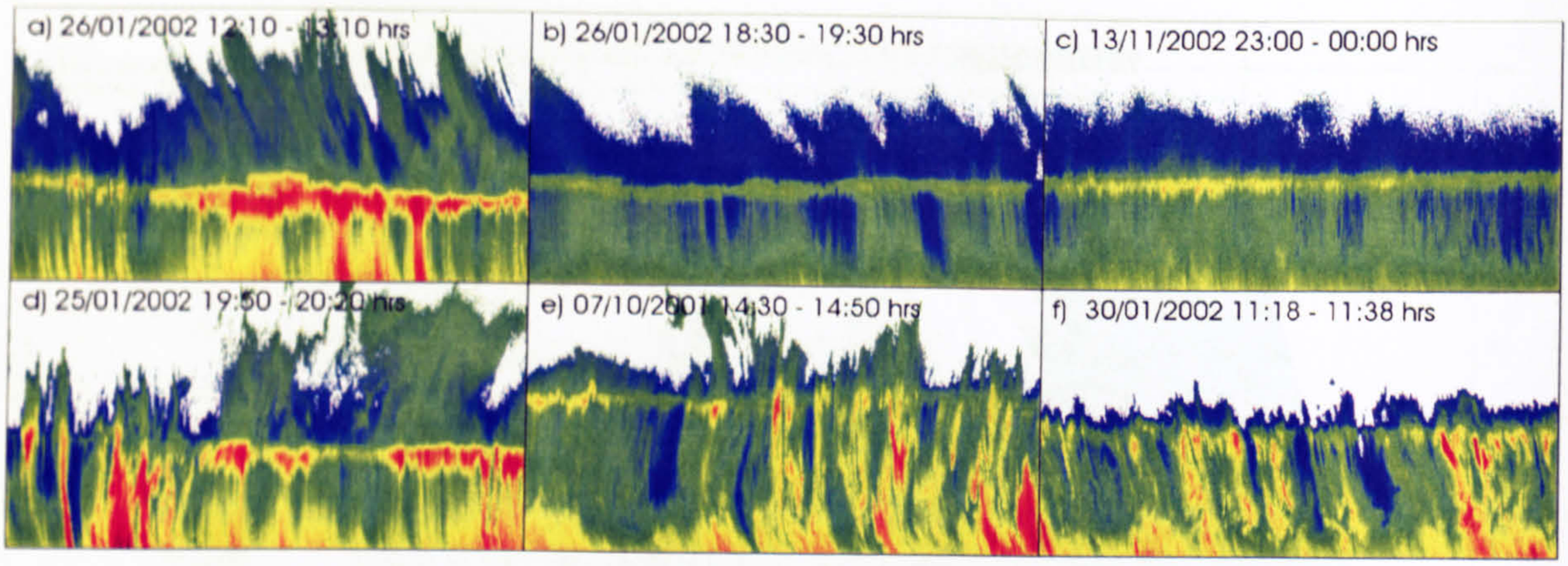

Fig. 4.2: Vertical reflectivity profiles from Bristol, UK. a) b) and c) Stratiform rainfall, d) e) and f) Stratiform-convective rainfall. All the events are from 100 m to 4100 m, spatial resolution 7.5 m and temporal resolution 1 s.

stratiform precipitation. Stratiform and stratiform-convective VRP have been analysed because they present the most important bright band features and the rest of the VRP defined by Fabry and Zawadzki (1995) and Towers (1996) are also important but they are out of the scope of this research.

Fig. 4.2 shows three different events presenting stratiform and stratiform-convective VRP's. Every image in Fig. 4.2 is composed of two signals: along the vertical every profile is described as a function of height $Z(h)$, whereas along the horizontal every profile is described as a function of time $Z(t)$; then every image is described by a function of time and height $Z(t,h)$. The continuous reflectivity $Z(h)$ (or $Z(t)$) can be represented as a discrete sequence $z[n]$ by:

$$z[n] = Z(nT), \qquad n = 0, 1, 2, ... \tag{4.2}$$

where T is the sampling period and it represents the space between two consecutive samples ($T = 7.5$ m for $Z(h)$ and $T = 1.0$ s for $Z(t)$). The reciprocal of the sampling period is called the sampling frequency ($F_s = 1/T$).

The transformation of a signal from time/height domain into the frequency domain plays a key role in the study of the signal frequency characteristics. Han (1991) explained the importance of spectral analysis in the temporal and spatial domain by choosing the right sampling frequency in order to prevent large aliasing errors from radar rainfall data. Frequency analysis of reflectivity profiles involves primarily the computation of the Fourier transform. The Discrete Fourier Transform (DFT) of $z[n]$ is given by (Mitra, 2001):

$$Z[k] = Z(e^{j\omega})|_{\omega=2\pi k/N} = \sum_{n=0}^{N-1} z[n]e^{-j2\pi kn/N}, \qquad 0 \leq k \leq N-1 \tag{4.3}$$

where N is the number of elements in the array and ω is the real frequency variable. The energy density spectrum of $Z[k]$ is given by (Mitra, 2001):

$$S_{zz}[k] = |Z[k]|^2 \qquad \text{or} \qquad S_{zz}(\omega) = |Z(\omega)|^2 \tag{4.4}$$

The energy density spectrum represents the distribution of energy for every frequency involved in the construction of the sequence $z[n]$. The total energy of the sequence is given by the integration of $S_{zz}(\omega)$ over all the frequencies:

$$\varepsilon_z = \frac{1}{2\pi} \int_{-\pi}^{\pi} S_{zz}(\omega) d\omega \tag{4.5}$$

The events shown in Fig. 4.2 are analyzed in the following way. For every event, the vertical reflectivity profiles $Z_j(h)$ are extracted and transformed to $z_j[n]$ using Eq. 4.2 and their DFT $Z_j[k]$ are calculated. The relationship containing all the frequencies involved in each vertical profile and for every event shown in Fig. 4.2 is calculated by:

$$Z_s[k] = \sum_{j=1}^{m} Z_j[k] \tag{4.6}$$

where m is the number of profiles. Similarly, in the temporal domain, all the profiles $Z_i(t)$ are extracted and transformed to $z_i[n]$ using Eq. 4.2 and their DFT $Z_i[k]$ are calculated. Only those profiles below 1500 m are taken into account because variations on the top of the precipitation are not important for hydrological purposes. The relationship containing all the frequencies involved along the time scale for every event shown in Fig. 4.2 is calculated by:

$$Z_t[k] = \sum_{i=1}^{n} Z_i[k] \tag{4.7}$$

where n is the number of profiles. $Z_s[k]$ represents the spatial variation of reflectivity, whereas $Z_t[k]$ represents the temporal variation of reflectivity. The magnitude of Eqs. 4.6 and 4.7 is standardized to unity removing the DC component. The DC component is not important for this analysis, but it may have a large impact in the results.

The spatial energy density spectrums for every one of the events shown in Fig. 4.2 are depicted in Fig. 4.3. The frequency is normalised to 1, which is equivalent to half the sampling frequency (*i.e.* $F_s/2$ with $F_s = 1/7.5\ \text{m}^{-1}$). For instance, a frequency of $\omega/\pi = 1$ corresponds to a signal with a sinusoidal component varying within 15 m; $\omega/\pi = 0.1$ corresponds to a signal with a sinusoidal component varying within 150 m and so on. The frequency scales of Fig. 4.3 are logarithmic to appreciate in detail the low-frequency signal characteristics. In all the events, the noise threshold is below -35 dB. Above this level,

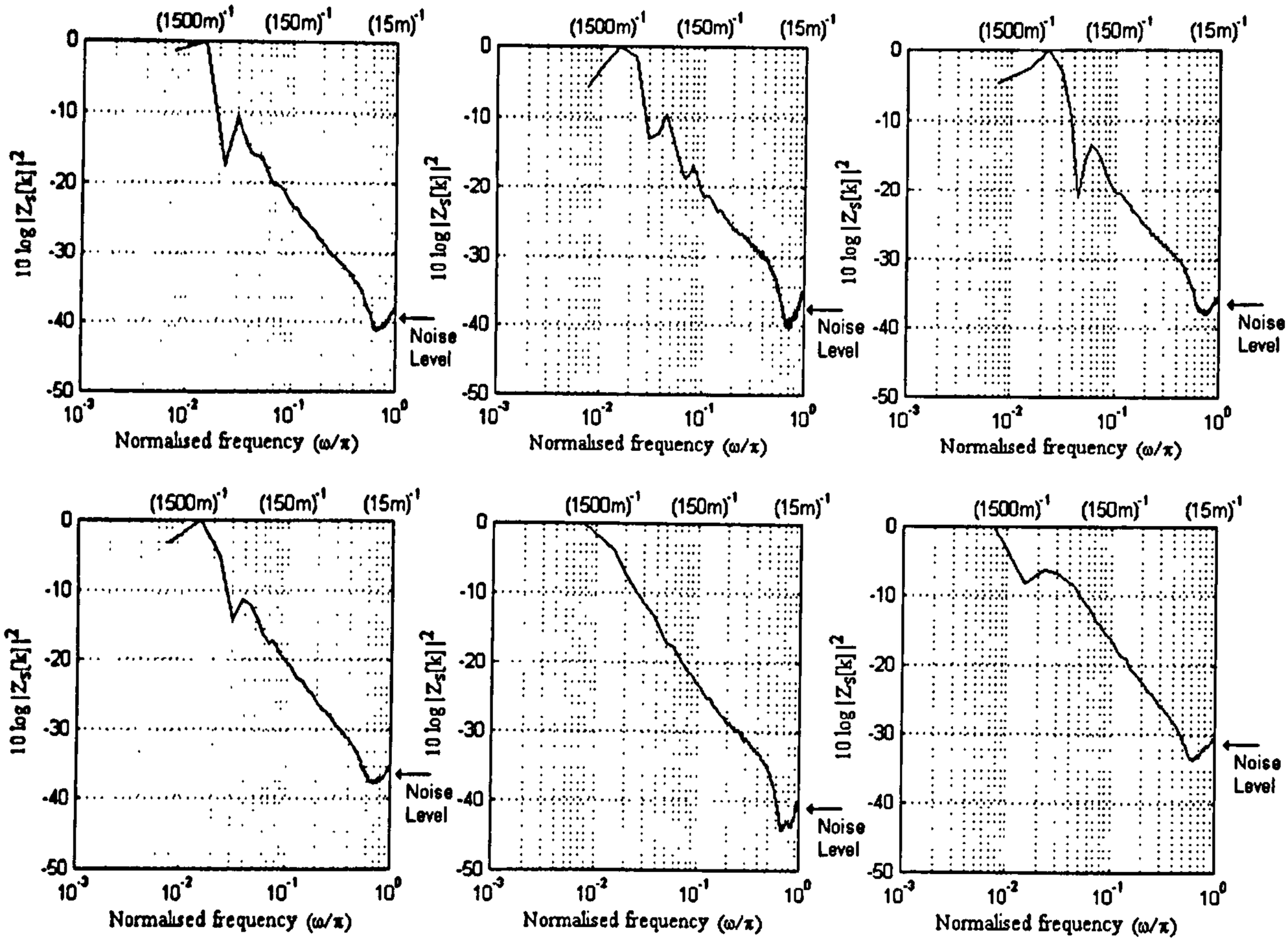

Fig. 4.3: Spatial power spectrum distribution for the events shown in Fig. 4.2.

there are important frequencies composing the vertical reflectivity profiles, but what is the threshold defining these important frequencies? Unfortunately there is not a rule to follow to obtain this threshold. In filter design for instance, the designer defines a point above the noise level, where there is an abrupt change in the behavior of the signal. Below this level the signal will be buried by noise. For the signals shown in Fig. 4.3 there is a decrease of energy as the frequency increases up to the point where the signal reaches the level of noise. Therefore, it is not straightforward to apply the same criteria. It is possible to assume that the level of noise is constant over all the frequencies and the noise can be modeled as a white noise. The power spectral density of the white noise has a constant value (σ^2) for all the frequencies (Mitra, 2001) and σ corresponds to the levels of noise depicted in Fig. 4.3 and it is different for every event. Therefore, the averaged energy of the signal without noise is calculated by:

$$\varepsilon_{s,t} = \frac{1}{2\pi} \int_{-\pi}^{\pi} |Z_{s,t}(\omega) - \sigma|^2 d\omega \tag{4.8}$$

The above expression represents the total energy of the signal considering the effects of the white noise. If the integration of Eq. 4.8 is carried out in an interval lower than $[-\pi, \pi]$, the result is a percentage of the total energy of the signal as a function of the fre-

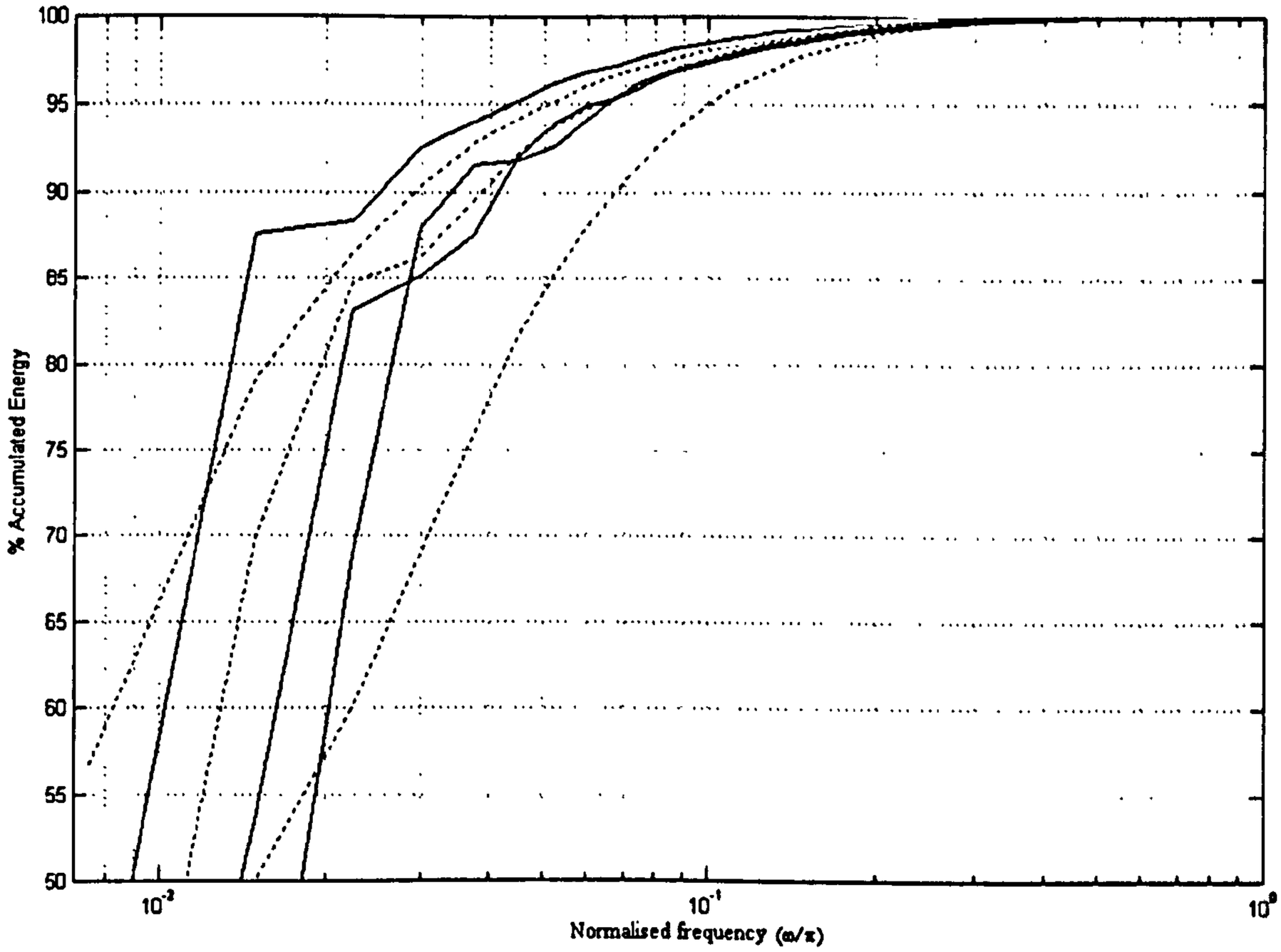

Fig. 4.4: Percentage of the total energy of the spatial power spectrum distribution as a function of the integrated frequencies for the events shown in Fig. 4.2. The solid line represents the results for stratiform precipitation and the dashed line for stratiform-convective precipitation.

quency. Following this procedure, the accumulative energy curve is depicted in Fig. 4.4. It is straightforward to establish that 95% of the total energy for stratiform and stratiform-convective VRP comprises frequencies smaller than 0.1 (*i.e.* $\omega/\pi < 0.1$). Therefore, the spatial frequency analysis shows that stratiform and mixed stratiform-convective precipitation present very similar characteristics. All the frequencies smaller than 0.1 contain 95% of the total energy of the signal and for the design of a low-pass filter, this value can represent the cut-off frequency of the filter.

The temporal energy density spectrums for the events shown in Fig. 4.2 are depicted in Fig. 4.5. Again, the frequency is normalised to 1, which is equivalent to half the sampling frequency (*i.e.* $F_s/2$ with $F_s = 1\ \mathrm{s}^{-1}$). A frequency of $\omega/\pi = 1$ represents a signal with a sinusoidal component with a frequency of 2 s; a frequency of $\omega/\pi = 0.1$ represents a signal with a sinusoidal component with a frequency of 20 s and so on. The Fig. 4.5 shows that there are high-frequency components due to noise and a similar procedure may be followed to obtain the percentage of the total energy of the signal as a function of frequency. The accumulative energy curve is shown in Fig. 4.6. 95% of the signal's energy comprises frequencies $\omega/\pi < 0.011$ for stratiform reflectivity profiles and $\omega/\pi < 0.033$ for stratiform-convective reflectivity profiles (See Table 4.2).

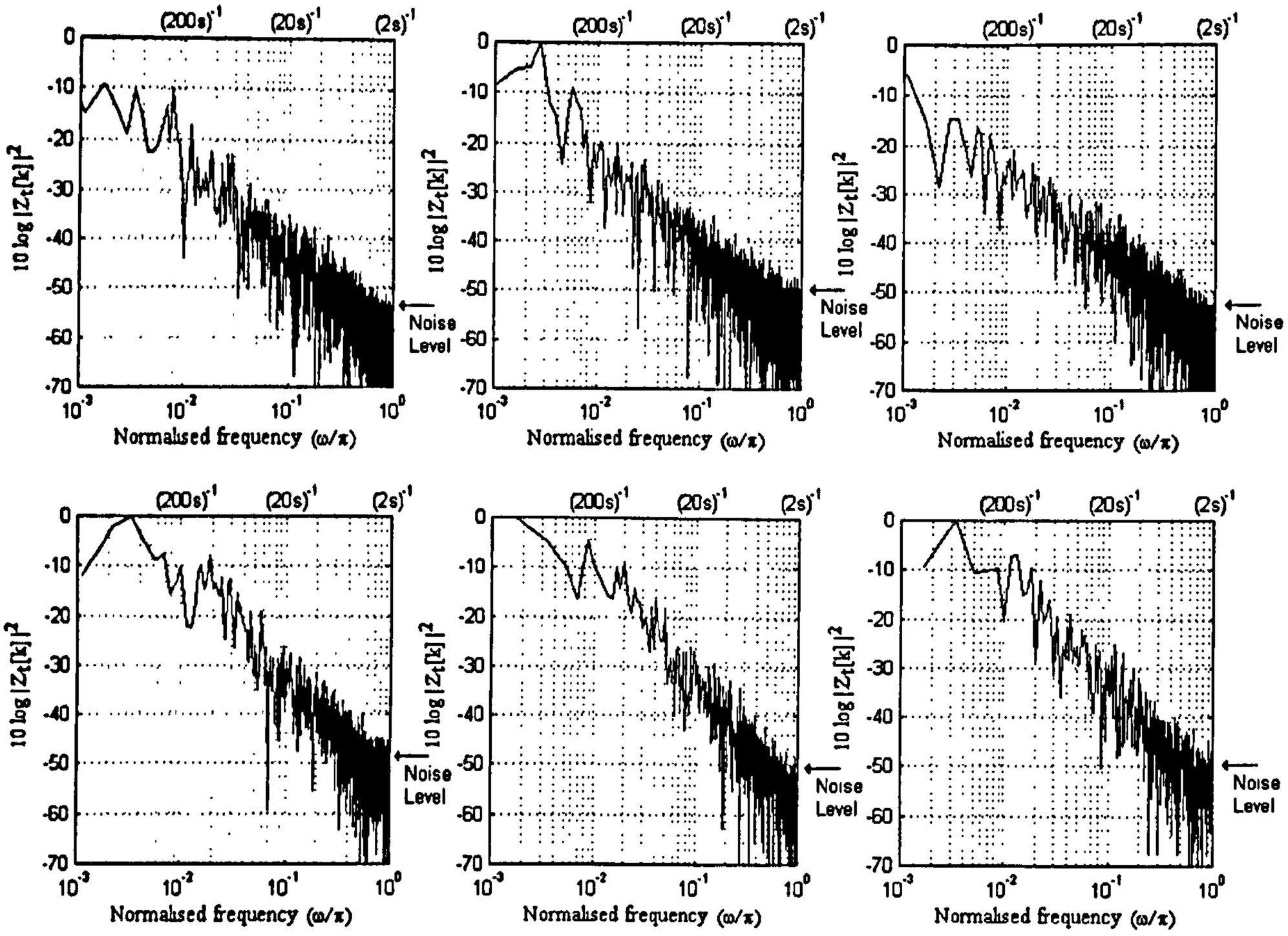

Fig. 4.5: Temporal power spectrum distribution for the events shown in Fig. 4.2.

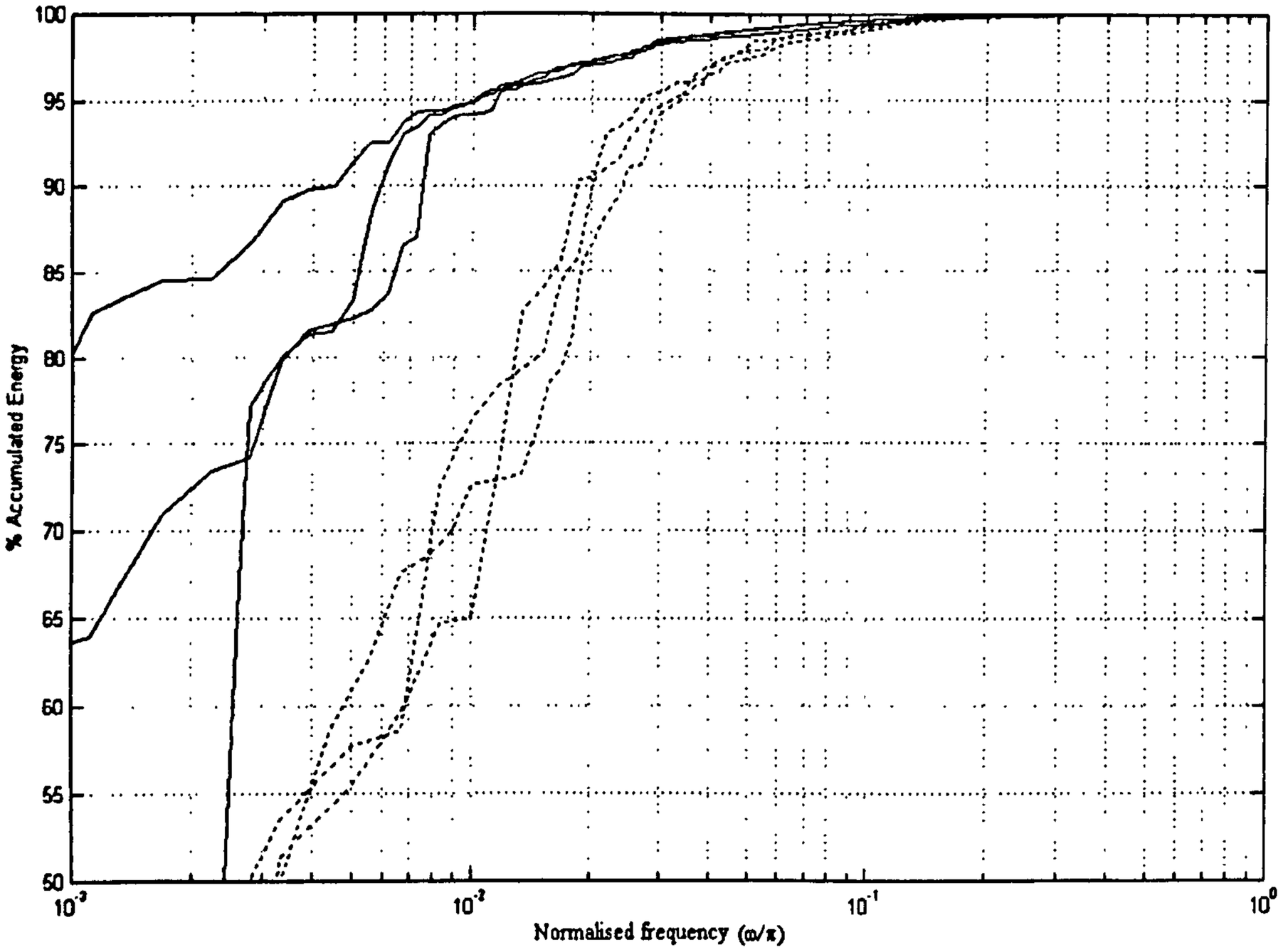

Fig. 4.6: Percentage of the total energy of the temporal power spectrum distribution as a function of the integrated frequencies for the events shown in Fig. 4.2. The solid line represents the results for stratiform precipitation and the dashed line for stratiform-convective precipitation.

Rainfall type	*Spatial analysis*	*Temporal analysis*
Stratiform	$F_c \approx 0.1/15$ m^{-1}	$F_c \approx 0.011/2$ s^{-1}
Stratiform-convective	$F_c \approx 0.1/15$ m^{-1}	$F_c \approx 0.033/2$ s^{-1}

Table 4.2: Cut-off frequencies from signals shown in Fig. 4.3 including the 95% of the total energy.

It is interesting to note that the reflectivity profiles from stratiform and stratiform-convective precipitation in the spatial domain $Z(h)$ present similar characteristics in the frequency domain $Z_s[k]$. However the reflectivity profiles in the temporal domain $Z(t)$ present different characteristics in the frequency domain $Z_t[k]$ depending on the precipitation type. The cut-off frequencies indicate that shorter temporal averages are allowed in stratiform-convective precipitation than in pure stratiform precipitation (See Section 4.4.1).

A general frequency spectrum covering the spatial and temporal frequency domains with its respective cut-off frequencies is depicted in Fig. 4.7. In the discrete domain the spectrum is repeated every $F_s/2$. From this figure is very clear that the spatial-temporal reflectivity signal can be resampled at a different frequency without losing the signal characteristics. The Nyquist theorem establishes that a signal can always be recovered given that the sampling frequency is more than twice the highest frequency component. Assuming that the highest frequency component is the cut-off frequency, the sampling frequency could be $F_s \geq 2F_c$. For instance, in the spatial frequency analysis the cut-off frequency is $F_c = 0.1/15$ m^{-1}; in the worst of the cases, the VRP could have been sampled every 75 m (*i.e.* $F_s = 1/75$ m^{-1}) and still would have similar frequency characteristics to the VRP sampled at 7.5 m. This is important in terms of designing a real-time VRP measurement system for on-line vertical reflectivity correction. Through the signal frequency

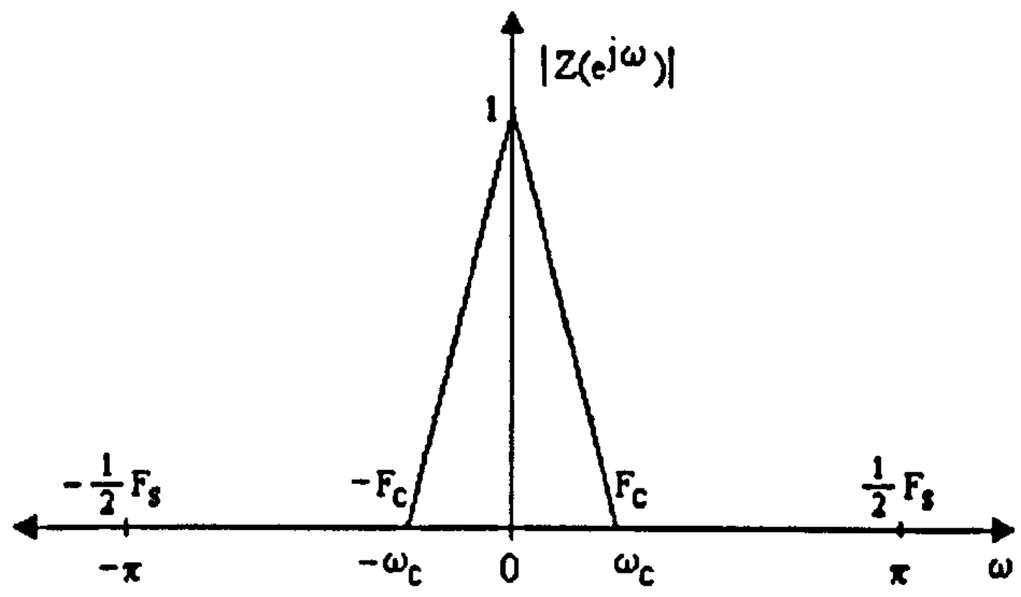

Fig. 4.7: Frequency spectrum of the spatial and temporal reflectivity profiles depicted in Figs. 4.3 and 4.5 respectively with cut-off frequencies shown in Table 4.2.

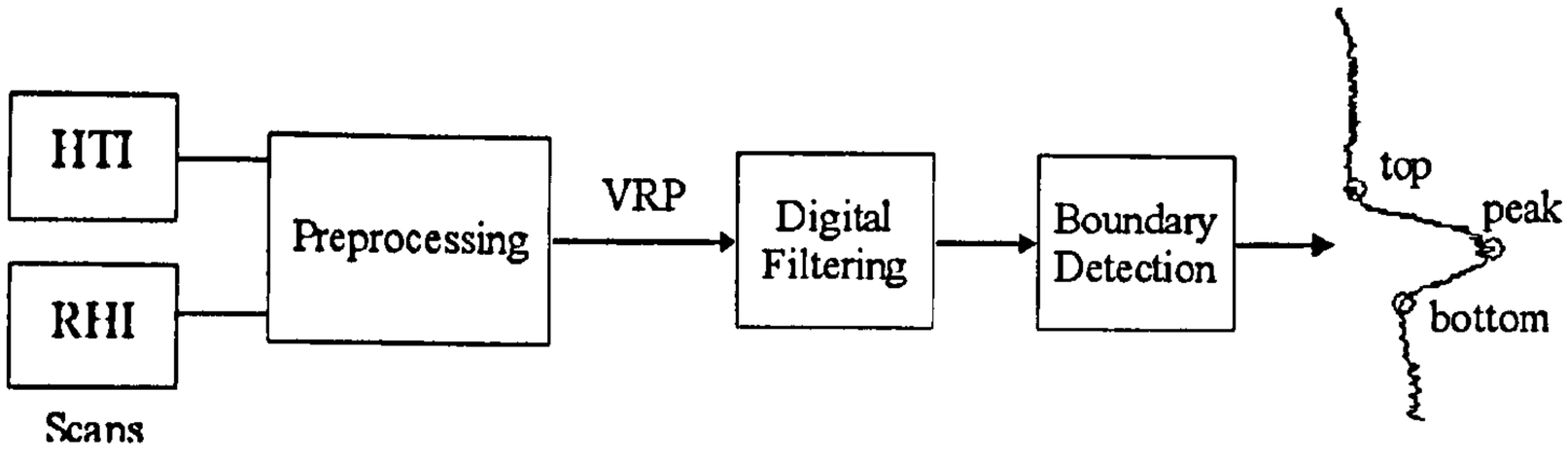

Fig. 4.8: Algorithm to detect the bright band.

analysis is straightforward to develop digital filters to remove the high-frequency noise of the reflectivity signal.

4.4 Bright band detection algorithm

A good estimate of the bright band boundaries conveys a deep understanding of the bright band characteristics. The better the way to detect the boundaries of the bright band, the better the interpretation of results among the reflectivities above, within and below the melting layer.

A general view of the algorithm to detect the bright band is shown in Fig. 4.8. The HTI or RHI scans are preprocessed independently to obtain the VRP. The VRP is the input to the bright band detection algorithm, which is divided in two blocks: digital filtering and boundary detection.

4.4.1 Preprocessing of HTI scans

The HTI scans are composed of VRP with a temporal resolution of 1 s. Every VRP can be filtered independently and the bright band boundaries can be detected at the same temporal resolution. However, it is not necessary to detect the bright band with such a high temporal resolution because the temporal variation of the reflectivity during stratiform precipitation occurs over a longer time scale. From Section 4.3, the temporal frequency response for different rainfall events has the shape shown in Fig. 4.7 with cut-off frequencies being $0.011/2$ s^{-1} and $0.033/2$ s^{-1} for stratiform and stratiform-convective precipitation respectively ($F_s = 1$ s^{-1}). This means that the VRP can be averaged and resampled over longer time intervals and still will have similar frequency characteristics to the VRP sampled at one-second temporal resolution. Therefore a compromise must be made between having enough measurements to smooth the vertical reflectivity profiles (Fabry and Zawadzki, 1995) while allowing the changes due to the dynamic nature of the storms. Two preprocessing tasks are applied to the VRP from HTI scans: temporal

averaging and resampling. Both of them depend on the cut-off frequency of the VRP in the temporal domain.

Temporal averaging is a type of filtering and it reduces the noise by the factor $1/\sqrt{N}$, where N is the number of samples. A moving-average filter of N coefficients has a rectangular impulse response $h[k] = 1/N$. This filter has the effect of smoothing a noisy signal by suppressing its high-frequency variations. The magnitude response of the moving-average filter is given by (Mitra, 2001):

$$|H(e^{j\omega})| = \left|\frac{1}{N}\frac{\sin(N\omega/2)}{\sin(\omega/2)}\right| \tag{4.9}$$

The normalised cut-off frequency (ω_c/π) of the moving-average filter can be calculated from Eq. 4.9 for $|H(e^{j\omega})| = 1/2$. Using numerical methods to solve Eq. 4.9, it is obtained that the cut-off frequency of the moving-average filter is estimated by:

$$\omega_c = 3.9107N^{-1.0078}, \qquad 2 \leq N \leq 100 \tag{4.10}$$

Thus, the number of coefficients of a moving-average filter as a function of the cut-off frequency is estimated by:

$$N = 3.8696\omega_c^{-0.9922}, \qquad 0 \leq \omega_c \leq \pi \tag{4.11}$$

The above expression indicates that the number of coefficients of a moving-average filter using the normalised cut-off frequencies 0.011 and 0.033 (From Table 4.2, $\omega_c = 0.011\pi$ and $\omega_c = 0.033\pi$ respectively) are approximately 109 and 36 for stratiform and stratiform-convective precipitation respectively.

On the other hand, resampling involves to take into account the highest frequency component of $Z(t)$. The sampling frequency must be at least twice the highest frequency component, that is, $F_s \geq 2F_c$. The sampling period is $T = 1/F_s$. The cut-off frequencies for stratiform and stratiform-convective precipitation are $F_c = 0.011/2$ s^{-1} and $F_c = 0.033/2$ s^{-1} respectively. Thus, the maximal sampling periods are 90 s and 30 s approximately.

Rainfall type	F_c	*Coefficients*	*Resampling*
Stratiform	$0.011/2$ s^{-1}	$\leq$109	$\leq$90 s
Stratiform-convective	$0.033/2$ s^{-1}	$\leq$36	$\leq$30 s

Table 4.3: Maximal number of coefficients of the moving-average filter and maximal resampling periods in stratiform and stratiform-convective precipitation.

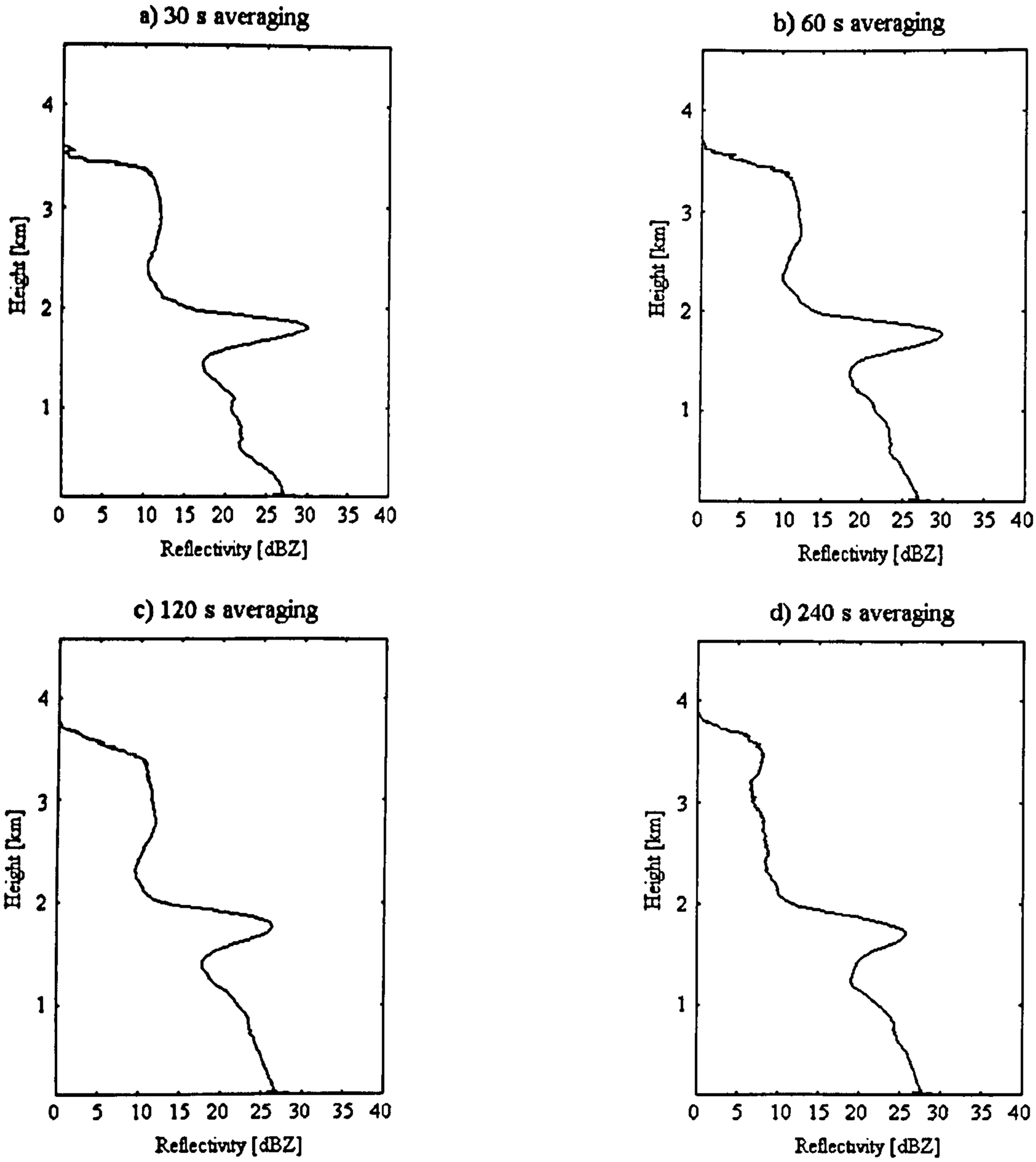

Fig. 4.9: Effects of temporal averaging of vertical reflectivity profiles.

The temporal averaging and resampling are summarised in Table 4.3. In stratiform precipitation is possible to apply a moving-average filter with up to 109 coefficients (*i.e.* up to 109 s of averaging interval) and the resampling interval can be up to 90 s. As soon as convection is present in stratiform precipitation, the number of coefficients of the moving-average filter is reduced to 36 (*i.e.* up to 36 s of averaging interval) and the resampling interval to 30 s. Fig. 4.9 shows the effects of averaging VRP from stratiform precipitation. The maximal reflectivity in the bright band has decreased from 30 dBZ to approximately 26 dBZ when averaging 120 s and 240 s respectively. This difference represents a big problem for the study of the bright band intensity and for the estimation to rainfall rate. Thus, the averaging interval should be small enough to deal with the temporal variation of reflectivity and consequent changes in the bright band. In this study, the number of

coefficients of the moving-average filter has been fixed to 30 (*i.e.* 30 s of averaging interval) and the resampling interval has been fixed to 30 s. These results can be extended to rainfall events presenting similar characteristics.

4.4.2 Preprocessing of RHI scans

On the other hand, an RHI scan has M beams at M different elevation angles from around 0 to 30 degrees, every one of them separated approximately with the same incremental angle. In order to extract the VRP, a transformation from polar to rectangular coordinates should be carried out. In an RHI scan, every pixel represents reflectivity at some specific range from the radar site and height above the earth surface. The horizontal resolution is related directly to the pulse width whereas the vertical resolution to the beamwidth and the number of elevation beams. Every VRP from an RHI scan is extracted from several beams at different elevation angles and at the same range from the radar site. All this process is carried out following the beam propagation under standard atmospheric conditions and taking into account the 4/3 earth curvature approximation. The transformation from polar to rectangular coordinates is a kind of resampling. The spatial resolution along the vertical has been fixed in 10 m, which can be supported with the frequency analysis carried out in the last section. The spatial resolution along the range has been fixed as half the pulse width of the radar beam, according to the Nyquist theorem.

An RHI scan is a composite image, which varies in space and time, but the variation between adjacent measurements is so small that the radar scan can be seen as a continuous image. It means that digital image processing techniques can be applied to RHI scans. The reflectivity values in an RHI scan are very noisy and the transformation from polar to rectangular coordinates will introduce more noise to the data. Using a two-dimensional average filter reduces considerably the noise in the RHI scan. With this filter, the echo intensity at some particular point is replaced with the average of the echo intensities in a square window around the echo. The resultant echo intensity depends on the window size and it is obtained directly by convolving the data with the window. The size of the window should be small to avoid taking into account reflectivity measurements too far away from the measurement in question. It has been found that with spatial resolutions of 10 m times 300 m in the vertical and horizontal scale respectively, the effects of noise are reduced considerably when using an average window of 5x5. Every value of this window has a weight of 1/25 and it represents an averaging of 50 m by 1500 m along the vertical and horizontal scales respectively.

The averaging is part of the preprocessing of the reflectivity signal in both HTI and

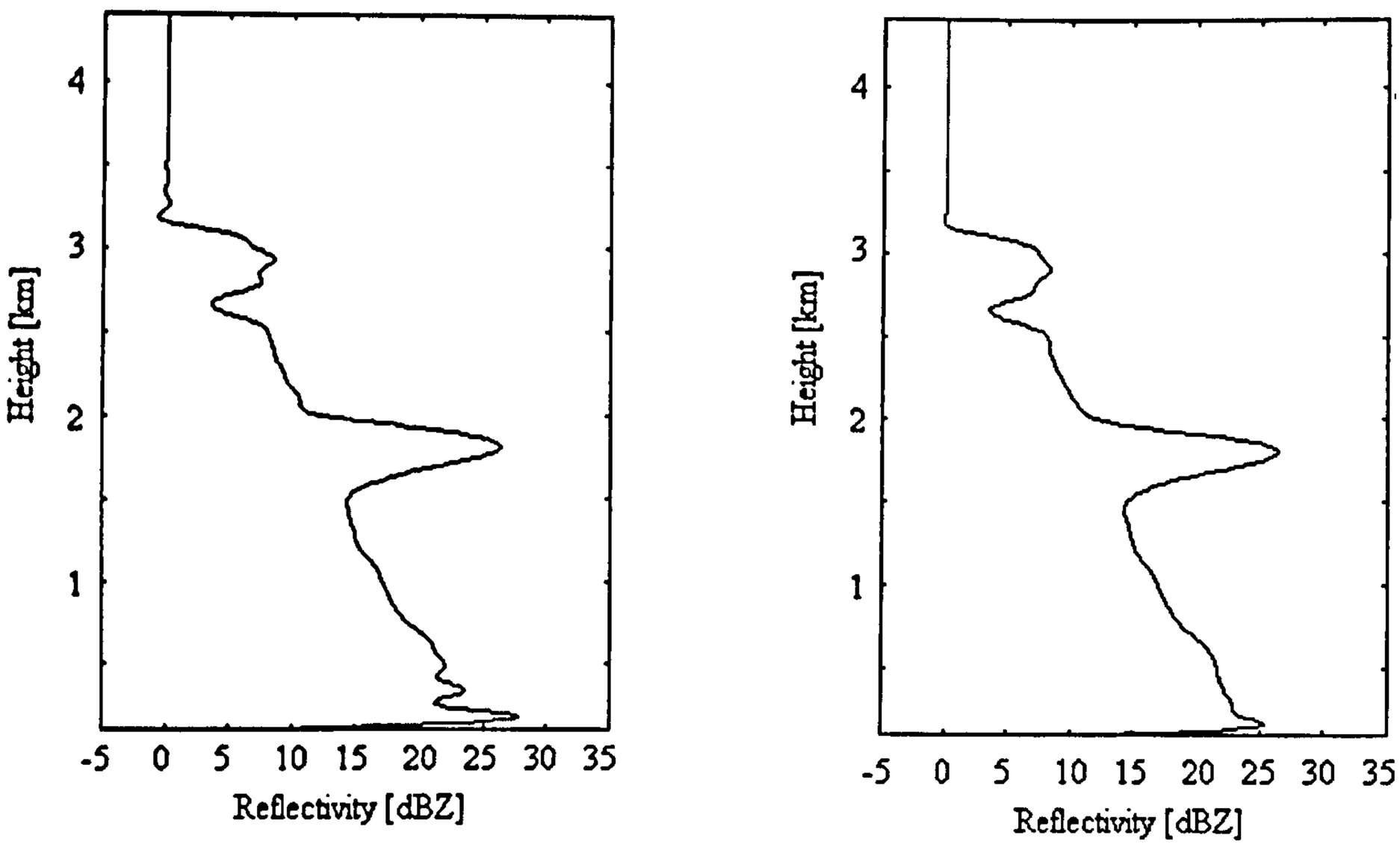

Fig. 4.10: Smoothed VRP using a low-pass a) IIR filter (9 coefficients) and b) FIR filter (66 coefficients). Both filters have a normalised cut-off frequency of 0.1 and a transition width of 0.05.

RHI scans. Without it, the detection of the bright band between consecutive vertical reflectivity profiles would be highly variable.

4.4.3 Digital filtering

The VRP may have unwanted high-frequency noise due to either sampling errors or the characteristics of the radar transceiver. In order to reduce the visible effects of noise a low-pass digital filter must be applied. The spatial frequency characteristics obtained is Section 4.3 are taken into account to design the appropriate low-pass digital filter. The VRP may come from either HTI or RHI scans (either $Z(t_i, h)$ or $Z(r_i, h)$).

The design of a low-pass digital filter is presented in Appendix B. Finite Impulse Response (FIR) filters are prefered instead of Infinite Impulse Response (IIR) filters to guarantee stability in the filtering process. Fig. 4.10 shows a comparison between a FIR and a IIR filter. Small ripples or instabilities appear in the VRP using a IIR filter, which can produce further errors in the bright band detection process. This is the main reason for using FIR filters.

The number and values of the filter coefficients $h[k]$ are based on the characteristics of the reflectivity signal. From the spatial frequency analysis carried out in Section 4.3, the reflectivity echoes along the vertical have the majority of their energy in the low-frequency spectrum. The most important parameter in digital filter design is the cut-off frequency,

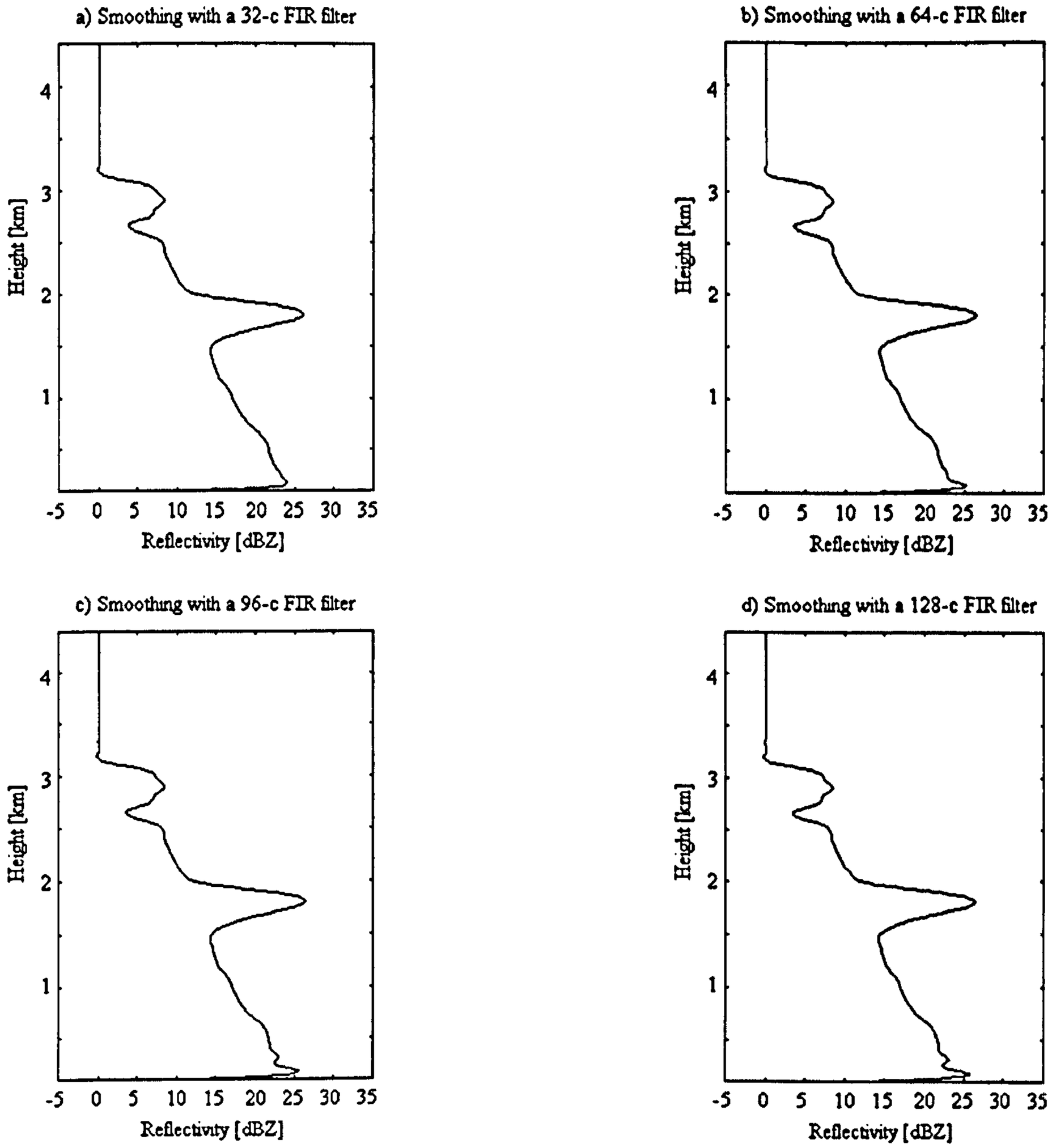

Fig. 4.11: Smoothed VRP using a low-pass FIR filter with a) 32, b) 64, c) 96 and d) 128 coefficients and a normalised cut-off frequency of 0.1.

which is $F_c = 0.1/15$ m^{-1} for stratiform and stratiform-convective VRP (See Section 4.3, Table 4.2).

Appendix B presents the design of a FIR filter using a Hamming window. The characteristics of the low-pass FIR filter are:

- The cut-off frequency has been established in $F_c = 0.1(F_s/2)$ with $F_s = 1/7.5$ m^{-1}. Thus, the normalised cut-off frequency is $\omega_c/\pi = 0.1$. Any change in the spatial resolution of the VRP will be reflected in a change of the normalised cut-off frequency of the filter. Therefore, the normalised cut-off frequency will change to $\omega_c/\pi = 0.1(T/7.5)$, where T is the new spatial resolution of the VRP and 7.5 is the spatial resolution proposed in this analysis. This is very important because in

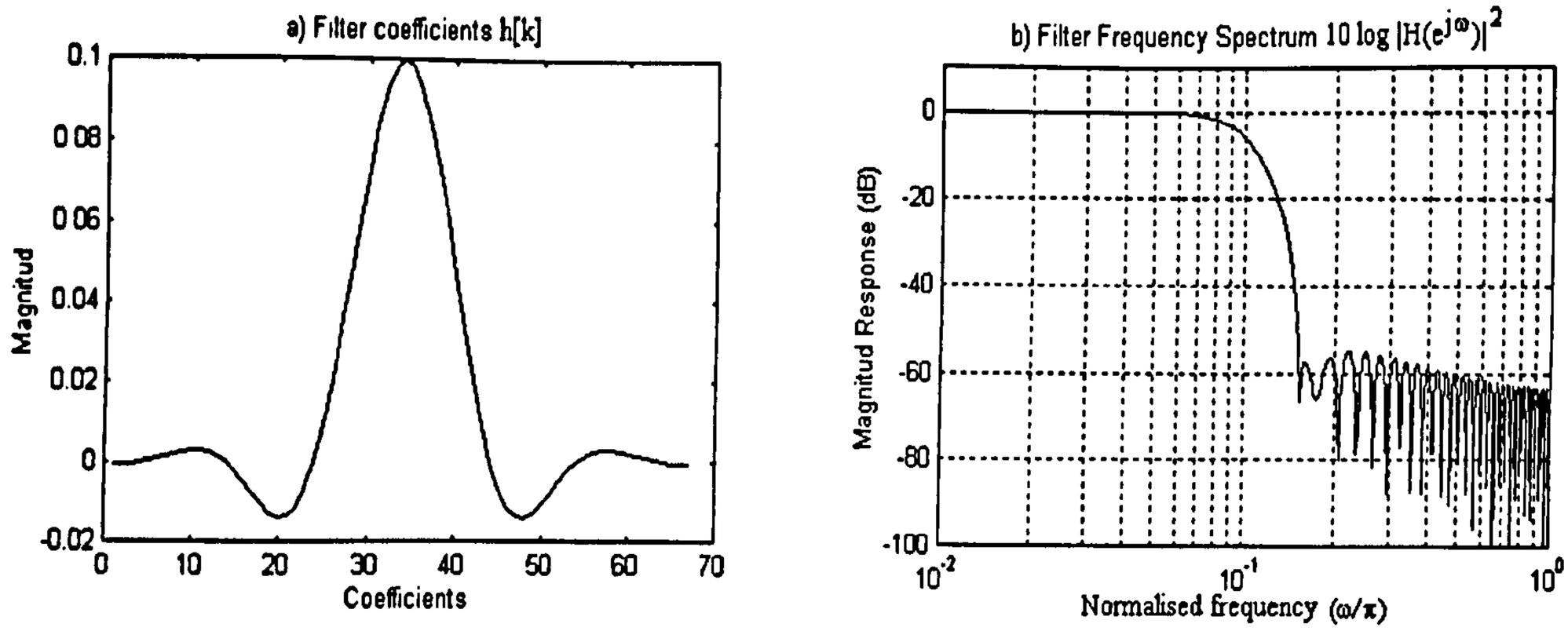

Fig. 4.12: a) Impulse response of a low-pass FIR filter with 66 coefficients. b) Frequency response of the same filter.

digital filter design a percentage of half of the sampling frequency ($F_s/2$) must be specified to calculate the filter coefficients.

- The number of filter coefficients is a function of the transition width. The higher the number of coefficients, the smaller the transition width and the sharper the frequency response of the filter. The transition width in a Hamming window is given by $\Delta\omega = 3.32\pi/N$ (See Appendix B). Fig. 4.11 shows the VRP after applying a FIR filter with 32, 64, 96 and 128 coefficients for the same cut-off frequency. As the number of coefficients increases, the filter frequency response becomes sharper and there are oscillations in the filtered VRP due to rapid changes of reflectivity. However, there is not a need to have a very sharp filter frequency response. A transition width being $\Delta\omega = 0.5(\omega_c)$ is good enough to smooth the VRP and to minimize the oscillations due to the filter frequency response. Therefore, the number of coefficients is $N = 6.6/(\omega_c/\pi)$.

- The stop-band attenuation of a Hamming window is 53 dB.

The frequency response of the filter used in this analysis is shown in Fig. 4.12.

4.4.4 Boundary detection

It has been explained in Section 2.8.1, that there are several factors contributing to the enhancement of reflectivity in the melting layer. A few kilometres above the bright band, aggregation of ice particles is dominant. This is reflected as a continuous increase in reflectivity. Towards the 0°C wet-bulb air temperature, there is a notable increase in reflectivity compared with the reflectivity above. This sudden change in reflectivity defines

the top of the bright band (Z_{snow}). In the bright band, the reflectivity increases reaching a maximal value (Z_{peak}) and then decreases until the ice is completely melted (Z_{rain}). This height defines the bottom of the bright band. Below this height, the reflectivity of water drops is approximately constant.

As it was mentioned in Section 4.1, most of the existing bright band detection algorithms take advantage in some way of the variation of dZ/dh and d^2Z/dh^2. During the development of this research, some tests were carried out taking into account the variation of dZ/dh without satisfactory results. The natural variation of reflectivity in the bright band makes it difficult to establish a general condition to obtain the boundaries. Therefore, it has been concluded that using the gradient of reflectivity to estimate the bright band boundaries is not the best solution.

The new proposal to detect the bright band is based on the rotation of coordinates to obtain clear boundaries. The detection starts on the point h_{peak} where the reflectivity of the bright band is a maximum. To get to this point, dZ/dh is calculated. The numerical differentiation of the vertical reflectivity profile $Z(h)$ at the height h_0 is estimated by (Burden and Faires, 2001):

$$\frac{\mathrm{d}Z(h_0)}{\mathrm{d}h} = \frac{1}{12\Delta h}[Z(h_0 - 2\Delta h) - 8Z(h_0 - \Delta h) + 8Z(h_0 + \Delta h) - Z(h_0 + 2\Delta h)] \quad (4.12)$$

where Δh is the sampling period. The conditions to locate a maximum on $Z(h)$ are:

$$\text{If } \begin{cases} \mathrm{d}Z(h_0 - \Delta h)/\mathrm{d}h > 0 \\ \mathrm{d}Z(h_0 + \Delta h)/\mathrm{d}h < 0 \end{cases} \Rightarrow Z(h_0) \text{ is maximum} \quad (4.13)$$

If the condition 4.13 is fulfilled, the maximum is located at the height h_0, then $h_{peak} = h_0$. This height can also be obtained from the maximum reflectivity in $Z(h)$. Following this concept, the boundaries of the bright band are well defined if they are seen from different coordinate systems. The new coordinate systems have the origin on the point $[h_{peak}, Z(h_{peak})]$. A translation of coordinates is performed on the original coordinate system $h - Z$ to obtain the coordinate systems $h'_{upper} - Z'_{upper}$ and $h'_{lower} - Z'_{lower}$ for the upper and lower parts of the bright band respectively (See Fig. 4.13). The coordinate systems $h''_{upper} - Z''_{upper}$ and $h''_{lower} - Z''_{lower}$ are obtained by performing a rotation of coordinates on the translated coordinate systems $h'_{upper} - Z'_{upper}$ and $h'_{lower} - Z'_{lower}$ respectively (See Fig. 4.14). This algorithm searches for the maximal value in the rotated coordinate system rather than take into account local variations of dZ/dh. The boundaries may not be well defined in the coordinate system $h - Z$, but they will have a unique value on the

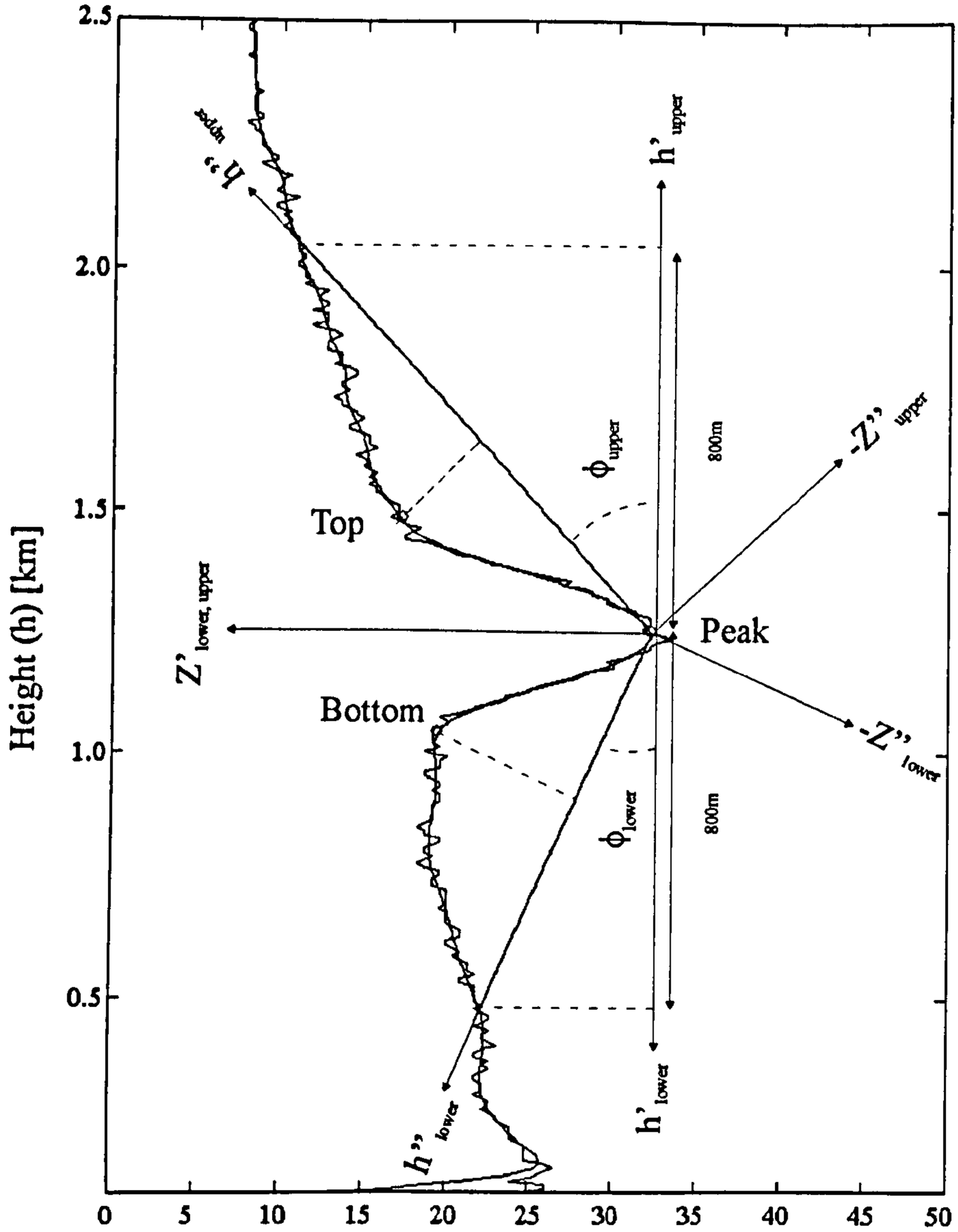

Fig. 4.13: Detection of the bright band boundaries by rotating the coordinate system. The VRP has been recorded at Bristol on 26/01/02 at 13:07 hr GMT.

coordinate system $h'' - Z''$. The location of the bright band boundaries depends on the rotation angle ϕ (See Fig. 4.13). In order to establish the value of ϕ, it must be considered that the h'' axis must intercept the reflectivity profile $Z(h)$ at a height of 800 m above and below h_{peak}, safe enough to guarantee it is outside the bright band boundaries. This value has been established, assuming that the upper and lower parts of the bright band were less than 800 m from h_{peak}. Fabry (1994a) found that in Montreal the total bright band thicknesses are from 150 m to less than 1000 m for rainfall reflectivities up to 40 dBZ. Kitchen et al. (1994) proposed a maximum bright band thickness of 700 m based on the Chilbolton weather radar observations to correct scanning weather radar measurements. It is important to mention that this algorithm may fail when a bright band is thicker than 1600 m, but a thickness of this magnitude is unlikely to occur.

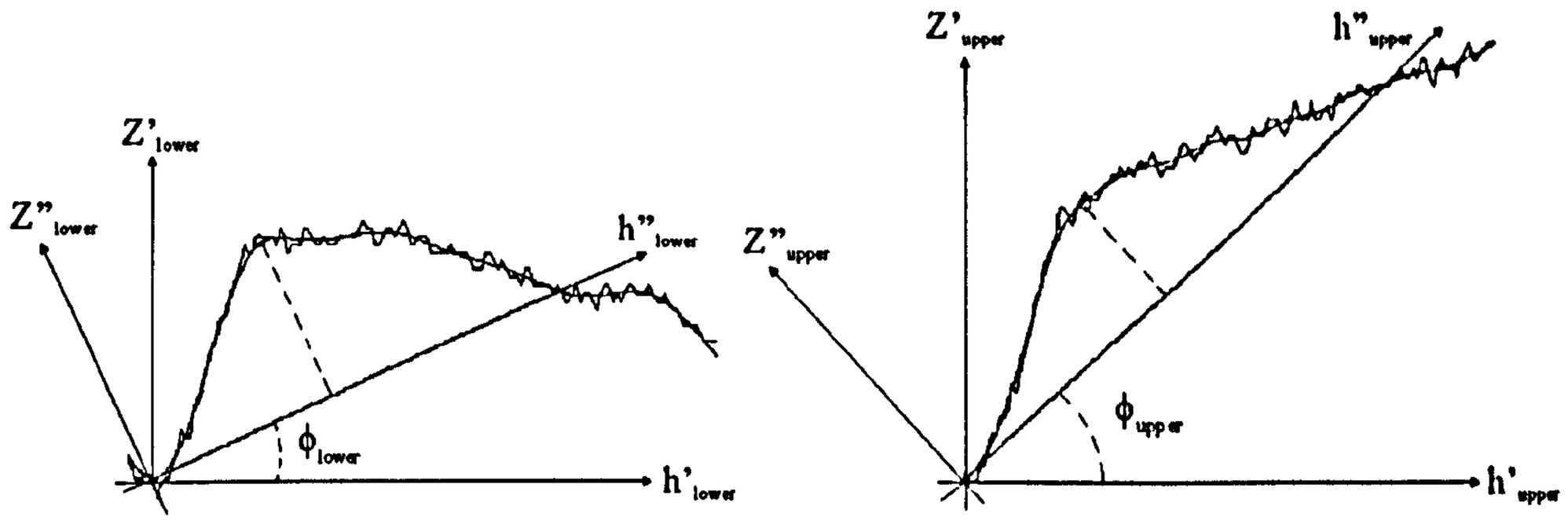

Fig. 4.14: Simplification of the detection of the bright band boundaries using coordinate rotation.

The rotation angle in the upper part of the bright band is calculated by:

$$\phi_{upper} = \tan^{-1}\left[\frac{Z(h_{peak}) - Z(h_{peak} + 800)}{800}\right] \tag{4.14}$$

and the rotation angle in the lower part of the bright band is calculated by:

$$\phi_{lower} = \tan^{-1}\left[\frac{Z(h_{peak}) - Z(h_{peak} - 800)}{800}\right] \tag{4.15}$$

where h_{peak} is the height of the maximum bright band reflectivity. Therefore, the rotated coordinate systems are calculated by (See Fig 4.14):

$$h''_{upper,lower} = h'_{upper,lower} \cos\phi_{upper,lower} + Z'_{upper,lower} \sin\phi_{upper,lower} \tag{4.16}$$

$$Z''_{upper,lower} = Z'_{upper,lower} \cos\phi_{upper,lower} - h'_{upper,lower} \sin\phi_{upper,lower} \tag{4.17}$$

The heights of the top and bottom of the bright band are those points in the rotated coordinate systems with the maximal values. The rotation algorithm avoids local maximums that could be misinterpreted by some other algorithms as possible boundaries. This algorithm searches for the maximal variation in the 800 m interval rather than local variations of reflectivity along the vertical. When the reflectivity value on the interception with the new axis h'' is less than or equal to zero, a new interval less than 800 m is defined until the value of reflectivity on the interception is greater than zero.

Following this procedure, a vertical reflectivity profile may have several possible "bright bands", but only one of them is due to melting snowflakes rather than to local variations of the reflectivity in the vertical. To overcome this problem, two more conditions have been defined. The first condition is to define an average gradient of reflectivity for the

lower and the upper part of the bright band. It has been found that a slope greater than 10 dBZ km^{-1} and smaller than -10 dBZ km^{-1} for the lower and upper part of the bright band respectively are good thresholds. Below these limits, possible peaks can be found, but they will be the natural variation of the vertical reflectivity profile rather than bright bands. The second condition, is to measure the power inside the bright band. The power in the bright band can be calculated by:

$$P_{BB} = \frac{1}{h_{top} - h_{bottom}} \int_{h_{bottom}}^{h_{top}} [Z(h)^2 - f(h)^2] \tag{4.18}$$

where $f(h)$ is the line equation defined by the points $[h_{bottom}, Z(h_{bottom})]$ and $[h_{top}, Z(h_{top})]$. The bright band is that enhancement with maximum power.

In convective situations the algorithm may fail in detecting the bright band because of the large gradients of reflectivity along the vertical. This applies to any algorithm that makes use of only reflectivity data. In this case, dual-polarisation radar measurements may help to overcome this problem (See Hines, 1983; Hopper et al., 1991).

4.5 Results

Fig. 4.15 shows a particular VRP with its gradient of reflectivity, dZ/dh, and its curvature function, $\rho(h)$. The bright band boundaries have been obtained using the rotation algorithm and the algorithms proposed by Tilford et al. (2001) and Fabry and Zawadzki (1995).

The asymmetrical shape of the bright band makes it difficult to extract the boundaries using Tilford et al.'s algorithm. The top of the bright band is around 150 m above the top detected by the rotation algorithm, although the value of reflectivity is approximately the same. In such a case, the overestimation is only in the bright band thickness and not in reflectivity. However, the bottom of the bright band is 75 m above the bottom detected by the rotation algorithm and the value of the bottom reflectivity is being overestimated.

Fabry and Zawadzki's algorithm takes into account the curvature of reflectivity to detect the boundaries. In this case the boundaries have been underestimated, resulting in the bright band thickness being underestimated and the top/bottom reflectivities overestimated. In order to detect the boundaries accurately through the curvature function, it is necessary for a strong curvature to exist on the boundaries.

Fig. 4.16 shows a HTI scan obtained from a VPR located at Bristol, UK. Every profile has been averaged and resampled over 30 s intervals, discarding no-rain periods. The rotation algorithm follows the bright band boundaries satisfactorily.

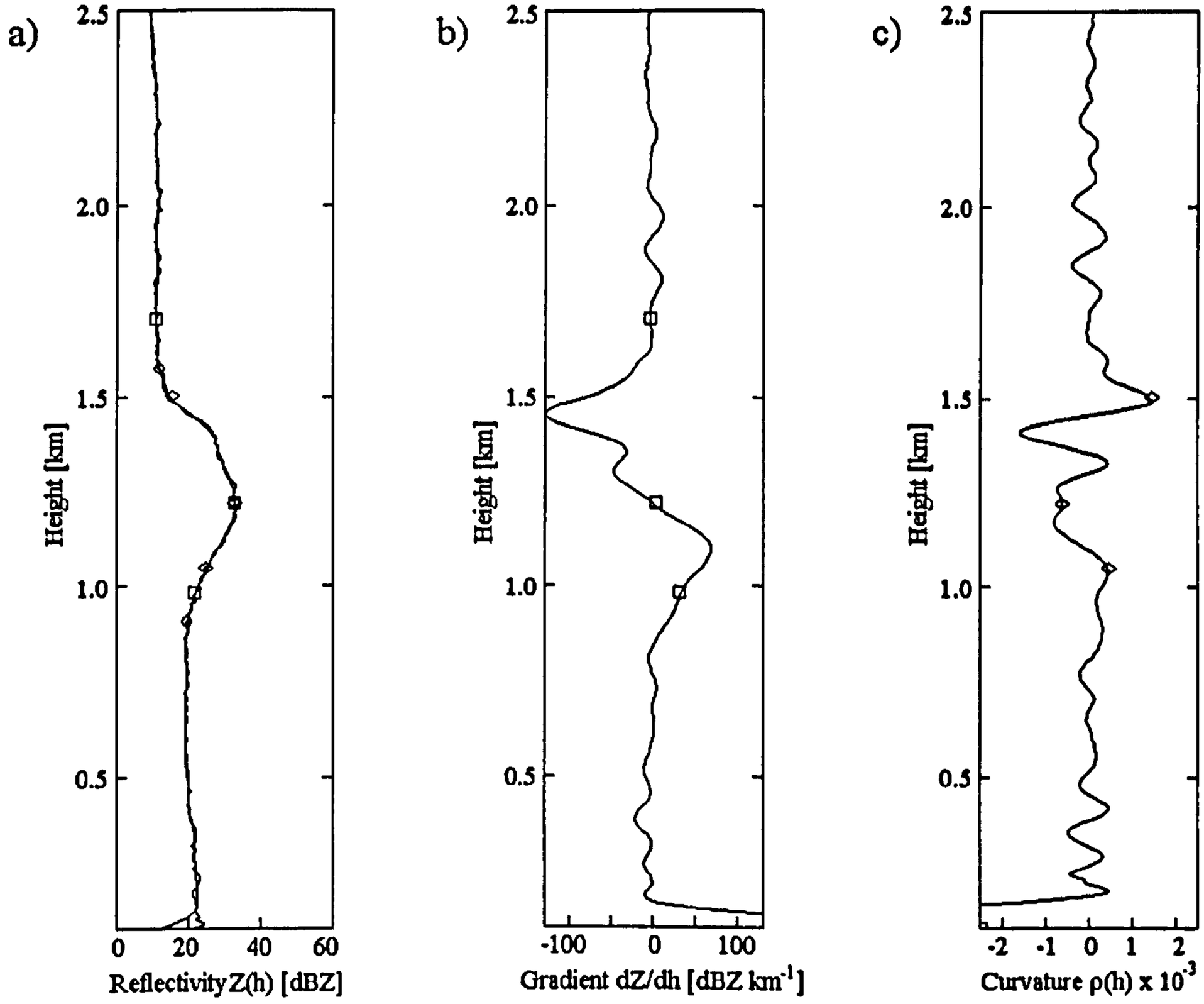

Fig. 4.15: Heights of the bottom, peak and top of the bright band from Bristol on 26/01/02 at 12:55 hr GMT. The boundaries are detected as follow: circles using the rotation algorithm, squares as in Tilford et al. (2001), diamonds as in Fabry and Zawadzki (1995).

The RHI shown in Fig. 4.17 presents a convective cell with high values of reflectivity. The algorithm avoids the convective cell. It is important to remark, that the condition of the average slope in the upper and lower part of the bright band avoids misinterpreting some peaks as possible bright bands. Additionally, the average power inside the bright band selects the strongest peak found in every VRP, which fulfills the conditions for detecting a likely bright band.

Fig. 4.18 shows an RHI scan from Chilbolton radar. The scan has been transformed from polar to rectangular coordinates and the VRP have been extracted individually and smoothed with a FIR filter to apply the boundary detection. In this case, there is no two-dimensional filtering in the RHI image. The result is reflected in the variation of the bright band boundaries between consecutive VRP. However, applying a two-dimensional averaging filter to the RHI image in rectangular coordinates, improves considerably the bright band detection, smoothing the variation between consecutive profiles (See Fig. 4.19).

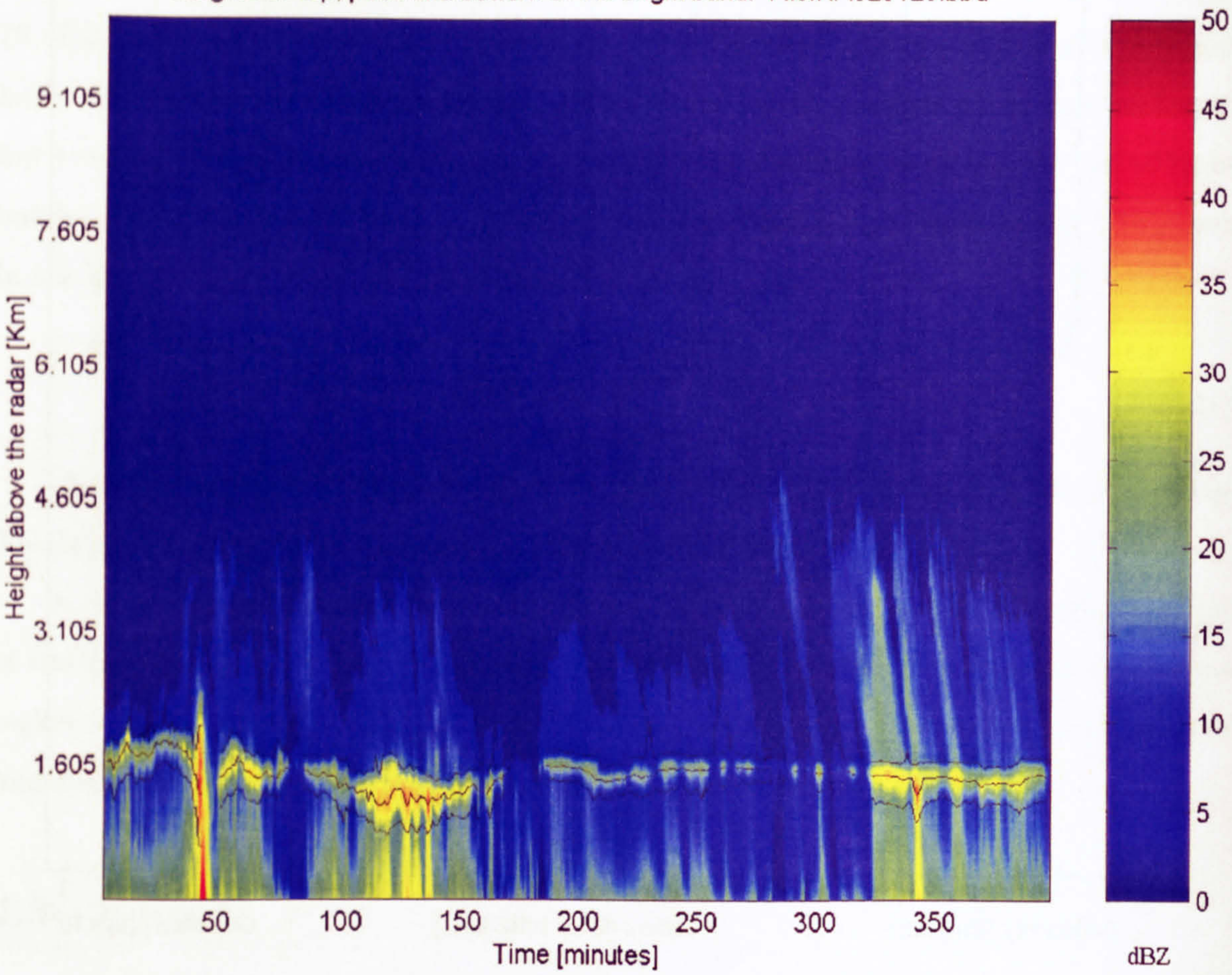

Fig. 4.16: Bright band boundaries on 26 January 2002 starting at 10:30 hr.

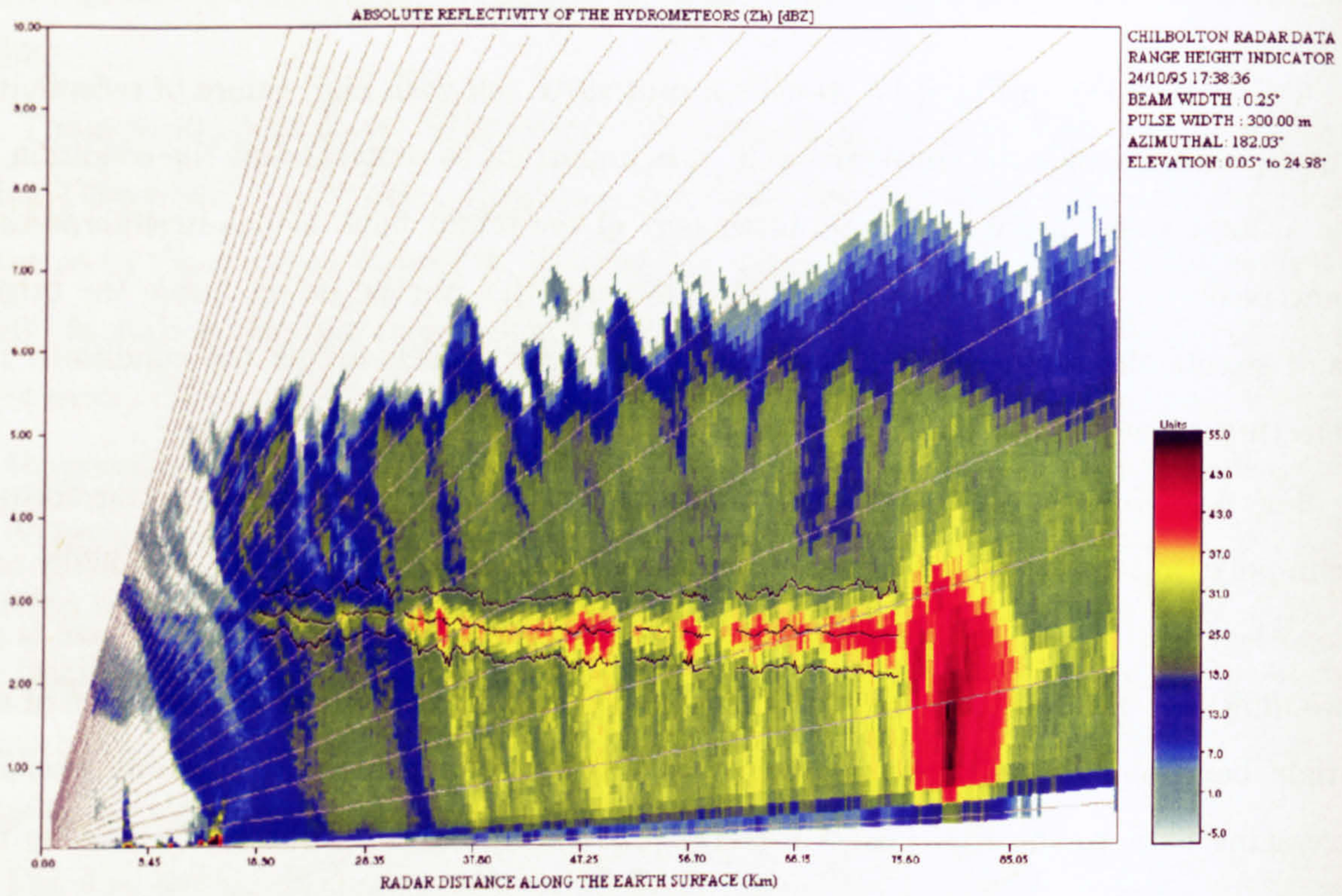

Fig. 4.17: Bright band boundaries on 24 October 1995. RHI from the Chilbolton radar.

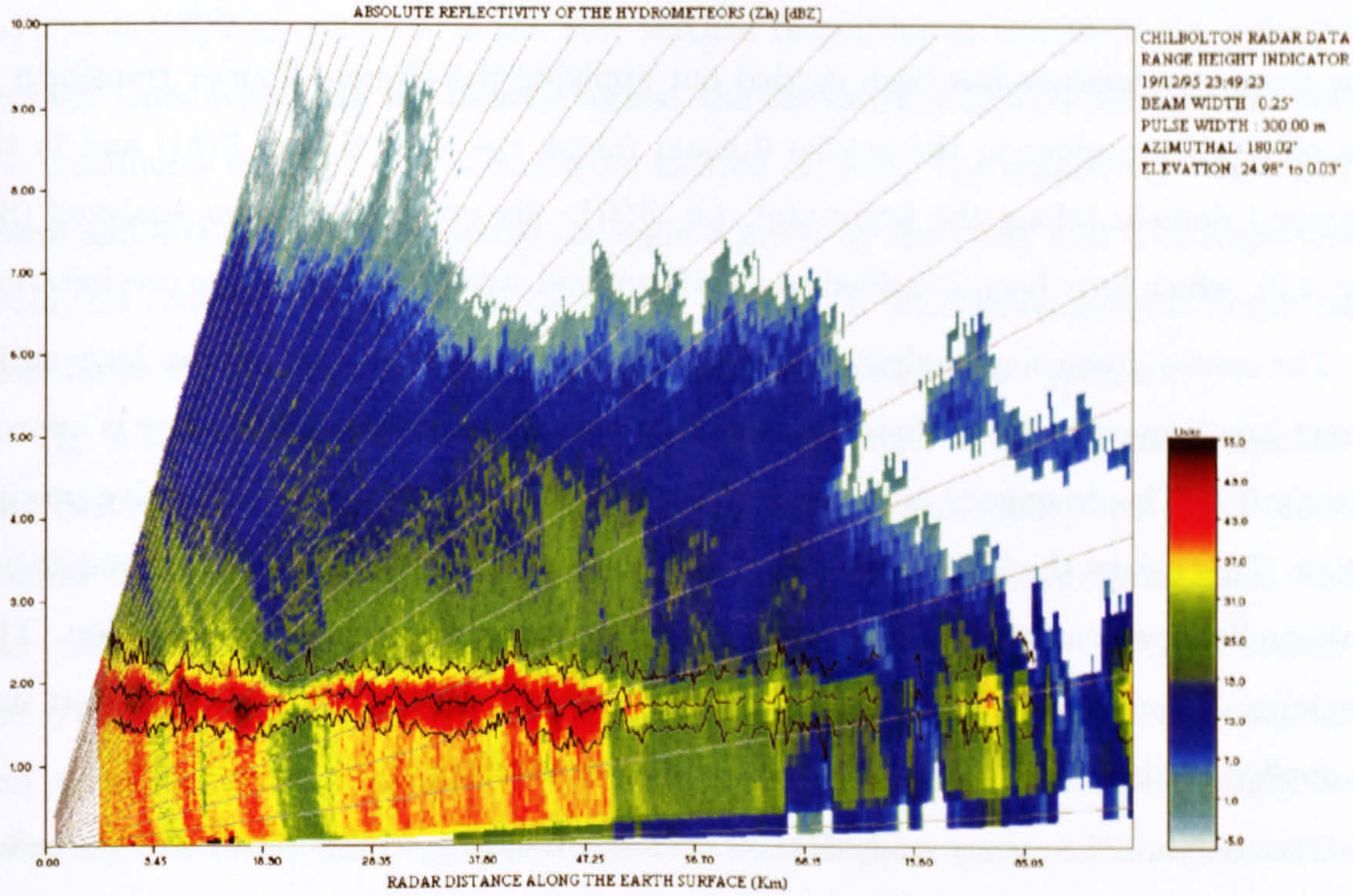

Fig. 4.18: Bright band boundaries on 19 December 1995. RHI from the Chilbolton radar without the two-dimensional filtering.

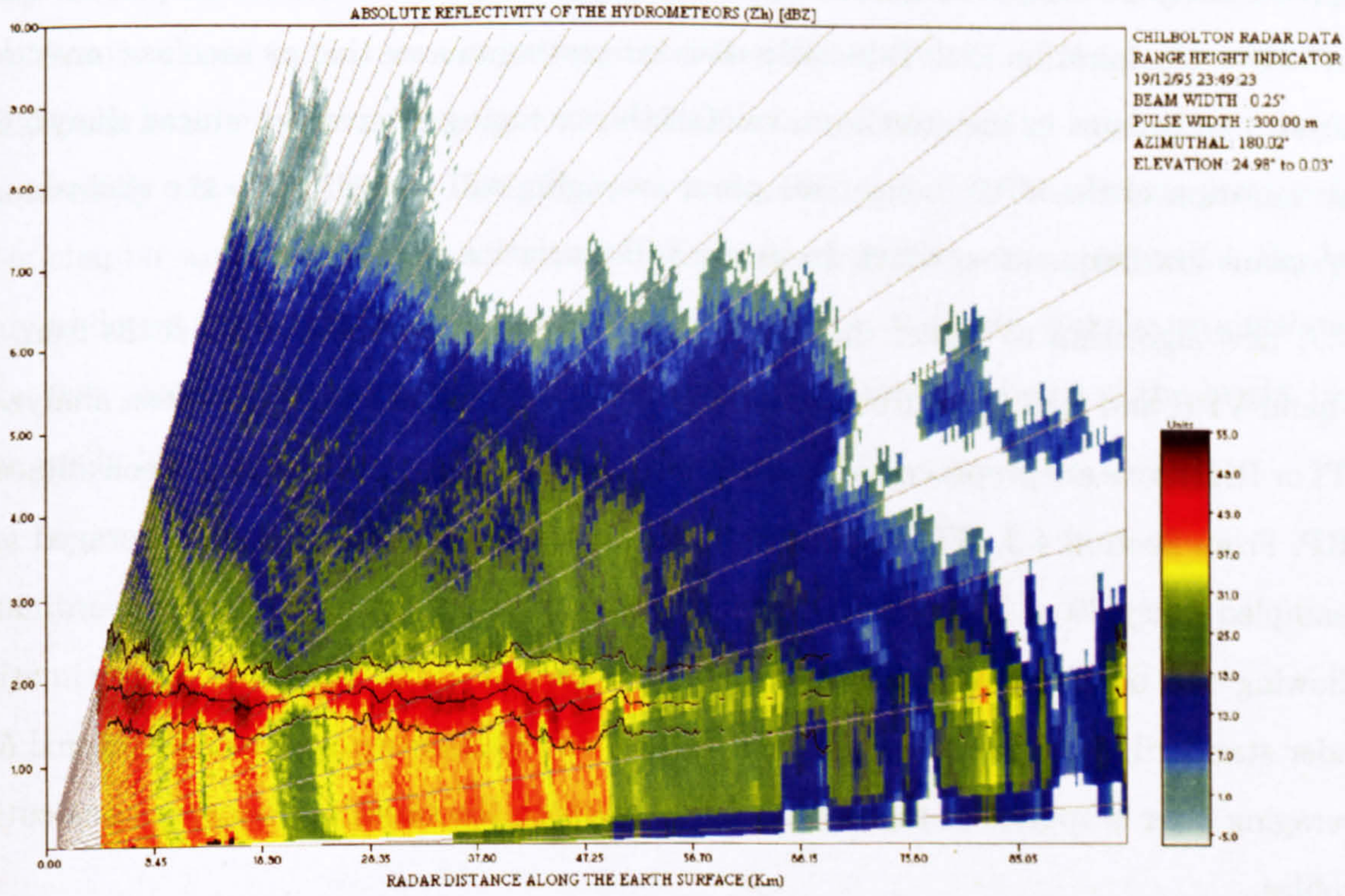

Fig. 4.19: Bright band boundaries on 19 December 1995. Pre-filtered RHI using a 5x5 averaging filter (50 m vertical x 1500 m horizontal).

4.6 Conclusions

The frequency analysis has been carried out applying the discrete Fourier transform to the reflectivity profiles in the spatial domain (along the vertical, *i.e.* $Z(h)$) and in the temporal domain (along the horizontal, *i.e.* $Z(t)$). Six events have been analyzed (See Fig. 4.2), which have been classified as stratiform and stratiform-convective precipitation.

The spatial frequency analysis shows that the vertical reflectivity profiles have an inherent low-frequency signal characteristic. The maximal normalised frequency is approximately 0.1. This frequency is the same for stratiform and stratiform-convective precipitation. This means the VRP from either stratiform or stratiform-convective precipitation have similar low-frequency characteristics independent of the type of precipitation. This frequency becomes the cut-off frequency for digital filter design and any filter that may be applied to the VRP should take into account this frequency.

The temporal frequency analysis shows the low-frequency characteristics of the reflectivity profiles in the temporal domain. The normalised cut-off frequencies for stratiform and stratiform-convective precipitation are 0.011 and 0.033 respectively. These cut-off frequencies indicate that the maximal temporal averaging between adjacent profiles and resampling of vertical reflectivity profiles without losing the dynamics of the storm is approximately 90 s for stratiform rainfall and approximately 30 s for mixed stratiform-convective precipitation (See Table 4.3). It is interesting to note that as soon as convection starts to be present in the stratiform rainfall the averaging interval is reduced due to the fast variation of the VRP. Longer temporal averaging will contribute to the exclusion of important low frequencies, which are part of the variation of precipitation.

A new algorithm to detect the bright band has been developed. HTI scans from an X-band VPR and RHI scans from an S-band scanning weather radar have been analyzed. HTI or RHI scans are preprocessed to avoid large variations or reflectivity between adjacent VRP. From Section 4.3, HTI profiles from stratiform precipitation may be averaged and resampled every 30 s. RHI scans are transformed from polar to rectangular coordinates following the beam propagation equations and the 4/3 earth curvature approximation under standard atmospheric conditions. Then, a convolution with a two dimensional 5x5 averaging filter is applied to the whole image to smooth the variations between consecutive profiles.

After the preprocessing has been carried out, the VRP are extracted from either HTI or RHI scans. Every VRP is extracted and filtered independently using a low-pass FIR filter. The normalised cut-off frequency of this filter is $\omega_c/\pi = 0.1$ for a sampling period

of 7.5 m. For a different sampling period, the normalised cut-off frequency would be $\omega_c/\pi = 0.1(T/7.5)$, where T is the new vertical resolution in metres of the reflectivity profiles. Once every VRP has been smoothed, the derivative of $Z(h)$ is calculated to obtain the maximums on $Z(h)$. For a maximum located on $Z(h)$, the reflectivity values 800 m above and 800 m below are rotated an angle ϕ given by Eqs. 4.14 and 4.15 respectively. From this rotation, a new coordinate system $h'' - Z''$ is established and the bright band boundaries are the maximal values reached in the new coordinate systems.

Fig. 4.15 has shown that this new technique to detect the bright band boundaries performs better than the algorithms proposed by Tilford et al. (2001) and Fabry (1994a), because the boundary detection relies on the value of reflectivity where the maximal change has taken place. For instance, the algorithm proposed by Tilford et al. (2001) relies on the symmetry of the upper and lower part of the bright band to detect the boundaries and when the maximal gradient of reflectivity is not the mid-point of the bright band boundary, the result will be an overestimation or underestimation of the real boundaries (See Fig. 4.15b). On the other hand, the curvature function tends to underestimate the bright band boundaries because it relies on a strong curvature around the bright band boundaries (See Fig. 4.15c).

It is clear that there is not a specific rule to detect the extent of the bright band using only single-polarisation vertical reflectivity profiles. Without additional information, the problem is closed to feature extraction, but when fall velocities of the hydrometeors or dual-polarisation measurements are available, the boundaries of the bright band may be more easily obtained (Hines, 1983; Hopper et al., 1991). All the conditions proposed in this chapter are based on the analysis of hundreds of profiles, concluding that the best way to detect the bright band is not directly the variation of dZ/dh, but the establishment of a new coordinate system rotated in such a way that the boundaries of the bright band are easily identified.

Chapter 5

Long-term bright band analysis at X-band frequencies

5.1 Introduction

There has been important and continuous research conducted to measure the Vertical Reflectivity Profiles (VRP) with Vertically Pointing weather Radars (VPR). All the research work presented in this chapter is based on the large amount of VPR data collected by Prof. Ian Cluckie since the building and commissioning of one VPR at Salford University in 1991 (Tilford and Cluckie, 1991). Several studies have been conducted since the installation of this VPR. Preliminary tests were carried out in April 1991 and later two mobile VPR devices were designed and commissioned during 1993 and 1994, operating at different sites within the Manchester region. Then, three VPR devices operated continously from 1991 to 1995 on the North West of England (Tilford and Cluckie, 1993; Tilford et al., 1995a); the sites included Liverpool, Warrington, Davyhulme, Salford, Audenshaw and Harrop Edge. In the second half of 1995 the VPR were deployed in the South West of England, during the HYdrological Radar EXperiment (HYREX) (Lane, 1997; Cluckie et al., 2000); the sites were Alhampton, Middle Wallop and Boscombe Down. Since 2001 onwards one of the VPR has been operating at Bristol, UK. The different deployments of the VPR within England are shown in Fig. 5.1.

Additionally, the VPR have been deployed in different climatological regions. On October 1996, one of the VPR was shipped and deployed in the Southern Alps of New Zealand during the Southern ALPs EXperiment (SALPEX) (Wratt et al., 1996). The microphysical characteristics of the reflectivity data were studied in Lane (1997), where orographic enhancement influenced in great measure weather radar rainfall measurements.

Fig. 5.1: VPR deployments in England from 1991 to 2002.

During Autumn 1998, one of the VPR was deployed in Marseille, on the South East French Mediterranean coast during the Hydromet Integrated Radar Experiment (HIRE) (Uijlenhoet et al., 1999).

Hundreds of hours of vertical reflectivity profiles were collected during this time with one, two and four seconds of temporal resolution and 7.5 m and 30 m of spatial resolution. The total hours of VRP recorded by the VPR are summarised in Table 5.1.

Gray et al. (2001) pointed out the need to have reflectivity measurements over different climatological areas in order to have a better understanding of the variability of the vertical reflectivity profile. It is quite important to study the variation in the vertical reflectivity profile, in particular when the bright band is present to support the development of algorithms to correct scanning weather radar measurements, which were contaminated with the high scattering of microwaves due to melting snowflakes. The influence of the bright band over rainfall measurements depends on its height, thickness and amount of increase. Some of these parameters are climate dependent and therefore determined by the climatological region, but others are related to the microphysics of precipitation and may be very similar even for different climatological regions. This chapter presents the analysis of the bright band from the long-term database of X-band VRP observations (See Table 5.1).

Site or region	Data period	Precipitation
North West, England	May 1991 to December 1994	1201.26 hr
South West, England	April to December 1995	354.99 hr
Bristol, England	June 2001 to December 2002	98.10 hr
The Southern Alps, New Zealand	October 1996	115.43 hr
Marseille, France	September to November 1998	65.93 hr

Table 5.1: Precipitation time recorded with the VPR from 1991 to 2002.

5.2 Data processing

The analysis of the bright band characteristics has been carried out in the following way. Every region shown in Table 5.1 has been analysed independently and although the analysis is very similar, different aspects of the radar bright band are covered individually in different sections.

All the vertical reflectivity profiles have been averaged over one-minute intervals to smooth the noise in the reflectivity but at the same time ensuring the variation in precipitation does not change too quickly from profile to profile. The temporal averaging of one minute is supported by the frequency analysis carried out in Section 4.3 for VRP in stratiform precipitation.

The bright band detection algorithm developed in Chapter 4 has been applied to the database of X-band VRP. The key parameters are the reflectivity in snow ($Z_{e(snow)}$) at the height of the bright band top, the maximal reflectivity inside the bright band ($Z_{e(peak)}$) at the height of the bright band peak, the reflectivity in rain ($Z_{e(rain)}$) at the height of the bright band bottom and the thickness of the bright band (T_{BB}). The seasonal dependence of the height of bright band top have also been obtained. Additional parameters around the bright band were obtained where required.

When describing the bright band increase in terms of dBZ units, it is important to remark, that dBZ units are a logarithmic scale and attention must be focused when comparing it to rainfall rates. For instance, 12 dBZ of bright band increase over rain reflectivities of 10 dBZ (0.15 mm hr^{-1}) results in an increment of +0.71 mm hr^{-1} but 12 dBZ increase over rain reflectivities of 20 dBZ (0.65 mm hr^{-1}) results in an increment of +2.99 mm hr^{-1}. The same concept applies when a standard deviation in dBZ units is evaluated.

Fabry et al. (1994) presented a similar analysis of the bright band characteristics over Montreal, Canada. He pointed out that whereas the relative frequency of the rainfall intensity depends on the climatological region, the reflectivity profiles are related to the

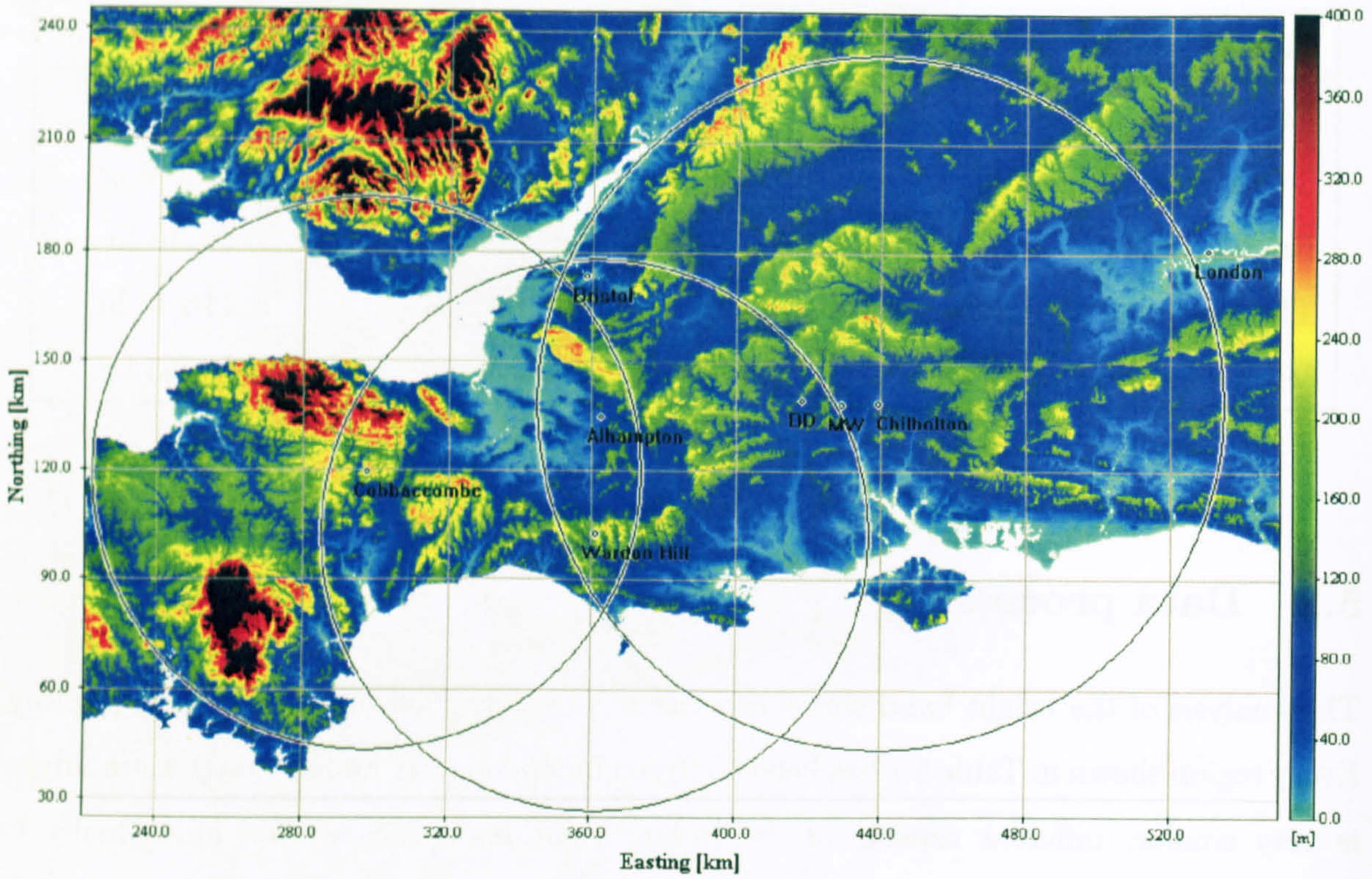

Fig. 5.2: HYREX radar sites. Two X-band VPR were located at Boscombe Down (BD), Middle Wallop (MW) and Alhampton; two C-band scanning radars located at Cobbacombe and Wardon Hill sites and one S-band radar located at Chilbolton.

microphysics of precipitation and then, similar characteristics of the variation of reflectivity in the bright band may be expected.

The general descriptions of the different radar experiments introduced in Section 5.1 are presented in the following subsections.

5.2.1 HYREX

HYREX was a UK Natural Environment Research Council (NERC) radar experiment carried out in the South West of England from May 1993 to April 1997. The objectives were to study the variability of precipitation as observed by weather radars in order to improve surface and radar estimates of rainfall for hydrological purposes.

The infrastructure comprised two single-polarisation C-band scanning weather radars from the national network at Wardon Hill and Cobbacombe Cross, an experimental dual-polarisation S-band scanning radar at Chilbolton operated by the Rutherford Appleton Laboratory and two mobile X-band vertically pointing weather radars deployed and commissioned by the Water Resource Research Group from Salford University (Cluckie et al., 2000). Additionally, a dense network of 49 recording rain gauges were deployed in the Brue catchment over an area of 135 km^2 (Moore et al., 2000). The VPR data were supported

with the deployment of automatic weather stations close to the radar sites (See Fig. 5.2). Initially, one of the VPR was deployed close to Chilbolton radar but two weeks later was relocated to Middle Wallop. At the same time, another VPR was deployed at Boscombe Down. During August, the VPR deployed at Boscombe Down was displaced to Alhampton on the Brue catchment. Therefore, two VPR were operating almost continuously within the South West region from April 1995 to December 1995.

The Chilbolton radar was operating continuously from February 1994 to May 1996. The data include Plan Position Images (PPI) with azimuthal angles from 225° to 315° and Range Height Images (RHI) with elevation angles from 0° to 25° above the regions where both, the VPR and rain gauges, were deployed.

5.2.2 SALPEX

SALPEX was developed to study the influence of the Southern Alps on the weather and climate of New Zealand (Wratt et al., 1996). During 1993 to 1995 the study was focused on the mountain influences on the South island. Later from 1996 to 1997 field experiments were carried out and an X-band VPR was shipped from Salford to New Zealand to study the microphysics of the rainfall in mountainous areas.

The infrastructure of SALPEX comprises a research aircraft equipped with atmospheric instruments, a high resolution X-band scanning radar developed by the Atmospheric Physics Group from the University of Auckland and located on the west coast and a Doppler weather radar operated by the New Zealand meteorological service. The VPR shipped from Salford to New Zealand was deployed in Otira, at 360 m above the mean sea level in the west coast. Additional instruments such as tipping bucket rain gauges, a high-resolution drop counting gauge, a disdrometer and a weather station were deployed near to the VPR site.

5.2.3 HIRE

The main objective of HIRE was to improve the estimation of rainfall over a large Mediterranean urban area by the integration of additional radar equipment supported by conventional rain gauges. Improving the quality of the radar data for hydrological modelling was one of the main focus points of HIRE.

The experiment took place in Marseille (South East French coast) between September and November 1998 (Uijlenhoet et al., 1999). The infrastructure comprised a network of 25 rain gauges, an S-band weather radar located 93 km North-West from Marseille which is part of the MeteoFrance Aramis radar network, an X-band weather radar operating in

RHI mode and a mobile X-band vertically pointing weather radar operated by the Water and Environmental Management Research Centre (WEMRC) (Dupasquier et al., 2000).

5.3 Climatology of the different sites

5.3.1 England

The geographic location of Britain is the main factor controlling its weather, combining the influence of the mid-latitude westerly winds and the North Atlantic drift bringing warm water from the tropics (Hulme and Barrow, 1997). The general weather conditions and the climate of Britain are shaped by atmospheric circulation (Sterling, 1982). Depending on the character of the surfaces over which the wind is flowing, the atmosphere will experience changes in temperature and humidity, giving rise to the four well-known air masses: maritime (humid), continental (dry), polar (cold) and tropical (warm) (Wheeler and Mayes, 1997). The sources and movement of air masses over the British Isles is a combination of those air masses and classified as tropical continental, polar continental, polar maritime and tropical maritime, the last two categories being the most common (Wheeler and Mayes, 1997).

Rainfall over the British Isles is produced from three sources: frontal systems, local atmospheric static instability (thunderstorms) and atmospheric uplift by hills and mountains (Hulme and Barrow, 1997). In addition, it has recently become recognized that mesoscale processes are also responsible for precipitation development in the UK. The highest amounts of rainfall are usually produced by cyclonic, southerly or westerly circulations (Hulme and Barrow, 1997), driving moist maritime air masses originated from the Gulf of Mexico, the Caribbean and the Azores. Orography plays a major role in the distribution of precipitation not only in England, but also in any region with high mountains. Orographic enhancement of precipitation occurs at low levels over hills exposed to strong moist maritime air flows. When the wind is forced to rise over hills, large quantities of cloud and rainfall are formed. According with this, zones around mountainous areas are prone to suffer orographic enhancement, resulting in large quantities of precipitation. Thus, precipitation is greater in the western half of the British Isles due to the combined effect of the orography and westerly wind circulations.

5.3.2 The Southern Alps, New Zealand

The climate in New Zealand is often classified as warm temperate. According to Garnier (1958), there are two dominant influences controlling the weather in New Zealand. The

first one is its oceanic position in the westerly wind belt of middle latitudes being exposed to the dominant flow of air. The second one is its orography, with very high mountains acting as a physical barrier to the atmospheric flows and contributing to most of the rainfall in some parts of the Islands. Both influences, work together to produce the diversity of climate in New Zealand.

The Southern Alps form a mountain chain extending from the southwest to the northeast in the South Island for a distance of 800 km, with peaks exceeding 2500 m and the highest extending to 3754 m. The orography of New Zealand has a remarkable effect on its climate and weather with higher annual precipitation on the west coast (3.5 m with peaks at around 11 m in the mountains) than on the east coast of the South Island (0.7 m) (Wratt et al., 1996). The Western South Island is regarded as a very wet place and it is commonly called the "rainy Westland" (Garnier, 1958). Northwesterly fronts are very common in New Zealand. As these fronts approach the main alpine divide, orographic rain takes place on the west coast but not always reaching the east coast, hence decreasing the distribution of precipitation. This is the main reason of the variation in precipitation between the west coast and the east coast.

5.3.3 Marseille, France

The particular distribution of land and sea over Europe is a shaping factor of the different regional climates of the continent. The warm seas bordering the continent give central and western Europe a temperate climate even when the greatest part of Europe lies in the northern latitudes. The atmospheric circulation over Europe is essentially determined by the interactions of three well defined pressure centres: the cyclonic centres stationed over the North Atlantic (the Icelandic Low) which are deeper in Winter, the Azores High which is reinforced in Summer and the continental highs and lows which are predominant in the months of Winter and Summer respectively (Martyn, 1992).

The prevailing westerly flows during most of the year, are warmed by their passage over the North Atlantic ocean currents bringing a great amount of precipitation, but its strength varies in response with the North Atlantic Oscillation (NAO)[1]. For instance, in the Mediterranean area the Summer is usually hot and dry and most of the rainfall in this area occurs during the Winter. Marseille belongs to western Europe and it lies on the Mediterranean coast. The annual precipitation in this region is around 546 mm.

[1]The NAO is an atmospheric-mass oscillation between the North Atlantic regions of subtropical high surface pressure and subpolar low surface pressure (Lamb and Peppler, 1987).

5.4 Statistics of the bright band in Marseille, France

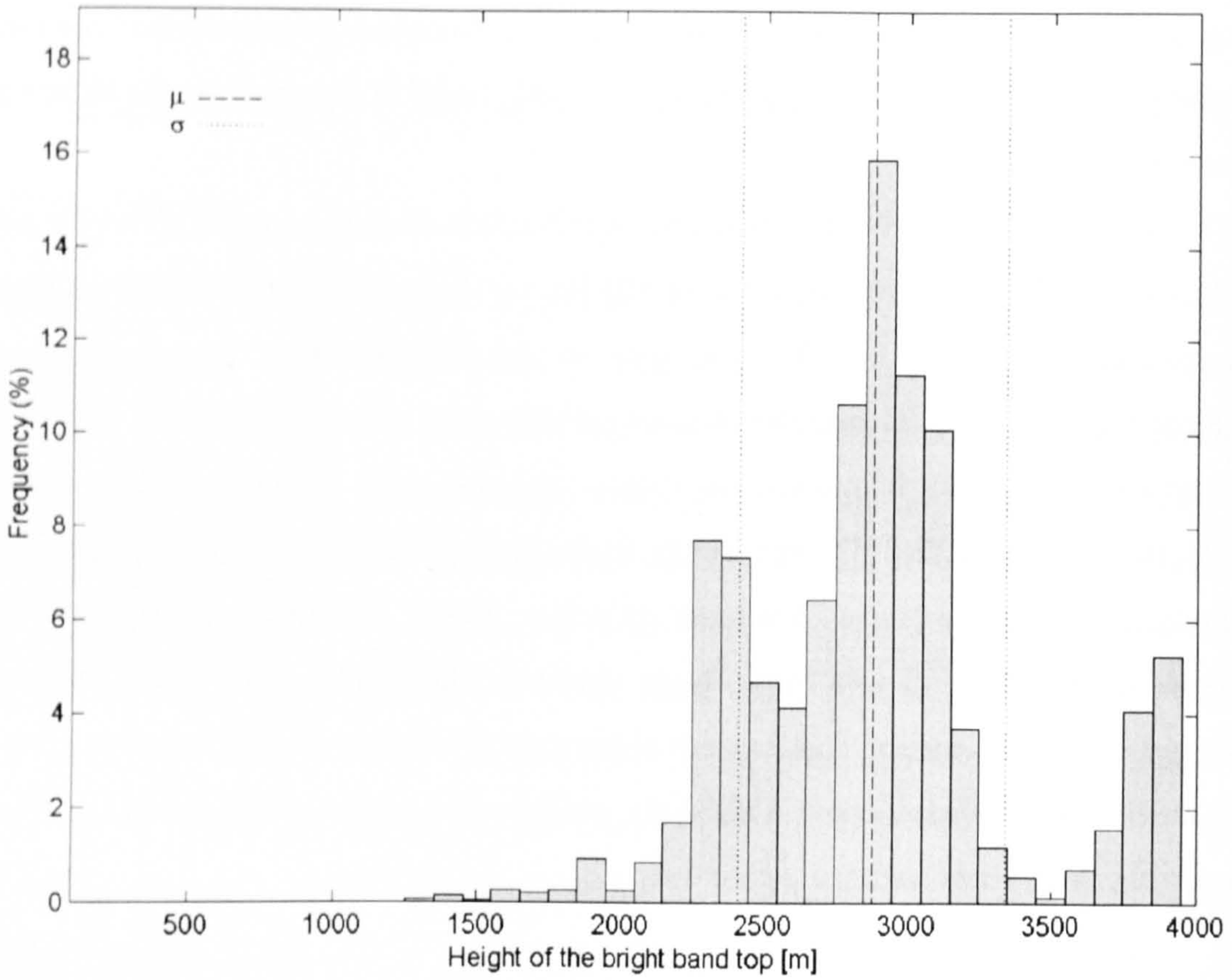

Fig. 5.3: Relative frequency of the height of bright band top over Marseille during September, October and November 1998 (100 m steps).

It is well known that melting starts from the height of the 0 °C wet-bulb air temperature (Klaassen, 1988; Stewart et al., 1984). Therefore, the height of the bright band top is influenced in great measure by the seasons. In Marseille, the VPR was deployed during the months of September, October and November 1998 and the distribution of the height of bright band top is depicted in Fig. 5.3. This distribution covers from around 1900 m to almost 4000 m, being the most frequent height at 2900 m. The mean height of bright band top is 2877 m with 463 m of standard deviation. This distribution is more typical from Summer, where the bright band is above 2 km, but the fluctuations observed below this height represent data taken at the end of November, where temperature starts dropping and the bright band is more frequent at lower altitudes.

Although the presence of the bright band in Marseille is limited to 21.67 hr, Fig. 5.4a depicts a broad distribution of rain reflectivities from 5 dBZ to almost 50 dBZ, with 23 dBZ being the most frequent rain reflectivity. Similar reflectivity distributions are presented for the maximum reflectivity in the bright band and for the reflectivity at the bright band top (Figs. 5.4b and 5.4c respectively). The distribution of $Z_{e(peak)}$ is shifted

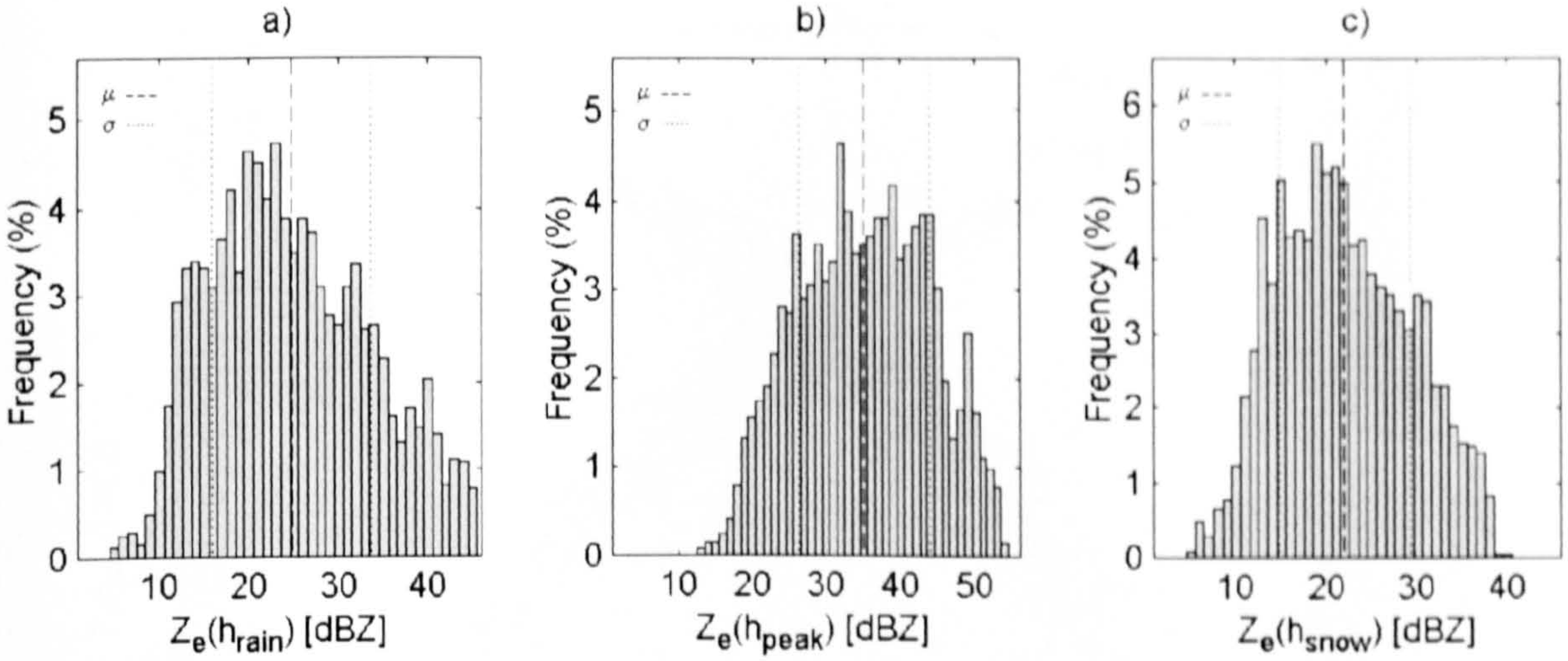

Fig. 5.4: Relative frequency of the reflectivities $Z_{e(rain)}$, $Z_{e(peak)}$ and $Z_{e(snow)}$ over Marseille (1 dBZ steps).

to higher reflectivities compared to the distribution of $Z_{e(rain)}$ because $Z_{e(peak)} > Z_{e(rain)}$. However, the distribution of $Z_{e(snow)}$ fits inside the distribution of $Z_{e(rain)}$ which suggests that usually $Z_{e(snow)} < Z_{e(rain)}$.

Fig. 5.5 shows the scatter plot of the maximum reflectivities within the bright band ($Z_{e(peak)}$) against the reflectivities at the bright band top ($Z_{e(snow)}$), where $Z_{e(peak)}$ is strongly dependent on the value of $Z_{e(snow)}$. The equations shown in the same figure were obtained through linear regression analysis of the scattered data getting a correlation of 0.91 and 3.63 dBZ of standard deviation. Both equations represent the same regression line but the difference is that the upper one is for values of reflectivity in dBZ units and the lower one for values of reflectivity in $mm^6\ m^{-3}$ units.

The slope of the regression line in dBZ units is very close to unity with an offset of 10.90 dBZ. Assuming for instance that the slope is unity, the maximum increase in reflectivity in the bright band for any possible value of snow reflectivity is approximately 10.90 dBZ.

However, the equations shown in Fig. 5.5 are a function of the snow reflectivity and in terms of comparisons it is better to show the scatter plots of $Z_{e(snow)}$ and $Z_{e(peak)}$ as a function of $Z_{e(rain)}$, because the latter is the important parameter that should be transformed to rainfall rate.

Fig. 5.6 shows the scatter plot of the maximum reflectivities within the bright band ($Z_{e(peak)}$) against the reflectivities at the bright band bottom ($Z_{e(rain)}$). In this figure it is observed that $Z_{e(peak)}$ is strongly dependent on the value of $Z_{e(rain)}$. The regression line has a greater value of correlation ($r = 0.94$) than the scatter plot shown in Fig. 5.5. The standard deviation for this line is 3.11 dBZ. The regression line in dBZ units has a slope

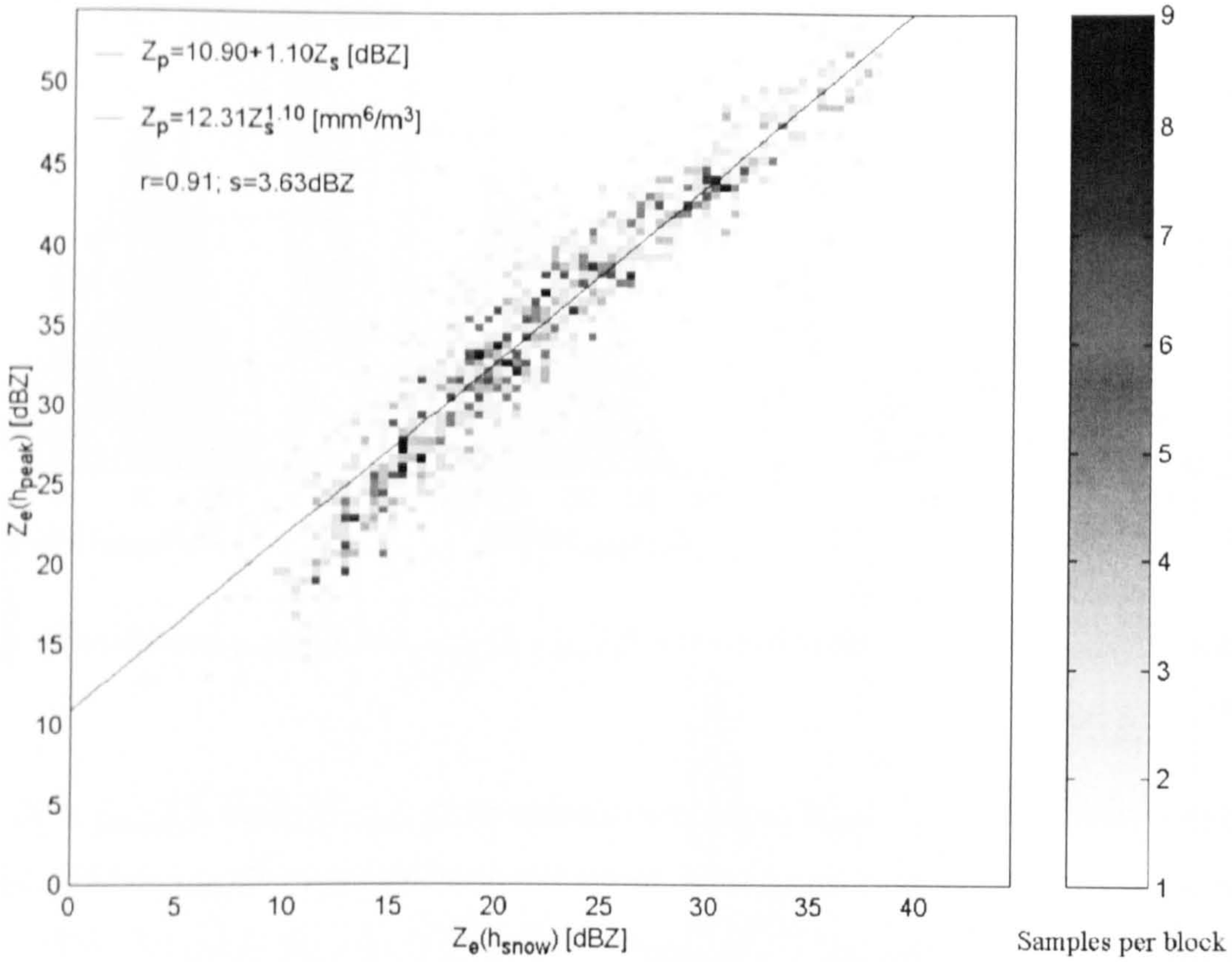

Fig. 5.5: Scatter plot of the maximum reflectivities within the bright band ($Z_{e(peak)}$) against the reflectivities at the bright band top ($Z_{e(snow)}$) at X-band frequencies over Marseille.

of 0.93 with an offset of 12.17 dBZ and it is given by:

$$Z_{e(peak)} = 12.17 + 0.93 Z_{e(rain)}; \qquad \text{dBZ} \tag{5.1}$$

Fig. 5.7 shows the scatter plot of the reflectivities at the bright band top ($Z_{e(snow)}$) against the reflectivities at the bright band bottom ($Z_{e(rain)}$). These data present more scatter than the data shown in Figs. 5.5 and 5.6. The regression analysis shows that the correlation between the regression line and the scattered data is 0.86 with a standard deviation of 3.70 dBZ . The regression line is given by:

$$Z_{e(snow)} = 4.53 + 0.71 Z_{e(rain)}; \qquad \text{dBZ} \tag{5.2}$$

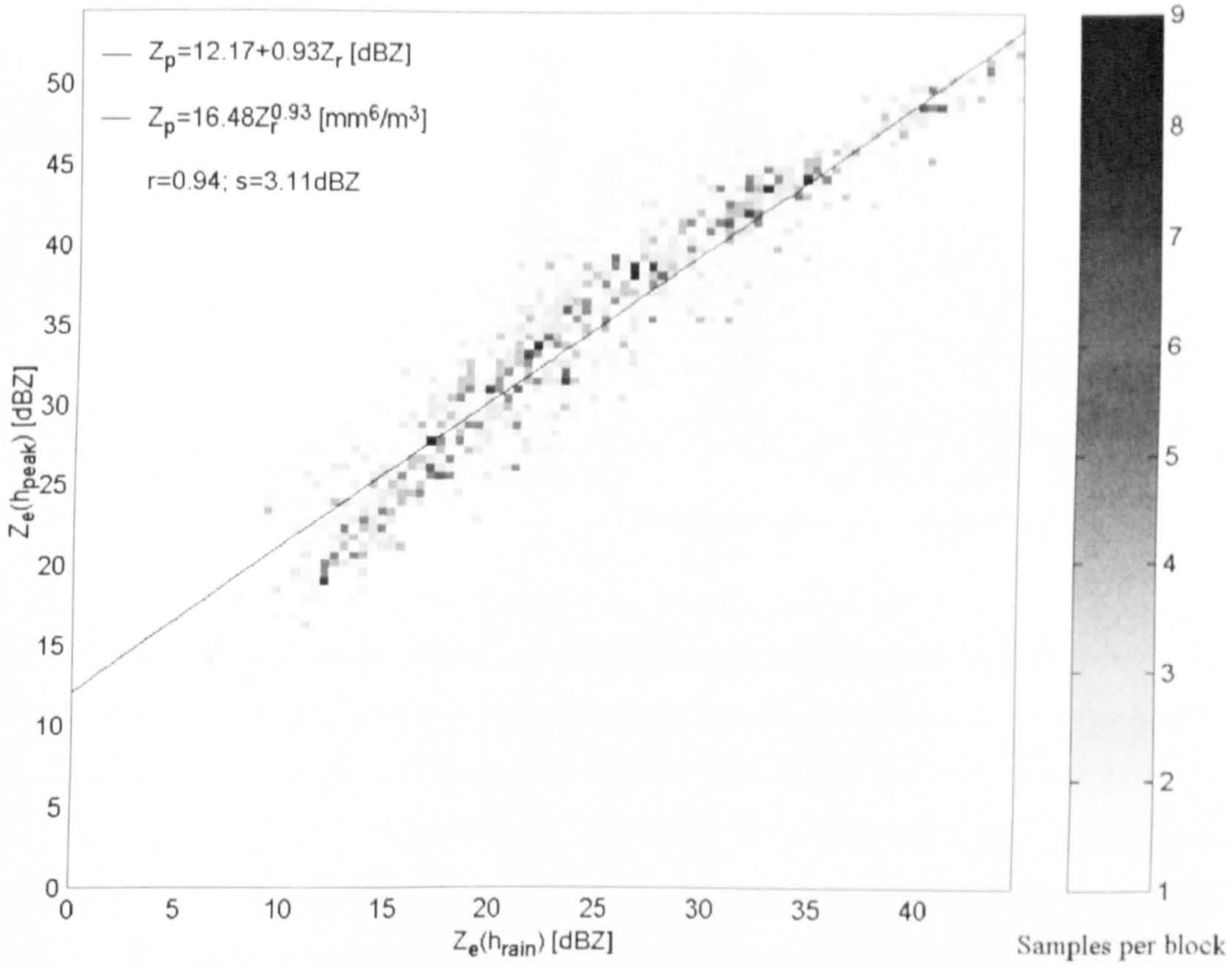

Fig. 5.6: Scatter plot of the maximum reflectivities within the bright band ($Z_{e(peak)}$) against the reflectivities at the bright band bottom ($Z_{e(rain)}$) at X-band frequencies over Marseille.

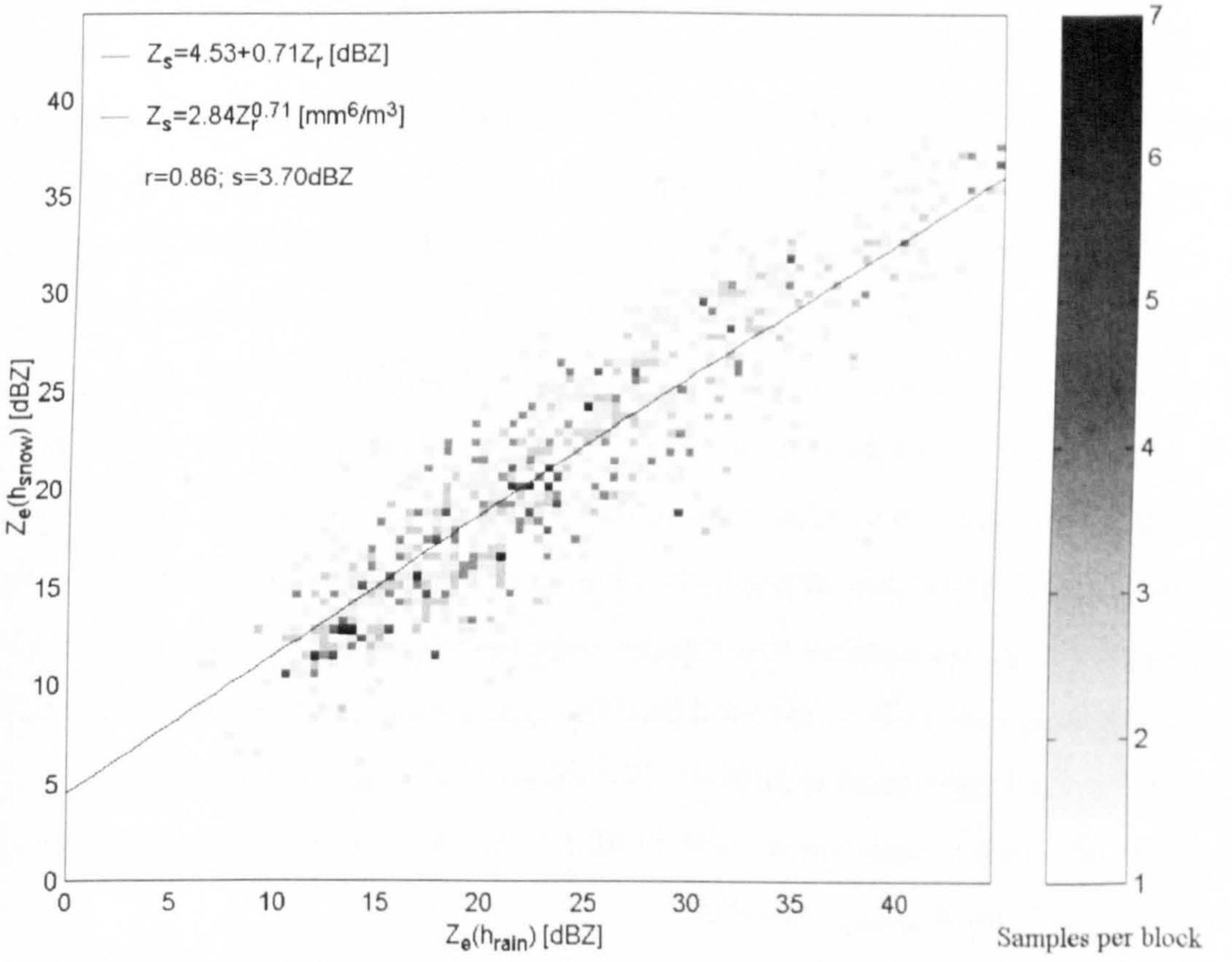

Fig. 5.7: Scatter plot of the reflectivities at the bright band top ($Z_{e(snow)}$) against the reflectivities at the bright band bottom ($Z_{e(rain)}$) at X-band frequencies over Marseille.

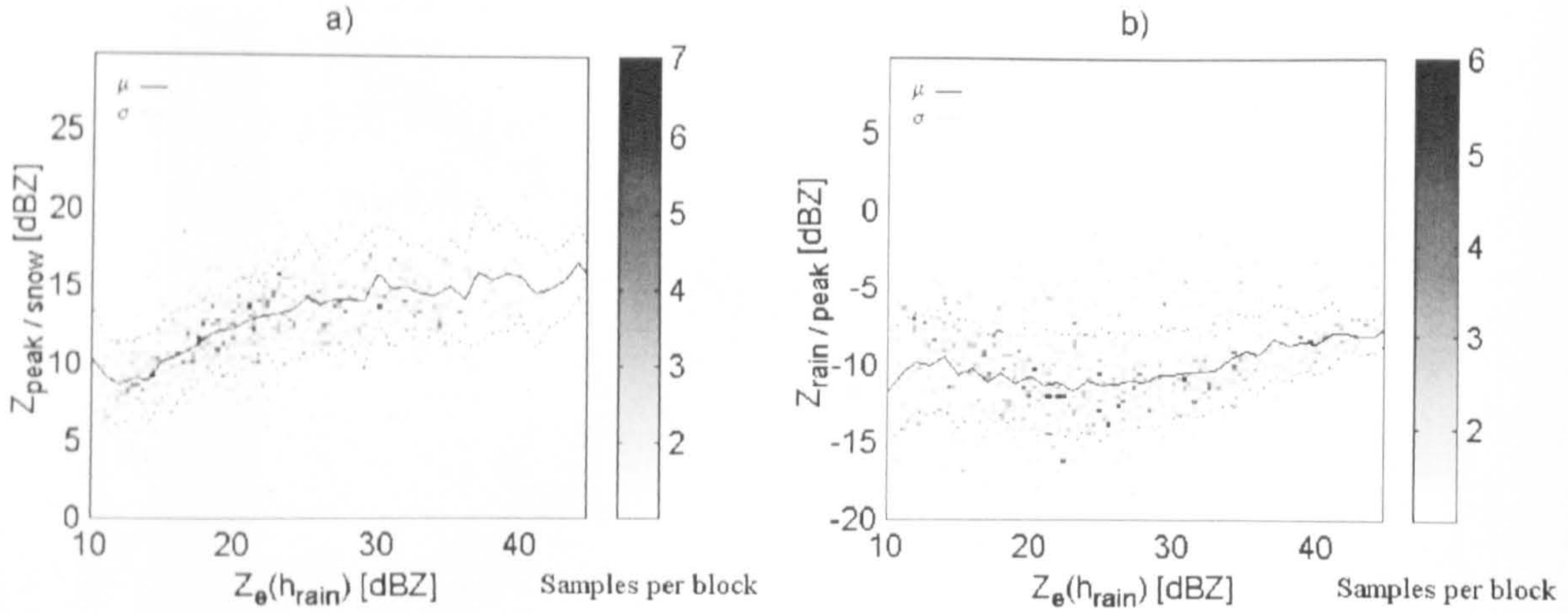

Fig. 5.8: Scatter plot of the increase-decrease in reflectivity in the bright band over Marseille at X-band frequencies. a) Increase from the top to the peak of the bright band as a function of $Z_{e(rain)}$. b) Decrease from the peak to the bottom of the bright band as a function of $Z_{e(rain)}$.

The scatter plot of the increase in reflectivity in the upper part of the bright band as a function of rain reflectivity is shown in Fig. 5.8a. There is a lot of scatter from the mean value, but it is possible to extract some features. There are two different regimes bounded by $Z_{e(rain)} \approx 25$ dBZ. For rain reflectivities between 10 dBZ to 25 dBZ the increase becomes more rapid from ≈ 8 dBZ to ≈ 14 dBZ; for rain reflectivities greater than 25 dBZ the increase is very slow and going from ≈ 14 dBZ to ≈ 15 dBZ. This change in increase in $Z_{e(rain)} \approx 25$ dBZ is also observed with a slight bending in the scatter plot depicted in Fig. 5.6. It is possible that this effect is due in part to the attenuation effects in the melting layer of electromagnetic waves at X-band frequencies. However, there is no reference point to corroborate this issue and at the moment, the bending will be seen as part of the parameterisation of the bright band at X-band frequencies.

A similar scatter plot for the decrease in reflectivity in the lower part of the bright band, from the maximum reflectivity to the bright band bottom as a function of the rain reflectivity is presented in Fig. 5.8b. The decrease in reflectivity is represented as a negative number in comparison with the increase and similar to the previous analysis, two regimes are observed in the scattered data. The value of $Z_{e(rain)} \approx 25$ dBZ seems to be the boundary in the bright band behaviour. For values of $Z_{e(rain)}$ between 10 dBZ to 25 dBZ there is an absolute enhancement from 10 dBZ to 12 dBZ and afterwards decreases up to a value of 8 dBZ for $Z_{e(rain)} \approx 45$ dBZ.

The increase-decrease in reflectivity in the bright band on Marseille suggests that there are two regimes bounded by $Z_{e(rain)} \approx 25$ dBZ. Fabry and Zawadzki (1995) from similar work carried out with a long term X-band VPR database from Montreal found three

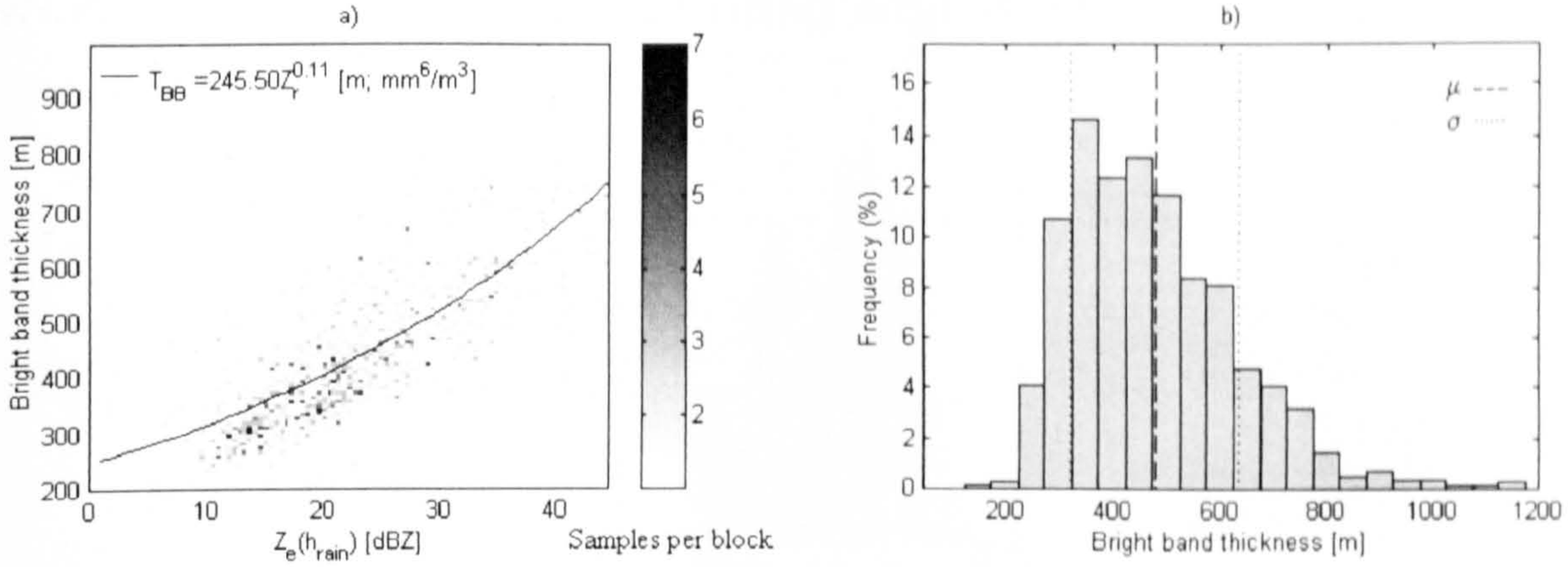

Fig. 5.9: Bright band thickness over Marseille. a) Scatter plot of the bright band thickness versus the rain reflectivity; b) Relative frequency of the bright band thickness (50 m steps).

different regimes bounded by $Z_{e(rain)} = 19$ dBZ and 25 dBZ. However, when comparing the measurements with an UHF profiler (914 MHz, $\lambda = 32.8$ cm), they concluded that the change in the bright band behaviour is a consequence of both, attenuation and the use of the Rayleigh approximation at X-band frequencies. It is very likely that both effects play a major role shaping the intensity of the bright band. However, this analysis is intended to establish the behavior of the bright band at X-band frequencies and it is in Chapter 6 that similar analysis has been carried out at S-band frequencies.

The thickness of the bright band as a function of rain reflectivity is depicted in Fig. 5.9a, revealing an increase in bright band thickness as the rain reflectivity increases, which is congruent with the results shown by Klaassen (1988) and Fabry and Zawadzki (1995). Large values of rain reflectivity are associated to large snowflakes melted over a larger depth, increasing the thickness of the bright band (Fabry et al., 1994). For rain reflectivities greater than 25 dBZ, the scatter is significant, which means that an equal value of rain reflectivity can produce bright bands with different depths.

Fig. 5.9b shows the distribution of the bright band thickness, being the most frequent depth of 350 m. The distribution presents values from 250 m to 1000 m, with a mean value of 479 m and 156 m of standard deviation. Such a distribution may not be the general trend during the rest of the year because of the lack of data from December to August.

5.5 Statistics of the bright band in the Southern Alps, New Zealand

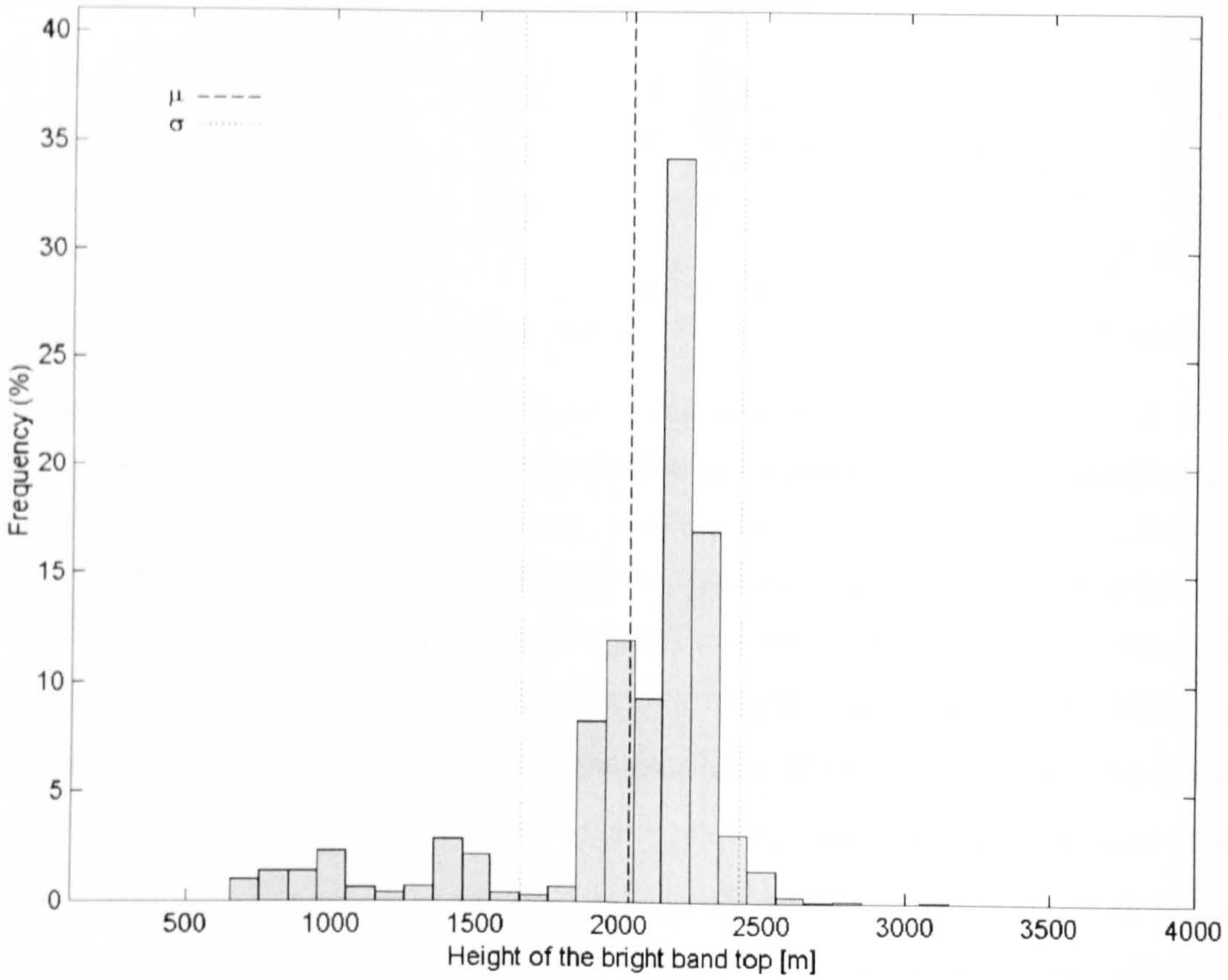

Fig. 5.10: Relative frequency of the height of bright band top over the Southern Alps, New Zealand during October 1996 (100 m steps).

In spite of the fact that the VPR was deployed for a shorter period in the Southern Alps than in Marseille, the bright band hours recorded by the VPR are almost twice that in the former (41.32 hr in the Southern Alps against 21.67 hr in Marseille), primarily because of the influence of the Alps in the Southern Island as explained in Section 5.3.2. The VPR was deployed during October 1996 and the distribution of height of the bright band top over the Southern Alps is shown in Fig. 5.10. The most frequent bright bands appear at 2200 m above the radar site, with a mean height of 2037 m and a standard deviation of 382 m. These results do not represent the general trend of the height of the bright band top during the rest of the year because the data were collected only during a period of one month, but they show the wide distribution collected during that month. The heights of bright band tops are from 700 m to almost 2500 m, although with less frequency below 1800 m.

Fig. 5.11 depicts the distributions of the reflectivities $Z_{e(rain)}$, $Z_{e(peak)}$ and $Z_{e(snow)}$. These reflectivities reveal bimodal distributions with two well defined maxima. For in-

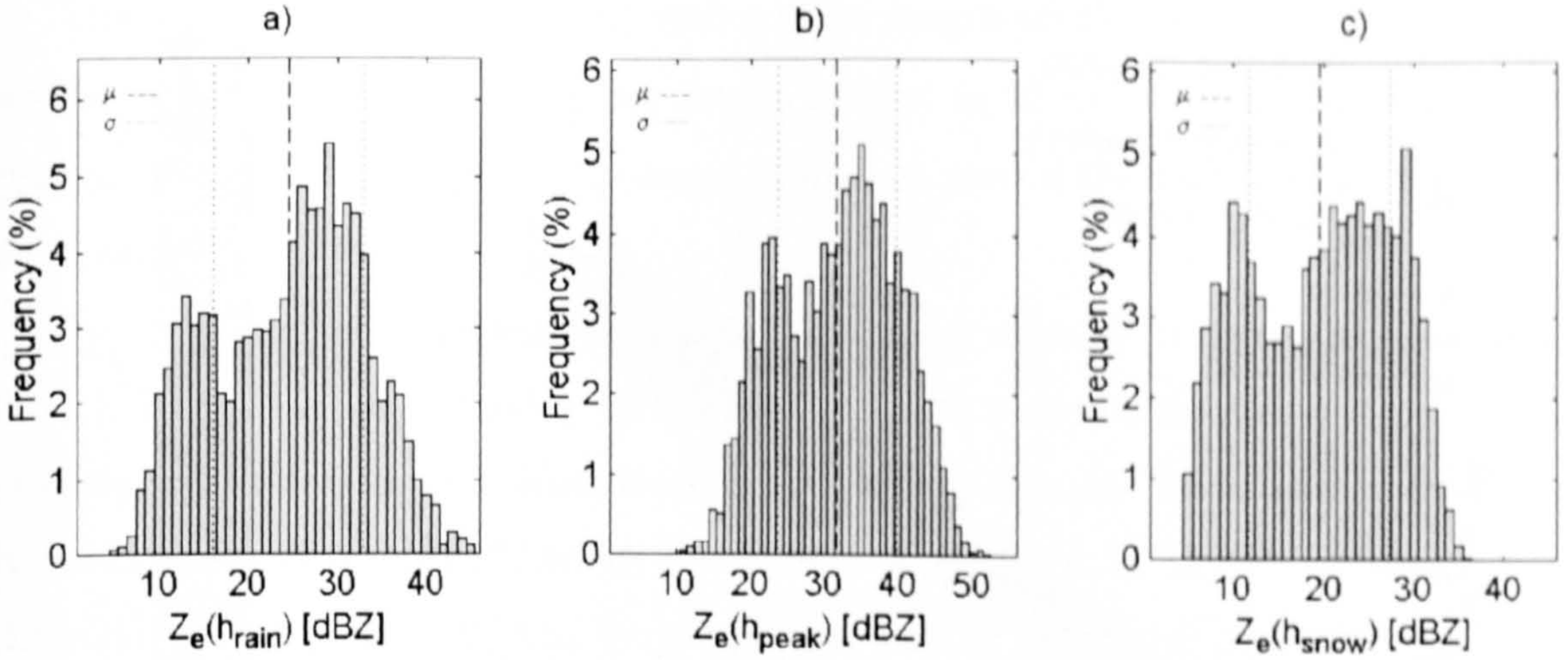

Fig. 5.11: Relative frequency of the reflectivities $Z_{e(rain)}$, $Z_{e(peak)}$ and $Z_{e(snow)}$ over the Southern Alps, New Zealand (1 dBZ steps).

stance, the distribution of rain reflectivities has two maxima around 13 dBZ and 29 dBZ. This means that not only high-intensity stratiform rainfall (> 3 mm hr^{-1}) is developed in the Southern Alps as expected because of the influence of the mountains, but also light rain with rates less than 0.24 mm hr^{-1}. The bimodal distribution in $Z_{e(rain)}$ is also reflected in the distributions of $Z_{e(peak)}$ and $Z_{e(snow)}$. As it was said before, the results are not the general trend prevailing in the Southern Alps during the rest of the year, but it is interesting to note that during a period of one month a very broad spectrum of rain reflectivities was recorded.

On the other hand, the scatter plots of the reflectivities at the top and peak of the bright band against the reflectivities at the bright band bottom represent the microphysics of precipitation that may be seen during the rest of the year in the Southern Alps (Figs. 5.12 and 5.14). Fig. 5.12 reveals that the variation in the peak reflectivity against the rain reflectivity follows a well defined straight line, with a correlation of 0.96 and a standard deviation of 2.20 dBZ. In the bright band analysis of Marseille, Fig. 5.6 revealed a kind of bending around 25 dBZ in $Z_{e(rain)}$ even when the estimated regression line fitted the data well. However, the bending is not appreciable in the bright band analysis of the Southern Alps. There are two factors, which must be considered to explain the differences.

The mobile VPR deployed in New Zealand was fitted with a new antenna and operated without the sidelobe suppression unit. Because of the new antenna, the VPR had to be recalibrated with another fixed VPR from New Zealand up to the point that both VPR achieved similar outputs (Lane, 1997). The fixed VPR in New Zealand was accurately calibrated.

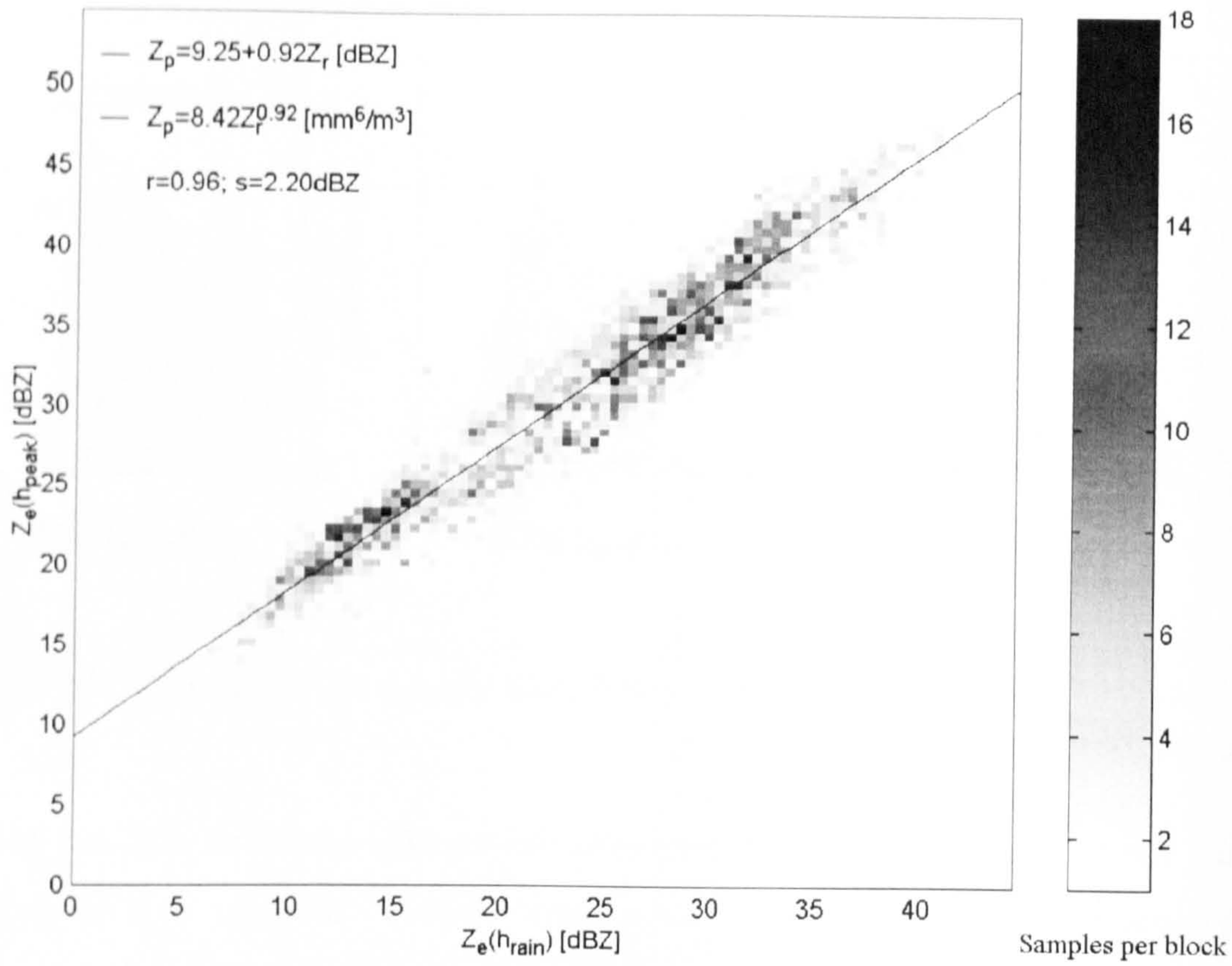

Fig. 5.12: Scatter plot of the maximum reflectivities within the bright band ($Z_{e(peak)}$) against the reflectivities at the bright band bottom ($Z_{e(rain)}$) at X-band frequencies over New Zealand.

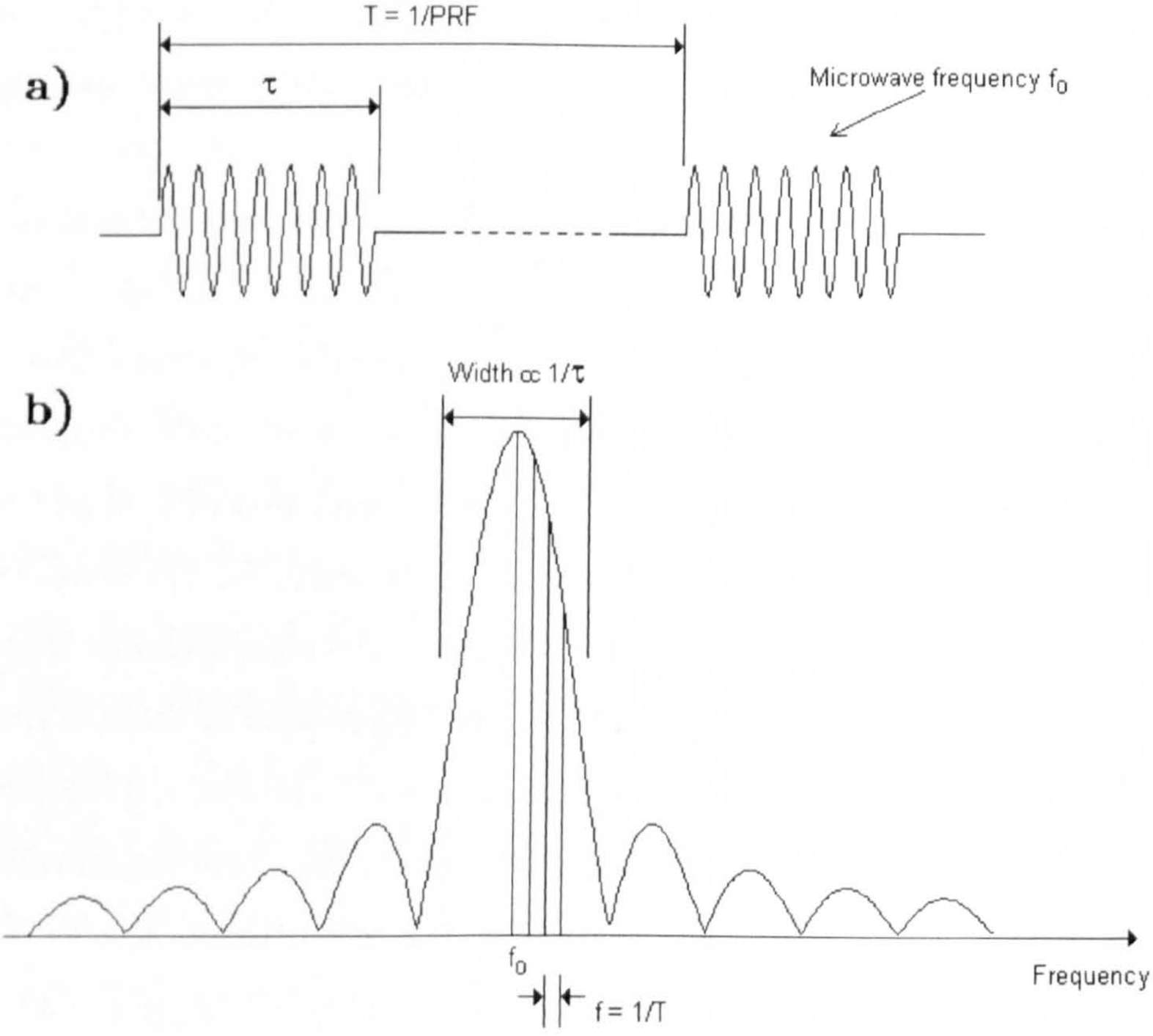

Fig. 5.13: a) Schematic representation of the pulses sent out by the transmitter. b) Idealised spectrum of the radar pulses (From Cole, 1992).

The mobile VPR was operating with a pulse length of 250 ηs. Usually to obtain a spatial resolution of 7.5 m, the pulse length is fixed to 50 ηs. A pulse length of 250 ηs changes the spatial resolution of the radar to 37.5 m, even if the data were sampled every 30 m as was the case.

By increasing the pulse length there is a notorious increase in Signal to Noise Ratio (SNR). The radar pulses leaving the transmitter have a carrier frequency f_0 in the microwave band (10 GHz at X-band frequencies). The pulses are modulated by the Pulse Repetition Frequency (PRF), which has a duty cycle given by the pulse length, τ, of the radar (See Fig. 5.13a). The frequency spectrum of the radar pulses is depicted in Fig. 5.13b. The envelope of the spectral lines follows a Sinc[2] function centred at the frequency f_0. It is noteworthy to remark that the narrower the pulse length, the wider the main lobe of its frequency spectrum and the higher the number of frequencies that construct the modulated pulses. The radar receiver must have the capability of receiving all those spectral lines being transmitted through a pass-band filter centred on f_0 with a limited Bandwidth (B). The optimal relationship between the pulse length and the bandwidth necessary to recover the signal through the receiver without distortion and maximizing the SNR is $B\tau = 1$. Therefore, for a pulse length of 50 ηs the bandwidth is equal to 20 MHz, but for a pulse length of 250 ηs the bandwidth is 4 MHz. A bandwidth of 20 MHz allows more components of noise to pass to the output of the receiver than a bandwidth of 4 MHz. The narrower the bandwidth the less the noise power at the output of the receiver, that is (See Skolnik, 1980):

$$P_n = kTB \tag{5.3}$$

where P_n is the thermal-noise power in the receiver, k is the Boltzmann's constant and T is taken to be 300 K (room temperature). Therefore, it is clear that the noise power increases proportionally with the receiver bandwidth. The SNR is given by:

$$\text{SNR} = \frac{P_r}{P_n} \tag{5.4}$$

where P_r is the power reflected from precipitation echoes. P_r is given by (From Eq. 2.19):

$$\bar{P}_r = \left(\frac{\pi^3 P_t G^2 \theta_h \theta_v c\tau}{1024\lambda^2 \ln 2}\right)\frac{|K|^2 Z}{r^2} = \frac{(C_o\tau)|K|^2 Z}{r^2} \tag{5.5}$$

[2]The Sinc function is given by $sinc(x) = sin(x)/x$.

where C_o depends on the radar characteristics. Substituting Eqs. 5.3 and 5.5 into Eq. 5.4, SNR becomes:

$$\mathrm{SNR} = \frac{C_o |K|^2 Z}{r^2 kT} \left(\frac{\tau}{B} \right) \tag{5.6}$$

If the product $B\tau$ is kept constant and equal to 1, the SNR is proportional to the square of the transmitted pulse width, that is (See also Doviak and Zrnić, 1993):

$$\mathrm{SNR} = \frac{C_o |K|^2 Z}{r^2 kT} \tau^2 \tag{5.7}$$

It is interesting to note the trade-off between having the smallest spatial resolution and having the highest SNR. A shorter pulse length leads to a smaller spatial resolution. As the pulse length increases, the SNR increases. The larger the pulse length the higher the SNR, but there is a loss in radar resolution. For instance, an increase in the length of the pulses sent out by the radar from 50 ηs to 250 ηs increases the SNR by 13.97 dB, but the spatial resolution of the radar increases from 7.5 m to 37.5 m. However, this factor is important when there are low-intensity echoes. An increase in SNR improves the ability of a radar to differentiate low-intensity echoes from noise, as on the top of the cloud. But in the bright band there are high-intensity echoes and the increase in SNR does not play a major role.

On the other hand, the processes producing heavy rain in the Southern Alps may be the shaping factors leading to a slightly different scatter plot between the maximal reflectivity in the bright band and the rain reflectivity below. The Southern Alps act as a natural barrier to the air flow. According to Revell et al. (2002), there are two possible trajectories of air parcels crossing the Southern Alps, which can produce lifting and therefore heavy precipitation. They are the normal flow perpendicular to the Alps and the barrier jet flow, where the flow is turned and lifted as it flows parallel to the divide. Revell et al. (2002) showed that in the barrier jet flow, the rising air in the layer between 1 and 2 km AMSL is saturated long enough to grow drizzle size drops, providing seeder drops that could grow quickly by coalescence as they fell into the intense updrafts at the foot of the Alps. Through this mechanism, they explain shallow convection producing very heavy precipitation. Although the bright band is the result of a cold process, the factor producing larger reflectivities compared to Marseille may be a continuous seeder-feeder mechanism operating within the melting layer. Studies carried out by Hill et al. (1981) in South Wales, UK showed that 80% of the precipitation growth takes place within 1.5 km over the hills, with very little enhancement occurring above 2 km. However, in

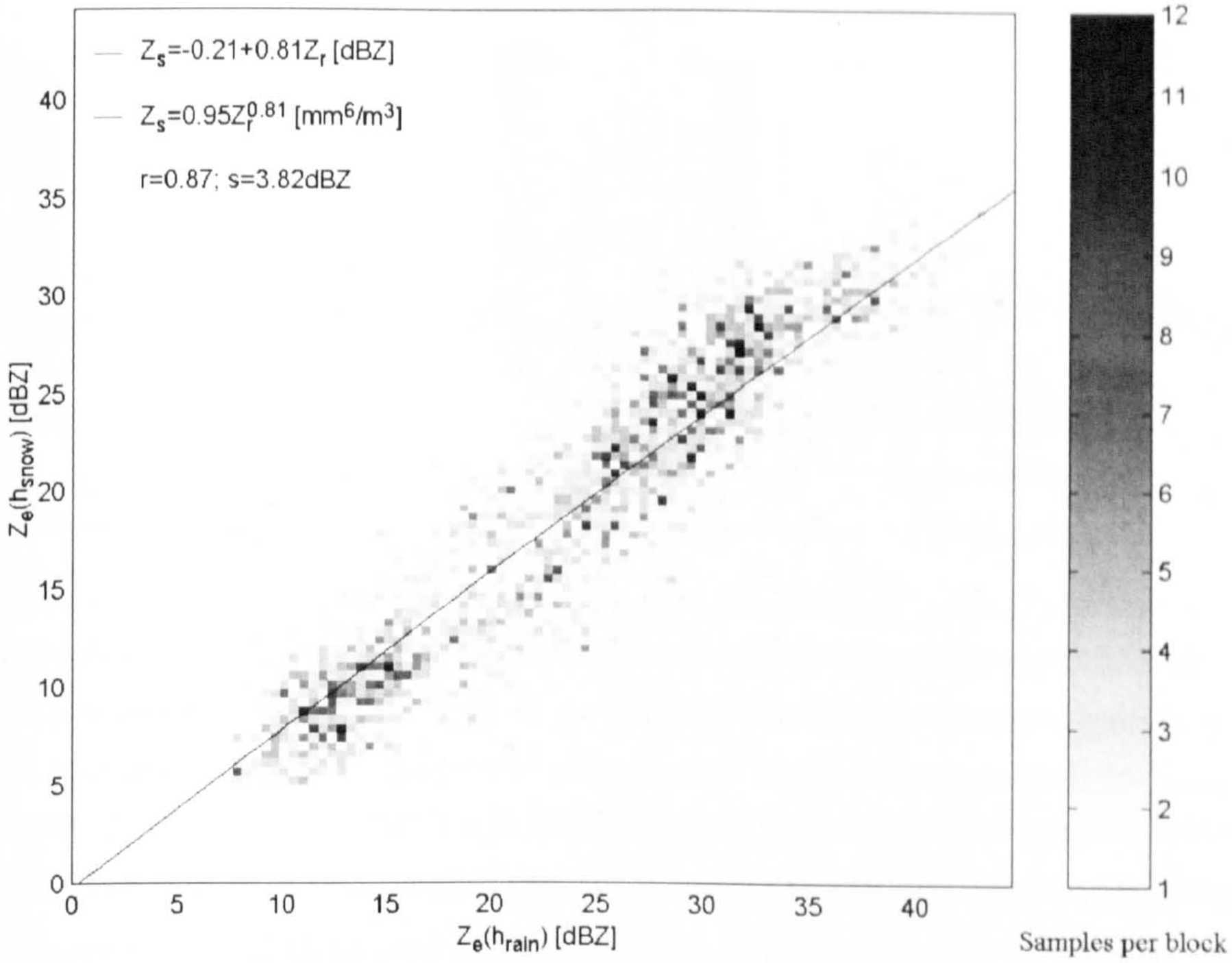

Fig. 5.14: Scatter plot of the reflectivities at the bright band top ($Z_{e(snow)}$) against the reflectivities at the bright band bottom ($Z_{e(rain)}$) at X-band frequencies over New Zealand.

the Southern Alps, the VPR was deployed close to the mountains, which are around 2 km in height on average with some peaks exceeding 2.5 km, and the orographic enhancement observed by Hill et al. (1981) in South Wales involves mountains with heights less than 800 m (the highest mountains in Wales are in the North with peaks around 1 km height). Most of the bright bands observed in New Zealand were below 2.1 km, (From Fig. 5.10), which suggests that not only orographic enhancement may take place at lower levels, but also within the melting layer causing an increase in the reflectivities in the bright band. Therefore, it is suggested that the Southern Alps play a major role in the development of heavy precipitation and they may be the main reason for the differences with the scatter plot observed in Marseille.

Fig. 5.14 shows the variation of $Z_{e(snow)}$ against $Z_{e(rain)}$. The regression line of the scattered data present a correlation of 0.87 with a standard deviation of 3.82 dBZ. The slope of the regression line is 0.81 with an offset of -0.21 dBZ. This means that the top reflectivity is smaller than the rain reflectivity by a factor of approximately 0.81.

Fig. 5.15a depicts the scatter plot of the increase in reflectivity from the bright band top to the bright band peak as a function of rain reflectivity. It is interesting to note that there are two regimes: one is for rain reflectivities below 32 dBZ where the increase is

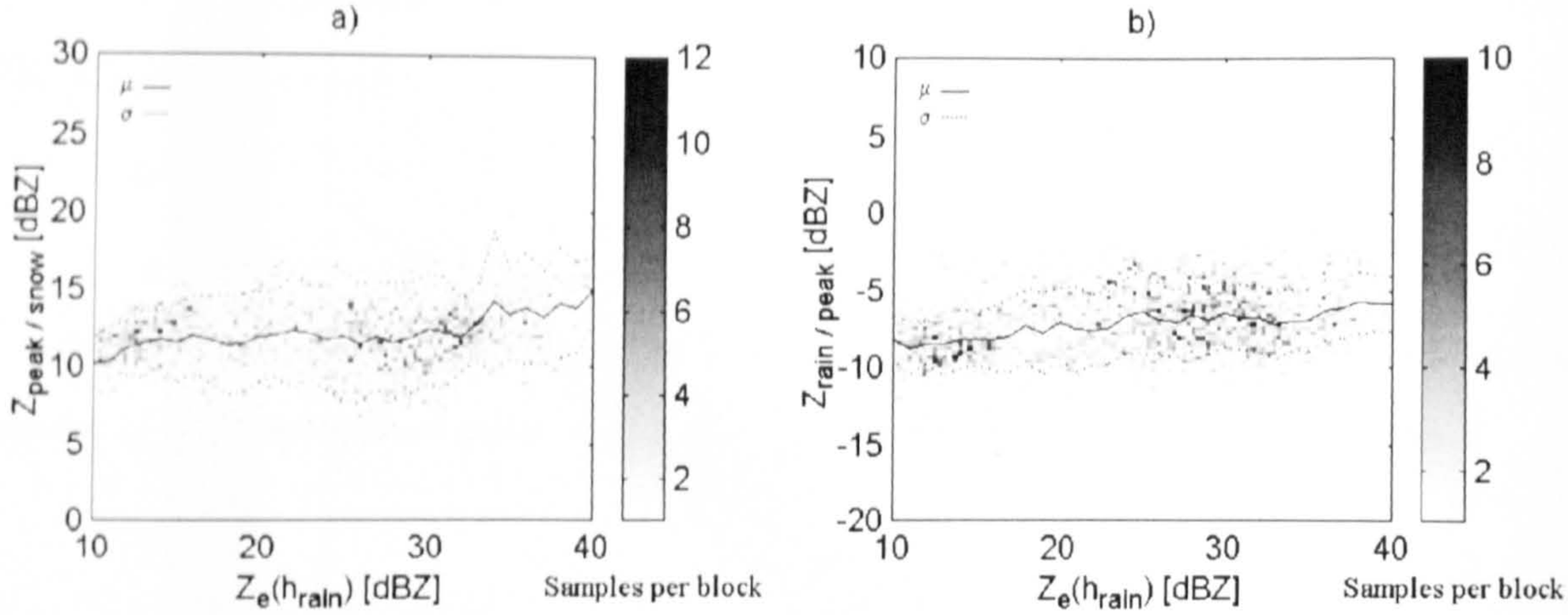

Fig. 5.15: Scatter plot of the increase-decrease in reflectivity in the bright band over the Southern Alps at X-band frequencies. a) Increase from the top to the peak of the bright band as a function of $Z_{e(rain)}$. b) Decrease from the peak to the bottom of the bright band as a function of $Z_{e(rain)}$.

approximately 12 dBZ and the other one is for rain reflectivities greater than 32 dBZ but smaller than 40 dBZ where there is a gradual increase from 12 dBZ up to approximately 15 dBZ.

The decrease in reflectivity in the bright band from the maximum value to the rain reflectivity is depicted in Fig. 5.15b. From this figure it is possible to establish that for rain reflectivities between 10 dBZ and 40 dBZ, there is an absolute enhancement from 8 dBZ to 6 dBZ.

The scatter plot of the bright band thickness against the rain reflectivity is shown in Fig. 5.16a. It is evident that there is a lower vertical resolution when compared to the scatter plot of the thicknesses observed in Marseille (Fig. 5.9a). In spite of this fact, the trend in increasing the thickness when increasing the precipitation rate is still observed. The trend is very similar to that in Marseille and the standard deviations differ only by $\Delta\sigma = 0.01 T_{BB}$. However, as it was observed before, there is a lot of scatter for greater values of rain reflectivity and may be well related to the number of variables that model the melting layer. This point is extended in Section 5.10.3.

The distribution of the bright band thickness is plotted in Fig. 5.16b where the most frequent is 400 m, with a mean value of 459 m and a standard deviation of 137 m. It is interesting to note that the distribution of the bright band thickness observed in Marseille presents a similar distribution to the bright band thickness observed in the Southern Alps. However, in Marseille the heights of the bright band tops are at higher altitudes ($>$ 2200 m) than the heights of the bright band tops observed in the Southern Alps ($<$ 2300 m). Fabry et al. (1994) found evidence that the bright band thickness may be

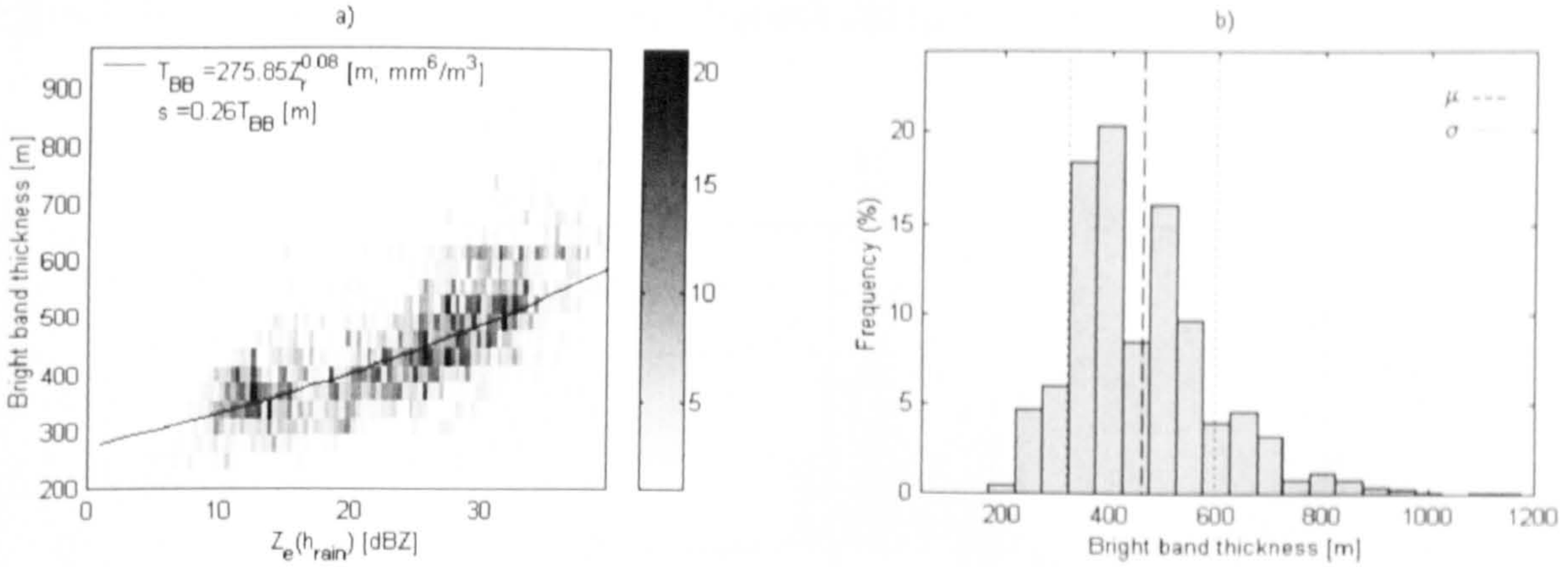

Fig. 5.16: Bright band thickness over the Southern Alps, New Zealand. a) Scatter plot of the bright band thickness versus the rain reflectivity; b) Relative frequency of the bright band thickness (50 m steps).

influenced by the altitude of the bright band. The comparisons carried out in this analysis represent two different climatological regions and there are several factors influencing the thickness of the bright band (See Section 5.10.3).

5.6 Statistics of the bright band in the South West of England

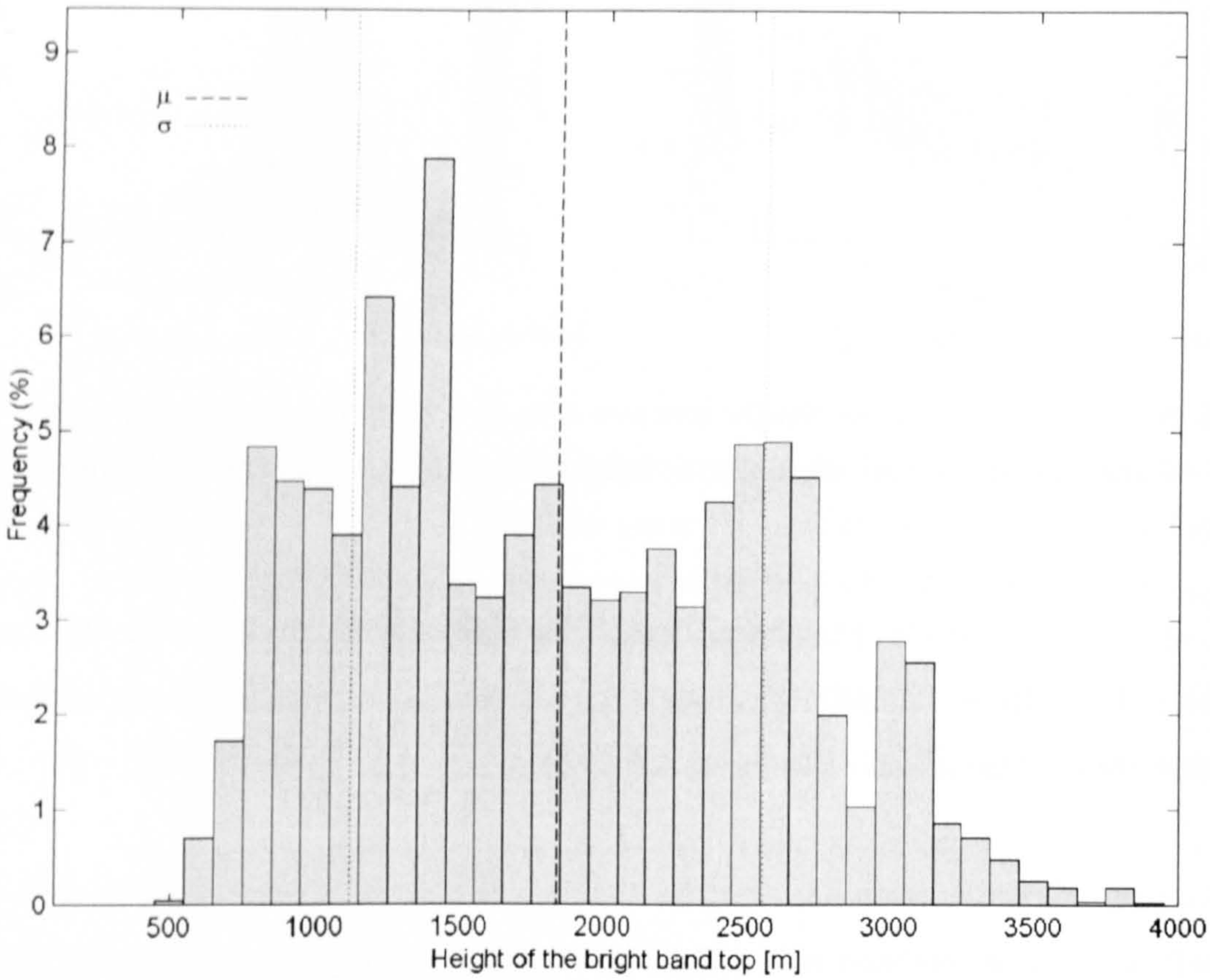

Fig. 5.17: Relative frequency of the height of bright band top over the South West of England from April 1995 to November 1995 (100 m steps).

The South West analysis covers only VPR data from HYREX. Despite the fact that no data are available during the Winter season, the height distribution of the bright band tops (Fig. 5.17) shows bright bands at very low altitudes (less than 1000 m). With the bright band at these lower altitudes, the low elevation angles of scanning weather radars will be contaminated by the increase in reflectivity in the melting layer. The height from the ground to the centre of the radar beam is given by Eq. 2.3, assuming standard refraction and the 4/3 earth approximation. For instance, the radar beam intercepts the bright band at 26 km away from the radar site, assuming that the bright band is 500 m above the ground surface and the beamwidth of the radar and elevation angle are 1° and 0.5° respectively. This means that not only the increase in reflectivity in the bright band will affect the estimation of precipitation using weather radars, but also the reflectivity in snow observed even further than 26 km needs correction to obtain a proper estimation of rainfall rate on the ground for hydrological purposes.

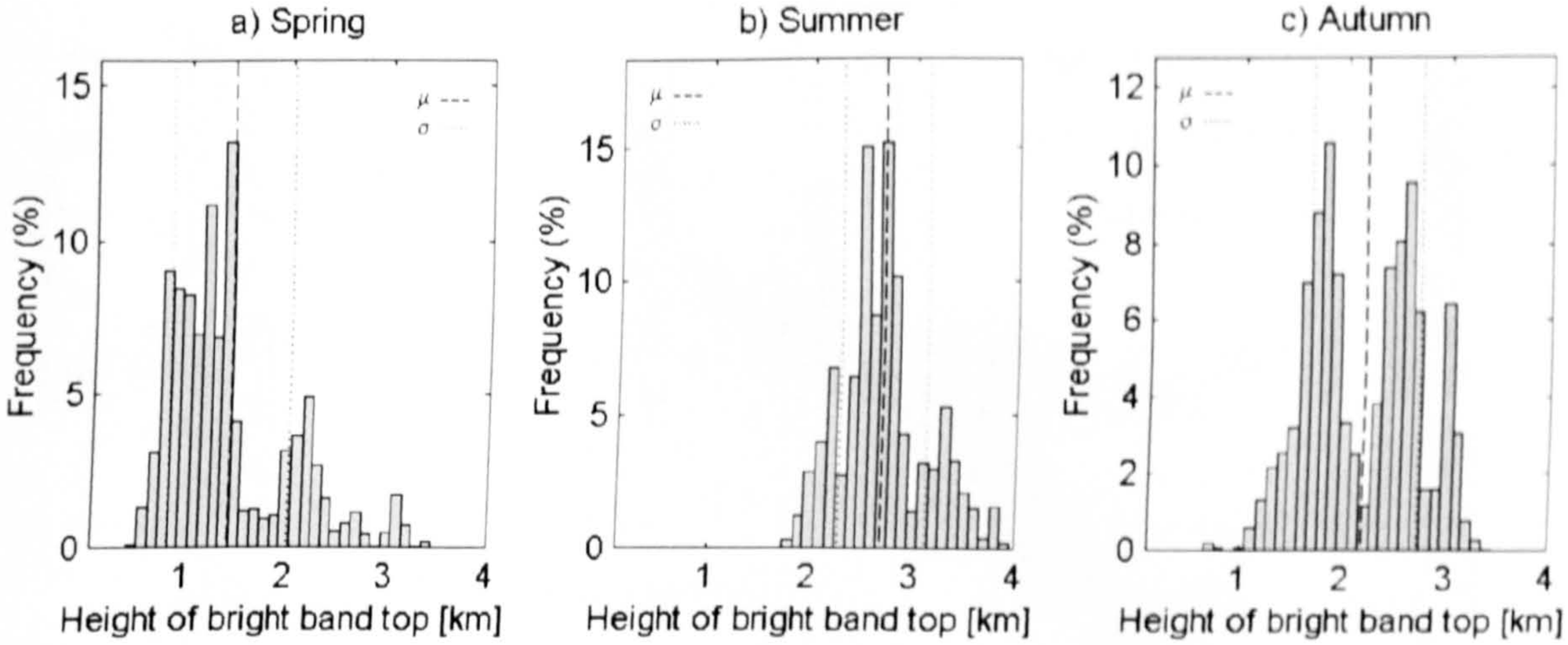

Fig. 5.18: Seasonal distributions of the height of the bright band top over the South West of England from April 1995 to November 1995 (100 m steps).

From Fig. 5.17, the mean height of bright band top is approximately 1839 m, but because the distribution is very uniform the standard deviation is very high ($\sigma = 721$ m). Fig. 5.18 shows the seasonal distribution of the height of the bright band top. During Spring (Fig. 5.18a), the influence of the recently ended Winter and the coming Summer produces fluctuations in temperature, which are reflected in a wide spectrum of bright band tops including those at low altitudes.

It is interesting to note that during Spring there is a bimodal distribution with maxima around 1000 m and 2200 m, which may be well related to the influence of the adjacent seasons. During Summer (Fig. 5.18b), the bright band may not represent a serious problem because generally is at higher altitudes with a mean value located at 2700 m. During Autumn (Fig. 5.18c) the distribution is very similar to Spring, although the height of the bright band top is more frequent at higher altitudes. Also the bimodal distribution is present, with maxima at 1800 m and 2600 m. Then, Spring and Autumn being the transitional seasons from Summer and Winter respectively, also represent a potential source of error because of the bright band contamination of scanning weather radar measurements at low elevation angles, although Spring to a higher degree.

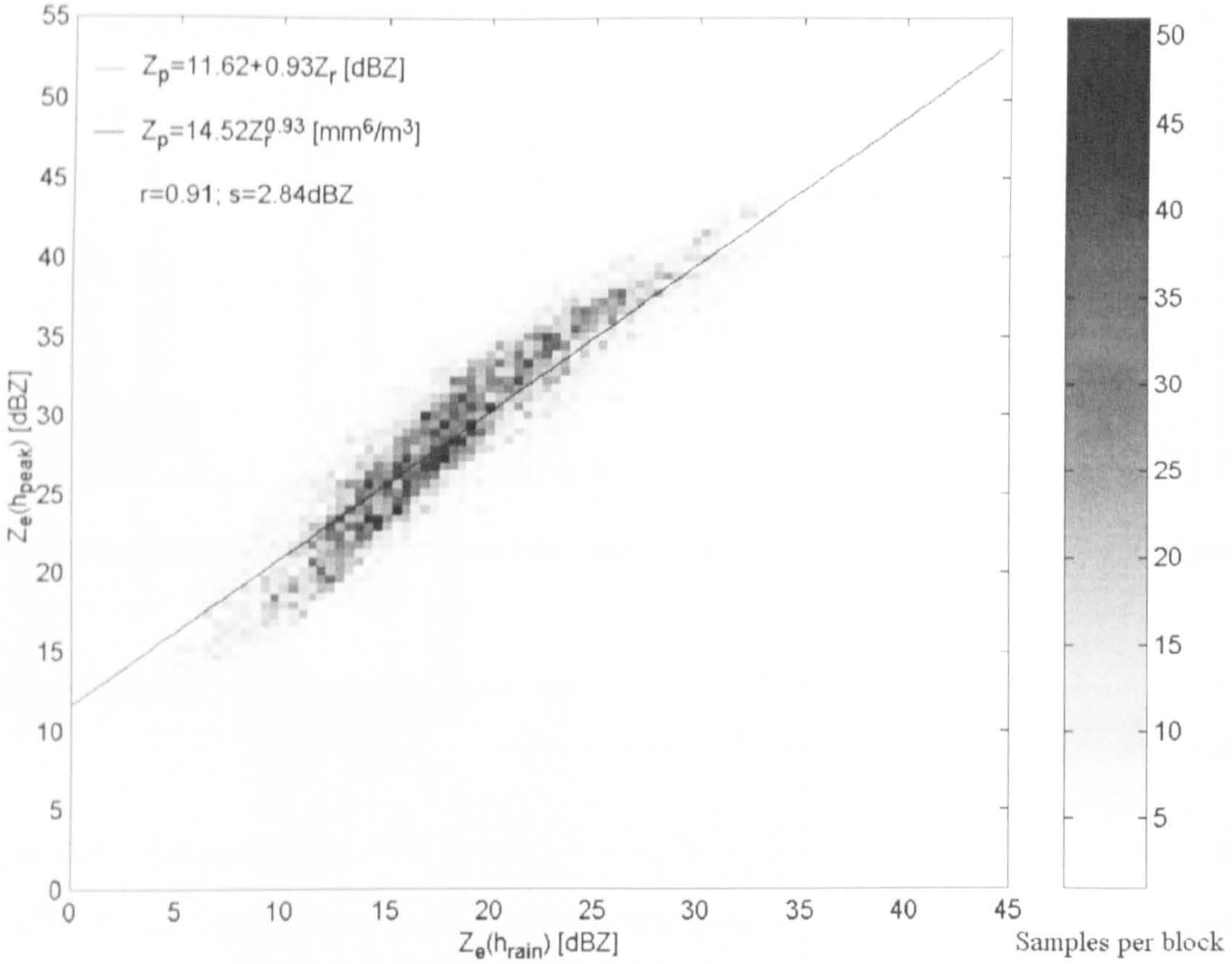

Fig. 5.19: Scatter plot of the maximum reflectivities within the bright band against the reflectivities at the bright band bottom at X-band frequencies over the South West of England.

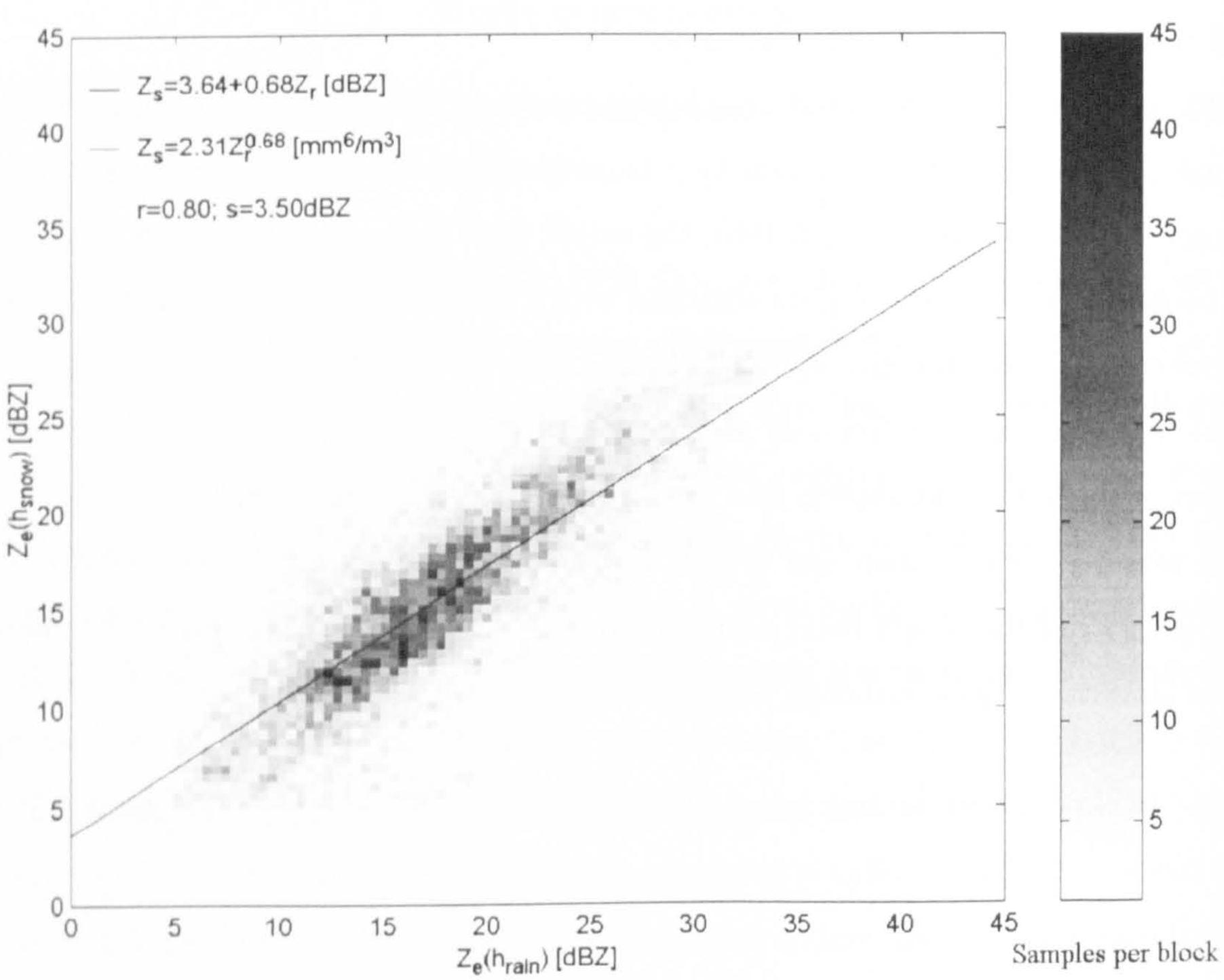

Fig. 5.20: Scatter plot of the reflectivities at the bright band top ($Z_{e(snow)}$) against the reflectivities at the bright band bottom ($Z_{e(rain)}$) at X-band frequencies over the South West of England.

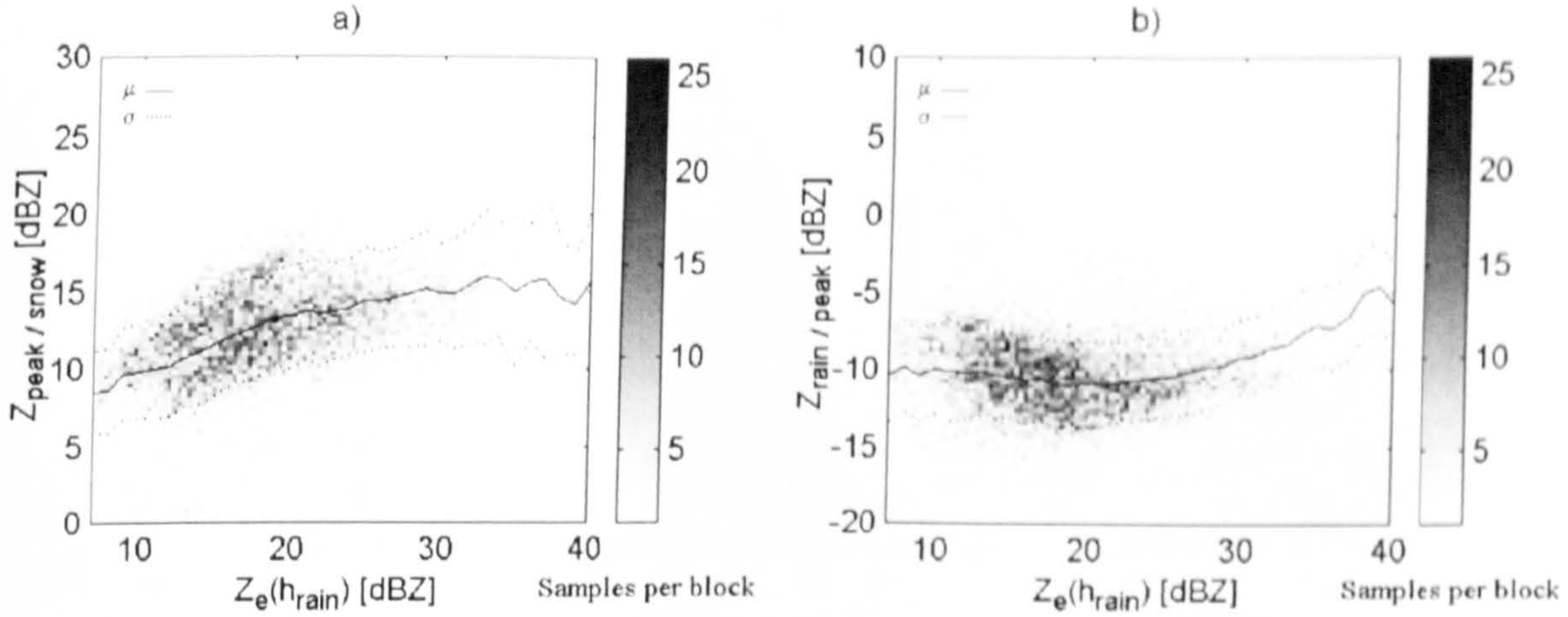

Fig. 5.21: Scatter plot of the increase-decrease in reflectivity in the bright band over the South West of England at X-band frequencies. a) Increase from the top to the peak of the bright band as a function of $Z_{e(rain)}$. b) Decrease from the peak to the bottom of the bright band as a function of $Z_{e(rain)}$.

Fig. 5.19 shows the scatter plot of the variation of $Z_{e(peak)}$ versus $Z_{e(rain)}$. This scatter plot presents a similar trend as the scatter plot obtained in Marseille (Fig. 5.6), with a slight bending around 20 dBZ in $Z_{e(rain)}$. The regression analysis of the scattered data in Fig. 5.19 gives:

$$Z_{e(peak)} = 11.62 + 0.93 Z_{e(rain)}; \qquad \text{dBZ} \tag{5.8}$$

From Eq. 5.8, it is obtained that the peak of the bright band is around 11.62 dBZ above the rain reflectivity but tends to decrease for higher values of $Z_{e(rain)}$. The scatter plots for $Z_{e(peak)}$ versus $Z_{e(rain)}$ for Marseille and the Southern Alps have also similar slopes and the differences are with the offsets of the regression lines.

Fig. 5.20 shows the variation between the reflectivity above and below the bright band, that is, $Z_{e(snow)}$ vs $Z_{e(rain)}$. The slope of the regression line is 0.68 with an offset of 3.64 dBZ. The standard deviation of this line is 3.50 dBZ, being the lowest value obtained up to now with such an amount of data. The equation is given by:

$$Z_{e(snow)} = 3.64 + 0.68 Z_{e(rain)}; \qquad \text{dBZ} \tag{5.9}$$

The scatter plot of the increase in reflectivity from the top to the peak of the bright band as a function of the rain reflectivity is depicted in Fig. 5.21a. There is a gradual increase in reflectivity from the bright band top from 10 dBZ to 15 dBZ for rain reflectivities between 10 dBZ and 28 dBZ afterwards remains constant in approximately 15 dBZ

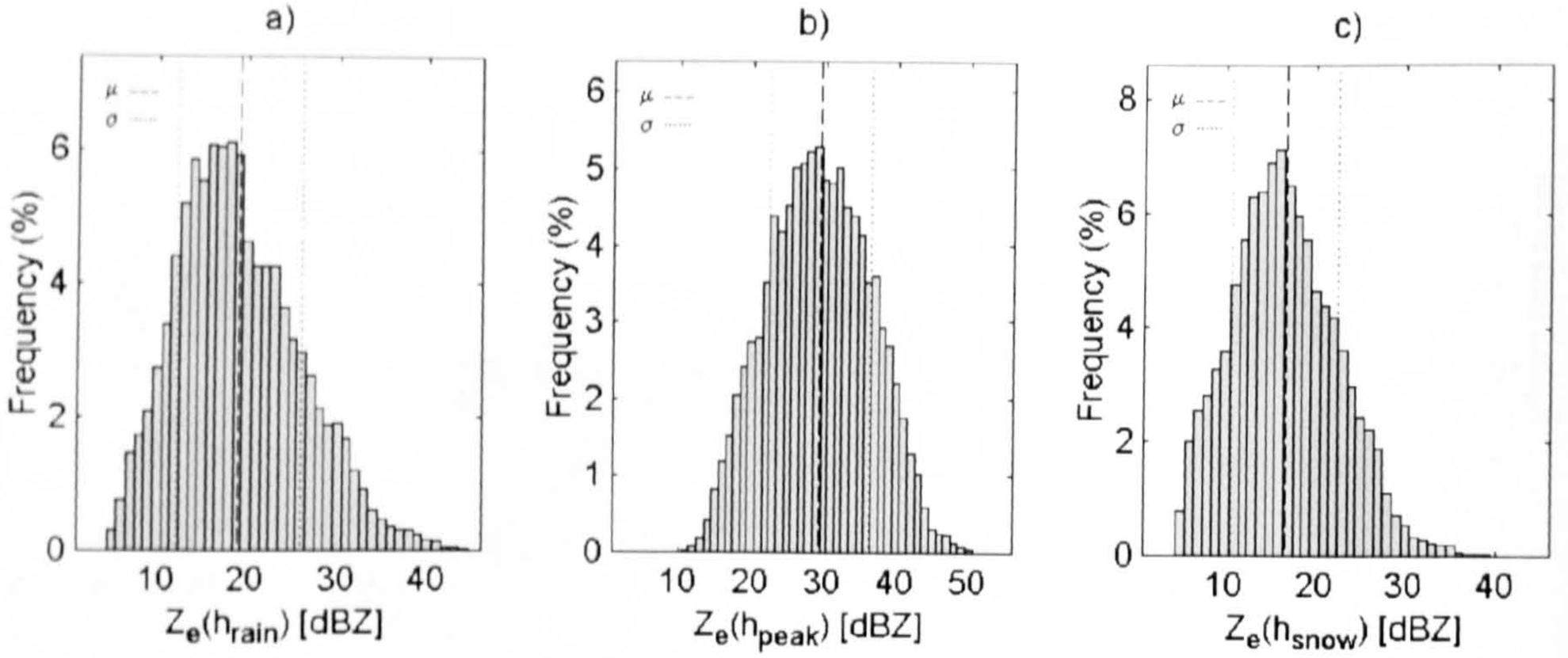

Fig. 5.22: Relative frequency of the reflectivities $Z_{e(rain)}$, $Z_{e(peak)}$ and $Z_{e(snow)}$ over the South West of England (1 dBZ steps).

for rain reflectivities up to 40 dBZ. Fig. 5.21b shows the scatter plot of the decrease in reflectivity from the peak to the bottom of the bright band. The enhancement is approximately 11 dBZ (See Eq. 5.8) for values of rain reflectivity lower than 25 dBZ, then there is an enhancement from 11 dBZ to 6 dBZ for rain reflectivities between 25 dBZ and 40 dBZ.

The distributions of the bright band reflectivities are shown in Fig. 5.22. The distribution of $Z_{e(rain)}$ has a range of reflectivities from 5 dBZ up to 42 dBZ (0.07 mm hr^{-1} to 15.37 mm hr^{-1}), with a mean value of 17 dBZ (0.42 mm hr^{-1}). From the distribution of $Z_{e(peak)}$, the range of reflectivities obtained in the bright band is from 10 dBZ to 50 dBZ (0.15 mm hr^{-1} to 48.62 mm hr^{-1}) with a mean reflectivity of 29 dBZ (2.36 mm hr^{-1}). The distribution of reflectivities at the bright band top presents values from 4 dBZ to around 35 dBZ (0.06 mm hr^{-1} to 5.61 mm hr^{-1}) with a mean reflectivity of 16 dBZ (0.36 mm hr^{-1}).

The scatter plot of the bright band thickness as a function of rain reflectivity is depicted in Fig. 5.23a. The trend is an increase in bright band thickness with the increase in rain reflectivity as in Marseille and New Zealand, although the data in the South West represent almost 9 continuous months. Fig. 5.23b depicts the distribution of the bright band thickness, the most frequent being at 300 m. The mean thickness is 395.40 m with a standard deviation of 130.44 m. Fig. 5.24b depicts the seasonal distribution of the bright band thickness. It is interesting to note that the bright band is thicker during the Summer and thinner during Spring and Autumn. For instance, in Spring the mean bright band thickness is approximately 350 m with 100 m of standard deviation. In Autumn the mean thickness is approximately 375 m with 125 m of standard deviation. However, in Summer

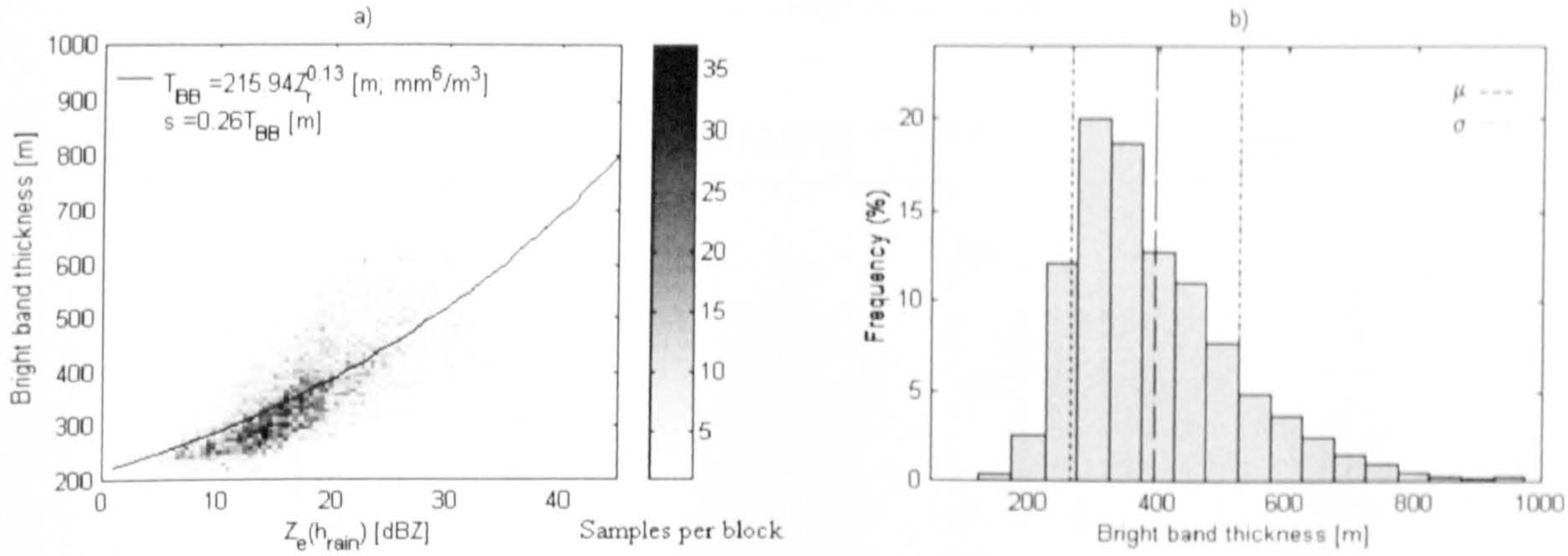

Fig. 5.23: Bright band thickness over the South West of England. a) Scatter plot of the bright band thickness versus the rain reflectivity; b) Relative frequency of the bright band thickness (50 m steps).

the mean thickness increases to 500 m with 150 m of standard deviation. Fabry et al. (1994) suggested that the seasonal dependence of the bright band thickness is due to the fact that they are higher and thicker during Summer than during Autumn or Spring. To corroborate this issue, the mean bright band thicknesses are plotted against their heights in Fig. 5.25. It is interesting to note that the higher the heights of the bright band tops are, the thicker the mean bright band thicknesses. However, the scatter increases at higher altitudes, presenting higher fluctuations around the mean thickness. This means that the height of the bright band top is an important factor influencing the bright band thickness, but there are also additional factors that may contribute to this effect.

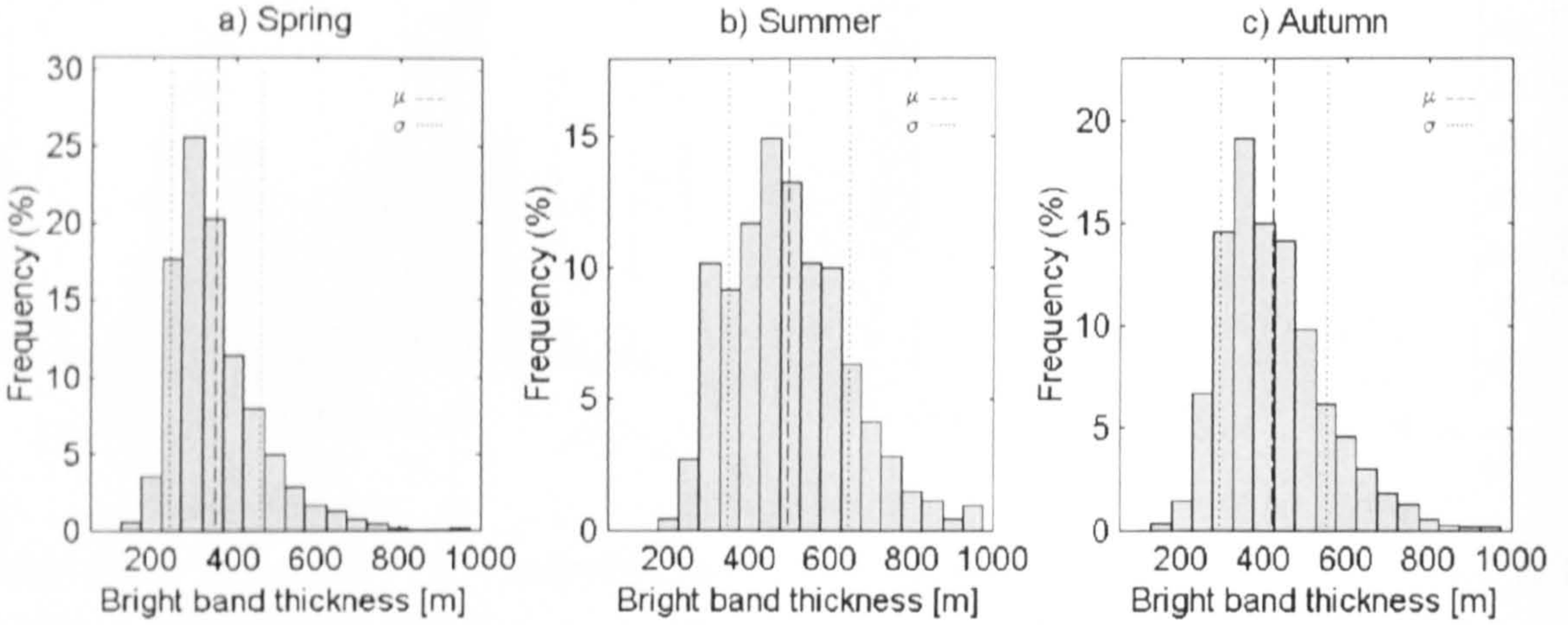

Fig. 5.24: Seasonal distributions of the bright band thickness over the South West of England (50 m steps).

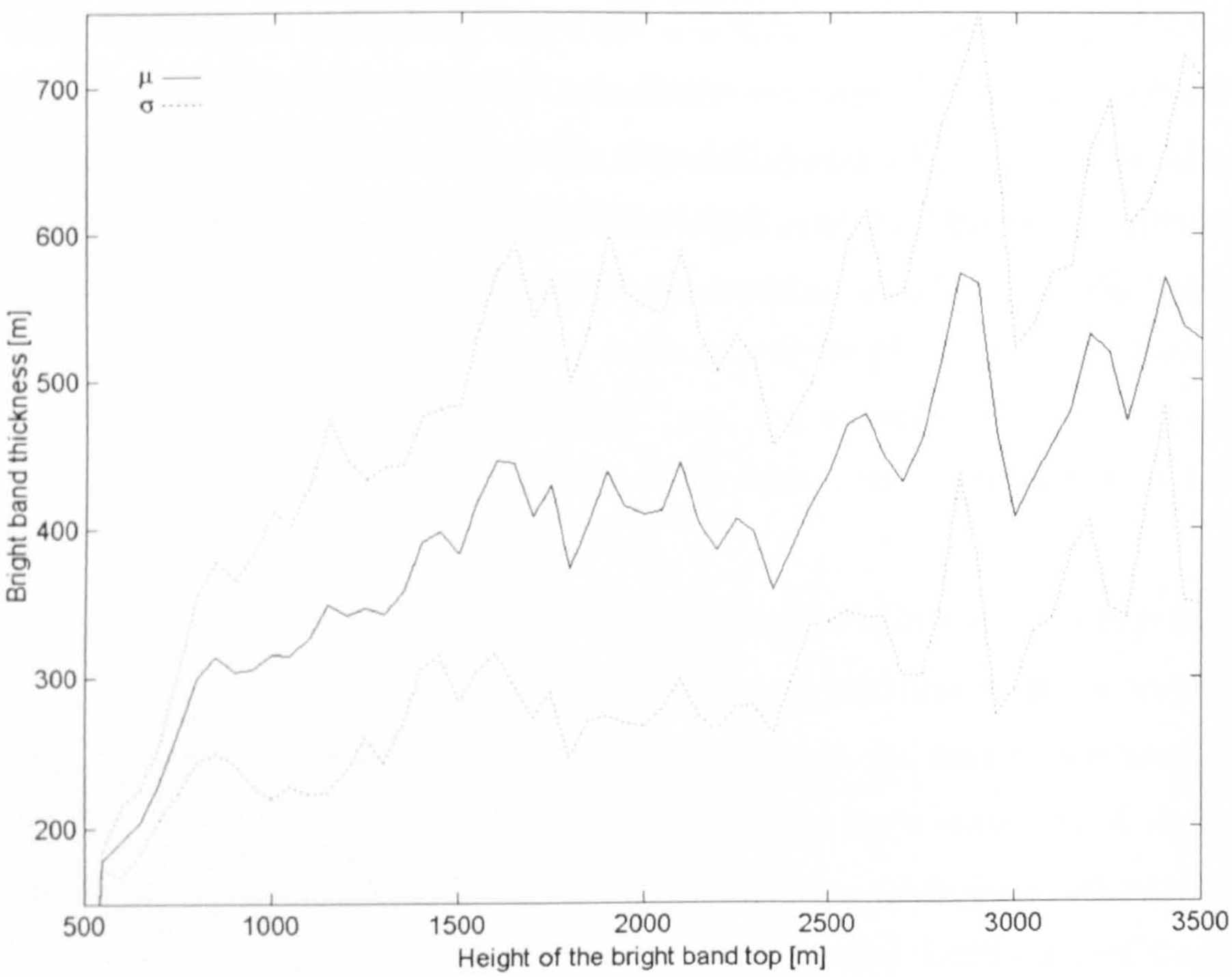

Fig. 5.25: Dependence of the bright band thickness with the height of the bright band top over the South West of England.

5.7 Statistics of the bright band in Bristol, UK

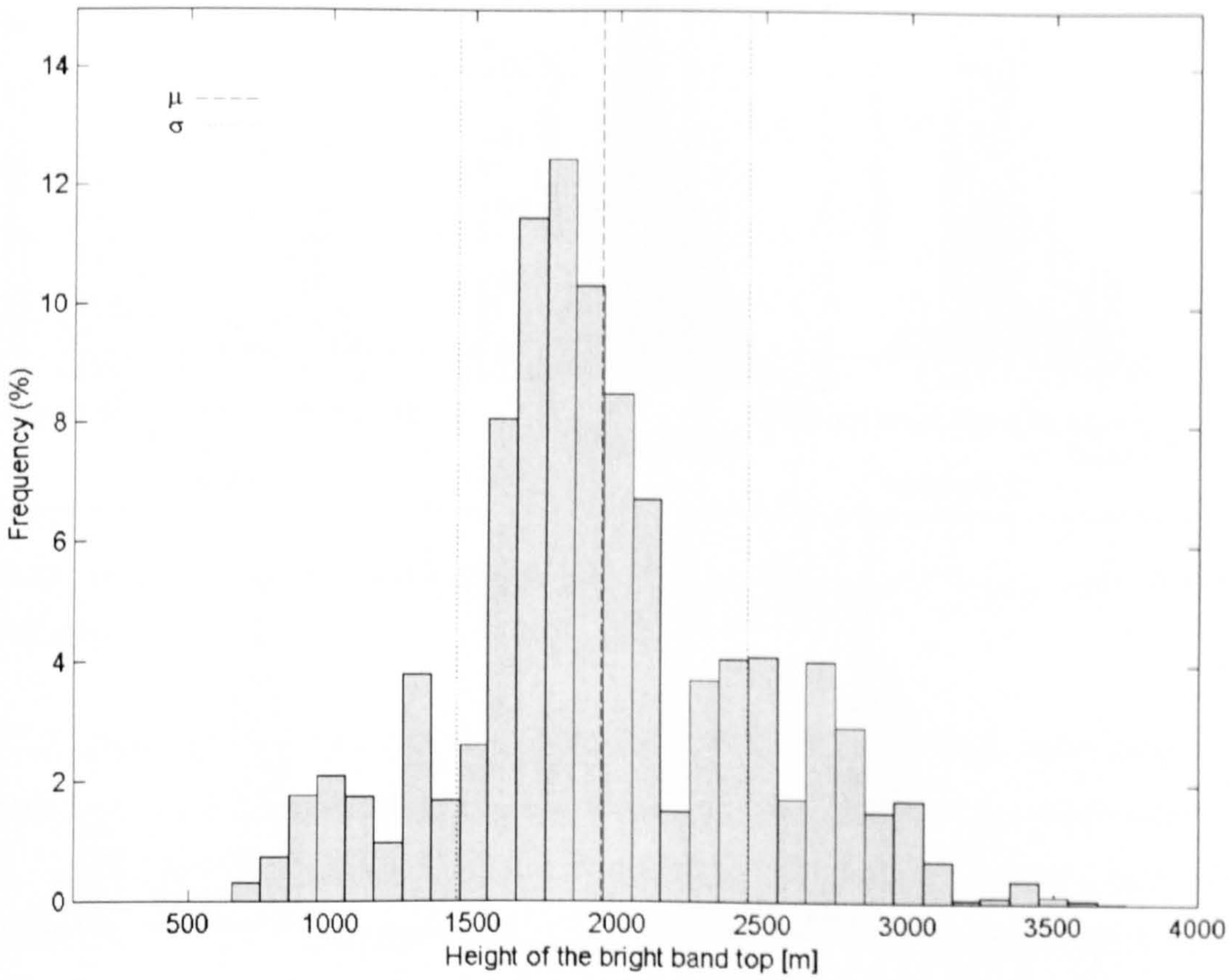

Fig. 5.26: Relative frequency of the height of bright band top over Bristol, UK from June 2001 to December 2002 (100 m steps).

The vertical reflectivity profiles from Bristol have been collected during the development of this research thesis from June 2001 to December 2002. The VPR has been deployed beside the WEMRC building. Due to security reasons, the VPR was switched off overnight and all the data have been collected during day time. Despite the fact that Bristol belongs to the South West of England, this analysis has been carried out independently from the South West analysis because the data have been collected at a different time and possible differences in the results may be more easily explained. The distribution of the height of the bright band top is depicted in Fig. 5.26. The heights of bright band tops are from 700 m to 3500 m, being the most frequent top at 1800 m. The mean bright band top is at 1943 m with 502 m of standard deviation.

The analysis of the distributions of the bright band top by seasons is depicted in Fig. 5.27. In the analysis from the South West region, there are no data available during Winter. Fig. 5.27a shows how low the bright band can be in Bristol during the months from January to March with bright bands seen as low as 700 m, being very critical for scanning weather radar measurements. The mean bright band top in Winter is at 1750 m.

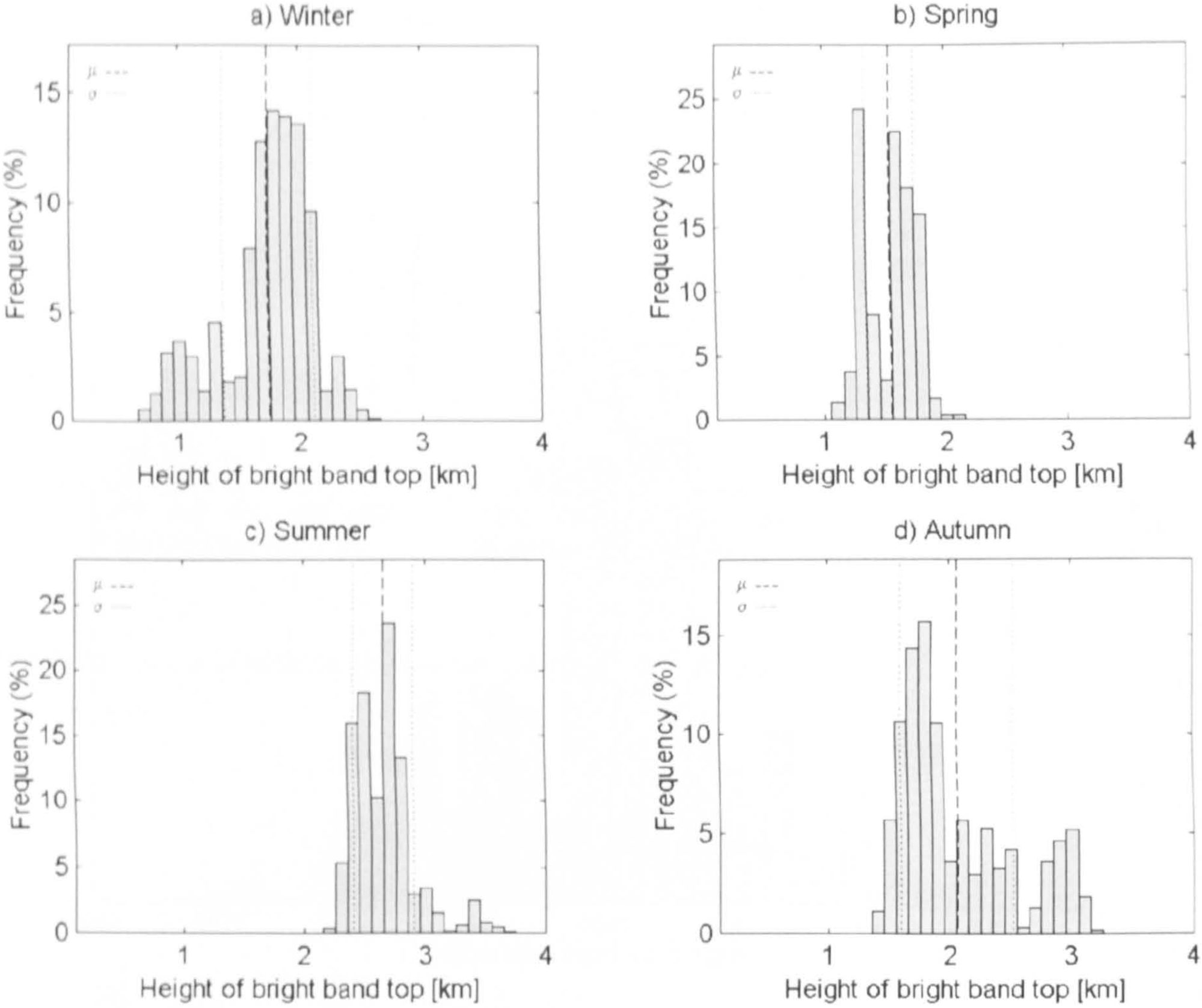

Fig. 5.27: Seasonal distributions of the height of the bright band top over Bristol, UK from June 2001 to December 2002 (100 m steps).

During Spring, the height of the bright band top is between 1100 m and 2000 m, disappearing completely at lower altitudes. In the South West analysis, during Spring the height of the bright band top is as low as 500 m (Fig. 5.18a). Obviously, this is climate dependent and it is directly related to temperature changes from year to year and different distributions can be expected in the coming years. In Summer, the distribution of the bright band top is between 2200 m and 3500 m with a mean value of 2650 m and 250 m of standard deviation. In Summer no bright bands are observed at lower altitudes. During Autumn, the bright band top is lower than during Summer (1400 m), but still with several fluctuations below 3100 m. It is important to remark that attention must be focused on scanning weather radar measurements during the Winter months, because the reflectivity data will be contaminated with the melting layer and any correction algorithm must perform accurately during this season.

The distributions for the reflectivities below, within and above the bright band are depicted in Fig. 5.28. The rain reflectivities follow a gamma distribution (See Appen-

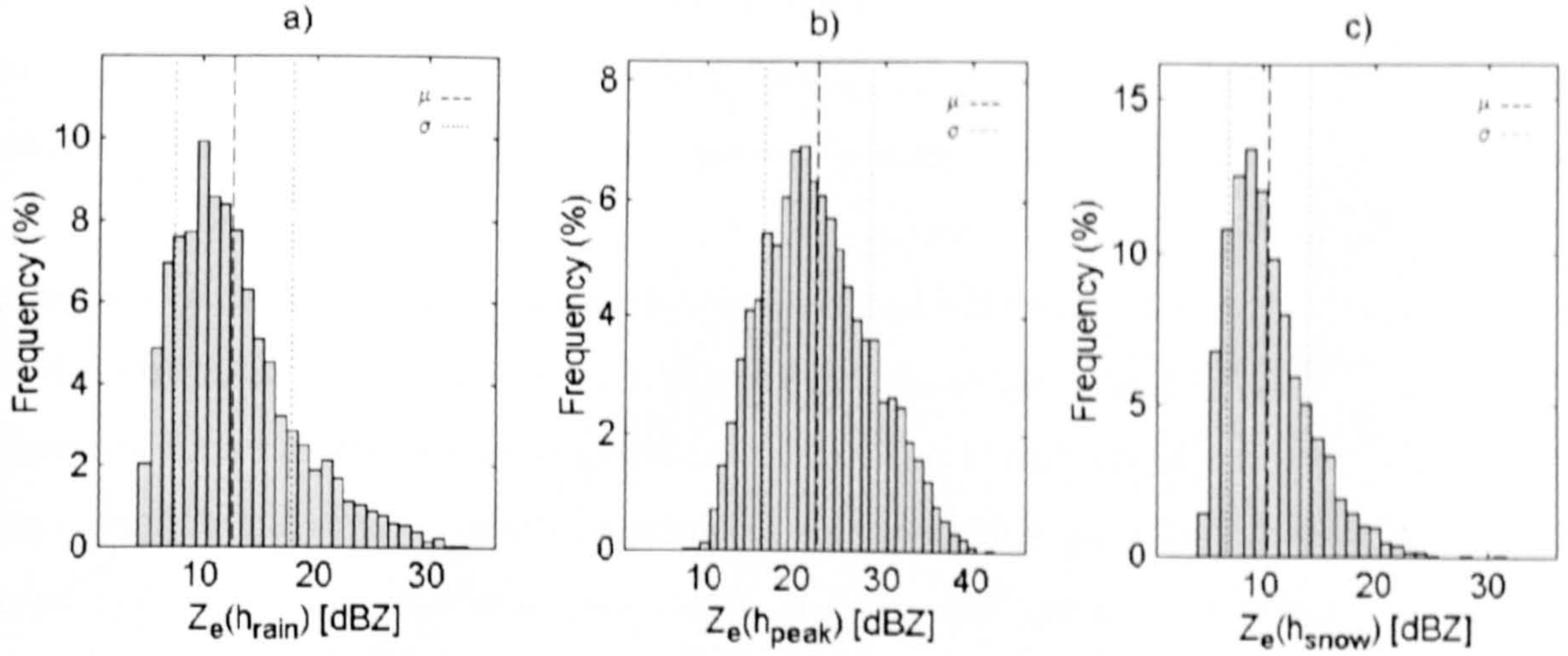

Fig. 5.28: Relative frequency of the reflectivities $Z_{e(rain)}$, $Z_{e(peak)}$ and $Z_{e(snow)}$ over Bristol, UK (1 dBZ steps).

dix C.2) given by Eq. C.2, with $\alpha = 6.35$ and $\lambda = 0.50$. In Bristol, stratiform rainfall is predominantly light because of the low values of reflectivities in the distribution. The mean value of this distribution is around 12.6 dBZ (0.2235 mm hr^{-1}) with 5 dBZ of standard deviation. The distribution of $Z_{e(snow)}$ (Fig. 5.28c) is quite similar to the $Z_{e(rain)}$ distribution, which is gamma distributed although the former is slightly narrower than the latter. The distribution of $Z_{e(peak)}$ (Fig. 5.28b) still presents the shape of a gamma distribution although it is very close to the Gaussian distribution. The mean reflectivity is 22.5 dBZ with 6 dBZ of standard deviation.

Fig. 5.29 shows the scatter plot of $Z_{e(peak)}$ against $Z_{e(rain)}$. From the regression analysis, it is obtained that the reflectivity $Z_{e(peak)}$ as a function of the reflectivity $Z_{e(rain)}$ is given by:

$$Z_{e(peak)} = 9.52 + 1.03 Z_{e(rain)}; \qquad \text{dBZ} \tag{5.10}$$

The correlation of Eq. 5.10 is 0.89 with 2.72 dBZ of standard deviation. It is straightforward to establish that the decrease in reflectivity from the peak of the bright band to the bottom as a function of rain reflectivity is approximately 9.52 dBZ for any value of rain reflectivity. However, the regression line was obtained with rain reflectivities not exceeding 30 dBZ (See Fig. 5.28a) and it is possible that higher values of reflectivity will produce a slightly different regression line.

The scatter plot between the reflectivities above and below the bright band are shown in Fig. 5.30. The regression line of the scattered data has an slope of 0.51 with an offset of 4.07 dBZ. The correlation is 0.75 and the standard deviation is 2.34 dBZ. This regression

line has the lowest slope found at the moment, but also has the lowest correlation. It is likely that a wider distribution of $Z_{e(rain)}$ will produce a regression line with a different slope, which may present similar trends as the regression lines observed in Marseille, New Zealand and the South West of England.

As expected, the thickness of the bright band increases as the rain reflectivity increases (Fig. 5.31a). Thinner bright bands are expected because of the low values of rain reflectivity. However, the bright bands in Bristol are thicker than the bright bands analysed in the South West region for similar values of rain reflectivity. This is one of the points that has been remarked in the last sections, where the complexity in the melting layer contributes to different values of bright band thicknesses for one particular value of rain reflectivity. The distribution of the bright band thickness for the whole data base is shown in Fig. 5.31b. The values range from 200 m to 800 m with a mean thickness of 449 m and a standard deviation of 122 m. The most frequent bright band thicknesses have 350 m depth. The seasonal distributions of the thickness of the bright band are shown in Fig. 5.32. As expected, thinner bright bands are found during Winter and thicker ones during Summer. But not only during Summer the bright bands are thicker, but also during Spring and Autumn. However, there is a lack of data during Summer and it is not possible to suggest that Spring and Autumn will present similar thicknesses.

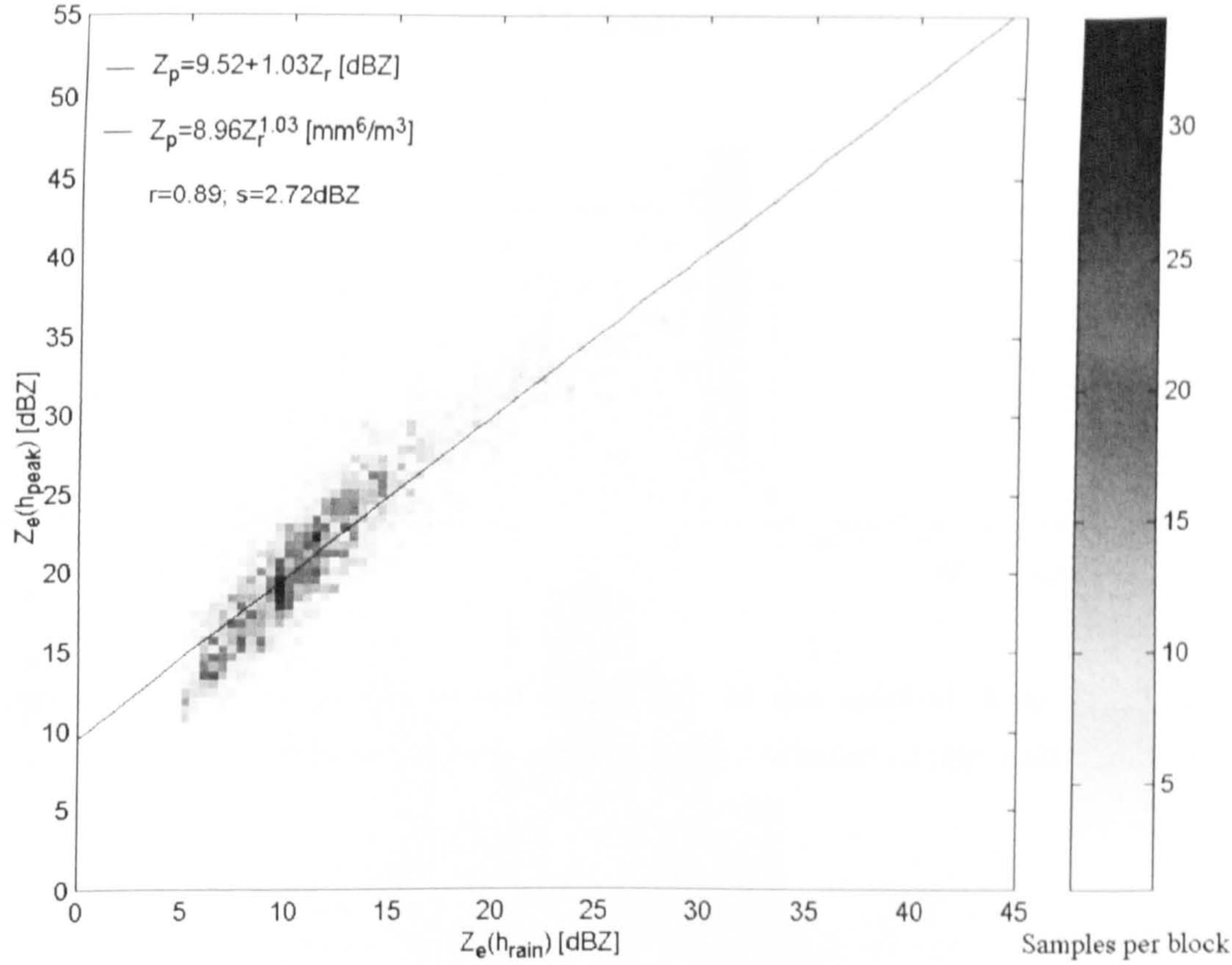

Fig. 5.29: Scatter plot of the maximum reflectivities within the bright band ($Z_{e(peak)}$) against the reflectivities at the bright band bottom ($Z_{e(rain)}$) at X-band frequencies over Bristol, UK.

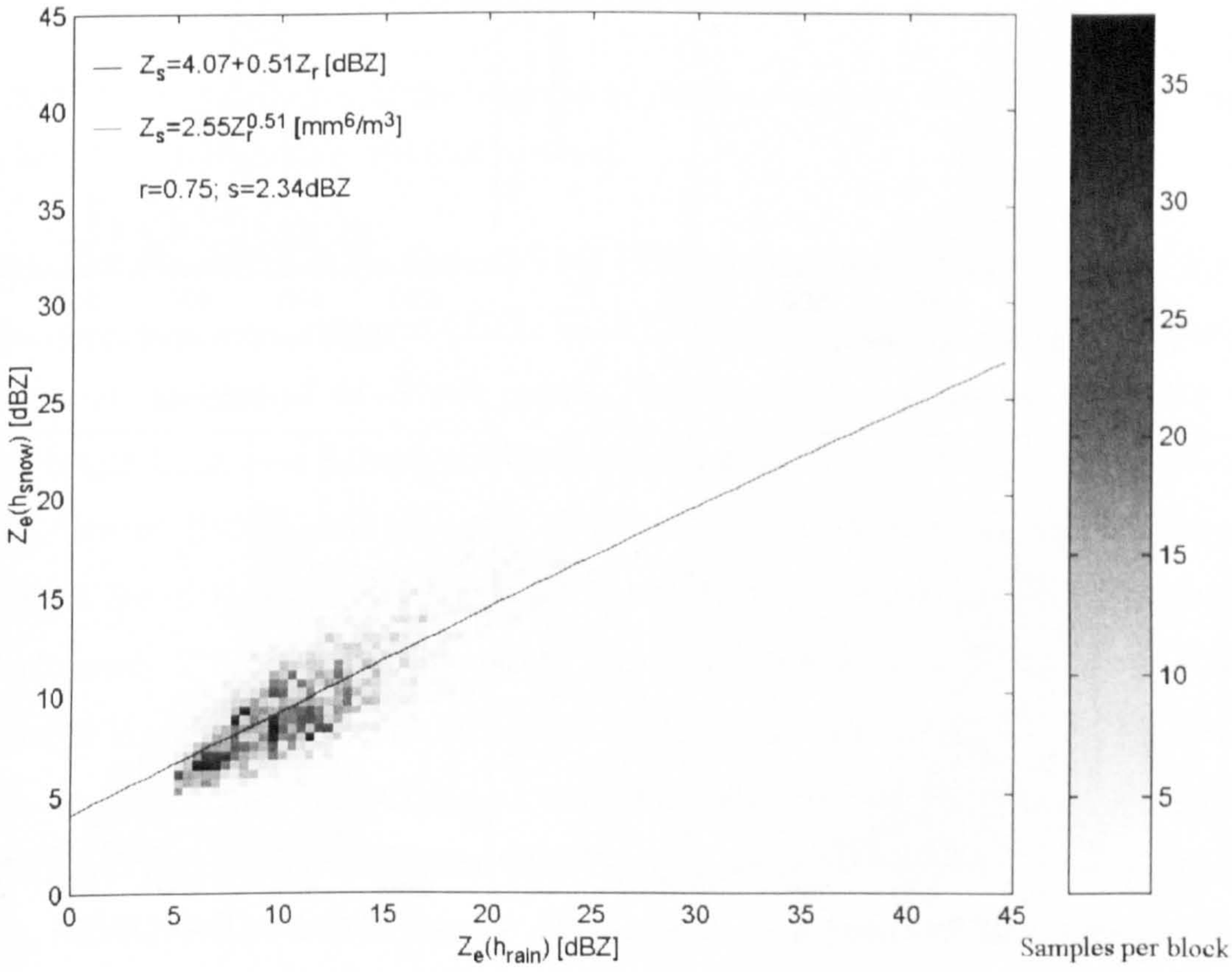

Fig. 5.30: Scatter plot of the reflectivities at the bright band top ($Z_{e(snow)}$) against the reflectivities at the bright band bottom ($Z_{e(rain)}$) at X-band frequencies over Bristol, UK.

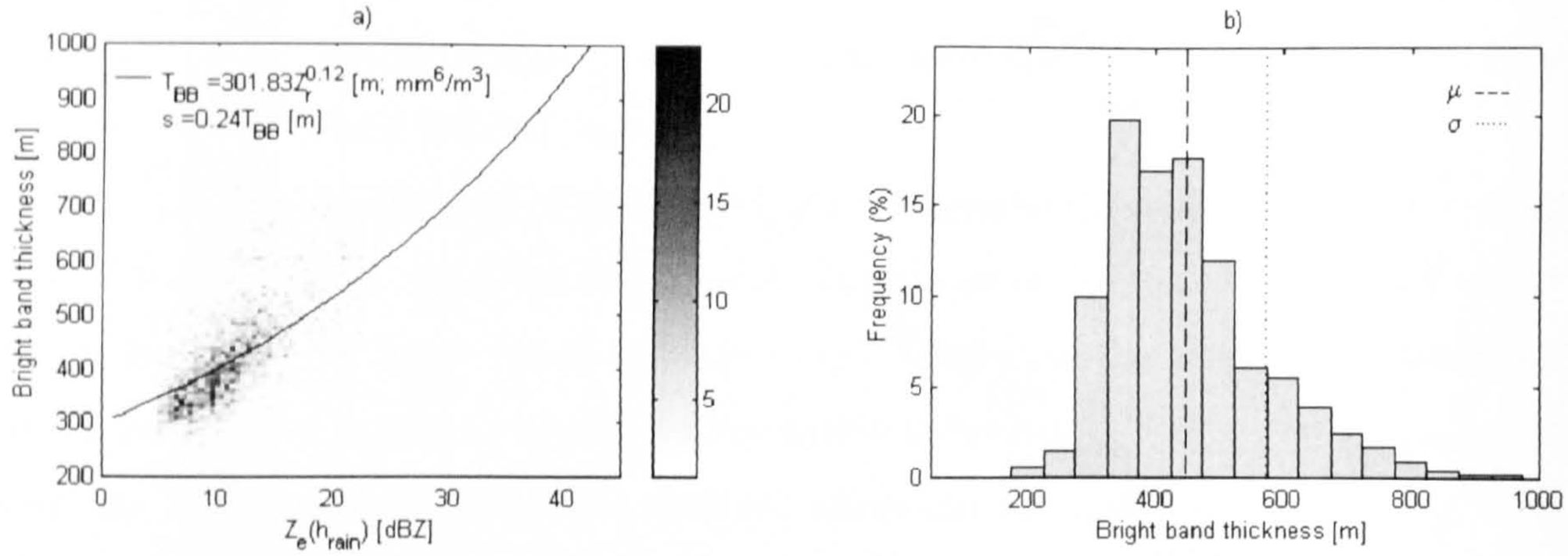

Fig. 5.31: Bright band thickness over Bristol, UK. a) Scatter plot of the bright band thickness versus the rain reflectivity; b) Relative frequency of the bright band thickness (50 m steps).

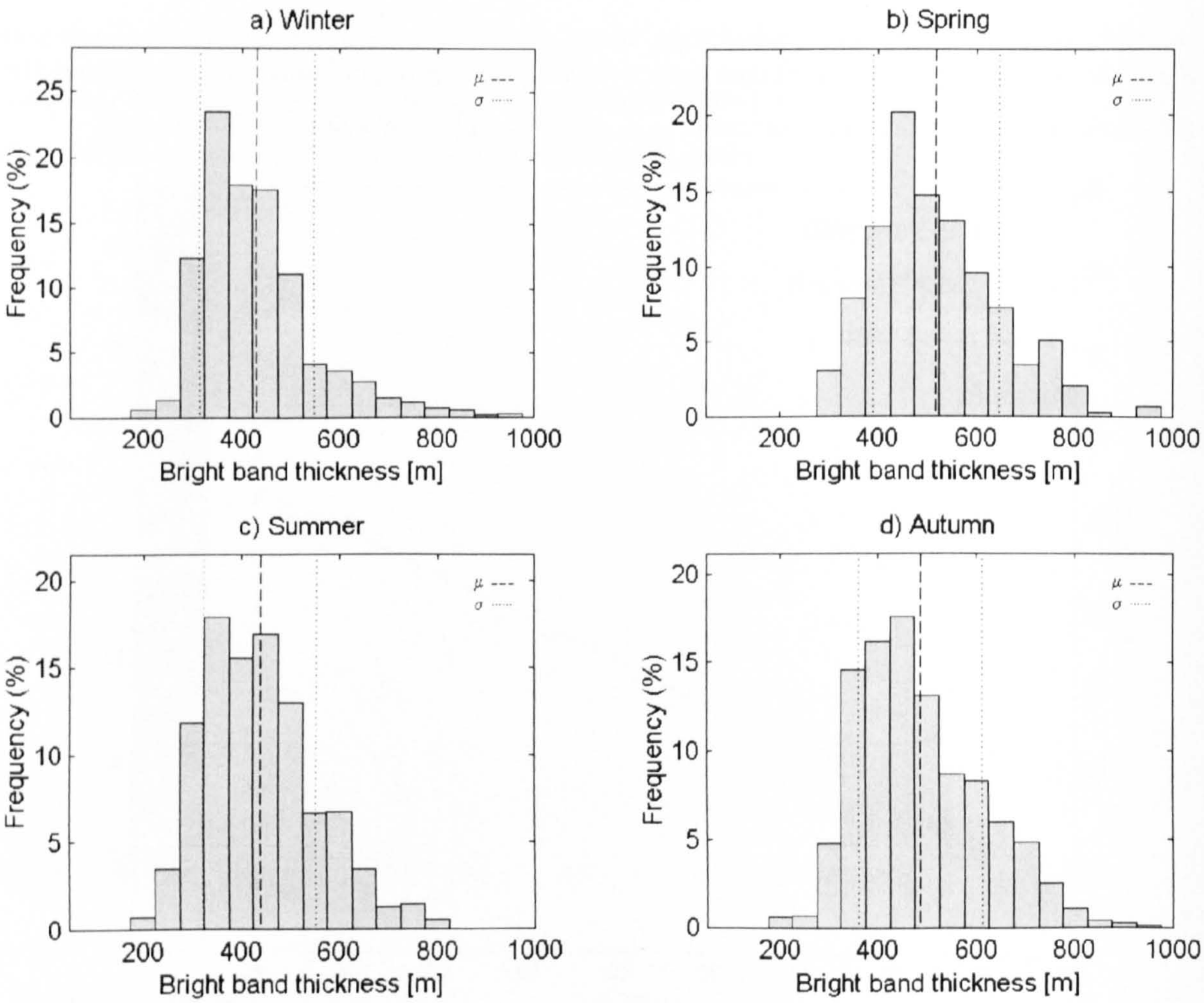

Fig. 5.32: Seasonal distributions of the bright band thickness over Bristol, UK (50 m steps).

5.8 Statistics of the bright band in the North West of England

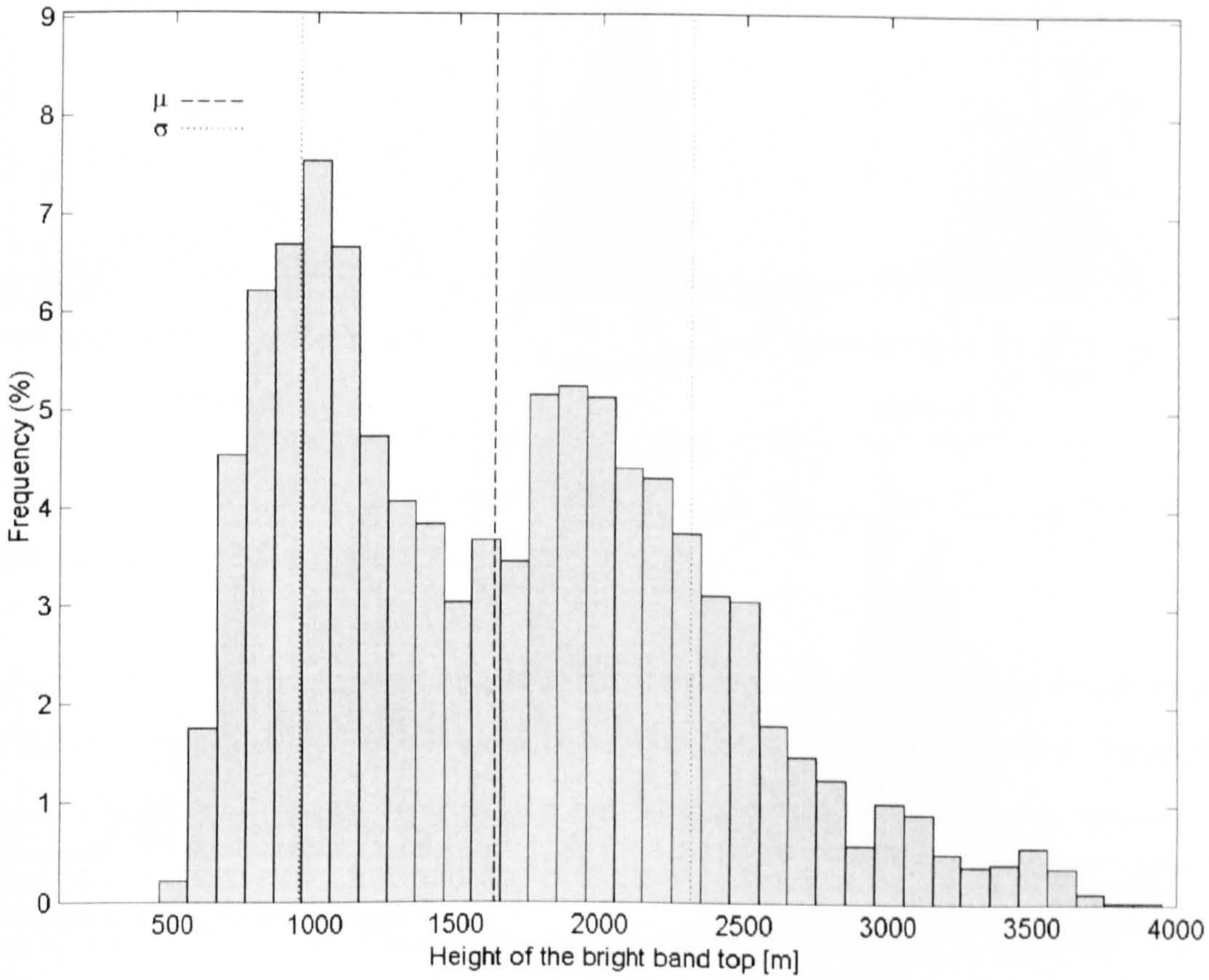

Fig. 5.33: Relative frequency of the height of bright band top over the North West of England from May 1991 to December 1994 (100 m steps).

Since the building of the Salford VPR (Tilford and Cluckie, 1991) several field experiments have been conducted (Tilford and Cluckie, 1992, 1993) in order to study the variation of the vertical reflectivity profile. Towers (1996) carried out a detailed study of the bright band over Salford and part of her results were published in Cluckie et al. (2000). Towers (1996) found that 82% of vertical reflectivity profiles over Salford present the bright band. However, Towers only selected 35 stratiform rainfall events, comprising approximately 270 hr of data in comparison with the 650 hr of bright bands found in the North West database. The corrupted data were not included by Towers (1996) nor in this analysis. Towers (1996) carried out the bright band analysis using the Automatic Bright Band Recognition Algorithm (ABBRA) developed at Salford (Tilford et al., 1992, 2001). However, there are remarkable differences found by using ABBRA to estimate the bright band boundaries (See Section 4.5, Fig. 4.15). Therefore, the analysis of 650 hr of bright band events observed over the North West of England using the rotation algorithm developed in Chapter 4 is presented in this Section.

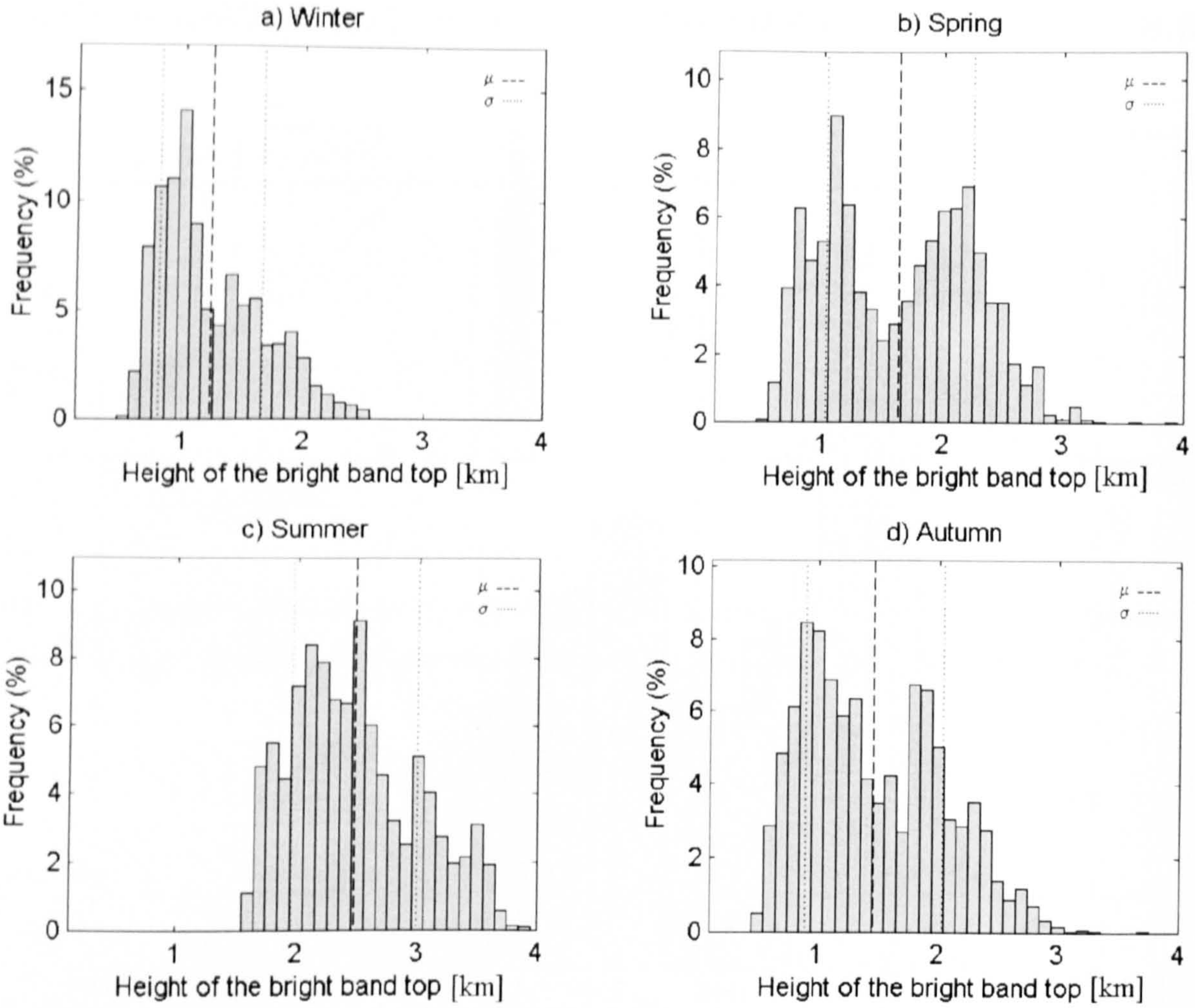

Fig. 5.34: Seasonal distributions of the height of the bright band top over the North West of England from May 1991 to December 1994 (100 m steps).

Fig. 5.33 shows the distribution of the height of the bright band top over the North West of England. The height of the bright band top is from 500 m to almost 3800 m, with a mean of 1628 m and 687 m of standard deviation. Similar distributions have been observed in the bright band analysis of the South West region, although with fewer data. It is interesting to note that Fig. 5.33 presents a bimodal distribution with two maxima at 1000 m and 1900 m. A similar distribution was obtained by Towers (1996) although not as well defined as in Fig. 5.33. The differences are due to the delineation technique employed in the algorithms to detect the bright band boundaries and the sizes of the databases. This bimodality is due to the existence of two prevalent 0 °C isotherm temperature regimes that may be related to the Winter and Summer seasons. The answer may be in the seasonal distribution of height of the bright band top (Fig. 5.34). During Winter, the bright band is more frequent at lower altitudes with a maximum height at 1000 m but with values ranging from 500 m to almost 2500 m (Fig. 5.34a). During this season, the bright band effect is a dominant source of error in the estimation of precipitation using weather

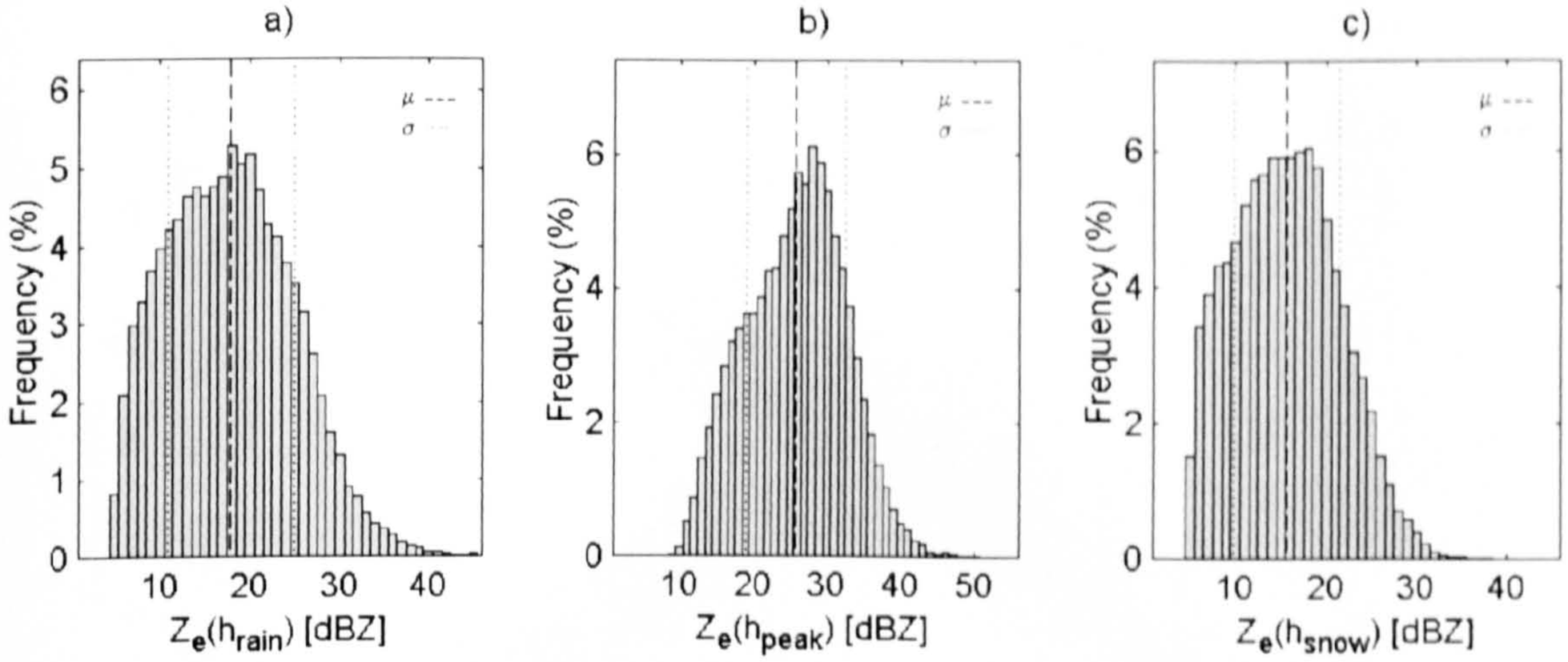

Fig. 5.35: Relative frequency of the reflectivities $Z_{e(rain)}$, $Z_{e(peak)}$ and $Z_{e(snow)}$ over the North West of England (1 dBZ steps).

radars. During Spring, there is a bimodal distribution in the height of the bright band top (Fig. 5.34b). This bimodality may be attributable to the transition between Summer and Winter reflected in temperature changes between the cold and the warm seasons. This pattern is also reflected in Autumn and it is clearly observed by the bimodal distribution shown in Fig. 5.34d. During Summer, the distribution of the bright band top is only at higher altitudes. The values range from 1600 m to almost 4000 m with a mean top of 2500 m.

Therefore, there are bimodal distributions during Spring and Autumn with maxima at 1000 m and 2000 m approximately. During Winter, the distribution is at low altitudes with one maximum at approximately 1000 m. During Summer, the distribution is at high altitudes with one maximum at approximately 2000 m. Thus, the distribution of the height of the bright band top during the whole year is a combination of the seasonal distributions and the result is a bimodal distribution with maxima at 1000 m and 2000 m approximately.

The distributions of the bright band reflectivities are shown in Fig. 5.35. The rain reflectivity distribution comprises values from 5 dBZ (0.07 mm hr^{-1}) to 40 dBZ (11.53 mm hr^{-1}), with a mean rain reflectivity of 18 dBZ (0.49 mm hr^{-1}) (Fig. 5.35a) . The distribution of $Z_{e(rain)}$ over Montreal presents a similar trend (Fabry and Zawadzki, 1995), although in the North West of England the most frequent rain reflectivity is 2 dBZ smaller than the most frequent rain reflectivity in Montreal. This suggests, that the rainfall rate in the North West of England is on average slightly less intense than in Montreal. It is interesting to note that the distribution of $Z_{e(snow)}$ has a similar shape than the distribu-

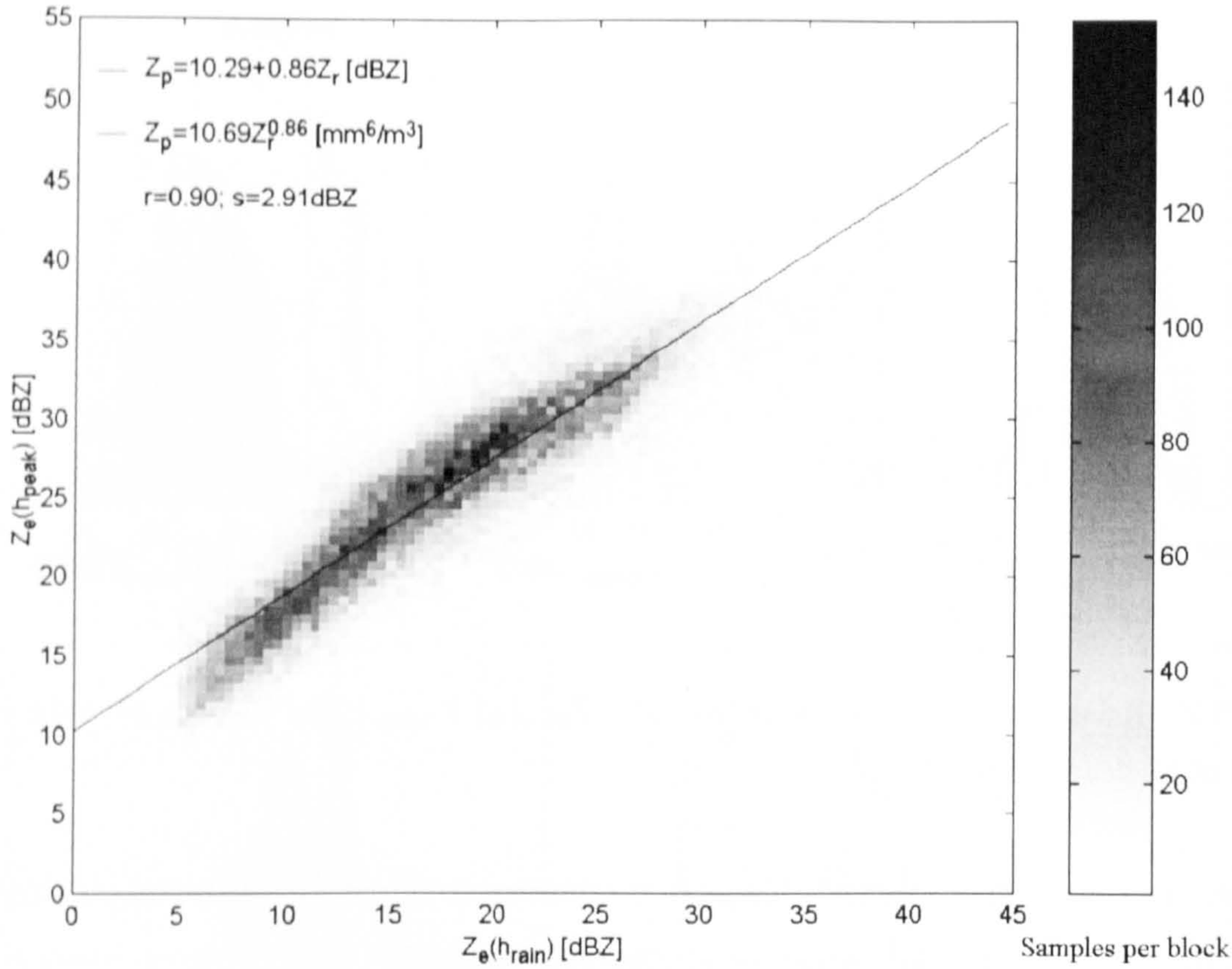

Fig. 5.36: Scatter plot of the maximum reflectivities within the bright band against the reflectivities at the bright band bottom at X-band frequencies over the North West of England.

tion of $Z_{e(rain)}$, although the former is slightly narrower than the latter (Fig. 5.35c). The distribution of $Z_{e(peak)}$ presents values from 10 dBZ to almost 50 dBZ with a mean peak reflectivity of 25.5 dBZ (Fig. 5.35b).

The scatter plot of the maximum reflectivity within the bright band against the rain reflectivity below is depicted in Fig 5.36. Regression analysis shows that there is a correlation of 0.90 between the scattered data and the regression line defined by:

$$Z_{e(peak)} = 10.29 + 0.86 Z_{e(rain)}; \qquad \text{dBZ} \tag{5.11}$$

The standard deviation of Eq. 5.11 is 2.91 dBZ. It is noteworthy to state that the bright band increase is lower than 10.29 dBZ as the rain reflectivity increases, because of the slope of 0.86 in Eq. 5.11. There is a light bending in the scattered data of Fig. 5.36 at approximately 22 dBZ in $Z_{e(rain)}$, similar to the bending observed in Marseille, Bristol and the South West of England.

Fig. 5.37 depicts the variation of the reflectivity above against the reflectivity below the bright band. There is a lot of scatter of data and the regression line presents a poor correlation of 0.78 with a standard deviation of 3.65 dBZ. The slope of the regression line is 0.65 with an offset of 3.92 dBZ. This equation is very similar to the one obtained in

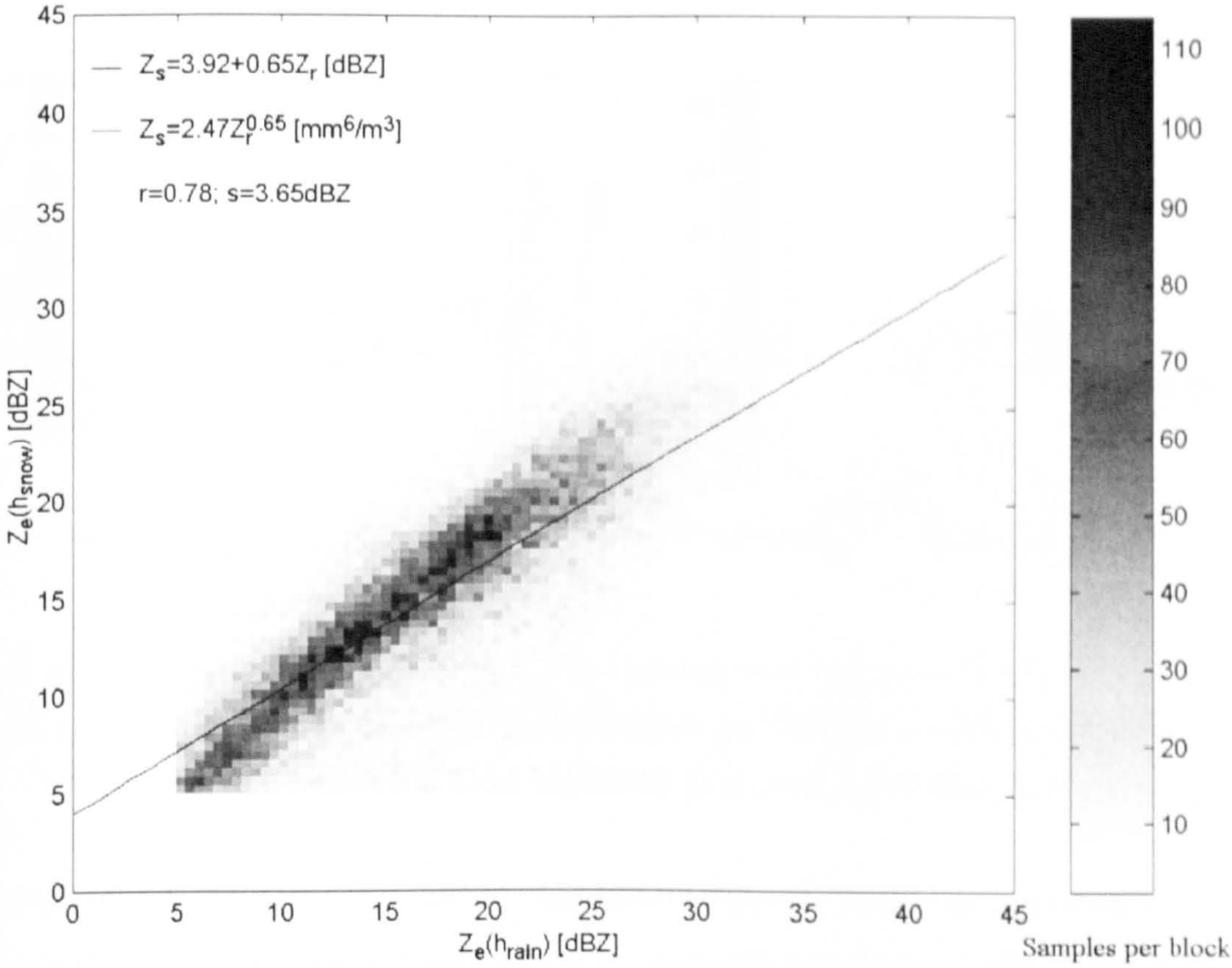

Fig. 5.37: Scatter plot of the reflectivities at the bright band top ($Z_{e(snow)}$) against the reflectivities at the bright band bottom ($Z_{e(rain)}$) at X-band frequencies over the North West of England.

the South West bright band analysis. The scatter may be due in part to the fact that the bright band top is not always well defined as the bright band bottom.

The increase in reflectivity from the top to the peak of the bright band as a function of the rain reflectivity is depicted in Fig. 5.38a. There are two regimes bounded by $Z_{e(rain)} = 20$ dBZ. For $Z_{e(rain)} < 20$ dBZ, there is an increase in reflectivity from the top to the peak of the bright band from 7 dBZ to 11 dBZ and for $Z_{e(rain)} \geq 20$ dBZ the increase in reflectivity is constant and equal to 11 dBZ. The decrease in reflectivity from the peak to the bottom of the bright band as a function of the rain reflectivity is depicted in Fig. 5.38b. For $Z_{e(rain)} < 18$ dBZ the decrease is ≈ 9 dBZ, afterwards decreasing up to ≈ 5 dBZ for $Z_{e(rain)} < 35$ dBZ.

Fig. 5.39a shows the scatter plot of the bright band thickness as a function of rain reflectivity. There is a lot of scatter from the mean value and the standard deviation is approximately 100 m. The mean bright band thickness shows that there is an increase from 350 m to 500 m for rain reflectivities between 5 dBZ to 30 dBZ (0.07 mm hr^{-1} to 2.73 mm hr^{-1}) and afterwards a decrease of 50 m for rain reflectivities of 35 dBZ. This last decrease may be explained by the lack of rain reflectivities greater than 30 dBZ (From Fig. 5.35a). Towers (1996) found no evidence of increasing bright band thicknesses when

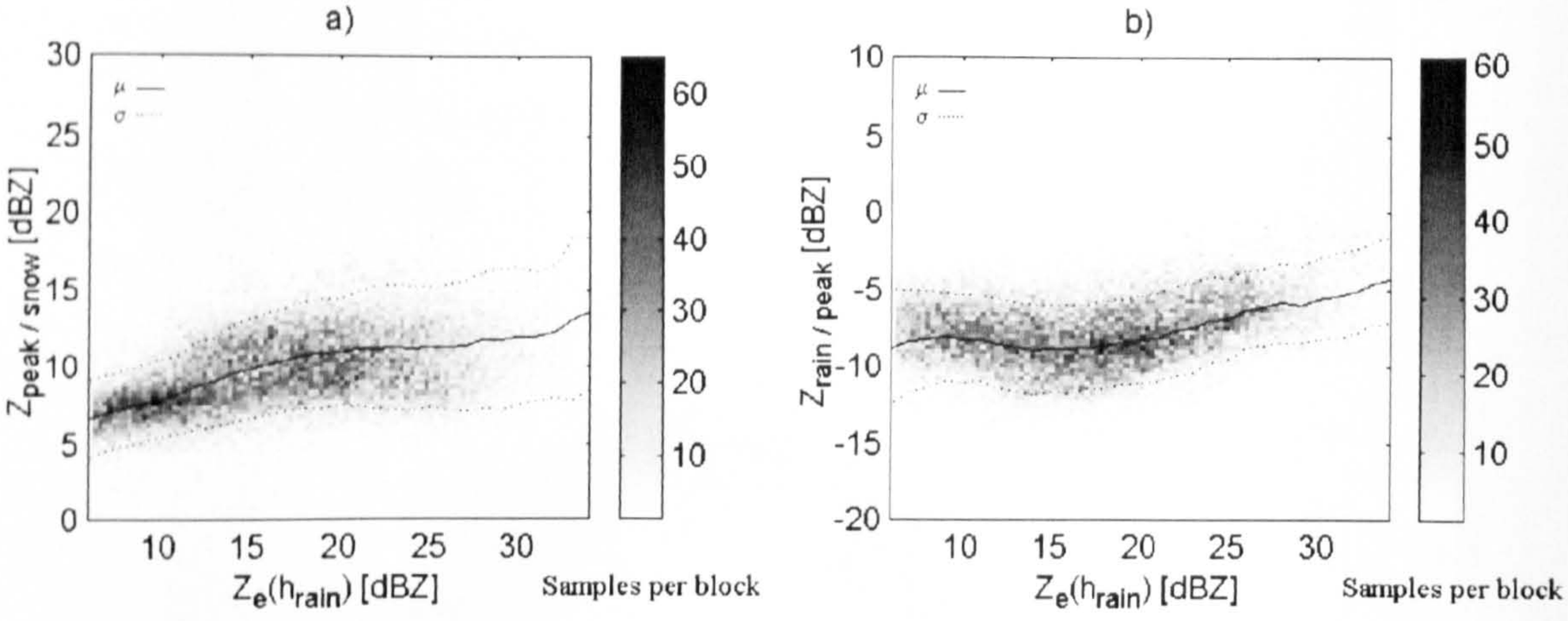

Fig. 5.38: Scatter plot of the bright band enhancement over the North West of England at X-band frequencies. a) Enhancement from the top to the peak of the bright band as a function of $Z_{e(rain)}$. b) Decrease from the peak to the bottom of the bright band as a function of $Z_{e(rain)}$.

the rain reflectivity increases. Towers attributed this effect to the intense precipitation trails passing over the bright band. However, it is true that the precipitation trails influence the accuracy of the estimation of the height of the bright band top, but the scatter in the bright band thickness is real and it depends on several factors such as the variation of the vertical temperature profile, the lapse rate and relative humidity among others around the melting layer. Then, even when there is a dependence of bright band thicknesses with precipitation intensity the scatter will be large and modelling the bright band thickness is not an easy task because it involves the integration of all the factors influencing the snowflake melting rate. The mean value of the bright band thickness is 425 m with 150 m of standard deviation (From Fig. 5.39b).

As pointed out in preceding sections, there is a certain dependence of the bright band thickness on the season of the year, where the height of the bright band top is very important. Fig. 5.40 shows this influence and it is interesting to note that when the bright band top is between 500 m and 1300 m, there is a clear increase in bright band thickness from $\approx$ 150 m to $\approx$ 450 m. However, when the bright band top is above 1300 m and up to 3500 m the thickness of the bright band only increases by around 50 m on average. This analysis takes into account the mean bright band thickness and its scatter is represented by the standard deviation in Fig. 5.40 (dotted line).

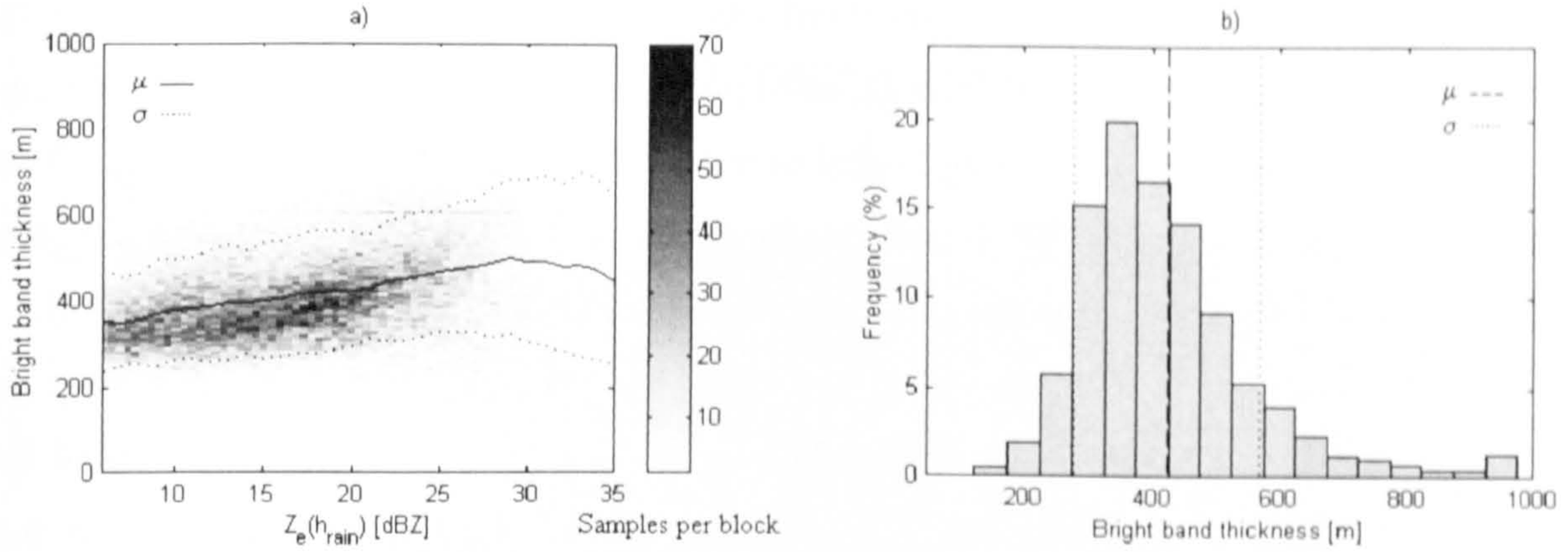

Fig. 5.39: Bright band thickness over the North West of England. a) Scatter plot of the bright band thickness versus the rain reflectivity; b) Relative frequency of the bright band thickness (50 m steps).

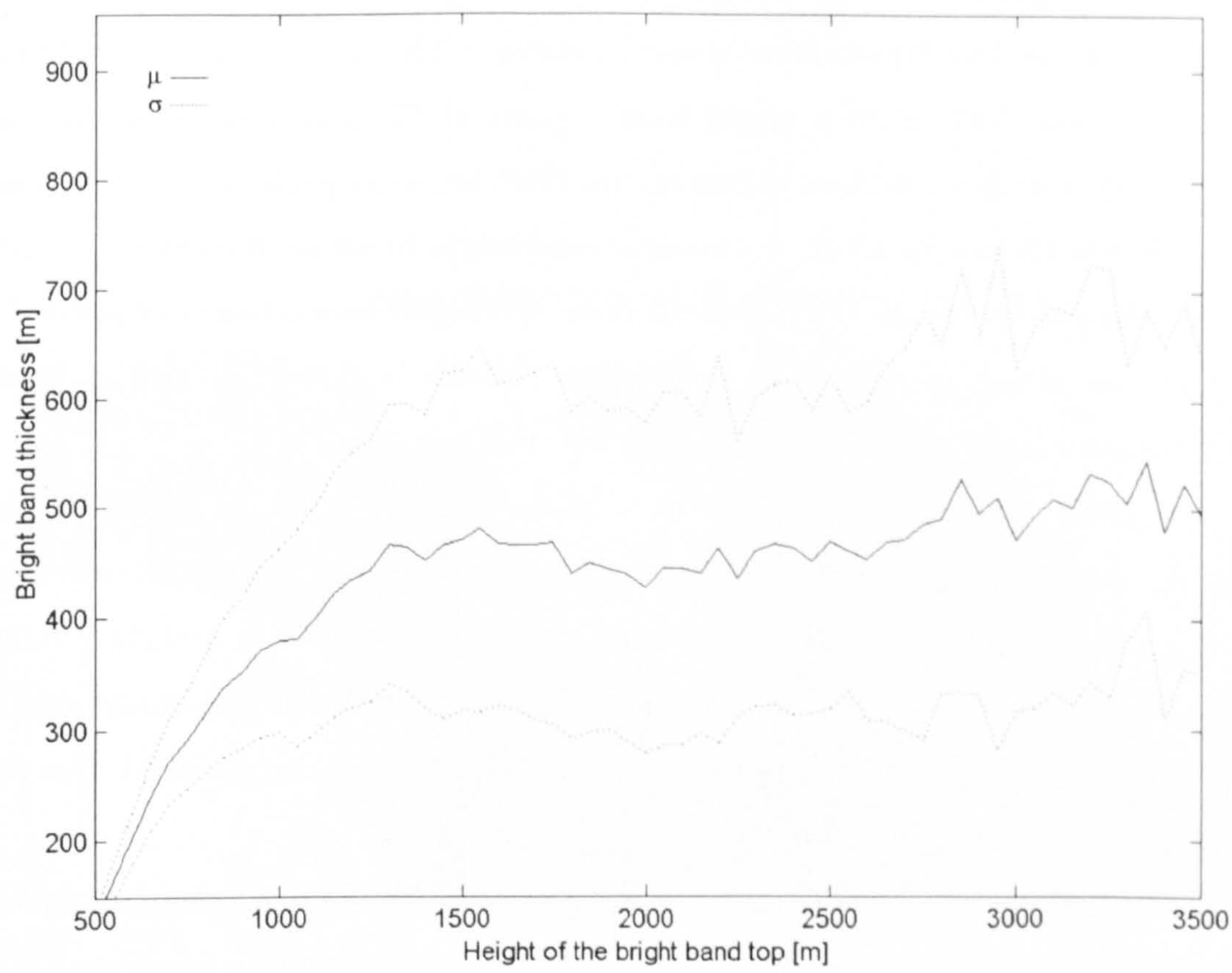

Fig. 5.40: Dependence of the bright band thickness with the height of the bright band top over the North West of England.

5.9 Multiple bright band events

A particularly interesting feature is observed when there are temperature inversions along the vertical. As ice particles fall through an upper 0 °C isotherm layer, they start melting, then re-freezing again until melting begins in another layer of sub-zero temperature. The result, when observed by a VPR is a double bright band. Usually, double bright bands are common in fronts, which cause temperature inversions (Hardaker, 1993; Fabry, 1994a).

A double bright band event recorded in Marseille on November 1998 is depicted in Fig. 5.41. At 23:48 hr the bright band top was around 2.5 km height, but at 23:50 hr a second bright band appears 400 m above the first one. Both of them remained for approximately 4 minutes. After that, the prevailing bright band was the one at 2.9 km height.

In Boscombe Down, UK, a double bright band event was recorded on 26th May 1995 (See Fig. 5.42). The top of the upper bright band was at 2.6 km with a thickness of approximately 300 m. The second bright band appeared at 1.8 km with a thickness of 300 m. Both bright bands stayed for around 25 minutes.

The most impressive multiple bright band event recorded in the long term database took place close to the Chilbolton radar facility during HYREX. The multiple bright bands are shown in Fig. 5.43. First a bright band appears at 12:50 hr, approximately 2.3 km above the VPR with a thickness of 300 m. At 12:55 hr, some pockets of instabilities are observed below 1.8 km. At 13:02 hr, two additional bright bands are formed; one at 1.6 km and the other one at 1.3 km. Finally at 13:14 hr, the higher bright band disappeared and the other two came together into a single highly variable bright band. This event shows clearly the complexity of the vertical reflectivity profile.

Fabry (1994a) reported a double and a triple bright band over Montreal. Towers (1996) reported around 50 min of double bright band events over Salford. In conventional scanning weather radars, double bright band events are observed in a slightly different way. Scanning radars usually scan over a wide area where fronts are easily identified. They may observe a double bright band as a very thick single bright band, due to the beam spreading at long ranges.

The bright band detection algorithm developed in Chapter 4 can be applied to double bright band events. If the bottom of the upper bright band is far away (more than 800 m) from the top of the lower bright band, the algorithm will detect the one with more power or area. However, if they are very close, the algorithm may see them as a very thick single bright band with the top from the upper one and the bottom from the lower one.

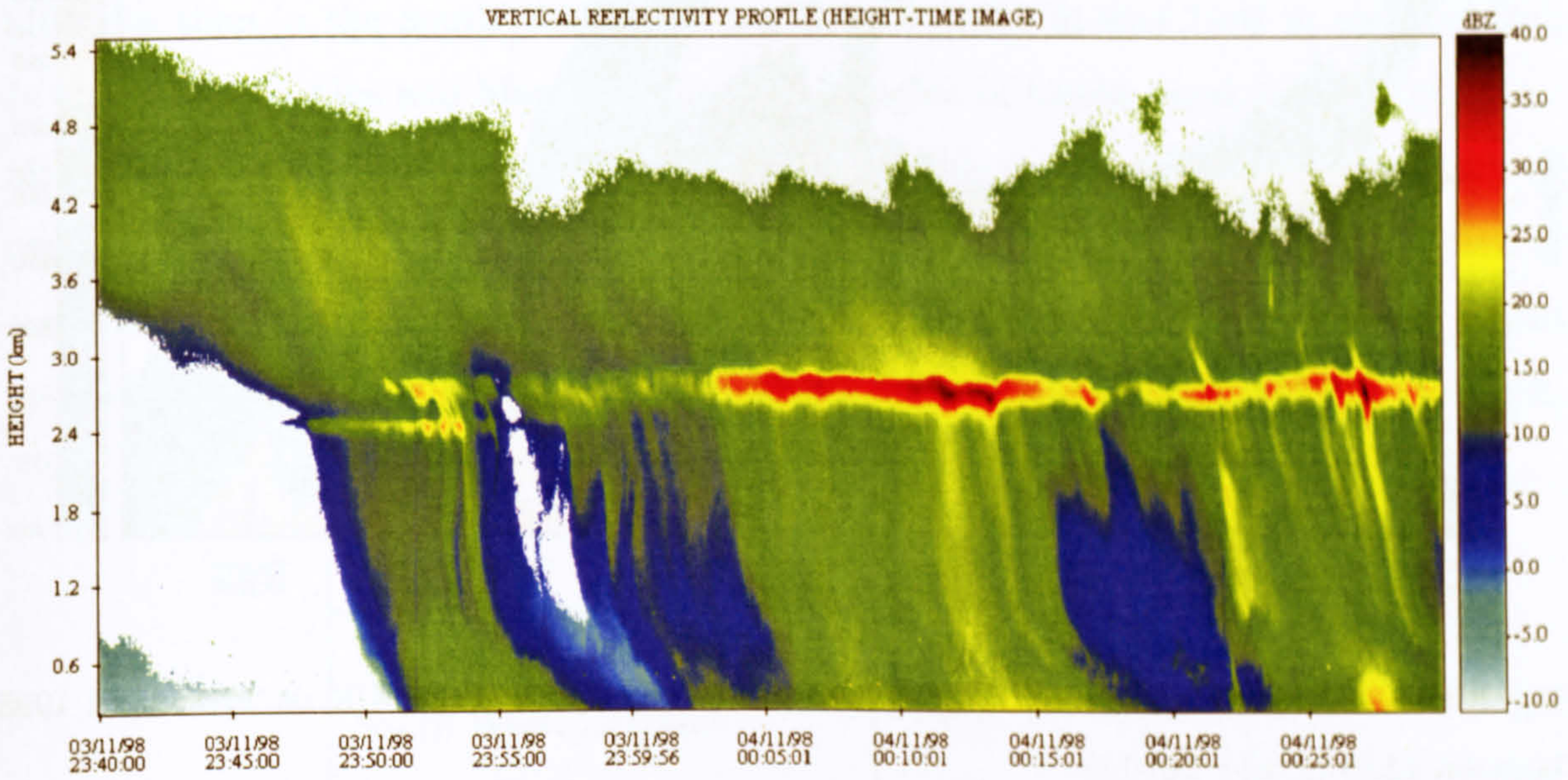

Fig. 5.41: Double bright band in Marseille, France on 3rd November 1998 between 23:50 hr and 23:54 hr, at 2.5 km and 2.9 km above the radar site.

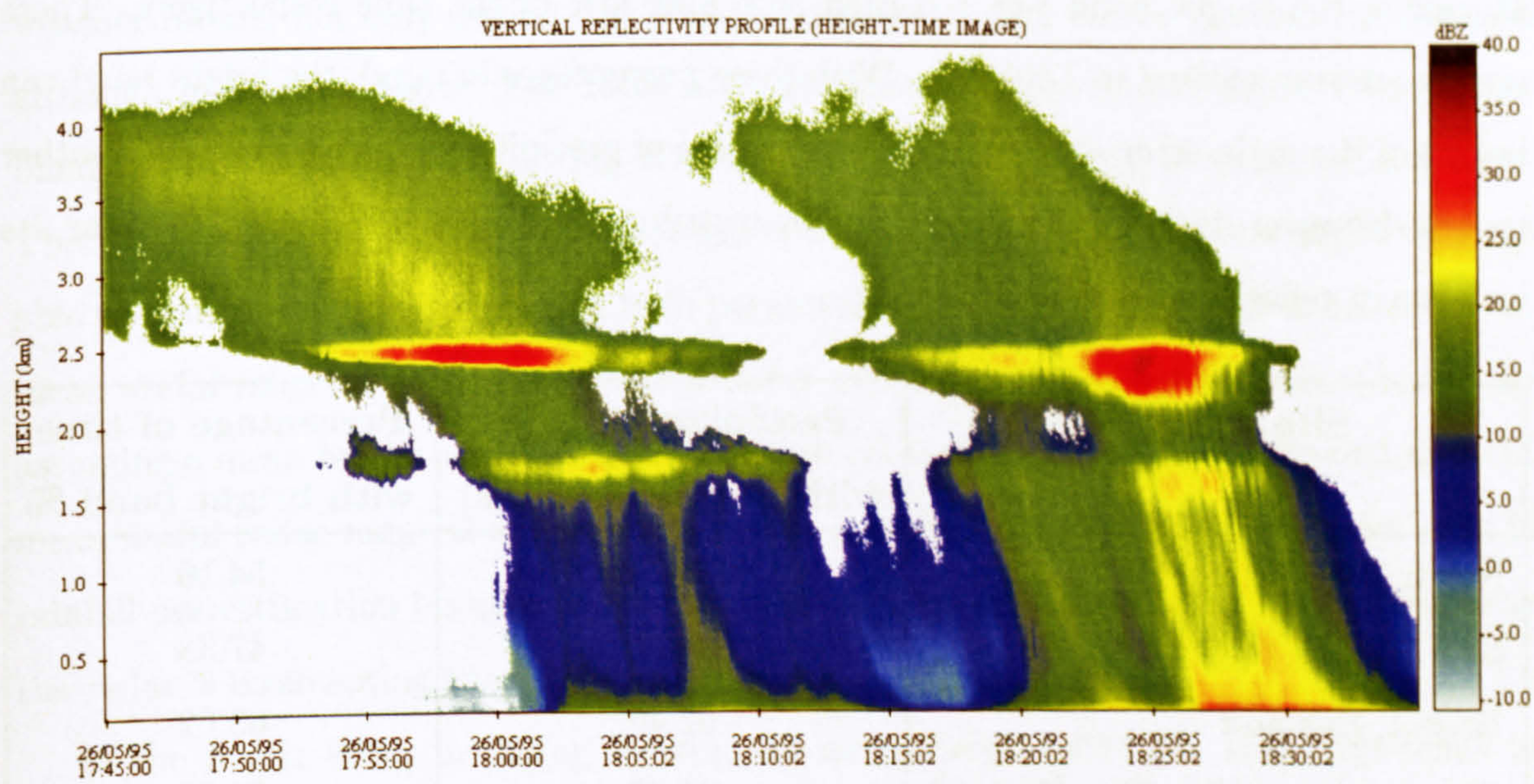

Fig. 5.42: Double bright band in Boscombe Down, UK on 26th May 1995.

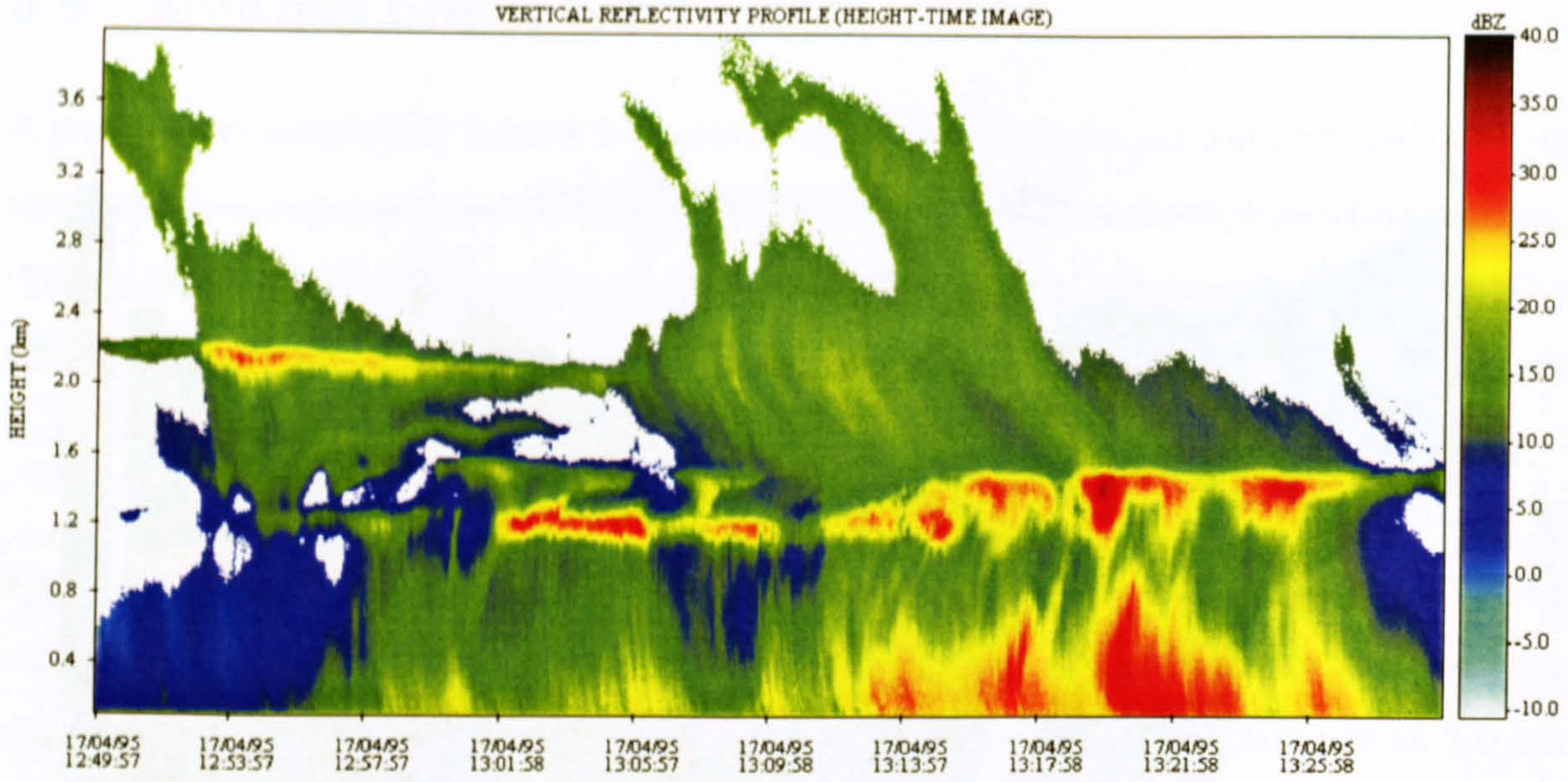

Fig. 5.43: Multiple bright bands in Chilbolton radar site, Oxfordshire, UK on 17th April 1995 between 12:55 hr and 13:10 hr.

5.10 Summary of results

It has been found that the bright band was recorded approximately 54% of the time in the North West, 47% in the South West and 63% in Bristol. In the Southern Alps and Marseille, the bright band was recorded 36% and 33% of the time respectively. These results are summarised in Table 5.2. With these percentages in mind, the bright band can be one of the main error sources on the estimation of precipitation using scanning weather radars. However, its impact depends on the distribution of its height during the year, its increase in reflectivity and its thickness.

Site or region	**Precipitation time with bright band (hr)**	**Percentage of time with bright band %**
North West, England	650.70	54.16
South West, England	168.21	47.38
Bristol, England	62.45	63.62
The Southern Alps, New Zealand	41.32	35.80
Marseille, France	21.67	32.87

Table 5.2: Precipitation time with bright band observed with the VPR from 1991 to 2002.

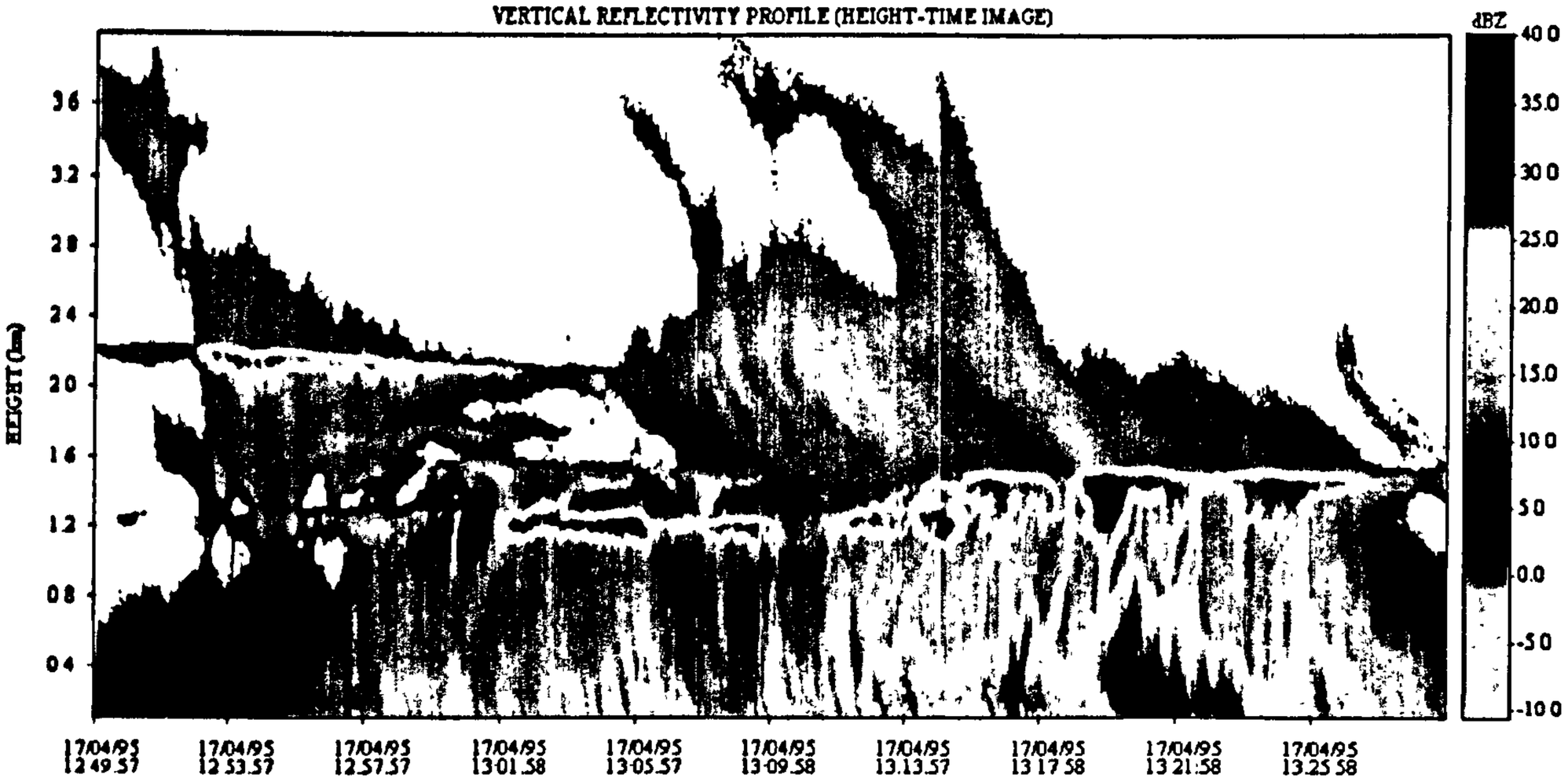

Fig. 5.43: Multiple bright bands in Chilbolton radar site, Oxfordshire, UK on 17th April 1995 between 12:55 hr and 13:10 hr.

5.10 Summary of results

It has been found that the bright band was recorded approximately 54% of the time in the North West, 47% in the South West and 63% in Bristol. In the Southern Alps and Marseille, the bright band was recorded 36% and 33% of the time respectively. These results are summarised in Table 5.2. With these percentages in mind, the bright band can be one of the main error sources on the estimation of precipitation using scanning weather radars. However, its impact depends on the distribution of its height during the year, its increase in reflectivity and its thickness.

Site or region	Precipitation time with bright band (hr)	Percentage of time with bright band %
North West, England	650.70	54.16
South West, England	168.21	47.38
Bristol, England	62.45	63.62
The Southern Alps, New Zealand	41.32	35.80
Marseille, France	21.67	32.87

Table 5.2: Precipitation time with bright band observed with the VPR from 1991 to 2002.

5.10.1 Height of bright band top

In England, the mean height of bright band top in the North West (1628 m) is at lower altitudes than in the South West including Bristol (1839 m and 1943 m respectively). In the Southern Alps and Marseille, the mean heights of bright band tops are at higher altitudes, although these results represent only a couple of months and they may not be representative during the rest of the year. The mean heights of the bright band tops of every site analysed in the past sections are summarised in Table 5.3. The sites are placed in descending order according to the number of bright band hours recorded by the VPR.

Site or Region	Bright band top	
	μ (m)	σ (m)
North West, England	1628	687
South West, England	1839	721
Bristol, England	1943	502
Southern Alps, New Zealand	2037	382
Marseille, France	2877	463

Table 5.3: Statistics of the height of bright band top recorded by the VPR from 1991 to 2002.

The seasonal analysis of the height of bright band top in England reveals that the bright band may be a potential error source in the estimation of precipitation using scanning weather radars, not only during the Winter months but also during Spring and Autumn although in a lesser degree (See Table 5.4). For instance, the mean height of the bright band top in the North West during Winter is 1225 m with 430 m of standard deviation. The UK weather radars have a beamwidth of 1° and the lowest elevation angle they are able to scan is at 0.5°. Considering both parameters and applying Eq. 2.3 to calculate the mean useful range of a scanning weather radar without intercepting the bright band and assuming a mean bright band thickness of 400 m (From Fig. 5.39a), it is obtained that the mean useful radar range is approximately 41.5 km. Beyond this limit, problems arise in rainfall overestimation because of the interception with the bright band and further away the radar is intercepting snow rather than rain.

In the South West, including Bristol, the mean height of bright band top tends to be higher than in the North West at least during Summer and Autumn, but not during Spring. During Winter, there is no way to compare with the results from the South West or Bristol, because of the lack of measurements in the former and the small amount of data obtained in the latter during the same season.

Site or region	Spring		Summer		Autumn		Winter	
	μ (m)	σ (m)	μ (m)	σ (m)	μ (m)	σ (m)	μ (m)	σ (m)
North West	1635	613	2474	518	1465	571	1225	430
South West	1429	597	2701	419	2176	532	-	-
Bristol	1546	205	2652	248	2055	466	1735	369

Table 5.4: Seasonal dependency of the height of bright band top in England.

$Z_{e(peak)}$ vs $Z_{e(rain)}$	r	σ	$Z_{e(snow)}$ vs $Z_{e(rain)}$	r	σ
The North West of England					
$Z_{e_1(peak)} = 10.29 + 0.86 Z_{e_1(r)}$ $Z_{e_2(peak)} = 10.69 Z_{e_2(rain)}^{0.86}$ $Z_{e_2(peak)} = 1018.27 R^{1.38}$	0.90	2.91	$Z_{e_1(s)} = 3.92 + 0.65 Z_{e_1(r)}$ $Z_{e_2(snow)} = 2.47 Z_{e_2(rain)}^{0.65}$ $Z_{e_2(snow)} = 77.33 R^{1.04}$	0.78	3.65
The South West of England					
$Z_{e_1(peak)} = 11.62 + 0.93 Z_{e_1(r)}$ $Z_{e_2(peak)} = 14.52 Z_{e_2(rain)}^{0.93}$ $Z_{e_2(peak)} = 2004.12 R^{1.49}$	0.91	2.84	$Z_{e_1(s)} = 3.64 + 0.68 Z_{e_1(r)}$ $Z_{e_2(snow)} = 2.31 Z_{e_2(rain)}^{0.68}$ $Z_{e_2(snow)} = 84.78 R^{1.09}$	0.80	3.50
Bristol, England					
$Z_{e_1(peak)} = 9.52 + 1.03 Z_{e_1(r)}$ $Z_{e_2(peak)} = 8.96 Z_{e_2(rain)}^{1.03}$ $Z_{e_2(peak)} = 2100.72 R^{1.65}$	0.89	2.72	$Z_{e_1(s)} = 4.07 + 0.51 Z_{e_1(r)}$ $Z_{e_2(snow)} = 2.55 Z_{e_2(rain)}^{0.51}$ $Z_{e_2(snow)} = 38.02 R^{0.82}$	0.75	2.34
The Southern Alps, New Zealand					
$Z_{e_1(peak)} = 9.25 + 0.92 Z_{e_1(r)}$ $Z_{e_2(peak)} = 8.42 Z_{e_2(rain)}^{0.92}$ $Z_{e_2(peak)} = 1102.20 R^{1.47}$	0.96	2.20	$Z_{e_1(s)} = -0.21 + 0.81 Z_{e_1(r)}$ $Z_{e_2(snow)} = 0.95 Z_{e_2(rain)}^{0.81}$ $Z_{e_2(snow)} = 69.43 R^{1.30}$	0.87	3.82
Marseille, France					
$Z_{e_1(peak)} = 12.17 + 0.93 Z_{e_1(r)}$ $Z_{e_2(peak)} = 16.48 Z_{e_2(rain)}^{0.93}$ $Z_{e_2(peak)} = 2274.65 R^{1.49}$	0.94	3.11	$Z_{e_1(s)} = 4.53 + 0.71 Z_{e_1(r)}$ $Z_{e_2(snow)} = 2.84 Z_{e_2(rain)}^{0.71}$ $Z_{e_2(snow)} = 122.19 R^{1.14}$	0.86	3.70

Table 5.5: Regression analysis results between the reflectivities $Z_{e(peak)}$ vs $Z_{e(rain)}$ (left side) and $Z_{e(snow)}$ vs $Z_{e(rain)}$ (right side) at X-band frequencies for the North West, South West and Bristol in England, the Southern Alps in New Zealand and Marseille in France. Z_{e_1} is in dBZ, Z_{e_2} in mm^6 m^{-3}, R in mm hr^{-1} and σ in dBZ. For the calculus of $Z_e(R)$, it is assumed the M-P Z-R relationship, *i.e.* $Z_{e(rain)} = 200 R^{1.6}$ (Marshall et al., 1955).

5.10.2 Reflectivities at the top, peak and bottom of bright band

The equations obtained in the last sections from regression analysis among the maximum reflectivities in the bright band, and the reflectivities at the top and bottom of the bright band are summarised in Table 5.5.

The maximal correlation between the variation of $Z_{e(peak)}$ and $Z_{e(rain)}$ has been found with the Southern Alps database ($r = 0.96$) and also with the lowest standard deviation ($\sigma = 2.20$ dBZ). Despite the fact that the Southern Alps database represents only one month of data, it contains a wide spectrum of rain reflectivities between 5 dBZ and almost 45 dBZ (See Fig. 5.11a). The reason for the higher correlation is due to the fact that the bending experienced in the other sites, does not exist in the Southern Alps database, fitting the regression line more accurately. It has been explained, that in the Southern Alps a longer pulse length was used to increase the SNR of the radar signal, trading-off resolution with SNR. However, an increase in SNR improves the ability of a radar to differentiate low-intensity echoes from noise, as on the top of the cloud. This is not the case in the bright band, which high-intensity echoes are expected. It has been suggested that orographic enhancement takes place not only at lower altitudes, but also within the melting layer because of the influence of the Alps, causing an increase in the bright band reflectivities.

Fig. 5.44 depicts the regression lines $Z_{e(peak)}$ against $Z_{e(rain)}$ for all the sites. It is interesting to note that the slopes of the regression lines are very close among them with a mean slope of 0.93. The differences are more remarkable in the offsets of the regression lines, with values from 9.25 dBZ for the Southern Alps to 12.27 dBZ in Marseille with a mean offset of 10.57 dBZ. Fabry and Zawadzki (1995) carried out a similar analysis in Montreal, using a similar X-band VPR and from their results, fitting a regression line to the scatter plot of $Z_{e(peak)}$ vs $Z_{e(rain)}$, it is found that $Z_{e(peak)} \approx Z_{e(rain)} + 10$ dBZ, which means the slope is slightly higher than the ones obtained in this analysis with an offset of 10 dBZ. Even when there are slight differences among the results obtained in this chapter for the different climatological regions, it is possible to suggest that at X-band frequencies the variation between the maximal reflectivity in the bright band and the rain reflectivity below presents a general trend given by:

$$Z_{e(peak)} \approx 10.57 + 0.93 Z_{e(rain)}; \qquad \text{dBZ} \tag{5.12}$$

Eq. 5.12 has been obtained by regression analysis among the Eqs. $Z_{e(peak)}$ vs $Z_{e(rain)}$ shown in Table 5.5.

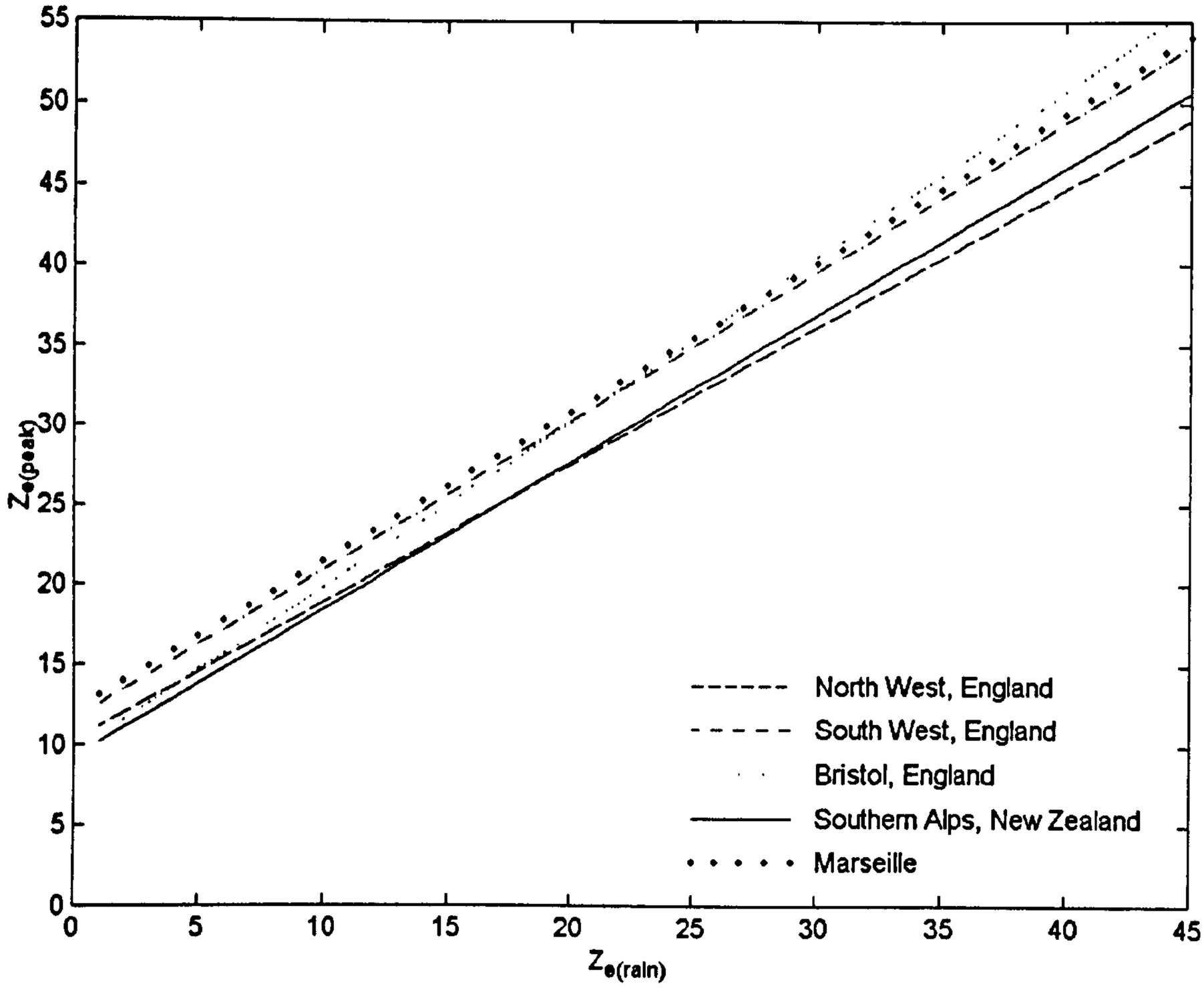

Fig. 5.44: Regression lines of the maximum reflectivities within the bright band ($Z_{e(peak)}$) against the reflectivities at the bright band bottom ($Z_{e(rain)}$) at X-band frequencies for all the sites.

On the other hand, the regression lines between the variation of $Z_{e(snow)}$ and $Z_{e(rain)}$ for all the sites are shown in Fig. 5.45. It is interesting to note that the regression lines from the North West, the South West and Marseille databases follow similar trends, but they are slightly different in the Southern Alps and Bristol databases. In Bristol, the bias may be explained by the lack of data with greater rain reflectivities (See Fig. 5.28a). The rain reflectivities prevailing on the regression line are those less than 20 dBZ (See Fig. 5.30). Therefore, a wider distribution of rain reflectivities in the Bristol database will produce a change in slope of the regression line shown in Fig. 5.45. On the other hand, the regression line in the Southern Alps database presents the highest correlation. The slope of the regression line is 0.81 with an offset of -0.21 dBZ. The difference between this regression line and the rest of the regression lines is more remarkable at low rain reflectivities ($Z_{e(rain)} < 20$ dBZ). There is always more uncertainty to locate the bright band top than the bright band bottom because the former is not as well defined than the latter. Fabry and Zawadzki (1995) found that reflectivities at the bright band top are approximately the same as the reflectivities at the bright band bottom. The differences with the results of Fabry and Zawadzki may be attributable in part to the algorithms to

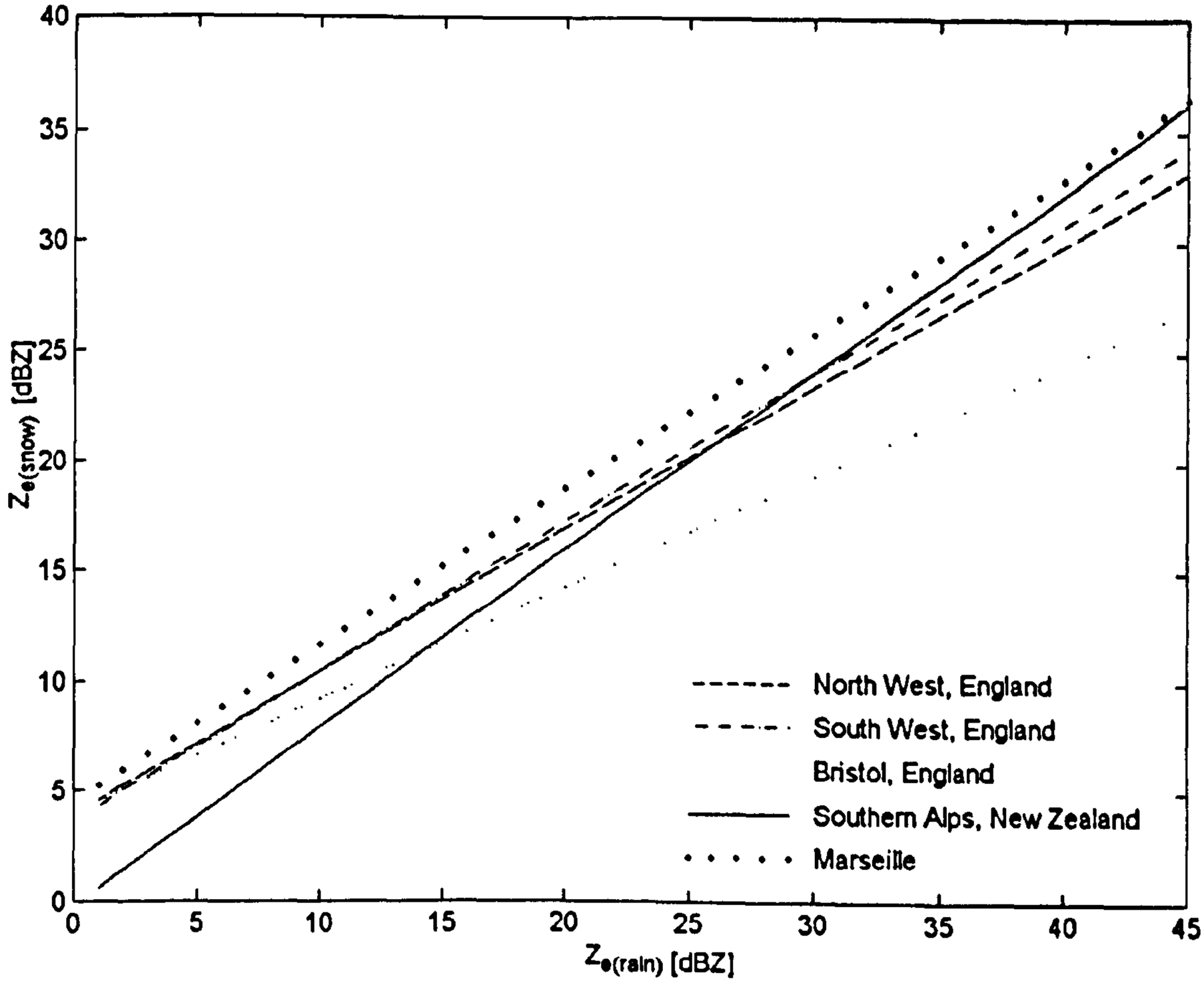

Fig. 5.45: Regression lines of reflectivities at the bright band top ($Z_{e(snow)}$) against the reflectivities at the bright band bottom ($Z_{e(rain)}$) at X-band frequencies for all the sites.

detect the bright band boundaries.

The results presented in this chapter are only valid at X-band frequencies and questions arise as to the validity of the equations presented in Table 5.5 at C-band or S-band frequencies. The reflectivity values presented in this analysis have been obtained making use of the Rayleigh approximation, valid only for small particles compared to the wavelength, but large aggregates are found in the melting layer (Barthazy et al., 1998) and the use of the Rayleigh approximation in the measurement of reflectivity may be no longer valid. Additionally, the effect of attenuation in rain at X-band frequencies is dependent on the rainfall rate (Battan, 1973), but in the melting layer the scattering effects of the melting particles will reduce the amount of power received by particles just above the melting layer. Both effects are difficult to quantify without the support of data at non-attenuating wavelengths. Chapter 6 presents a similar analysis of the bright band at S-band frequencies.

5.10.3 Bright band thickness

The mean bright band thicknesses are shown in Table 5.6. The mean value obtained in the North West of England (424 m) is greater than the mean value obtained in the South West (395 m) even when the mean height of the bright band top was higher in the latter. In Marseille, thick bright bands have been observed, correlating well with the mean height of the bright band top. However, in the Southern Alps of New Zealand, the mean bright band thickness is 459 m, slightly smaller than in Marseille, but with the difference that in the latter, the distribution of the height of the bright band top is centred at higher altitudes than the distribution experienced in New Zealand (See Figs. 5.3 and 5.10).

Table 5.7 presents the equations relating the thickness of the bright band and the rain reflectivity. The equation relating the bright band thickness to the reflectivity in the North West is not presented because of the large amount of scatter from the mean value (See Fig. 5.39a). On the other hand, the equations modelling the bright band thickness in the Southern Alps, the South West and Marseille present similar characteristics.

Klaassen (1988) found a relationship between the bright band thickness and the rain reflectivity given by:

$$T_{BB} = 100 Z_{e(rain)}^{0.17}; \qquad \text{m} \tag{5.13}$$

with a scatter of 100 m and for rain reflectivities between 20 dBZ and 45 dBZ. The equations presented in Table 5.7 result in thicker bright bands compared to the one proposed by Klaassen (1988). Fabry and Zawadzki (1995) found slightly thinner bright bands in Canada for rain reflectivities between 0 dBZ and 40 dBZ than the equations presented in Table 5.7. Gray et al. (2001) found thicknesses of 150 m at 10 dBZ and increasing to around 250 m at 25 dBZ, which are more similar to Eq. 5.13. Some of the differences between the bright band thicknesses observed by all these researchers may be attributable

Site	BB thickness	
	μ (m)	σ (m)
North West, England	424	146
South West, England	395	130
Bristol, England	449	122
Southern Alps, New Zealand	459	137
Marseille, France	479	156

Table 5.6: Statistics of the bright band thickness at X-band frequencies.

Site	BB thickness (m)
South West, England	$T_{BB} = 215.94 Z_{e(rain)}^{0.13}$
Bristol, England	$T_{BB} = 301.83 Z_{e(rain)}^{0.12}$
Southern Alps, New Zealand	$T_{BB} = 275.85 Z_{e(rain)}^{0.08}$
Marseille, France	$T_{BB} = 245.50 Z_{e(rain)}^{0.11}$

Table 5.7: Equations relating the bright band thickness as a function of rain reflectivity at X-band frequencies. $Z_{e(rain)}$ is given in mm^6 m^{-3} and T_{BB} in m.

to the algorithms to detect the bright band boundaries as it was pointed out by Fabry and Zawadzki (1995). However, in this analysis the algorithm employed to estimate the bright band boundaries is the same and even here, different equations have been obtained relating the bright band thickness and the rain reflectivity.

The thermodynamic equation relating the rate of melting of ice particles is a balance between the latent heat release due to melting and the rate of heat transfered through the layer of water on the ice particle (Cotton and Anthes, 1989). Therefore, the melting rate is extremely dependent on the initial density of the snowflakes, the vertical temperature profile ($T(h)$) and the lapse rate (dT/dh). Any change in the temperature profile will increase or decrease the thickness of the bright band to some degree even if the initial density of the snowflakes remains constant. In the bright band model presented by Hardaker (1993), the thickness of the bright band is strongly dependent on the lapse rate and the relative humidity. Both parameters have a large effect on the speed of melting. Higher values of relative humidity speed up the melting process because the latent heat of condensation is released as water condenses onto the particle (Hardaker, 1993). The scatter in the parameterisation of the bright band thickness is real and even when there is a general trend of increasing the bright band thickness with the rain reflectivity, there is not a single solution to relate both variables. These are some of the factors causing most of the scatter in the depth of the bright band.

5.11 Conclusions

The bright band detection algorithm developed in Chapter 4 has been applied to the long-term database of X-band vertical reflectivity profiles collected since the building and commissioning of the original VPR at Salford University in 1991. In the UK, the sites have been classified into two regions: the North West and the South West of England. In the latter the Bristol database has been analysed independently. Additionally, vertical

reflectivity profiles from experiments carried out in the Southern Alps in New Zealand and Marseille in France have been also analysed (See Table 5.1).

In the North West of UK, it has been found that 54.16% of the precipitation time contains the bright band signature (650.70 hr), whereas in the South West and Bristol 47.38% (168.21 hr) and 63.62% (62.45 hr) of the time respectively. In Marseille, the VPR was deployed for three months and the bright band was detected only 32.87% (21.67 hr) of the time. This is perhaps to be expected of a Mediterranean catchment subjected to Autumn thunderstorm activity, but the real surprise is that even in a highly convective situation that 32% of the precipitation time was classified as containing bright band. Despite the fact that the VPR was deployed for only one month in the Southern Alps, the bright band signature was present 35.80% (41.32 hr) of the time, more frequent than in Marseille.

In the North West of England, the height of the bright band top during Winter is as low as 500 m, being very critical in the estimation of precipitation using scanning weather radars. During Spring and Autumn, it has been found that the distribution of the height of the bright band top presents two maxima, one of them centred at lower altitudes and the other one at higher altitudes (See Fig. 5.34b and 5.34d). It has been suggested that this bimodal distribution is due to the fact that Spring and Autumn are transitional seasons between the Summer and Winter, which explains the changes in temperature influencing the height of the bright band top. A similar bimodal distribution has been obtained in the South West database during the Spring and Autumn months (See Figs. 5.18a and 5.18c). This is quite important in the estimation of precipitation using scanning weather radars because not only in Winter is the height of the bright band critical but also to some extent during Spring and Autumn. To some extent this fact also compromises existing bright band correction algorithms. In Summer, the height of the bright band does not represent a real threat in the estimation of precipitation using radars, being on average above 2000 m.

The reflectivities at the top, peak and bottom of the bright band have been analysed. The results from all the sites show that there is in general a strong relationship between the maximum reflectivity in the bright band with the reflectivity at the bright band bottom, that is: $Z_{e(peak)}$ vs $Z_{e(rain)}$. On average, the maximal reflectivity observed at X-band frequencies is 10.57 dBZ above the rain reflectivity and decreasing slightly as the rain reflectivity increases at a rate of 0.93 (From Eq. 5.12).

There is an increase in the bright band thickness as the rain reflectivity increases, but there is a lot of scatter from the mean thickness. It is strongly suggested that this

scatter is real and due to the variation in the vertical temperature profile, which may increase or decrease the bright band thickness. To some extent, some relationships between the bright band thickness and the rain reflectivity have been found (See Table 5.7), but in the development of a bright band correction algorithm for scanning weather radar measurements, it is likely that a parameterisation of the bright band thickness will lead to further errors. A proper parameterisation of the bright band thickness must include the vertical temperature profile in order to estimate accurately its dependence on the rain reflectivity.

It has been found that there is a relationship between the thickness of the bright band and the height of the bright band top (See Figs. 5.25 and 5.40). The thickness of the bright band increases as the height of the bright band top increases. This suggests that during Summer the bright bands are thicker than during Winter.

Chapter 6

Long-term bright band analysis at S-band frequencies

6.1 Introduction

Weather radar rainfall measurements at S-band frequencies are less affected by attenuation effects. Attenuation of microwaves occurs as a result of both, absorption of energy by the medium and scattering of energy out of the radar beam (Battan, 1973). In the absence of precipitation, the attenuation of radar energy is due to the presence of oxygen and water vapour (Battan, 1973; Skolnik, 1980). In this case, the gases act as absorbers and this type of attenuation is negligible at frequencies lower than 10 GHz. Attenuation of radar signals by hydrometeors is the result from both, absorption and scattering. Ryde (1946) showed that attenuation by raindrops is a function of both, the radar wavelength and the rainfall rate. At S-band frequencies (3 GHz), this dependency is almost negligible and becomes independent of the rainfall rate.

On the other hand, in the measurement of reflectivity at S-band frequencies, all the hydrometeors act as Rayleigh scatterers and are small particles when compared to the wavelength and therefore their backscattering cross sections are proportional to the sixth power of their diameters. They therefore reflect more energy as backscatter as the diameter of the particle increases.

This chapter presents the analysis of the reflectivity in the melting layer at S-band frequencies. The study of the bright band at S-band frequencies minimizes to some extent the uncertainties experienced at X-band frequencies, which are due to both, the attenuation effects and the use of the Rayleigh approximation for the measurement of reflectivity within the melting layer. In addition, the polarimetric measurements in the melting layer

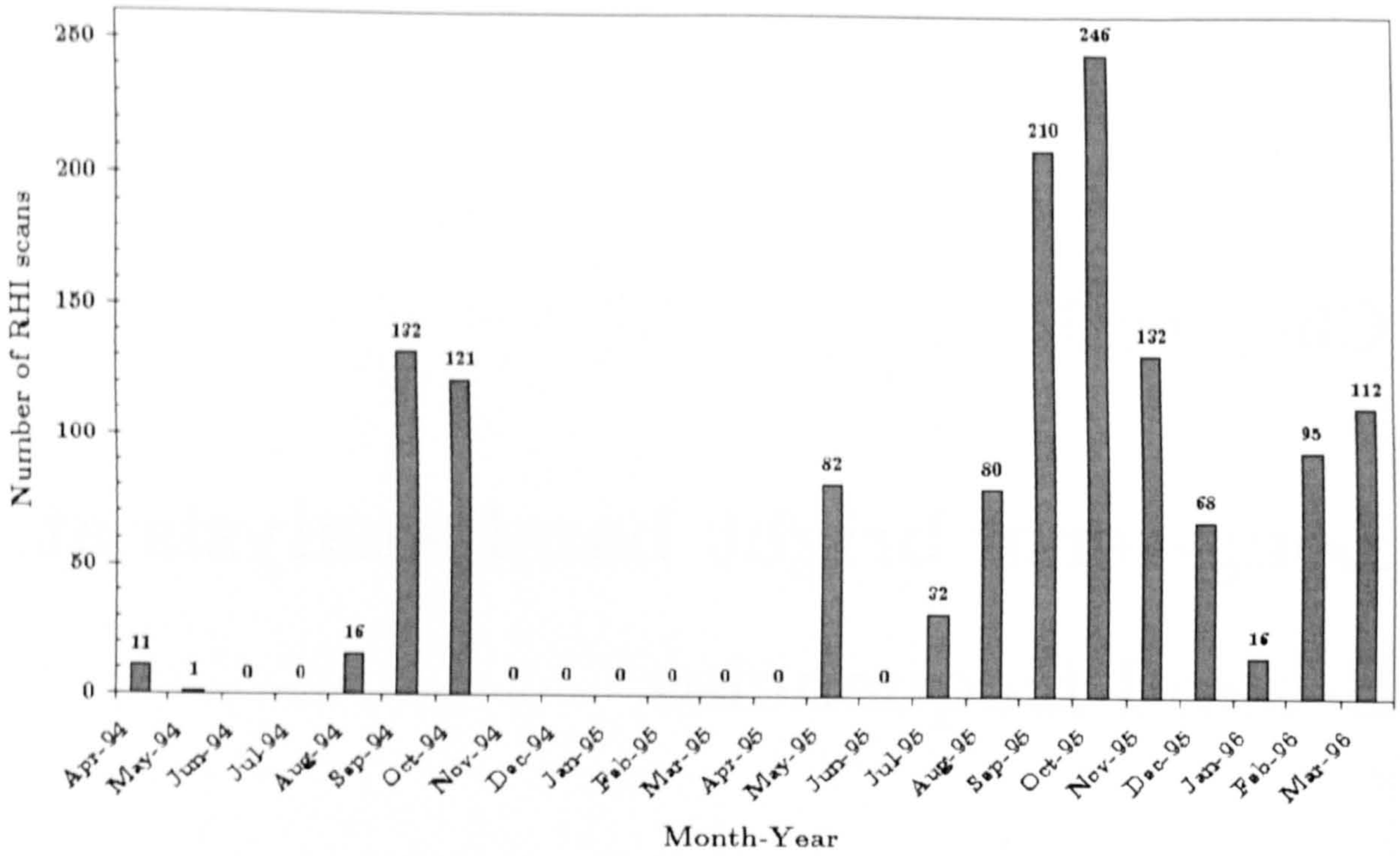

Fig. 6.1: Distribution of the RHI scans during HYREX.

are also evaluated.

6.2 Data processing

The S-band reflectivity data have been obtained from the Chilbolton radar[1] during the HYdrological Radar EXperiment (HYREX) (See Section 5.2.1). During HYREX, the Chilbolton radar operated almost continuously from February 1994 to May 1996. The Chilbolton data set comprises Range Height Indicator (RHI) and Plan Position Indicator (PPI) scans. The PPI scans are centred on the Brue catchment (West of Chilbolton) covering around 100° azimuthally. The RHI scans are from 0° to either 25° or 30° in elevation in the direction of the Brue catchment. Two X-band Vertically Pointing weather Radars (VPR) were deployed in three different sites to the West of Chilbolton, recording the precipitation passing overhead. The radar sites are shown in Fig. 5.2.

The RHI scans comprise a set of 1354 scans, most of them being recorded during 1995. The distribution of the RHI scans during the whole experiment is depicted in Fig. 6.1. It is evident that during September and October a great number of RHI scans were recorded (covering part of the Summer and Autumn respectively) whereas during June no scans were recorded (covering part of Spring). The RHI scans have been transformed to rectangular coordinates assuming standard refraction and following the beam propagation equations

[1]The overall characteristics of Chilbolton radar are given in Goddard et al. (1994).

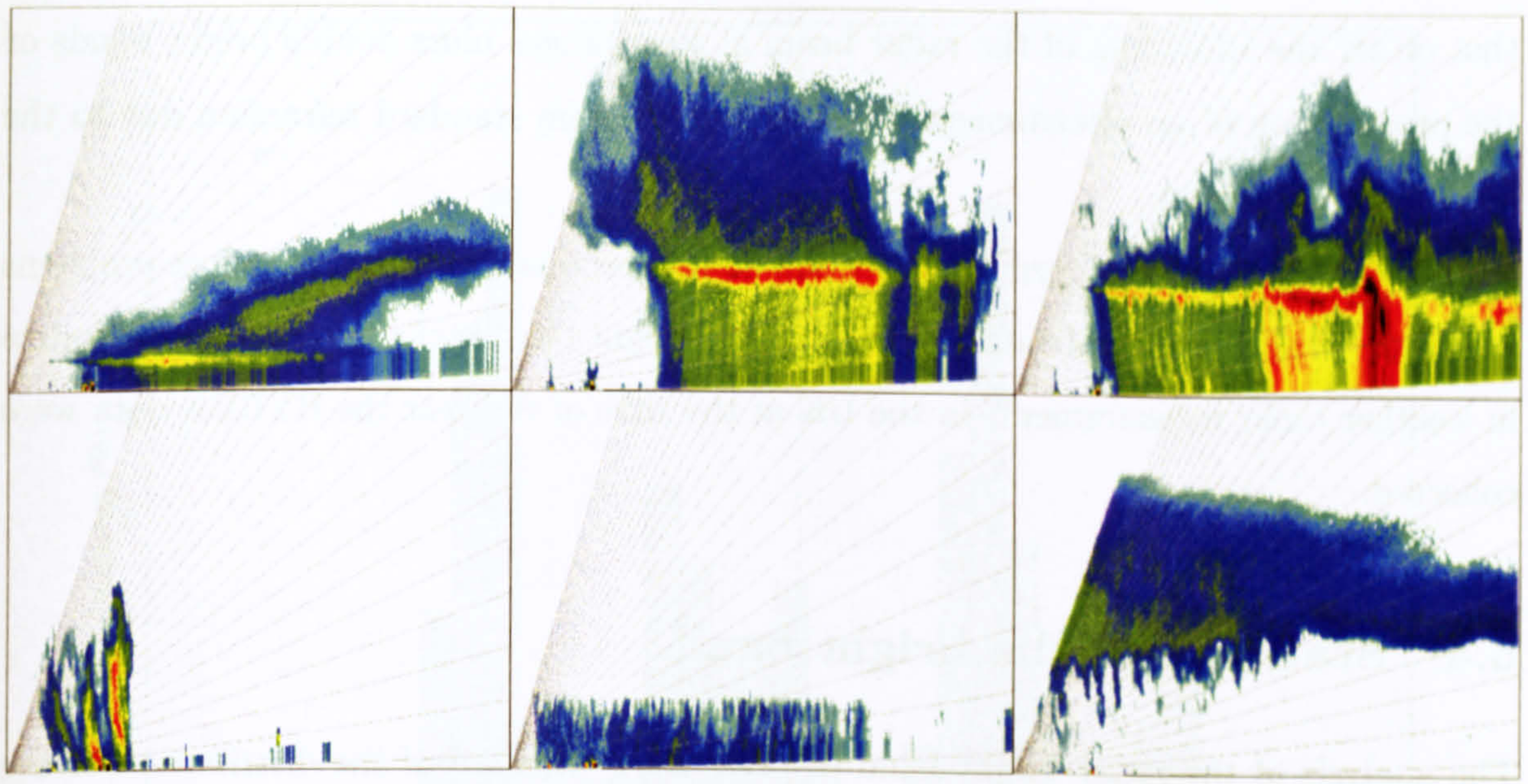

Fig. 6.2: Classification of precipitation events as observed by the Chilbolton radar during HYREX. a) Stratiform rainfall with snow trails; b) Stratiform rainfall c) Convection embedded in stratiform rainfall; c) Showers; d) Low level rainfall; e) Low level evaporation (The RHI scans are from 0 to 95 km in range and from 0 to 10 km in height).

given in Section 2.4 (Eqs. 2.3 and 2.6).

An RHI scan in rectangular coordinates is composed of Vertical Reflectivity Profiles (VRP) at different distances from the radar. Only those profiles closer to the radar site (within 30 km in range) have been extracted to avoid the spreading of the radar beam with range. The bright band detection algorithm developed in Chapter 4 has been applied to the whole set of VRP. The reflectivities above, within and below the bright band are analysed in the following sections.

6.3 RHI classification

The different sorts of precipitation events recorded in the RHI scans are summarised in Fig. 6.2. Stratiform rainfall is a dominant signature in most of the events presenting a well defined bright band. This type of signature has been found in 83.08% of the RHI scans. Convective precipitation has been found only in 6.64% of the RHI scans with high values of reflectivity along the vertical. Most of the convective cells in the RHI scans are embedded in stratiform rainfall. Showers are in 6.42% of the RHI scans. A typical signature of precipitation without bright band classified as low level rainfall by Fabry and Zawadzki (1995) has been found only in 0.88% of the RHI scans. Precipitation echoes with evaporation below the radar beam have been found in 0.81% of the RHI scans. Only one double bright band event has been found very close to the radar because it is very likely

that either the spreading of the radar beam at long ranges blurs double bright bands or the propagation of an electromagnetic wave departs from standard refraction due to the temperature inversion.

It is evident that stratiform precipitation dominates this set of data, therefore problems associated with the radar beam intercepting the bright band is the dominant error source in weather radar measurements in the UK at the time of the year the HYREX data were collected.

6.4 Statistics of the bright band

The analysis of the radar bright band involves the estimation of the distribution of the height of the bright band top, the scatter plots among the reflectivities above, within and below the bright band and the scatter plot between the bright band thickness and its dependency on rainfall intensity. The results are compared to the long-term bright band analysis at X-band frequencies carried out in Section 5.6 over the South West region.

The main source of discrepancies between the X-band and S-band bright band analysis is attributable to the attenuation effects and the use of the Rayleigh approximation for the estimation of reflectivity within the bright band. However, additional discrepancies may be attributable to the fact that the VPR data are point measurements whereas the RHI scans are measurements along the range. In RHI scans, only VRP no further than 30 km in range have been analysed to minimize the spreading of the radar beam with range. An additional source of discrepancy could be the fact that the S-band database covers a longer period compared to the X-band measurements.

6.4.1 Height of the bright band top

The distribution of the height of the bright band top is depicted in Fig. 6.3. The heights of the bright band tops present a very broad distribution with heights ranging from 800 m to 3900 m. The mean height of the bright band top is centred at 2124 m with a standard deviation of 782 m. However, in the X-band analysis, the mean height of the bright band top is slightly lower at 1839 m with 721 m of standard deviation.

The seasonal analysis of the distributions of the height of the bright band top is presented in Fig. 6.4. During Winter, the mean height of the bright band top is 1236 m with 303 m of standard deviation. These results are biased by the lack of data during January and the large amount of data during March. The distribution also presents some data above 2000 m of relative low frequency compared with the ones at lower altitudes.

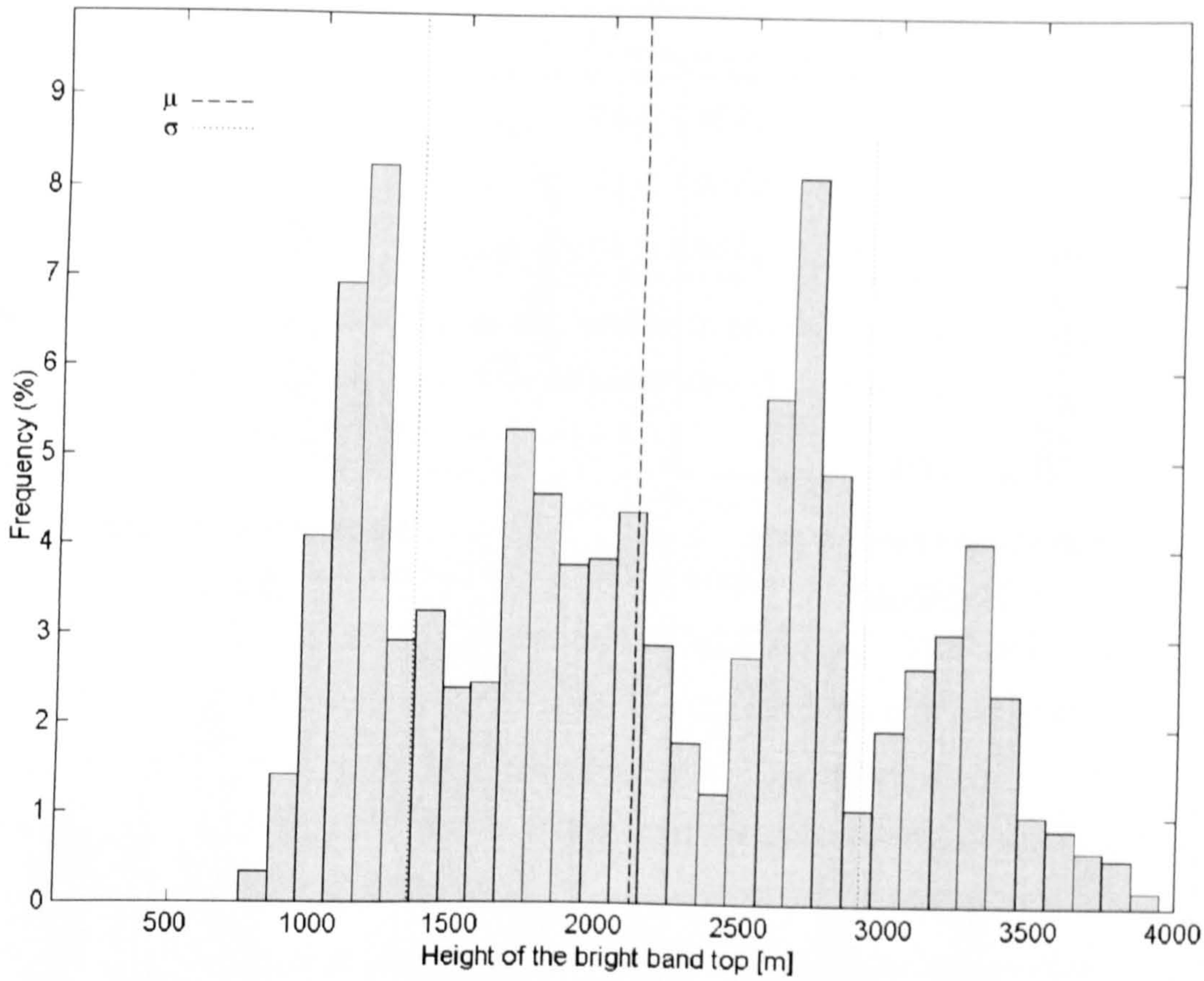

Fig. 6.3: Relative frequency of the height of the bright band top over the South West of England from March 1994 to February 1996 (100 m steps).

During Spring, the bias of the distribution is greater, because the database covers only the month of May with a small amount of data during April and no data during June. The mean height of the bright band top is 1320 m with a standard deviation of 266 m. During Summer, the distribution presents three well defined maxima above 1500 m. The mean height of the bright band top is 2611 m with more spread in the standard deviation (σ = 625 m). The maxima at 2700 m and 3400 m shown in Fig. 6.4c also appears in the X-band bright band analysis over the South West (See Fig. 5.18b). However, the maximum at 1700 m does not exist in the X-band results because the S-band data set contains RHI scans from the Summer of 1994 and 1995. During Autumn, there are three well defined maxima, which are also present in the X-band analysis. They are at 2000 m, 2600 m and 3200 m, with a mean of 2438 m and 532 m of standard deviation.

The seasonal analysis of the height of bright band top marks the temperature regimes prevailing during those days and clearly shows the variation of the height of the bright band during a relatively short period of time. Not only during Winter the bright band is at lower altitudes, but also during Spring and Autumn although to a lesser degree.

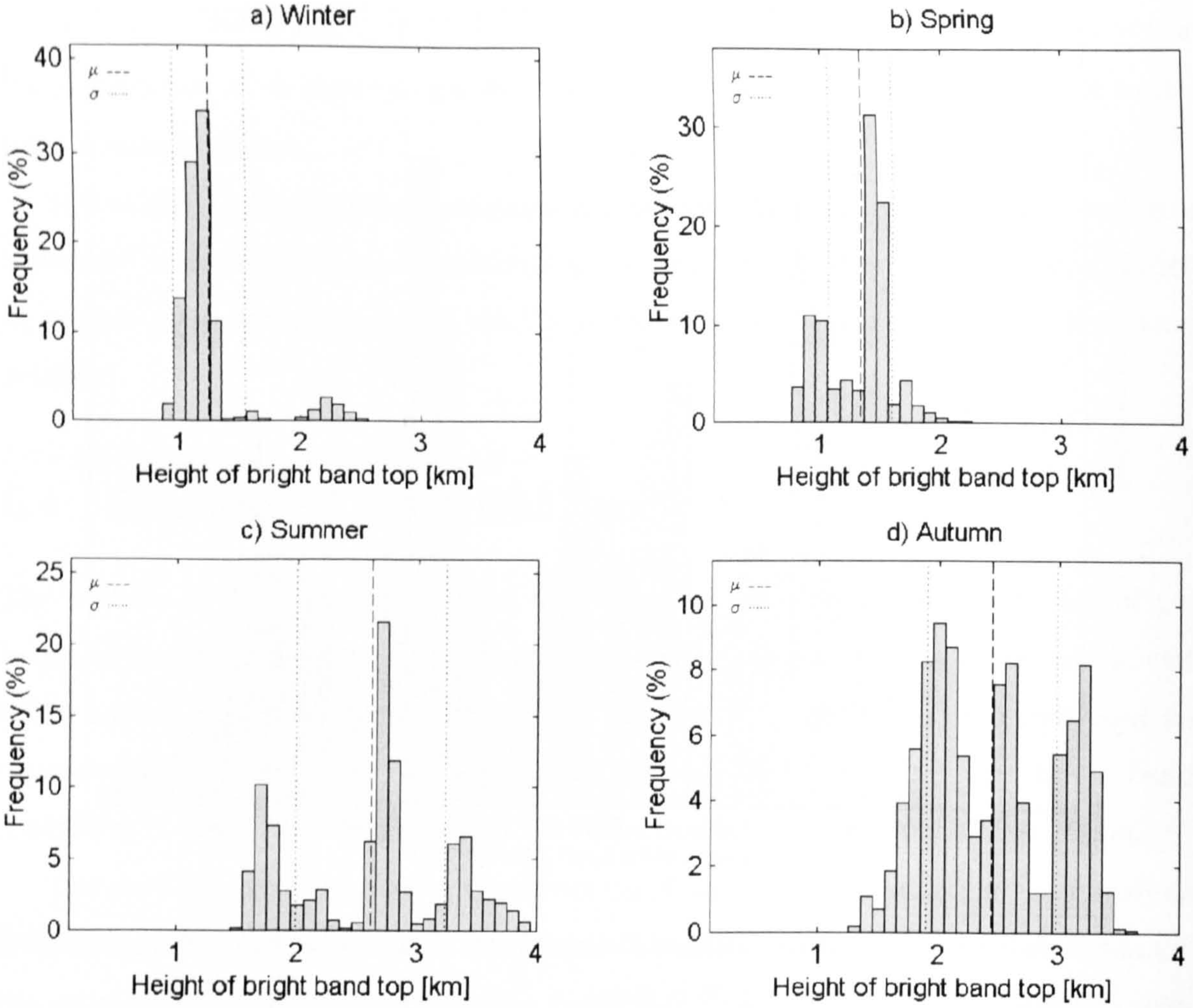

Fig. 6.4: Seasonal distributions of the height of the bright band top over the South West of England from April 1995 to November 1995 (100 m steps).

6.4.2 Reflectivities in the bright band

The scatter plot showing the relationship between the reflectivities $Z_{e(peak)}$ and $Z_{e(snow)}$ is depicted in Fig. 6.5. The regression line of the scattered data is given by:

$$Z_{e(peak)} = 9.72 + 1.09 Z_{e(snow)}; \qquad \text{dBZ} \tag{6.1}$$

Eq. 6.1 indicates that the increase in reflectivity from the top to the peak of the bright band is 9.72 dBZ and increases linearly by a factor of 1.09 with $Z_{e(snow)}$. However, in order to compare the amount of increase in the bright band, it is more convenient to obtain the scatter plot between the reflectivities $Z_{e(peak)}$ and $Z_{e(rain)}$ (See Fig. 6.6). This scatter plot does not exhibit the bending on $Z_{e(rain)} \approx 20$ dBZ obtained in the X-band bright band analysis over the South West of England. On the contrary, the scattered data follow a well defined regression line given by:

$$Z_{e(peak)} = 8.34 + 1.05 Z_{e(rain)}; \qquad \text{dBZ} \tag{6.2}$$

Range	$Z_{e(peak)}$ vs $Z_{e(rain)}$	r	σ
00 - 30 km	$Z_{e(peak)} = 8.34 + 1.05 Z_{e(rain)}$	0.93	2.70
30 - 60 km	$Z_{e(peak)} = 7.14 + 1.06 Z_{e(rain)}$	0.94	2.68
60 - 90 km	$Z_{e(peak)} = 6.04 + 1.06 Z_{e(rain)}$	0.94	2.54

Table 6.1: Regression equations relating the increase in reflectivity from the bottom to the peak of the bright band at different ranges from the radar site. (The reflectivities are in dBZ units and the beamwidth of the radar is 0.25 °).

Therefore, the increase in reflectivity from the bottom to the peak of the bright band is 8.34 dBZ and increases linearly by a factor of 1.05 with $Z_{e(rain)}$. The correlation of Eq. 6.2 is 0.93 with a standard deviation of 2.70 dBZ. Eq. 6.2 has been obtained from the analysis of VRP within 30 km in range from the radar site. The results from a similar analysis between $Z_{e(peak)}$ vs $Z_{e(rain)}$ at different ranges from the radar are summarised in Table 6.1. It is interesting to note that as the range increases by 30 km, the increase in reflectivity in the bright band decreases in average approximately 1.1 dBZ. The slopes of the regression equations remain constant in approximately 1.05. This decrease in bright band intensity is because of the spreading of the radar beam with range. However, the results presented in Table 6.1 are strongly dependent on the beamwidth of the radar and a fatter beamwidth will produce more spreading, reducing even more the increase in reflectivity in the bright band. Therefore, the effect of beam spreading in scanning weather radar measurements is an important factor to take into account in any correction algorithm for the bright band effect (See Chapter 7).

The scatter plot showing the relationship between $Z_{e(snow)}$ and $Z_{e(rain)}$ is depicted in Fig. 6.7. The regression line of the scatter data has a correlation of 0.88 with a standard deviation of 3.06 dBZ and it is given by:

$$Z_{e(snow)} = 1.05 + 0.85 Z_{e(rain)}; \qquad \text{dBZ} \tag{6.3}$$

Eq. 6.3 presents more scatter than Eq. 6.2 because the height of the bright band top is always more difficult to locate than the height of the bottom. The reason for this is because sometimes the snow trails above the bright band blur the precise location of the height of the bright band top. Eq. 6.3 indicates that the reflectivities at the height of the bright band top are always smaller than reflectivities at the height of the bright band bottom, except for rain reflectivities below 7 dBZ.

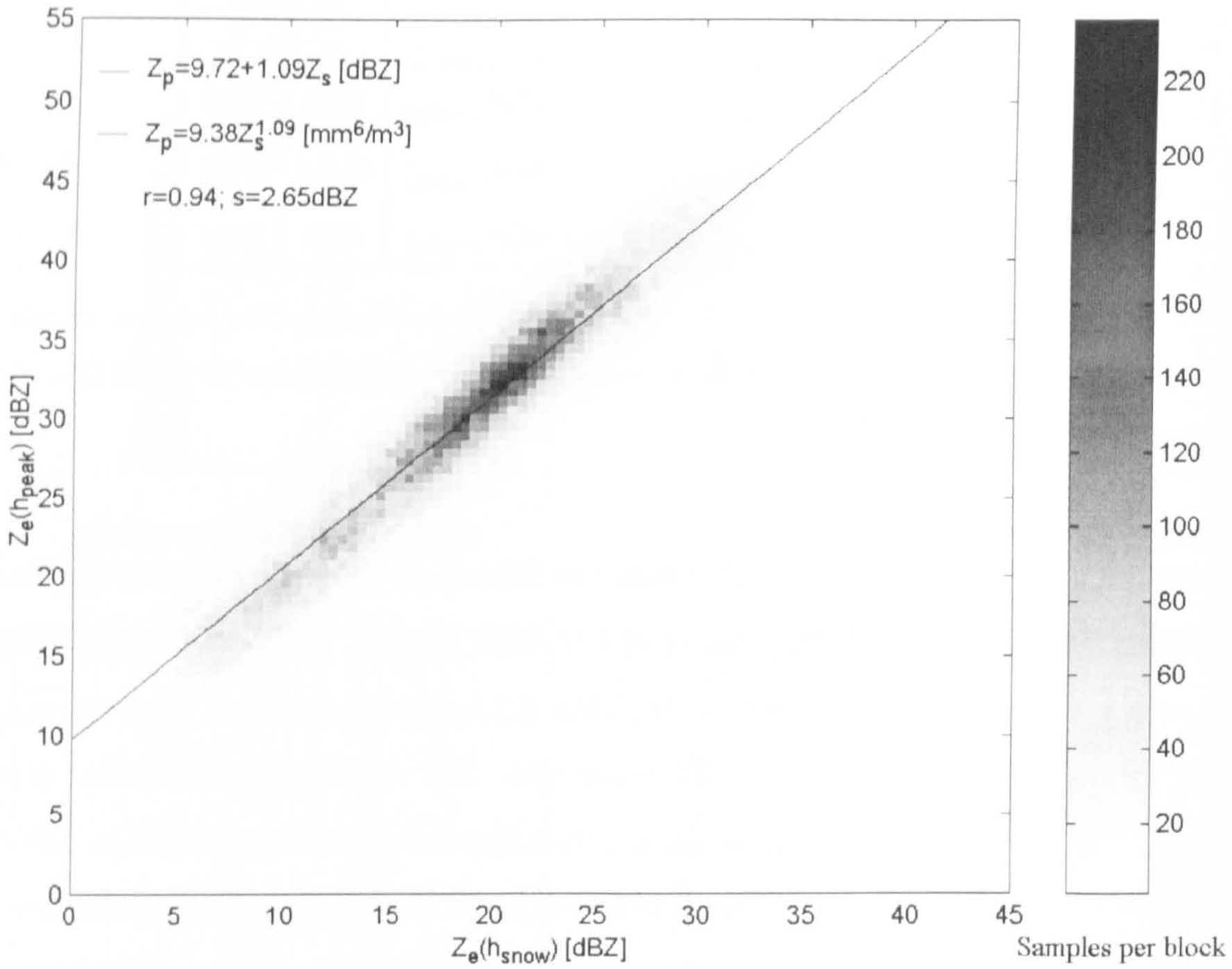

Fig. 6.5: Scatter plot of the maximal reflectivities within the bright band against the reflectivities at the bright band top at S-band frequencies over the South West of England.

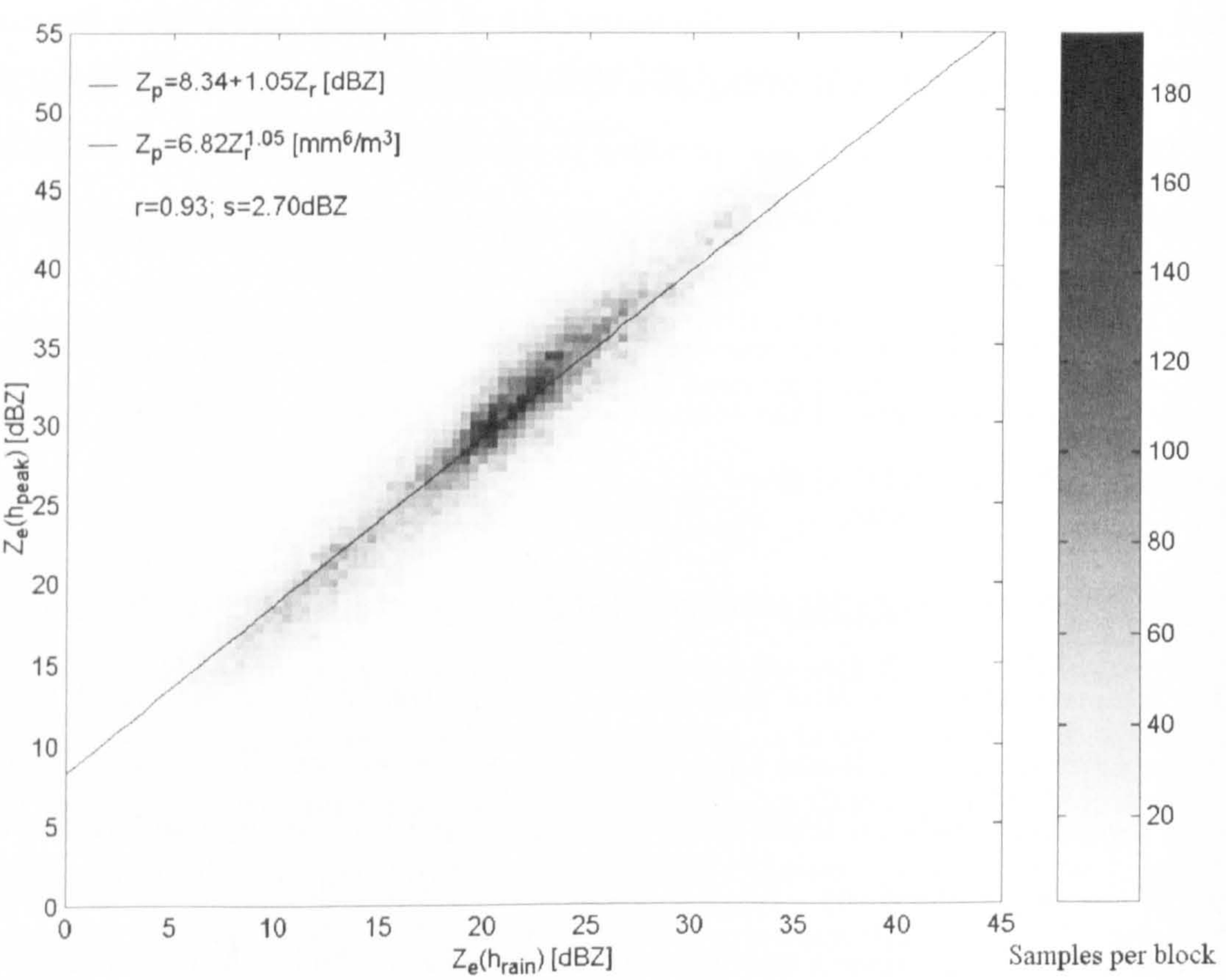

Fig. 6.6: Scatter plot of the maximal reflectivities within the bright band against the reflectivities at the bright band bottom at S-band frequencies over the South West of England.

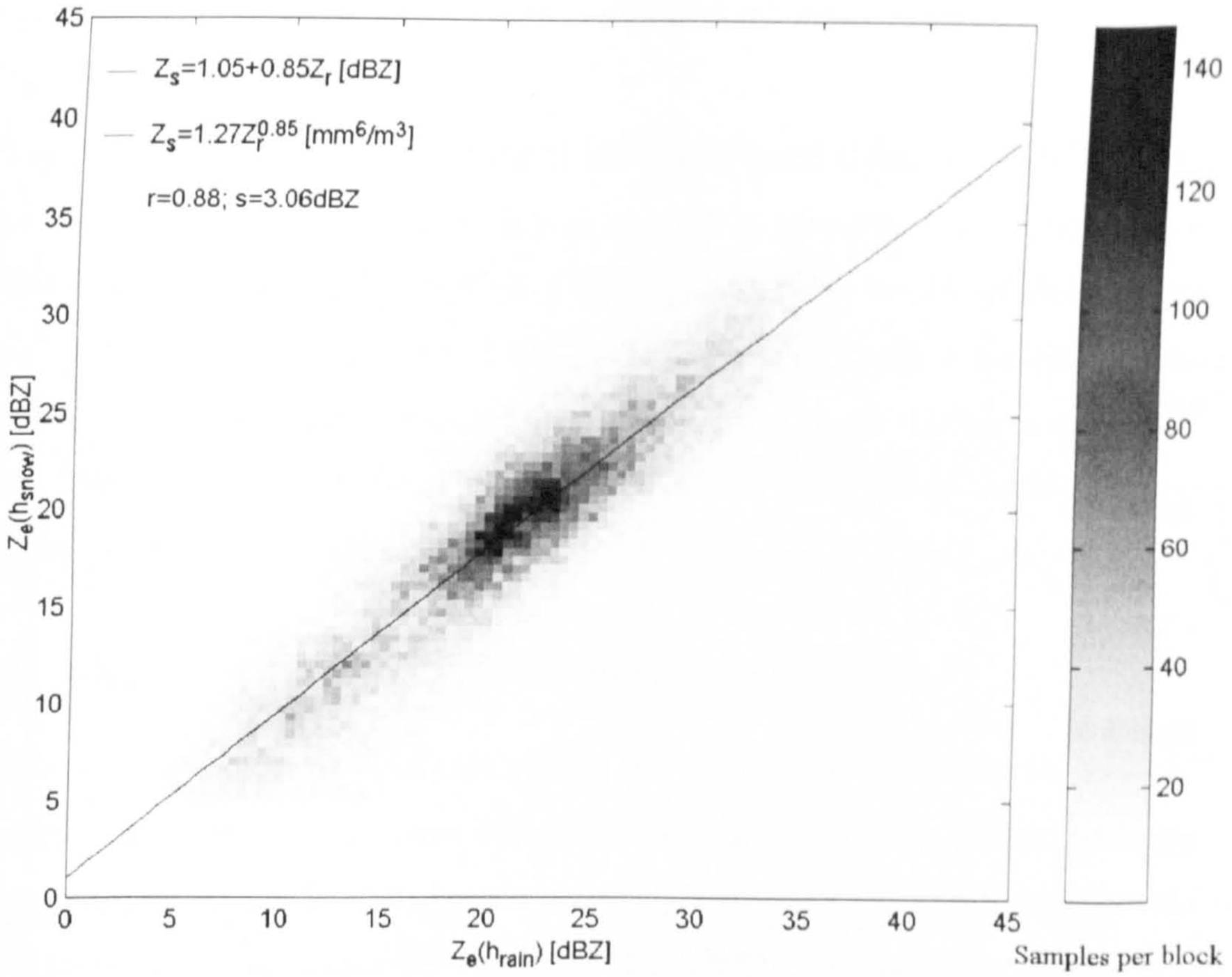

Fig. 6.7: Scatter plot of the reflectivities at the bright band top against the reflectivities at the bright band bottom at S-band frequencies over the South West of England.

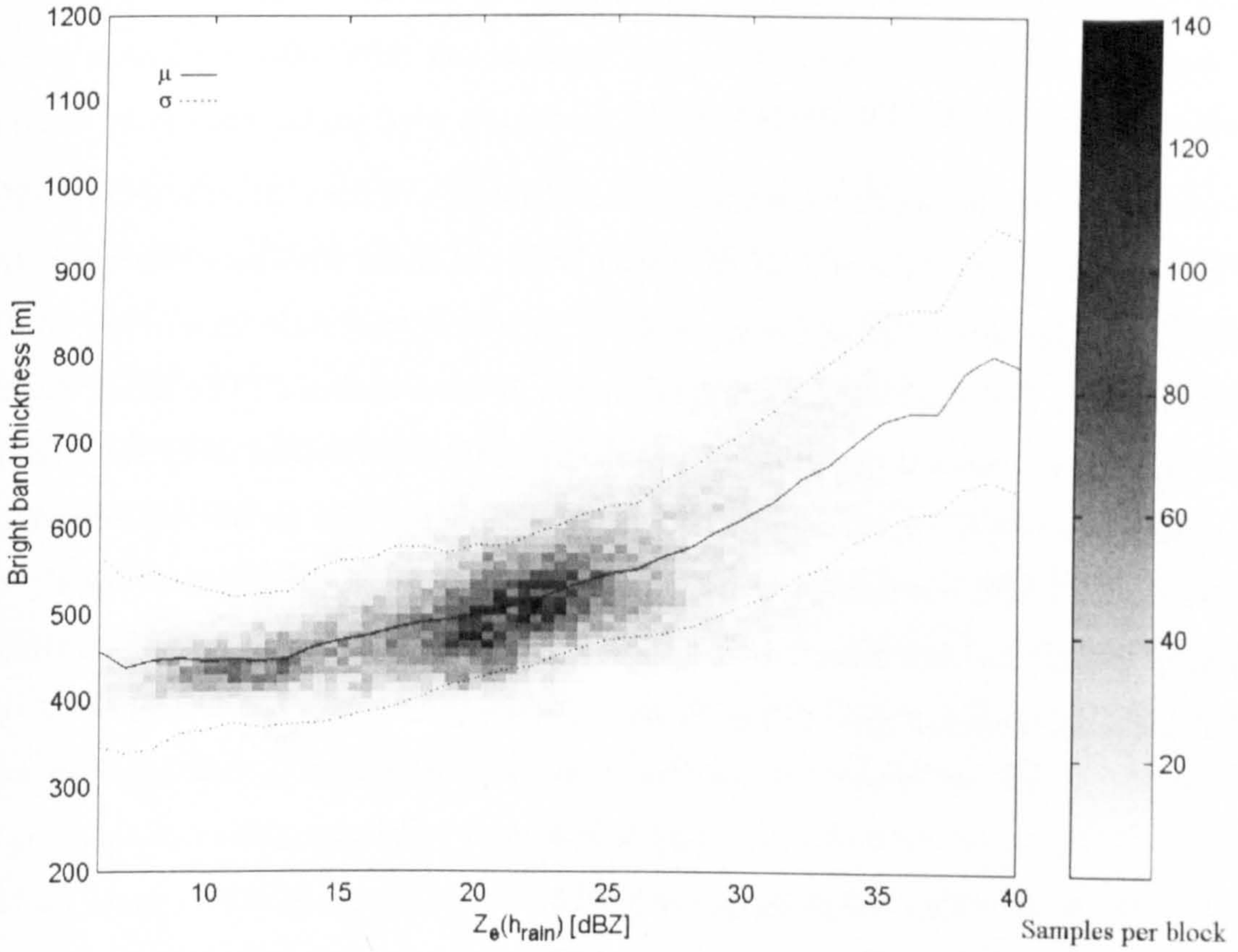

Fig. 6.8: Scatter plot between the bright band thickness and the rain reflectivity at S-band frequencies over the South West of England.

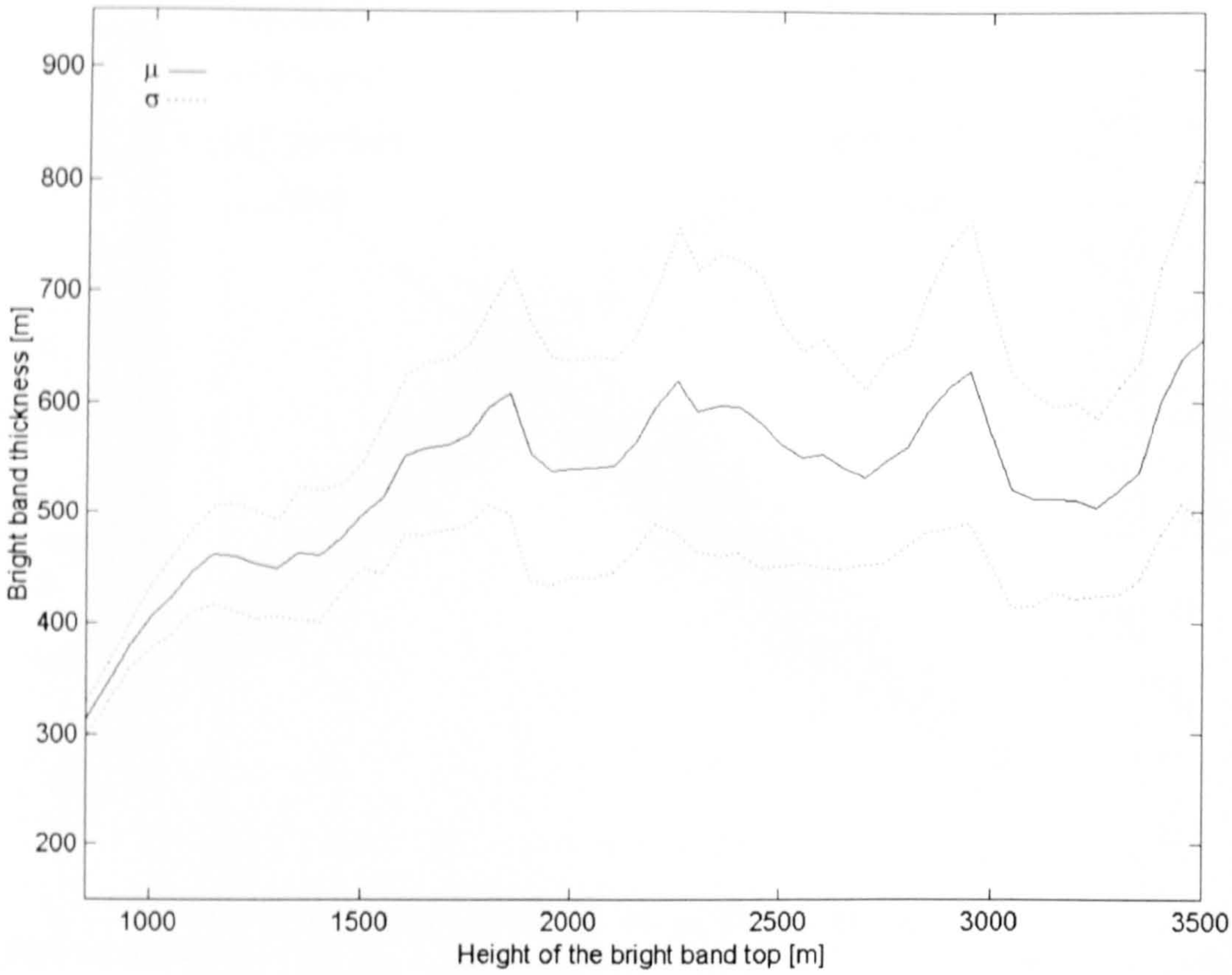

Fig. 6.9: Dependence of the bright band thickness with the height of the bright band top over the South West of England.

6.4.3 Thickness of the bright band

The scatter plot of the bright band thickness as a function of the rain reflectivity is shown in Fig. 6.8. Although there is a lot of scatter from the mean thickness, there is a trend of increasing the bright band thickness when increasing the rain reflectivity, which is congruent with the observations obtained in the X-band analysis. The mean thickness is 529 m with a standard deviation of 109 m. For rain reflectivities lower than 13 dBZ, the mean thickness is approximately constant and equal to 450 m; for rain reflectivities greater than 13 dBZ but smaller than 28 dBZ the mean thickness increases linearly from 450 m to 580 m; for rain reflectivities greater than 28 dBZ but smaller than 40 dBZ the mean thickness increases from 580 m to 800 m. That is:

$$\begin{aligned} T_{BB} &= 450; & Z_{e(rain)} &\leq 13 \\ T_{BB} &= 8.66 Z_{e(rain)} + 337.33; & 13 \leq Z_{e(rain)} &\leq 28 \\ T_{BB} &= 18.33 Z_{e(rain)} + 66.66; & 28 \leq Z_{e(rain)} &\leq 40 \end{aligned} \tag{6.4}$$

where T_{BB} is in m and $Z_{e(rain)}$ is in dBZ. In the X-band analysis of the South West region, the bright bands are thinner. This effect can be due in part to the combination of

the lower resolution of the S-band data set and to the effect of beam spreading, although the latter to a lesser degree.

There is also a certain dependency of the bright band thickness with the height of the bright band top as suggested by Fabry et al. (1994) (See Fig. 6.9). This dependency is indicative of thinner bright bands during Winter and thicker bright bands during Summer. When the height of the bright band top is below 1900 m, there is a clear increase in the thickness of the bright band, but above this height, the mean thickness seems to oscillate around 550 m. These oscillations may be indicative of the limit of the bright band depth for higher altitudes.

6.4.4 Slopes of the VRP in stratiform precipitation

Stratiform precipitation is characterized by a very specific signature in the VRP. This signature can be divided into three different zones: the reflectivity below the bright band, which corresponds to echoes from raindrops; the bright band, which corresponds to the zone of high scattering of microwaves due to the melting of snowflakes and the reflectivity above the bright band, which corresponds to echoes from snowflakes and ice particles. The VRP obtained from a VPR or constructed from an RHI scan does not always represent the true profile, because it is affected by the trails of precipitation, which are usually slanted altering the shape of the VRP. For instance, the trails of snow are formed by echoes from ice particles or snow falling with a constant speed from the snow-generating cells leaving a trail in their descent (Battan, 1973; Dennis and Hitschefeld, 1990). A similar effect is observed in rain. The shape of the trails of precipitation is controlled by the terminal velocity of the precipitation particles and the wind shear effects. Large raindrops fall faster than snowflakes (See Fig. 2.4). Thus, snowflakes are affected more by the constant wind shear leaving a remarkable trail in their descent.

To some extent it is possible to estimate the average slope above the bright band with some degree of certainty (See Fig. 6.10a). The average slope for every VRP is estimated from the top of the precipitation, once the formation of ice crystals in the generating cells begins, to the height of the bright band top. The positive slope is indicative of the growth of ice particles and it is interesting to note that in approximately 85% of the profiles, the growth occurs at a rate lower than 6 dBZ km^{-1}. If a column of saturated air with a constant lapse rate with height is to be lifted, the amount of water that would condense (becoming available to develop rain) would decrease markedly with height, because the saturation vapour pressure of air is strongly dependent on temperature (Gray, 1991). Therefore, the amount of condensation of the lifted column will decrease with height,

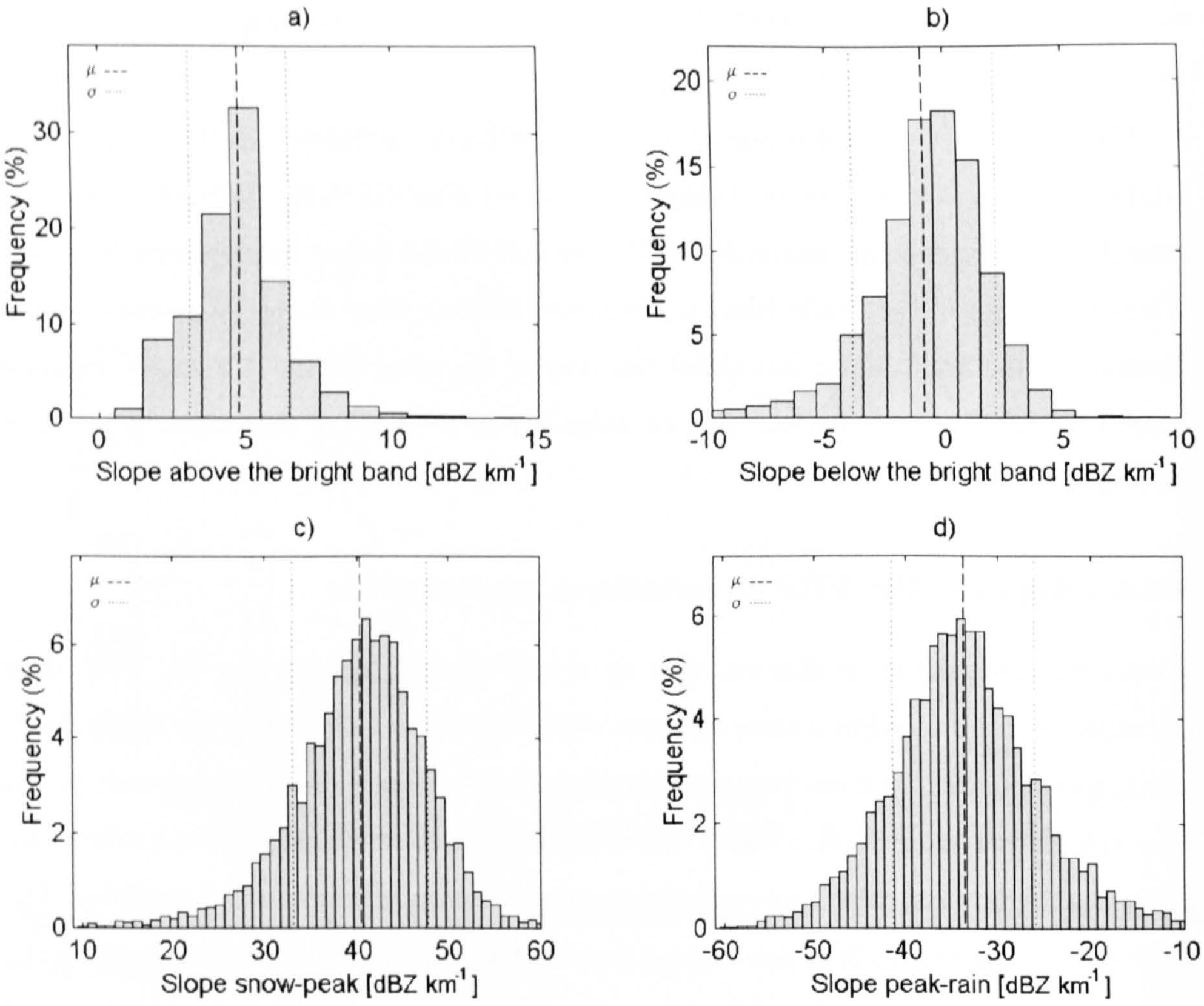

Fig. 6.10: Distributions of the average slopes of the VRP from stratiform precipitation. a) Average slope above the bright band (ice particles and snowflakes). b) Average slope below the bright band (raindrops). c) Average slope in the upper part of the bright band (melting snowflakes). d) Average slope in the lower part of the bright band (melting snowflakes and raindrops). A positive slope indicates an increase in reflectivity, whereas a negative slope a decrease in reflectivity from precipitation particles along their descent.

because the temperature in the troposphere also decreases with height. This is the main reason for the decrease in reflectivity with increasing height (or the increase in reflectivity with decreasing height). The mean growth rate is 4.75 dBZ km^{-1} with a standard deviation of 1.68 dBZ km^{-1}. Fabry and Zawadzki (1995) found that there was an increase in reflectivity of 7 dBZ km^{-1} in the last kilometre just above the melting layer of data collected above Montreal in Canada, but with little dependence on precipitation intensity. The scatter plot of the average slope above the bright band against the rain reflectivity below is shown in Fig. 6.11, revealing that there is an increase in the growth rate of snowflakes as the rain reflectivity increases. This means that the slope of the reflectivity above the bright band may be a clear indicator of bright band thickness and rainfall intensity. However, factors such as the saturation due to ice being different from water

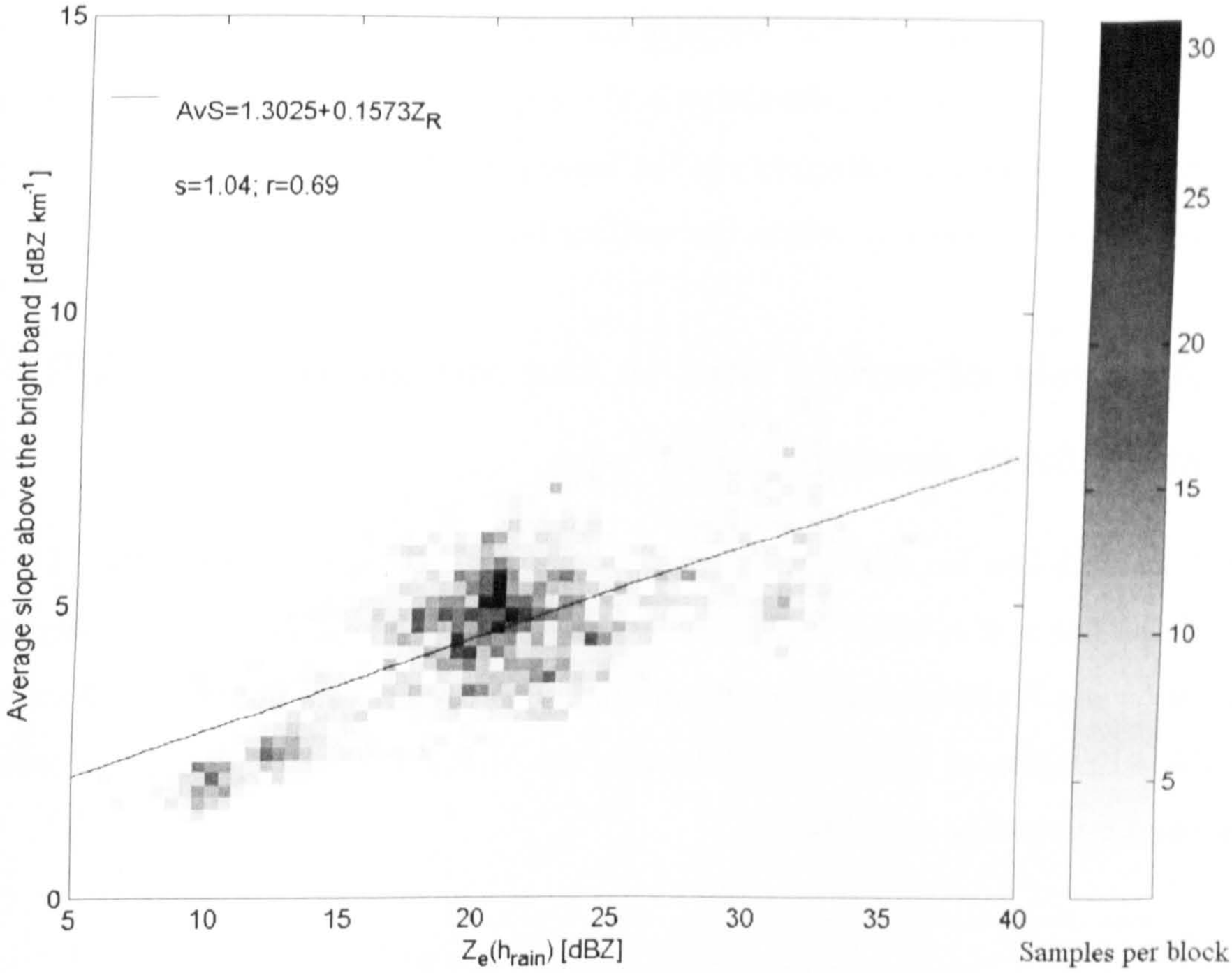

Fig. 6.11: Scatter plot of the average slope above the bright band against the rain reflectivity below in stratiform precipitation. This plot is indicative of the growing rate of ice particles at different rain intensities. Although the spread of the scattered data is high, there is certain tendency of increasing the growing rate of ice particles with the rain reflectivity.

means that the lapse rate is never constant in the bright band and the refractive index will strongly drive the reflectivity. Fig. 6.11 presents a lot of scatter and the regression line shown in the same figure has a relatively poor correlation of 0.69. The scatter may also be a consequence of the variation of the lapse rate with height.

The distribution of the average slope below the bright band is depicted in Fig. 6.10b. The distribution is approximately Gaussian with a mean of -0.91 dBZ km^{-1} and a standard deviation of 3.05 dBZ km^{-1}. The spread of the distribution is due mainly to the variation of the drop size distribution within the resolution volume being illuminated by the radar beam. In addition, the average slope below the bright band is affected by the trails of precipitation, which define zones of different precipitation intensities from one VRP to the next.

The distributions of the average slopes in the upper and the lower part of the bright band are depicted in Figs. 6.10c and 6.10d respectively. In the upper part of the bright band, the mean slope is at 40.29 dBZ km^{-1} with a standard deviation of 7.28 dBZ km^{-1}, whereas in the lower part the most frequent slope is at -33.84 dBZ km^{-1} with a standard

deviation of 7.77 dBZ km^{-1}. If the depths of the upper and lower part of the bright band were the same, the increase in reflectivity in the upper part of the bright band would be greater than the decrease in reflectivity in the lower part. The spread of both distributions is indicative of the complexity within the melting layer.

6.5 Analysis of errors due to the variation of the VRP in stratiform precipitation

Eqs. 6.2 and 6.3 can be represented, in terms of rainfall rate, following the M-P Z-R relationship, that is $Z = 200R^{1.6}$ (Marshall et al., 1955), where Z is the reflectivity factor in $mm^6\ m^{-3}$ and R the rainfall rate in mm hr^{-1}. If the radar beam intercepts the melting layer, the estimation of rainfall rate following the M-P Z-R relationship on the maximal bright band reflectivity would be:

$$R_{peak} = 3.92R_{rain}^{1.05}; \qquad \text{mm hr}^{-1} \tag{6.5}$$

and the rainfall rate just above the bright band would be:

$$R_{snow} = 0.71R_{rain}^{0.85}; \qquad \text{mm hr}^{-1} \tag{6.6}$$

The maximal overestimation of rain in the melting layer using Eq. 6.5 is depicted in Fig. 6.12. It is important to observe that the slope shown in this figure, is related to the exponent 1.05 of Eq. 6.5 (See also Eq. 6.2) and the amount of overestimation to the coefficient 3.92. A slightly change in the exponent will cause a remarkable change in slope. For instance, an exponent of 1.0 causes a constant value of overestimation for any value of rainfall rate. From Fig. 6.12, it follows that interception of the radar beam with the melting layer can cause overestimation of rain up to a factor of 3.5 at 0.1 mm hr^{-1} and up to a factor of 5 at 100 mm hr^{-1}. However, these values are also dependent on the volume of melting layer being intercepted by the radar beam and therefore the overestimation will tend to decrease with range (See Chapter 7).

On the other hand, the rainfall rate observed by the radar just above the melting layer is depicted in Fig 6.13. The trend is an underestimation of rain because of the fact that the reflectivity in snow is lower than the reflectivity in rain. The underestimation is even more severe as the radar beam reaches several kilometres above the melting layer because as explained in the previous section, the reflectivity in snow tends to decrease with height.

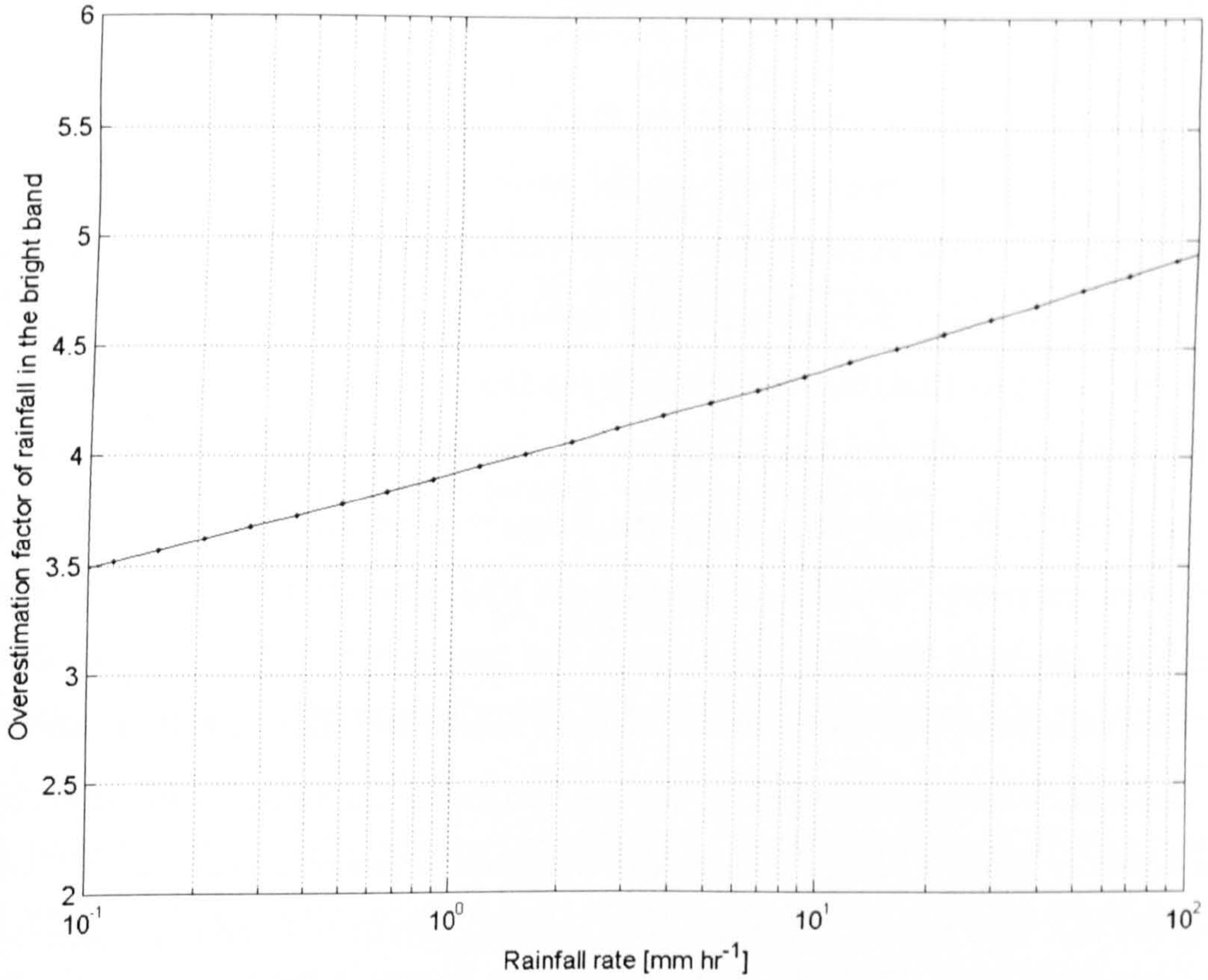

Fig. 6.12: Overestimation of rain when the radar beam intercepts the melting layer.

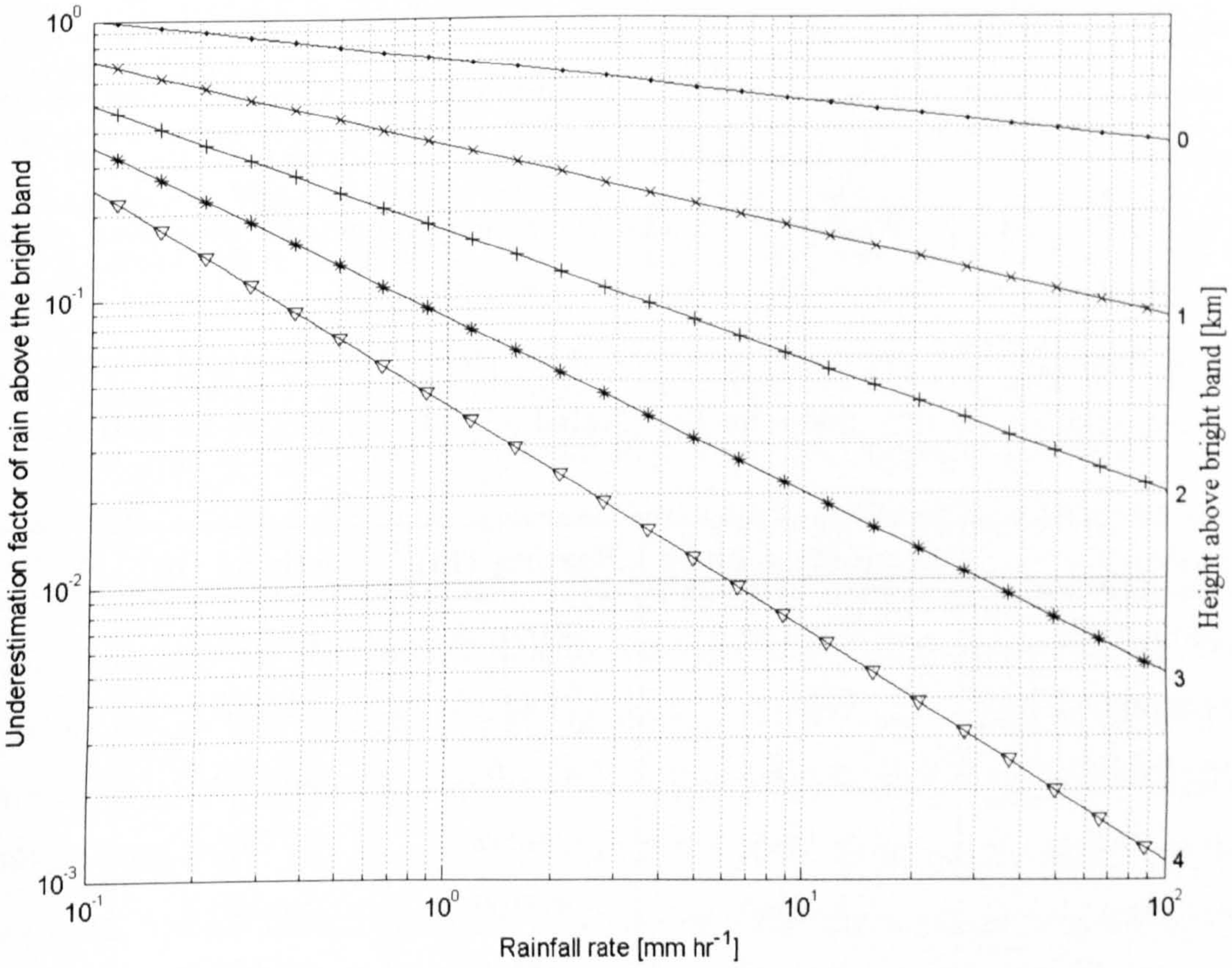

Fig. 6.13: Underestimation of rain when the radar beam is above the melting layer.

deviation of 7.77 dBZ km^{-1}. If the depths of the upper and lower part of the bright band were the same, the increase in reflectivity in the upper part of the bright band would be greater than the decrease in reflectivity in the lower part. The spread of both distributions is indicative of the complexity within the melting layer.

6.5 Analysis of errors due to the variation of the VRP in stratiform precipitation

Eqs. 6.2 and 6.3 can be represented, in terms of rainfall rate, following the M-P Z-R relationship, that is $Z = 200R^{1.6}$ (Marshall et al., 1955), where Z is the reflectivity factor in $mm^6\ m^{-3}$ and R the rainfall rate in mm hr^{-1}. If the radar beam intercepts the melting layer, the estimation of rainfall rate following the M-P Z-R relationship on the maximal bright band reflectivity would be:

$$R_{peak} = 3.92R_{rain}^{1.05}; \qquad \text{mm hr}^{-1} \tag{6.5}$$

and the rainfall rate just above the bright band would be:

$$R_{snow} = 0.71R_{rain}^{0.85}; \qquad \text{mm hr}^{-1} \tag{6.6}$$

The maximal overestimation of rain in the melting layer using Eq. 6.5 is depicted in Fig. 6.12. It is important to observe that the slope shown in this figure, is related to the exponent 1.05 of Eq. 6.5 (See also Eq. 6.2) and the amount of overestimation to the coefficient 3.92. A slightly change in the exponent will cause a remarkable change in slope. For instance, an exponent of 1.0 causes a constant value of overestimation for any value of rainfall rate. From Fig. 6.12, it follows that interception of the radar beam with the melting layer can cause overestimation of rain up to a factor of 3.5 at 0.1 mm hr^{-1} and up to a factor of 5 at 100 mm hr^{-1}. However, these values are also dependent on the volume of melting layer being intercepted by the radar beam and therefore the overestimation will tend to decrease with range (See Chapter 7).

On the other hand, the rainfall rate observed by the radar just above the melting layer is depicted in Fig 6.13. The trend is an underestimation of rain because of the fact that the reflectivity in snow is lower than the reflectivity in rain. The underestimation is even more severe as the radar beam reaches several kilometres above the melting layer because as explained in the previous section, the reflectivity in snow tends to decrease with height.

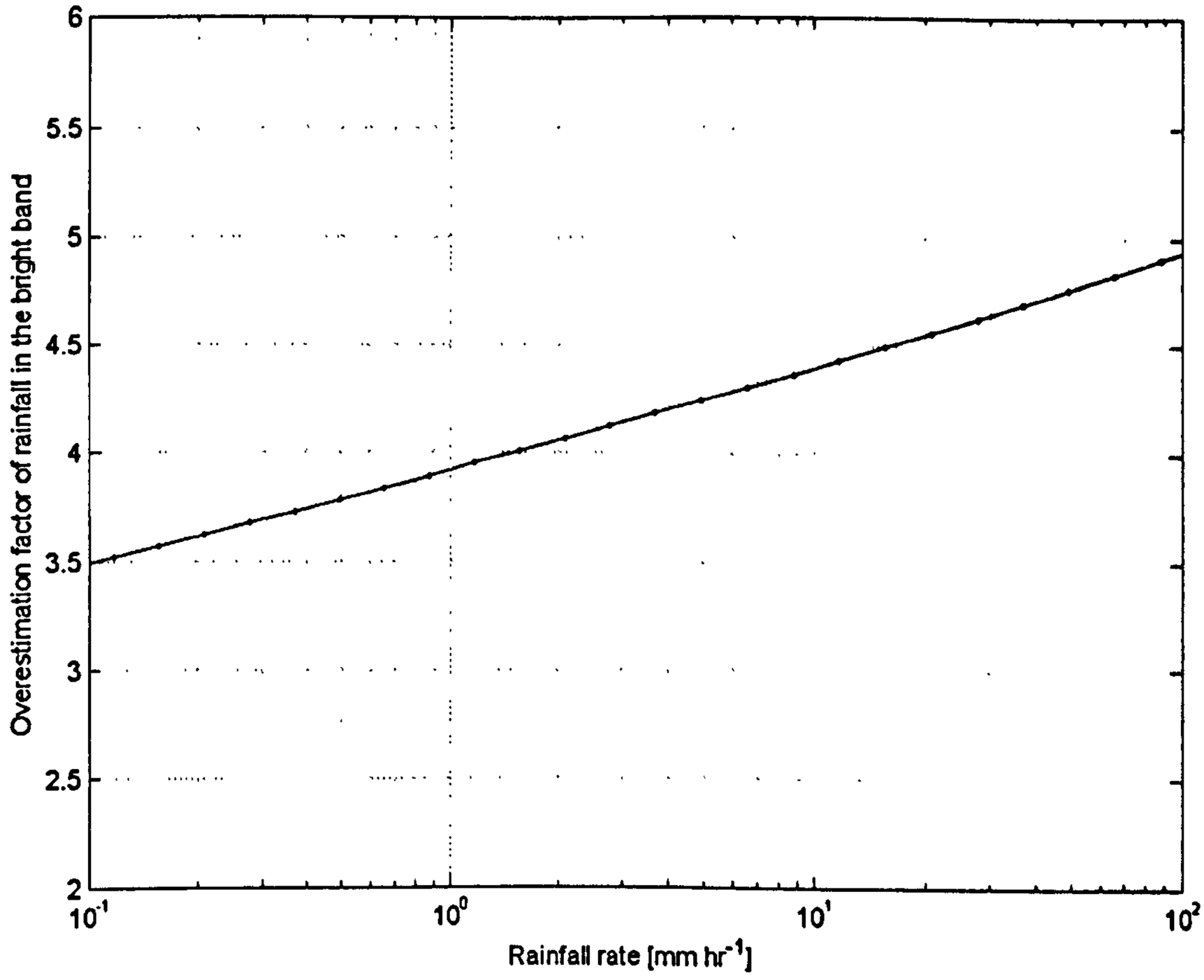

Fig. 6.12: Overestimation of rain when the radar beam intercepts the melting layer.

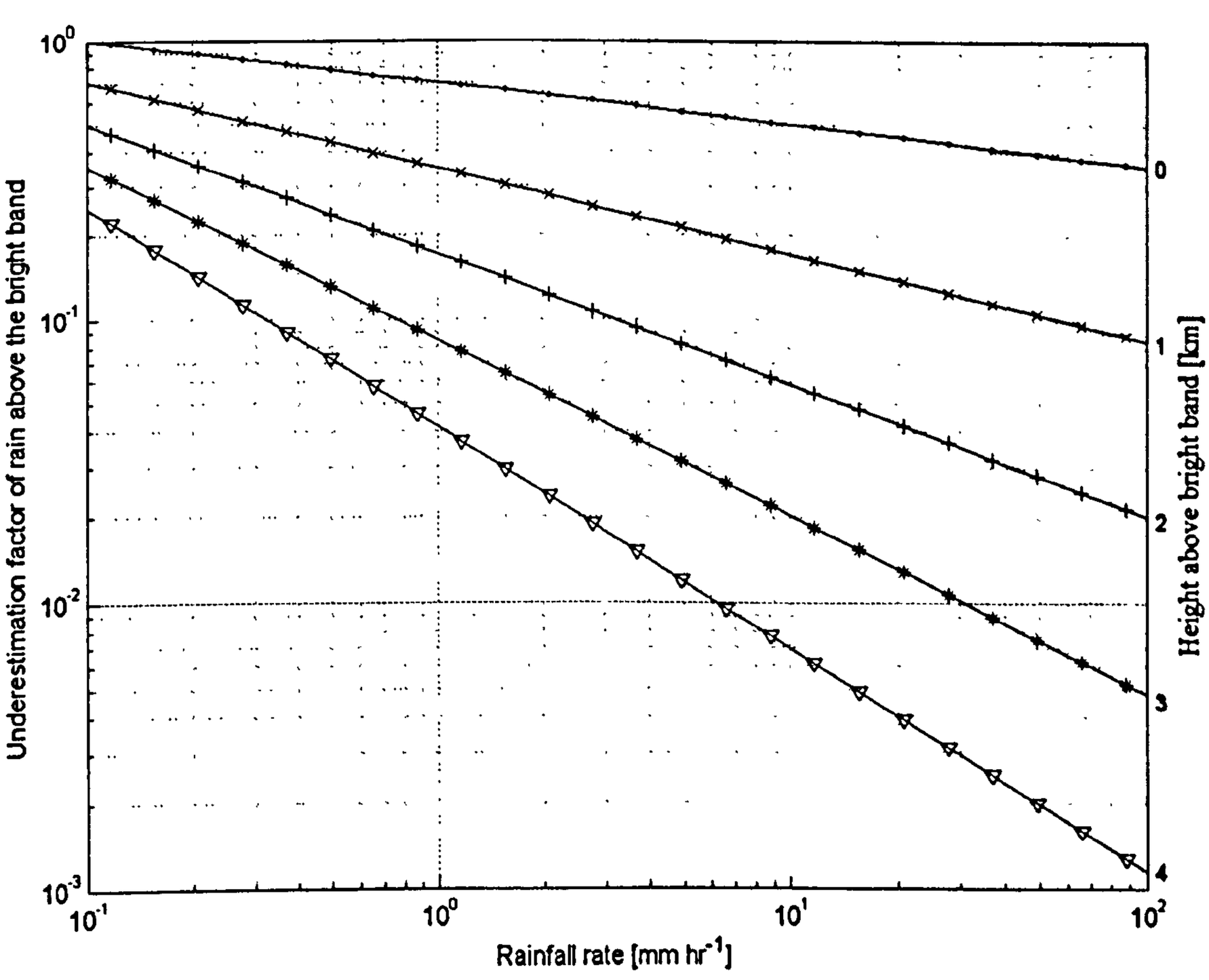

Fig. 6.13: Underestimation of rain when the radar beam is above the melting layer.

6.6 X-band VRP versus S-band VRP

The infrastructure of HYREX comprised two single polarisation C-band scanning weather radars from the national network at Wardon Hill and Cobbacombe Cross, an experimental dual-polarisation S-band scanning radar at Chilbolton operated by Rutherford Appleton Laboratory and two mobile X-band vertically pointing weather radars deployed and commissioned by the Water Resources Research Group from Salford University (Cluckie et al., 2000). The locations of the weather radars are summarised in Table 6.2 (See also Fig. 5.2).

During HYREX, the Chilbolton radar was performing RHI scans in the direction of the vertically pointing radars. In order to compare the VRP observed by the Chilbolton radar with the VRP observed by the X-band radars was necessary to obtain the true distance and the true azimuthal angle between the X-band radars and the Chilbolton radar.

The coordinate system employed in Table 6.2 to locate the radars is described by the Ordnance-Survey (2002). These coordinates are used to locate a position with respect to a map (in this case the UK National Grid System), which is a two-dimensional plane surface depicting features of the curved surface of earth. This map is a projection of a curved surface and therefore is not a perfect representation.

The true distance between two points has to be estimated using the curved surface and applying adequate corrections. The equations relating the true distance and the true azimuth between two points are given in Ordnance-Survey (1998). The results are summarised in Table 6.3. The true azimuth is measured clockwise from the west.

The VRP at Middle Wallop, Boscombe Down and Alhampton sites were extracted from Chilbolton RHI scans for the ranges and azimuths given in Table 6.3. The VRP obtained from the VPR were averaged over N seconds. The averaging interval has to be proportional to the time taken for the Chilbolton radar to acquire an RHI scan. The

Location	Frequency band	Easting (m)	Northing (m)	Altitude (m)
Wardon Hill	C-band	360910.5	102350.0	244
Cobbacombe Cross	C-band	298090.0	119245.0	286
Chilbolton	S-band	439378.8	138565.3	84
Middle Wallop	X-band	429292.0	137958.0	61
Alhampton	X-band	362500.0	134500.0	46
Boscombe Down	X-band	418500.0	139500.0	107

Table 6.2: Locations of the weather radars during HYREX in the UK National Grid System.

Location (1)	Location (2)	True Distance (1-2)	True Azimuthal (1-2)
Chilbolton	Middle Wallop	10109.0 m	356.9927°
Chilbolton	Alhampton	77016.5 m	357.4114°
Chilbolton	Boscombe Down	20907.8 m	363.0016°

Table 6.3: Distances and azimuths between the X-band radars and the Chilbolton radar during HYREX.

acquisition time of an RHI scan in seconds can be estimated by:

$$N = 0.210k; \qquad \text{s} \tag{6.7}$$

where 0.210 is the averaging interval in seconds of 64 independent pulses typical for the Chilbolton radar (Goddard et al., 1994) and k is the number of rays in the RHI scan.

A primary source of discrepancy between the X-band and S-band VRP is that the X-band VRP are single point measurements whereas the S-band VRP are constructed from reflectivity data acquired in several elevation angles. Therefore, the spatial and temporal variation of precipitation may influence slightly the comparisons.

The event to analyse took place on 11th of May 1995. Rainfall lasted for approximately ten hours with intensities no more than 1.4 mm hr^{-1} and with accumulations of 3.6 mm in Boscombe Down and 2.1 mm in Middle Wallop. The variation of reflectivity in the temporal domain as observed by the VPR is depicted in Figs. 6.14 and 6.15 for Boscombe Down and Middle Wallop respectively. The top of the bright band was located at 1.1 km with a depth of 300 m at 15:00 hr, but descends approximately 400 m during the 10 hr interval.

The RHI scans from Chilbolton along the line of the VPR are depicted in Fig. 6.16. The same colour scale has been used in HTI and RHI scans. The height of the bright band top in every RHI scan is approximately constant and its descent can only be observed between consecutive RHI scans. From Table 6.3, the azimuths between Chilbolton and the VPR are 357° and 363° for Middle Wallop and Boscombe Down respectively, but the nearest RHI scans are at 358° and 362° (See Fig. 6.16). In both cases, there is one degree of difference, which represents reflectivity measurements 175 m away from the VPR located at Middle Wallop and 349 m away from the VPR located at Boscombe Down. However, in stratiform precipitation, reflectivity measurements separated 350 m may not represent a big difference.

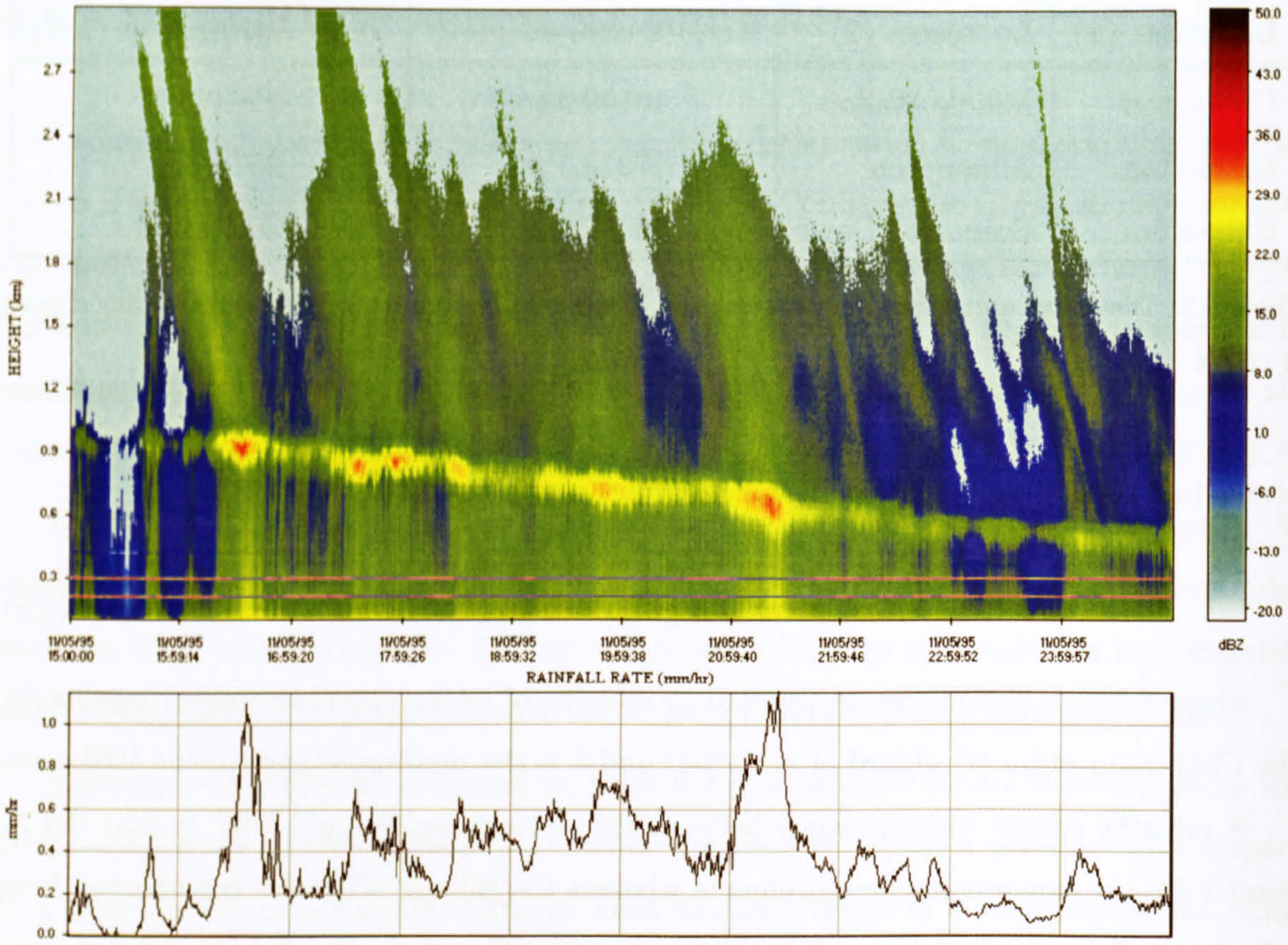

Fig. 6.14: HTI scan from a VPR located at Boscombe Down on 11/05/95. The rainfall rate is estimated between 200 m and 300 m using the relationship $Z = 200R^{1.6}$ (Marshall et al., 1955).

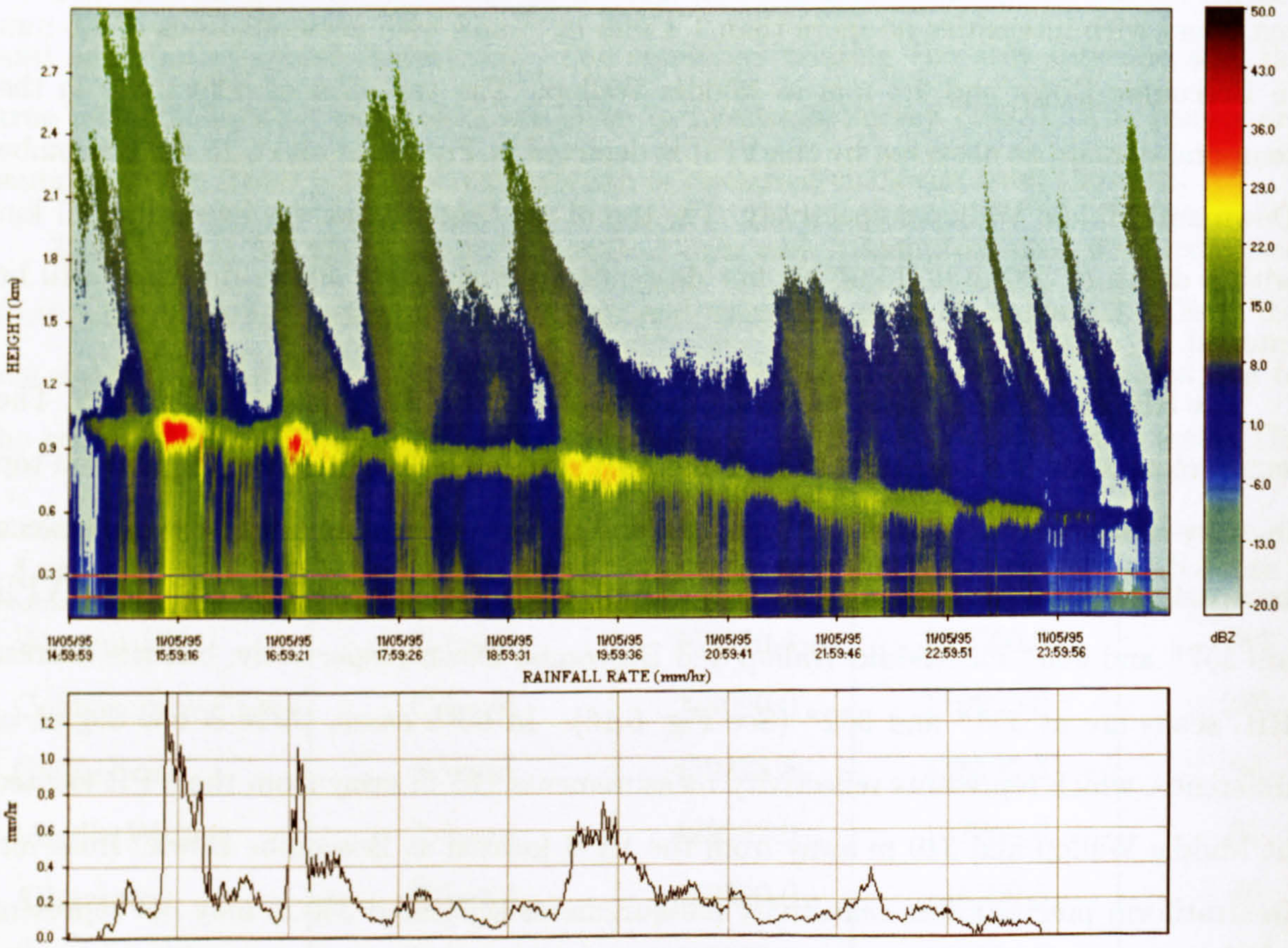

Fig. 6.15: HTI scan from a VPR located at Middle Wallop on 11/05/95. The rainfall rate is estimated between 200 m and 300 m using the relationship $Z = 200R^{1.6}$ (Marshall et al., 1955).

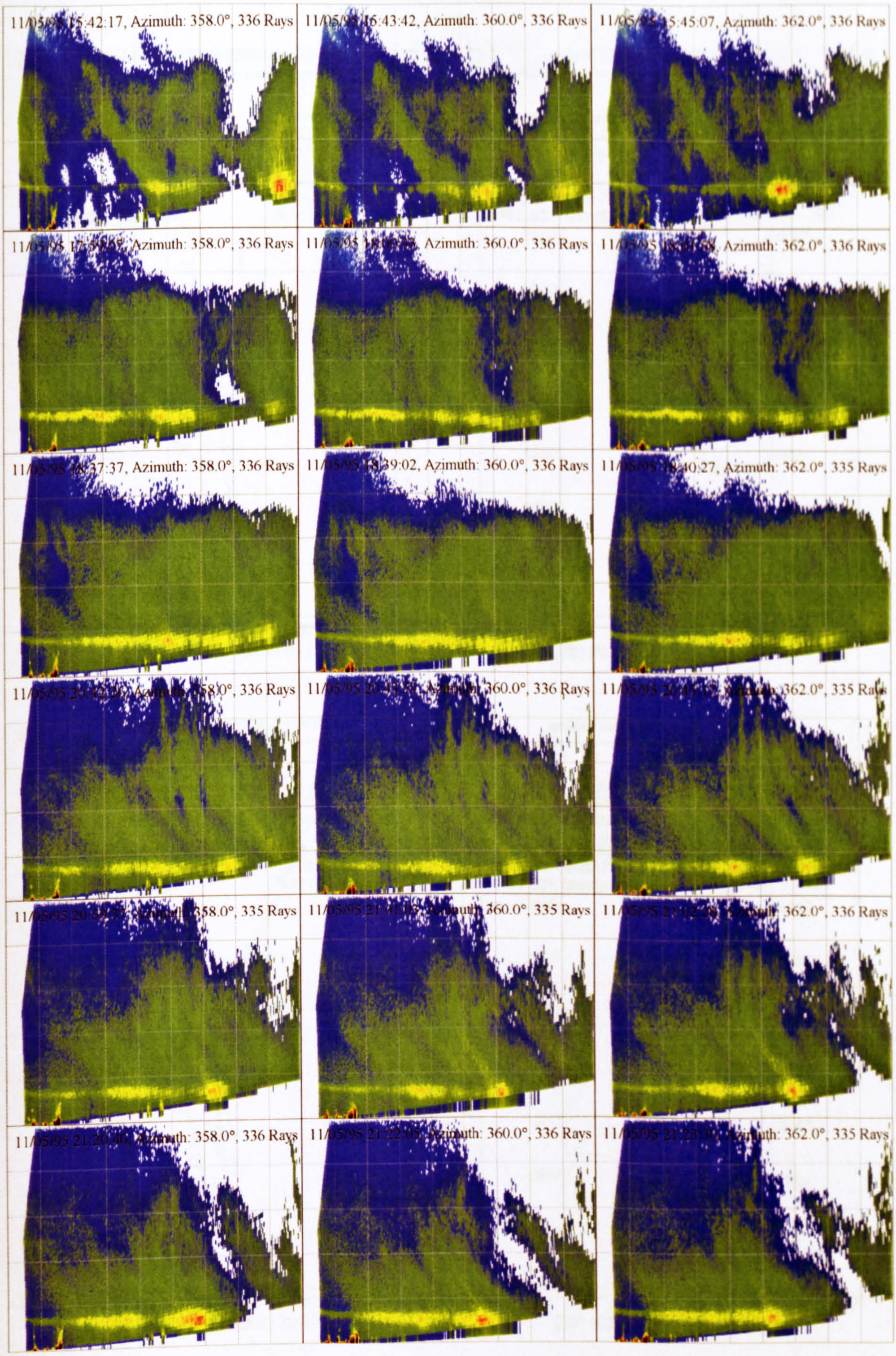

Fig. 6.16: RHI scans from Chilbolton on 11th of May 1995. The scans are from 0 to 90 km in range and from 0 to 5 km in height. The azimuths are measured clockwise from the west.

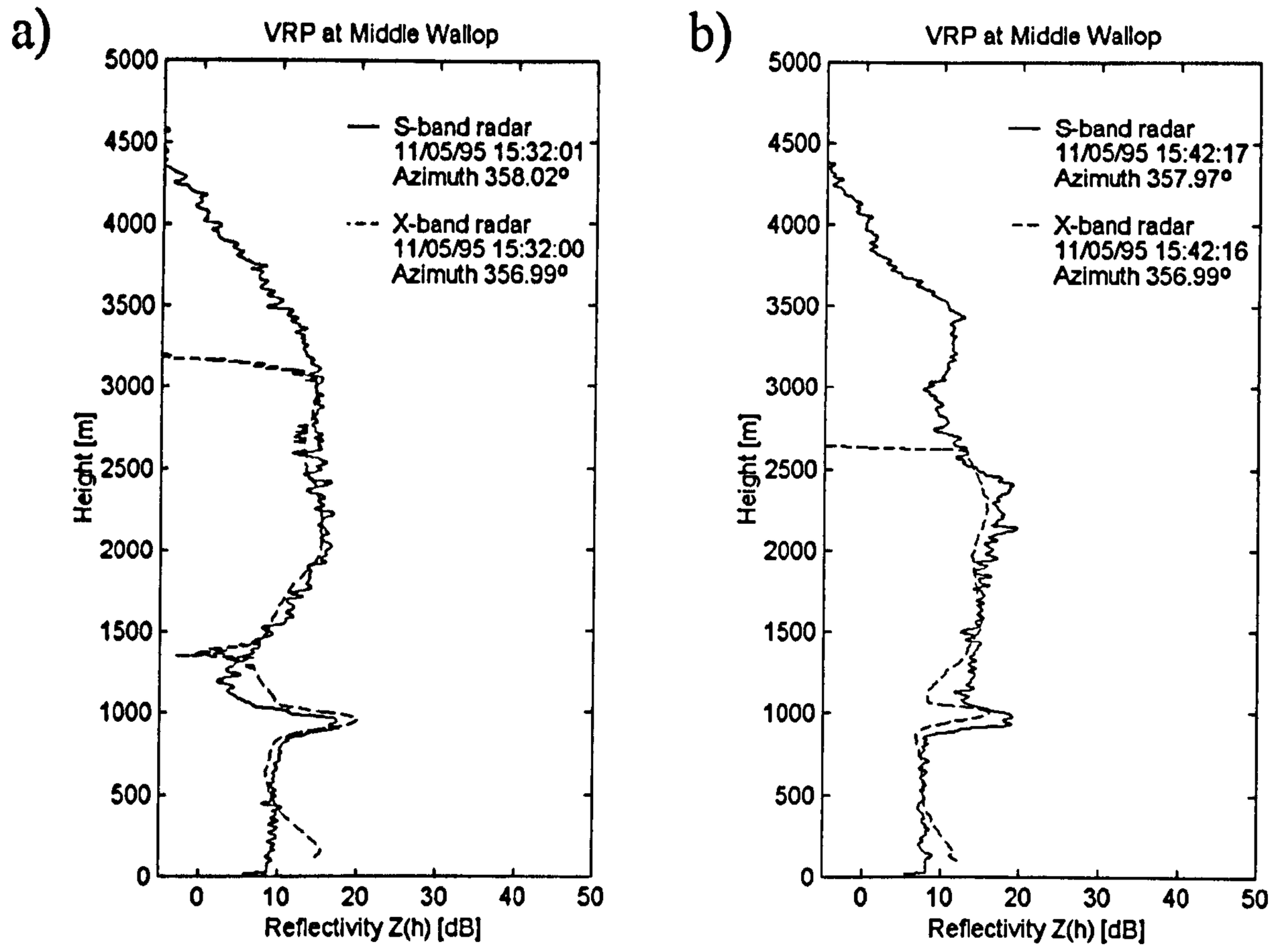

Fig. 6.17: VRP at Middle Wallop at X-band and S-band frequencies on 11/05/95.

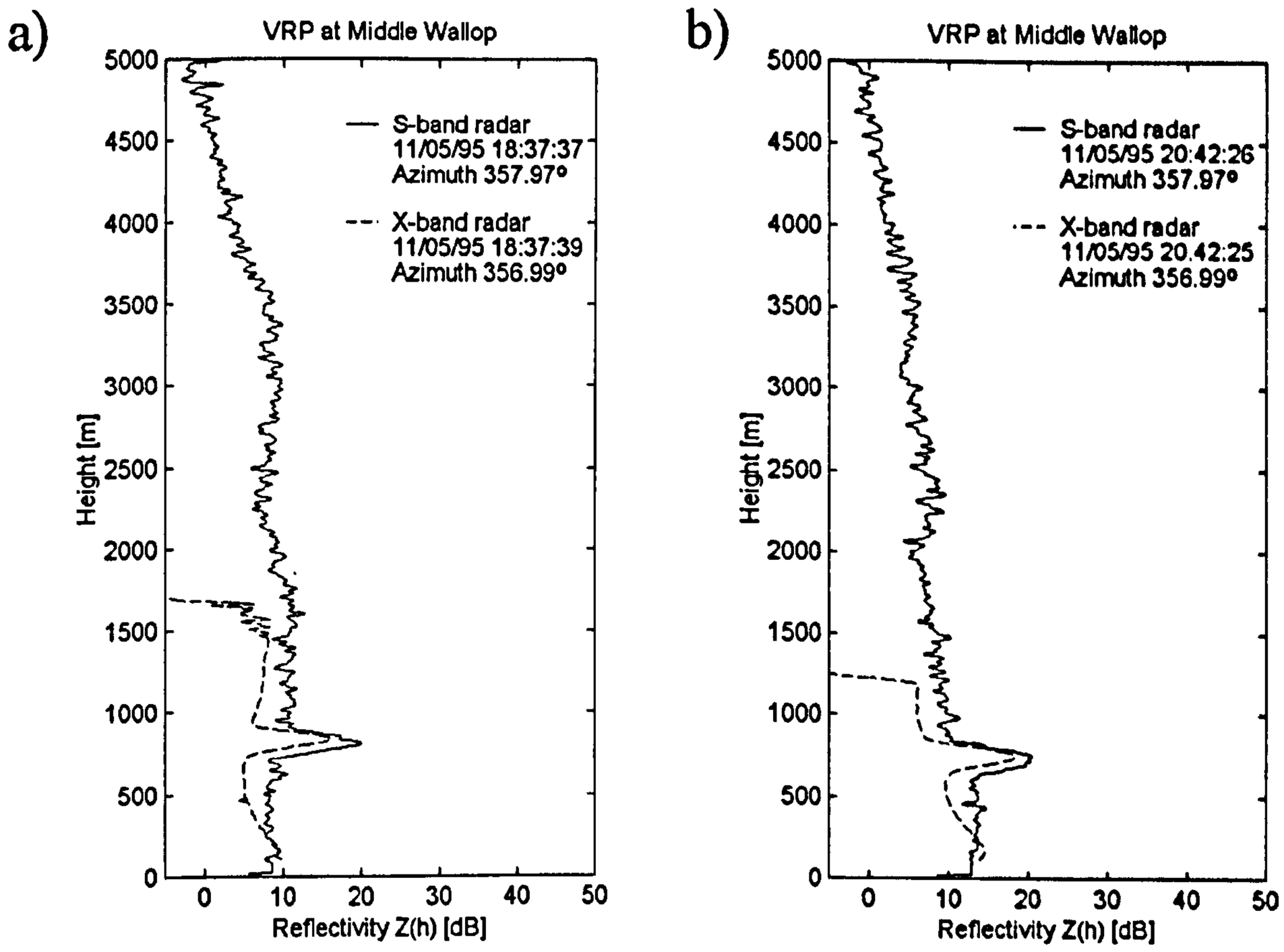

Fig. 6.18: VRP at Middle Wallop at X-band and S-band frequencies on 11/05/95.

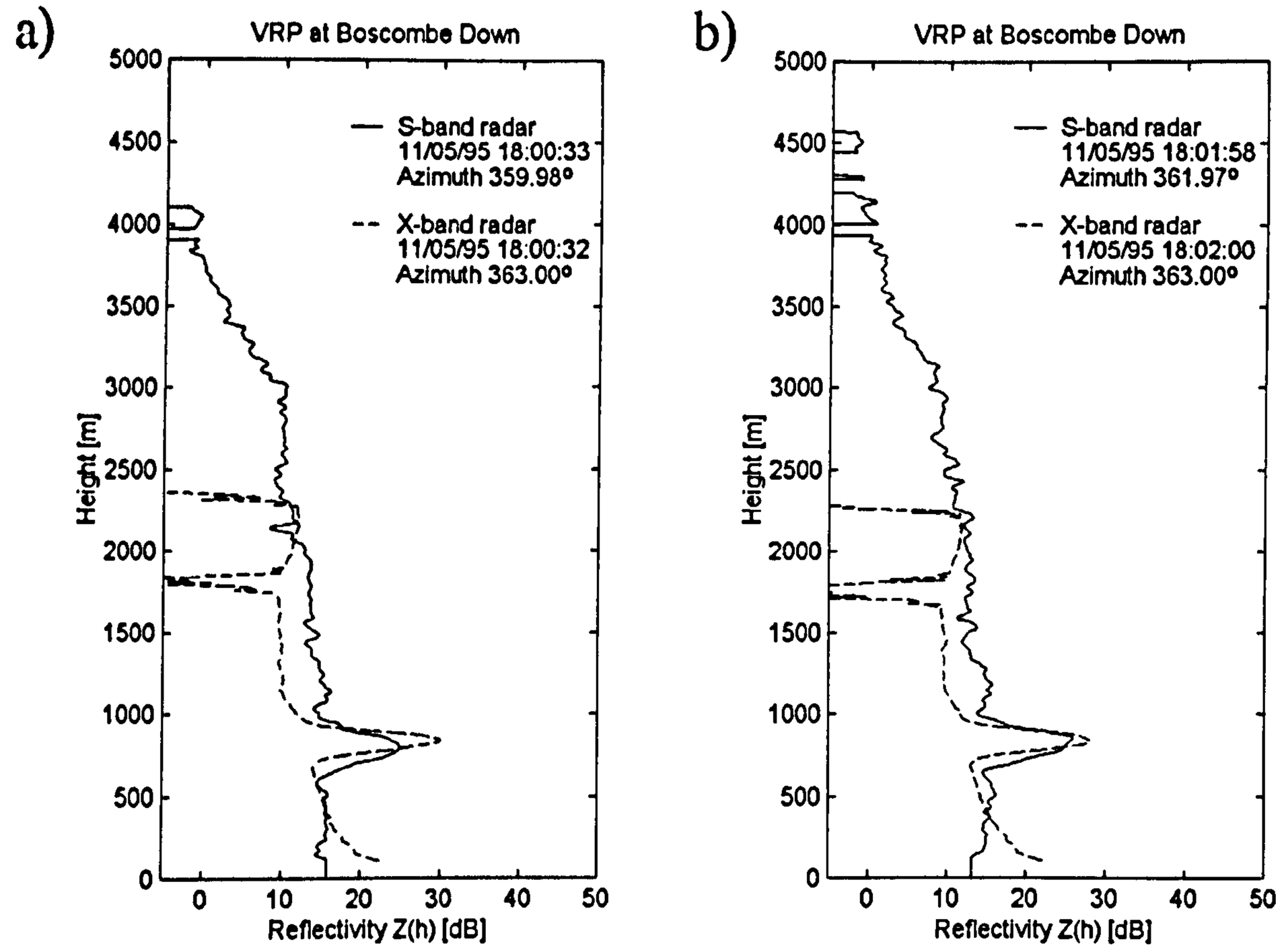

Fig. 6.19: VRP at Boscombe Down at X-band and S-band frequencies on 11/05/95.

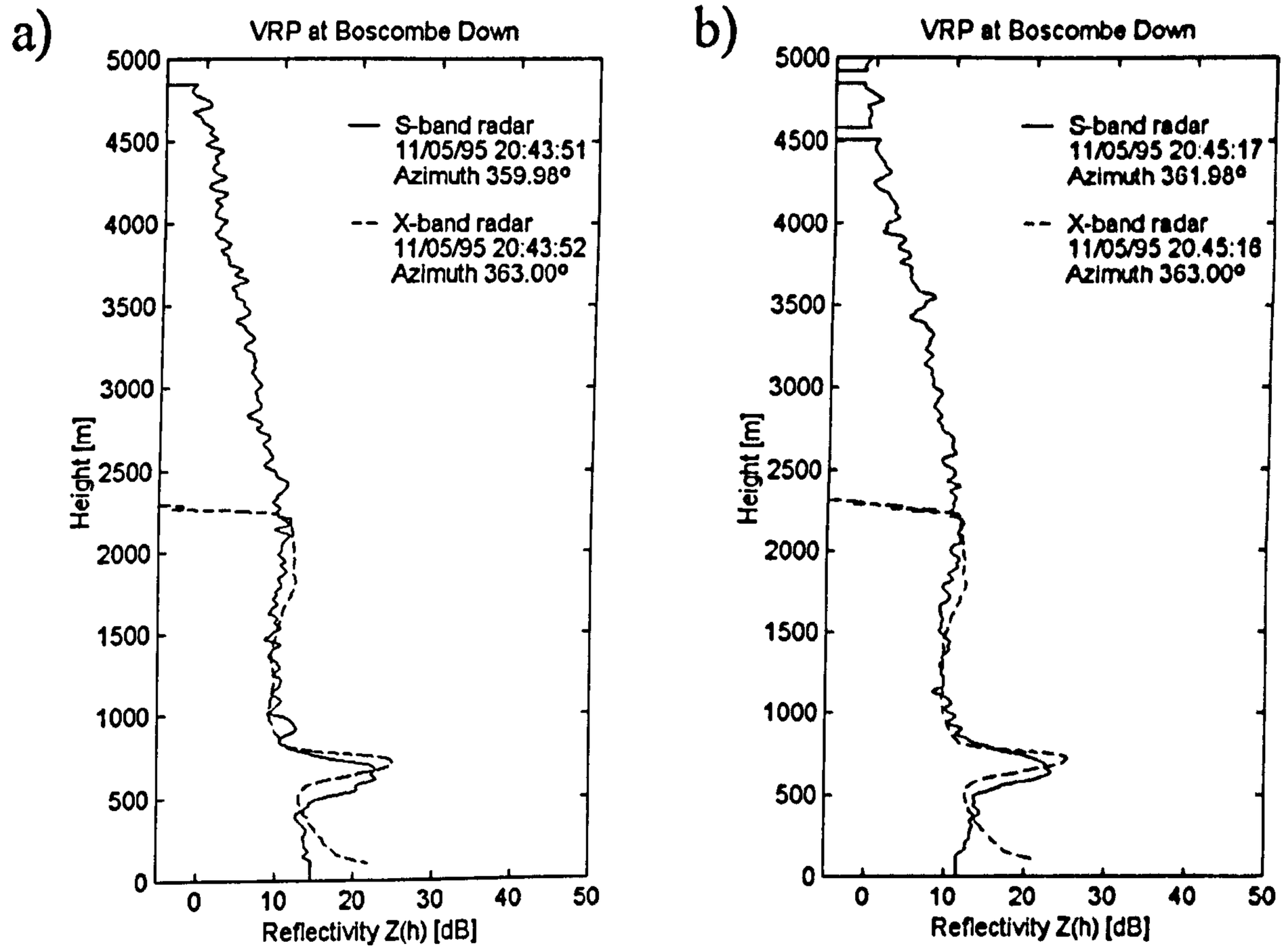

Fig. 6.20: VRP at Boscombe Down at X-band and S-band frequencies on 11/05/95.

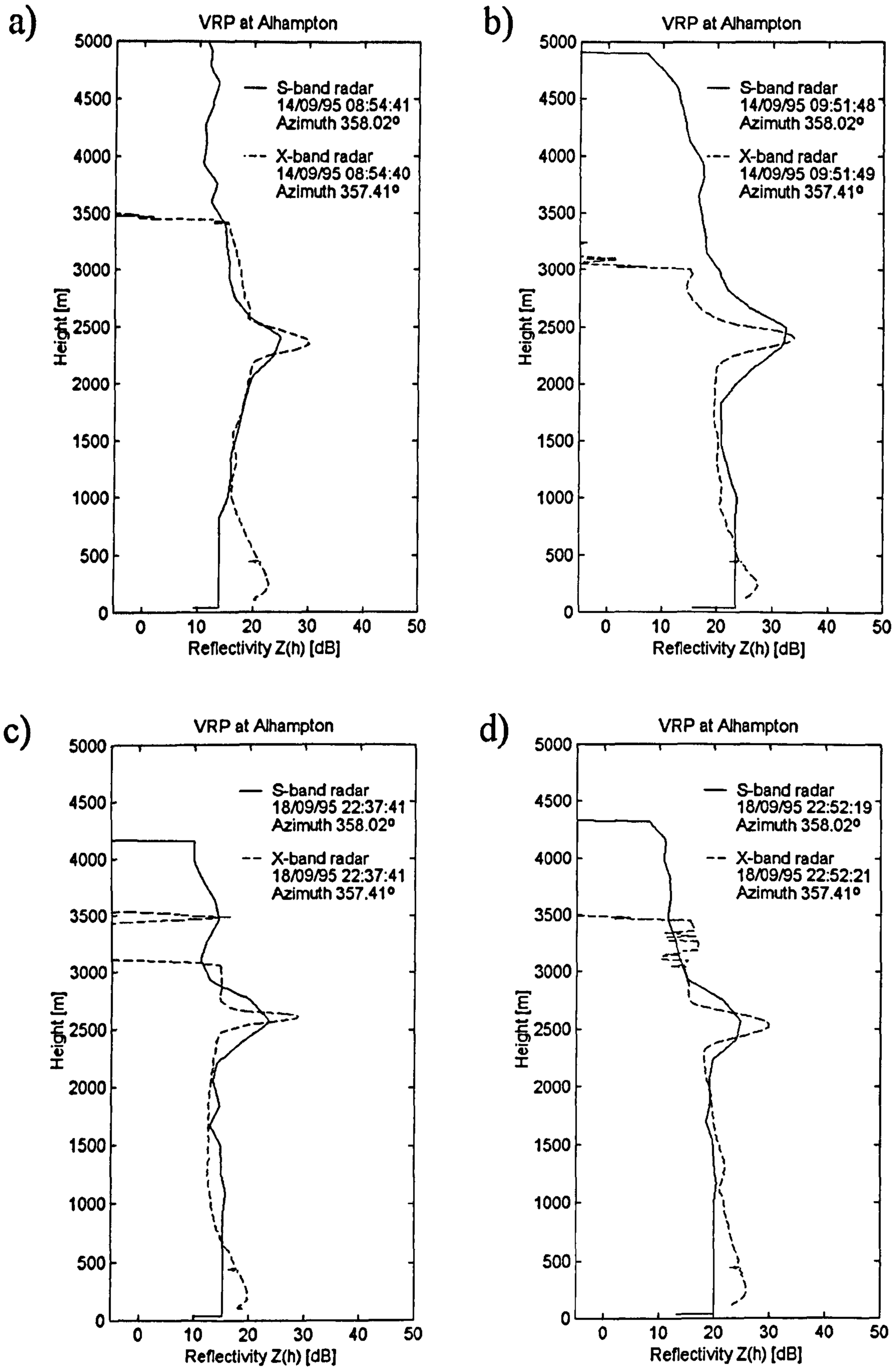

Fig. 6.21: VRP at Alhampton at X-band and S-band frequencies on 14/09/95 and 18/09/95.

The X-band and S-band VRP comparisons are shown in Figs. 6.17 and 6.18 for Middle Wallop, Fig. 6.19 and 6.20 for Boscombe Down and Fig. 6.21 for Alhampton. The X-band profiles at Middle Wallop are quite similar to the S-band profiles at low altitudes, but the former disappear long before the latter. At Boscombe Down, the X-band profiles seem to have higher values of reflectivity at lower altitudes than the S-band profiles. This effect could be due to the calibration slope of the receiver of the X-band radar employed to estimate the reflectivity. At Alhampton, it is evident that at long ranges the effect of beam spreading of the S-band profiles produces an increase in the bright band thickness and reduces the intensity of the maximal reflectivity in the bright band.

It is evident that the vertical reflectivity profiles are quite similar in both frequencies, but the most remarkable difference between them is that the X-band profiles disappear at lower altitudes than the S-band profiles. For instance, in Fig. 6.17a, the X-band profile ends up at 3200 m while the S-band profile ends up at 4400 m. This discrepancy among the profiles may be attributable to several effects:

a) The effect of the pulse length (τ).- The Chilbolton radar operates with a pulse length of 0.5 μs (Goddard, 1995), which gives a gate resolution of 75 m. In order to increase the number of independent pulses, an additional range-averaging over groups of four gates is performed decreasing the gate resolution to 300 m (Goddard et al., 1994). In order to recover the pulses sent out by the transmitter, the radar receiver should have a pass-band filter with a limited bandwidth (B). The relationship between the pulse length and the bandwidth necessary to recover the signal through the receiver without distortion is given by $B\tau = 1$ (Cole, 1992). The bandwidth of the receiver in the Chilbolton radar is 4 MHz (Goddard et al., 1994). On the other hand, the pulse length of the VPR during HYREX was set to 50 ηs (the spatial resolution is 7.5 m) and the bandwidth of the receiver is 20 MHz (See Table 3.1). The effect of increasing the pulse length of the radar has a direct effect on the bandwidth of the receiver. A narrow bandwidth maximizes the Signal to Noise Ratio (SNR) (Jameson et al., 1997). Jameson et al. (1997) stated that the detection of rain depends only on the SNR of the radar. Therefore, a short pulse length (as in the case of the VPR) increases the spatial resolution of the radar but does not help to improve the SNR of the system. On the other hand, a large pulse length (as in the case of Chilbolton) increases the SNR of the system but decreases the spatial resolution. Doviak and Zrnić (1993) stated that if $B\tau$ is constant, the SNR of a distributed scatterer is proportional to the square of the transmitted pulse length (See also Eq. 5.7). In addition, the maximal SNR is obtained as $B \rightarrow 0$. Therefore, there is a trade-off between choosing the right pulse length to guarantee the detection of echoes from precipitation by increasing the SNR while

maintaining an appropriate spatial resolution of the radar.

b) The radar receiver characteristics .- The signals from precipitation echoes are amplified through logarithmic amplifiers. The VPR exhibits good log-linearity over a 50 dB range, while the Chilbolton radar uses a pair of log amplifiers with overlapping transfer characteristics that increase the dynamic range of the radar to 90 dB (Goddard et al., 1994). The weakest echoes received by the VPR fall in the range of the non-linear characteristics of the receiver. If the non-linearities are taken into account, they should be defined accurately by proper calibration (See Fig. 3.3). In the VPR, it is assumed that a constant calibration slope applies over the whole interval. Therefore, it is very likely that the characteristics of the receiver influence heavily the detection of the weakest echoes on the top of the precipitation. This is one of the main reasons for the differences between the X-band VRP and the S-band VRP.

c) Attenuation .- There is no doubt that attenuation effects at shorter wavelengths must be taken into account (See Battan, 1973). The attenuation effect at X-band frequencies is a function of the rainfall rate. The total effect is a decrease in signal strength with range rather than a sudden extinction. For instance, the VRP at X-band frequencies shown in Fig. 6.17 disappear around 2500 m in average, but in Fig. 6.18 disappear below 1500 m even when in the latter the VRP present lower values of reflectivities along the vertical than the former. Therefore, the X-band VRP suffering extinction is more likely due to the characteristics of the radar receiver rather than attenuation, but there is no doubt that attenuation due to the melting layer is not negligible.

The correlations between the X-band and S-band VRP just below the height where the reflectivity of the X-band VRP is extinct are presented in Fig. 6.22. The correlations oscillate between 0.6 and 0.9. These values are not too bad considering the low-cost involved in the construction of the VPR compared to Chilbolton. However, there is a need of improvement to detect weak echoes, by choosing a longer pulse length to increase the SNR and improving the characteristics of the receiver.

In order to evaluate the differences in reflectivity in the melting layer at both frequencies, it is necessary to compare the results obtained in the last sections. Figs. 6.23a and 6.23c depict the scatter plots of the peak reflectivities in the bright band against the reflectivities in rain, just below the bright band at X-band and S-band frequencies respectively (From Figs. 5.19 and 6.6). In order to obtain a more accurate comparison, the outliers of the scattered data have been removed following an approach discussed by Barnett and Lewis (1994, Chap. 8). As a first approximation, a regression curve (either of first or second order) is fitted to the scattered data; then a test of discordancy is applied to examine

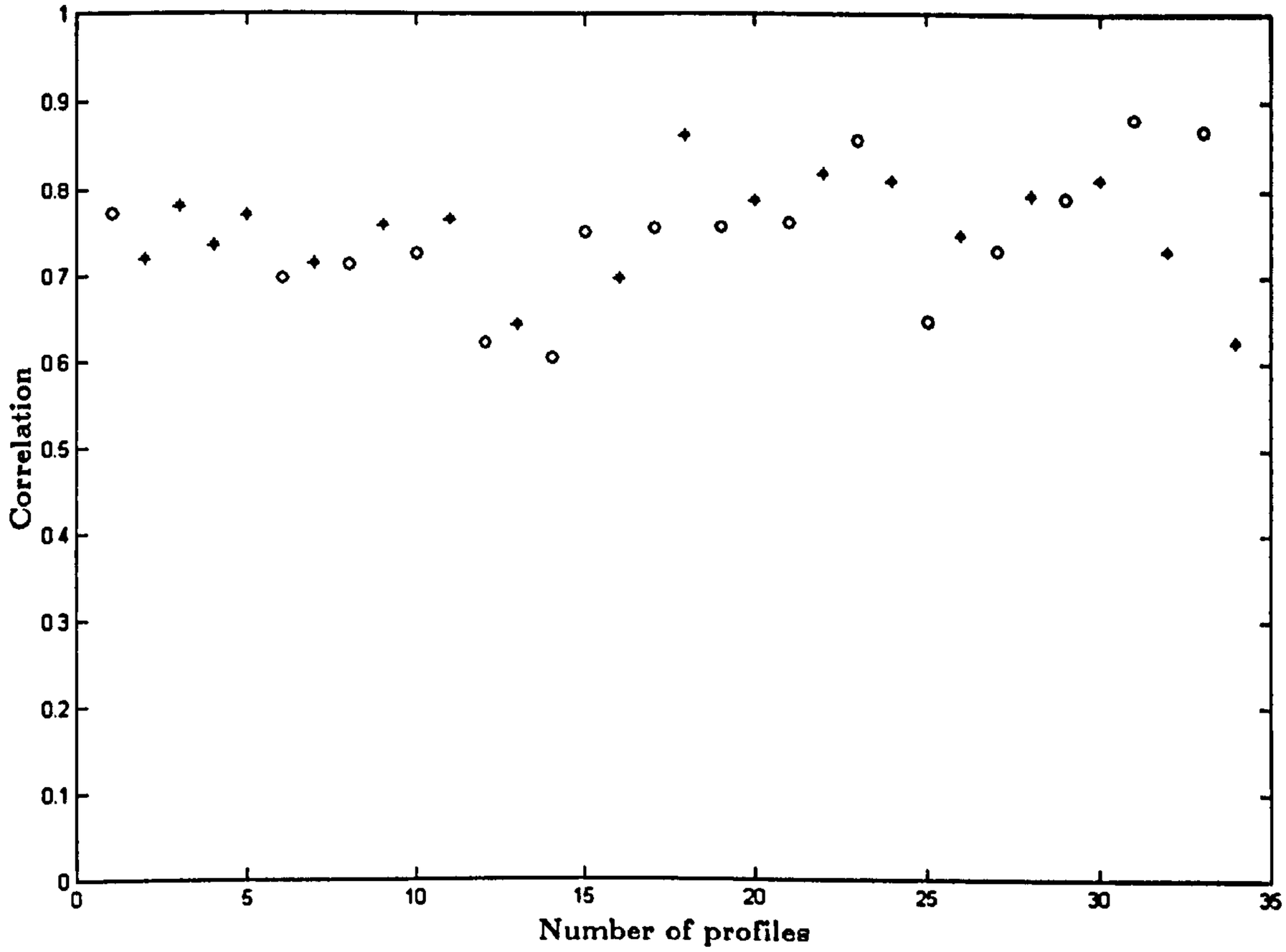

Fig. 6.22: Correlations from 35 pairs of VRP at X-band and S-band frequencies. The circles represent the VRP at Boscombe Down and the asterisks the VRP at Middle Wallop on 11/05/95.

the *studentized residuals* e_j. The studentized residuals provide an intuitively appealing measure of the aberrance of the separate observations (Barnett and Lewis, 1994). They are given by:

$$e_j = \frac{\varepsilon_j}{s_j} \tag{6.8}$$

where ε_j are the residuals between the scattered data and the regression curve and s_j^2 is an unbiased estimate of the variance of the residuals ε_j (See Barnett and Lewis, 1994, for further details). The test of discordancy of a single outlier is:

$$t = max|\varepsilon_j/s_j| \tag{6.9}$$

When the value of t is sufficiently large, the observation yielding this value is a discordant outlier. From the scattered data obtained in the analysis of the bright band, the distributions of ε_j are Gaussian. Therefore, values of $t \leq 2$ represent 95% of the scattered data and for $t > 2$ have been considered as outliers. A new regression curve is fitted to the modified scattered data and the results are shown in Figs. 6.23b and 6.23d. It is clear that there is an improvement in the correlations and standard deviations as much in the X-band analysis as in the S-band analysis. The maximal reflectivity in the bright band at

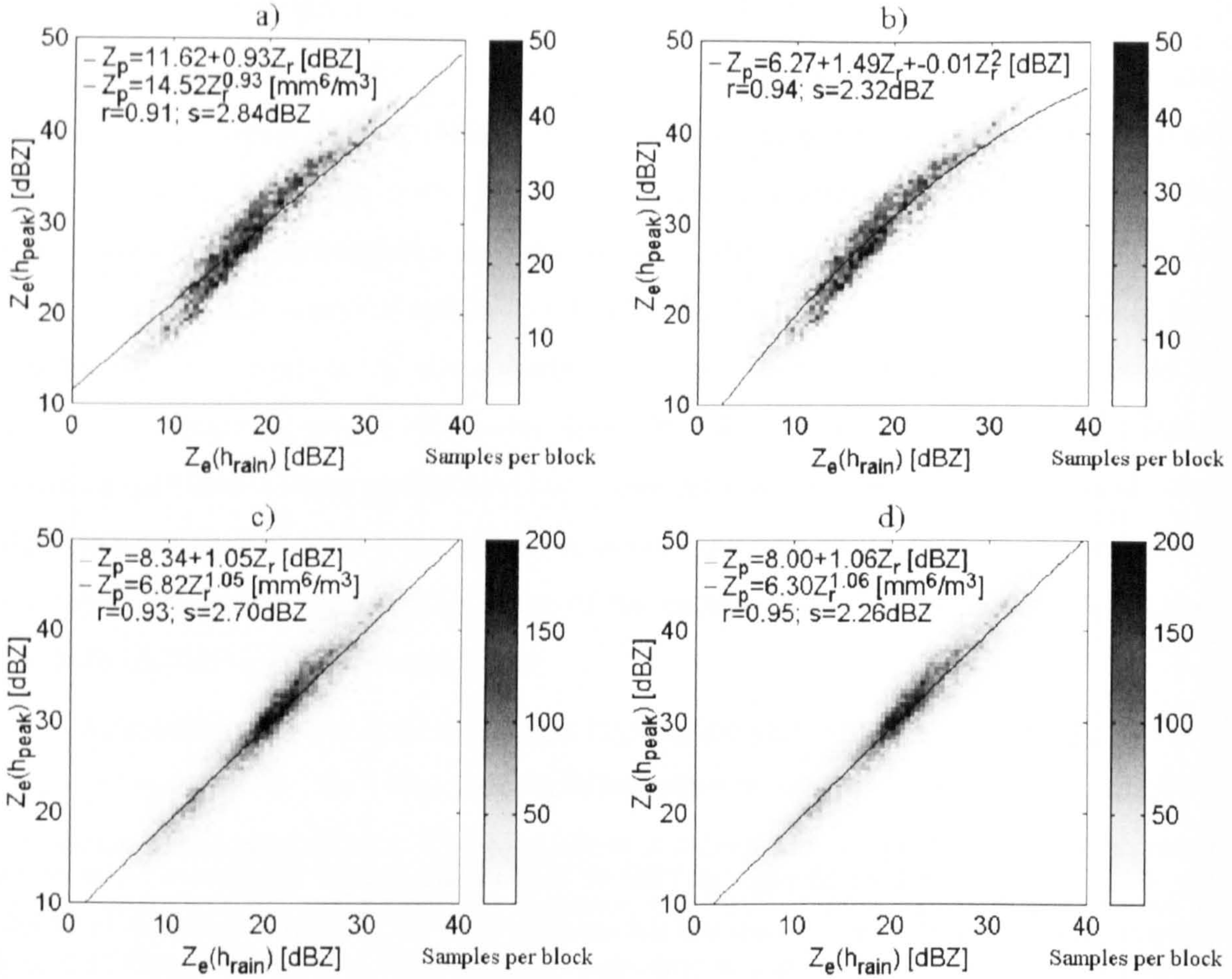

Fig. 6.23: Scatter plots of the maximal reflectivities in the bright band against the rain reflectivities below at X-band and S-band frequencies. a) Original scatter plot at X-band frequencies; b) Scatter plot at X-band frequencies removing outliers; c) Original scatter plot at S-band frequencies; d) Scatter plot at S-band frequencies removing outliers.

X-band frequencies as a function of the rain reflectivity is given by the regression curve:

$$Z_{e(peak)} = 6.2728 + 1.4917 Z_{e(rain)} - 0.0130 Z^2_{e(rain)}; \qquad \text{dBZ} \tag{6.10}$$

At S-band frequencies the regression line is given by:

$$Z_{e(peak)} = 7.9954 + 1.0637 Z_{e(rain)}; \qquad \text{dBZ} \tag{6.11}$$

It is interesting to note that the bending in the scatter plot at X-band frequencies departs considerably from the S-band analysis for rain reflectivities higher than 28 dBZ. Both regression curves are approximately the same for rain reflectivities below 28 dBZ and their differences may be attributable to the calibration of the X-band radar, but for higher rainfall intensities their differences become more remarkable and due to a combination of attenuation and the use of the Rayleigh approximation to estimate the reflectivity at

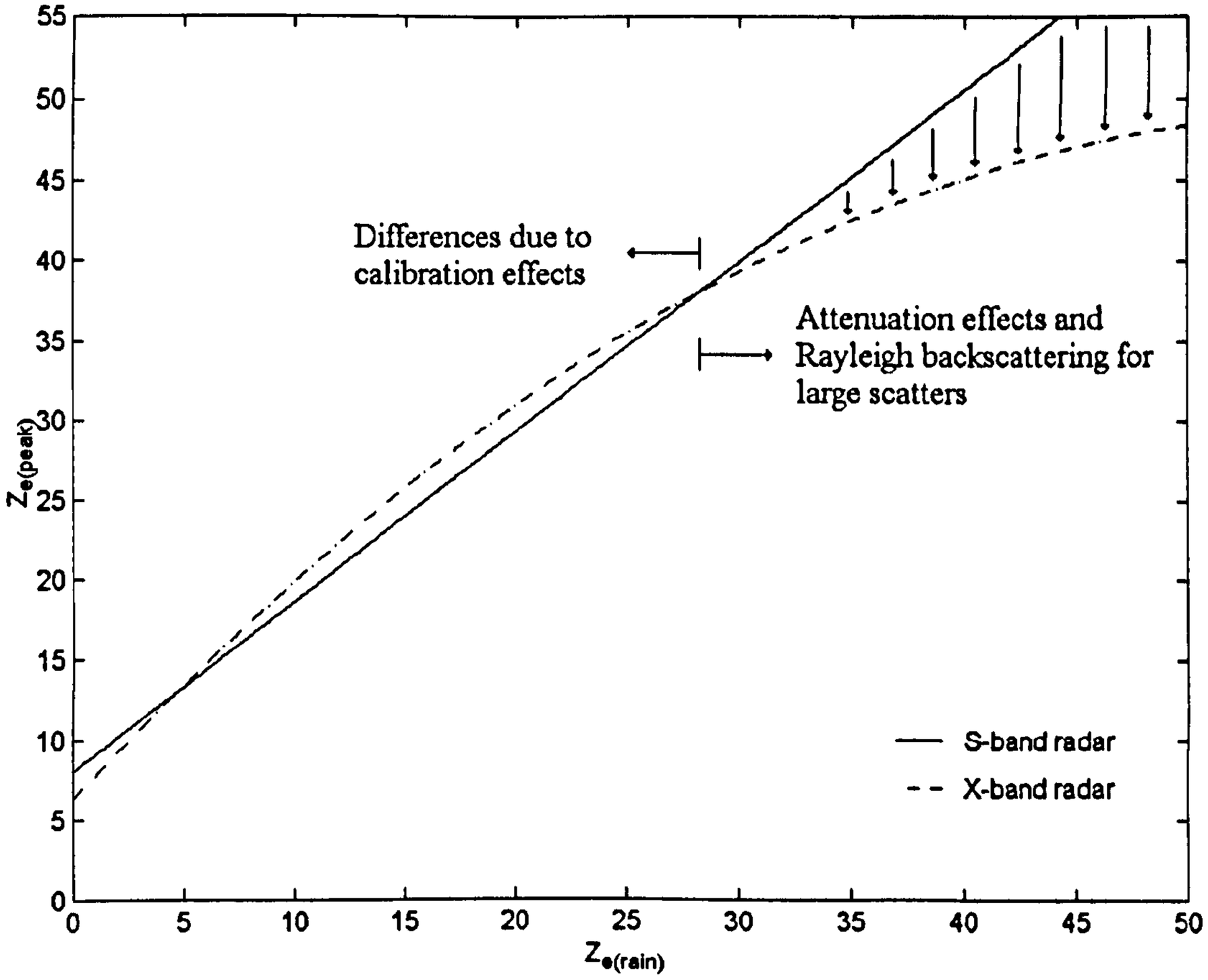

Fig. 6.24: Regression curves between the maximal reflectivities in the bright band against the rain reflectivity below at S-band and X-band frequencies.

X-band frequencies. The "differences" in dBZ units are given by:

$$\Delta Z_{S-X} = 1.7226 - 0.4280 Z_{e(rain)} + 0.0130 Z_{e(rain)}^2, \qquad 28 \leq Z_{e(rain)} \leq 40 \text{ dBZ} \quad (6.12)$$

This equation gives an estimation of the differences observed at X-band frequencies when the radar beam passes through the melting layer. The differences can be considered negligible when the rain reflectivity is lower than 28 dBZ, but should be taken into account when greater values of reflectivity are involved. For instance, an X-band vertically pointing radar measuring 40 dBZ in rain just before passing through the bright band will suffer a decrease in reflectivity of approximately 5.4 dBZ in the maximal bright band reflectivity.

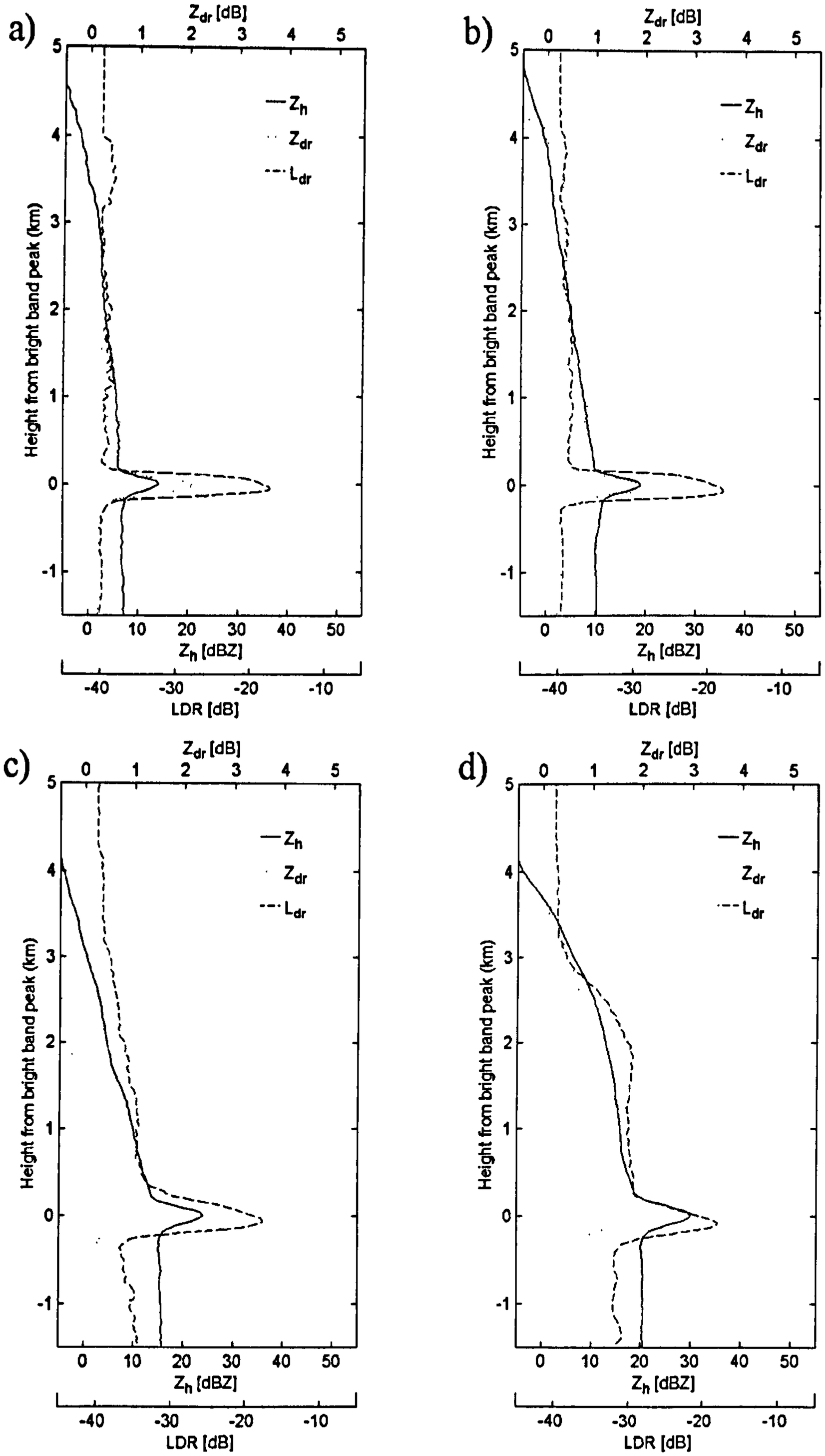

Fig. 6.25: Average vertical profiles of Z_h, Z_{dr} and LDR at S-band frequencies in stratiform precipitation. To generate the profiles, the height of an individual profile has been normalised with the height of the bright band peak. The averages have been performed for values of $Z_{h(r)}$ ± 0.5 dBZ, being $Z_{h(r)}$ the rain reflectivity below the bright band. $Z_{h(r)}$ = a) 5, b) 10, c) 15 and d) 20 dBZ.

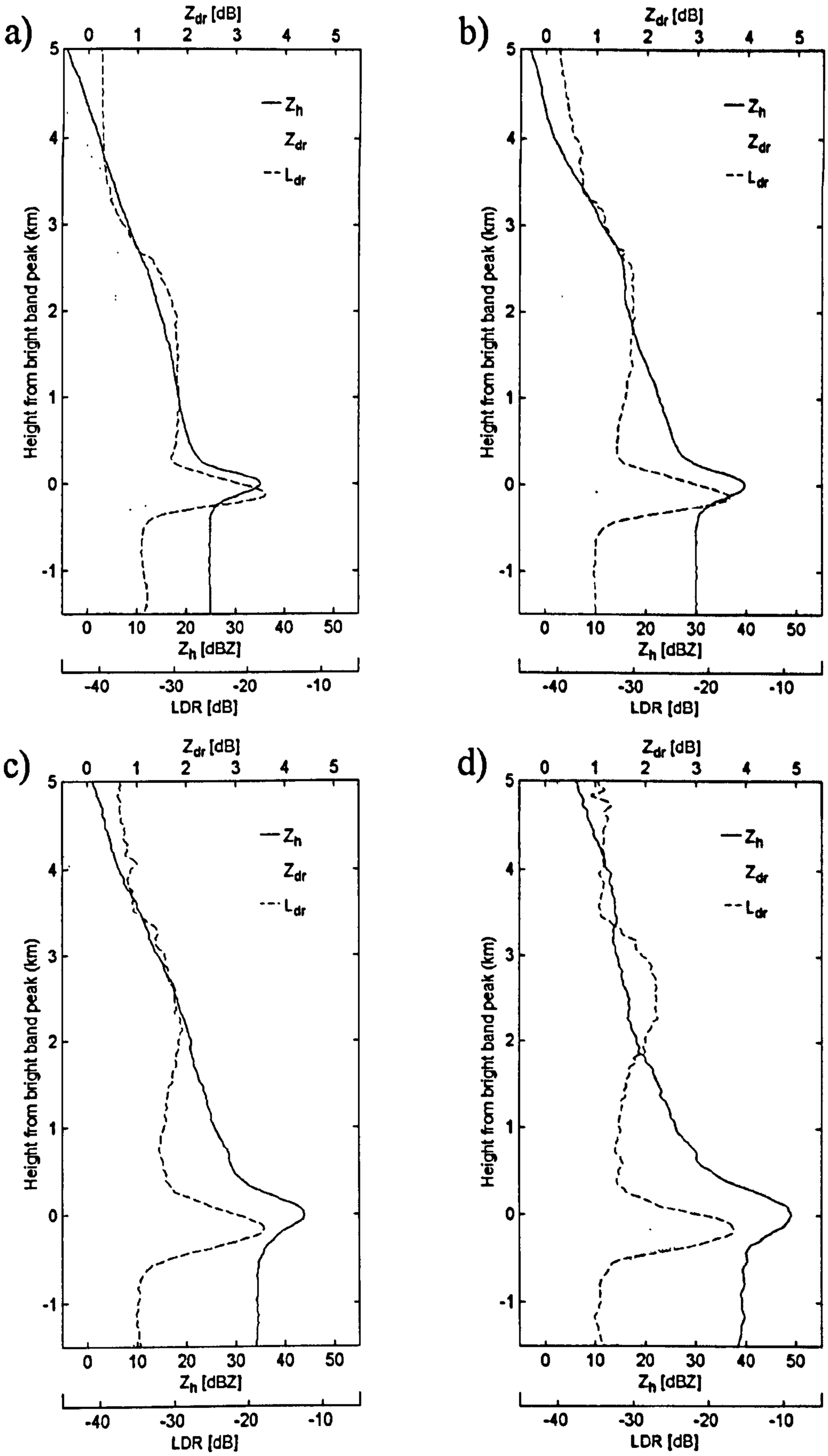

Fig. 6.26: Average vertical profiles of Z_h, Z_{dr} and LDR at S-band frequencies in stratiform precipitation. To generate the profiles, the height of an individual profile has been normalised with the height of the bright band peak. The averages have been performed for values of $Z_{h(r)}$ ±0.5 dBZ, being $Z_{h(r)}$ the rain reflectivity below the bright band. $Z_{h(r)}$ = a) 25, b) 30, c) 35 and d) 40 dBZ.

6.7 Polarimetric signatures in stratiform precipitation

Figs. 6.25a-d and 6.26a-d show averaged vertical profiles of Z_h, Z_{dr} and LDR for stratiform precipitation at different intensities of rain reflectivity. The vertical profiles have been constructed from RHI scans from the Chilbolton radar. Only those vertical profiles closer to the radar have been extracted to obtain the dual-polarisation measurements from ground level to 10 km in height, while minimizing the effect of beam-spreading with range. Profiles very close to the radar are not useful because of the truncation caused by the sweep of the radar from 0 to 30° in elevation, and profiles far from the radar are affected because of the spread of the beam with range. The optimal range is around 20 km and only the vertical profiles within 18-22 km from the radar have been analysed. The profiles represent hundreds of observations with similar characteristics, but taken from different precipitation events. The most striking features are the bright band signatures in Z_{dr} and LDR at different precipitation intensities.

6.7.1 Dual-polarisation measurements in the bright band

Figs. 6.25a-d and 6.26a-d show the evolution of the vertical profiles of Z_{dr} as the rain reflectivity increases. There are several interesting features in such an evolution. For low values of rain reflectivity ($Z_h < 20$ dBZ as in Figs. 6.25a-c), the maximum on Z_h (its height is $h_{peak(Z_h)}$) is approximately at the same height than the maximum on Z_{dr} (its height is $h_{peak(Z_{dr})}$). However, as the rain reflectivity increases ($Z_h > 20$ dBZ), the maximum on Z_{dr} starts to descend and then $h_{peak(Z_{dr})} < h_{peak(Z_h)}$ (See Figs. 6.25d and 6.26a-d). This effect can be observed clearly when plotting the scatter between Z_h in rain and the value of Z_{dr} at the height $h_{peak(Z_h)}$ (See Fig. 6.27a). In this figure, the values of Z_{dr} at the height $h_{peak(Z_h)}$ seem to decrease, but the reality is that the Z_{dr} bright band signature is descending.

Returning to Figs. 6.25a-d and 6.26a-d, it is interesting to note that below 20 dBZ in the rain reflectivity, not only the maxima on Z_h and Z_{dr} are approximately at the same height, but also the bright band thickness in both parameters has the same depth (See Figs. 6.25a-d). However, for rain reflectivities between 20 and 30 dBZ, the bright band thickness of Z_{dr} is reduced to approximately half the bright band thickness in Z_h (See Figs. 6.26a-b). For rain reflectivities above 30 dBZ, the bright band thickness of Z_{dr} remains approximately half of the thickness of Z_h (See Figs. 6.26b-d).

A possible explanation could be as follows. The maximum on Z_h in the bright band is caused by the largest particles (Barthazy et al., 1998) whereas large values of Z_{dr} are caused

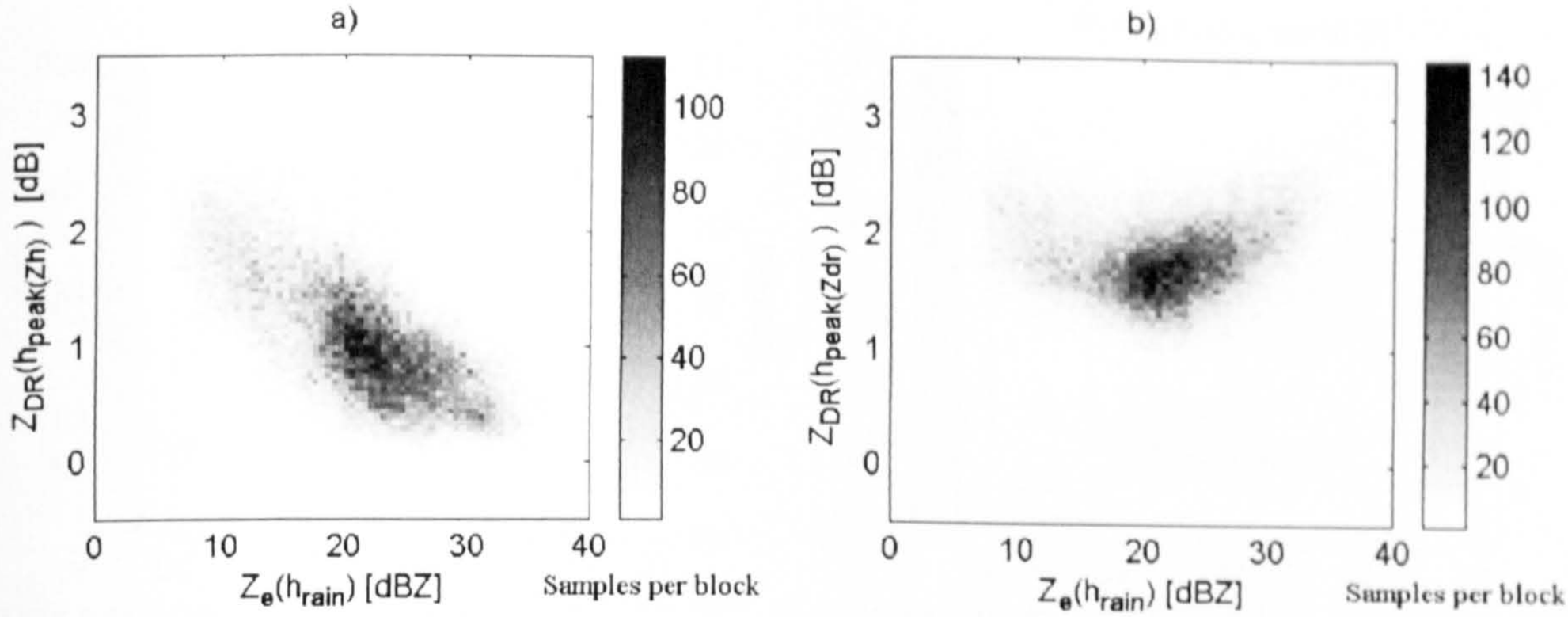

Fig. 6.27: Scatter plot between the differential reflectivity in the bright band and the rain reflectivity below at S-band frequencies. h_{rain} is the height of the rain reflectivity just below the bright band, $h_{peak(Z_h)}$ is the height of the maximal Z_h in the bright band and $h_{peak(Z_{dr})}$ is the height of the maximal Z_{dr} in the bright band.

by very oblate particles, which are horizontally oriented (Seliga and Bringi, 1976). In the bright band, large melting aggregates, which are almost, but not completely melted, will produce large values of differential reflectivity because they behave like raindrops getting oblate as they fall. Therefore, it may be possible that when low rainfall intensities are involved (rain reflectivities less than 20 dBZ as in Figs. 6.25a-c), the largest particles at the height $h_{peak(Z_h)}$ are relatively large melting aggregates, which are almost melted and can be observed by the radar as oblate raindrops producing large values on Z_{dr} at the height $h_{peak(Z_h)}$. As the rainfall intensity increases (rain reflectivities between 20-30 dBZ as in Figs. 6.25d and 6.26a-b), the melting aggregates at the height $h_{peak(Z_h)}$ are much bigger than for low rainfall intensities taking a longer time to complete their melting. In this case, the melting aggregates will be observed by the radar as oblate raindrops a few tens of metres just below $h_{peak(Z_h)}$. For high rain reflectivities (greater than 30 dBZ as in Figs. 6.26c-d), very large melting aggregates are formed at the height $h_{peak(Z_h)}$. They are so big that the melting takes place in a deeper layer and they still do not have a specific orientation at the height $h_{peak(Z_h)}$, presenting heavy tumbling and therefore Z_{dr} values very close to zero. These large melting aggregates will be observed by the radar as very oblate raindrops a few hundred metres below $h_{peak(Z_h)}$ producing large values of Z_{dr} at the height of $h_{peak(Z_{dr})}$.

This may be the reason that the maximum value of Z_{dr} is descending as the rain reflectivity increases. However, there is a lack of in-situ measurements to corroborate this issue and the suggested explanation is mainly based on the definition of the differential reflectivity.

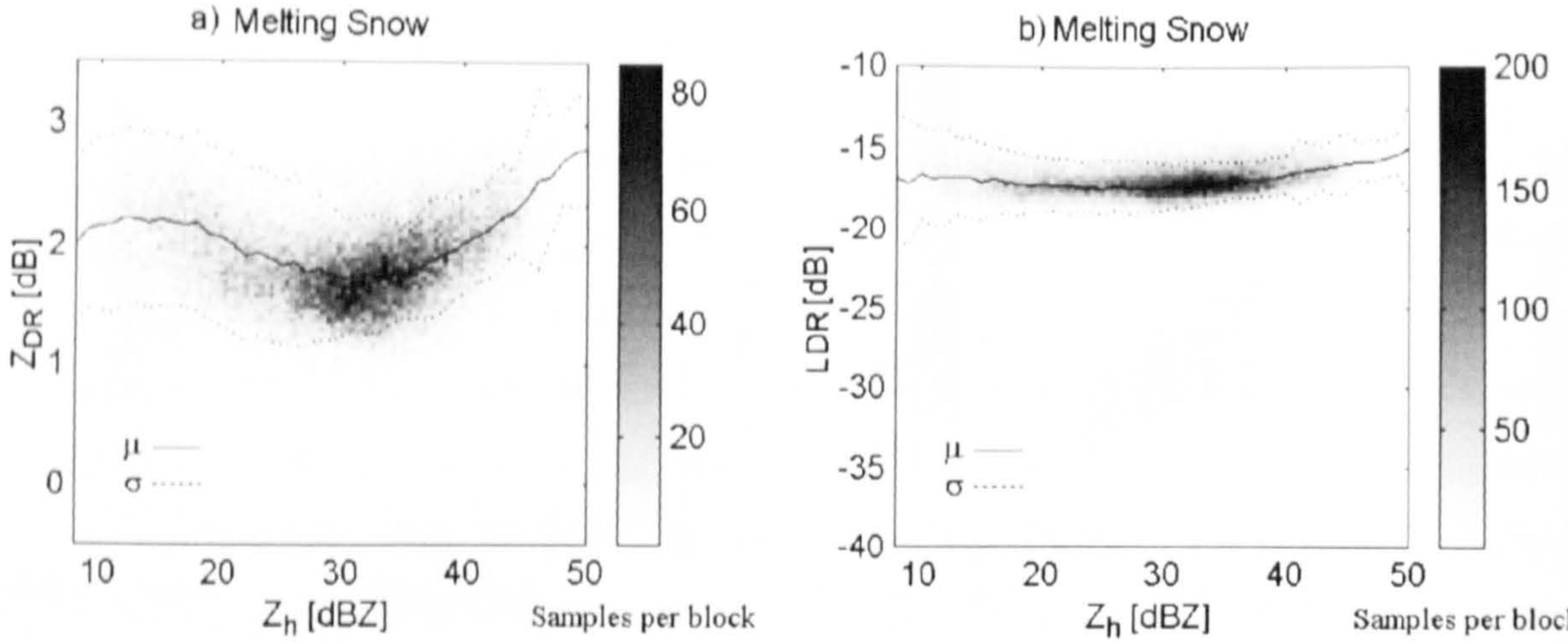

Fig. 6.28: Scatter plot between the horizontal reflectivity Z_h and the polarimetric variables Z_{dr} and LDR in the bright band at S-band frequencies.

Fig. 6.27b depicts the scatter plot between Z_{dr} at $h_{peak(Z_{dr})}$ in the bright band and the rain reflectivity below. This scatter plot presents an "U" shape, where Z_{dr} presents large values for low rain reflectivities, small values for intermediate rain reflectivities (20-30 dBZ) and large values again for high rain reflectivities. This may be well related to the descent of the Z_{dr} bright band signature, but it is not clear why the maximum value of Z_{dr} decreases its intensity during its descent.

On the other hand, the response of LDR to melting aggregates is quite remarkable. Melting snowflakes associated with the radar bright band produce a strong LDR signature (See Hopper et al., 1991; Herzegh and Jameson, 1992; Illingworth, 2003). The maximum value of LDR is almost at the height $h_{peak(Z_h)}$ for rain reflectivities less than 20 dBZ, but is always below $h_{peak(Z_h)}$ for rain reflectivities greater than 20 dBZ. According to Hagen et al. (1994) the maximum value of LDR is observed at higher altitudes than the maximum value of Z_{dr}, indicating that the melting particles are first tumbling and later fall horizontally oriented. The same effect is observed in this analysis, although is only valid for rain reflectivities above 20 dBZ, because for low rain reflectivities, the maxima of Z_h, Z_{dr} and LDR are approximately located at the same height and the thicknesses of their signatures have approximately the same depth.

Fig. 6.28 depicts the variation between the horizontal reflectivity and the polarimetric variables Z_{dr} and LDR in the melting layer. These scatter plots form the basis for melting snow classification in a two-dimensional space.

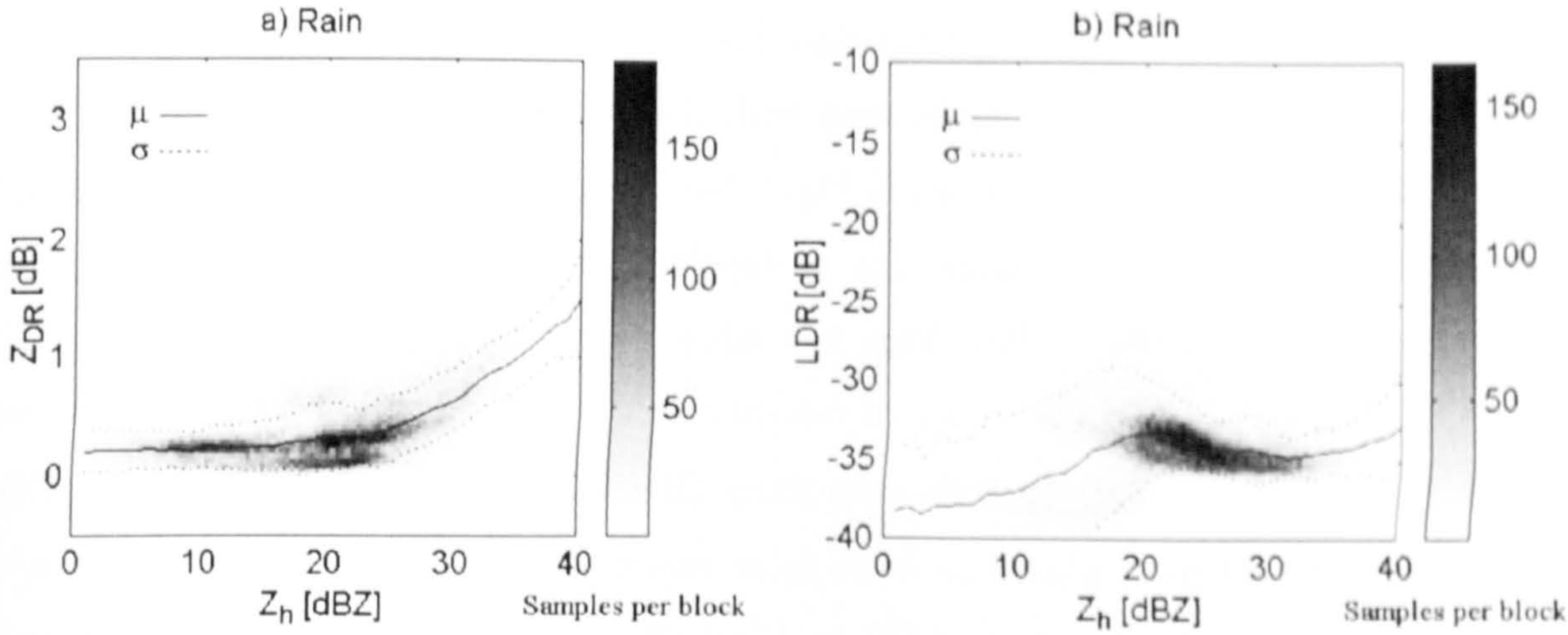

Fig. 6.29: Scatter plot of the differential reflectivity and the linear depolarisation ratio below the bright band against the rain reflectivity at S-band frequencies.

6.7.2 Dual-polarisation measurements from raindrops

Below the bright band, the differential reflectivity of raindrops increases with the rain reflectivity. This increase is more remarkable for rain reflectivities above 15 dBZ as shown in Figs. 6.25d and 6.26a-d. The scatter plot relating the differential reflectivity in rain to the rain reflectivity is shown in Fig. 6.29a. For rain reflectivities below 15 dBZ, the distribution of Z_{dr} is Gaussian with a mean of 0.23 dB and a standard deviation of 0.18 dB. These low values of Z_{dr} are typical for drizzle, where raindrops are almost spherical and Z_{dr} presents values very close to zero. For rain reflectivities greater than 15 dBZ, raindrops get more oblate and therefore the values of Z_{dr} become larger. A particular value of rain reflectivity Z_h has a wide spectrum of Z_{dr} values. Therefore, if the differential reflectivity is related to the mean volumetric diameter of raindrops (Seliga and Bringi, 1976), this can take a wide spectrum of values for one specific value of rain reflectivity and hence the drop size distribution will take a different shape. This has been one of the main problems in the estimation of rainfall rate using weather radars, because the same value of reflectivity can be obtained from different drop size distributions.

Bringi et al. (1991) modelled raindrops as oblate spheroids using a gamma drop size distribution (See Eq. 2.41) and assuming an empirical approximation for the shape of large raindrops as oblate spheroids with axis ratio given by:

$$a/b = 1.03 - 0.62D \tag{6.13}$$

where D is the diameter in cm of an equivalent spherical drop. They estimated the values of Z_{dr} and Z_h at S-band and C-band frequencies by varying the gamma parameters (N_o, D_o, μ) over a wide range of values covering a great diversity of rainfall types. They

obtained a scatter plot relating Z_h with Z_{dr}. The theoretical results that they obtained at S-band frequencies are in good agreement with the dual-polarisation radar observations obtained in this analysis and depicted in Fig. 6.29a (See also Fig. 1 in Bringi et al., 1991).

On the other hand, the scatter plot of depolarisation of raindrops against the rain reflectivity is shown in Fig. 6.29b. Very low values of depolarisation LDR ($<< -40$ dB) are associated with very small values of reflectivity Z_h (less than 15 dBZ). LDR is often limited to regions of relatively high reflectivity (Herzegh and Jameson, 1992) and LDR becomes significant only when the cross-polar power is above the noise level. In fact, the antenna limits the minimum LDR in Chilbolton to about -34 dB (Eastment and Illingworth, 1995). For reasons of analysis, the values of LDR have been set to -40 dB when is below the noise level of Chilbolton. Therefore the mean and standard deviation shown in Fig. 6.29b are more accurate for large values of reflectivity.

As the reflectivity increases, the values of LDR become significant, presenting values between -30 and -35 dB for reflectivities greater than 15 dBZ. These results suggest that the canting angle of oblate raindrops is small (high values of depolarisation represent heavy tumbling and canting) as shown with the theoretical results presented by Beard and Jameson (1983), who estimated that the mean canting of raindrops is Gaussian distributed with a mean of zero and a standard deviation of less than five degrees.

6.7.3 Dual-polarisation measurements from snowflakes

From to the top of the precipitation to the height of the bright band top there is a gradual increase in reflectivity (See Section 6.4.4), which is indicative of the growth of ice particles by aggregation forming large snowflakes. This process can also be observed in the vertical profiles of Z_h shown in Figs. 6.25a-d and 6.26a-d. However, the vertical profiles of Z_{dr} do not present any gradual increase and the values are very close to zero. The response of Z_{dr} for snowflakes is different from that for water, because not only the shapes of ice particles and water are different, but also the dielectric constant of the hydrometeors (Herzegh and Jameson, 1992). Therefore, the sensitivity of Z_{dr} to the shapes of snowflakes is very weak.

Fig. 6.30a shows the scatter plot between Z_h and Z_{dr} above the bright band. The Z_{dr} values are narrowly distributed between 0 and 1 dB. The values of Z_{dr} decrease considerably towards zero as the snow reflectivity increases. According to Battan (1973), snowflakes tend to be preferentially oriented, with their long dimensions mostly horizontal. The results shown in Fig. 6.30a suggest that there is certain degree of orientation for low values of reflectivity. However, as the rain reflectivity increases, Z_{dr} values are closer to zero, which suggests that the aggregation of ice particles makes them lose orientation and

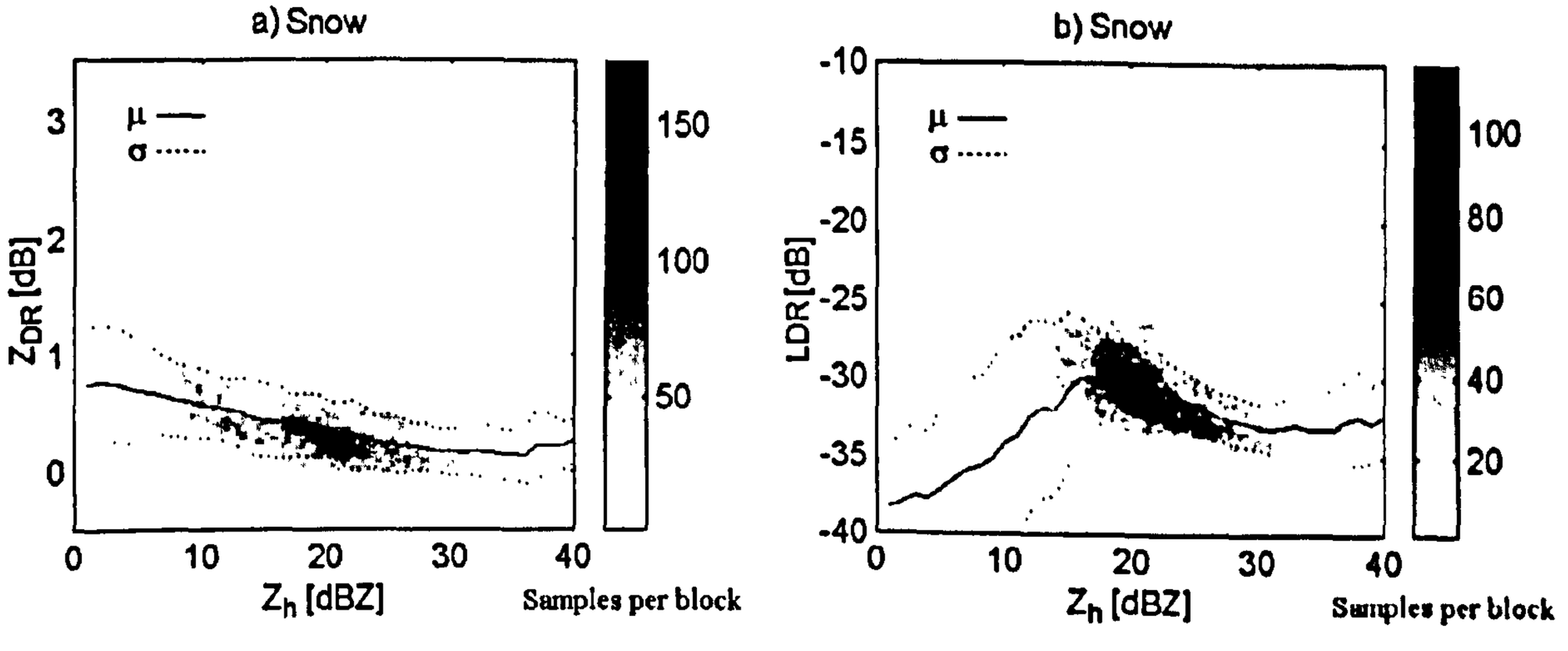

Fig. 6.30: a) Scatter plot between Z_h and Z_{dr} at the top of the bright band at S-band frequencies. b) Scatter plot between Z_h and LDR at the top of the bright band at S-band frequencies.

starting them to tumble during their descent and presenting very low values of Z_{dr}.

The scatter plot between LDR and Z_h above the bright band is shown in Fig. 6.30b. For low values of reflectivities, LDR is very small (less than -40 dB) and below the noise level as the case for very small raindrops. As the reflectivity increases, LDR is between -35 and -25 dB. The values of LDR in snow are slightly greater than in rain, but there is not a clear boundary between them (See Figs. 6.30b and 6.29b respectively).

LDR observations in rain and snow usually present small values, but they are clear indicators of melting. This parameter, in conjunction with Z_{dr} can provide indications of mixed-phase hydrometeors using dual-polarisation radar measurements. Taking advantage of this fact, it is possible to detect the bright band without the need of knowing the height of the melting level. With this, a correction algorithm can be applied to eliminate the increase in reflectivity due to melting snow, which affects the estimation of rainfall using weather radars.

6.8 Conclusions

The results obtained in this chapter can form the basis of a hydrometeor classification system. By classifying melting snowflakes is possible to apply a correction to estimate the expected reflectivity in rain from bright band contaminated reflectivity data. However, the spreading of the radar beam with range is an important point that must be taken into account. The results presented in this chapter represent measurements close to the radar with a very narrow beamwidth of 0.25° that for practical purposes, the spreading of the radar beam can be neglected at short ranges. However, when correcting scanning

weather radar measurements with conventional radars this effect must be considered and evaluated before any correction can be applied.

Chapter 7

Effects of beam spreading at long ranges

7.1 Introduction

The effect of the beamwidth at long ranges is an issue, which has not had much attention. This effect, after the variation of the vertical reflectivity profile of precipitation, is also an important factor that may influence the estimation of precipitation at long ranges using weather radars. This chapter describes the effect of beam spreading with range on weather radar measurements, in particular when polarimetric radar measurements are available.

7.2 The sampling theorem

The Vertical Reflectivity Profile (VRP) of precipitation ($Z(h)$) at some specific location can be represented by the sequence $z[n]$, with Fourier transform $Z(e^{j\omega})$ (See Section 4.3). If the VRP is obtained with a high-resolution Vertically Pointing weather Radar (VPR) and sampled along the vertical at a rate F_s, the frequency spectrum of $Z(e^{j\omega})$ is between the interval $[-F_s/2, F_s/2]$. However, as stated in Section 4.3, the VRP is a low-frequency signal, which is well reflected in its Fourier transform $Z(e^{j\omega})$. Therefore, the VRP has a range of important frequencies in the interval $[-F_{max}, F_{max}]$, where F_{max} is the highest frequency component of the continuous VRP. From the sampling theorem, the sampling rate has to be equal to or greater than twice the highest frequency component, that is:

$$F_s \geq 2F_{max} \tag{7.1}$$

Therefore, the VRP may be recovered always that the condition 7.1 is fulfilled. When this is not the case, the result is an overlapping of spectrums and the true VRP is lost due

to the incorrect selection of sampling frequency.

7.3 The antenna's radiation pattern

In the case of Range Height Indicator (RHI) scans, the radar sweeps from low-elevation angles, *e.g.* 0.5°, to around 30°. Therefore, the reflectivity signal obtained from an RHI scan is a function of the elevation angle θ and the range from the radar along the beam r, that is $Z(\theta, r)$. A similar reflectivity function can be obtained in Plan Position Indicator (PPI) scans, although in this scanning strategy the radar scans at different azimuths by keeping constant the elevation angle.

Assuming for instance that there are not large spatial variations of reflectivity along the range, it is possible to suggest that the VRP of precipitation at a range r_o from the radar can be well represented by the function $Z(\theta, r_o)$, which θ is varying from low elevation angles to elevations up to 30°. Therefore, there is a strong correlation between the profiles $Z(h)$ (obtained with a vertically pointing radar) and $Z(\theta, r_o)$ (extracted from an RHI scan), where h and θ are the independent variables respectively. The reflectivity profile $Z(\theta, r_o)$ depends exclusively on the dimensions of the volume of the radar beam illuminating the precipitating particles.

The two-way response of the beam power profile relative to the beam centre is given by (Brown et al., 1991):

$$P(\theta) = \left[\frac{sin(k\theta)}{k\theta}\right]^4 \tag{7.2}$$

where k depends on the beamwidth of the radar, *e.g.* $k = 159.46$ for 1° beamwidth (See Fig. 7.1). Divjak (1995) gives another approximation of the horizontally averaged two-way beam pattern based on an exponential function given by:

$$P(\theta) = \frac{1}{\theta_1\sqrt{\pi}} e^{-\theta^2/\theta_1^2} \tag{7.3}$$

where $\theta_1 = \theta_0/\sqrt{8ln2}$, being θ_0 the antenna beamwidth at half power. Eqs. 7.2 and 7.3 represent only approximations of the real antenna's radiation pattern, because in reality, it presents irregularities of considerable magnitude[1]. According to Hardaker (1993), Eq. 7.2 is more representative when comparing with the true antenna patterns of Plessey radars.

The averaged reflectivity factor weighted by the beam power profile and observed by the radar at some range and elevation angle is given by (adapted from Brown et al., 1991):

[1]The radome geometry and its framework shadowing contribute in some measure to the degradation of the antenna radiation pattern (http://www.radome.net/tl.html, http://www.afcsat.com).

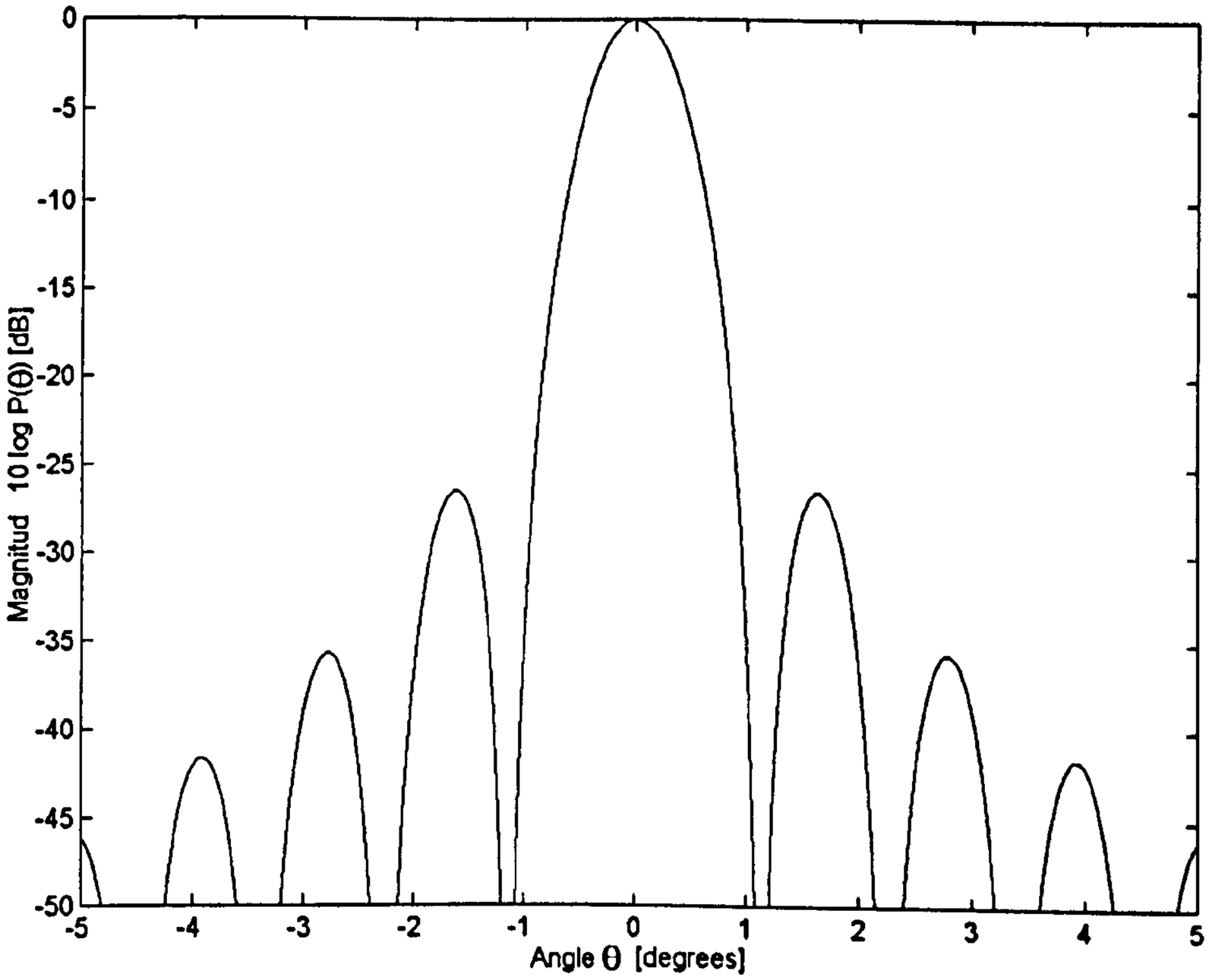

Fig. 7.1: Two-way response of antenna power pattern for a radar with a beamwidth of 1°.

$$Z_{ave}(\theta_i) = \int_{\theta_i - \tau/2}^{\theta_i + \tau/2} Z(\theta) f(\theta) d\theta \tag{7.4}$$

where θ_i is the elevation angle, τ is the half power beamwidth of the antenna, $Z(\theta)$ is the ideal reflectivity profile that can only be obtained with a very narrow beamwidth that its effects can be considered negligible and $f(\theta)d\theta$ is the fraction of the radar beam power in the range from θ to $\theta + d\theta$. This fraction is given by:

$$f(\theta)d\theta = P(\theta)d\theta / \int_{\theta_i - \tau/2}^{\theta_i + \tau/2} P(\theta)d\theta \tag{7.5}$$

where $P(\theta)$ is the beam power profile. Eq. 7.5 is considered negligible outside the range $\theta_i \pm \tau/2$. Eq. 7.4 indicates that the reflectivity measured by a weather radar involves all the reflectivities weighted by the beam power profile within the sampled volume. The most important of Eq. 7.4 is that the equivalent reflectivity measured by a radar is a direct convolution between the reflectivity profile $Z(\theta)$ and the beam power profile $P(\theta)$. This means that the beam acts as a filter and $Z_{ave}(\theta_i)$ is a filtered version of reflectivity.

The filtering characteristics of the beam radiation pattern depend on the range from the radar site to the precipitation measurements. At some range from the radar, the vertical depth in meters of the beam becomes increasingly large. Fig. 7.2 shows this effect, assuming standard propagation of the radar beam (Eq. 2.3).

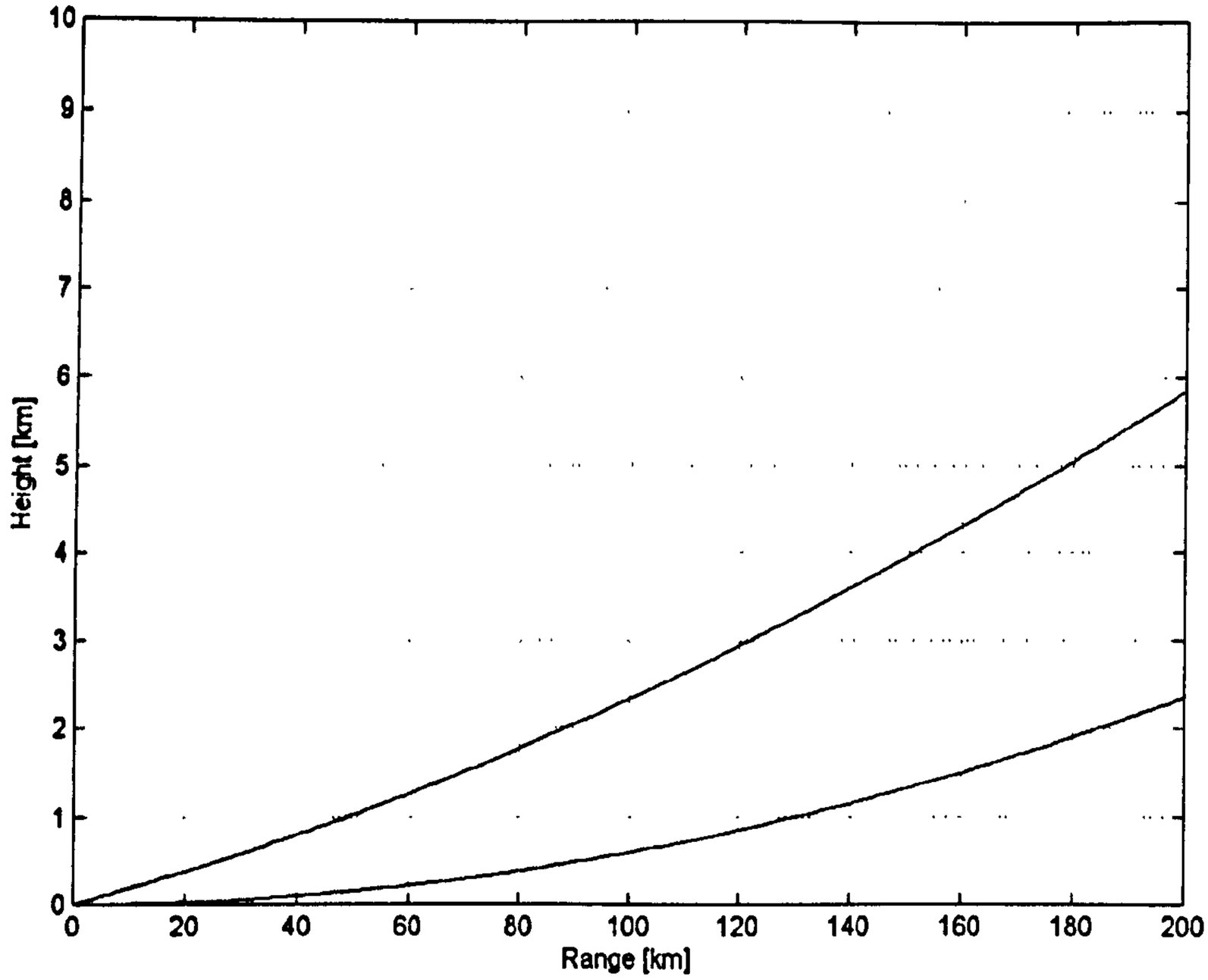

Fig. 7.2: Beam propagation through standard atmosphere (elevation 0.5° and beamwidth 1°).

As the range increases from the radar, the beamwidth is spread into a deeper distance along the vertical. Fig. 7.3 show this effect at 10 km, 30 km and 80 km from the radar site. It is interesting to note the effect of the antenna's radiation pattern in the frequency domain. In all the cases, the radiation pattern acts as a "low-pass filter", smoothing the natural variation of the vertical reflectivity profile. The characteristics of this filtering effect depend on the range where the measurement takes place. At shorter ranges from the radar, the filter has a wide pass-band, but as the range increases the pass-band becomes narrower (Compare Figs. 7.3a and 7.3c for 10 km and 80 km from the radar site respectively; in both cases $P(e^{j\omega})$ is the Discrete Fourier Transform (DFT) of the beam power profile $p[n]$). The effect is a decrease of the cut-off frequency of the filtering characteristics of the beam radiation pattern as the range increases from the radar.

Fig. 7.4 shows a plot of the normalised cut-off frequencies as a function of range of the frequency response of the beam radiation pattern for 1° and 0.25° beamwidths. It is interesting to note that there is a logarithmic decrease of the cut-off frequency of the "low-pass filtering" characteristics caused by the effect of the beam radiation pattern as the range increases from the radar.

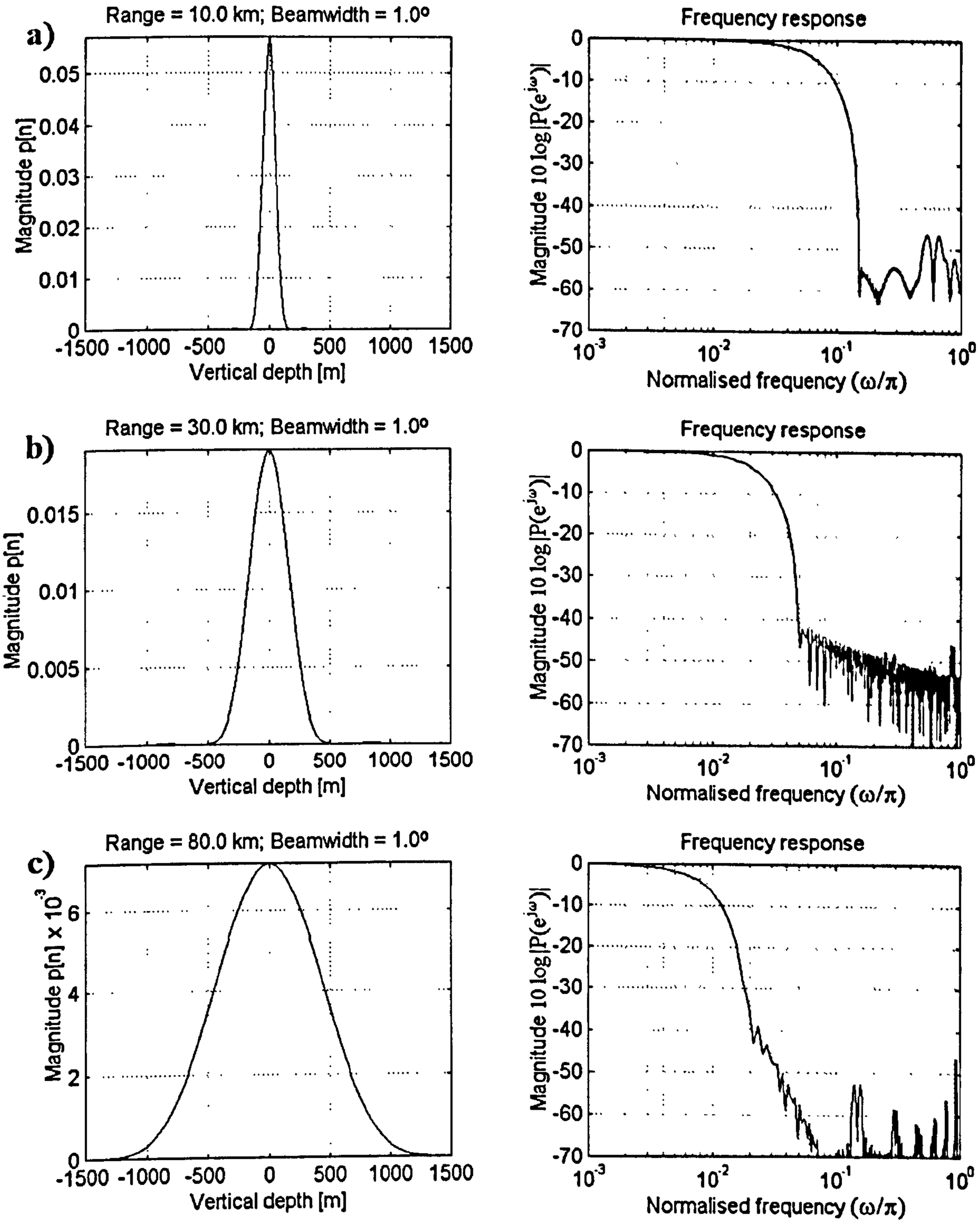

Fig. 7.3: Two-way response of antenna power pattern and its frequency response using the DFT, assuming a window of 3 km at a) 10 km, b) 30 km and c) 80 km from the radar. (The antenna power pattern has been sampled every 7.5 m in the vertical with respect to the beam centre, assuming 1 ° beamwidth and 0.5 ° elevation angle).

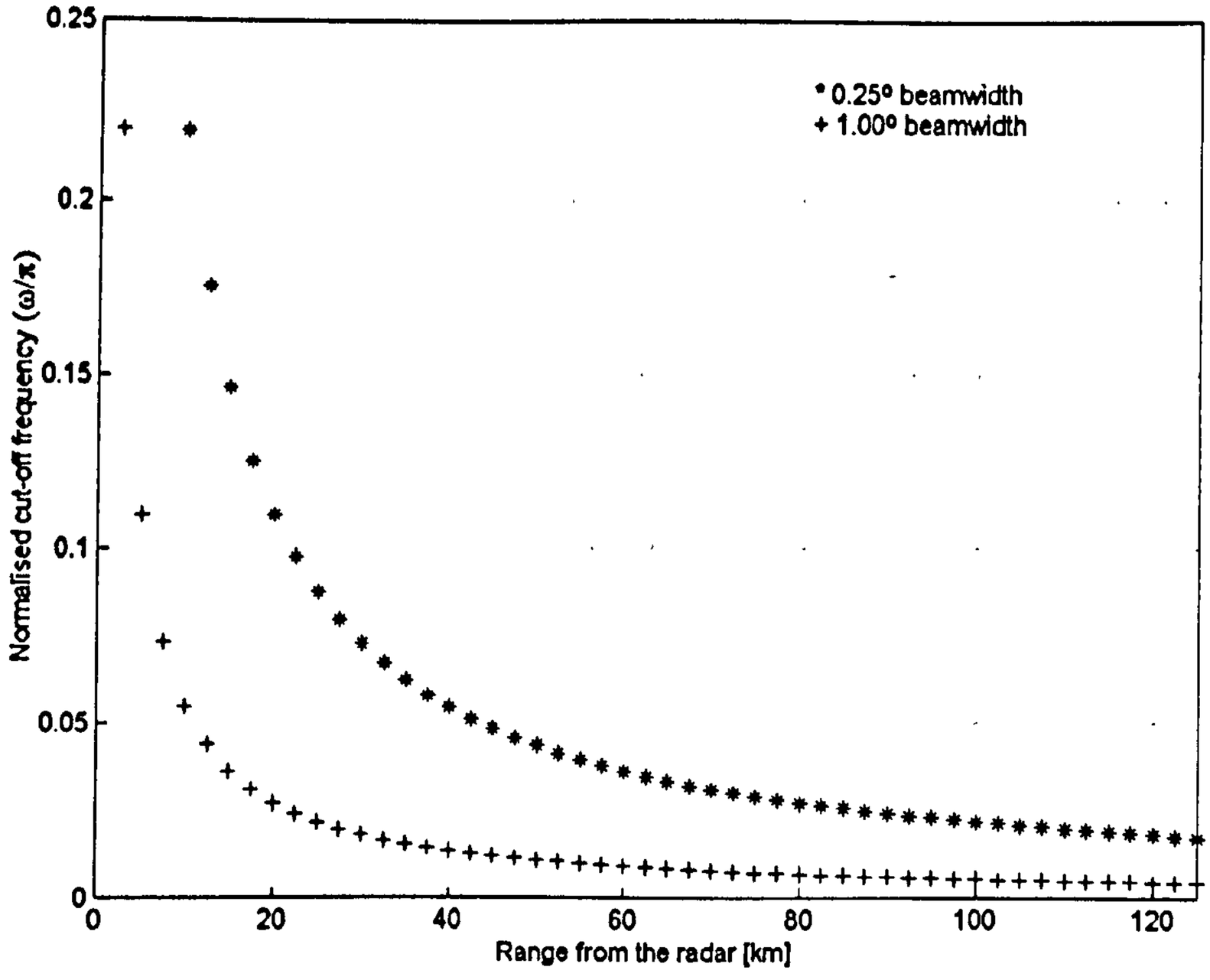

Fig. 7.4: Normalised cut-off frequencies at -3 dB points of the frequency response of the low-pass filtering characteristics of the two-way response of the antenna power pattern as a function of range.

In order to establish whether or not the frequency response of the low-pass filter affects the VRP of precipitation, it is necessary to know the frequency response of the VRP. From the results obtained in Section 4.3, the VRP is a low-frequency signal. The maximal frequency component (F_{max}) of the VRP during stratiform and stratiform-convective precipitation is $\omega_c/\pi = 0.1$ (the frequency is normalised to 1, being 1 half of the sampling frequency and the VRP has been sampled every 7.5 m in the vertical). This means that the VRP has a maximal sinusoidal component varying within 150 m. Faster variations can be considered noise in the VRP. These results were obtained using a high-resolution vertical pointing radar. Therefore, any low-pass filter applied to a signal with such characteristics should have a cut-off frequency greater or equal to 0.1, otherwise important frequency components will be lost. If the beam radiation pattern acts as a low-pass filter when receiving precipitation echoes, this filter should also have a cut-off frequency greater or equal than 0.1. For instance, returning to Fig. 7.4, a radar with a beamwidth of 0.25° (as the case of the Chilbolton weather radar, See Goddard et al., 1994), has an effective range of around 25 km without losing the highest frequency components involved in the natural variation of the VRP of precipitation. However, a radar with a beamwidth of 1° (as the case of the UK weather radars and most of the weather radars in the world) has an

effective range less than 10 km. This does not mean that beyond 10 km the data obtained are not useful, but this means that beyond 10 km the reflectivity obtained by the radar will be affected to some extent by the smoothing effect of the beam radiation pattern.

There are techniques for digital image restoration, where an acquired image (whichever the source of) has been affected or degraded due to effects of the sensors (antenna) and the noise of the system (See Andrews and Hunt, 1977; Rico-Ramirez, 2000). However, any restoration algorithm is only valid when the signal has been sampled at least twice the highest frequency component, that is, the sampling theorem has been fulfilled. In this case, the filter effect of the beam radiation pattern has a large impact on the VRP causing an overlapping of spectrums in the frequency domain. Therefore, rather than trying to correct for the effect of the low-pass filtering characteristics of the beam radiation pattern, it is more convenient to evaluate its impact more directly on the weather radar measurements.

7.4 Simulations of the effect of a one-degree beamwidth

The impact of the beam radiation pattern is simulated taking into account typical functions of vertical reflectivity profiles (Z_h) in stratiform precipitation. The reflectivity profiles have been obtained in Chapter 6 at different rain reflectivities. In addition, the effects of the beam radiation pattern on the polarimetric variables are also simulated using typical vertical profiles of Z_{dr} and LDR.

The aim is to convolve the beam radiation pattern with the vertical profiles of Z_h, Z_{dr} and LDR at different ranges from the radar. Vertical profiles with six different rain reflectivities: 15 dBZ, 20 dBZ, 25 dBZ, 30 dBZ, 35 dBZ and 40 dBZ were chosen. The convolution with the beam radiation pattern has been simulated at 10 km, 30 km and 80 km ranges from the radar site. The beamwidth of the radar has been fixed at 1°, which complies with the beamwidth of most weather radars in the world. The results are shown in Figs. 7.5, 7.6 and 7.7.

The most remarkable effect in all the results is that the beam radiation pattern does not affect at all either the reflectivity profile Z_h or the polarimetric variables Z_{dr} and LDR in the rain and snow regions. This is due to the fact that there are not high frequency fluctuations of reflectivity Z_h and the polarimetric variables Z_{dr} and LDR above and below the bright band. Therefore any echo in these regions represent accurately that part of the vertical profiles of Z_h, Z_{dr} and LDR. However, Z_h in the bright band, presents a reduction of enhancement in the medium range (around 30 km) and the total extinction of the bright band signature at long ranges (farther than 80 km). In the medium range is where most

weather radars struggle with the bright band enhancement. This obviously depends on the height of the bright band and there is a seasonal dependency (See Chapters 5 and 6). In addition, the filtering characteristics of the beam radiation pattern increase the depth of the bright band in proportion to the beamwidth.

The smoothing effect on the Z_{dr} signature in the bright band is similar to that in Z_h. In the medium range (around 30 km) the Z_{dr} signature in the bright band is reduced in intensity, but at long ranges (farther than 80 km) disappears completely. It is interesting to note that for rain reflectivities greater than 35 dBZ, the Z_{dr} signature in the bright band is a smooth transition between snow and rain (See Figs. 7.7a-b for Z_{dr}). This is mainly due to the fact that Z_{dr} in rain has much larger values than in snow when the rain reflectivity exceeds 35 dBZ due to oblate raindrops.

The smoothing effect on LDR in the bright band is not as remarkable as in Z_h and Z_{dr} for high rain reflectivities. The reason of this is that melting snowflakes have quite remarkable depolarization characteristics. For instance, at high rain reflectivities (greater than 30 dBZ) even at long ranges (around 80 km) the LDR signature represents the enhancement due to the large depolarization of melting snowflakes (See Figs. 7.7a-b for LDR).

However, at low rain reflectivities (less than 20 dBZ) the analysis of the linear depolarization ratio turns out to be incorrect. In reality, the behavior of LDR at low rain reflectivities is slightly different. In Chapter 6, it has been stated that when low rain reflectivities are involved, the depolarization is so small that it is impossible to measure it. For reasons of analysis, the lowest depolarization has been set to -40 dB, although the antenna limits the minimum LDR to about -35 dB (Eastment and Illingworth, 1995). Therefore, when low rain reflectivities are involved at far ranges, LDR in the bright band disappears because the radar beam may cover either part of the rain or snow or both and because their respective depolarizations are very small ($<< -40$ dB), the total effect is the extinction of LDR in the bright band.

7.5 Conclusions

The effect of the beamwidth is to smooth the vertical reflectivity profile of precipitation. It resembles a low-pass filter, smoothing the high-frequency fluctuations of the vertical reflectivity profile. This filter has a variable cut-off frequency, which decreases as the range increases from the radar. This means, that measurements taken far from the radar suffer more smoothing than the closer ones. In stratiform precipitation, the effect of the

beamwidth is very remarkable in the bright band. At far ranges (more than 80 km), the enhancement of reflectivity caused by melting snowflakes is smoothed and eliminated by the effect of the beamwidth (assuming one-degree beamwidth). However, the problem at these ranges is that the radar beam is intercepting snow rather than rain, which will cause underestimates of rainfall rates when applying the conventional Marshall and Palmer relationship. On the other hand, the effect of the beamwidth on the bright band in the medium range (less than 80 km) is a big problem in the estimation of precipitation using weather radars. This is because the enhancement of reflectivity is reduced depending on how far the measurement is from the radar site. At the same time, the bright band increases its thickness in proportion to the depth of the beamwidth at that range.

In addition, the polarimetric variables Z_{dr} and LDR are also affected by the beamwidth. At far ranges from the radar (more than 80 km) the bright band signature in Z_{dr} disappears completely. When high rain reflectivities are involved at these ranges, the result is a smooth transition from small values of Z_{dr}, which are due to tumbling snowflakes, to large values of Z_{dr}, which are due to oblate raindrops. The bright band signature is no longer available at these ranges, but the transition between snow and rain is clearly discernible (See Figs. 7.7a-b for Z_{dr}).

It is clear that the bright band enhancement at far ranges (more than 80 km) is not a big problem. At these ranges the bright band is eliminated by the effect of the beamwidth. However, at these ranges the estimation of precipitation is affected by the snow particles illuminating the radar beam. For ranges less than 80 km, the bright band affects the estimation of precipitation depending on its enhancement and thickness as well as the beamwidth of the radar and the range of the measurement from the radar site.

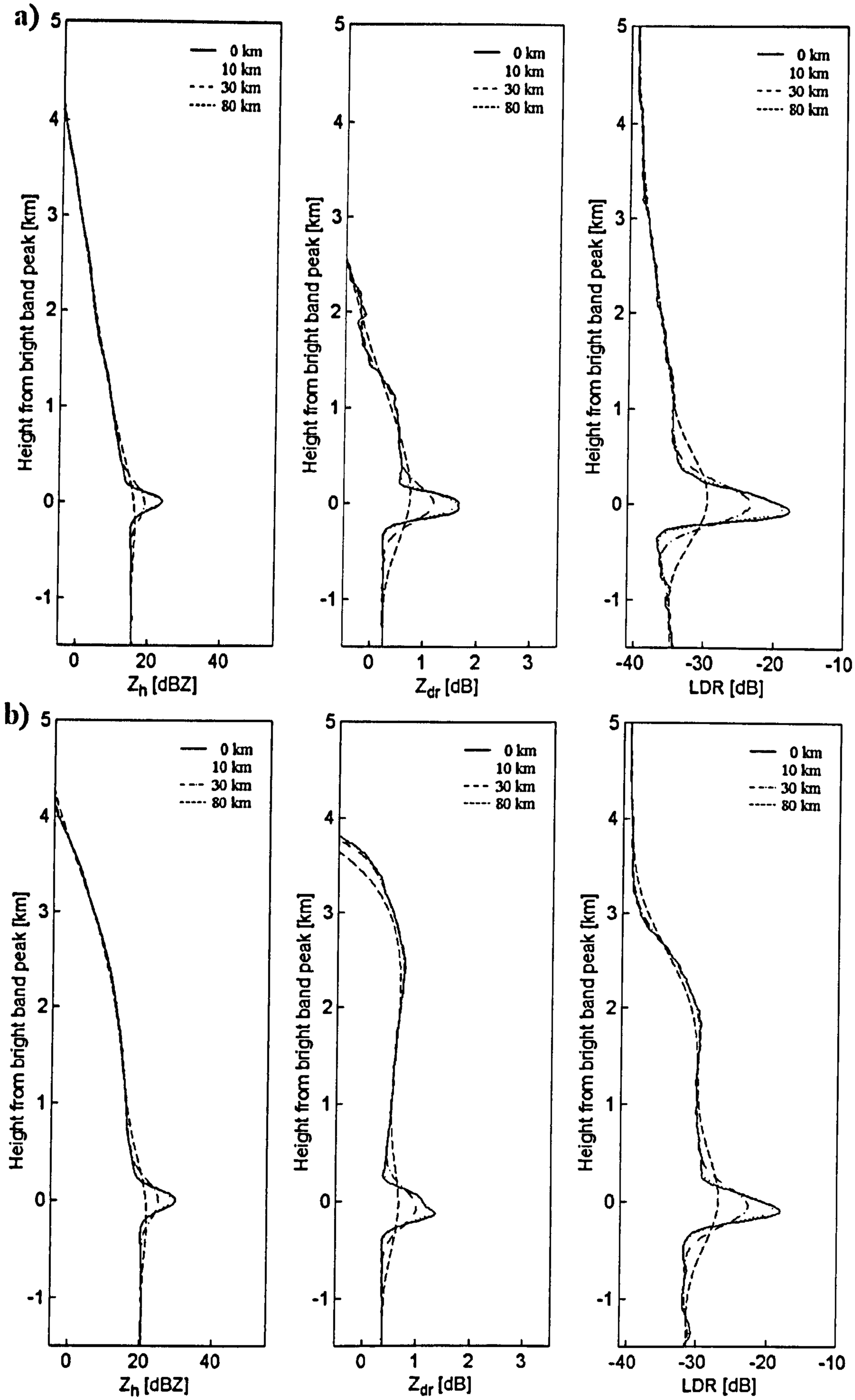

Fig. 7.5: Smoothing effect of a 1° beamwidth on vertical profiles of Z_h, Z_{dr} and LDR in stratiform precipitation at different ranges from the radar. $Z_h(h_{rain})$ = a) 15 dBZ and b) 20 dBZ.

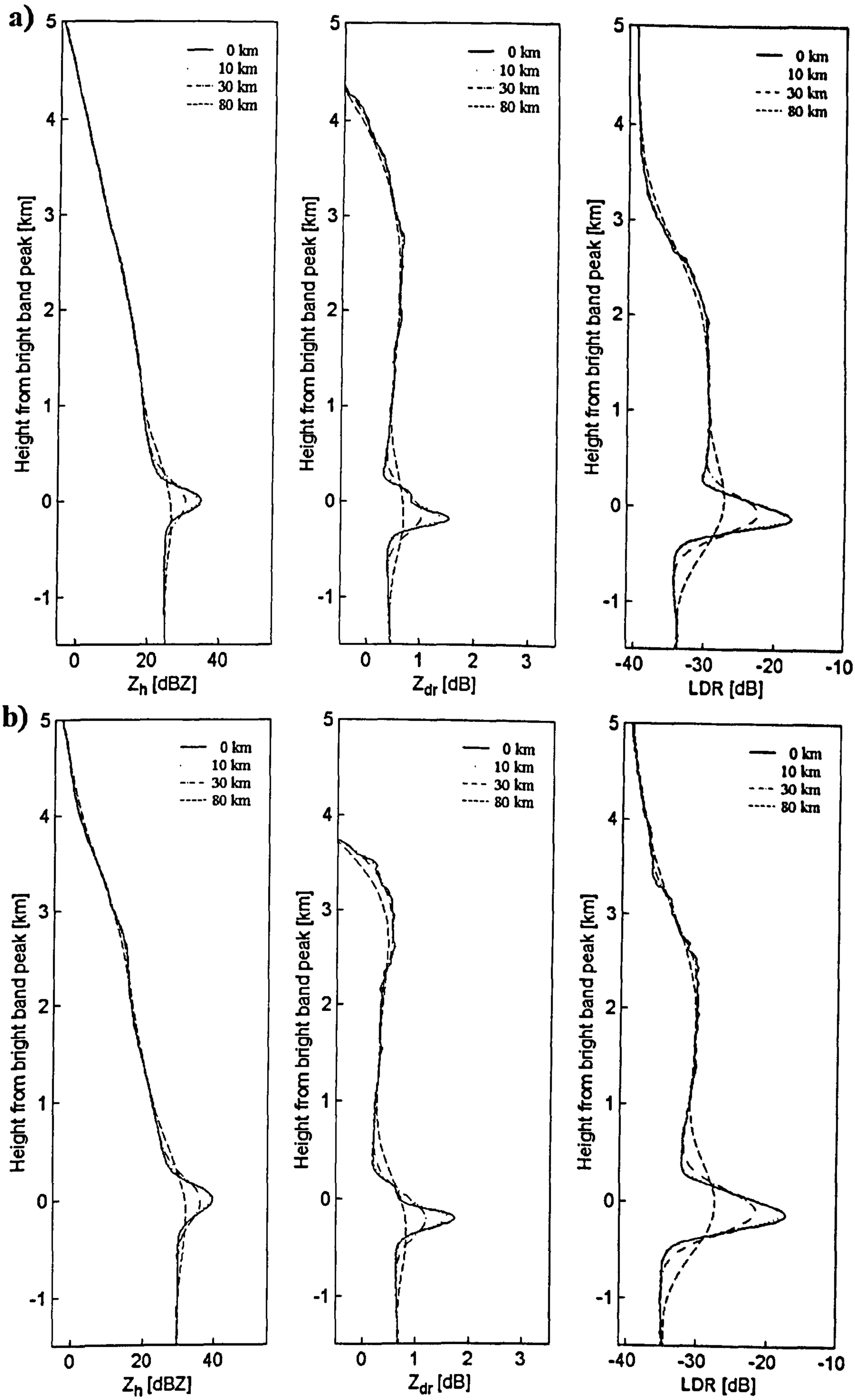

Fig. 7.6: Smoothing effect of a 1 ° beamwidth on vertical profiles of Z_h, Z_{dr} and LDR in stratiform precipitation at different ranges from the radar. $Z_h(h_{rain})$ = a) 25 dBZ and b) 30 dBZ.

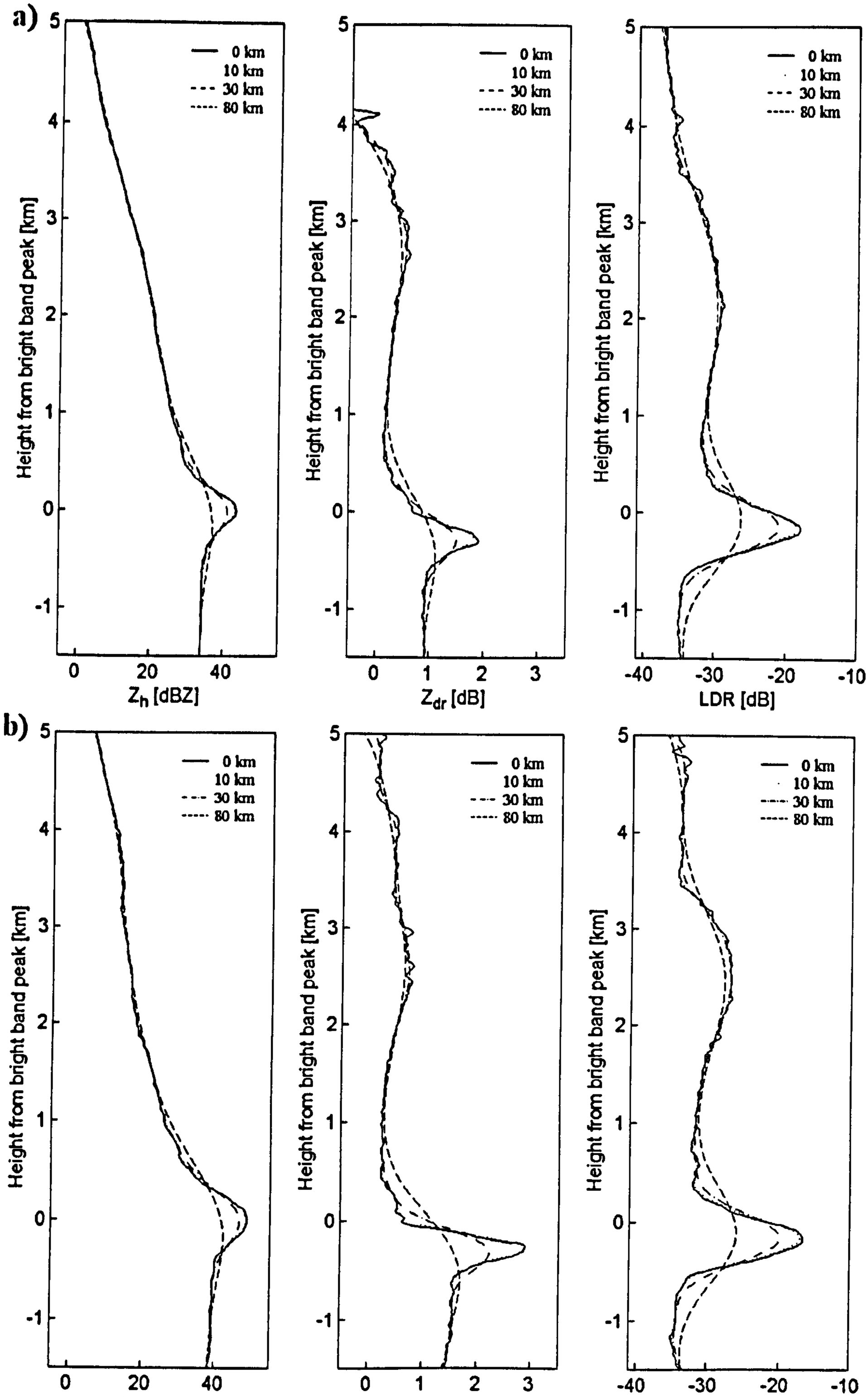

Fig. 7.7: Smoothing effect of a 1° beamwidth on vertical profiles of Z_h, Z_{dr} and LDR in stratiform precipitation at different ranges from the radar. $Z_h(h_{rain})$ = a) 35 dBZ and b) 40 dBZ.

Chapter 8

Fuzzy logic system to classify hydrometeors

8.1 Introduction

A fundamental prerequisite for accurate estimation of precipitation amount using weather radars is knowing what precipitation type is reaching the ground (Zrnić et al., 2001). Weather radars with dual-polarisation capability allow measurements of hydrometeors characteristics such as size, shape, spatial orientation and discrimination of thermodynamic phase (Doviak and Zrnić, 1993). There are several schemes developed to classify hydrometeors. According to Liu and Chandrasekar (2000) the potential techniques that can be used for automatic hydrometeor classification are the decision tree method, classic statistical decision theory, neural network techniques and fuzzy logic. The decision tree method has predefined boundaries or thresholds to discriminate between the different hydrometeors. There is a fair amount of overlap between polarimetric observables for different precipitation types and therefore the use of predefined boundaries can lead to misclassification of hydrometeors (Vivekanandan et al., 1999). Doviak and Zrnić (1993), Straka and Zrnić (1993), Holler et al. (1994), Hagen et al. (1995) and Zeng et al. (2001) used decision tree methods to classify hydrometeors. In statistical decision theory, the probabilities of detection and false alarm have to be established, but the major drawback is the prior knowledge of the joint probability distribution of polarimetric variables being measured (Zrnić, 1995). Neural network techniques require a considerable number of training sets to tune the network, which are often not available. For instance, Da Silveira and Holt (2001) proposed a neural network method to classify clutter and precipitation, based on the use of circular polarisation parameters such as the circular depolarisation

ratio (CDR) and the degree of polarisation (p). On the other hand, the values of the polarimetric radar observables that delineate different types of particles overlap and they are not well defined as it is assumed with decision tree methods. Therefore, the problem is suitable for fuzzy logic classifiers. In addition, a Fuzzy Logic System (FLS) handles uncertainty in a very natural way (Mendel, 1995). Zrnić and Ryzhkov (1999), Vivekanandan et al. (1999), Liu and Chandrasekar (2000) and Zrnić et al. (2001) used FLS to classify hydrometeors. Both, decision tree methods and fuzzy logic classifiers have been widely utilised to classify hydrometeors and therefore, the following paragraphs explain briefly the different systems employed up to date to classify hydrometeors.

Doviak and Zrnić (1993) proposed a range of values that polarimetric variables as the reflectivity factor (Z_h), the differential reflectivity (Z_{dr}), the correlation coefficient ($\rho_{hv}(0)$), the specific differential phase (K_{DP}) and the linear depolarisation ratio (LDR) are likely to have from different forms of precipitation. They stated that although the proposed range of values come from modelling, measurements and experience, much more modelling and verification has to be done before the full potential of dual-polarisation can be achieved.

The scheme developed by Straka and Zrnić (1993) is based on the spaces $Z_h - Z_{dr}$, $Z_h - K_{DP}$, $Z_h -$ LDR and $Z_h - \rho_{hv}(0)$. This boolean decision logic is utilised to classify ten different classes of hydrometeors (drizzle, rain, dry snow, dense snow, wet snow, dry graupel, wet graupel, small hail, rain/hail and large hail). This scheme is important and has been the departure point for different hydrometeor classification algorithms based on fuzzy logic.

Holler et al. (1994) studied hailstorm processes in a convective storm using multiparameter radar observations. They developed a hydrometeor classification scheme based on Z_{dr} and LDR excluding Z_h because of its strong dependence on maximum particle size as well as particle concentration. In addition, they used the height of the freezing level to distinguish between snow and rain. They stated that this hydrometeor classification scheme is somewhat empirical and needs to be confirmed by further numerical and observational studies.

Hagen et al. (1995) developed a classification scheme for rain, graupel and melting aggregates using a two-dimensional parameter space between the polarimetric variables Z_{dr} and LDR. They supported the radar observations with in-situ measurements of 2D optical and precipitation probes. There are clear overlapping areas among rain, graupel and melting aggregates in the two-dimensional $Z_{dr} -$ LDR space. They concluded that rain or snow is not always easy to discriminate. In addition, they stated that additional or

redundant information could be gained using K_{DP} and $\rho_{hv}(0)$, pointing out that additional parameters could introduce additional error sources into the hydrometeor classifier.

Zeng et al. (2001) developed a simple hydrometeor identification algorithm based on Z_h, Z_{dr} and LDR to classify regions within the rain and snow portions of the storm volumes that included hail, graupel and supercooled rain. In this algorithm, the classification of rain and snow is strongly dependent on temperature.

Vivekanandan et al. (1999) developed a fuzzy logic algorithm for hydrometeor particle identification. They stated that in a fuzzy logic-based approach there is a smooth transition in the boundaries of the polarimetric radar measurements among different types of hydrometeors. They constructed two-dimensional membership functions in the spaces $Z_h - Z_{dr}$, $Z_h - K_{DP}$, $Z_h -$ LDR and $Z_h - \rho_{hv}(0)$. In order to make easier the implementation of the membership functions in a fuzzy-logic based system, the two-dimensional functions were decomposed into several one-dimensional membership functions depending on the value of the reflectivity Z_h. In addition, the temperature (T) and the reflectivity (Z_h) are also one-dimensional membership functions. Therefore, in this fuzzy logic system, there are six different observations (Z_h, Z_{dr}, K_{DP}, LDR, $\rho_{hv}(0)$ and T), which are fuzzified using the corresponding one-dimensional membership functions. The results of the fuzzifications are weighted depending on the general accuracy of the variable (the weights for Z_h, Z_{dr} and T were set twice the weights for the rest of the variables). The six weighted results were summed to produce a single aggregated value for each of the fifteen different hydrometeors (cloud drops, drizzle, light rain, moderate rain, heavy rain, hail, rain/hail, graupel/small hail, dry snow, wet snow, ice crystals, irregular ice crystals, supercooled liquid droplets and insects). One important parameter in this classification scheme is the temperature profile, which is not available in real-time at every point of a radar scan. For instance, the hydrometeors with small values of reflectivity above the freezing level were classified as dry snow, ice crystals or supercooled liquid droplets whereas that below the freezing level were classified as drizzle or cloud drops. Thus, this fuzzy logic scheme is strongly dependent on the temperature profile and care should be taken when this parameter is not available.

Another fuzzy logic system based on polarimetric radar measurements to classify hydrometeors was proposed by Liu and Chandrasekar (2000). They combined a fuzzy logic system to infer hydrometeor types and a neural network for automatic adjustment of the parameters of the fuzzy logic system as new in-situ measurements become available. The system receives five polarimetric radar measurements (Z_h, Z_{dr}, K_{DP}, $\rho_{hv}(0)$, LDR) and one additional parameter to indicate the altitude of the measurement. The membership

function for Z_{dr} in rain is constructed from a two-dimensional membership function between Z_h and Z_{dr} assuming a given value of Z_h. The output of the fuzzy logic system produces ten different hydrometeor types for Summer storms (drizzle, rain, low density dry ice, high density dry ice, wet ice crystals, dry graupel, wet graupel, small hail, large hail and rain/hail) and five different hydrometeor types for Winter storms (drizzle, rain, dry snow, oriented ice crystal and wet snow).

Straka et al. (2000) compiled a considerable number of observational and modelling studies to deduce the dominant polarimetric data signatures for different type of hydrometeors. With this information, a fuzzy logic-based hydrometeor classification system was built and the results and sensitivity tests of the polarimetric radar measurables are described in Zrnić et al. (2001). The FLS described by Zrnić et al. (2001) uses two-dimensional functions in the space of Z_h and any polarimetric variable (Z_{dr}, K_{DP}, LDR and $\rho_{hv}(0)$) to classify eleven hydrometeor classes (light rain, moderate rain, heavy rain, rain dominated by large drops, rain/hail mixture, graupel/small hail, hail, dry snow, wet snow, horizontally oriented ice crystals and vertically oriented ice crystals). The system also uses the vertical temperature profile (T) obtained from a proximity sounding. Straka et al. (2000) argued that the use of temperature is important in minimizing some unreasonable ambiguities; for instance, neither rain would be expected at $-30\,°C$ nor ice crystals at $15\,°C$. The results obtained by Zrnić et al. (2001) reveal that the combination of the reflectivity factor and the differential reflectivity have the strongest discriminating power in the fuzzy logic-based hydrometeor classifier. In addition, the temperature profile plays an important role eliminating a substantial number of spurious errors, but without it the classification results are not far from the results obtained by adding this parameter.

As presented in this section, there are several approaches dealing with FLS to classify hydrometeors and although most of them include melting snowflakes in their classification, there is a lack of in-situ measurements to refine the system. Straka et al. (2000) stated that it is very difficult to obtain comprehensive in-situ measurements of different types of hydrometeors and amounts in order to validate the polarimetric radar data. With the exception from disdrometer measurements at the ground, there are some in-situ measurements with aircraft, but they have limited temporal and spatial resolutions. The study of the radar bright band in Chapter 6 at orthogonal polarisations and S-band frequencies has provided important characteristics of the polarimetric radar measurements (Z_{dr} and LDR) above, within and below the melting layer. Taking into account all these results, a simple method has been proposed to define the membership functions of the FLS, whose values are the degree to which a given variable is a member of a fuzzy set such as rain,

snow and melting snow. The FLS to classify hydrometeors is described in the following sections. A simple algorithm to correct for the increase in reflectivity in the melting layer is proposed, which uses the output of the FLS to start the correction.

8.2 Description of the FLS to classify hydrometeors

A fuzzy logic system is a non-linear mapping of an input space into an output space (Mendel, 1995). The fuzzy sets have been proposed as a faster and cheaper method to model human reasoning. Fuzzy logic is tolerant of imprecise data. Fuzziness is concerned with the lack of predefined boundaries of the set of objects to which some symbol refers. This reflects linguistic imprecision and a degree of uncertainty. Mendel (1995) remarks that a fuzzy logic system is able to handle uncertainty in a very natural way, because it is embedded in the framework of the system. The conventional boolean logic is either 0 or 1, while the fuzzy principle establishes that everything is a matter of degree and the values can go from 0 to 1.

The FLS uses expert knowledge to build the system and therefore is an expert system. This type of system is capable of resolving problems that require human experience. The FLS has four components: fuzzifier, rules, inference engine and defuzzifier (Mendel, 1995). The *fuzzifier* maps the precise measurements into fuzzy sets. *Rules* are provided by experts or extracted from numerical data. The rule base contains all possible fuzzy relations between input and outputs. They are expressed in the form of IF-THEN statements. The way in which the rules are combined is handled by the *inference engine*. The inference engine takes into account all the rules and transform a set of inputs to corresponding outputs. The *defuzzifier* converts the resulting fuzzy outputs from the fuzzy inference engine into precise numbers.

Fig. 8.1 depicts a block diagram of the FLS to classify hydrometeors. The FLS receives four input measurements: the conventional reflectivity factor (Z_h), the differential reflectivity (Z_{dr}), the linear depolarisation ratio (LDR) and the height of the hydrometeor (H_o). The output gives any of the three different hydrometeor types: rain (subdivided in drizzle, moderate rain and heavy rain), snow and melting snow. The four input measurements are fuzzified by using membership functions. The main element in the fuzzifier system is the membership function and it can be defined by:

$$\mu_A(x) : U \rightarrow [0, 1] \tag{8.1}$$

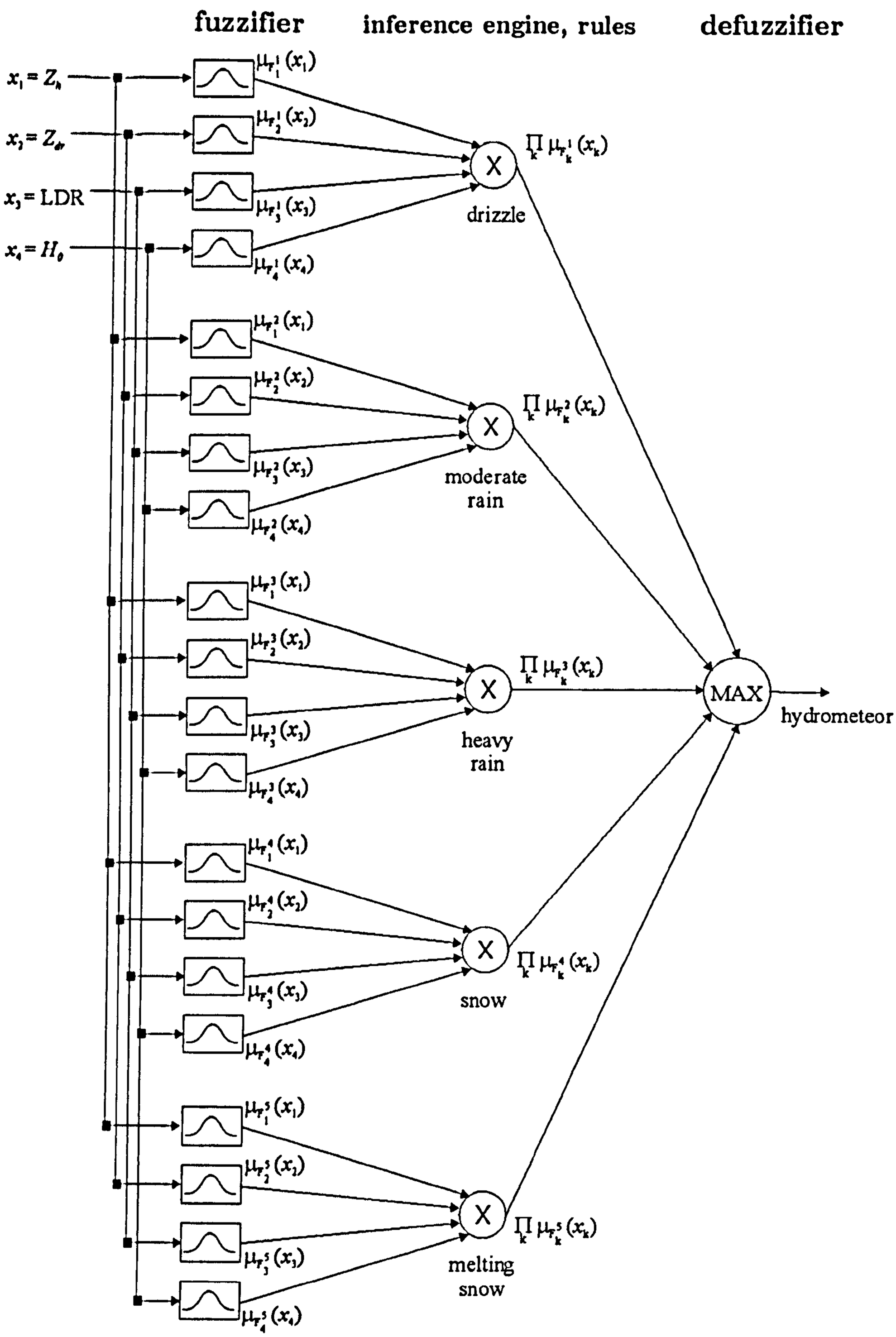

Fig. 8.1: A fuzzy logic system to classify hydrometeors (After Liu and Chandrasekar, 2000).

This function represents a specific fuzzy set A, of a universe U with a continuous function in the interval from 0 to 1. From Fig. 8.1, the membership functions for Z_h, Z_{dr}, LDR and H_o are $\mu_{F_1^r}(x)$, $\mu_{F_2^r}(x)$, $\mu_{F_3^r}(x)$ and $\mu_{F_4^r}(x)$ respectively, where $r = 1$ in drizzle, $r = 2$ in moderate rain, $r = 3$ in heavy rain, $r = 4$ in snow and $r = 5$ in melting snow. For instance, drizzle is very light rain composed of small sphericals raindrops, which present values of Z_{dr} very close to zero. This membership function may be well represented as a Gaussian function with mean 0 and standard deviation of a few tenths of dB. However, according to Liu and Chandrasekar (2000), the specification of the membership functions is a critical point in the classification performance. Therefore, it is necessary to analyse the Z_{dr} signature for a set of small spherical raindrops in order to specify the shape of the membership function.

The problem in obtaining this knowledge is the lack of in-situ measurements of different types of hydrometeors. The method proposed here, makes use of the bright band detection algorithm developed in Chapter 4, which has been applied to a considerable amount of S-band vertical reflectivity profiles with bright band. This analysis has been carried out in Chapter 6. From this analysis, the $Z_h - Z_{dr}$ and $Z_h -$ LDR spaces for rain, snow and melting snow are constructed and shown in Figs. 8.2 and 8.3 respectively (From Figs. 6.28, 6.29 and 6.30).

There is a large overlapping region in the $Z_h - Z_{dr}$ space between rain and snow for $Z_h < 30$ dBZ. This represents a serious problem in classifying either rain or snow using only these variables. On the other hand, for heavy precipitation ($Z_h > 38$ dBZ) the overlapping region is between rain and melting snow. Although there is a lack of polarimetric radar data for rain reflectivities greater than 40 dBZ, it is relatively easy to follow the trend for the classification of rain. The same applies for snow ($Z_h > 40$ dBZ) and for melting snow ($Z_h < 8$ dBZ).

In the $Z_h -$ LDR space there is also a very large overlapping region between rain and snow and it is clearly discernible that LDR does not make a clear distinction between rain and snow. However, the classification of melting snow does not present any overlapping region and therefore LDR is a clear indicator of the bright band.

For a given value of reflectivity, the two-dimensional spaces ($Z_h - Z_{dr}$ and $Z_h -$ LDR) for rain, snow and melting snow are decomposed into six different Gaussian membership functions for Z_{dr} and LDR in rain, snow and melting snow. The membership functions for Z_{dr} in drizzle, moderate rain and heavy rain are the same, that is, $\mu_{F_2^1}(x) = \mu_{F_2^2}(x) = \mu_{F_2^3}(x)$. The same occurs for the membership functions for LDR in drizzle, moderate rain and heavy rain, that is, $\mu_{F_3^1}(x) = \mu_{F_3^2}(x) = \mu_{F_3^3}(x)$.

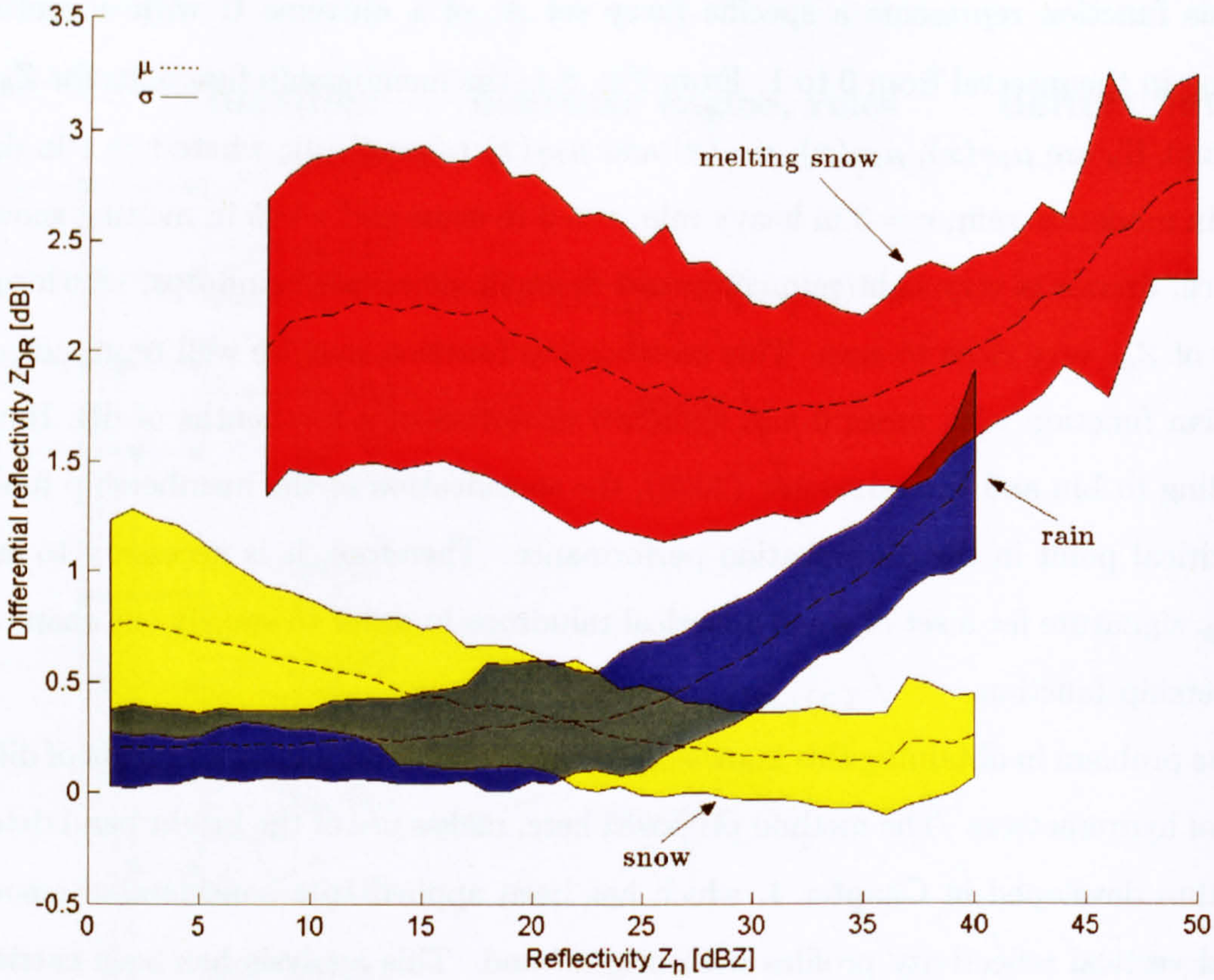

Fig. 8.2: Classification of rain, snow and melting snow in the Z_h-Z_{dr} space. The dashed line represents the mean μ and the solid line the standard deviation σ.

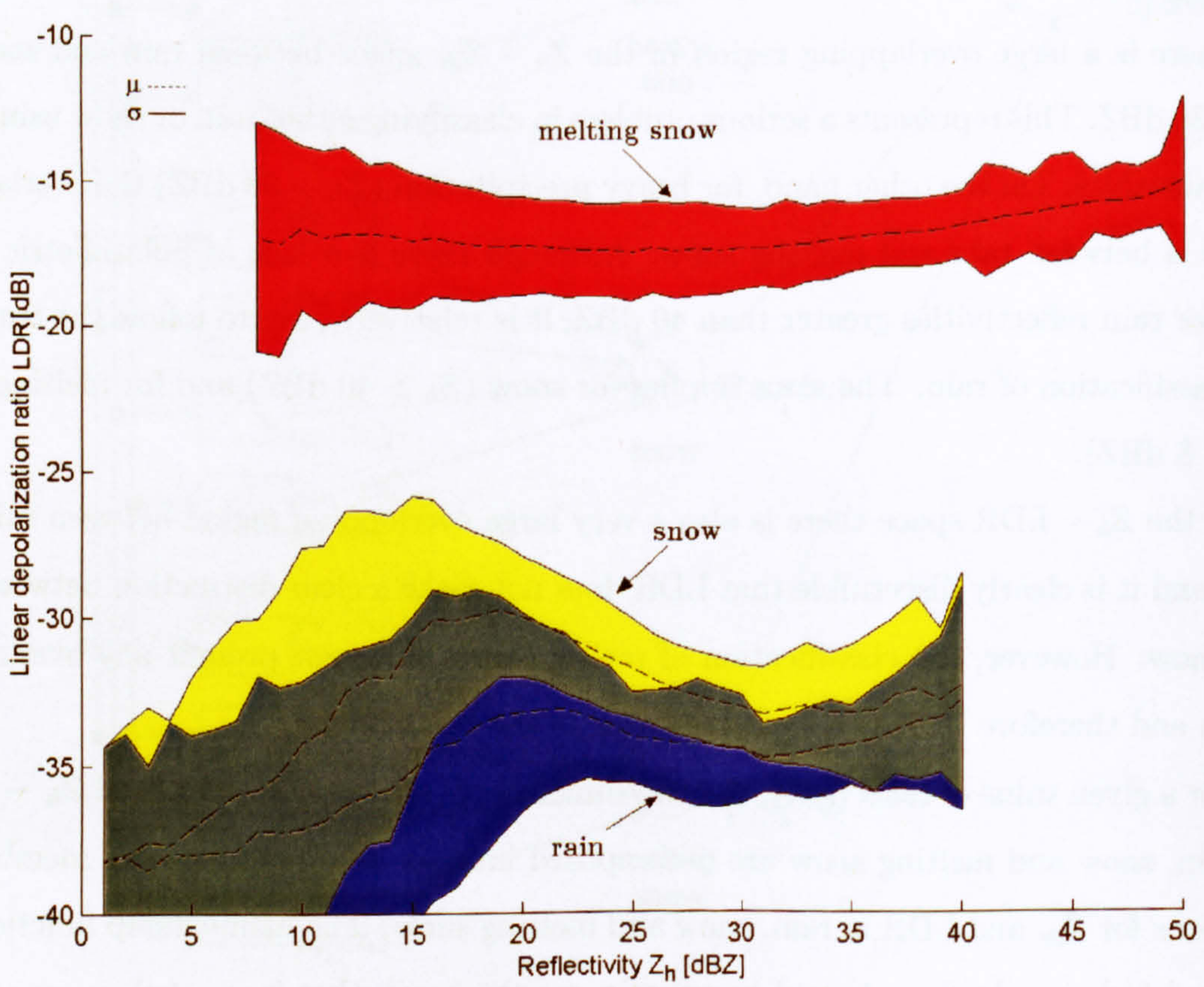

Fig. 8.3: Classification of rain, snow and melting snow in the Z_h-LDR space. The dashed line represents the mean μ and the solid line the standard deviation σ.

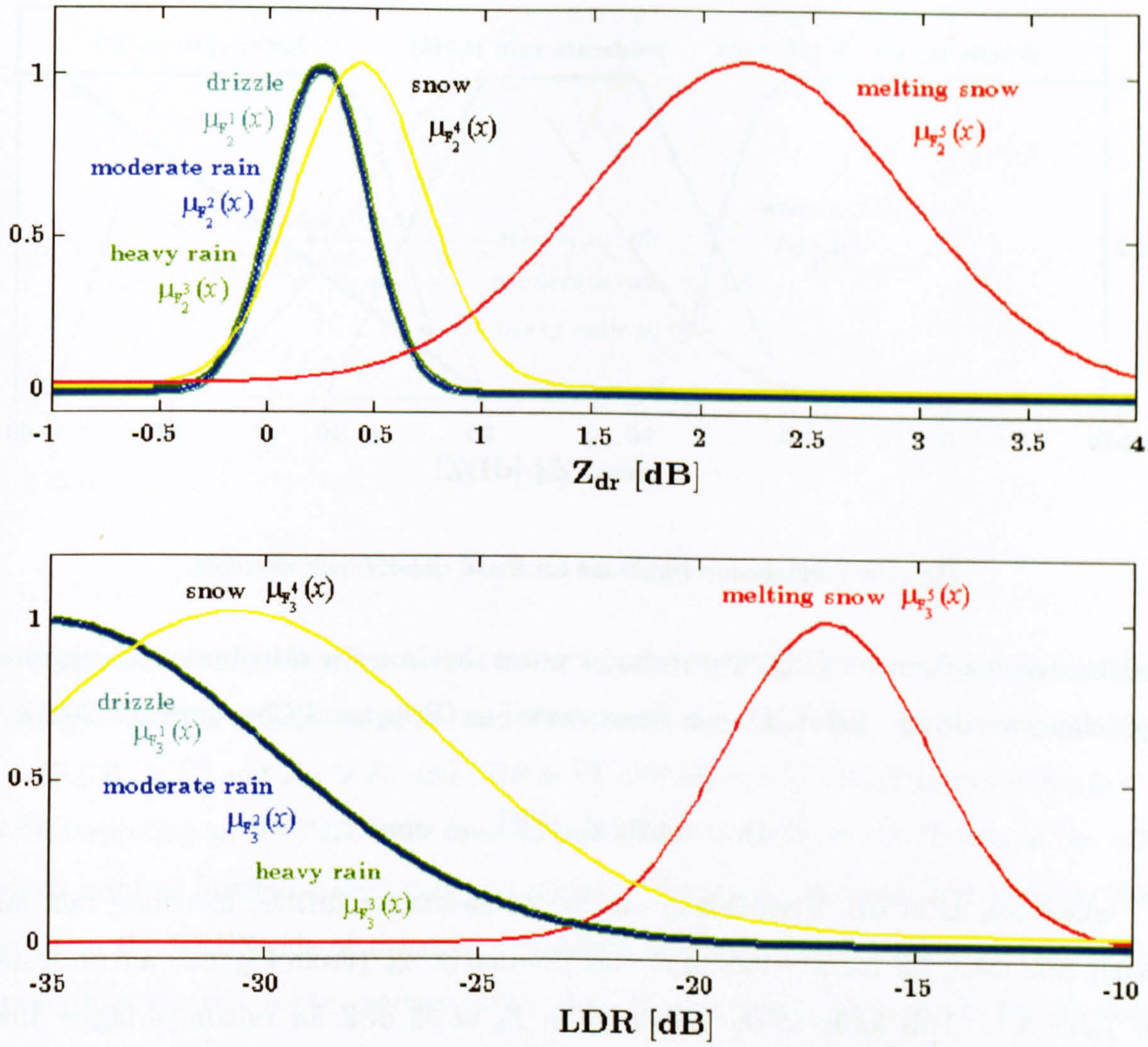

Fig. 8.4: Membership functions for Z_{dr} and LDR when $Z_h = 15$ dBZ (extracted from Figs. 8.2 and 8.3 respectively).

For instance, assuming a value of reflectivity of 15 dBZ, the membership functions of Z_{dr} and LDR are extracted from Figs. 8.2 and 8.3 respectively and they are shown in Fig. 8.4. The advantages of Gaussian membership functions are of being smooth and non-zero at all points. In addition, in a very noisy environment, the membership functions may be modified by increasing their standard deviation allowing the FLS to handle the noise of the polarimetric radar measurements easily.

The membership functions for Z_h are shown in Fig. 8.5. The class corresponding to rain has been subdivided into three subclasses, namely, drizzle, moderate rain and heavy rain. The boundaries among them have been defined as follows. Fig. 8.2 shows that the distributions of Z_{dr} in rain present similar characteristics for any value of reflectivity below 15 dBZ. The mean Z_{dr} is around 0.23 dB and this mean value represents measurements from small raindrops. Therefore, this region has been defined as drizzle. On the other hand, the boundary between moderate rain and heavy rain has been obtained using the

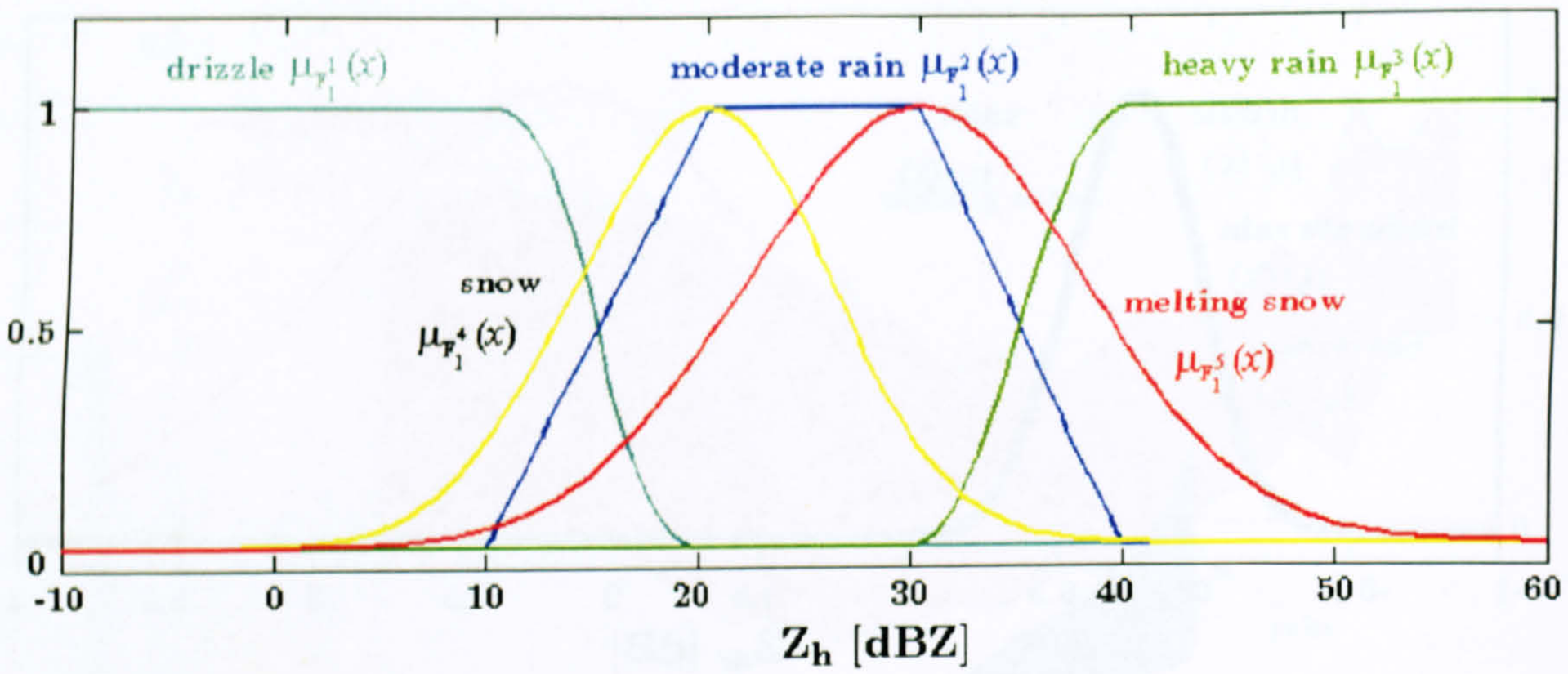

Fig. 8.5: Membership functions for Z_h to classify hydrometeors.

median volume diameter (D_o), which characterizes the drop size distribution as suggested by Seliga and Bringi (1976). D_o can be expressed as (Bringi and Chandrasekar, 2001):

$$D_o = 1.529(Z_{dr})^{0.467}; \qquad \text{mm} \tag{8.2}$$

where Z_{dr} is in dB. The median volume diameters for drizzle, moderate rain and heavy rain using the mean values of the distribution of Z_{dr} (From Fig. 8.2) are presented in Table 8.1. This leads to the boundary in Z_h of 35 dBZ for raindrops bigger than 1.5 mm. Then, trapezoidal membership functions for drizzle, moderate rain and heavy rain are defined to allow some degree of fuzziness around the boundary (See Fig. 8.5).

From the analysis of the height of the bright band top carried out in Chapter 6, it has been found that the height of the bright band top is above 500 m (See Fig. 6.3). However, this represents the height of the bright band top and the melting takes place within the 400 or 500 m below this height. Therefore, the distribution of the existence of melting snowflakes has been slightly modified to cover between 0 to 4 km and the membership functions of the height H_o of the different types of hydrometeors is shown in Fig. 8.6. The membership functions for rain and snow present high degree of fuzziness because both classes depend on the membership function of melting snow.

Type of rain	$\bar{Z}_{dr}$ [dB]	D_o [mm]	Z_h [dBZ]
Drizzle	$\bar{Z}_{dr} \approx 0.23$	$D_o \leq 0.8$	$0 \leq Z_h \leq 15$
Moderate	$0.23 < \bar{Z}_{dr} < 1.00$	$0.8 < D_o < 1.5$	$15 \leq Z_h \leq 35$
Heavy	$\bar{Z}_{dr} \geq 1.00$	$D_o \geq 1.5$	$Z_h \geq 35$

Table 8.1: Median volume diameters for drizzle, moderate rain and heavy rain applying Eq. 8.2.

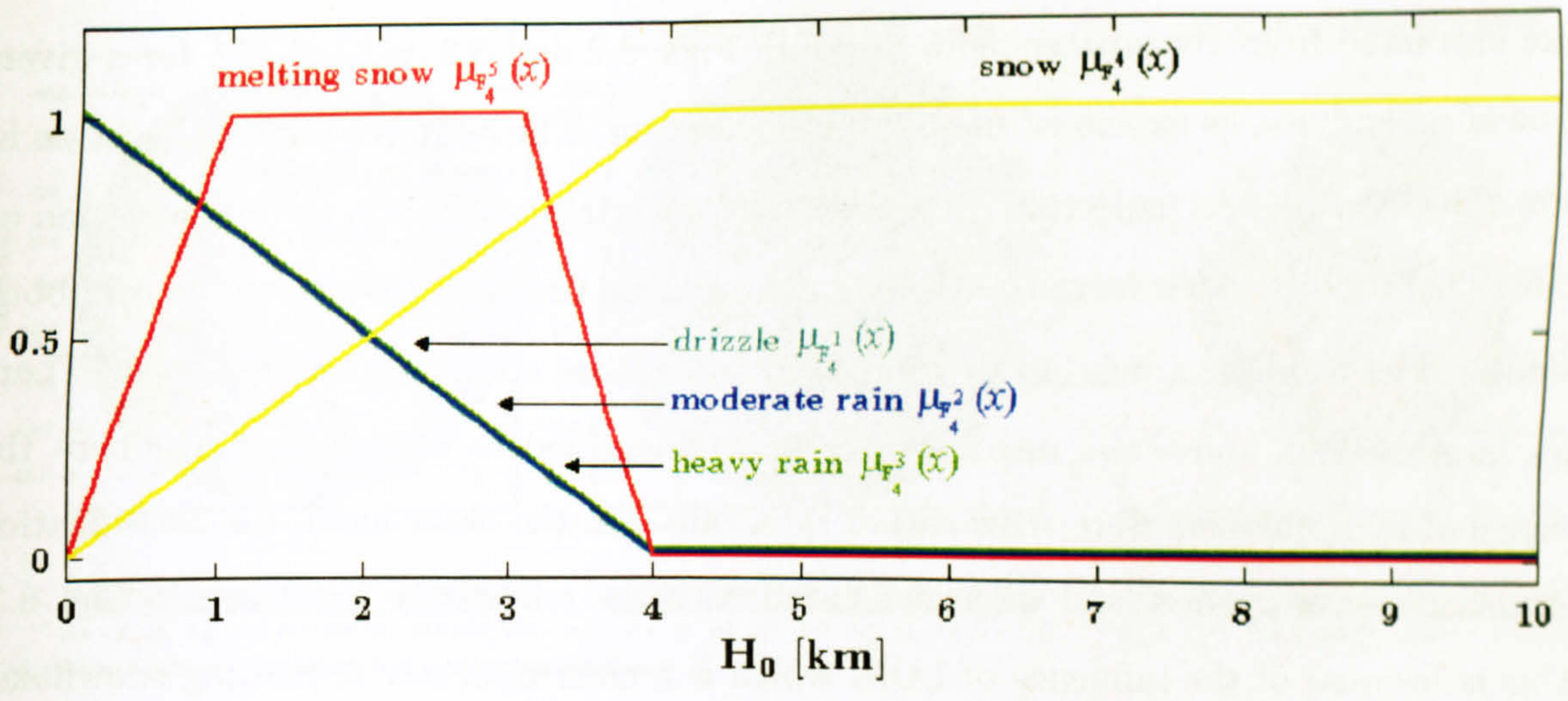

Fig. 8.6: Membership functions for H_o to classify hydrometeors.

The rules of the FLS are expressed in the form of IF-THEN statements. There are five rules ($r = 1...5$ for drizzle, moderate rain, heavy rain, snow and melting snow respectively):

IF (Z_h is F_1^r and Z_{dr} is F_2^r and LDR is F_3^r and H_o is F_4^r) THEN hydrometeor is r

Interpreting an IF-THEN rule involves two steps: to evaluate the IF-side of the rule, which involves fuzzifying the input and applying the fuzzy operator, and to apply that result to the THEN-side of the rule. The fuzzy operator ("and") used to evaluate the strength of the rule is the product rather than the minimum, because the former takes into account the product among the membership degree of all the inputs and the latter only the value with minimal membership. Thus, the strength of each rule can be obtained by evaluating the product among the membership functions by (See Fig. 8.1):

$$S_r = \prod_{k=1}^{4} \mu_{F_k^r}(x_k) \tag{8.3}$$

where x_k is a single value, that is, $x_1 = Z_h$, $x_2 = Z_{dr}$, $x_3 =$ LDR and $x_4 = H_o$. The hydrometeor type is the one in that rule with maximal strength.

8.3 Hydrometeor classification

The FLS developed in Section 8.2 to classify hydrometeors has been applied to several scans from the Chilbolton radar. These scans have been obtained from a precipitation event that took place on the 1st of December 2003 over the South West of UK. The type of precipitation was stratiform with very intensive rainfall rates and a clear bright band around 1 km above the ground surface (See Figs. 8.7 and 8.8).

The four different observations (Z_h, Z_{dr}, LDR and H_o) were fuzzified according to their corresponding membership functions. The membership functions for Z_{dr} and LDR

were extracted from the scatter plots shown in Figs. 8.2 and 8.3 respectively, for a given value of reflectivity, as explained in the previous section. The hydrometeor classification is shown in Fig. 8.10. As expected, there is a lot of uncertainty between the classification of rain and snow due to the large overlapping areas among the membership functions of both classes. The result is a misclassification of hydrometeors above the melting level. There are large regions above the melting layer being identified as moderate rain, where the expected hydrometeors were snow rather than rain. On the other hand, the classification of melting snow is successful when compared with the reflectivity Z_h shown in Fig. 8.7. This is because of the influence of LDR, which is a clear indicator of melting snowflakes (See Fig. 8.3). Taking into account this fact, an additional improvement can be obtained when a primary classification is used to establish the mean height of melting snowflakes (See Fig. 8.9). Using the mean height of melting snowflakes, new membership functions are constructed to modify the height of the different hydrometeors (H_o) reducing the uncertainty between the classification of rain and snow.

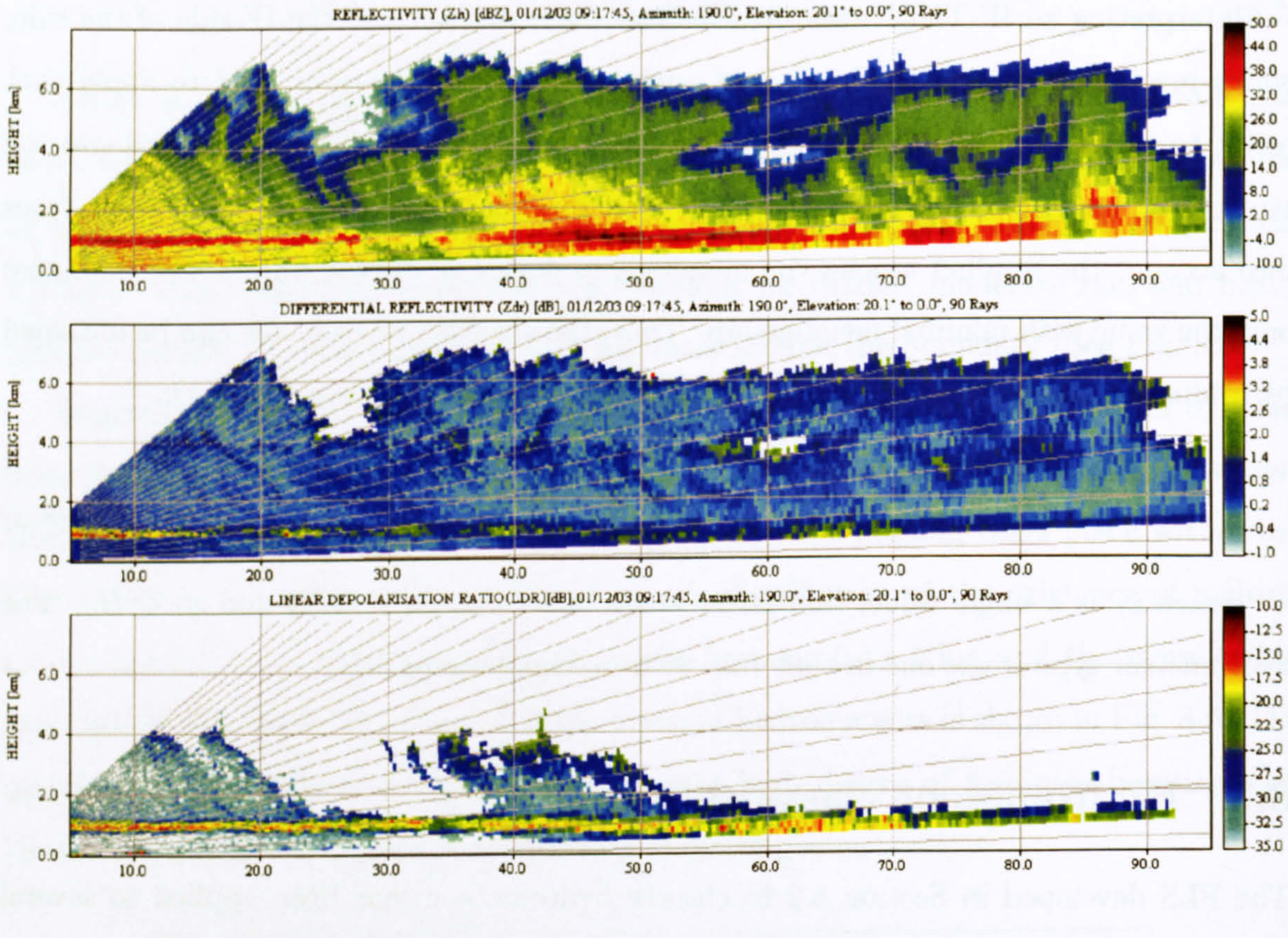

Fig. 8.7: RHI scans from Chilbolton radar on 01/12/03 at 09:17:45 hr (azimuthal 190° from the North).

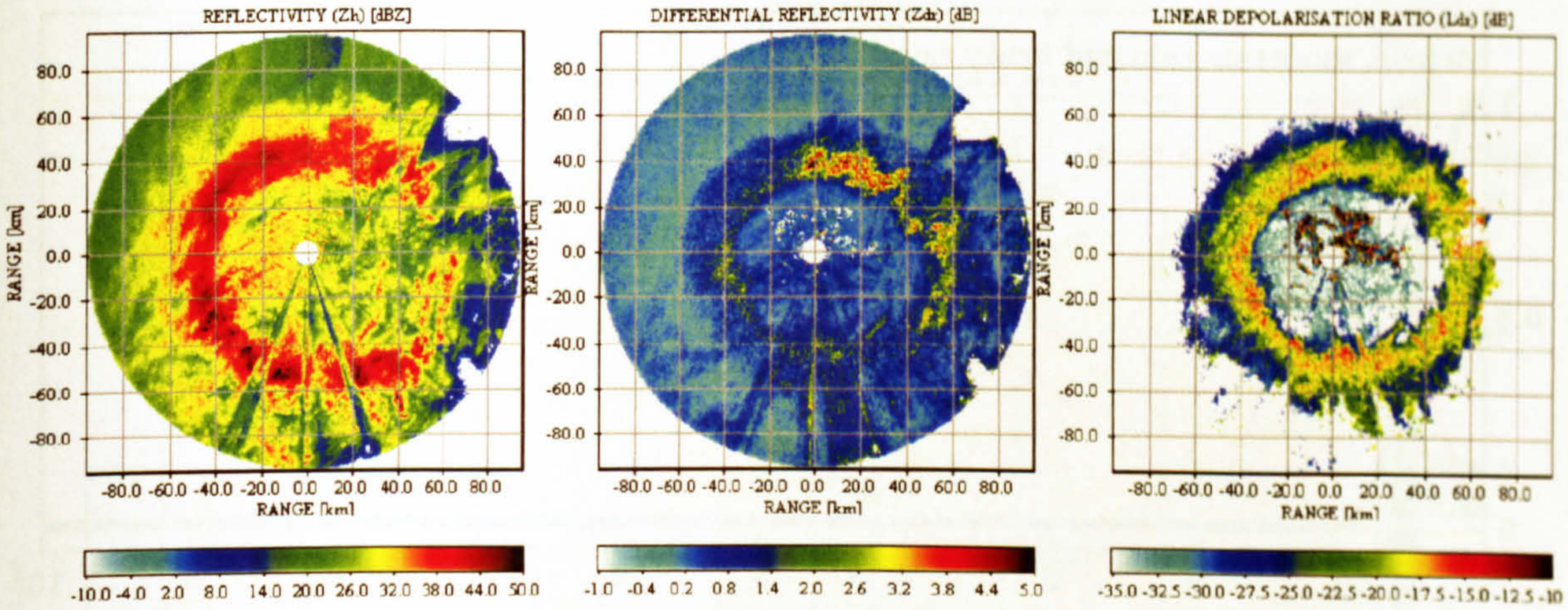

Fig. 8.8: PPI scans from Chilbolton radar on 01/12/03 at 09:26:25 hr.

The result of the secondary classification is shown in Fig. 8.11. Other hydrometeor classifications are shown in Figs. 8.12, 8.14 and 8.16, which present some regions of heavy precipitation. The secondary hydrometeor classifications for these events are shown in Figs. 8.13, 8.15 and 8.17 respectively.

These results present some regions very close to the radar and at lower altitudes classified as melting snow. This is because of the fact that LDR is very easily contaminated with ground clutter or partial blocking by the mountains causing significant depolarisation. There are several alternatives to deal with this problem. One is by taking into account the Digital Elevation Model (DEM) surrounding the radar and ignoring regions prone to clutter contamination. The second alternative is by incorporating the DEM into the FLS and adding a new class called ground clutter. This is obviously an issue of further research, because LDR is prone to clutter contamination not only by the mainlobe of the antenna radiation pattern, but also by the sidelobes. The third alternative is the incorporation of the correlation coefficient ($\rho_{hv}(0)$) into the FLS, which is also susceptible to the presence of mixed-phase precipitation (Zrnić and Ryzhkov, 1999). LDR just as $\rho_{hv}(0)$ do not provide quantitative estimates of precipitation, but they are important indicators of the presence of mixed-phase precipitation. Unfortunately $\rho_{hv}(0)$ is not available on Chilbolton, but the incorporation of this parameter into the FLS may give more reliability to the classification procedure. Straka et al. (2000) suggested that self-consistency among the polarimetric variables may reduce classification ambiguities. That is, the classification system should be more reliable if two or more polarimetric variables suggest a certain type of hydrometeor.

The FLS has also been applied to the PPI scans shown in Fig. 8.8. The result is shown in Fig. 8.18. This classification assumes a certain melting level from a previous

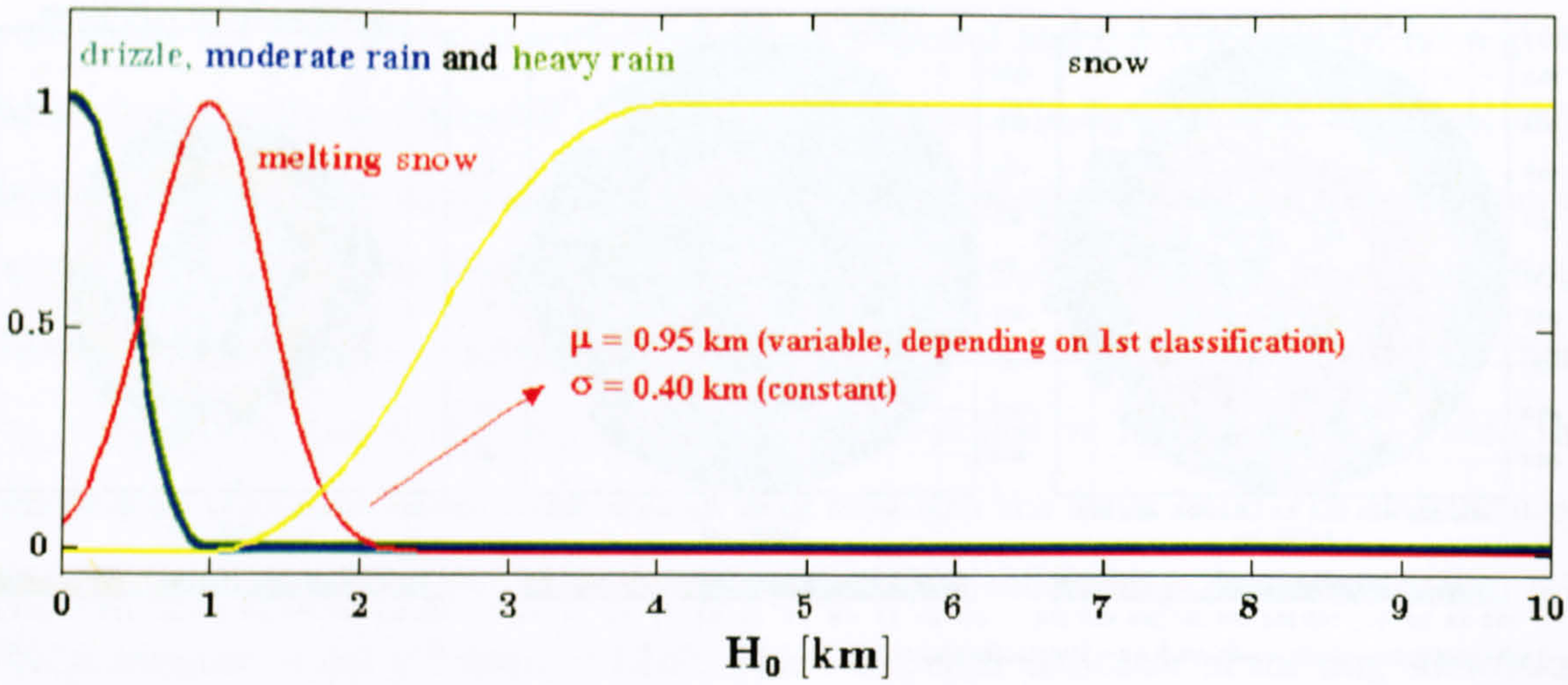

Fig. 8.9: Variable membership functions for H_o to classify hydrometeors. The mean value (μ) of the melting level has been obtained from a previous classification.

classification as in the case of RHI scans. The melting level has been obtained as an average of melting levels at every azimuth of the overall PPI scan. However, the variation of the height of the melting level causes some regions to be misidentified. For instance, there are some regions identified as snow below melting snow along the azimuths between 90° and 170° from the North. The only way to avoid this is by sectorizing the PPI scans into small regions allowing small variations in the height of the melting level. This can be particularly useful in fronts, where the radar may see two different melting levels. Sectorizing the PPI scan every 30° allows flexibility in the variation of the melting level. This is shown in Fig. 8.19. In this new classification, the regions misidentified as snow below the melting level have been classified as rain. Sectors of 30° are a trade-off between having enough azimuths to estimate the height of the melting level whereas allowing the natural variation of its height.

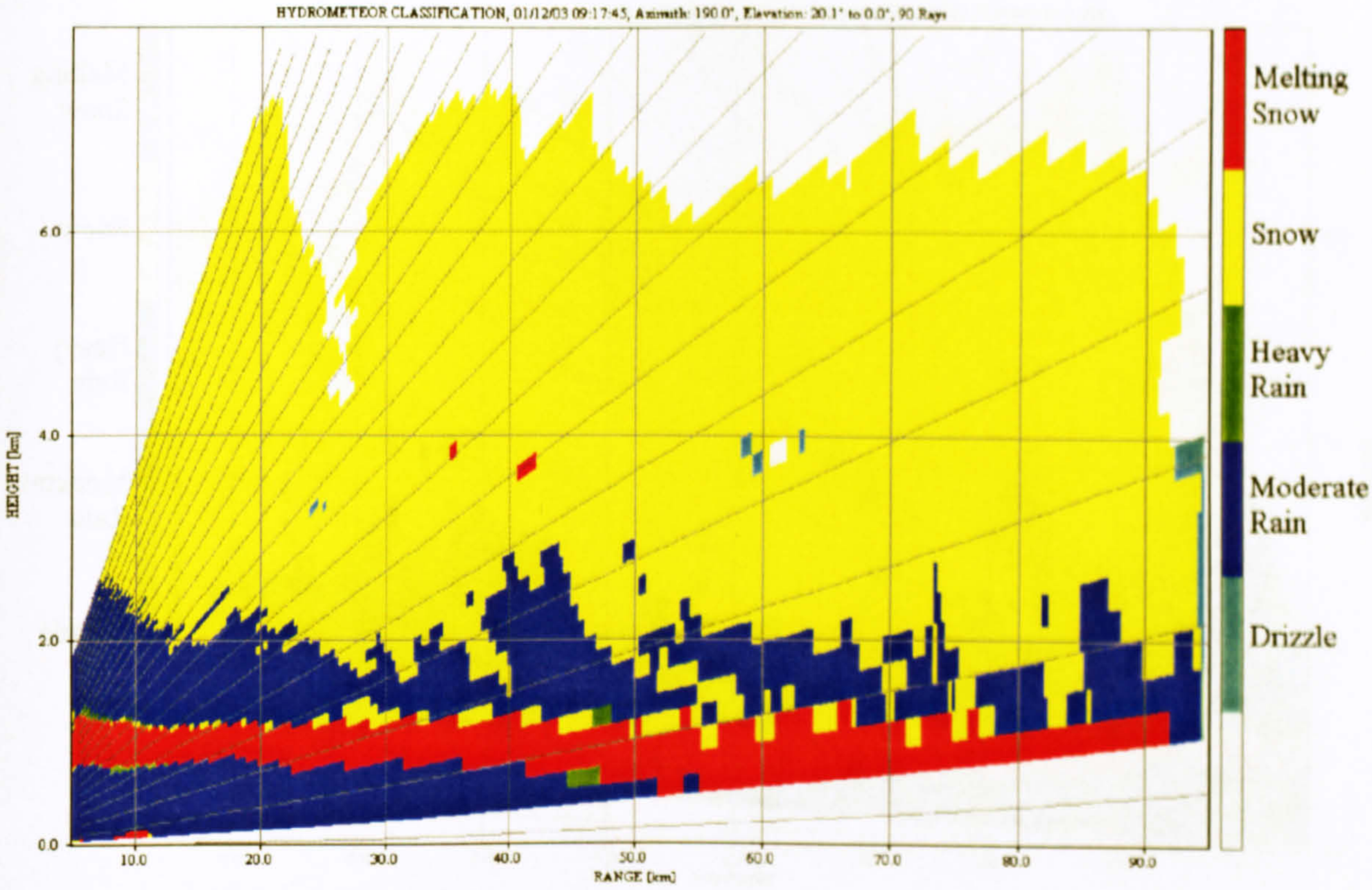

Fig. 8.10: Hydrometeor classification using 2D membership functions.

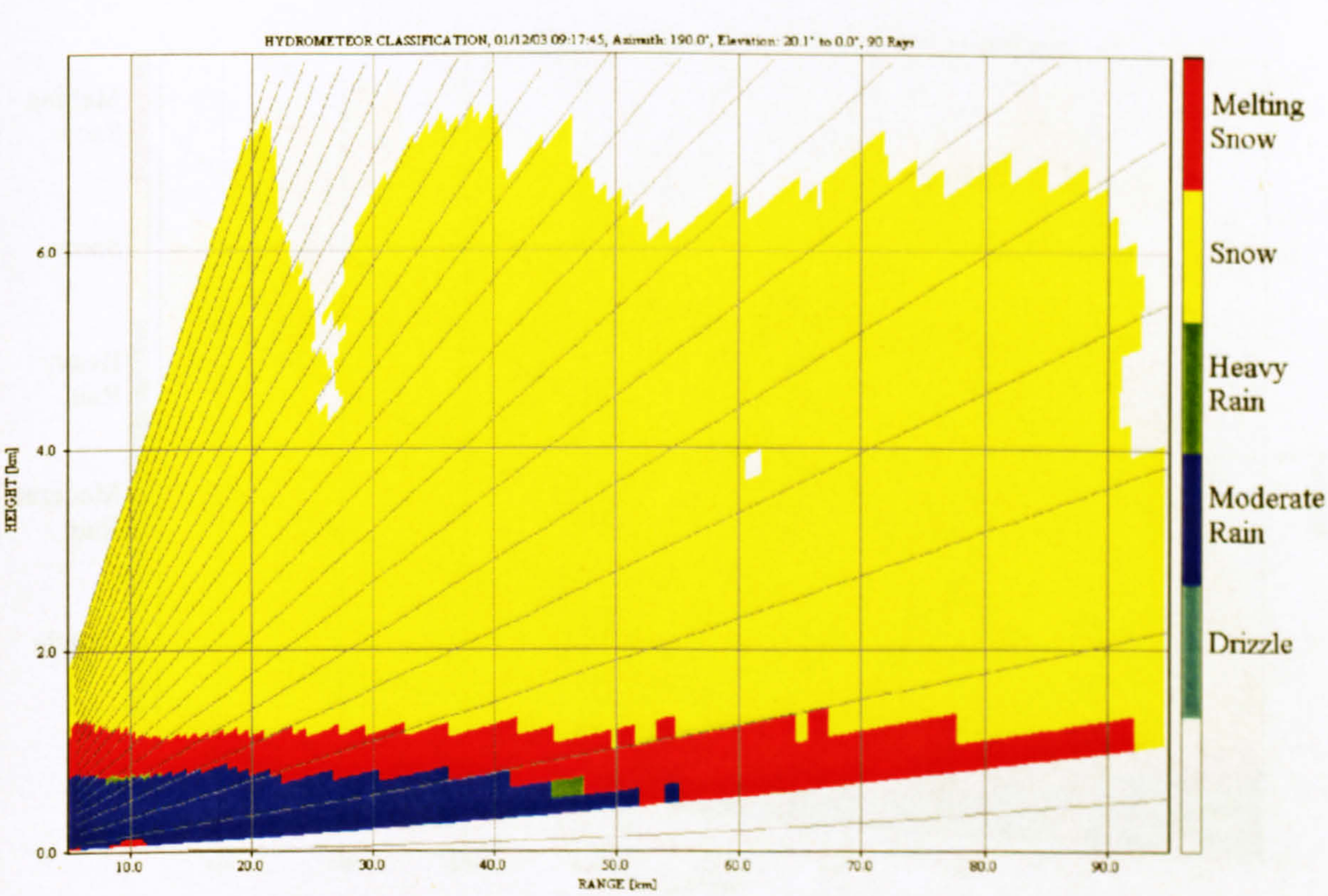

Fig. 8.11: Hydrometeor classification using 2D membership functions. The melting level has been obtained from a previous classification.

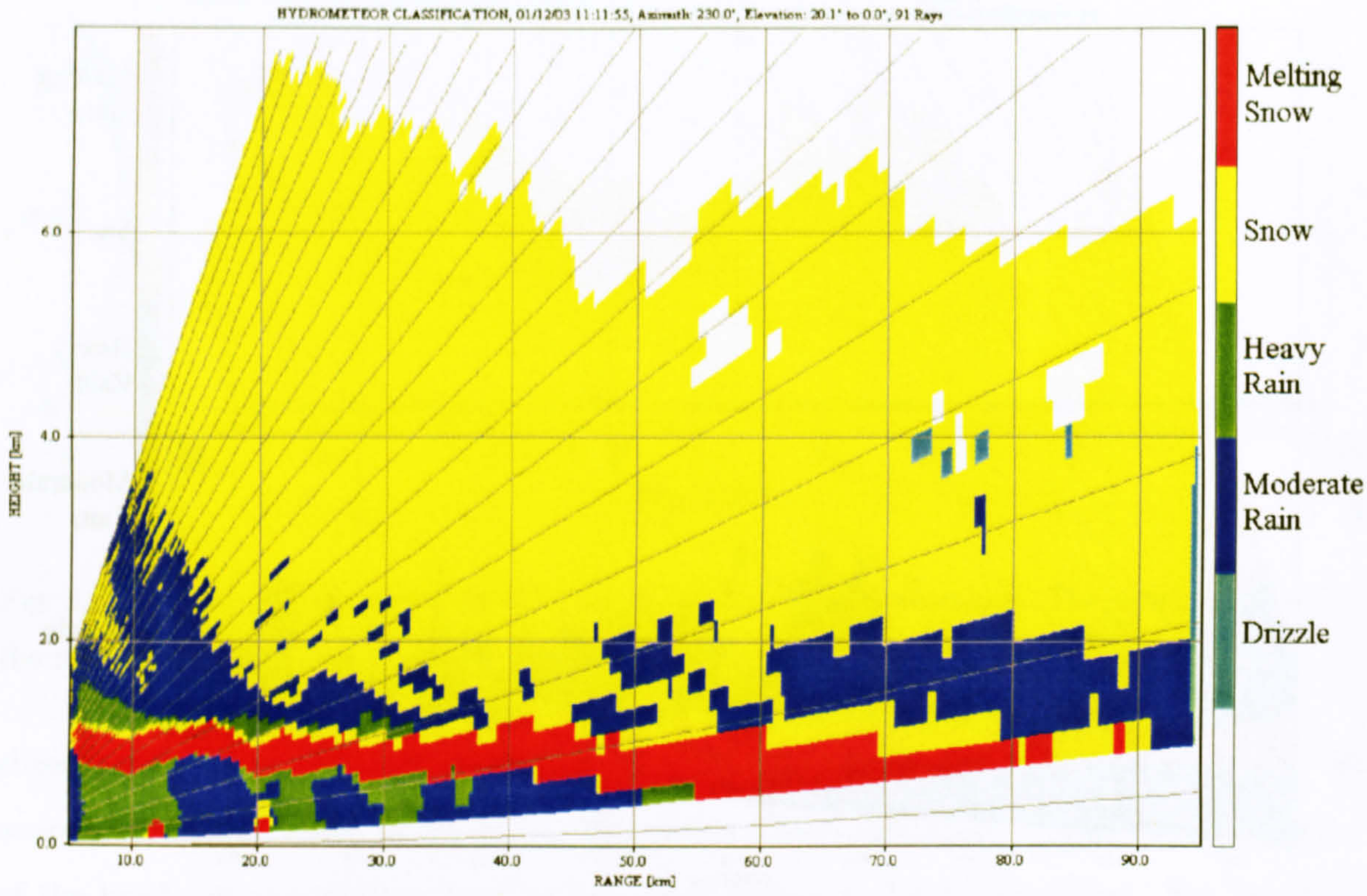

Fig. 8.12: Hydrometeor classification using 2D membership functions.

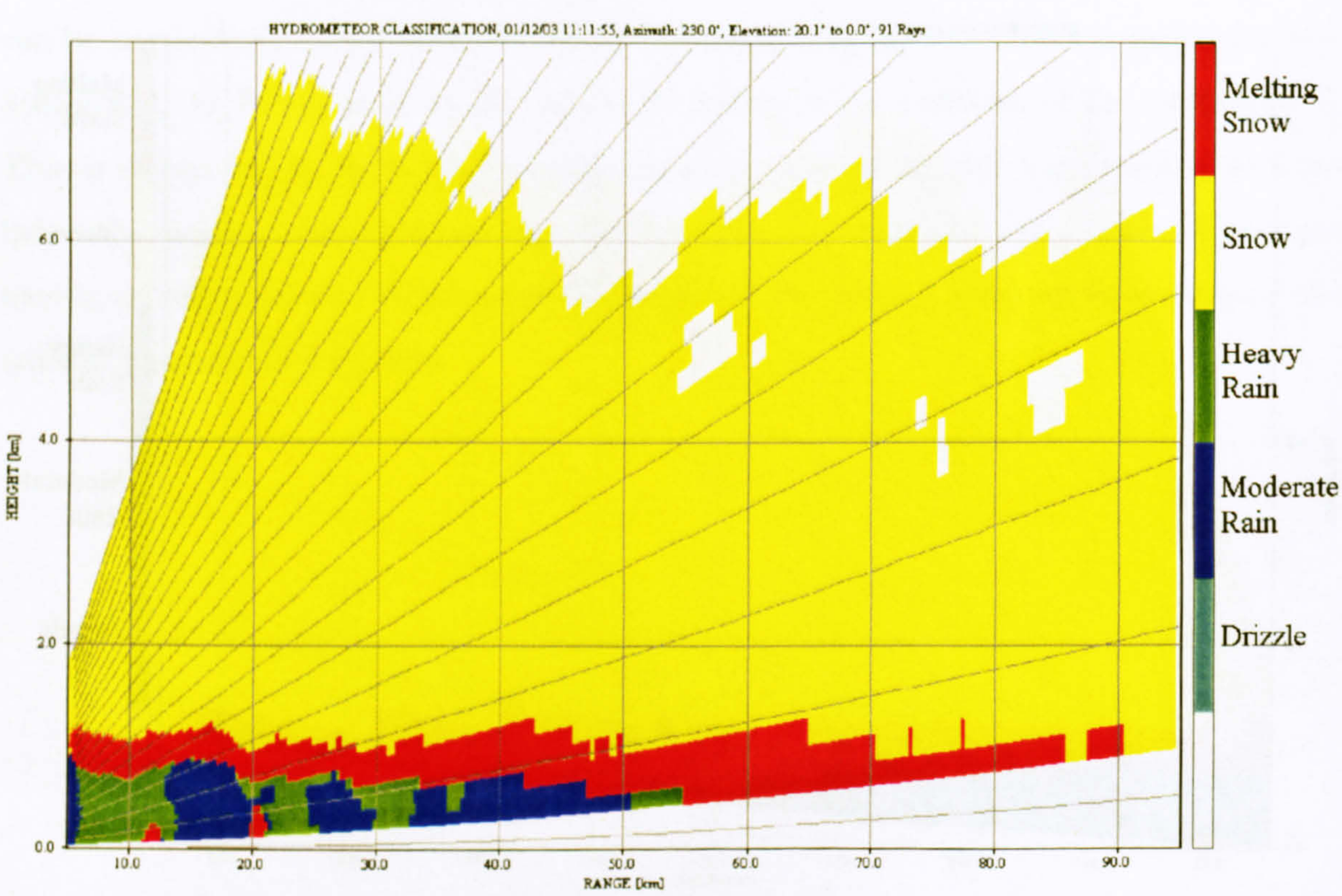

Fig. 8.13: Hydrometeor classification using 2D membership functions. The melting level has been obtained from a previous classification.

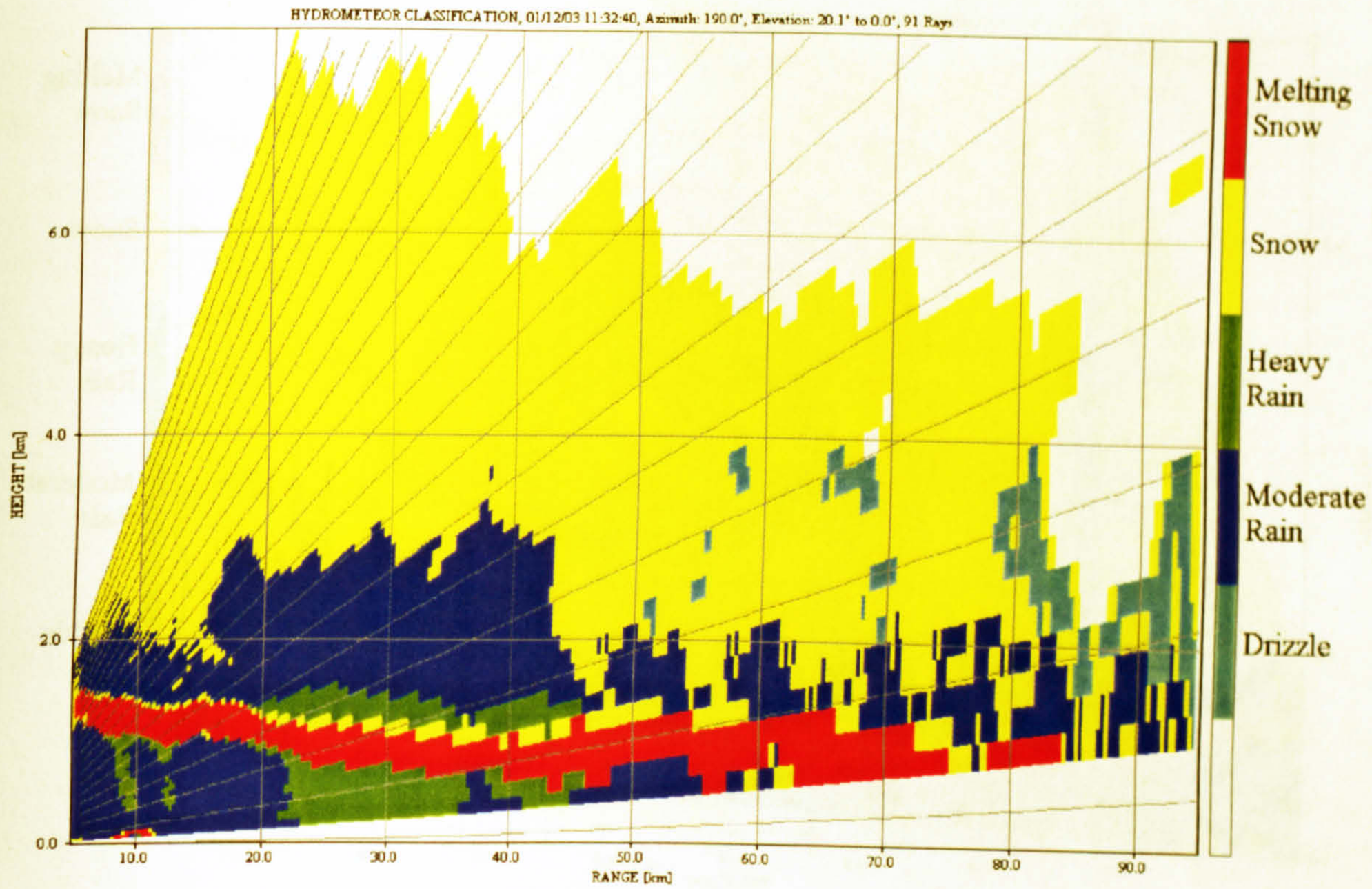

Fig. 8.14: Hydrometeor classification using 2D membership functions.

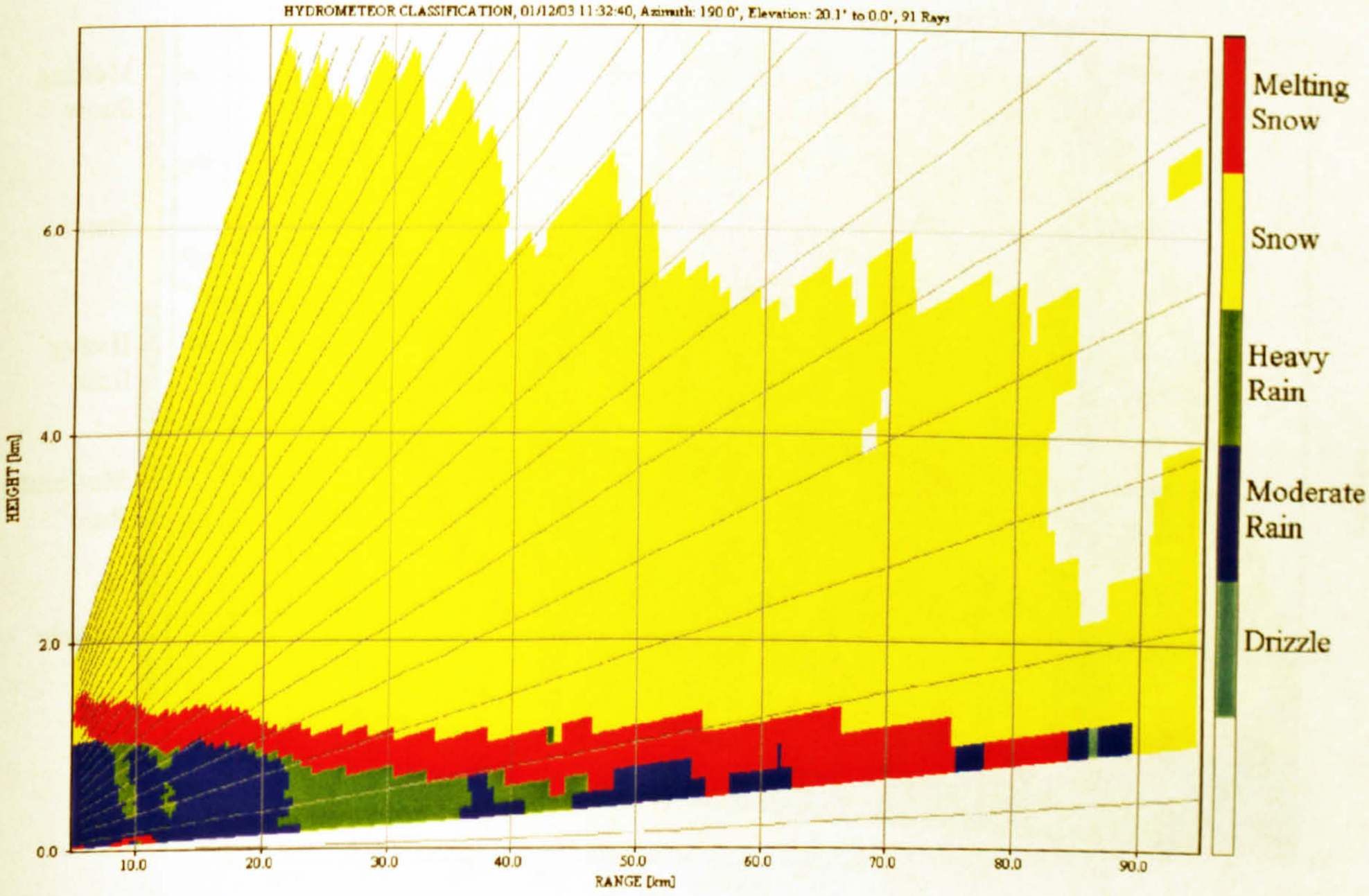

Fig. 8.15: Hydrometeor classification using 2D membership functions. The melting level has been obtained from a previous classification.

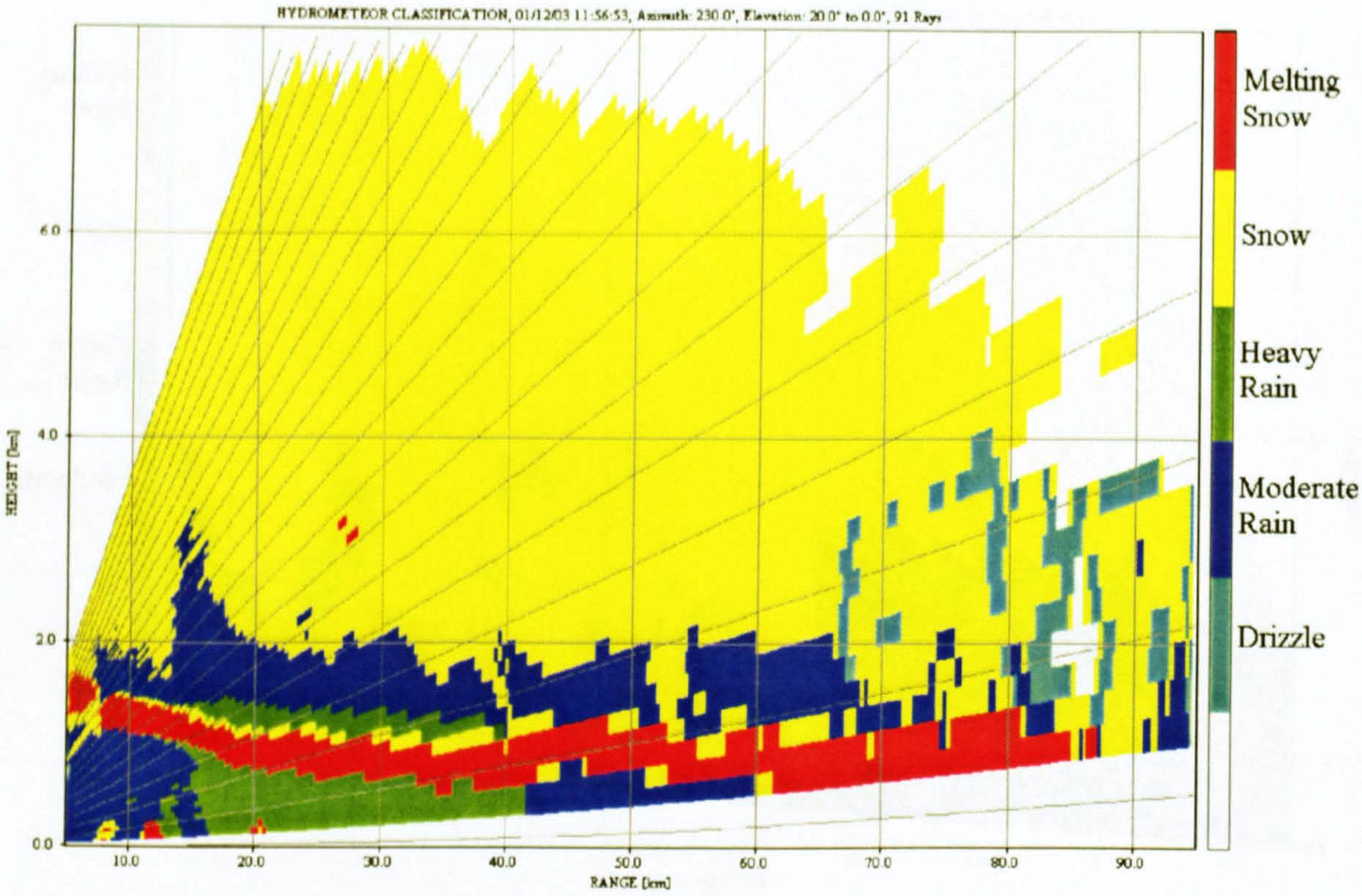

Fig. 8.16: Hydrometeor classification using 2D membership functions.

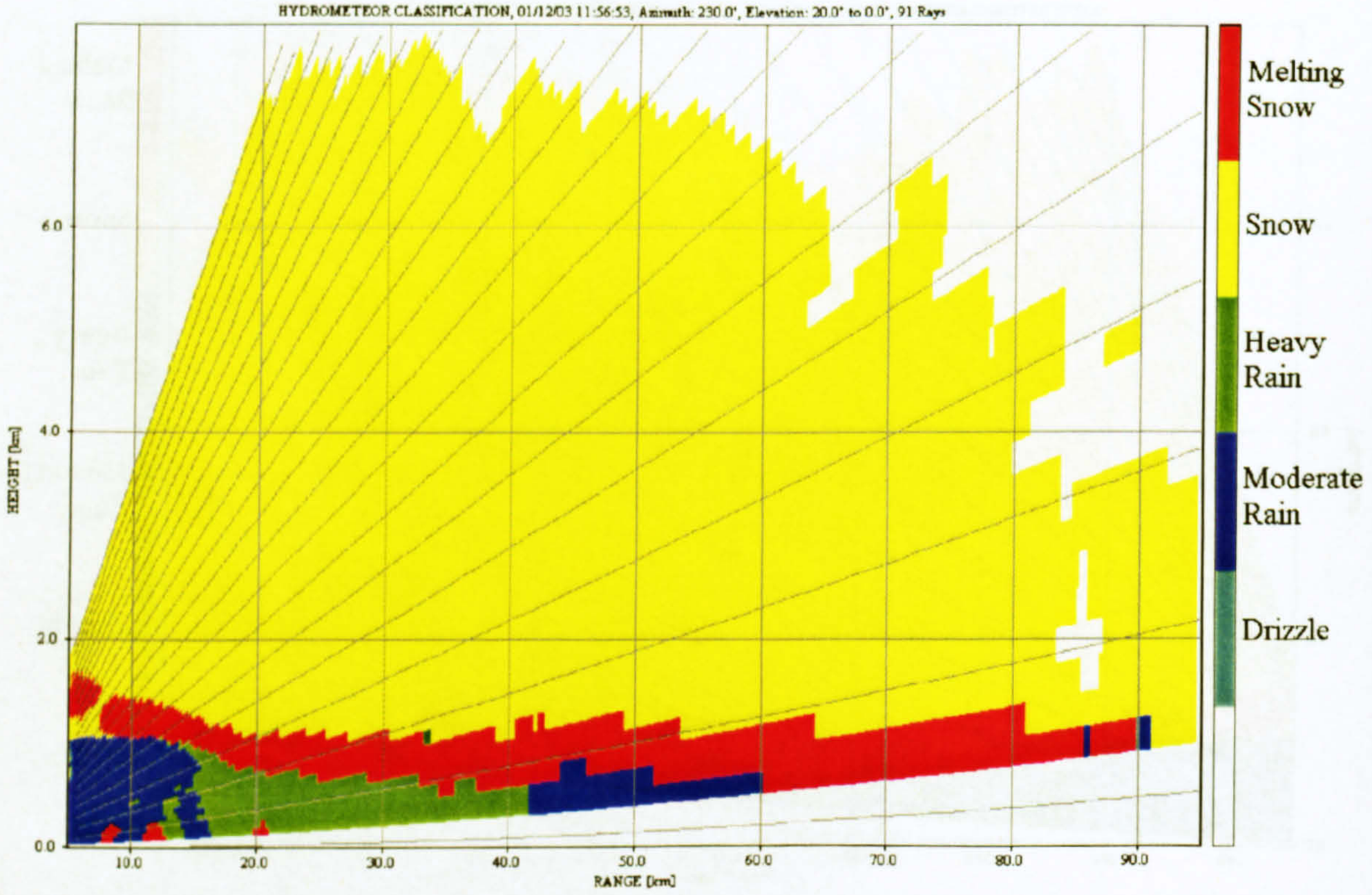

Fig. 8.17: Hydrometeor classification using 2D membership functions. The melting level has been obtained from a previous classification.

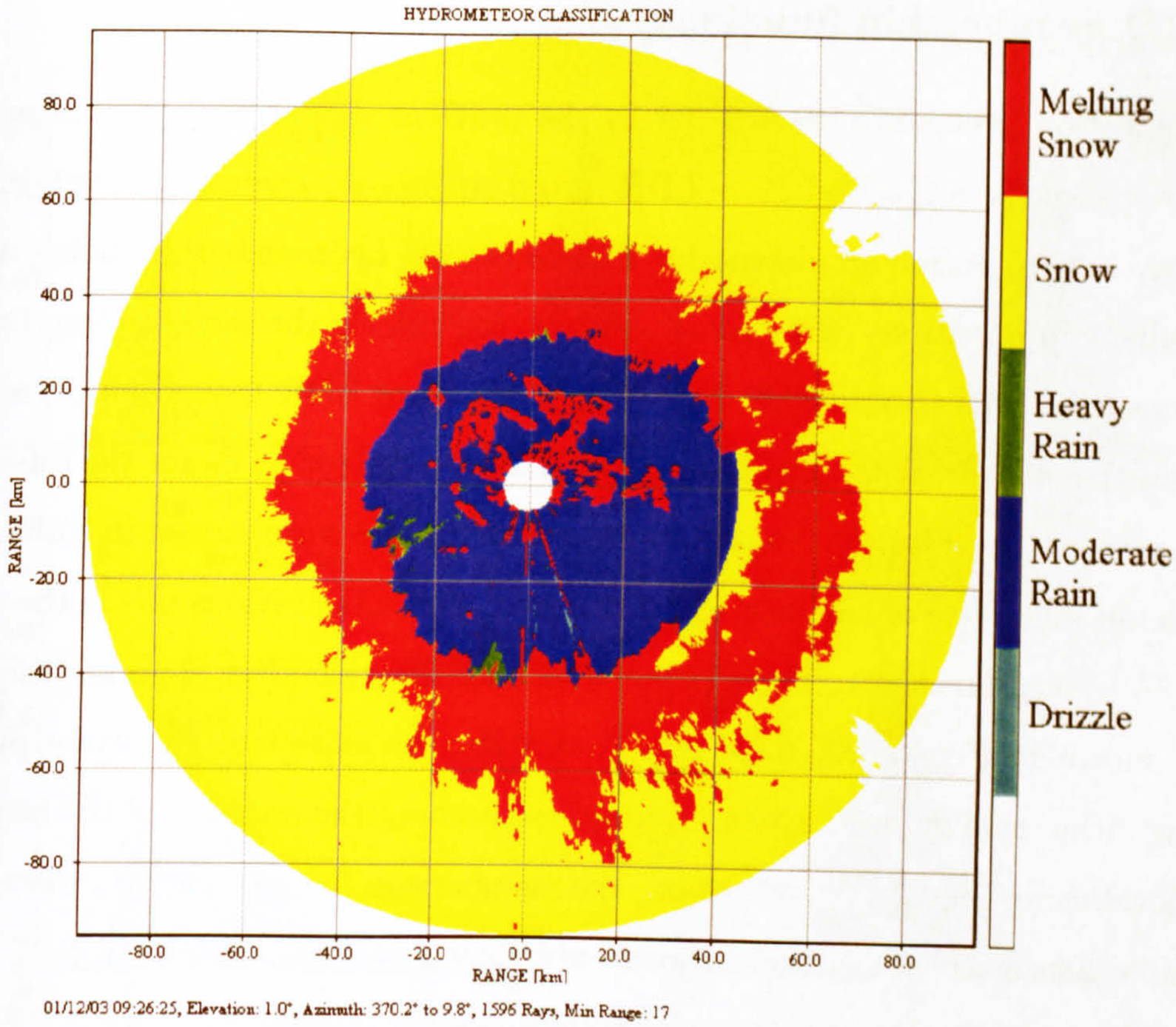

Fig. 8.18: Hydrometeor classification using 2D membership functions. The melting level has been obtained from the whole PPI scan.

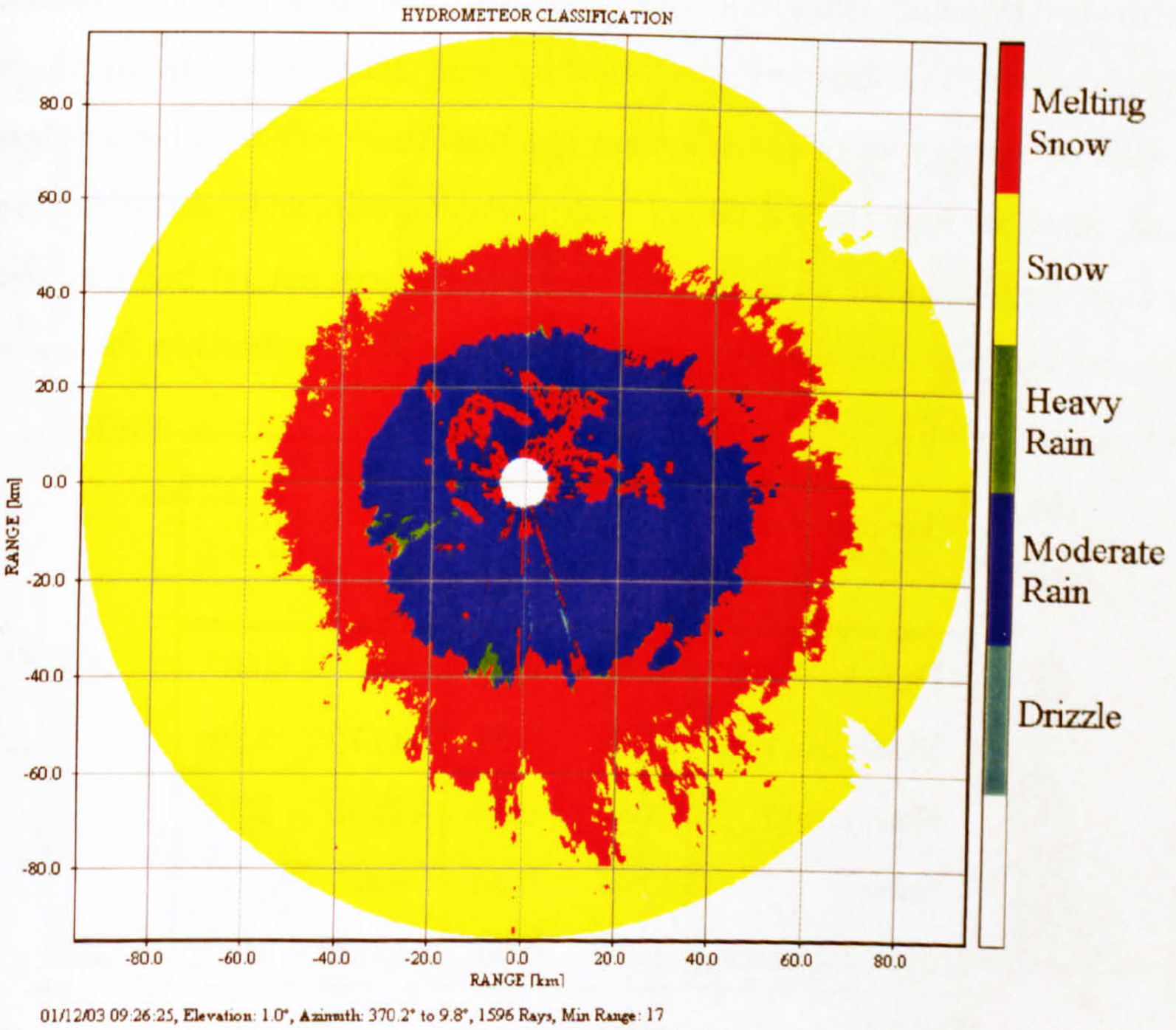

Fig. 8.19: Hydrometeor classification using 2D membership functions. The melting level has been obtained in sectors of 30 °.

8.3.1 1D membership functions

The classification procedure carried out in the previous section makes a decomposition of the 2D spaces $Z_h - Z_{dr}$ and $Z_h -$ LDR into a single one, assuming a certain value of reflectivity. In this section an alternative FLS to classify hydrometeors is being described. The Membership Functions (MF) for Z_h and H_o are exactly the same as described in the previous section. The membership functions for Z_{dr} and LDR have been obtained from their respective distributions according to the intervals defined in Z_h for the different type of hydrometeors (See Figs. 8.20 and 8.21 respectively) and summarised in Table 8.2.

The main difference of the new FLS compared with the previous one is the definition of 1D membership functions. The results of the classification after applying the modified FLS are shown in Figs. 8.22, 8.24, 8.26 and 8.28. As expected, the same problem in classifying either rain or snow exists. Taking into account the estimate of the height of the melting level using the first classification, the membership functions for H_o were modified. The results of the secondary classification are shown in Figs. 8.23, 8.25, 8.27 and 8.29. The secondary and 30-degree sectorization hydrometeor classifications for a PPI scan are shown in Figs. 8.30 and 8.31 respectively.

In general, the hydrometeor classifications using the 2D membership functions in comparison with the 1D membership functions are very similar. It is difficult to establish which FLS performs better. The answer may be that by using 2D membership functions with the incorporation of more types of precipitation particles there will be a better classification. In this case, there are only three different hydrometeors: rain, snow and melting snow, but there are large regions in the $Z_h - Z_{dr}$ and $Z_h -$ LDR spaces not yet being categorized. In this study the hydrometeor classification using 1D or 2D membership functions conveys practically to the same results.

Hydrometeor	Z_{dr} [dB]		LDR [dB]	
	μ	σ	μ	σ
Drizzle	0.23	0.18	-40^{+}	6.66^{+}
Moderate rain	0.42	0.31	-33.76	2.89
Heavy rain	1.22	0.34	-33.46	2.74
Snow	0.41	0.34	-40^{+}	6.66^{+}
Melting snow	1.93*	0.60*	-17.03	1.71

Table 8.2: 1D Gaussian MF for Z_{dr} and LDR for the different types of hydrometeors (* represents a Gamma MF and $^{+}$ represents an adapted Gaussian MF).

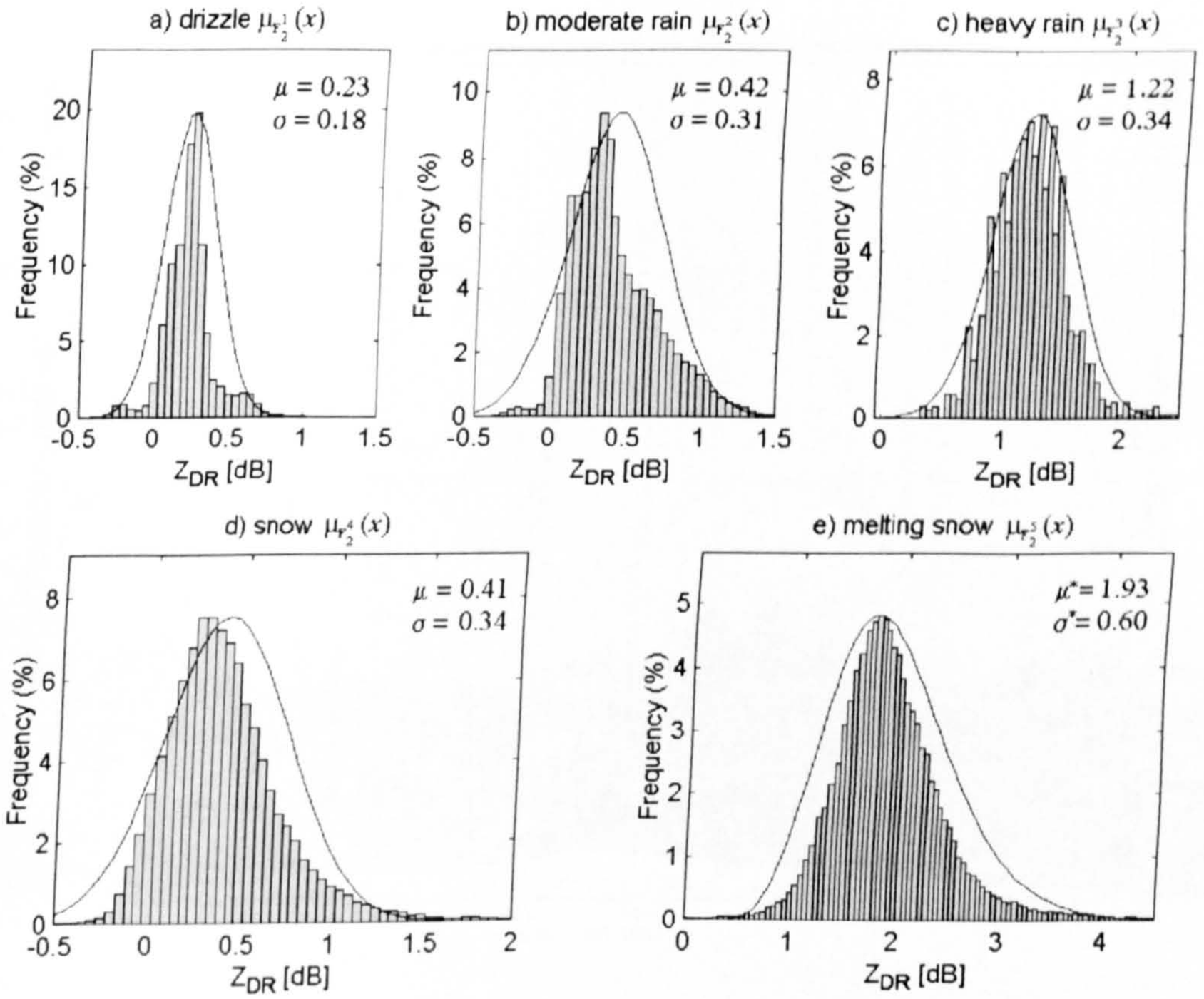

Fig. 8.20: 1D Gaussian MF for Z_{dr} (* represents a Gamma MF).

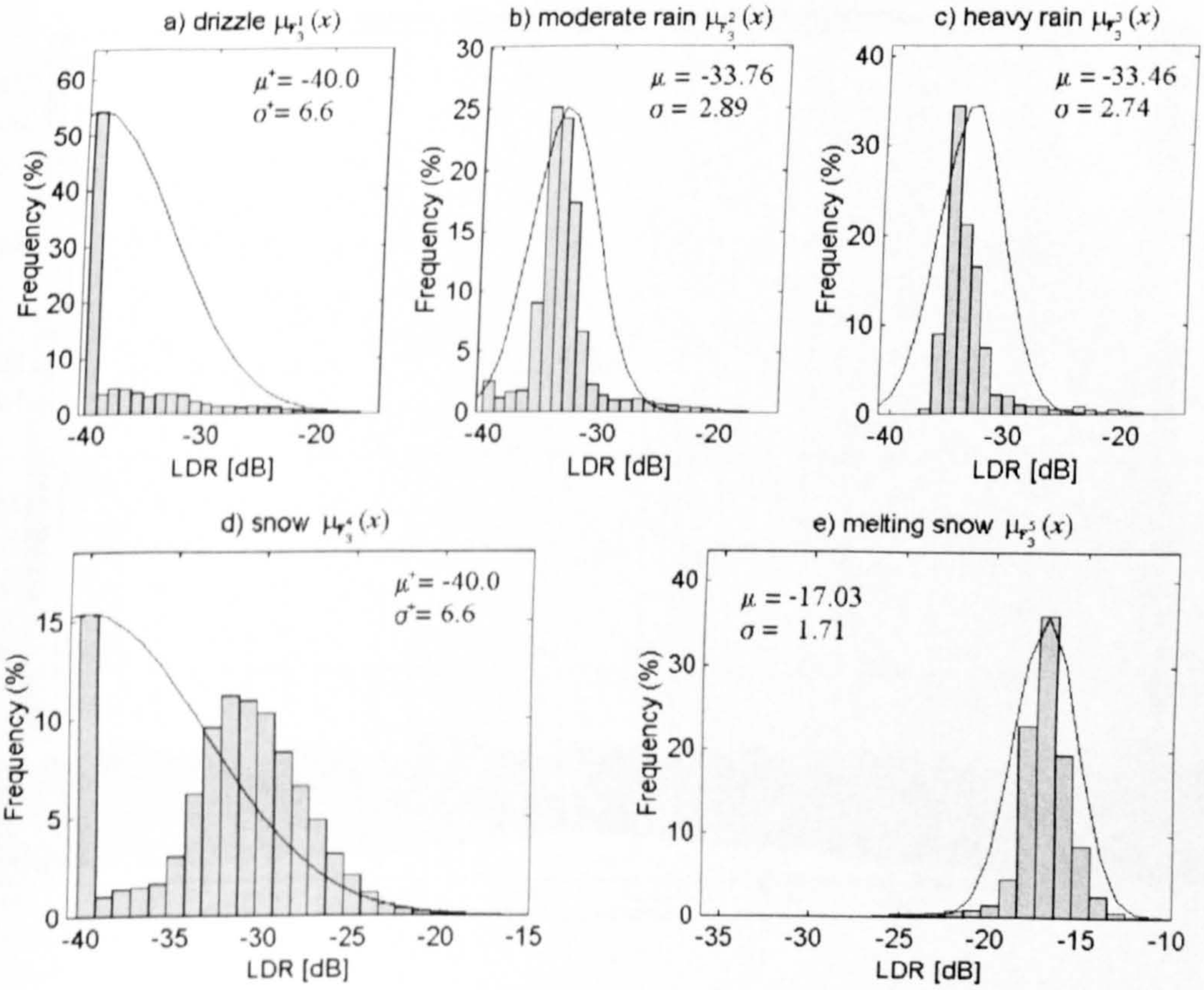

Fig. 8.21: 1D Gaussian MF for LDR ($^+$ represents an adapted Gaussian MF).

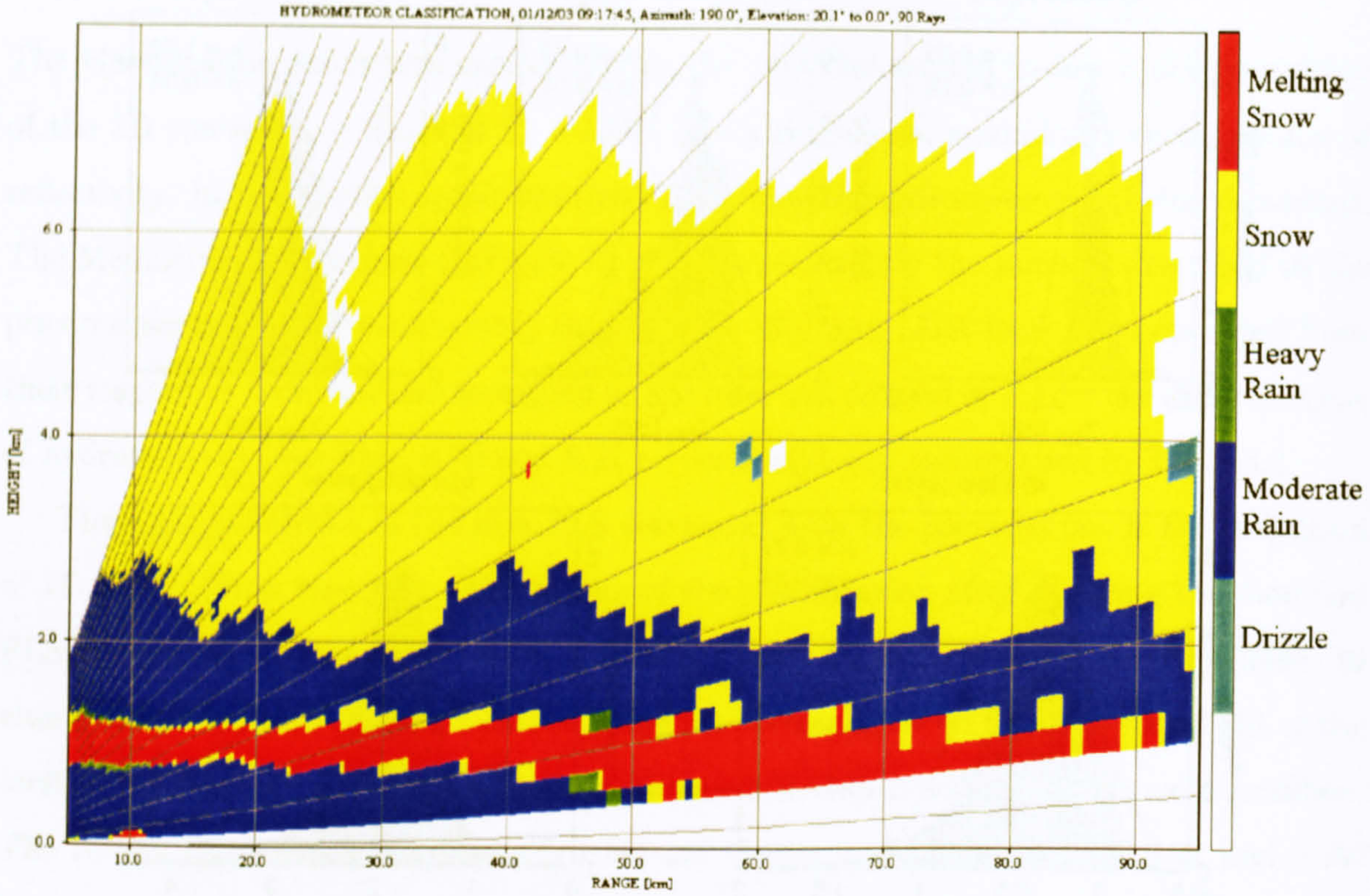

Fig. 8.22: Hydrometeor classification using 1D membership functions.

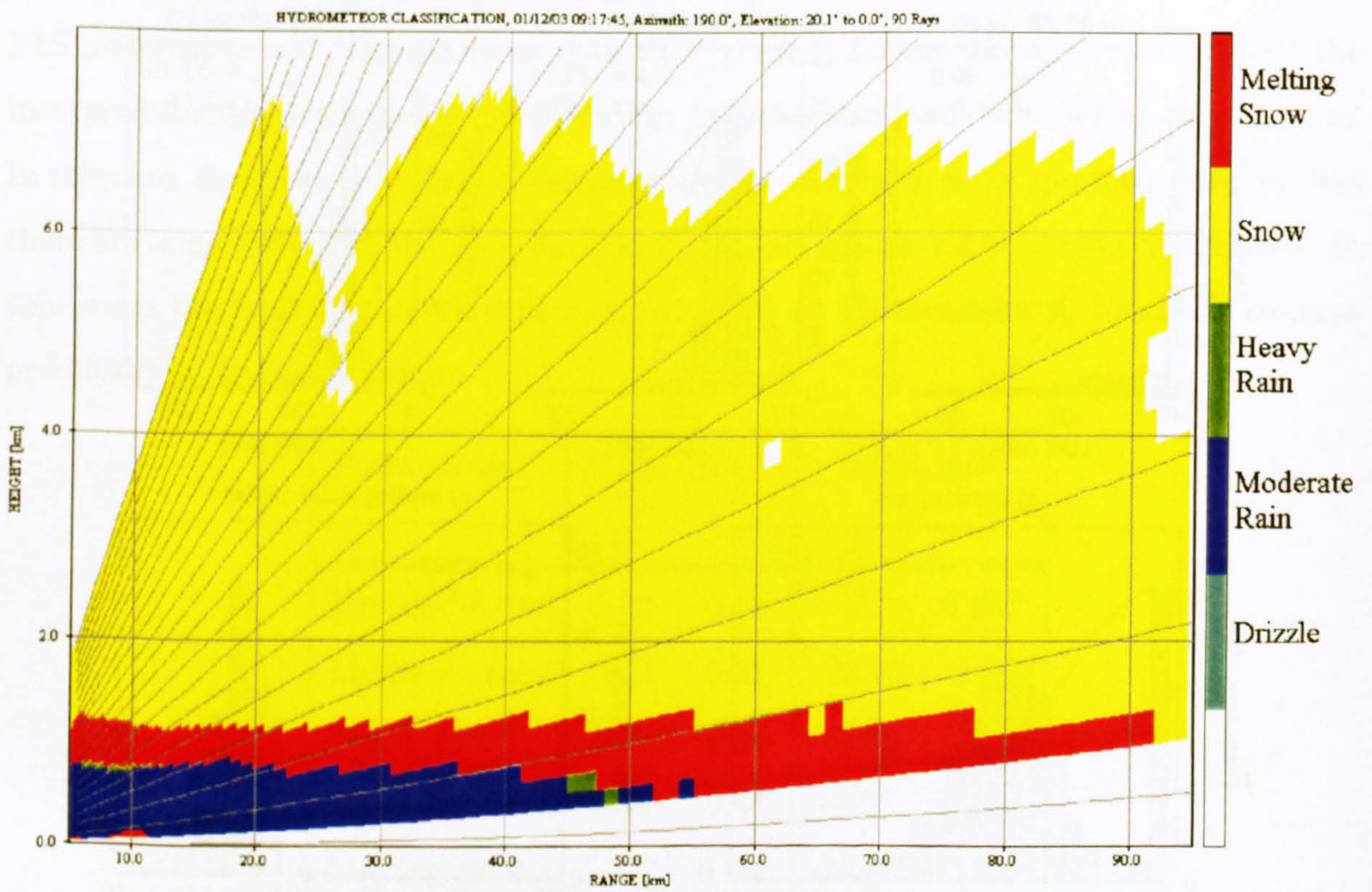

Fig. 8.23: Hydrometeor classification using 1D membership functions. The melting level has been obtained from a previous classification.

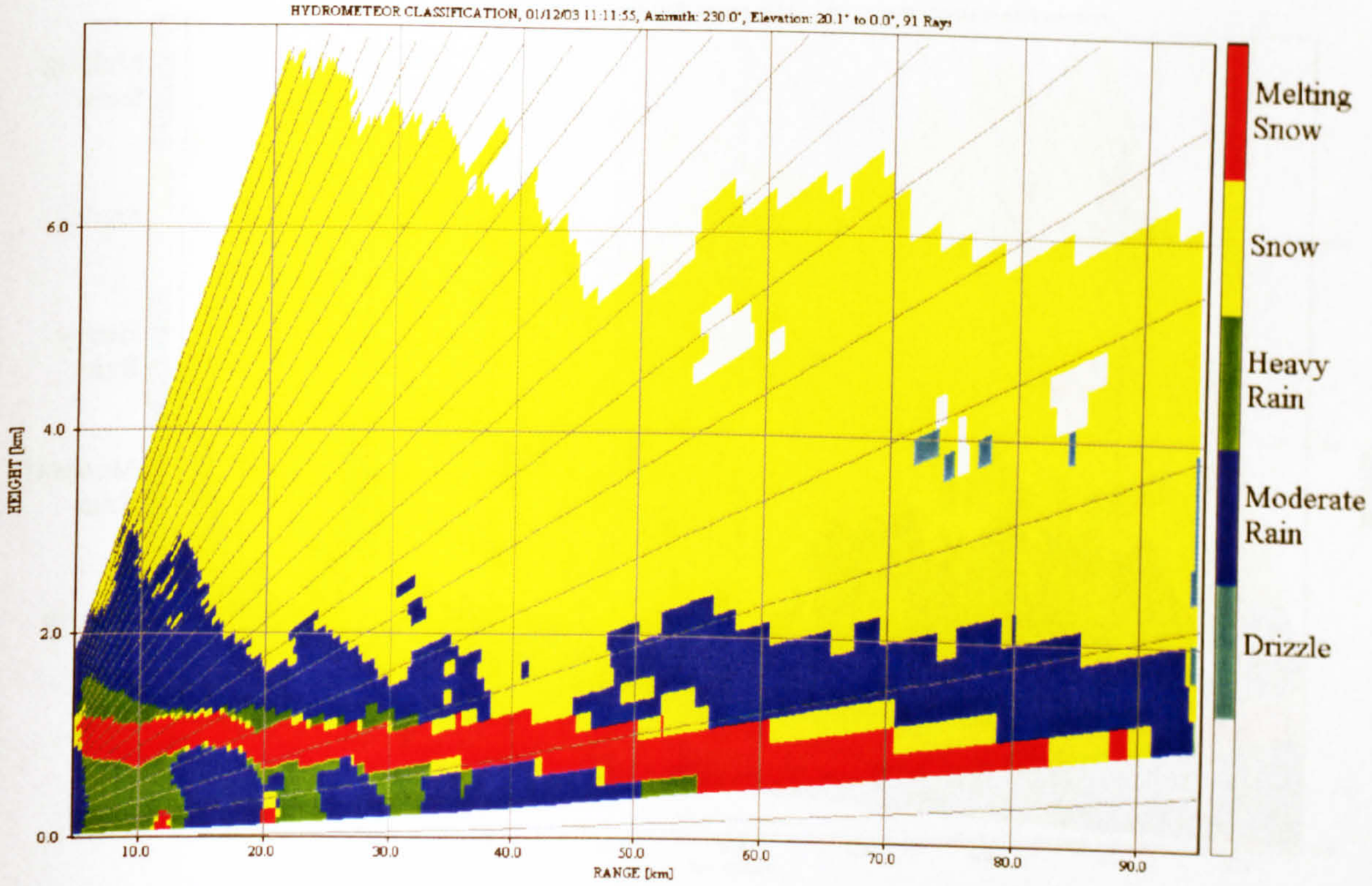

Fig. 8.24: Hydrometeor classification using 1D membership functions.

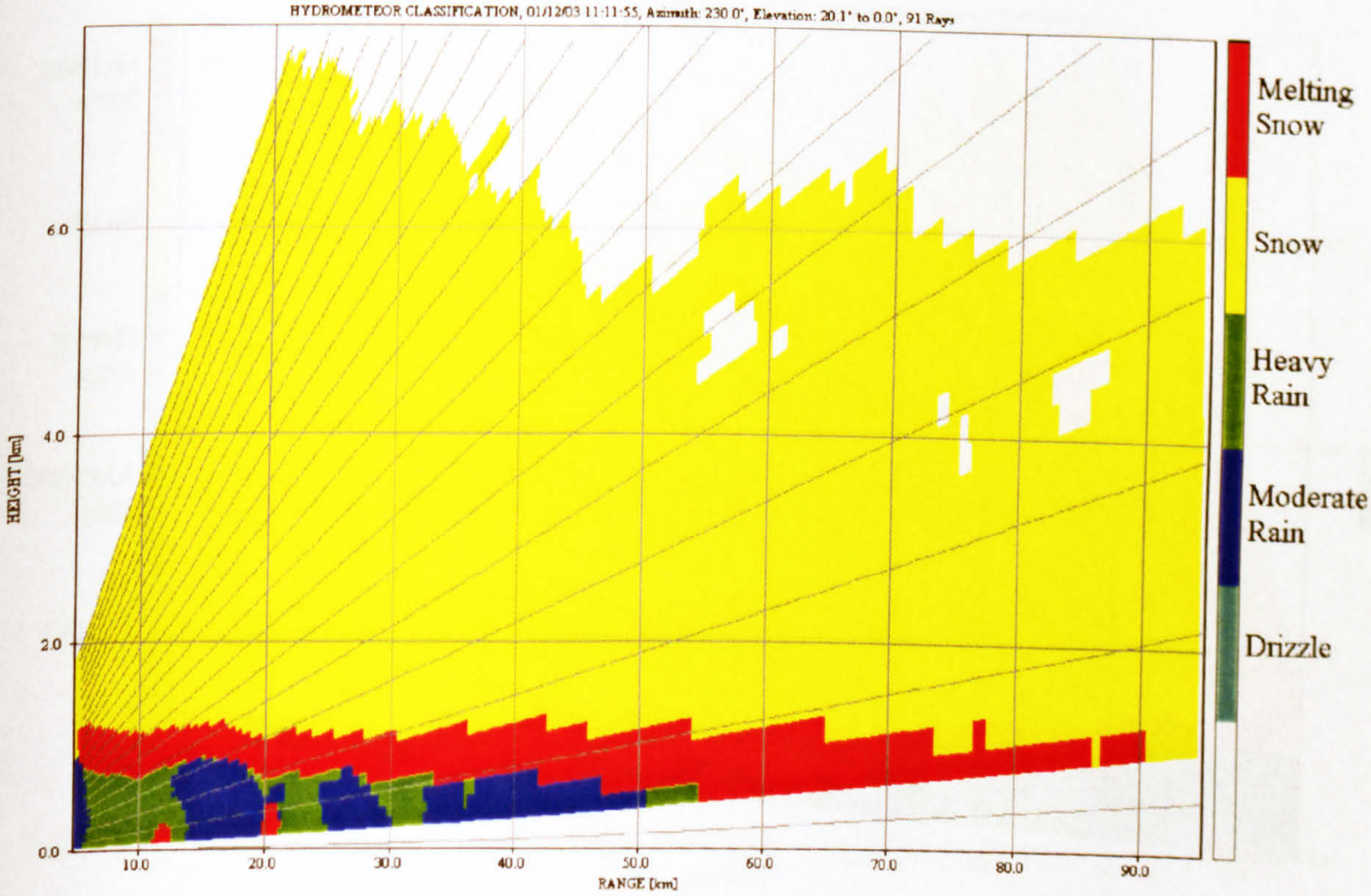

Fig. 8.25: Hydrometeor classification using 1D membership functions. The melting level has been obtained from a previous classification.

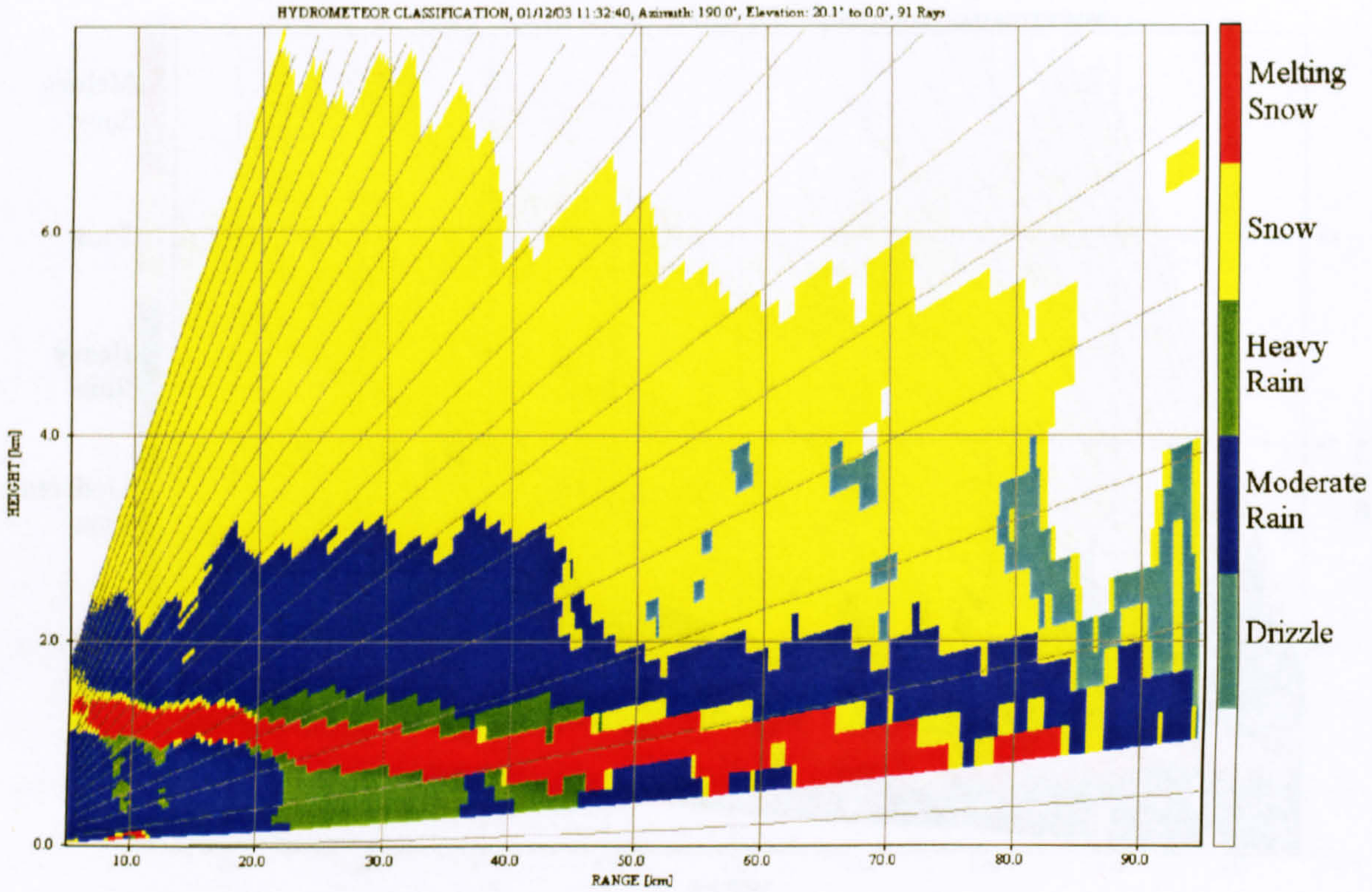

Fig. 8.26: Hydrometeor classification using 1D membership functions.

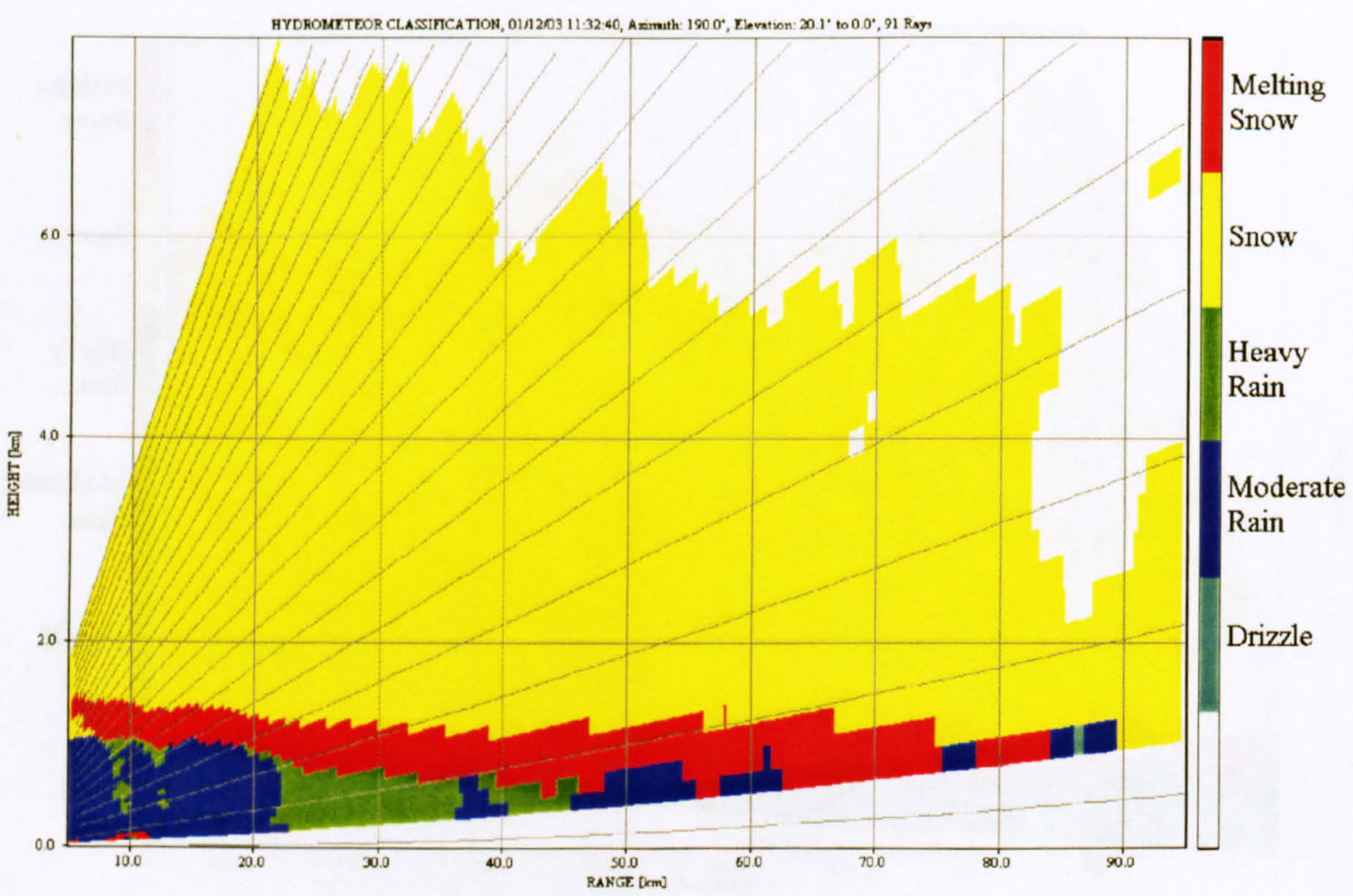

Fig. 8.27: Hydrometeor classification using 1D membership functions. The melting level has been obtained from a previous classification.

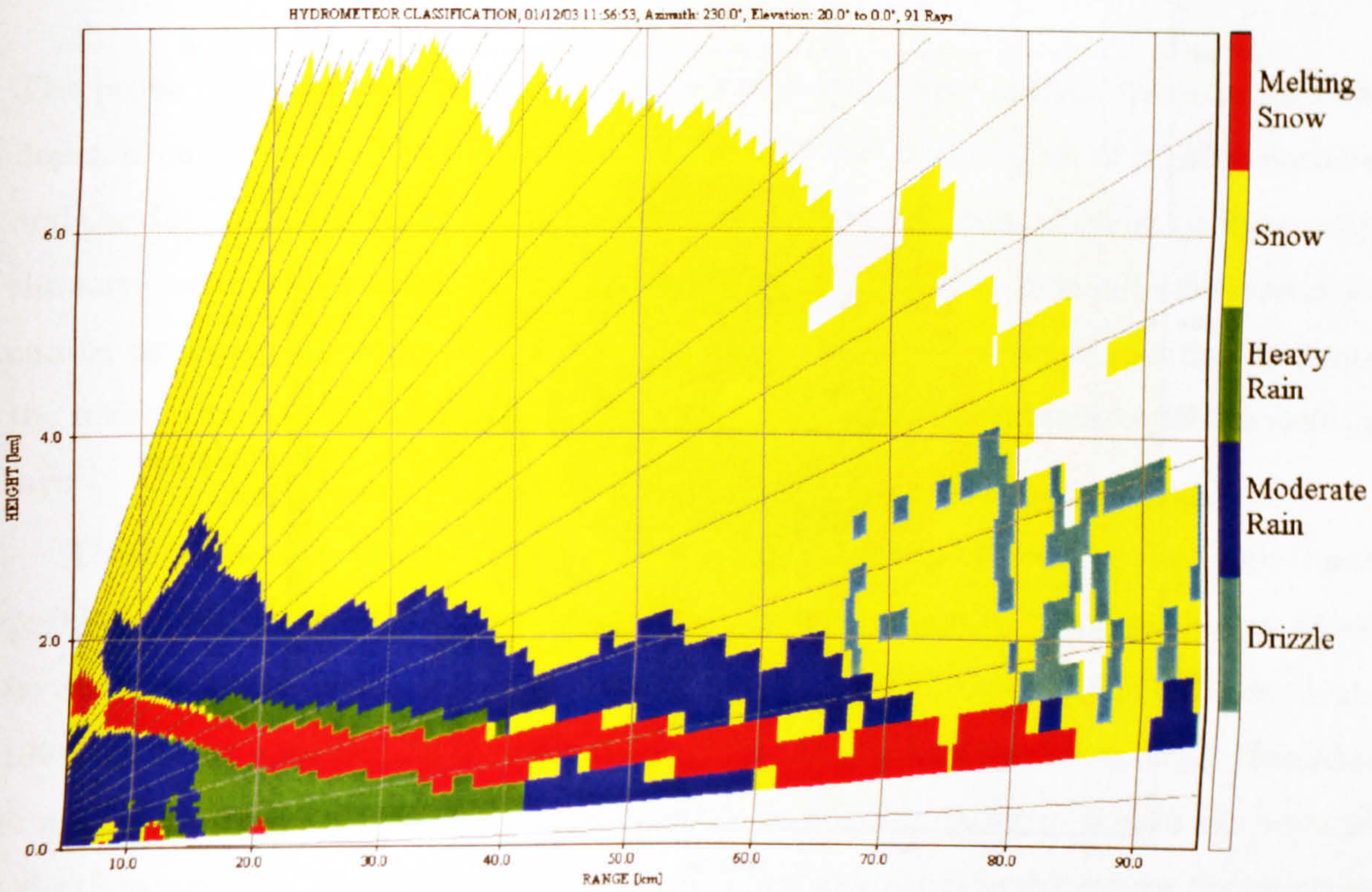

Fig. 8.28: Hydrometeor classification using 1D membership functions.

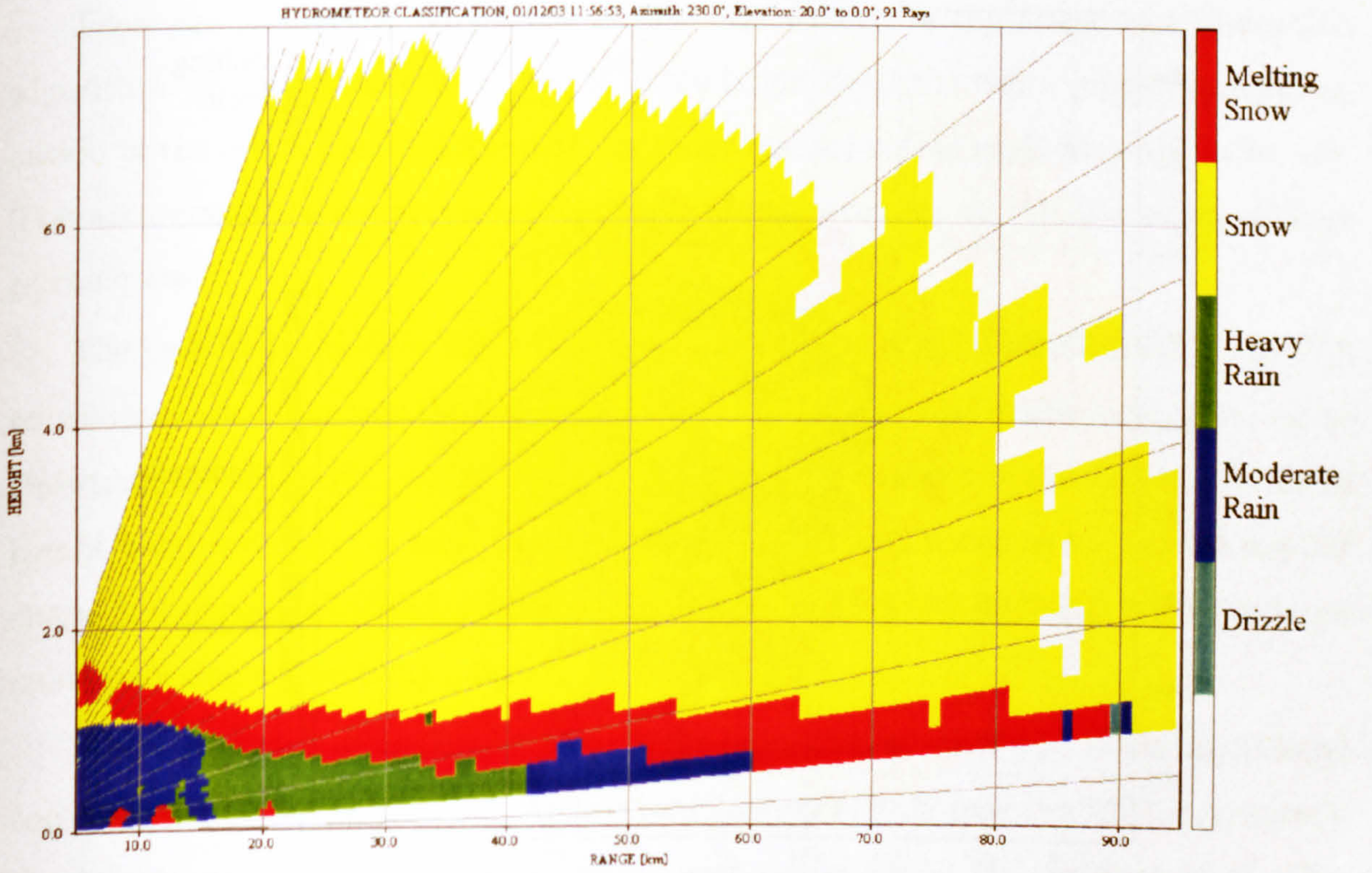

Fig. 8.29: Hydrometeor classification using 1D membership functions. The melting level has been obtained from a previous classification.

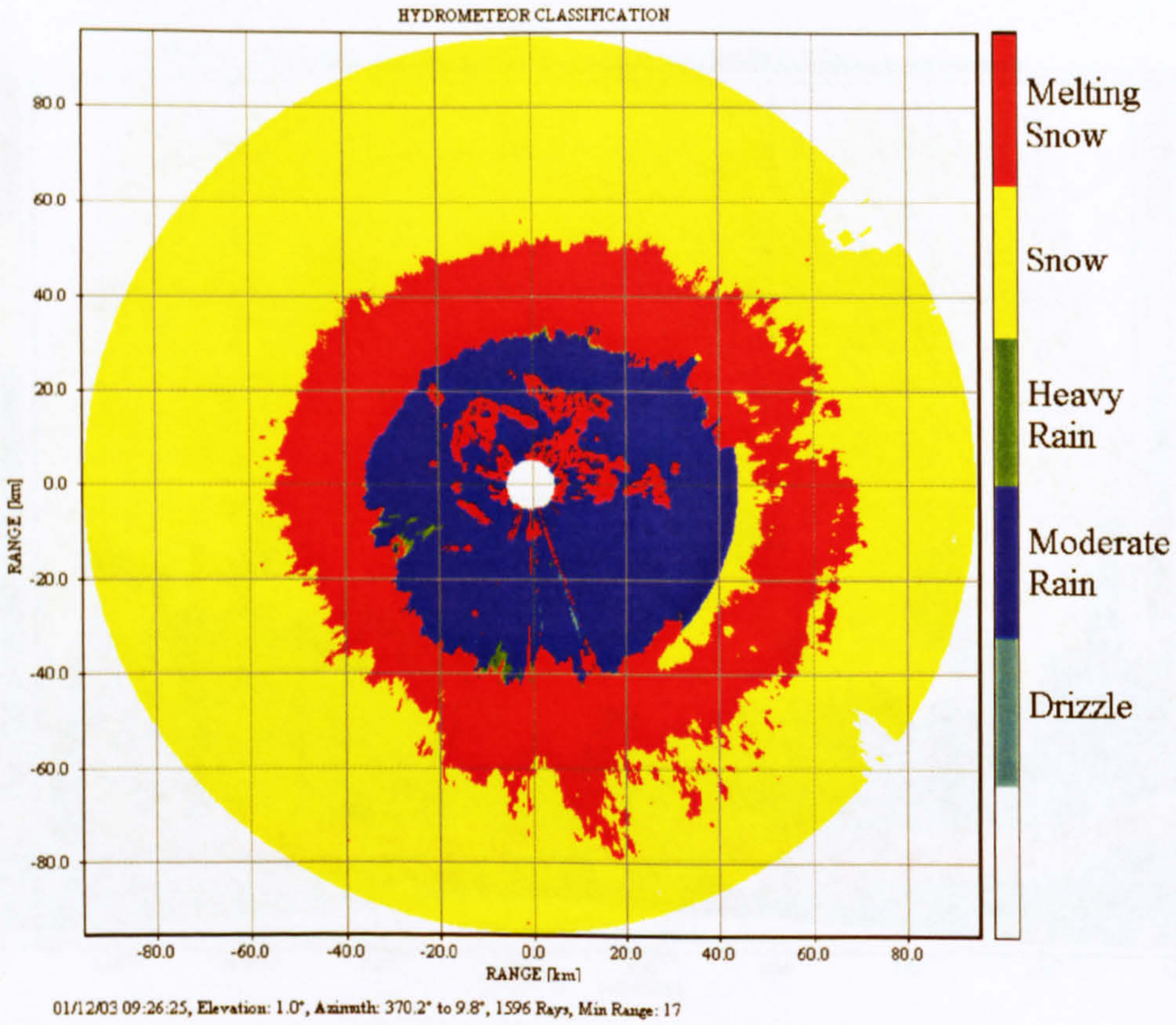

Fig. 8.30: Hydrometeor classification using 1D membership functions. The melting level has been obtained from the whole PPI scan.

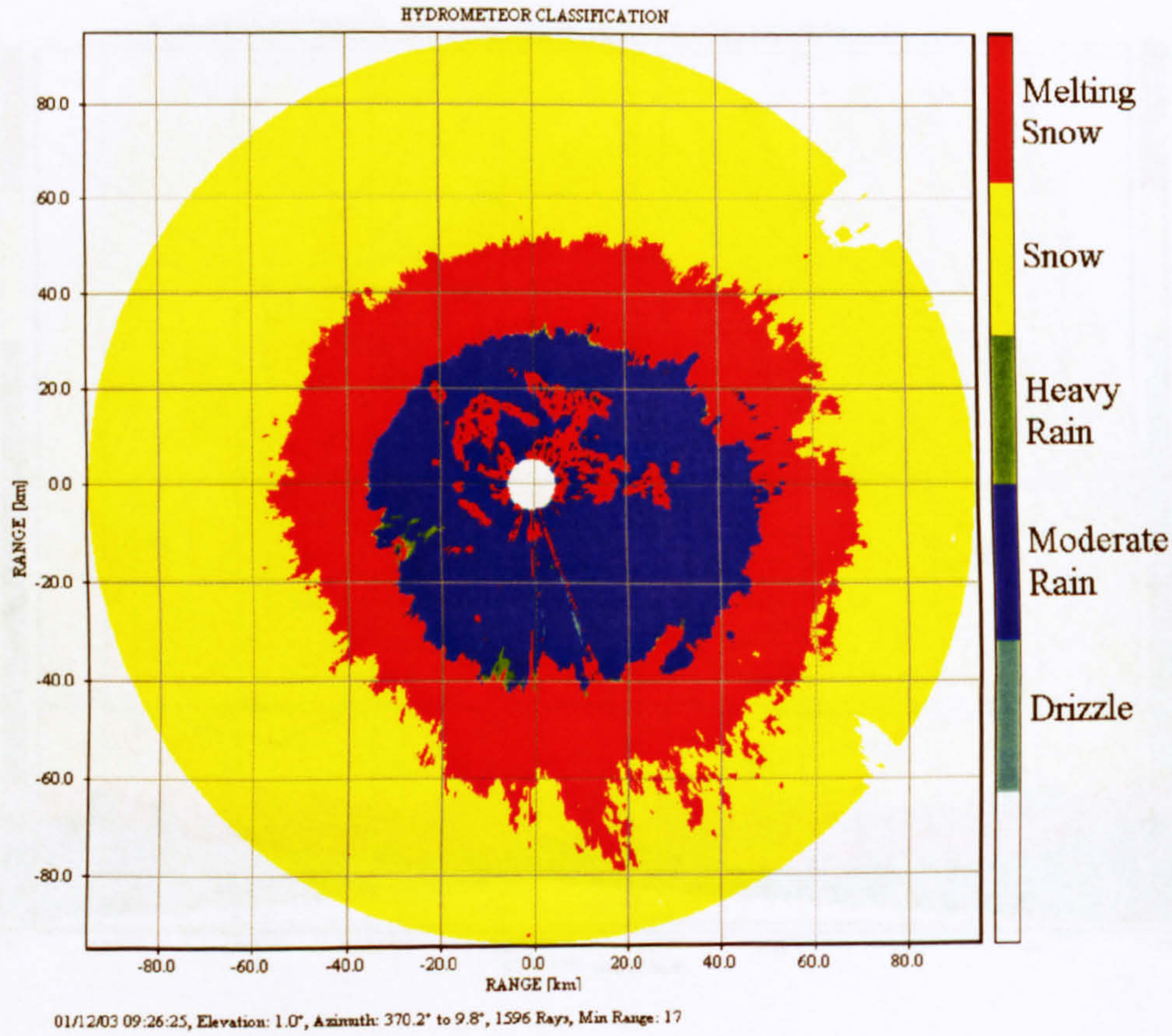

Fig. 8.31: Hydrometeor classification using 1D membership functions. The melting level has been obtained in sectors of 30 °.

8.4 Bright band correction

The problem of the radar beam intercepting the melting layer is that, the echo intensity depends on factors such as the variation of the drop size distribution of melting particles and the distribution of water within the snowflakes. However, even when observing exactly the same melting layer at two different ranges from the radar, two different echo intensities can be obtained. Therefore, it is not straightforward to apply a single equation to relate the reflectivity factor to the rainfall intensity when the radar beam intercepts the melting layer.

There are several algorithms that have been proposed to correct for the bright band problem using single-polarisation radar measurements; some of them are either based on a parameterised vertical reflectivity profile (Smith, 1986; Gray, 1991; Kitchen et al., 1994), or using a melting layer model to generate the profiles (Hardaker, 1993; Hardaker et al., 1995; Gray et al., 2001) or using a vertically pointing radar to obtain the vertical reflectivity profile (Lane, 1997). In this section, a new algorithm to correct for the increase of reflectivity in the melting layer is being proposed. This algorithm uses the output of the fuzzy logic system to identify the melting snow and then a correction is applied in order to obtain an estimate of the expected reflectivity below the bright band.

There are two critical parameters to take into account in any bright band correction algorithm: the estimation of the height of the bright band top and a proper parameterisation of the bright band thickness at any range and azimuthal angle from the radar site. The accuracy of the correction is proportional to the accuracy in the estimation of those parameters.

The proposed correction algorithm for bright band, is based on the output of the FLS to estimate with accuracy the height of the bright band top and bright band thickness as shown on the left of Fig. 8.32. The proposal of using the output of the FLS to detect the bright band is due to the fact that most of the time it does not have the typical annular shape in a single-polarisation channel and it is difficult to detect its height and boundaries using only single reflectivity values.

However, there is an important point in the estimation of the height of the bright band top from the output of the FLS. A close examination reveals that the LDR signature in the bright band typically occurs a few hundred metres below the signature of Z_h. For instance, Ikeda and Brandes (2003) found that the LDR extreme was usually 200 m below the Z_h maximum. Thus, it is necessary to apply a correction to estimate more accurately the height of the bright band top.

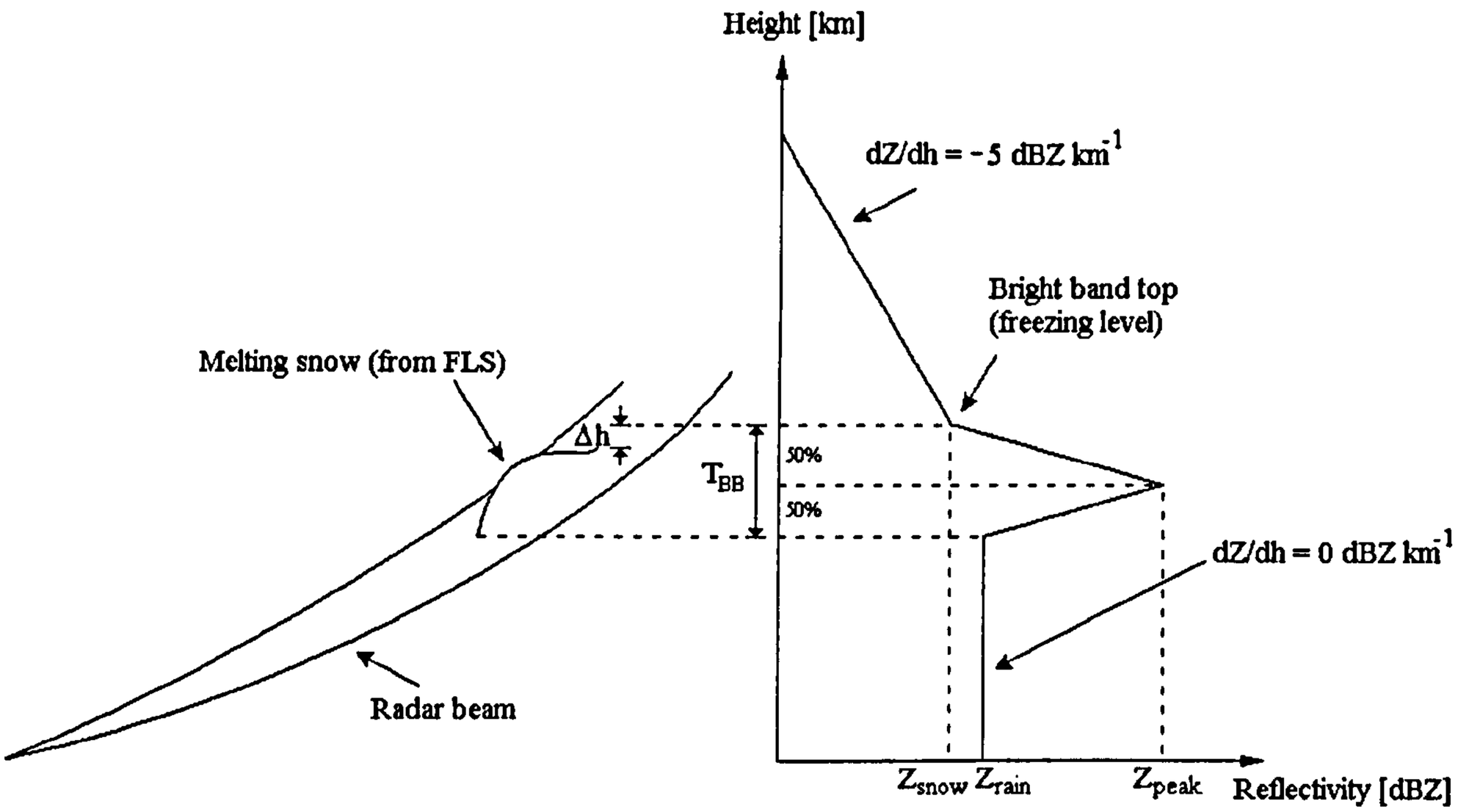

Fig. 8.32: Parameterisation of the vertical reflectivity profile in stratiform precipitation.

The scatter plot between Z_h maximum and the difference in altitudes between LDR and Z_h maxima in the bright band is depicted in Fig. 8.33. So, there is a relationship, which depends on the maximal reflectivity in the bright band in order to obtain an estimate of the shift of the height of the bright band top. This relationship is given by:

$$\Delta h = 58 - 2.40 Z_p + 0.12 Z_p^2; \qquad \text{m} \tag{8.4}$$

where Z_p is the maximal reflectivity obtained in the bright band in dBZ units along the beam and Δh is the shift in metres of the real height of the bright band top.

Knowing the heights of the bright band top and bottom, an idealised vertical reflectivity profile similar as the one proposed by Smith (1986) and Kitchen et al. (1994) is constructed. This new parameterisation is supported with the long-term S-band bright band analysis carried out in Chapter 6. For a given value of rain reflectivity (Z_{rain}), the maximal reflectivity in the bright band (Z_{peak}) is given by Eq. 6.2, whereas the reflectivity above the bright band (Z_{snow}) is given by Eq. 6.3. Below the bright band, the slope of the reflectivity has been set to 0 dBZ km^{-1} (From Fig. 6.10b), whereas above the bright band is approximately 5 dBZ km^{-1} (From Fig. 6.10a). The proposed idealised vertical reflectivity profile in stratiform precipitation is shown in Fig. 8.32.

Depending on the beamwidth of the radar and its elevation angle, at some point the radar beam will be intercepting some part of the melting layer. Following the correction proposed by Brown et al. (1991) and adopted by Kitchen et al. (1994), the reflectivity

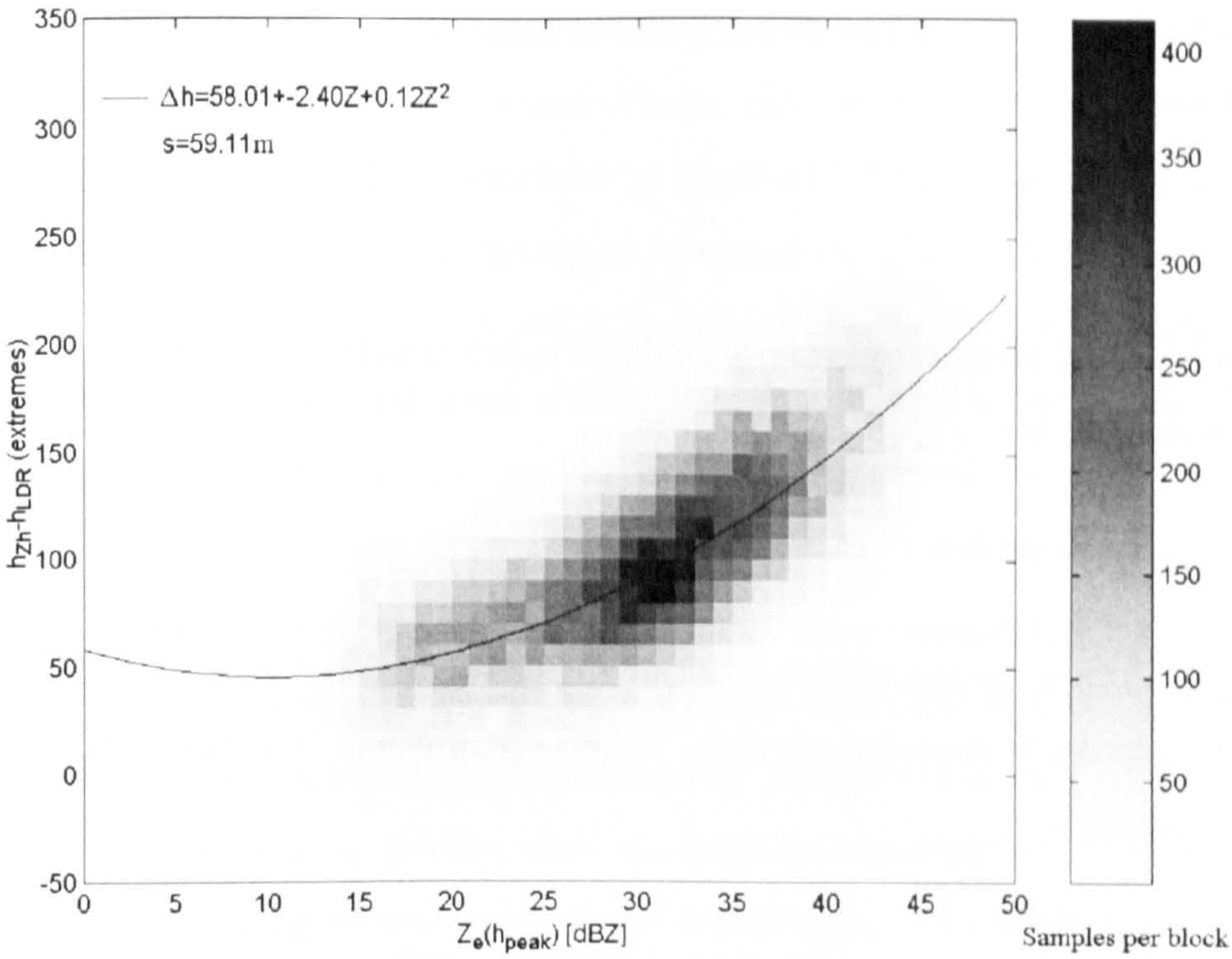

Fig. 8.33: Scatter plot between Z_h maximum and the difference in altitudes between LDR and Z_h maxima in the bright band.

observed by the radar is the result of weighting the beam power profile with the "real" vertical reflectivity profile and it is equivalent to:

$$Z_{ave} = \int_{\alpha}^{\beta} Z(\theta) f(\theta) d\theta \tag{8.5}$$

where α and β are the lower and upper elevation angles corresponding to the -3 dB (half power) of the beam power profile, Z_{ave} is the averaged reflectivity observed by the radar, $Z(\theta)$ is the "real" vertical reflectivity profile and $f(\theta)d\theta$ is a fraction of the beam power at the angle θ. This fraction is given by:

$$f(\theta)d\theta = \frac{P(\theta)d\theta}{\int_{\alpha}^{\beta} P(\theta)d\theta} \tag{8.6}$$

where $P(\theta)$ is the beam power profile, which is obtained according with the characteristics of the radar antenna.

From the output of the FLS along any particular beam at any elevation and azimuthal angles can be obtained an estimate of the height of the bright band top and bright band thickness, following the correction proposed in Eq. 8.4. Thus, an idealised vertical reflectivity profile ($Z(\theta)$) is constructed assuming an estimate of rain reflectivity just below the bright band, that is, Z_{rain}. As a first approximation, Z_{rain} can be equal to Z_{ave}, which is the averaged reflectivity observed by the radar. The idealised vertical reflectivity profile

is weighted following Eq. 8.5 resulting in an estimate of the reflectivity $\hat{Z}_{ave}$. The error is then evaluated by:

$$error = \hat{Z}_{ave} - Z_{ave} \tag{8.7}$$

A new idealised vertical reflectivity profile is constructed with a different value of Z_{rain}, which is estimated by:

$$Z_{rain}[n] = Z_{rain}[n-1] - error \tag{8.8}$$

where $Z_{rain}[n]$ is the new estimate of the rain reflectivity and $Z_{rain}[n-1]$ is the previous value. The process is repeated until the error is minimized. The threshold for the error has been fixed to:

$$|error| < 0.0001; \qquad \text{dBZ} \tag{8.9}$$

Usually, Eq. 8.9 converges in less than five iterations. The correction process is applied pixel by pixel to the bright band contaminated reflectivity data. When the correction has been performed, the rain reflectivity can be transformed to an estimate of rainfall rate assuming the conventional M-P Z-R relationship.

8.4.1 Results

The bright band correction algorithm has been applied to several RHI scans from Chilbolton for the precipitation event that took place on 1st December 2003. For this particular precipitation event, one of the major problems has been to compare the results applying the correction with reflectivity measurements from lower elevation beams. This is because the height of the bright band was at a very low altitude (less than 1 km) and sometimes even the lowest elevation beams were contaminated with the bright band.

Some of the results are shown in Figs. 8.34a-c and 8.35a-c. The main characteristics of the correction algorithm proposed in this section is the use of the output of the FLS to identify the bright band boundaries to apply the correction, in comparison with Kitchen et al.'s correction, which uses the output of the mesoscale model to obtain the height of the 0 °C isotherm and assumes a constant depth of 700 m (See Section 2.8.1).

The Root Mean Squared Errors (RMSE) between the estimated rain reflectivity and the actual rain reflectivity from lower elevation beams oscillate between 1 and 3.5 dBZ. The estimated and the actual rain reflectivity profiles seem to have a shift between them. This is specially remarkable on reflectivity maxima and minima even when a correction has

been applied to compensate the differences in range with the elevation angle. The reason for the shift is because of the wind shear effects, that is, the change in wind velocity with height. This effect was first described by Marshall (1953). Raindrops falling from a particular point adopt the horizontal speed of the wind at each different height. This forms a kind of trail in their descent and it is difficult to establish a correction for this effect without knowing the wind shear speed. By using the mean radial velocity of the hydrometeors obtained with Doppler radars, it may be possible to apply a correction. Although this procedure was not implemented, it may help to reduce slightly the RMSE.

In a real operational environment, a weather radar has a beamwidth of 1° rather than 0.25° and questions arises about the performance of this algorithm with fatter beamwidths. Fig. 8.36 presents a comparison between reflectivity profiles obtained with 1° and 0.25° beamwidths. The reflectivity profiles with one-degree beamwidth have been simulated according to Eq. 8.5 using several beams from a RHI scan. The bright band correction algorithm has been applied to both profiles obtaining very similar results. The RMSE between the estimated rain reflectivity at 1° and 0.25° are 0.8 and 1.32 dBZ as shown in Fig. 8.36. This is consistent with the definition of the model, where the effect of the beamwidth is taken into account in order to estimate the rain reflectivity.

From the results obtained in Figs. 8.34, 8.35 and 8.36, there are some points that need to be observed. The bright band correction algorithm depends on the output of the FLS to estimate the thickness of the bright band and the height of the bright band top. All the misclassification errors due to clutter or partial blocking, which are reflected in the linear depolarisation ratio, have to be removed before applying the bright band correction algorithm. Second, the height of the bright band top estimated from the output of the FLS has to be corrected due to differences in height between the signatures of Z_h and LDR. The correction for the height of the bright band top depends on the maximum reflectivity value within bright band contaminated data and it has a standard error of around 50 m (See Fig. 8.33). Third, the parameterisation of the Vertical Reflectivity Profile (VRP) with the bright band feature is based on the analysis of a considerable amount of S-band VRP observations. This parameterisation is a general trend and there are standard errors associated with it (See Chapter 6). The triangular shape has been adopted from the parameterisation carried out by Smith (1986) and Kitchen et al. (1994) although with different values. Fourth, the proposal for bright band correction assumes that the triangular shape of the bright band has the same depth along one particular beam, which is not always the case. Usually along the 30 or 40 km that the radar beam passes through the bright band there are growths and decays of precipitation, which will

produce thicker and thinner bright band depths respectively. In summary, the total error associated with the estimated rain reflectivity assuming all the aforementioned sources of errors are from 1 to 3.5 dBZ compared to errors of 7-8 dBZ for the reflectivity contaminated by the melting layer.

8.5 Conclusions

The FLS developed in this chapter to classify hydrometeors presents several differences compared to existing classification systems. First, a method to obtain the MF for the different types of hydrometeors has been proposed. This method avoids the need of having in-situ observations of different types of hydrometeors, which are always difficult to obtain. From this analysis, the classification of rain, snow and melting snow has been defined in two-dimensional spaces, that is, $Z_h - Z_{dr}$ and $Z_h -$LDR. These spaces are slightly different from previous hydrometeor classification algorithms. For instance, the classification of wet snow in the space $Z_h - Z_{dr}$ from Vivekanandan et al. (1999) and Straka et al. (2000) present smaller values in Z_{dr} than the values observed in Fig. 8.2. The reason is because the Chilbolton radar data present less smoothing than radar data at 1 ° beamwidth.

The FLS with the 2D MF has been applied to several scans from Chilbolton during the precipitation event that took place in December 2003. The classification procedure presents a lot of uncertainty to classify either rain or snow because of the large overlapping regions between both type of hydrometeors. Knowing the height of the melting level is an important parameter in any hydrometeor classification algorithm. However, this parameter is not available in real-time and for every scan of the radar. The fuzzy logic algorithm proposed in this chapter carries out a primary classification to identify mainly melting snowflakes because their depolarisation characteristics are very remarkable. Knowing the mean height of melting snowflakes, it is possible to modify the MF for the height of the different type of hydrometeors in a more constrained way. A second classification is then performed with these new MF providing much improved classification.

An alternative FLS with one-dimensional MF has been proposed as an easy way to carry out the classification. This system has proved to have a similar performance to the one using the 2D MF. There is no doubt that 2D MF will provide a better classification when incorporating more types of hydrometeors, but 1D MF are sufficient to classify rain, snow and melting snow.

The linear depolarisation ratio is without a doubt a very important parameter in the classification of melting snow. However, an important issue of using LDR is that

this polarimetric variable is more vulnerable to noise than any other variable for the simple reason that it is 30 or 40 dB smaller than the reflectivity, which in terms of power measurements is 3 or 4 orders of magnitude smaller than the co-polar signal. One way to deal with this is by incorporating the correlation coefficient into the FLS to obtain a much more reliable classification. In addition, Z_h, Z_{dr} and LDR are not immune to propagation effects at frequencies higher than 3 GHz and the measurements are biased by attenuation and differential attenuation due to rain (Zrnić and Ryzhkov, 1999). In this analysis, both effects were neglected because of the 3 GHz frequency, but using data from C-band or X-band radars, they should be taken into account. Bringi and Chandrasekar (2001) described alternative power relations using the differential phase shift (ϕ_{dp}) to correct for these effects.

In the last section a bright band correction algorithm to estimate the rain reflectivity just below the bright band has been proposed. The algorithm estimates the expected reflectivity below the melting layer, assuming a simple bright band model, which has been adapted from Smith (1986) and Kitchen et al. (1994). The RMSE of the estimated rain reflectivity when compared to a lower elevation beam not contaminated with the bright band are between 1 and 3.5 dBZ.

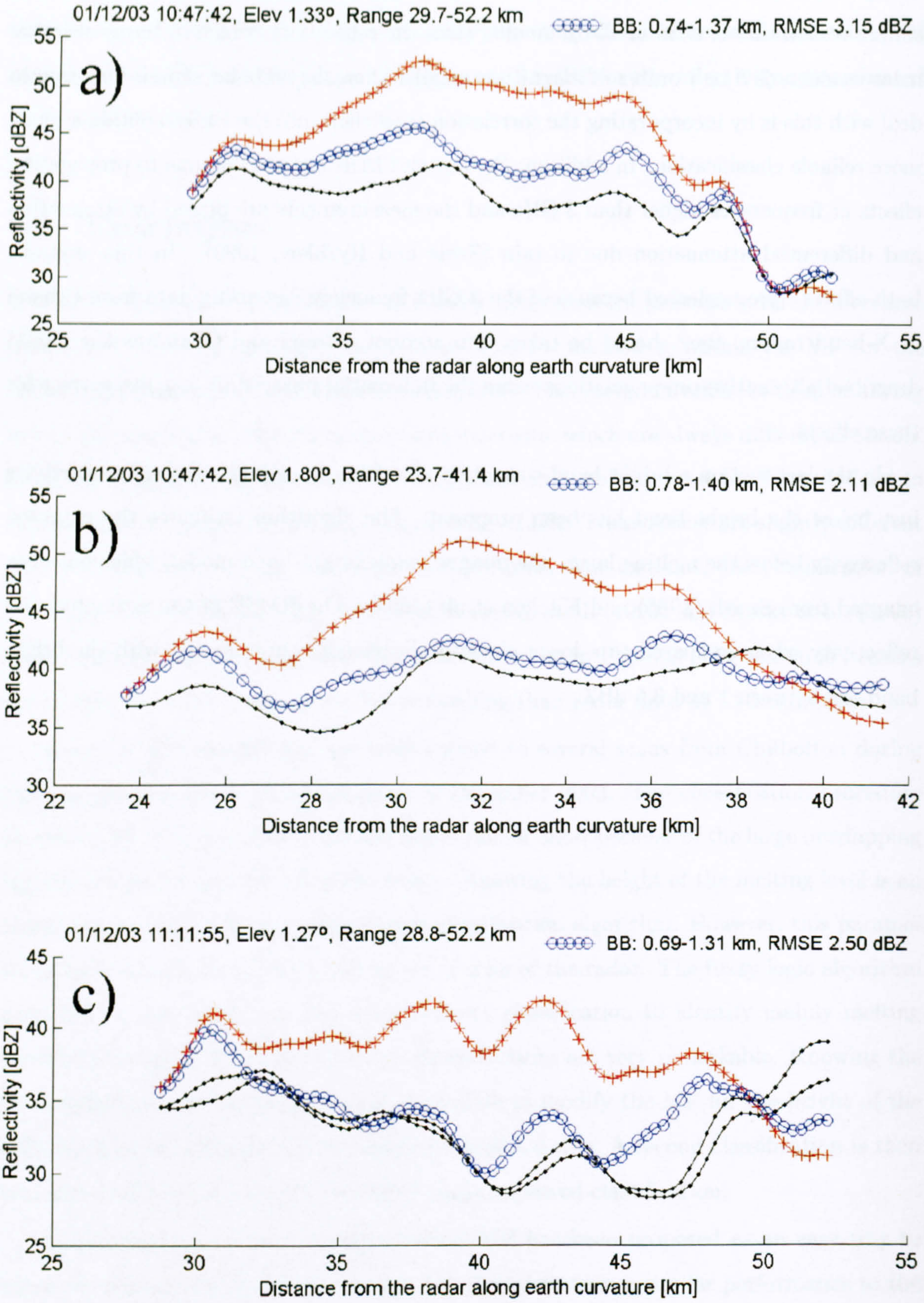

Fig. 8.34: Estimation of the rain reflectivity from bright band contaminated reflectivity data. The plus marks are the bright band reflectivities, the circles are the estimated rain reflectivities following the correction proposed in Section 8.4 and the points are the actual rain reflectivities from a lower elevation beam no contaminated with the bright band.

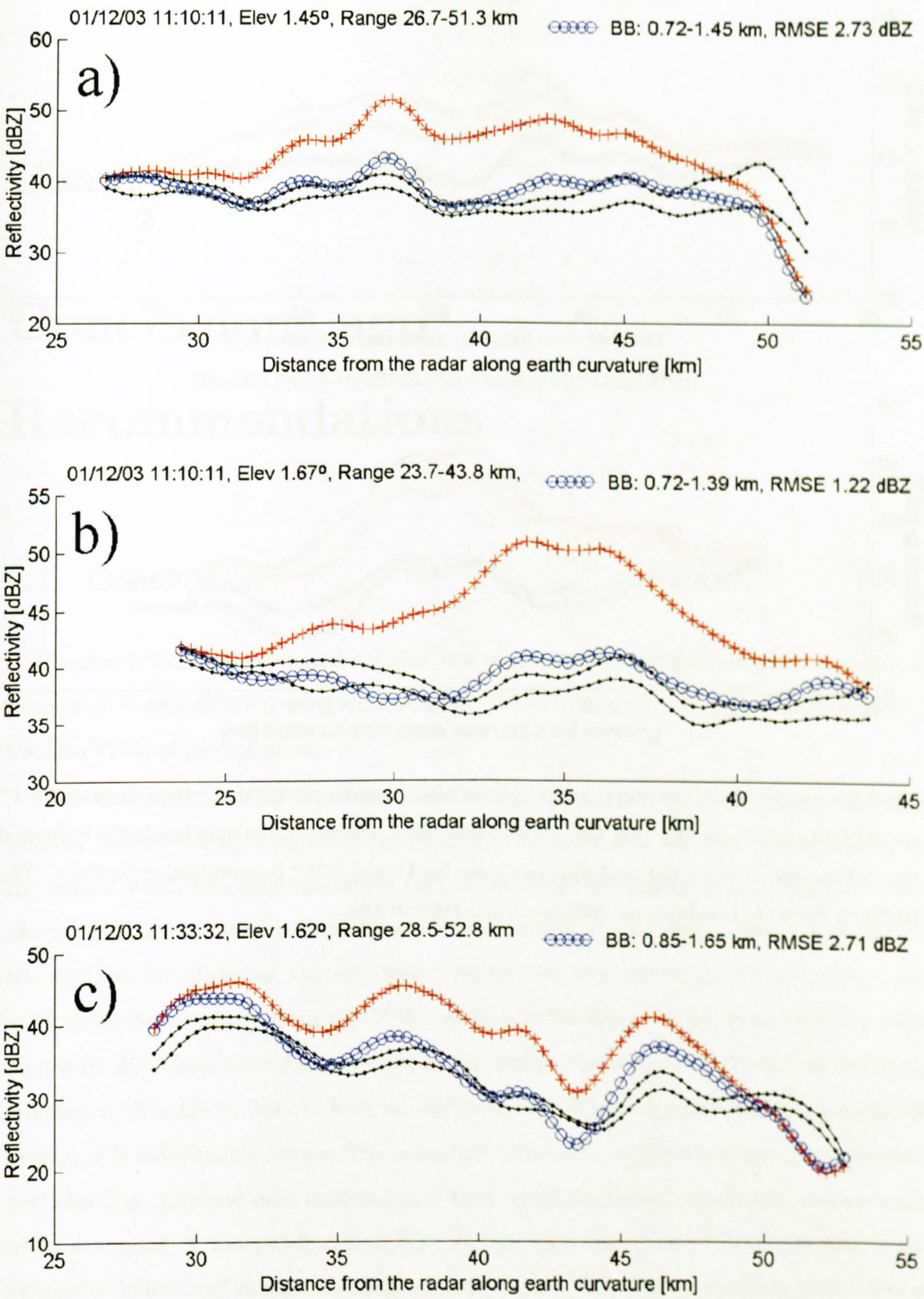

Fig. 8.35: Estimation of the rain reflectivity from bright band contaminated reflectivity data. The plus marks are the bright band reflectivities, the circles are the estimated rain reflectivities following the correction proposed in Section 8.4 and the points are the actual rain reflectivities from a lower elevation beam no contaminated with the bright band.

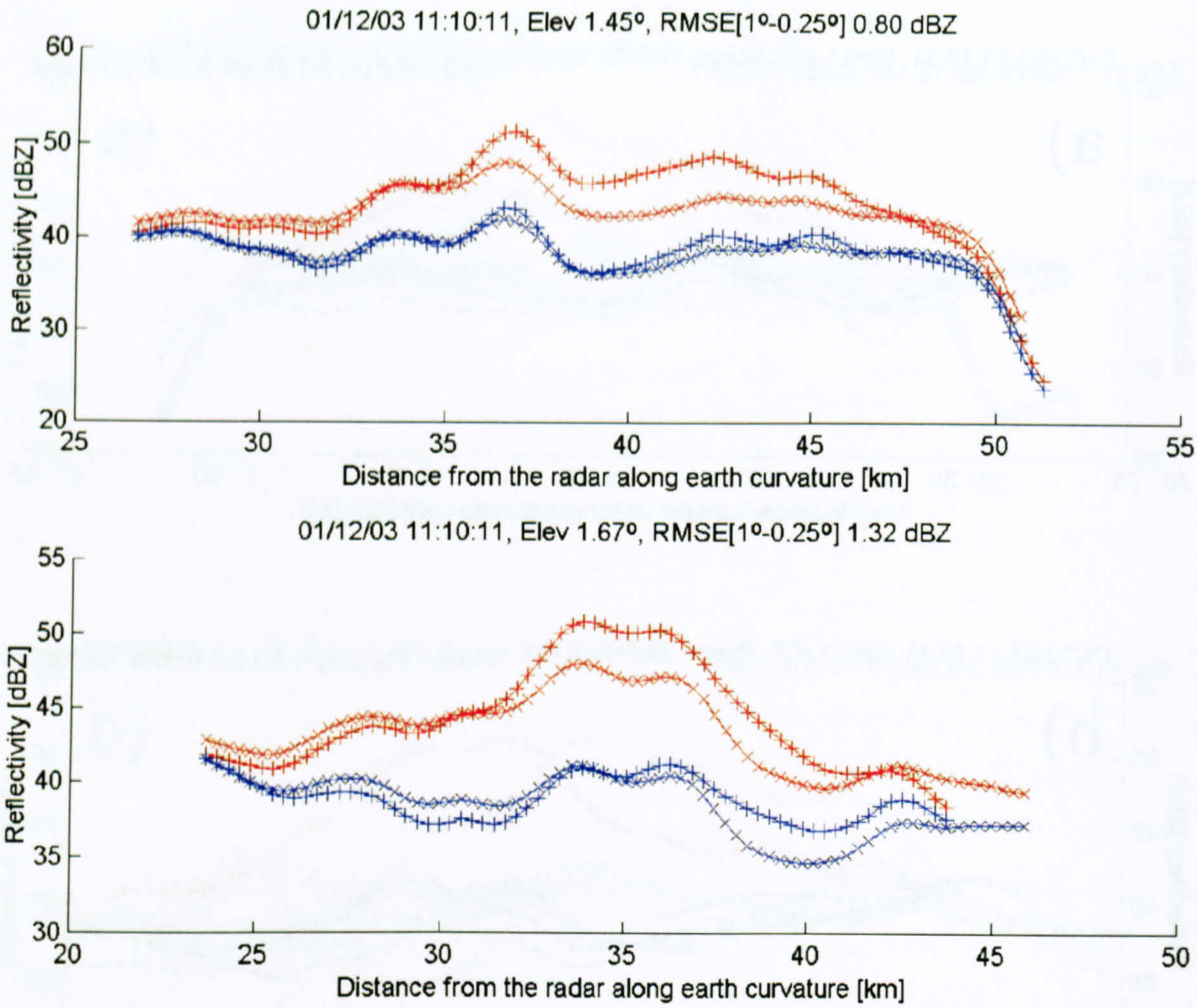

Fig. 8.36: Estimation of the rain reflectivity from bright band contaminated reflectivity data for 1° and 0.25° beamwidths. The red line is the bright band reflectivity, the blue line is the estimated rain reflectivity. The x-mark and plus mark are for 1° and 0.25° beamwidths respectively. The RMSE is calculated between the estimated rain reflectivities.

Chapter 9

Conclusions and Recommendations

9.1 Conclusions

In Chapter 2, it has been pointed out that one of the most important errors sources in the estimation of precipitation using weather radars is the variation of the Vertical Reflectivity Profile (VPR) of precipitation.

The study of the VRP has been possible thanks to the use of Vertically Pointing weather Radars (VPR). Chapter 3 described the hardware and software characteristics of the Bristol VPR. The most important part of the signal processing is the acquisition and averaging of precipitation echoes. New assembler routines have been written to initialize the digitizer board, to set the acquisition parameters and to obtain the average power of N independent arrays from the VPR, using a PCIP-Scope board from Keithley (See Appendix A). These assembler routines can be easily linked to a high level programming language such as C++, Basic or Fortran, directing the full processor power in acquiring and averaging N independent arrays. The intensities of the echo fluctuations from precipitation particles (Fig. 3.5) have been analysed in order to estimate the standard error σ associated when averaging N independent samples. It has been found that the fluctuating echo intensities follow well defined Gaussian distributions (Fig. 3.6) with a zero mean and a standard deviation (standard error) given by $\sigma = 3.9250N^{-0.3883}$ [dBZ] (Fig. 3.7), for a time between successive pulses of 2.5 ms. For instance, 256 independent pulses produce a standard error of approximately 0.45 dBZ. In order to decrease further the error during shorter averaging intervals, the use of real-time digital filters has been proposed. The suggested digital filters are Finite Impulse Response (FIR) filters mainly because the

transfer function of this type of filter is always stable. In addition, FIR filters have a linear phase response over the whole frequency range, which produces a constant lag between unfiltered and filtered reflectivity signals. The echo fluctuations produce high-frequency variations in the reflectivity signal, which can be removed using a low-pass FIR filter (See Fig. 3.9). Two different real-time applications have been developed to acquire VPR data. One of the applications runs under Microsoft Windows (MW) and the other under DOS. The former has been programmed in Visual C++, but it has been found to be dependent on the MW events and not reliable in real-time. The latter has been programmed in C++ under DOS being possible to obtain a temporal resolution of 1 second averaging 256 samples with 2048 data points. The main advantage of this new software with respect to the TRAILER version is the modularity within the source code, facilitating to plug-in new real-time algorithms. Moreover, the processing of the reflectivity signal has been improved with the analysis of the echo fluctuations to produce a more accurate reflectivity signal. In addition, an off-line application running under MW has been developed in order to study the variation of the vertical reflectivity profile of precipitation.

To study the characteristics of the bright band, a new algorithm has been proposed to detect the bright band boundaries from single-polarisation VRP (Chapter 4). The algorithm involves digital filtering and boundary detection through axis rotation. From the spatial frequency analysis of reflectivity, it has been shown that the VRP has an inherent low-frequency signal characteristic. The maximal frequency is approximately $0.1/15$ m^{-1} for either stratiform or stratiform-convective VRP. On the other hand, from the temporal frequency analysis of reflectivity, the maximal frequencies were $0.011/2$ s^{-1} and $0.033/2$ s^{-1} for stratiform and stratiform-convective precipitation respectively (See Table 4.2). These boundaries are important to define the cut-off frequencies of the digital filters to smooth the high-frequency variations of reflectivity, which are due to noise rather than precipitation. For instance, the temporal analysis of reflectivity indicates that the maximal averaging and resampling intervals of the VRP without losing the dynamics of the storm are approximately 90 s and 30 s for stratiform and stratiform-convective precipitation respectively. The bright band boundary detection is performed by rotating the upper and lower part of the bright band (See Figs. 4.13 and 4.14). This algorithm performs better than conventional algorithms based on the variation of the gradient of reflectivity dZ/dh (See Fig. 4.15).

The bright band detection algorithm has been applied to a long-term database of X-band VPR data (Chapter 5). The VPR data were obtained from experiments carried out in the North West and South West of UK, Bristol, UK, the Southern Alps in New Zealand

and Marseille in France. The percentages of data with bright band were 54%, 47%, 64%, 36% and 33% for all the sites respectively (Table. 5.2). The reflectivities above (Z_{snow}), within (Z_{peak}) and below (Z_{rain}) the bright band have been extracted as well as their corresponding heights. There is a seasonal dependency on the height of the bright band in UK (Table 5.4, Figs. 5.18, 5.27 and 5.34), which reveals that not only during Winter the bright band may be a potential error source in the estimation of precipitation using scanning weather radars, but also during Spring and Autumn. From the regression lines relating Z_{peak} and Z_{rain} (Table 5.5, Fig. 5.44), it has been shown that on average the maximal reflectivity in the bright band is $Z_{peak} \approx 10.57 + 0.93 Z_{rain}$. The regression lines between Z_{peak} and Z_{rain} presents similar trends for all the sites, except in the Southern Alps. It has been suggested that orographic enhancement may contribute to the increase in reflectivity in the melting layer because of the influence of the Southern Alps. On average, above the bright band the reflectivities were smaller than the reflectivities below (See Table 5.5). There was an increase in the bright band thickness as the rain reflectivity increased, but there was a lot of scatter about the mean thickness. It is strongly suggested that this scatter is real and due to the variation in the vertical temperature profile, which may increase or decrease the bright band thickness.

The bright band detection algorithm has been also applied to a long-term database of S-band radar data. The regression line between Z_{peak} and Z_{rain} (Fig. 6.6) reveals that the reflectivity enhancement ($\Delta Z = Z_{peak} - Z_{rain}$) is approximately constant and increases slightly with the rain reflectivity. The peak reflectivity is $Z_{peak} = 8.34 + 1.05 Z_{rain}$. Above the bright band, the snow reflectivity is lower than the rain reflectivity below and it is given by $Z_{snow} = 1.05 + 0.85 Z_{rain}$ (Fig. 6.7). The errors due to the variation of the VRP in stratiform precipitation were as follows. In the bright band, at rainfall rates of 0.1 mm hr^{-1} the overestimation factor is approximately 3.5 and increases up to a factor of 5 for rainfall rates of 100 mm hr^{-1} (See Fig. 6.12). These errors depend on the volume of melting layer being illuminated by the radar beam and tend to decrease with range. The rainfall rate estimated from reflectivity measurements obtained above the bright band suffers underestimation and decreases even more at high rainfall intensities (See Fig. 6.13). For instance, at rainfall rates of 10 mm hr^{-1}, the underestimation factor is around 0.5 whereas at low rainfall intensities (< 0.1 mm hr^{-1}) is approximately zero. Above the melting layer, reflectivity measurements tend to decrease with height, decreasing even further the rainfall estimates (See Fig. 6.13). On average, the gradients were approximately 5 dBZ km^{-1} (See Fig. 6.10a), but this estimate is somewhat dependent on the rain intensity (See Fig. 6.11). The combined effect due to attenuation and the use of the Rayleigh

approximation for the calculation of the reflectivity factor at X-band frequencies suggests that the maximal reflectivity in the bright band is underestimated for reflectivities between 28 dBZ and 50 dBZ when compared to bright bands obtained at S-band frequencies. The differences are a function of the rain reflectivity and they are given by $\Delta Z_{S-X} = 1.7226 - 0.4280 Z_{rain} + 0.0130 Z_{rain}^2$ (See Figs. 6.23 and 6.24). The differential reflectivity (Z_{dr}) and the linear depolarisation ratio (LDR) above, within and below the bright band have been also studied. The combined values of Z_h, Z_{dr} and LDR within, below and above the bright band form the basis of a hydrometeor classifier for melting snow, rain and snow respectively (See Figs. 6.28, 6.29 and 6.30 respectively).

The spreading of the radar beam with range has been analysed in Chapter 7. The effect of the spreading is to smooth the VRP of precipitation. It resembles a "low-pass filter", smoothing the high-frequency fluctuations of the VRP. This "filter" has a variable cut-off frequency, which decreases as the range increases from the radar (See Fig. 7.4). For one-degree beamwidths, the filtering effect of the beam radiation pattern will affect the VRP of precipitation from ranges of around 10 km.

A Fuzzy Logic System (FLS) to classify rain, snow and melting snow has been proposed (Chapter 8). The input parameters are Z_h, Z_{dr}, LDR and the height of the measurement (H_0). The Membership Functions (MF) of the FLS for Z_{dr} and LDR are extracted from the two-dimensional (2D) spaces $Z_h - Z_{dr}$ and Z_h – LDR (Figs. 8.2 and 8.3) for a given value of reflectivity Z_h. The MF for Z_h and H_0 have been proposed according to the analysis carried out in Chapter 6 (See Figs. 8.5 and 8.6 for Z_h and H_0 respectively). The classification of hydrometeors using 2D MF is very similar than using 1D MF (Figs. 8.20 and 8.21) mainly because there are only three types of hydrometeors. By incorporating more hydrometeors into the FLS it is prefered to use the 2D MF because the boundaries of every hydrometeor are well defined. The classification procedure presents a lot of uncertainty to classify either rain or snow because of the large overlapping regions between both hydrometeors. Knowing the height of the melting level is an important parameter in any hydrometeor classification algorithm, but unfortunately this parameter is not available in real-time and for every scan of the radar. The FLS performs a primary classification to classify melting snowflakes because their depolarisation characteristics are very remarkable. Knowing the mean height of melting snowflakes, it is possible to modify the MF of H_0 in a more constrained way (See Fig. 8.9). A second classification is then performed with the new MF providing much improved classification. Using the output of the FLS for melting snow it is possible to correct reflectivity measurements using an idealised VRP (Fig. 8.32). The RMSE are between 1 and 3.5 dBZ but the novelty of this technique is that the correction

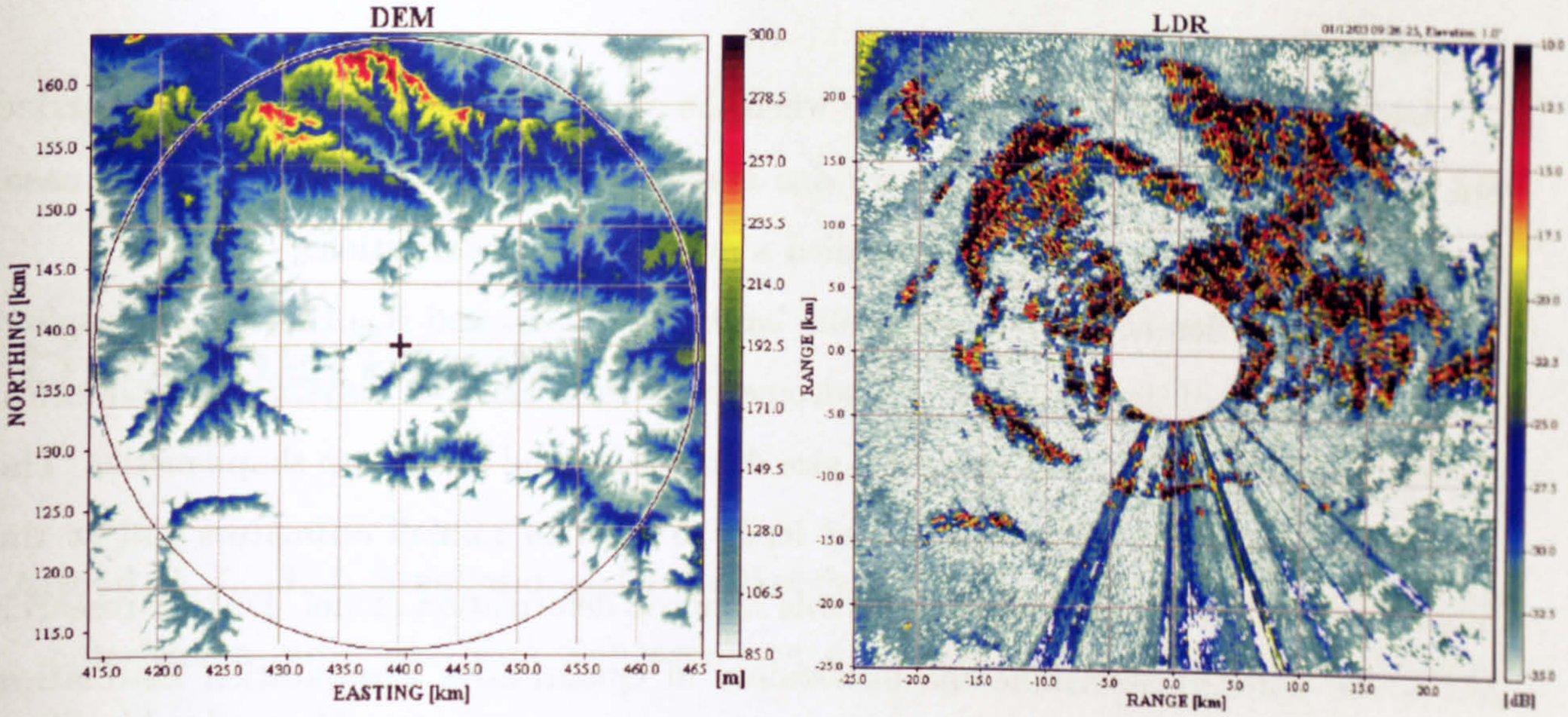

Fig. 9.1: Digital elevation model surrounding Chilbolton radar and linear depolarisation ratio (LDR) on moderate precipitation.

is performed only to reflectivity measurements contaminated with the melting layer as indicated by the output of the FLS. The classification of hydrometeors can be a previous step to improve the estimation of precipitation using weather radars.

9.2 Recommendations for future work

Dual-polarisation over single-polarisation weather radar measurements offer several advantages. Polarimetric radar measurements have the potential to classify hydrometeors (See Chapter 8), which provides the possibility of applying different rainfall estimation algorithms depending on the output of the classification.

The FLS to classify hydrometeors can be extended. For instance, an additional characteristic of the linear depolarisation ratio (LDR) is its sensitivity to ground clutter contamination. This characteristic can be exploited as an alternative to detect partial blocking by mountains. Fig. 9.1 presents the Digital Elevation Model (DEM) with a coverage of 25 km around the Chilbolton radar. The radar is located approximately 85 m above mean sea level and any mountain below this height is represented with a white color. The DEM is being represented according to the UK national grid system (See Ordnance-Survey, 2002). High mountains when compared to the altitude of the radar site are easily identified. On the same figure is shown LDR on moderate precipitation. As expected, there is a high correlation between large depolarisation values and high mountains. By analysing LDR and the rest of the polarimetric variables in regions contaminated with ground clutter and with the support of the DEM, it may be possible to incorporate this knowledge into the proposed FLS to classify regions contaminated with ground clutter and anomalous

propagation.

Additional research has to be done when the classification of hydrometeors is carried out at C-band or X-band frequencies due mainly to propagation effects. In this case, attenuation corrections have to be applied a priori to the classification.

There are different rainfall estimators based on Z_h, Z_{dr} and K_{dp} that can be applied when the output of the classification hydrometeor is rain. However, any rainfall estimation algorithm is obtained assuming a drop size distribution and a raindrop shape model. The latter is an important relationship that leads to different rainfall estimators and at the moment there is no consensus of a suitable raindrop deformation model. Further research has to be done to determine the uncertainty in Quantitative Precipitation Estimation (QPE) when using different raindrop shape models and the propagation of this uncertainty in river flow simulations. The performance of the different rainfall estimators based on Z_h, Z_{dr} and K_{dp} or any combination between them has to be investigated, not only when the radar measurements are in rain, but also in snow. In addition, a detail study of the effects of noise has to be realised in the measurements Z_h, Z_{dr} and K_{dp} for QPE.

Another key aspect of future research is the use of low-power high-resolution dual-polarisation X-band and C-band scanning weather radars to estimate precipitation in small catchments or to control urban drainage systems. In both cases the problems of attenuation can be addressed to some extent by the use of differential phase measurements. One of the great advantages of both systems is that the problems due to the variation of the vertical reflectivity profile of precipitation are minimized by scanning at short ranges (*e.g.* < 30 km). In the case of C-band systems, the impact of using small antennas has to be investigated to allow measurements with beamwidths of 2 or 3 degrees.

The EPSRC, in collaboration with the DEFRA/EA Joint R&D programme on Flood and Coastal Defence, UKWIR, NERC and the Scottish Executive, has agreed to fund an interdisciplinary research Consortium (Flood Risk Management Research Consortium - FRMRC) investigating the prediction and management of flood risk. The research portfolio for the Consortium has been formulated to address key issues in flood risk management through a multi-disciplinary research programme. One of the research areas in the FRMRC is "weather radar and remote sensing". This area will investigate the real-time application potential of polarisation diversity weather radar and this will be possible with the installation of the first UK operational C-band dual-polarisation weather radar at a site in Kent during 2005. The recommendations for future work proposed in this Section will be addressed in post-doctoral research work identified and funded by the FRMRC Consortium.

Bibliography

Alford, J. L., J. J. Stagliano, and **J. J. Helvin** (2002) Commercial simultaneous dual polarization radar. In *Sixth Symposium on Integrated Observing Systems*. Orlando, Florida, Amer. Meteor. Soc.

Andrews, H. C. and **B. R. Hunt** (1977) *Digital Image Restoration*. Prentice-Hall, Inc.

Atlas, D. and **C. W. Ulbrich** (1977) Path- and area-integrated rainfall measurement by microwave attenuation in 1-3 cm band. *J. Appl. Meteor.*, 16:1322–1331.

Atlas, D. and **C. W. Ulbrich** (1990) Early foundations of the measurement of rainfall by radar. In D. Atlas, editor, *Radar in Meteorology: Battan Memorial and 40th Anniversary Radar Meteorology Conference*, pages 86–97. American Meteorological Society.

Atlas, D., C. W. Ulbrich, and **R. Meneghini** (1984) The multiparameter remote measurement of rainfall. *Radio Sci.*, 19(1):3–21.

Austin, P. M. and **A. C. Bemis** (1950) A quantitative study of the "bright band" in radar precipitation echoes. *J. Meteor.*, 7:145–151.

Bandera, J., A. D. Papatsoris, P. A. Watson, J. Tan, and **J. W. Goddard** (1998) Method for detecting the extent of the melting layer. *J. Electronics Letters*, 34(22).

Barnett, V. and **T. Lewis** (1994) *Outliers in Statistical Data*. John Wiley & Sons, Ltd.

Barthazy, E., W. Henrich, and **A. Waldvogel** (1998) Size distribution of hydrometeors through the melting layer. *J. Atmos. Res.*, 47-48:193–208.

Battan, L. J. (1973) *Radar observation of the atmosphere*. The University of Chicago Press.

Beard, K. V. and **A. R. Jameson** (1983) Raindrop canting. *J. Atmos. Sci.*, 40:448–454.

Bendat, J. S. and **A. G. Piersol** (2000) *Random Data, Analysis and Measurement Procedures*. John Wiley & Sons, Inc.

Borland (1990) *Turbo C++, Library Reference*. Borland International, Inc.

Brandes, E. A., A. V. Ryzhkov, and **D. S. Zrnić** (2001) An evaluation of radar rainfall estimates from specific differential phase. *J. Atmos. Oceanic Technol.*, 18(3):363–375.

Bringi, V. N. and **V. Chandrasekar** (2001) *Polarimetric Doppler Weather Radar, Principles and applications*. Cambridge University Press.

Bringi, V. N., V. Chandrasekar, P. Meischner, J. Hubbert, and **Y. Golestani** (1991) Polarimetric radar signatures of precipitation at S- and C-bands. *IEE Proceedings*, 138(2):109–119.

Bringi, V. N. and **A. Hendry** (1990) Technology of Polarization Diversity Radars for Meteorology. In D. Atlas, editor, *Radar in Meteorology: Battan Memorial and 40th Anniversary Radar Meteorology Conference*, pages 153–190. American Meteorological Society.

Bringi, V. N., T. D. Keenan, and **V. Chandrasekar** (2001) Correcting C-band radar reflectivity and differential reflectivity data for rain attenuation: A self-consistent method with constraints. *IEEE Trans. Geosci. Remote Sensing*, 39(9):1906–1915.

Brown, R., G. P. Sargent, and **R. M. Blackall** (1991) Range and orographic corrections for use in real-time radar data analysis. In I. D. Cluckie and C. G. Collier, editors, *Hydrological Applications of Weather Radar*, pages 219–228. Ellis Horwood.

Browne, I. C. and **N. P. Robinson** (1952) Cross polarization of the radar melting band. *Nature*, 170:1078–1079.

Burden, R. L. and **J. D. Faires** (2001) *Numerical Analysis*. Wadsworth Group.

Calheiros, R. V. and **I. Zawadzki** (1987) Reflectivity-rain rate relationships for radar hydrology in Brazil. *J. Climate Appl. Meteor.*, 26(1):118–132.

Cluckie, I. D., R. J. Griffith, A. Lane, and **K. A. Tilford** (2000) Radar hydrometeorology using a vertically pointing radar. *J. Hydrology and Earth System Sciences*, 4:565–580.

Cole, H. W. (1992) *Understanding Radar*. Blackwell Scientific Publications.

Collier, C. G. (1996) *Applications of weather radar systems: a guide to uses of radar data in Meteorology and Hydrology*. Praxis Publishers, John Wiley & Sons.

Cotton, W. R. and **R. A. Anthes** (1989) *Storm and Cloud Dynamics*, volume 44 of *International Geophysics Series*. Academic Press, Inc.

Da Silveira, R. B. and **A. R. Holt** (2001) An automatic identification of clutter and anomalous propagation in polarization-diversity weather radar data using neural networks. *IEEE Trans. Geosci. Remote Sens.*, 39(8):1777–1788.

Dennis, A. S. and **W. F. Hitschefeld** (1990) Advances in precipitation physics following the advent of weather radar. In D. Atlas, editor, *Radar in Meteorology: Battan Memorial and 40th Anniversary Radar Meteorology Conference*, pages 98–108. American Meteorological Society.

Divjak, M. (1995) Radar measurement of precipitation: The use of vertical reflectivity profiles. In C. G. Collier, editor, *Cost 75 Weather Radar Systems*, pages 73-84. European Commission.

Doviak, R. J., V. Bringi, A. Ryzhkov, A. Zahrai, and **D. Zrnić** (2000) Considerations for Polarimetric Upgrades to Operational WSR-88D Radars. *J. Atmos. Oceanic Technol.*, 17:257–278.

Doviak, R. J. and **D. S. Zrnić** (1993) *Doppler Radar and Weather Observations*. Academic Press.

Duncan, M. R. (1993) *The universal multifractal nature of radar echo fluctuations*. Ph.D. thesis, McGill University, Montreal, Canada.

Dupasquier, B., H. Andrieu, G. Delrieu, R. J. Griffith, and **I. Cluckie** (2000) Influence of the VRP on high frequency fluctuations between radar and raingauge data. *Phys. Chem. Earth*, 25:1021–1025.

Eastment, J. D. and **A. J. Illingworth** (1995) A hardware implementation of LDR and Doppler measurements. In C. G. Collier, editor, *Cost 75 Weather Radar Systems*, pages 527–538. European Commission.

Ekpenyong, B. E. and **R. C. Srivastava** (1970) Radar characteristics of the melting layer - a theoretical study. In *Preprints 14th Int. Conf. on Radar Meteorology*, pages 161–166. Tucson, Arizona, Amer. Meteor. Soc.

Fabry, F. (1994a) *Observations and uses of high resolution radar data from precipitation*. Ph.D. thesis, McGill University, Montreal, Canada. Available online at http://grappa.meteo.mcgill.ca/publications/ (checked October 2003).

Fabry, F. (1994b) *Trailer 4.0, Real-time Vertically Pointing Radar Data Collection Software.*

Fabry, F., A. Bellon, and **I. Zawadzki** (1994) Long term observations of the melting layer using vertically pointing radars. Technical Report MW-101, Cooperative Centre for Research in Mesometeorology, Université du Québec à Montréal. Available online at http://grappa.meteo.mcgill.ca/publications/ (checked October 2003).

Fabry, F. and **I. Zawadzki** (1995) Long term radar observations of the melting layer of precipitation and their interpretation. *J. Atmos. Sci.*, 52:838–851.

Garnier, B. J. (1958) *The Climate of New Zealand.* Edward Arnold LTD.

Goddard, J. W. F. (1995) The chilbolton radar facility. In *IEE Colloquium on "Radar Meteorology" (Digest No. 1995/034).*

Goddard, J. W. F., J. D. Eastment, and **M. Thurai** (1994) The Chilbolton Advanced Meteorological Radar: a tool for multidisciplinary atmospheric research. *J. IEE Electronics and Communication Eng.*, 6:77–86.

Gorgucca, E., G. Scarchilli, and **V. Chandrasekar** (1994) A robust estimator of rainfall rate using differential reflectivity. *J. Atmos. Oceanic Technol.*, 11(2):586–592.

Gray, W. R. (1991) *The vertical profile of reflectivity and errors in radar estimates of rainfall.* Ph.D. thesis, University of Reading, UK.

Gray, W. R., I. D. Cluckie, and **R. J. Griffith** (2001) Aspects of melting and the radar bright band. *J. Meteorol. Appl.*, 8:371–379.

Gray, W. R., M. J. Uddstrom, and **H. R. Larsen** (2002) Radar surface rainfall estimates using a typical shape function approach to correct for the variations in the vertical profile of reflectivity. *Int. J. Remote Sensing*, 23:2489–2504.

Gunn, K. L. S. and **R. S. Marshall** (1958) The distribution of size of aggregate snowflakes. *J. Meteorol.*, 15:452–466.

Hagen, M., M. Holler, and **P. F. Meischner** (1995) Multiparameter radar characterization of precipitation particles with in situ measurements. In C. G. Collier, editor, *Cost 75 Weather Radar Systems*, pages 519–526. European Commission.

Hagen, M., J. Hubbert, C. Richter, V. N. Bringi, and **P. Meischner** (1994) Melting Layer Observations with Radar and Aircraft. *IEEE Geoscience and Remote Sensing Symposium*, pages 372–374.

Han, D. (1991) *Weather radar information processing and real-time flood forecasting.* Ph.D. thesis, Water Resources Research Group, University of Salford, UK.

Hardaker, P. J. (1993) *A study of the melting layer in single polarisation radar echoes with application to operational weather radar.* Ph.D. thesis, University of Essex, UK.

Hardaker, P. J., A. R. Holt, and **C. G. Collier** (1995) A melting layer model and its use in correcting for the bright band in single polarization radar echoes. *Quart. J. Roy. Meteor. Soc.*, 121:495–525.

Harrison, D. L., S. J. Driscoll, and **M. Kitchen** (2000) Improving precipitation estimates from weather radar using quality control and correction techniques. *Meteorol. Appl.*, 6:135–144.

Herzegh, P. H. and **A. R. Jameson** (1992) Observing precipitation through dual-polarization radar measurements. *Bull. Amer. Meteor. Soc.*, 73:1365–1374.

Hill, F. F., K. A. Browning, and **M. J. Bader** (1981) Radar and raingauge observations of orographic rain over south Wales. *Quart. J. Roy. Meteor. Soc.*, 107:643–670.

Hines, E. L. (1983) *Image processing techniques for the detection of the radar bright band.* Ph.D. thesis, University of Bradford, UK.

Holler, H., V. N. Bringi, J. Hubbert, M. Hagen, and **P. F. Meischner** (1994) Life cycle and precipitation formation in a hybrid-type hailstorm revealed by polarimetric and Doppler radar measurements. *J. Atmos. Sci.*, 51:2500–2522.

Holt, A. R. (1982) The scattering of electromagnetic waves by single hydrometeors. *Radio Sci.*, 17(5):929–945.

Hooper, J. E. N. and **A. A. Kippax** (1950) The bright band - a phenomenon associated with radar echoes from falling rain. *Quart. J. Roy. Meteor. Soc.*, 76:125–132.

Hopper, S. E., A. J. Illingworth, and **I. J. Caylor** (1991) Bright-band errors in rainfall measurement: identification and correction using linearly polarized radar returns. In I. D. Cluckie and C. G. Collier, editors, *Hydrological Applications of Weather Radar*, pages 240–249. Ellis Horwood.

Hulme, M. and **E. Barrow** (1997) *Climates of the British Isles.* Routledge.

Ifeachor, E. C. and **B. W. Jervis** (1999) *Digital signal processing: a practical approach.* Addison Wesley.

Ikeda, K. and **E. A. Brandes** (2003) Freezing level determinations with polarimetric radar: retrieval model and application. In *31st International Conference on Radar Meteorology*. AMS, Seattle, Washington.

Illingworth, A. (2003) Improved precipitation rates and data quality by using polarimetric measurements. In *Advanced Applications of Weather Radar*. Springer.

Illingworth, A. J. and **T. M. Blackman** (2002) The need to represent raindrop size spectra as normalized gamma distributions for the interpretation of polarization radar observations. *J. Appl. Meteor.*, 41(3):286–297.

Jameson, A. R. and **D. B. Johnson** (1990) Cloud microphysics and radar. In D. Atlas, editor, *Radar in Meteorology: Battan Memorial and 40th Anniversary Radar Meteorology Conference*, pages 323–340. American Meteorological Society.

Jameson, A. R., F. K. Li, S. L. Durden, Z. S. Haddad, B. Holt, T. Fogarty, E. Im, and **R. K. Moore** (1997) SIR-C/X-SAR Observations of Rain Storms. *Remote Sens. Environ.*, 59:267–279.

Joss, J. and **A. Waldvogel** (1990) Precipitation measurement and hydrology. In D. Atlas, editor, *Radar in Meteorology: Battan Memorial and 40th Anniversary Radar Meteorology Conference*, pages 577–606. American Meteorological Society.

Keeler, R. J. and **R. E. Passarelli** (1990) Signal processing for atmospheric radars. In D. Atlas, editor, *Radar in Meteorology: Battan Memorial and 40th Anniversary Radar Meteorology Conference*, pages 199–229. American Meteorological Society.

Keithley (1996) *PCIP-SCOPE User's Guide*. Keithley Instruments, Inc.

Kitchen, M., R. Brown, and **A. G. Davies** (1994) Real time correction of weather radar data for the effects of bright band, range and orographic growth in widespread precipitation. *Quart. J. Roy. Meteor. Soc.*, 120:1231–1254.

Klaassen, W. (1988) Radar observations and simulation of the melting layer of precipitation. *J. Atmos. Sci.*, 45:3741–3753.

Lamb, P. J. and **R. A. Peppler** (1987) North Atlantic Oscillation: Concept and Application. *Bull. Amer. Meteor. Soc.*, 68:1218–1225.

Lane, A. (1997) *Real time weather radar correction using a vertically pointing radar*. Ph.D. thesis, Water Resources Research Group, Telford Research Institute, University of Salford, UK.

Lhermitte, R. M. and **D. Atlas** (1963) Doppler fall speed and particle growth in stratiform precipitation. In *Proc. Tenth Weather Radar Conf.*, pages 218–223. Boston, Amer. Meteor. Soc.

Liu, H. and **V. Chandrasekar** (2000) Classification of hydrometeors based on polarimetric radar measurements: development of fuzzy logic and neuro-fuzzy systems, and in situ verification. *J. Atmos. Oceanic Technol.*, 17:140–164.

Marion, P. M. and **A. J. Illingworth** (2003) Comparison of model-derived and radar-observed freezing-level heights: Implications for vertical reflectivity profile-correction schemes. *Quart. J. Roy. Meteor. Soc.*, 129:83–95.

Marshall, J. S. (1953) Precipitation trajectories and patterns. *J. Meteor.*, 10(1):25 29.

Marshall, J. S. and **W. Hitschfeld** (1953) Interpretation of the fluctuating echo from randomly distributed scatterers, pt. i. *Canadian J. Physics*, 31:962–994.

Marshall, J. S., W. Hitschfeld, and **K. L. S. Gunn** (1955) Advances in radar weather. *Advances in Geophysics*, 2:1–56.

Marshall, J. S., R. C. Langille, and **W. McK. Palmer** (1947) Measurement of rainfall by radar. *J. Meteor.*, 4:186–192.

Marshall, J. S. and **W. McK. Palmer** (1948) The distribution of raindrops with size. *J. Meteor.*, 5:165–166.

Martyn, D. (1992) *Climates of the World*. Elsevier.

McGill (1992) *McGill Vertically Pointing Weather Radar, User Manual Version 2.0*. McGill Radar Weather Observatory.

Mendel, J. M. (1995) Fuzzy Logic Systems for Engineering: A Tutorial. *Proc. IEEE*, 83:345–377.

Mie, G. (1908) Beiträge zur optik trüber medien, speziell kolloidaler metallösungen [contribution to the optics of suspended media, specifically colloidal metal suspensions]. *Ann. Phys.*, 25:377–445.

Mitra, S. K. (2001) *Digital Signal Processing A computer-based approach*. McGraw-Hill.

Moore, R. J., D. A. Jones, D. R. Cox, and **V. S. Isham** (2000) Design of the HYREX raingauge network. *J. Hydrology and Earth System Sciences*, 4:523–530.

Ohtake, T. (1969) Observations of the size distributions of hydrometeors through the melting layer. *J. Atmos. Sci.*, 26:545–557.

Ordnance-Survey (1998) *The ellipsoid and the Transverse Mercator projection. Geodetic information paper No 1.* Available online at http://www.geovrml.org/archive/pdf00000.pdf (checked October 2003).

Ordnance-Survey (2002) *A guide to coordinate systems in Great Britain. An introduction to mapping coordinate systems and the use of GPS datasets with Ordnance Survey mapping.* Available online at http://www.gps.gov.uk/guidecontents.asp (checked October 2003).

Proakis, J. G. and **D. G. Manolakis** (1996) *Digital signal processing: principles, algorithms and applications*. Prentice-Hall Int.

Probert-Jones, J. R. (1962) The radar equation in meteorology. *Quart. J. Roy. Meteor. Soc.*, 88:485–495.

Probert-Jones, J. R. (1990) A history of radar meteorology in the United Kingdom. In D. Atlas, editor, *Radar in Meteorology: Battan Memorial and 40th Anniversary Radar Meteorology Conference*, pages 54–60. American Meteorological Society.

Pruppacher, H. R. and **K. V. Beard** (1970) A wind tunnel investigation of the internal circulation and shape of water drops falling at terminal velocity in air. *Quart. J. Roy. Meteor. Soc.*, 96:247–256.

Racal (1988) *X-band Transceiver Manual*. Racal Decca Ltd.

Revell, M. J., J. H. Copeland, H. R. Larsen, and **D. S. Wratt** (2002) Barrier jets around the Southern Alps of New Zealand and their potential to enhance alpine rainfall. *Atmospheric Research*, 61:277–298.

Rice, J. A. (1995) *Mathematical Statistics and Data Analysis*. Duxbury Press.

Rico-Ramirez, M. A. (2000) *Conformación adaptiva de haz para formación y restauración de imágenes digitales*. Master's thesis, Facultad de Ingeniería Mecánica, Eléctrica y Electrónica, Universidad de Guanajuato, México. Available online at http://www.cen.bris.ac.uk/civil/pgra/mrr/Personal/docs/htms/references.htm (checked October 2003).

Rosenfeld, D., D. B. Wolff, and **E. Amitai** (1994) The window probability matching method for rainfall measurements with radar. *J. Appl. Meteor.*, 33(6):682–693.

Ryde, J. W. (1946) The attenuation and radar echoes produced at centimetre wavelengths by various meteorological phenomena. *Meteorological Factors in Radio Wave Propagation*, pages 169–188. Physical Society, London.

Ryzhkov, A. and **S. Giangrande** (2004) Measurements of rain with polarimetric WSR-88D radar. Operational demonstration. In *Sixth International Symposium on Hydrological Applications of Weather Radar. Success Stories in Radar Hydrology*. Melbourne, Australia.

Ryzhkov, A. V. and **D. S. Zrnić** (1996) Assessment of rainfall measurements that uses specific differential phase. *J. Appl. Meteor.*, 35(11):2080–2090.

Sachidananda, M. and **D. S. Zrnić** (1987) Differential propagation phase shift and rainfall rate estimation. *J. Atmos. Oceanic Technol.*, 4(4):588 598.

Seliga, T. A. and **V. N. Bringi** (1976) Potential Use of Radar Differential Reflectivity Measurements at Orthogonal Polarizations for Measuring Precipitation. *J. Appl. Meteor.*, 15:69–76.

Serafin, R. J. and **J. W. Wilson** (2000) Operational Weather Radar in the United States: Progress and Opportunity. *Bull. Amer. Meteor. Soc.*, 81(3):501–518.

Skolnik, M. I. (1980) *Introduction to Radar Systems*. McGraw-Hill International Editions.

Smith, C. J. (1986) The Reduction of Errors Caused by Bright Bands in Quantitative Rainfall Measurements Made Using Radar. *J. Atmos. Oceanic Technol.*, 3:129–141.

Staelin, D. H., A. W. Morgenthaler, and **J. A. Kong** (1994) *Electromagnetic Waves*. Prentice-Hall Inc.

Sterling, R. (1982) *The weather of Britain*. Fakenham Press.

Stewart, R. E., J. D. Marwitz, J. C. Pace, and **R. E. Carbone** (1984) Characteristics through the melting layer of stratiform clouds. *J. Atmos. Sci.*, 41:3227–3237.

Straka, J. M. and **D. S. Zrnić** (1993) An algorithm to deduce hydrometeor types and contents from multi-parameter radar data. In *Preprints*, 26^{th} *Conference on Meteorology*, pages 513–515. Boston, MA, American Meteorological Society.

Straka, J. M., D. S. Zrnić, and **A. V. Ryzhkov** (2000) Bulk hydrometeor classification and quantification using polarimetric radar data: synthesis of relations. *J. Appl. Meteor.*, 39:1341–1372.

Szyrmer, W. and **I. Zawadzki** (1999) Modelling of the melting layer. Part I: Dynamics and Microphysics. *J. Atmos. Sci.*, 56:3573–3592.

Tan, J. and **W. F. Goddard** (1995) The use of dual-polarisation techniques for bright-band detection with ppi-based radars. In *IEE Colloquium on "Radar Meteorology" (Digest No. 1995/034)*.

Testud, J., S. Oury, R. A. Black, P. Amayenc, and **X. Dou** (2001) The concept of "normalized" distribution to describe raindrop spectra: A tool for cloud Physics and cloud remote sensing. *J. Appl. Meteor.*, 40(6):1118 1140.

Tilford, K. A. and **I. D. Cluckie** (1991) Build, commission and field test of vpr. vertically pointing radar project. Technical Report 1-Q4.91, Department of Civil Engineering, Water Resources Research Group, University of Salford.

Tilford, K. A. and **I. D. Cluckie** (1992) Preliminary results from vpr field application. vertically pointing radar project. Technical Report 2-Q2.92, Department of Civil Engineering, Water Resources Research Group, University of Salford.

Tilford, K. A. and **I. D. Cluckie** (1993) Vpr field application results. vertically pointing radar project. Technical Report 5-Q2.93, Department of Civil Engineering, Water Resources Research Group, University of Salford.

Tilford, K. A., I. D. Cluckie, R. J. Griffith, and **A. Lane** (2001) Vertical reflectivity characteristics and bright band correction. In R. J. Griffith, I. D. Cluckie, G. L. Austin, and D. Han, editors, *Radar Hydrology for Real Time Flood Forecasting, Proceedings of an advanced study course*. European Communities.

Tilford, K. A., I. D. Cluckie, and **S. Y. Towers** (1992) Preliminary analysis of vertical reflectivity data and bright band study. vertically pointing radar project. Technical Report 4-Q4.92, Department of Civil Engineering, Water Resources Research Group, University of Salford.

Tilford, K. A., I. D. Cluckie, A. Wild, S. Y. Towers, and **A. Lane** (1995a) Local real-time adjustment techniques. vertically pointing radar project. Technical Report 6-Q3.93, Department of Civil Engineering, Water Resources Research Group, University of Salford.

Tilford, K. A., D. Han, and **I. D. Cluckie** (1995b) Vertically pointing and urban weather radars. In K. A. Tilford, editor, *Hydrological Uses of Weather Radar*, pages 147–165. British Hydrological Society.

Towers, S. Y. (1996) *Vertical reflectivity profiles and the correction of operational radar rainfall data*. Ph.D. thesis, Water Resources Research Group, Telford Research Institute, University of Salford, UK.

Uijlenhoet, R., H. Andrieu, G. L. Austin, E. Baltas, M. Borga, et al. (1999) Hydromet Integrated Radar Experiment (HIRE): experimental setup and first results. In 29^{th} *Int. Conf. on Radar Meteorology*, pages 926–930.

Ulbrich, C. W. (1983) Natural variations in the analytical form of raindrop size distributions. *J. Clim. & Appl. Meteorol.*, 22:1764–1775.

Vivekanandan, J., D. S. Zrnić, S. M. Ellis, R. Oye, A. V. Ryzhkov, and J. Straka (1999) Cloud microphysics retrieval using S-band dual-polarization radar measurements. *Bull. Amer. Meteor. Soc.*, 80:381–388.

Wexler, R. (1955) An evaluation of the physical effects in the melting layer. In *Proc. Fifth Weather Radar Conf.*, pages 329–334. Fort Monmouth, N.J., Amer. Meteor. Soc.

Wexler, R. and D. Atlas (1963) Radar reflectivity and attenuation of rain. *J. Appl. Meteor.*, 2:276–280.

Wheeler, D. and J. Mayes (1997) *Regional Climates of the British Isles*. Routledge.

Willis, P. T. and A. J. Heymsfield (1989) Structure of the melting layer in mesoscale convective system stratiform precipitation. *J. Atmos. Sci.*, 46:2008–2025.

Wilson, J. W. and E. A. Brandes (1979) Radar Measurement of Rainfall - A Summary. *Bull. Amer. Meteor. Soc.*, 60(9):1048–1058.

Wratt, D. S., R. N. Ridley, M. R. Sinclair, H. Larsen, S. M. Thompson, et al. (1996) The New Zealand Southern Alps Experiment. *Bull. Amer. Meteor. Soc.*, 77:683 692.

Zeng, Z., S. E. Yuter, and R. A. Jr. Houze (2001) Microphysics of the rapid development of heavy convective precipitation. *Mon. Wea. Rev.*, 129:1882–1904.

Zhang, W. (1994) Scattering of radiowaves by a melting layer of precipitation in backward and forward directions. *J. IEEE Trans. Antennas Propagat.*, 42:347–356.

Zrnić, D. S. (1995) Weather radar polarimetry-trends toward operation applications. *Bull. Amer. Meteor. Soc.*, 77:1529–1534.

Zrnić, D. S. and **A. Ryzhkov** (1996) Advantages of rain measurements using specific differential phase. *J. Atmos. Oceanic Technol.*, 13(2):454–464.

Zrnić, D. S., A. Ryzhkov, J. Straka, Y. Liu, and **J. Vivekanandan** (2001) Testing a procedure for automatic classification of hydrometeor types. *J. Atmos. Oceanic Technol.*, 18:892–913.

Zrnić, D. S. and **A. V. Ryzhkov** (1999) Polarimetry for weather surveillance radars. *Bull. Amer. Meteor. Soc.*, 80:389–406.

Appendix A

Assembler routines

The following code contains the assembler routines that can be linked to C++, Basic or Fortran languages in order to initialize the digitizer board, to set the acquisition parameters and to obtain the average power of N independent arrays from a weather radar, using a PCIP-Scope board from the Keithley manufacturer[1].

```
.model small
.386
.code

; ROUTINES AVAILABLES IN THIS CODE
PUBLIC _InitDigitizer     ; Digitizer initialization
PUBLIC _UpdateParameters  ; Setting Acquistion Parameters
PUBLIC _GetAveragePower   ; Getting 2^K Averaged Independent Arrays


; DIGITIZER PORTS
MEMORY           EQU 300h
CLOCK_CONTROLLER EQU 301h
TRIGGER_LEVEL    EQU 302h
CHANNEL_A        EQU 303h
CHANNEL_B        EQU 304h
TRIG_TIME        EQU 305h
RESET            EQU 306h
STATUS           EQU 307h


; ROUTINE TO INITIALIZE THE DIGITIZER CARD
; void InitDigitizer()
_InitDigitizer PROC NEAR
      push ax
      push bx
      push cx
```

[1] http://www.keithley.com.

```
        push dx

sID:    mov dx, RESET               ; Write any value to RESET port
        mov al, 0
        out dx, al

        mov cx, 8                   ; Write any 8 values to CLOCK_CONTROLLER port
        mov dx, CLOCK_CONTROLLER
        mov al, 6
lp1:    out dx, al
        dec cx
        jnz lp1

        mov dx, RESET               ; Read RESET port
        in  al, dx

        mov dx, STATUS              ; Read STATUS port
        in  al, dx

        mov cx, 5
lp2:    mov dx, CLOCK_CONTROLLER
        mov al, 6
        out dx, al
        mov dx, STATUS              ; Read STATUS port
        in  al, dx
        and al, 5                   ; Compare until bits LOAD_ADD y DONE are low
        jz  eID
        dec cx
        jnz lp2
        jmp  sID                    ; ERROR! Try again (Possible board failure)

eID:    pop dx
        pop cx
        pop bx
        pop ax

        ret
_InitDigitizer ENDP


; ROUTINE TO SET THE DIGITIZER ACQUISTION PARAMETERS
; void UpdateParameters(short TRIGGER_LEVEL, short CHAN_A_SENSITIVITY,
;                       short CHAN_B_SENSITIVITY, short TRIGGER_TIME)
_UpdateParameters PROC NEAR
        ARG TL:WORD, CHNA:WORD, CHNB:WORD, TT:WORD

        push bp
        mov bp, sp

        push ax
        push dx
```

```
mov dx, TRIGGER_LEVEL   ; Write the value for the TRIGGER_LEVEL port
mov AX, TL              ; Zero level = 127d
out dx, al              ; Trigger should be above this level
out dx, al

mov dx, CHANNEL_A       ; Set sensitivity of Channel A
mov AX, CHNA            ; 21 = 4V
out dx, al
out dx, al

mov dx, CHANNEL_B       ; Set sensitiviry of Channel B.  0 = not used
mov AX, CHNB
out dx, al
out dx, al

mov dx, TRIG_TIME       ; Write the value for the TRIGGER_TIME port
mov AX, TT              ; 88h external trigger
out dx, al              ; 48h trigger on Channel A
out dx, al              ; 08h trigger on Channel B

pop dx
pop ax

pop bp
ret
_UpdateParameters ENDP

; ROUTINE TO AVERAGE 2^K INDEPENDENT ARRAYS
; void GetAveragePower(long* POINTER_ARRAY, short NUMBER_OF_DATA,
;                      short K, short CHANNEL)   AVERAGE=2^K
_GetAveragePower PROC
      ARG plong: WORD, N: WORD, K: WORD, CHANNEL: WORD

      push bp
      mov bp, sp

      mov cx, [N]               ; Clearing array
      mov bx, [plong]
      mov eax, 0
lpAv2:mov [bx], eax
      add bx, 4                 ; every 4 bytes
      dec cx
      jnz lpAv2

      mov dx, 1                 ; Getting AVE = 2^K = dx
      mov ax, [K]
lpAv3:cmp ax, 0
      jz  lpGetD
      shl dx, 1
      dec ax
      jmp  lpAv3
```

```
lpGetD:push dx                  ; Saving AVE

       mov dx, STATUS           ; Write 5 to STATUS port to acq data from Chan A
       mov AX, CHANNEL          ; Write 3 to STATUS port to acq data from Chan B
       out dx, al

       mov dx, STATUS           ; Read STATUS port until bit D1 is low
       in  al, dx
       and al, 0Fh
       cmp al, 02h              ; With trigger would be 0Ah, without 02h.
       jz  lp4
       call _InitDigitizer      ; ERROR! Try to initialize digitizer again!

lp4:   mov dx, CLOCK_CONTROLLER; Write once more to CLOCK_CONTROLLER port
       mov al, 06h
       out dx, al

       mov dx, STATUS
       in al, dx
       and al, 02h
       jnz lp4

       mov dx, CLOCK_CONTROLLER; Write once more to CLOCK_CONTROLLER port
       mov al, 06h
       out dx, al

       mov dx, STATUS
lp5:   in al, dx                ; The digitizer is getting data. Wait.
       and al,05                ; until START bit is low
       jnz lp5

       mov dx, STATUS           ; Addresing the MEMORY of the digitizerdata
       mov al, 5                ; DONE & LOAD_ADD biTS are low
       out dx, al

       mov bx, [plong]          ; pointer where the data are going to be saved
       mov cx, [N]              ; array size
       mov dx, MEMORY           ; READING THE NEW DATA!
lp6:   mov eax, 0
       in al, dx
       add eax, [bx]
       mov [bx], eax            ; Writing the data to other memory locations
       add bx, 4
       dec cx
       jnz lp6

       pop dx
       dec dx
       jnz lpGetD               ; Get next array

       mov bx, [plong]          ; Averaging by bit rotation
```

```
        mov cx, [N]

lpAv7:push cx

        mov dx, [K]
        mov eax, [bx]
lpAv8:cmp dx, 0
        jz  lpAv9
        shr eax, 1
        dec dx
        jmp lpAv8

lpAv9:and eax, 00FFh
        mov [bx], eax
        add bx, 4                   ; increasing pointer

        pop cx
        dec cx
        jnz lpAv7

        pop bp

        ret
_GetAveragePower ENDP
        END
```

Appendix B

Finite Impulse Response Filter Design

B.1 Introduction

Digital filters are divided into two classes: Finite Impulse Response (FIR) filters and Infinite Impulse Response (IIR) filters (See Proakis and Manolakis, 1996; Ifeachor and Jervis, 1999; Mitra, 2001).

The transfer function of a FIR filter is given by:

$$H(z) = \sum_{k=0}^{N} h[k] z^{-k} \tag{B.1}$$

In the time-domain the input-output relation of the FIR filter is given by the convolution sum:

$$y[n] = \sum_{k=0}^{N} h[k] x[n-k] \tag{B.2}$$

where $h[k]$ represents the impulse response sequence of the filter with N number of coefficients, $y[n]$ and $x[n]$ are the output and input sequences, respectively. In other terms, $x[n]$ may represent the unfiltered radar signal and $y[n]$ the filtered radar signal.

The input-output relation of an IIR filter is given by the convolution sum:

$$y[n] = \sum_{k=0}^{N} a_k x[n-k] - \sum_{k=1}^{M} b_k y[n-k] \tag{B.3}$$

where a_k and b_k are the filter coefficients.

There are two important points that should be taken into account in the design of digital filters: the election between an FIR or an IIR filter and the specification of the filter frequency response.

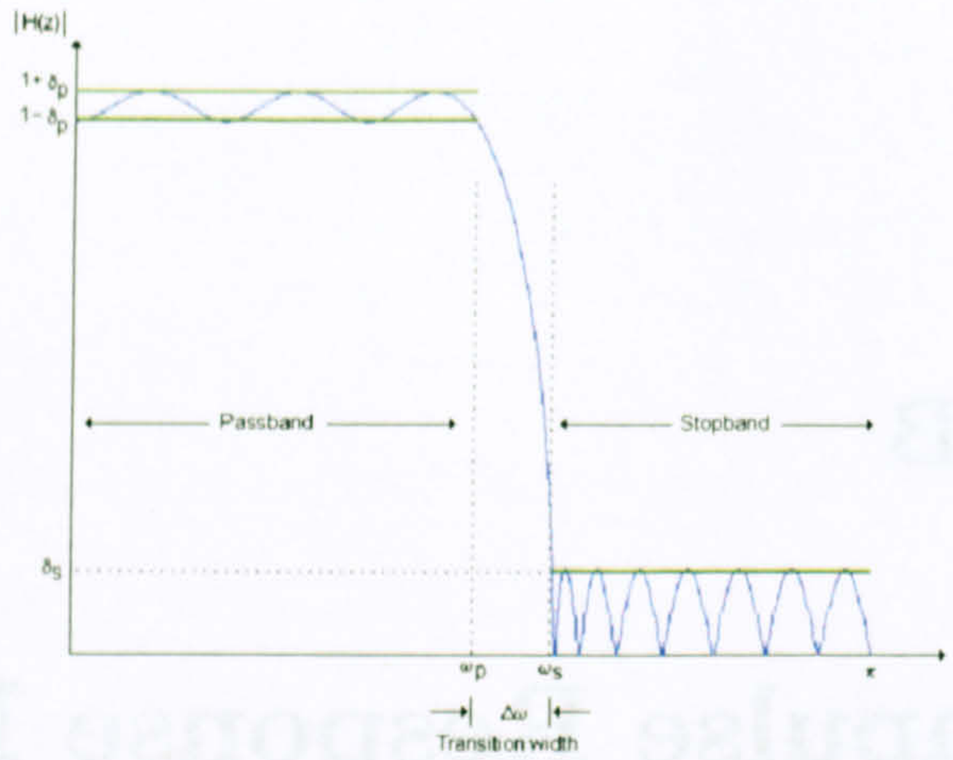

Fig. B.1: Frequency response of a low-pass filter.

The output of a FIR filter is a function only of past and present values of the input (See Eq. B.2) being the filter always stable. Additionally, a FIR filter can be designed to provide a linear phase response over the whole frequency range. On the other hand, the output of an IIR filter is a function of past outputs as well as present and past input samples (See Eq. B.3). Computationally an IIR filter is easier to implement than a FIR filter for similar frequency responses. IIR filters allow sharper cut-off frequencies with fewer coefficients than FIR filters may require, but the former may be unstable because of its dependency of $y[n-k]$. Therefore, a FIR filter is prefered over an IIR filter.

The filter frequency response depends on the requirements of the system where the filter will be employed. The design of FIR filters involves several conditions:

- *Filter specification.* There are low-pass, band-pass, high-pass and band-stop filters. The desired amplitude and phase responses and the cut-off frequency must be specified.

- *Coefficient calculation.* The coefficients of the transfer function $H(z)$ are calculated according to the filter specification. There are several methods to calculate the filter coefficients: the window, optimal and frequency sampling methods.

- *Realization and implementation.* It involves converting the transfer function $H(z)$ into a suitable filter network or structure and producing the software (or hardware) to perform the actual filtering.

B.2 Filter specification

The amplitude response of a FIR filter is specified in the form of a tolerance scheme. The Fig. B.1 shows such a scheme for a low-pass filter. The parameters of interest are the peak

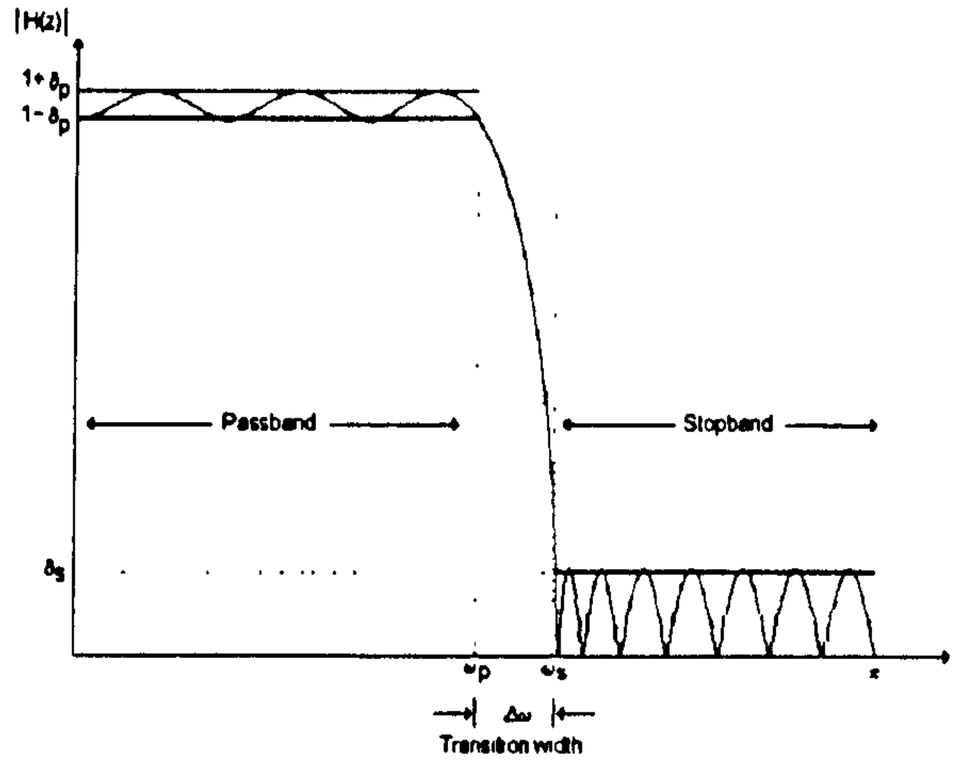

Fig. B.1: Frequency response of a low-pass filter.

The output of a FIR filter is a function only of past and present values of the input (See Eq. B.2) being the filter always stable. Additionally, a FIR filter can be designed to provide a linear phase response over the whole frequency range. On the other hand, the output of an IIR filter is a function of past outputs as well as present and past input samples (See Eq. B.3). Computationally an IIR filter is easier to implement than a FIR filter for similar frequency responses. IIR filters allow sharper cut-off frequencies with fewer coefficients than FIR filters may require, but the former may be unstable because of its dependency of $y[n-k]$. Therefore, a FIR filter is prefered over an IIR filter.

The filter frequency response depends on the requirements of the system where the filter will be employed. The design of FIR filters involves several conditions:

- *Filter specification.* There are low-pass, band-pass, high-pass and band-stop filters. The desired amplitude and phase responses and the cut-off frequency must be specified.

- *Coefficient calculation.* The coefficients of the transfer function $H(z)$ are calculated according to the filter specification. There are several methods to calculate the filter coefficients: the window, optimal and frequency sampling methods.

- *Realization and implementation.* It involves converting the transfer function $H(z)$ into a suitable filter network or structure and producing the software (or hardware) to perform the actual filtering.

B.2 Filter specification

The amplitude response of a FIR filter is specified in the form of a tolerance scheme. The Fig. B.1 shows such a scheme for a low-pass filter. The parameters of interest are the peak

passband deviation (δ_p), the stopband deviation (δ_s), the passband edge frequency (ω_p) and the stopband edge frequency (ω_s). The values of δ_p and δ_s are expressed in decibels. The difference between ω_s and ω_p gives the transition width $\Delta\omega$ of the filter. The cut-off frequency (ω_c) is determined by:

$$\omega_c = \frac{\omega_p + \omega_s}{2} \tag{B.4}$$

Another important parameter is the filter length N, which defines the number of filter coefficients. The question arises: What is the maximum number of coefficients for the digital filter? The answer will depend on the particular application which the filter was designed to operate with, and how small the transition width is, in order to obtain the optimal response of the filter.

It is difficult to specify uniquely what constitutes the best choice for one of the parameters mentioned above, so we may have to deduce in most of the cases by a trial and error process.

B.3 Coefficient calculation. Window method

Once the specifications of the filter have been established, the filter coefficients must be calculated. There are several methods available to obtain $h[k]$. The method used in this study is the window method. The frequency response of a filter, $H_d(e^{j\omega})$, and the corresponding impulse response, $h_D[k]$, are related by the inverse Fourier transform:

$$h_d[k] = \frac{1}{2\pi}\int_{-\pi}^{\pi} H_d(e^{j\omega})e^{j\omega k}d\omega \tag{B.5}$$

The subscript d is utilised to make a distinction between the ideal and the practical impulse responses. Thus, given a frequency response specification $H_d(e^{j\omega})$, it is possible to compute $h_d[k]$ using Eq. B.5 and hence determine the transfer function $H_d(z)$. For an ideal low-pass filter, $H_d(e^{j\omega}) = 1$, with a normalized cut-off frequency w_c, the impulse response of the filter is:

$$\begin{aligned} h_d[k] &= \frac{1}{2\pi}\int_{-\omega_c}^{\omega_c} e^{j\omega k}d\omega \\ &= \frac{\omega_c \sin(k\omega_c)}{\pi k\omega_c}, \quad -\infty \leq k \leq \infty \end{aligned} \tag{B.6}$$

Although the value of $h_d[k]$ decreases as $k \to \pm\infty$, the magnitude is never zero. With an infinite number of coefficients, it is of course impossible to have a FIR filter. One way to

avoid this is truncating the ideal impulse response by setting $h_d[k] = 0$ for k greater than N. However, this introduces undesirable ripples and overshoots in the frequency response of the filter $H_d(\omega)$. This procedure is similar to multiply the ideal impulse response by a rectangular window. A practical approach is to multiply the ideal response, $h_d[k]$, by a suitable window function, $w[k]$, whose duration is finite. In this way, the resulting impulse response decays smoothly towards zero. There are several window functions. The most widely used is the Hamming window because its simplicity. Hamming window is given by:

$$w[k] = 0.54 + 0.46\cos\left(\frac{2\pi k}{2N+1}\right), \qquad -N \leq k \leq N \tag{B.7}$$

The relation between the transition width for a filter designed with the Hamming window and filter length is given by:

$$\Delta\omega = 3.32\pi/N \tag{B.8}$$

where N is the filter length and $\Delta\omega$ the transition width. The maximum stopband attenuation is 53 dB and the minimum peak passband ripple is about 0.0194 dB. The magnitude of the passband and stopband ripples for this type of window is the same ($\delta_p = \delta_s$).

B.4 Realization and implementation

Knowing the functions $h_d[k]$ and $w[k]$, from Equations B.6 and B.7 respectively, the filter coefficients are given by:

$$h[k] = h_d[k]w[k] \tag{B.9}$$

Finally, the input signal $x[n]$ can be filtered using Eq. B.2 and Eq. B.9.

Appendix C

Probability distributions

C.1 Gaussian distribution

The Gaussian distribution is given by:

$$p(x) = \frac{1}{\sigma\sqrt{2\pi}} e^{-(x-\mu)^2/2\sigma^2} \qquad -\infty < x < \infty \tag{C.1}$$

where μ and σ are the mean and standard deviation respectively of the normal density.

C.2 Gamma distribution

The gamma density function depends on two parameters, α and λ, and it is given by:

$$p(x) = \frac{1}{\Gamma(\alpha)} \lambda^{\alpha} x^{\alpha-1} e^{-\lambda x} \qquad x \geq 0 \tag{C.2}$$

The gamma function, $\Gamma(\alpha)$, is defined as:

$$\Gamma(\alpha) = \int_0^{\infty} u^{\alpha-1} e^{-u} du \qquad \alpha > 0 \tag{C.3}$$

The parameter α is called the shape parameter and λ is called the scale parameter.

The estimates of $\hat{\lambda}$ and $\hat{\alpha}$ using the method of moments are given by (See Rice, 1995):

$$\hat{\lambda} = \frac{\mu}{\sigma^2} \tag{C.4}$$

$$\hat{\alpha} = \frac{\mu^2}{\sigma^2} \tag{C.5}$$

where μ and σ are the mean and standard deviation respectively of the data set.

C.3 Rayleigh distribution

The Rayleigh distribution is given by (See Bendat and Piersol, 2000):

$$p(x) = \frac{x}{\sigma_r^2} e^{-x^2/2\sigma_r^2} \qquad x \geq 0 \tag{C.6}$$